

UNCLASSIFIED

AD NUMBER

AD361768

CLASSIFICATION CHANGES

TO: **unclassified**

FROM: **secret**

LIMITATION CHANGES

TO:
Approved for public release, distribution unlimited

FROM:
**Distribution authorized to DoD only;
Specific Authority; 2 Sep 61. Other
requests shall be referred to Chief,
Defense Atomic Support Agency, Attn: STTI,
Washington, DC.**

AUTHORITY

**Defense Threat Reduction Agency ltr., dtd
October 11, 2000.; Same.**

THIS PAGE IS UNCLASSIFIED

SECRET

WT-1383

This document consists of one

No. of 205 copies, etc.

AD 361768

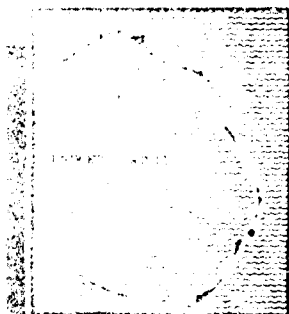
Operation **REDWING**

PACIFIC PROVING GROUNDS

Project 5.7

THERMAL FLUX AND ALBEDO MEASUREMENTS
FROM AIRCRAFT (U)

Issue Date: September 12, 1961



FORMERLY RESTRICTED DATA

Handle as Restricted Data in foreign dissemination. Section 144b, Atomic Energy Act of 1954.

This material contains information affecting the national defense of the United States within the meaning of the espionage laws, Title 18, U.S.C., Secs. 793 and 794, the transmission or revelation of which in any manner to an unauthorized person is prohibited by law.

HEADQUARTERS FIELD COMMAND, DEFENSE ATOMIC SUPPORT AGENCY
SANDIA BASE, ALBUQUERQUE, NEW MEXICO

EXCLUDED FROM AUTOMATIC
RESPONDING: DOD DIR 5206.10
DOES NOT APPLY

NO CONTROL
NO CONTROL

SECRET

Inquiries relative to this report may be made to

Chief, Defense Atomic Support Agency
Washington 25, D. C.

When no longer required, this document may be
destroyed in accordance with applicable security
regulations.

DO NOT RETURN THIS DOCUMENT

SECRET

WT-1333

OPERATION REDWING—PROJECT 5.7

**THERMAL FLUX AND ALBEDO MEASUREMENTS
FROM AIRCRAFT (U)**

R. L. Dresser, Maj, USAF

Project Officer

H. P. Gauvin

G. W. Wares

R. G. Walker

R. E. Ellis

C. A. Doherty

Air Force Cambridge Research Center

L. G. Hanscom Field, Massachusetts

I. L. Kofsky

J. C. Johnson

FORMERLY RESTRICTED DATA

Handle as Restricted Data in foreign dissemination. Section 144b, Atomic Energy Act of 1954.

This material contains information affecting the national defense of the United States within the meaning of the espionage laws, Title 18, U.S.C., Secs. 793 and 794, the transmission or revelation of which in any manner to an unauthorized person is prohibited by law.

**Technical Operations, Incorporated
Burlington, Massachusetts**

3 - 4

SECRET

ABSTRACT

The primary objective was to obtain and evaluate experimental data of the basic thermal phenomena associated with the nuclear and thermonuclear explosions detonated between 5 May and 22 July 1956 at the Pacific Proving Grounds (PPG). The phenomena of interest were those of significance in the prediction of the thermal radiant exposure and irradiance at a point in space as a result of a surface or low-altitude nuclear explosion.

An array of suitable instrumentation was placed in each of four aircraft for data acquisition from medium and high altitudes over the point of detonation. Records of radiant exposure and irradiance were obtained from calorimeters and radiometers aimed directly at the fireball, aimed toward the water underneath the aircraft (albedo study), and aimed away from the fireball (backscatter study). Filters were used with many of these thermal instruments, yielding data covering various parts of the visible and near-infrared spectrum. Spectral data from the detonation was obtained with modified N-9 gun sight aiming point cameras employing an Air Force Cambridge Research Center spectroscopic nosepiece; photographic records were secured by similar cameras aimed at the detonation site or its environment.

Thermal and photographic data for 10 events and spectral data for 11 events were analyzed.

The thermal records reaffirm the reduced transmission of radiant energy in the near infrared because of absorption by water vapor and carbon dioxide.

An equation for predicting the radiant exposure on a horizontal surface and its modification to a surface oriented normal to the fireball (Reference 1) was tested against the collected data and was found to satisfactorily predict the radiant exposure. A simplified equation is also presented and tested against the data. The uniform meteorological conditions accompanying these tests allow the use of the simpler equation.

Comparison between the air drop event (Cherokee) and a barge shot of similar yield (Zuni) indicated no significant differences in the irradiances or radiant exposures measured at the aircraft.

Measurements of the backscattered radiation, where available, were found to be two or three orders of magnitude lower than the radiant energy received directly from the fireball, with the exception of a single instrument reading on a single event on which the B-52 flying in severe cloud conditions measured 50-percent backscatter into the cockpit.

The spectral histories of all events appear quite similar, regardless of the yield; a large amount of NO_2 is formed quite early and persists throughout the entire event.

The photographic records from cameras having various fields of view were taken at 64 frames/sec on 16-mm high-resolution emulsions, from aircraft at slant ranges on the order of several kilometers from surface zero. Each record covers the entire thermal pulse. The cameras were paired utilizing infrared (0.70 to 0.90 micron) and blue (0.35 to 0.45 micron), and linearly polarized (vertical and horizontal, 0.40 to 0.70 micron) filter systems. The primary intensity information was gained from microdensitometer traces of each negative strip; further information came from size measurements on the film and from qualitative observation of the developing phenomena.

Such ancillary features as the Wilson cloud, plume, and bright spots appearing near shock wave breakaway were found to perturb the thermal output by less than 15 percent. The air shock appears to attenuate the blue light; the shocked volume is visible in the infrared because of scattering from the denser air. No polarization phenomena, other than the expected difference in specular scattering from the undisturbed ocean surface, were resolved.

It was found that an attenuating mantle (absorption shell) surrounds the fireball from after breakaway until the end of the thermal pulse. This shell develops to a thickness of about a

fourth of the fireball radius; it is somewhat more strongly attenuating in the blue than in the infrared. Properties of this absorbing shell such as dimensions versus time and effect on limb darkening (decrease in brightness toward the edges of the fireball) are discussed.

Aureole (air-scattered) light is found to be an order of magnitude more intense than the light reflected from the unshocked water surface, for the typical moist atmospheric conditions at the PPG. This aureole is white and unpolarized. The shock-froth albedo is about 12 times the unshocked water albedo. In general, the total red light reflected or scattered into the typical camera fields of view—from aureole, clouds, and water—was about equal to the direct flux from the fireball. Most of this was scattered from the shock-frothed water. The blue albedo was lower, presumably because of the air shock attenuation. Furthermore, the blue fireball showed considerably more limb darkening.

Both air shock and fireball dimensions were found to obey the predicted scaling laws. There is evidence that the fireball surface temperature is not symmetric with azimuth in some cases, as the thermal flux appears higher from certain (large) regions.

Reproductions of several series of photographs containing different views of Shot Dakota (1.1 Mt) are presented, as well as a typical series for each of the other detonations having photographic coverage; the photographs are discussed.

Suggestions for the further analysis of existing data and for improved data acquisition from future tests are presented.

FOREWORD

This report presents the final results of one of the projects participating in the military-effect programs of Operation Redwing. Overall information about this and the other military-effect projects can be obtained from WT-1344, the "Summary Report of the Commander, Task Unit 3." This technical summary includes: (1) tables listing each detonation with its yield, type, environment, meteorological conditions, etc.; (2) maps showing shot locations; (3) discussions of results by programs; (4) summaries of objectives, procedures, results, etc., for all projects; and (5) a listing of project reports for the military-effect programs.

PREFACE

The authors acknowledge the cooperation received from the personnel of Projects 5.1 through 5.6, the Naval Radiological Defense Laboratory, and Edgerton, Germeshausen and Grier, Inc.

Further acknowledgment is given the efforts of D. Thomas, C. Dieter, and W. Burke in obtaining field data; J. Cahill in the final compilation of calorimetric data; S. Locke, E. Lilly, and N. Pass in preparation of photographic data; Dr. R. Brownell in the analysis of photographic data; Dr. R. Meyerott and Lt O. Greenberg in the theoretical analysis of the absorption shell; Dr. R. Meyerott, Dr. S. Schwebel, and Dr. J. Sokoloff, who wrote the theoretical analysis of the absorption shell; Dr. J. Garing in contributing to the early development of the spectral experiment; S. Clough in designing the high-precision microdensitometer spectral film reader, and in the electronic modification of the filter photography microdensitometer; D. Siegel, A. McNally, H. Lockhart, and C. Spooner in spectral data reduction and Lt R. Hunter in spectral data presentation; and Lt J. Reed, J. Cahill, and L. Mercier in editing and preparing the final report.

Previous page was blank, therefore not filmed.

CONTENTS

ABSTRACT	5
FOREWORD	7
PREFACE	7
CHAPTER 1 INTRODUCTION	15
1.1 Objectives	15
1.2 Background and Theory	15
CHAPTER 2 PROCEDURE	18
2.1 Operations	18
2.1.1 Thermal Measurements	18
2.1.2 Photographic Coverage	18
2.2 Planned Shot Participation	18
2.3 Instrumentation	18
2.3.1 Radiometers and Calorimeters	19
2.3.2 Photographic	20
2.3.3 Spectrographic Instrumentation	20
2.3.4 Aircraft	21
2.3.5 Ground Stations	22
2.4 Data Requirements	22
2.5 Radiometer and Calorimeter Calibration and Data Reduction	23
2.5.1 Procedure	23
2.5.2 Filter Characteristics	23
2.6 Photographic Calibration and Data Reduction	24
2.6.1 Development and Sensitometry	24
2.6.2 Microdensitometry	24
2.6.3 Dynamic Range and Camera Flare	25
2.6.4 Analysis of Microdensitometer Records	25
2.7 Spectrographic Data Reduction and Calibration	25
CHAPTER 3 RESULTS	40
3.1 Calorimeter and Radiometer Results	40
3.1.1 Summary of Cumulative Thermal Radiation Data	40
3.1.2 Time History of Thermal Radiation Measurements	41
3.1.3 Backscattered Radiation	42
3.2 Photographic Results	42
3.2.1 Qualitative Picture of a Detonation	43
3.2.2 Shot Erie	44
3.2.3 Shot Lacrosse	44
3.2.4 Shot Huron	45
3.2.5 Shot Flathead	45
3.2.6 Shot Apache	45
3.2.7 Shot Zuni	46
3.2.8 Shot Cherokee	47

3.2.9 Shot Navajo	47
3.2.10 Shot Tewa	47
3.2.11 Shot Dakota	47
3.3 Spectrographic Results	49
CHAPTER 4 DISCUSSION	82
4.1 Atmospheric Attenuation	82
4.1.1 Absorption by the Atmosphere	82
4.1.2 Climatological Conditions and Atmospheric Optical Effects	82
4.1.3 Spectrographic Scattering Experiment	84
4.2 Analysis of Calorimeter and Radiometer Data	84
4.2.1 Data Reliability	84
4.2.2 Comparison of Observed Data with Predictions	86
4.2.3 Comparison of Thermal Yield from Air Drop and Barge Shot	87
4.2.4 Determination of Irradiance from Calorimeter Data for Shot Dakota	88
4.2.5 Radiometric Determination of the Source Color Temperature	88
4.3 Analysis of Low-Resolution Spectrographic Data	90
4.3.1 Structure Identification	90
4.3.2 Spectrographic Determination of Color Temperature	90
4.3.3 Time to Second Maximum Spectral Dependence	91
4.3.4 Fireball Diameter Correlation	92
4.4 Analysis of Photographic Data	92
4.4.1 Hot Spots	92
4.4.2 Plume	93
4.4.3 Wilson Cloud	94
4.4.4 Air and Water Scattering	94
4.4.5 Hydrodynamics—Air Shock and Shock Froth Phenomenon	97
4.5 Analysis of Shot Dakota	99
4.5.1 Hydrodynamics	99
4.5.2 Partition of Light; Relative Albedo Contribution	100
4.5.3 Time Variation of Fireball Brightness	103
4.5.4 Comparison of Polaroid Pictures of Shot Dakota	104
4.5.5 Asymmetry	106
4.6 Absorption Shell Phenomenon	108
4.6.1 General Properties	108
4.6.2 Hydrodynamics	108
4.6.3 Absorption Coefficient	109
4.6.4 Limb Darkening	111
4.6.5 Discussion	114
CHAPTER 5 CONCLUSIONS AND RECOMMENDATIONS	169
5.1 Conclusions	169
5.1.1 Thermal Exposure	169
5.1.2 Backscattered Radiation	169
5.1.3 Thermal Exposure of Air Versus Ground Bursts	169
5.1.4 Spectral Distribution of Thermal Radiation	170
5.1.5 General Conclusions	170
5.2 Recommendations	171
5.2.1 Calorimetric and Radiometric Measurements	171
5.2.2 Further Analysis of Photographic Data	171
5.2.3 Future Data	173
REFERENCES	175

TABLES

2.1	Planned Participation	26
2.2	Shot Statistics	26
2.3	Basic Aircraft Instrumentation	27
2.4	Calibration Factors	27
3.1	Aircraft Positions at Time Zero	51
3.2	Effectiveness of Thermal Instrumentation	52
3.3	Thermal Exposure and Maximum Irradiance	53
3.4	Filter Nomenclature	60
3.5	Ratio of Backscattered Radiant Exposure to Direct Radiant Exposure as Observed at B-47	60
3.6	Effectiveness of Photographic Instrumentation	61
3.7	Photographic Parameters	62
4.1	Transmission of Thermal Energy Through Pacific Air	119
4.2	Meteorological Data	119
4.3	Atmospheric Transmission for Aircraft Positions, Shot Dakota	120
4.4	Solar Color Temperatures Extrapolated to Zero Air Mass	120
4.5	Effect of Combining Data from Various Filtered Detectors	120
4.6	Amounts of NO_2	121
4.7	Temperatures at t_{max} for $\Delta\lambda$ Range of 4,400 to 6,000 Å	121
4.8	Integrated Temperatures	122
4.9	$K(\lambda)$ as a Function of Wavelength	122
4.10	Comparison of Measured and Calculated Values of t_{max}	122
4.11	Fireball Diameter at t_{max} as a Function of Yield	123
4.12	Maximum Fireball Diameter as a Function of Yield	123
4.13	Wilson Cloud Effects	123
4.14	Optics of Contoured Photographs	124
4.15	Partition of Thermal Flux, Frames 15 through 375	124
4.16	Partition of Thermal Flux, Frame 65	125
4.17	Intercomparison of Series 36236 Red Frames	125
4.18	Comparisons at Thermal Flux Maxima	125
4.19	Corrected Albedo Ratios	126
4.20	Absorption Shell (Red), Shot Zuni	126
4.21	Limb Darkening Results, Shot Dakota	126

FIGURES

2.1	Typical locations of aircraft instrumentation	28
2.2	Sensitivity as a function of wavelength for the Red, Blue, and Polaroid systems	29
2.3	Complete assembly of N-9 camera with spectroscopic attachment	30
2.4	Exploded view of N-9 camera with spectroscopic attachment	31
2.5	Response of spectriograph over various fields of view	32
2.6	Tail instrumentation mound, B-47 (rear view)	33
2.7	Tail instrumentation mount, B-47 (side view)	33
2.8	Tail instrumentation mound, B-52 (rear view)	34
2.9	Tail instrumentation mount, B-52 (side view)	34
2.10	Tail instrumentation mount, B-57 (rear view)	35
2.11	Tail instrumentation mount, B-57 (side view)	35
2.12	Tail instrumentation mount, B-66 (rear view)	36
2.13	Tail instrumentation mount, B-66 (side view)	36
2.14	Radiant exposure as a function of time	37

3.15 Transmittance of Filter B (Corning 7-56) as a function of wavelength	38
3.16 Typical microdensitometer trace across the fireball and its associated albedo elements	39
3.1 Geometry of a vertically oriented receiver	63
3.2 Radiant exposure as a function of time for Shot Dakota as measured from B-57	63
3.3 Irradiance as a function of time for Shot Dakota as measured from B-56	64
3.4 Radiant exposure as a function of time for Shot Dakota as measured from B-66	65
3.5 Irradiance as a function of time for Shot Dakota as measured from B-66	66
3.6 Radiant exposure as a function of time for Shot Apache as measured by three calorimeters on the same aircraft	67
3.7 Schematic diagram of a surface detonation	68
3.8 Chronological spectral history, Shot Apache	69
3.9 Chronological spectral history, Shot Cherokee	70
3.10 Chronological spectral history, Shot Dakota	71
3.11 Chronological spectral history, Shot Erie	72
3.12 Chronological spectral history, Shot Flathead	73
3.13 Chronological spectral history, Shot Huron	74
3.14 Chronological spectral history, Shot Lacrosse	75
3.15 Chronological spectral history, Shot Mohawk	76
3.16 Chronological spectral history, Shot Navajo	77
3.17 Early time spectra, Shot Tewa	78
3.18 Chronological spectral history, Shot Tewa	79
3.19 Chronological spectral history, Shot Zuni	80
3.20 Comparison of zero time spectra	81
4.1 Infrared spectrum of water vapor and carbon dioxide	127
4.2 Absorption spectrum of NO_2 and N_2O_4	128
4.3 Specific thermal energy as a function of slant range	129
4.4 E as a function of θ and $E/\cos^2 \theta$ as a function of θ	130
4.5 Correlation between predicted and observed radiant exposure	131
4.6 Correlation between predicted and observed radiant exposure	132
4.7 Ratio of specific thermal yield and specific irradiance	133
4.8 Irradiance as a function of time for narrow spectral region, Shot Dakota	134
4.9 Irradiance as a function of time for downward instrumentation, Shot Dakota	135
4.10 Color temperature as a function of time, Shot Dakota	136
4.11 Black body temperature	137
4.12 Absorption spectrum of NO_2	138
4.13 Comparison of N_2 absorption spectra with typical shot spectra	139
4.14 Scattering of light from region surrounding Shot Dakota, in Red light	140
4.15 Scattering of light from region surrounding Shot Dakota, in Blue light	141
4.16 Scattering of light from the upper right section of the region surrounding Shot Zuni, in Red light	142
4.17 Comparison of fireball to sun and flashbolt aureoles	143
4.18 Hydrodynamic growth of Shot Lacrosse	144
4.19 Hydrodynamic growth of Shot Huron	145
4.20 Hydrodynamic growth of Shot Zuni	146
4.21 Mature fireball radius as a function of yield	147
4.22 Location of Dakota and covering aircraft	148
4.23 Growth of fireball, Shot Dakota	149
4.24 Growth of absorption shell	150

4.25	Growth of shock froth, Shot Dakota	151
4.26	Typical brightness plot of fireball, Shot Dakota	152
4.27	Partition of thermal flux from one Red photograph, Shot Dakota	153
4.28	Maximum brightness history of fireball, Shot Dakota	154
4.29	Cloud and water brightness in Red Series 36236, Shot Dakota	155
4.30	Aureole of Shot Dakota, Frame Zero, in two polarizations	156
4.31	Aureole brightness on Frames 36240 (θ) and (ϕ), measured on a central scan to the right of the fireball, Shot Dakota	157
4.32	Brightness as viewed on eight scans, Shot Dakota	158
4.33	Speed of growth of fireball and shock froth radii	159
4.34	Location of absorption shell attenuation scans	160
4.35	Scan Line A in Red Frame 83, Shot Zuni	161
4.36	Red brightness ratio and μ' , Shot Zuni	162
4.37	Red brightness profile of a central scan line, Shot Dakota	163
4.38	Red brightness profile of a central scan line, Shot Dakota (continued)	164
4.39	Blue brightness profile of a central scan line, Shot Dakota	165
4.40	Observed and calculated limb darkening fireball, Shot Dakota	166
4.41	Blue fireball brightness contour	167
4.42	Red fireball brightness contour	168
A.1 through A.15,	Shot Erie, Series 34585	178
A.16 through A.28,	Shot Lacrosse, Series 31587	185
A.29 through A.41,	Shot Huron, Series 37505	192
A.42 through A.56,	Shot Flathead, Series 35157	198
A.57 through A.67,	Shot Apache, Series 37214	206
A.68 through A.78,	Shot Apache, Series 37218	211
A.80 through A.92,	Shot Zuni, Series 34383	217
A.93 through A.108,	Shot Cherokee, Kodachrome Positive, F-84	224
A.109 through A.127,	Shot Navajo, Series 36808	232
A.128 through A.140,	Shot Tewa, Series 37477	241
A.141 through A.158,	Shot Dakota, Series 34377	248
A.159 through A.171,	Shot Dakota, Series 35923	257
A.172 through A.182,	Shot Dakota, Series 36231	263
A.183 through A.191,	Shot Dakota, Series 36233	269
A.192 through A.204,	Shot Dakota, Series 36236	273
A.205 through A.211,	Shot Dakota, Series 36241	280
A.212 through A.215,	Shot Dakota, Series 36242	283
A.216 through A.223,	Shot Dakota, Series 36249	285
A.224 through A.232,	Shot Dakota, Series 36250	289
A.233 through A.251,	Shot Dakota, Series 36299	294
A.252 through A.256,	Shot Dakota, Series 36300	303

SECRET

Previous page was blank, therefore not filmed.

Chapter 1

INTRODUCTION

In the definition of the capabilities of present-day high-performance aircraft to deliver nuclear weapons of high yield, thermal radiation appears to be the limiting criterion. In order to predict the thermal effects of a nuclear explosion on aircraft structures, it is first necessary to be able to predict the intensity, wavelength distribution, and time irradiancy relationship of the thermal radiation incident upon critical surfaces, which may have any orientation and location in space.

1.1 OBJECTIVES

The primary objective was to obtain and evaluate experimental data of the basic thermal phenomena associated with the nuclear and thermonuclear explosions detonated between 5 May and 22 July 1956 at the Pacific Proving Grounds (PPG). This data was to be obtained from airborne instrumentation.

The phenomena of interest were those of significance in the prediction of the thermal radiant exposure and irradiance at a point in space as a result of a nuclear explosion.

The phenomena included: (1) fireball geometry, including size, shape, and rate of rise; (2) fireball characteristics as a thermal-energy source, including black-body quality, emissivity, and color temperature; (3) albedo effects of the earth's surface and of clouds; (4) effects of shadowing of the earth's reflecting surface (decrease in effective albedo at smaller angles of incidence because of surface roughness) and the obscuration by the fireball; (5) degree to which the emitted thermal radiation is anisotropic; (6) effects due to scattering and absorption as functions of wavelength; and (7) variation of the spectral distribution of the thermal energy in the visible region as a function of time from the first minimum to about 10 times the time to the second maximum.

1.2 BACKGROUND AND THEORY

With the advent of thermonuclear weapons, thermal radiant exposure became one of the limiting factors in the delivery capability of aircraft. In the preliminary estimate of thermal inputs to be received by the delivery aircraft (Reference 1), many assumptions and approximations were necessary because of lack of data and the difficulty of any analytical solution. Many significant parameters can be investigated adequately only at a nuclear test operation. (These parameters are listed as the objectives of this project.)

Methods used to predict the thermal radiant exposure received at a point in space consider such parameters as fireball size, shape, rate of rise, and color temperature. Additional factors are the albedo effects of clouds and of the earth's surface, atmospheric effects of scattering and water vapor absorption, and variation of spectral distribution as a function of time, yield, and height of burst. If these additional factors are neglected, the following equation for an airburst is obtained (References 1 and 2):

SECRET

FORMERLY RESTRICTED DATA

$$Q = 3.77 \times 10^7 (W^{0.4}/d^2)$$

Where: Q = radiant exposure, cal/cm²

W = weapon yield, kt

d = distance between fireball center and receiver, ft

In Reference 1, consideration of some of the above mentioned factors resulted in modifications to the basic equation as follows:

$$Q_E = Q_N [F_V (T_V \cos \theta + T_V' \rho \gamma) + F_{IR} (T_H T_W \cos \theta + T_H' T_W' \rho \gamma)] \Delta \quad (1.2)$$

Where: Q_E = thermal radiant exposure on a horizontal receiver, cal/cm²

Q_N = thermal radiant exposure on a receiver oriented normally to a radial from the fireball center in a vacuum, cal/cm²

Δ = fraction of the total thermal energy released in either the hemispherical or spherical fireball phase (Figure 7 in Reference 1)

F_V = fraction of the total thermal energy in the visible region of the spectrum from 0.3 to 0.7 micron

F_{IR} = fraction of the total thermal energy in the infrared region in the explosion radiation spectrum at wavelength greater than 0.7 micron

$\cos \theta$ = cosine of the angle between the vertical through the fireball center and the slant range line

T_V = fractional transmission due to scattering in the visible region for the direct radiation

T_V' = fractional transmission due to scattering in the visible region for the ground-reflected radiation

T_H = fractional transmission due to scattering in the haze layer over the entire spectrum for the direct radiation

T_H' = fractional transmission due to scattering in the haze layer over the entire spectrum of the explosion radiation for the reflected radiation

T_W = fractional transmission in the infrared region of the explosion spectrum due to water vapor absorption of the direct radiation

T_W' = fractional transmission in the infrared region of the explosion spectrum due to water vapor absorption of the reflected radiation

ρ = average ground albedo (Table 5 in Reference 1)

γ = ratio of the ground-reflected energy per unit area on a horizontal receiver to the direct energy per unit area on a receiver oriented normally to a radial from the fireball center at a particular point in space, in a vacuum, for unit albedo and for either a surface hemispherical or an air spherical fireball (Tables 7 and 8 in Reference 1).

Equation 1.1 was developed as a reasonably valid analytical expression for treating all air, surface, and intermediate-height bursts with yields of 500 kt or less. Although this equation seems to give results that are in better agreement with test data than other methods, many parameters have received only cursory consideration. In consequence, it was determined that Air Force Cambridge Research Center (AFCRC) participation during Operation Redwing was

desirable to acquire additional data. The desirability of combining efforts with the Wright Air Development Center (WADC) aircraft weapon-effect projects was obvious. The utilization of Naval Radiological Defense Laboratory (NRDL) instrumentation and calibration facilities, to avoid costly duplication and to permit correlation with the results of previous tests, was also desirable. Conferences including representatives of WADC, NRDL, and AFCRC established the test plan. It was agreed that the breakdown of responsibilities in this effort would be as follows:

1. AFCRC would assume responsibility for the technical aspects of the basic thermal portion of the operation on four WADC aircraft (B-47, B-52, B-57, and B-66), and serve as technical consultants to WADC and NRDL. Specifically, AFCRC, with assistance from Edgerton, Germer,hausen and Grier, Inc. (EG&G), would determine correct film, filters, lenses, exposure times, and film-transfer rates. The reduced thermal data would be analyzed by AFCRC for information on the parameters outlined in the objectives of this project.
2. WADC would provide funds for NRDL equipment and services, N-9 gun sight aiming point (GSAP) cameras, recorders, amplifiers, and control circuits. The WADC contractors would install and flight-check the instrumentation.
3. NRDL would supply the radiometers and calorimeters, make electrical and thermal calibrations before and after the test, and carry the data reduction through the tabulating, plotting, and correction phases.
4. All agencies concerned would provide necessary personnel at the test site.

Thus, the desired data would be available as results from the calorimetric, radiometric, photographic, and spectrographic recordings from each event.

It was expected that much of the information desired would be obtained from the film records of the GSAP cameras. From 20 to 35 cameras were utilized on each event. Some were filtered to obtain fireball pictures in the blue portion of the spectrum (3,400 to 4,500 Å) or in the red (6,800 to 8,800 Å). Other cameras were equipped with spectroscopic attachments developed at AFCRC to obtain spectral distribution information as a function of time in the spectral region from 3,200 to 9,000 Å. More detailed information of the instrumentation appears elsewhere in this report.

Densitometric measurements of the fireball films would provide an illumination-versus-area record of thermal radiation sources within the fields of view of the instrumentation, supplementing the spectrographic and calorimetric data.

Analysis of the spectral data would give information on color temperature. If the fireball is assumed to have black-body qualities, the spectral distribution of its radiant energy can be characterized by an effective color temperature, i.e., the temperature at which the relative intensity, as a function of wavelength, is distributed according to Planck's law of radiation.

Planck's law of radiation can be approximated by Wein's formula when $\lambda T \ll 3,000$ micron degrees, as follows:

$$\log I \lambda^5 = (-0.4343 c / \lambda T) + \log K \quad (1.3)$$

Where: I = intensity of radiation per unit wavelength

λ = wavelength, microns

T = temperature, °K

c = 1.4385×10^4 micron degrees

K = a constant, the numerical value of which depends on the units of I and λ .

If intensity measurements are corrected for absorption of the air by extrapolation to zero distance, they should follow the above law. Therefore, a straight-line fit to a plot of $0.4343 c / \lambda$ versus $\log I \lambda^5$ should have a slope equal to $-1/T$.

Chapter 2

PROCEDURE

2.1 OPERATIONS

The two-atoll (Bikini and Eniwetok) arrangement at the PPG and the wide variation of weapon yields compounded the problem of properly instrumenting each aircraft for each event of the operation.

2.1.1 Thermal Measurements. Aircraft positions were obtained from the individual projects as soon as possible. Instrument-sensitivity selections were made utilizing a combination of extrapolation of Operation Castle data and the method of Reference 1, as reduced to a nomograph form for Operation Redwing (Reference 3). The NRDL personnel furnished the instruments to the individual contractor for installation and accomplished the preflight electrical calibrations. After the event, the individual contractor performed initial data reduction.

2.1.2 Photographic Coverage. Following the establishment of aircraft positions, a detailed photographic plan was accomplished. Some variations of the basic camera configuration were made to take advantage of aircraft positions. Films, lenses, filters, camera speeds, and aperture settings were selected. Film requirements were given to Task Unit 5, which assisted in the field effort by providing loaded magazines, processing exposed film, repairing damaged cameras, and serving in a consultative capacity. Cameras were prepared and furnished to the individual contractor for installation. Installation was accomplished on the evening of D-1 day or the morning of D-day. After the event, the film was returned to Task Unit 5 for processing. The film was reviewed by project personnel for qualitative analysis of results. Films were then returned to the continental United States for further processing and analysis.

2.2 PLANNED SHOT PARTICIPATION

The coverage of basic thermal measurements from aircraft was quite extensive in the number of aircraft involved, the number of instruments per aircraft, and the number of events in which the aircraft participated.

Participation was planned for every event in which any of the four aircraft carrying Project 5.7 instrumentation participated, although in several cases the aircraft were positioned for other than thermal effects. The planned participation for the operation is given in Table 2.1, and the event statistics are given in Table 2.2.

Partial instrumentation for a backup ground station was planned to cover all events, except Shots Yuma and Osage.

2.3 INSTRUMENTATION

Twenty-one channels of thermal information were recorded on each aircraft. In addition, the B-47 and the B-52 were instrumented to measure the thermal radiation that would be back-scattered to the cockpit. This instrumentation is discussed later in this report.

Eighteen channels recorded the outputs of sensors located in the tail section of each aircraft (Station 1, Figure 2.1). These sensors were preset on the ground to point at the fireball during

the thermal pulse and were suitably filtered to obtain broadband spectral-distribution information. Various fields of view (21° to 160°) were utilized.

The three remaining sensors of the basic instrumentation were oriented vertically to the earth's surface and located in the lower fuselage of each aircraft (Station 2). The purpose of this instrumentation was to measure the thermal radiant exposure incident upon a horizontal surface. Each one of these sensors was fashioned with a hemispherical filter that had a 160° field of view. Two of these filters were of quartz, which transmits nearly all of the spectrum (essentially 0.2 to 4.5 microns), and the other was of red Jena glass, which transmits principally in the infrared (0.7 to 2.5 microns). Because of the proximity of these instruments to each other and to other obstructions, one of the quartz 160° filters on each aircraft was replaced, for the last few events, with a 90° filter. This was accomplished to assist in the evaluation of effects of obstructions within the field of view of the instruments. In the case of the B-57, it was possible to add the 90° instrument without removing a 160° instrument.

Each of the aircraft carried some additional thermal instrumentation that was not provided for within the scope of Project 5.7. This instrumentation consisted of two thermal sensors located within the radome of each aircraft. The B-47 also had a calorimeter oriented at right angles to the sensors in Station 1 and another mounted vertically in the left rear horizontal stabilizer.

In addition to the thermal sensors, N-9 GSAP cameras were used in these two stations in each aircraft. Two cameras were located in the lower fuselage (Station 2) with the same orientation as the three thermal sensors. These had a large field of view and obtained photographs of the albedo surface. Six cameras were located in the tail instrumentation section (Station 1) of each aircraft and were pointed at the fireball. Four of these were of primary interest and were fitted with red and blue filters to obtain photographs in the spectral regions of 0.34 to 0.45 and 0.68 to 0.88 micron. Lenses were selected to obtain as large a fireball image as possible but with some conservatism because of the pointing errors that it was reasonable to expect. In the case of the B-57 and the B-86, two of the four cameras were equipped with the spectroscopic attachment. The purpose of the other two cameras was to provide information, in the field, of the aircraft orientation with respect to the fireball. Although these cameras were the responsibility of the individual aircraft project, the film was of value to this project. Arrangements were made for AFCRC to be provided with the original negatives and with prints of these films.

In addition to the cameras included here in the basic instrumentation, there were other cameras, on three aircraft, which were incorporated as the project progressed. These included one camera in the backscatter mount on the B-47 (Station 3), two additional cameras on the B-52 in the camera housing aft of the cockpit (Station 4), and four to six additional cameras on the B-86 in Station 2. The additional cameras on the B-47 and B-52 were installed to provide photographic coverage of the thermal backscatter instrumentation. The additional camera mounts that became available on the B-86 were utilized to provide additional coverage between the directions of the radial to the fireball, and vertically down. Information on the additional cameras is furnished later.

More detailed information of the basic instrumentation in Stations 1 and 2, including field-of-view and filtering information, is given in Table 2.3. In some instances, more than one instrument had the same field of view and filter in order to cover a sensitivity range.

2.3.1 Radiometers and Calorimeters. The calorimeters and radiometers were furnished by NRDL in several sensitivity ranges to cover all anticipated input values. Calibration of these instruments was accomplished by NRDL, before and after the operation, by the utilization of standard techniques. The installation was accomplished by the aircraft projects' contractors, in each case, under the cognizance of NRDL and AFCRC. This information, with but one exception, was recorded on Consolidated recorders. The B-47 backscatter information was recorded on an Ampex 814 magnetic tape recorder. This resulted from the lack of oscillographic channels at the time the requirement for the backscatter measurements arose. The

calorimeter outputs frequency-modulated a carrier frequency over a 30-kc maximum range. A dc amplifier was utilized to amplify the signals (which were of the order of 1 mv) to the order of a volt, as required for the recorder input. The recorder response was 10 kc per volt.

2.3.2 Photographic. The N-9 GSAP cameras, supplied by WADC, had been modified by EG&G in accordance with criteria furnished by Cook Research Laboratory. These cameras have a focal plane and a 0.001-second shutter, employ 16-mm perforated film, and operate at 64 frames/sec. The purpose of the modifications was to eliminate nonessential features that had been found to be the source of certain malfunctions. Personnel of EG&G checked all cameras for proper running condition and collimated the desired lenses with each camera; the camera speed was checked over a range of temperatures and battery voltage variations, and found to be within acceptable limits. It was found, however, that occasionally in field operation the shutter opening time varied somewhat (order of 25 percent) from frame to frame; this point will be discussed later.

The cameras were mounted at Station 1 of the aircraft. Four to six of these cameras were located in the tail section of the four aircraft, and were adjusted before the flight to point at the expected position of the fireball. Lenses were selected to obtain as large a fireball image as possible, with the reservation that a considerable pointing error was to be expected. Lenses with 10-mm, 17-mm, and 25-mm focal lengths were used; these were collimated and carefully shimmed for sharp focus. The field of view of the 10-mm lenses is 61° by 43.5° ; of the 17-mm lenses, 35.5° by 25.5° ; and of the 25-mm lenses, 24.5° by 17.5° . The lenses were stopped to apertures between $f/5.6$ and $f/22$.

The cameras were operated in pairs, in that either infrared and blue filters, or horizontal and vertical linear polarizers, were used on alternate cameras having lenses with the same focal length. The blue filters (Jena BG-12) and the polarizers (Tiffen type) were used with Kodak SO-1,112 Microfile fine grain (~ 300 lines/mm) film. With the infrared (Jena RG-8) filters, a slow-speed infrared film, Type IV-N (~ 120 lines/mm) was used. These systems will henceforth be referred to as Red, Blue, and Polaroid. In addition, some of the series were filtered by Jena NG-5 neutral-density-1 filters.

The overall spectral response of these systems, in absolute units, is shown in Figure 2.2. These curves were compounded from the spectral response of the emulsions as furnished by the manufacturer and from the measured (with a spectrophotometer) response of the filters and polarizer. Since it was found that the heights of the attenuation-wavelength curves of the neutral density filters were subject to considerable variation (presumably they vary in thickness), the curves are to be regarded as representative only. The Red sensitivity extends from 6,800 to 9,000 Å, and the Blue sensitivity, which is less clearly delineated, from about 3,800 to 4,500 Å. The equivalent ASA speeds of these film-filter systems (less the neutral density filters) are about 1.

2.3.3 Spectrographic Instrumentation. The spectrographic instrumentation consisted of 16-mm, N-9 motion-picture cameras modified by the addition of AFCRC spectroscopic attachments. The assembled instrument is shown in Figure 2.3 and an exploded view in Figure 2.4.

The spectroscopic attachment employed a Bausch and Lomb 3-prism dispersing element and associated lenses. A second type, developed to extend the spectral coverage (3,200 to 9,000 Å), utilized a grating for the dispersing element.

The former attachment consisted of a slit, collimating lens, and a 3-prism Amici dispersing element. The slit is of the step variety consisting of five steps whose widths vary logarithmically from 10 to 800 microns. The widths were chosen to give equally spaced exposures along the "H and V" curve of the emulsion; thus, it was possible to determine the relative intensity response of the film at each wavelength on each frame of data. This is necessary for obtaining a fair degree of accuracy in the measurement of the relative intensity as a function of wavelength by holding to a minimum the errors introduced by nonuniformities in the emulsion and film processing.

The collimating lens is a cemented achromat with 7-mm diameter and 35-mm focal length. The Amici prism, manufactured by the Bausch and Lomb Optical Company, is a typical one composed of two crown glass prisms and one flint glass prism properly orientated to give a straight-through or direct-vision system in the spectral region of 4,000 to 8,000 Å.

A shade and an opal disk placed before the slit provide a simple means of varying the field of view of the instrument as well as assuring uniform illumination along the length of the slit.

A filter holder placed between the prism and camera lens allows for the insertion of neutral density filters for extending the range of the instrument and the inclusion of a Didymium filter to provide known absorption lines in the spectrum for wavelength calibration.

The standard 35-mm f/2.8 lens supplied with the N-9 camera is used as the camera lens for the spectrograph, thus retaining an optical system of unit magnification.

The N-9 camera was chosen for its versatility in the selection of exposures and the time resolution available with the 1-msec and 0.5-msec shutter speeds. A complete discussion of the N-9 camera may be found in References 4 and 5.

During the tests, the spectrographs were, in general, installed as follows: two each in the tail mount of the B-57, in the tail mount of the B-66, in the after fuselage mount of the B-66, and in the photo tower on Site William or Site Elmer. Exceptions to this occurred on shots in which the B-57 did not participate and when attempts were made to measure backscattered light. In these cases, the B-52 was instrumented.

The time interval of major interest was from the first minimum to about 10 times the time to the second maximum; thus, the camera speed normally used was 64 frames/sec with a time resolution for an individual frame of 1 msec.

Exceptions to this occurred for cameras located at long slant ranges for shots of high yield where it was determined that 32 frames/sec was optimum.

Three fields of view were used on the spectrographs during the operation. A plot of the measured relative response of the spectrograph over these fields is shown in Figure 2.5. The field defined by the opal with no shade approximated a Lambert surface over a total field of 180°. This field was used on all aircraft installations. The addition of a shade to the opal limited the field to about 40°. This combination was used for all data taken from the photo tower on Site William. Replacing the opal with a ground quartz diffuser resulted in a still narrower field but with an increase in sensitivity of a factor of 2 at the peak. This combination was used to advantage on the medium- and low-yield events recorded from the photo tower on Site Elmer.

The experimental procedure was straightforward. Loaded film cassettes for the N-9 cameras were obtained from EG&G. The film was titled, then loaded into the spectrographs, and operated to check that the cameras were running properly and that the film was traveling freely. Each spectrograph was then exposed to the radiation from a high-pressure mercury arc. This resulted in a few frames of mercury spectra on the leader of each film to serve as the wavelength calibration. The prepared cameras were installed in the aircraft several hours before the scheduled mission and the optics cleaned just prior to takeoff.

Upon completion of a mission, the cameras were removed from the aircraft and the exposed film delivered to EG&G for processing, after which it was reviewed for exposure level and then sent to AFCRC for data reduction.

2.3.4 Aircraft. The four aircraft used were the B-47 (Project 5.1), B-52 (Project 5.2), B-57 (Project 5.4), and B-66 (Project 5.3).

The instrumentation of the B-47 included all the basic instrumentation. In addition, extensive coverage of the backscattered radiation was provided by six of the sensitive (7- and 20-junction) NRDL calorimeters. Two of these were mounted in a camera housing on top of the fuselage about 8 feet aft of the canopy (Station 4). The instruments were oriented 15° above the horizontal, with one 30° to the left and the other 30° to the right of the aircraft nose. The other four calorimeters were mounted in the navigator's compartment (Station 3) and pointed forward at 65° above the horizontal. These instruments covered the area between the fields of view of the two calorimeters mounted aft. A camera was mounted parallel to the four calorimeters in Sta-

tion 3 to provide photographic coverage. Photographs of the tail instrumentation appear as Figures 2.6 and 2.7.

The B-52 carried the complete basic instrumentation, as well as two calorimeters and two cameras to obtain backscatter information. One maximum-sensitivity (20-junction) calorimeter was mounted close to the windshield behind the thermal curtain. The second calorimeter was mounted externally a short distance forward. Calorimeters and cameras were pointed forward with an angle of elevation of about 50° above the horizontal. The cameras for the backscatter instrumentation coverage were in a camera mount corresponding to Station 4. Photographs of the tail installation appear as Figures 2.8 and 2.9.

The B-57 carried the basic instrumentation. No backscattering measurements were made from this aircraft. The only variation from the basic instrumentation was made midway through the operation when a calorimeter with a 90° field of view was added to the vertical station (Station 2). The tail instrumentation station is pictured in Figures 2.10 and 2.11. The vertical station was mounted in the aft hatch door.

The B-66 instrumentation was similar to that in the B-57, and no instrumentation for measuring backscattered radiation was included. The instrumentation differed from that in the other three aircraft in that the tail turret, into which the tail instrumentation was incorporated, could be depressed to only 70° below the horizontal. With the inclusion of smaller yield weapons, this limitation became a major problem; because if the aircraft were positioned for receiving desired inputs, the tail instrumentations could not be pointed at the fireball. This was solved by fabrication of a second instrumentation container to be mounted in the lower fuselage station. This container could be tilted fore and aft up to 30° from the vertical and cover the region that the tail instrumentation could not cover. It was planned that, on those shots where the optimum position would not permit use of the tail turret, selected sensors of the tail instrumentation would be transferred to the lower fuselage station. The camera mounts were utilized on most events to obtain more complete photographic coverage. Photographs of the tail instrumentation appear as Figures 2.12 and 2.13. These photographs depict a bad case of instrumentation fouling by dirt, water, hydraulic fluid, and the waste products of the JATO units.

2.3.5 Ground Stations. The ground effort of this project was limited, but analysis of the data establishes its importance. Arrangements were made with EG&G for the operation of two N-9 cameras at a ground station on each atoll. These cameras were equipped with the spectroscopic attachment. Inclusion of this effort resulted in a capability of making direct correlation between data obtained on the ground and data taken with identical instrumentation from aircraft.

Data was also taken with an N-9 camera fitted with the spectroscopic attachment and using the sun as a source, to provide atmospheric transmission information to be utilized in the analysis of photographic data.

2.4 DATA REQUIREMENTS

The data requirements of the project were as follows: (1) measurements of thermal radiant exposure and irradiance as a function of spectral region and instrument field of view from points in space, for various weapon yields, heights of burst, meteorological conditions, and instrument orientations; (2) measurements of radiant exposure of thermal energy scattered by the atmosphere under various geometries and meteorological conditions; (3) photography of the fireball in the red (6,800 to 8,800 Å) and blue (3,400 to 4,500 Å) regions of the spectrum for various weapon yields, heights of burst, meteorological conditions; (4) photography of various albedo surfaces, such as the earth's surface, clouds, and the white shock-frothed water surface; and (5) spectral photography, such as was required with spectroscopic attachments mounted on N-9 cameras in the spectral region of 3,200 to 9,000 Å.

Data requirements from other projects and agencies included supplementary information required for interpretation and analysis of the thermal measurements and such photographic records as aircraft positions in space, meteorological conditions, weapon yield, height of burst,

and similar factors. Thermal and atmospheric transmission data obtained by other projects was to be correlated with the data resulting from this effort.

2.5 RADIOMETER AND CALORIMETER CALIBRATION AND DATA REDUCTION

The calorimeters and radiometers were furnished by NRDL in several sensitivity ranges to cover all anticipated input values. Calibration of these instruments was accomplished by NRDL, before and after the operation, by the utilization of standard techniques. All data presented was reduced at AFCRC using constants supplied by NRDL and Projects 5.1, 5.2, 5.3, and 5.4 (contractors).

2.5.1 Procedure. Essentially, the data reduction for the calorimeters (a description of the NRDL Mark 6F calorimeter is given in Reference 6) consisted of the following:

1. Converting the galvanometer deflection, as measured, to galvanometer deflection corrected for the heat lost by the instrument through conduction and radiation. This step corresponds to correcting the solid curve of Figure 2.14 to the dashed curve of the same figure. This is a typical calorimeter problem.
2. Converting the corrected galvanometer scale deflections to millivolts across the thermocouple, to temperature rise, and to energy received during the course of the event.
3. Correcting for the average reflectivity of the windows and filters.
4. Differentiating numerically the resulting curve of radiant exposure in respect to time to obtain the irradiance.

The reduction of the radiometer data followed a similar procedure essentially, except for Steps 1 and 4.

Two calibrations of each calorimeter and radiometer were made, both at NRDL. The instruments were precalibrated before they were mounted on the aircraft. At the conclusion of Operation Redwing, the instruments were dismounted and shipped to NRDL for a postcalibration. It was this postcalibration that was used in the final reduction of the data. Both calibrations were made in the laboratory with neither window nor filter in front of the detector surface. Table 2.4 lists some of the calibration factors selected at random.

An inspection of Table 2.4 shows that the calorimeters were apparently more stable toward holding their calibration than were the radiometers. However, the difference in the pre- and postcalibration factors will not completely explain the randomness of the data as observed. For one thing, a two-point calibration in which the instruments have the variation shown gives no reliable information as to the proper calibration factor for any particular event. Furthermore, the variability in data (an example of which is shown in Figure 4.3) indicates that this particular calibration technique may have been inadequate. The data, however, was not in a form where it was possible to make detailed comparisons of the performance of several individual calorimeters or radiometers as a function of event.

As no facilities were available in the field for calibration purposes, individual filters or quartz windows were not calibrated during the test series. It was assumed that no changes occurred in the transmission properties of the filters or windows. This assumption may not be uniformly true, considering the intense heat to which the filters were subjected. A certain amount of variance in calibration, not shown in Table 2.4, may be ascribed to unobserved changes that may have occurred in the properties of the filters.

2.5.2 Filter Characteristics. In Table 3.4, filters used on the project are listed together with the wavelength regions through which they transmit energy.

Standard Corning filters were used to determine the amount of radiant energy that can be expected in various broad regions of the spectrum between 0.2 and 4.5 microns. For data collected under these circumstances to be of greatest utility, it is necessary to know in detail the transmission properties of the filters as a function of wavelength. Ideally, this knowledge should extend to the spectral transmission properties of the intervening atmosphere and finally to the

spectral characteristics of the source. Otherwise, caution must be exercised in applying conclusions drawn from the data to other situations that are not optically similar.

As an example of the transmission properties of a particular filter, Table 3.4 lists a Filter B that transmits between 0.9 and 2.5 microns. This particular filter is a Corning 7-56, whose transmission (uncorrected for reflection of the surfaces) is given by the manufacturer (Reference 7) as that shown in Figure 2.15. From the figure, it will be observed that approximately two-thirds of the energy (64 percent) from a white source would be transmitted within the nominal limits of 0.9 to 2.5 microns. Similar statements can be made about the other filters.

In some respects, the statements made are a bit misleading, because some of these filters transmit a significant amount of energy outside the limits given. This statement is reinforced when these filters are coupled to a moist Pacific atmosphere and a high-temperature source. In this case, the absorption by water vapor has only a few windows in the infrared spectral region, while the absorption by the same water vapor allows a much greater percentage of energy to be transmitted in the visible spectral region. This is further enhanced by the increased ratio of visible to infrared radiation emitted by a high-temperature source. Such arguments were used as the basis of filter limits tabulated in Table 3.4.

2.6 PHOTOGRAPHIC CALIBRATION AND DATA REDUCTION

2.6.1 Development and Sensitometry. After each detonation, the films were processed by EG&G personnel in their field unit. Processed under the same conditions was a strip of film that had been exposed with a step tablet and an EG&G Mark VI sensitometer. The films were developed to a gamma (contrast) of about 1.0. The step tablet was an Eastman Kodak 2, with 21 steps and densities up to 3.0. The sensitometer used an FT 110 Xenon lamp, at 5,000 meter-candle seconds; in some cases this exposure was reduced by use of a mask. The lamp flash time was about the same as the field shutter time, roughly 1 msec, to minimize reciprocity-failure effects. Wratten W29 red and W38 + 38A blue filters were used on the Red and Blue film strips, respectively. These filters do not have the same characteristics as the Jena filters, and the lamp does not, of course, have the same spectral composition as the light from the detonation; this is expected to introduce only a small error in the calibration (Figure 176 of Reference 8). Unfortunately, however, the sensitometric exposure was often insufficient to expose the film to the high photographic densities observed in the field. Furthermore, some of the step tablets were lost in transit back to the continental United States.

2.6.2 Microdensitometry. A Jarrell-Ash Company Jaco JA 2310 recording microphotometer was modified to accept the film reels and to read optical density instead of transmission. With it, the optical density of the films could be measured semiautomatically. The instrument recorded (narrow-beam) optical densities from 0 to 4.0, sensed by a 931-A photomultiplier, on a Bristol strip chart recorder. The image of the frame could be projected onto a ground-glass viewing screen, with linear magnification 15X. A reticule was placed over this screen to locate the scan positions. The microdensitometer slit was set at 55 by 100 microns as a compromise between resolution and sensitivity without excessive noise. The slit height appears on the photographs (Figures A.1 through A.256 in the Appendix) to the right of symbol ".1"; note that it is not as small as could be desired. Similarly the scanning speed was chosen as 2.5 mm/min; the time for a complete horizontal scan is about 4 minutes. The stage on which the film was mounted could be rotated, and scans through various features on each frame could be taken. A typical trace is shown in Figure 2.16. The noise is presumably due to the granularity of the film (see Chapter 24 and especially Figure 358 of Reference 8).

The image on the viewing screen of each of the frames that was scanned was photographed with a Linhof Technika camera fitted with a Land Polaroid back. An attachment to the microdensitometer console allowed the camera to be quickly swung into position. Polaroid 48L film, which makes a positive transparency, was used; from this transparency enlargements were made. Such enlargements are shown in the Appendix.

2.6.3 Dynamic Range and Camera Flare. The GSAP cameras are designed for general duty rather than for accurate film photometry. Consequently, in spite of their being fitted with coated lenses, it is expected that flare light scattered from the interior (shutter blades, diaphragm) and exterior (filters, lens barrel) parts of the cameras (as well as from the lenses) will reduce the contrast to a dynamic range of brightnesses below 10^3 . The situation is aggravated by the heating of the lenses, filters, and other external camera parts during the thermal pulse, and by dust and spray on the lenses. Furthermore, the fireball typically covers an important fraction of the camera field of view, and so there is a large amount of light available to be smeared over the dimmer features of the photographs.

The existence of this flare light is borne out by the albedo measurements of Chapter 4, in which the lowest albedo points, near the photograph edges, are never less bright than 10^{-2} times the brightest fireball surface areas. Consequently, the lowest brightness points are subject to some error, and results of low-intensity measurements must be interpreted carefully.

2.6.4 Analysis of Microdensitometer Records. Hurter and Driffeld curves (H and D, density versus log exposure) for the various films that were scanned were prepared from the sensitized film strips. The microdensitometer traces could be analyzed with the aid of transparent plastic scales, engraved with the appropriate reticule gridwork numbers; these enabled the brightness at various positions on the image of the nuclear detonation to be found. Brightness maps of selected frames were prepared (Chapter 4), and isophot contour maps were made by connecting up points of equal brightness.

2.7 SPECTROGRAPHIC DATA REDUCTION AND CALIBRATION

At AFCEC, the spectral films were reduced through use of a microdensitometer to curves of film density versus wavelength. H and D curves were then constructed at selected wavelengths from the step slit calibration and the densities at 100-Å intervals converted to relative intensities. The variation of relative intensity with wavelength due to emulsion response and instrument transmission was corrected through calibration of the instrument and film against a tungsten standard lamp supplied by the National Bureau of Standards.

TABLE 2.1 PLANNED PARTICIPATION

Event	Planned Participation				Ground Station
	B-47	B-52	B-57	B-44	
Cherokee	x	x	x	x	x
Lacrosse	x	x	x	x	x
Zuni	x	x	x	x	x
Erie	x	x	x	x	x
Seminole	x	x	x	x	x
Yuma	x	x	x	x	x
Flathead	x	x	x	x	x
Blackfoot	x	x	x	x	x
Inca	x	x	x	x	x
Navajo	x	x	x	x	x
Huron	x	x	x	x	x
Dakota	x	x	x	x	x
Osage	x	x	x	x	x
Kickapoo	x	x	x	x	x
Apache	x	x	x	x	x
Mohawk	x	x	x	x	x
Tewa	x ^a	x ^a	x ^a	x ^a	x ^a

^a Participation in this event was planned only if justified because of not acquiring sufficient data on other shots.

TABLE 2.2 SHOT STATISTICS

Shot	Date	Location	Approximate Yield	Type Shot
			kt	
Lacrosse	5 May	Eniwetok, Yvonne	39.5	Surface
Cherokee	21 May	Bikini, Charlie	3,800	Air drop over water at 5,000 feet
Zuni	28 May	Bikini, Fare	3,380	Surface
Yuma	28 May	Eniwetok, Sally	0.19	200-foot tower
Erie	31 May	Eniwetok, Yvonne	14.9	300-foot tower
Seminole	6 June	Eniwetok, Irene	13.7	Surface
Flathead	12 June	Bikini, off Dog	365	Barge
Blackfoot	12 June	Eniwetok, Yvonne	8.5	200-foot tower
Kickapoo	16 June	Eniwetok, Sally	1.49	300-foot tower
Osage	16 June	Eniwetok, Yvonne	1.7	Air drop at 700 feet
Inca	22 June	Eniwetok, Pearl	15.2	200-foot tower
Dakota	26 June	Bikini, off Dog	1,100	Barge
Mohawk	3 July	Eniwetok, Ruby	360	300-foot tower
Apache	9 July	Eniwetok, Mike crater	1,850	Barge
Navajo	11 July	Bikini, off Dog	4,500	Barge
Tewa	21 July	Bikini, off Dog	4,600	Barge
Huron	22 July	Eniwetok, Mike crater	250	Barge

TABLE 2.3 BASIC AIRCRAFT INSTRUMENTATION

Aircraft	Instrument		Filter	Field of View or Focal Length	Station Number	Spectral Range
	Type	Number		degree or mm		
All	Radiometers	2	Quartz, flat	90	1	0.2 to 4.5
All	Calorimeters	3	Quartz, flat	90	1	0.2 to 4.5
All	Calorimeter	1	3-69, flat	90	1	0.5 to 2.5
All	Calorimeter	1	2-73, flat	90	1	0.57 to 2.5
All	Calorimeters	2	2-58, flat	90	1	0.63 to 2.5
All	Calorimeters	2	RG-8(Jena), flat	90	1	0.7 to 2.5
All	Calorimeters	2	7-56, flat	90	1	0.90 to 2.5
All	Calorimeters	2	Ge-7-56, flat	90	1	2.0 to 2.5
All	Calorimeter	1	Quartz, dome	160	1	0.2 to 4.5
All	Calorimeter	1	Quartz, flat	45	1	0.2 to 4.5
All	Calorimeter	1	Quartz, flat	21	1	0.2 to 4.5
All	Calorimeters	2	Quartz, dome	160	2	0.2 to 4.5
All	Calorimeter	1	RG-8(J), dome	160	2	0.7 to 2.5
B-47	Calorimeters	6	Quartz, flat	140	3 and 4	0.2 to 4.5
B-52	Calorimeters	2	Quartz, flat	140	3	0.2 to 4.5
All	Cameras	2	ND and/or GG 14	10	2	0.57 to 0.7
All	Cameras	1 or 2 ^a	Blue, (BG 12)	10, 17, 25	1	0.34 to 0.45
All	Cameras	1 or 2 ^a	Red, (RG-8)	10, 17, 25	1	0.7 to 0.88
B-57 and B-66	Cameras	2	Spectroscopes	25 to 160	1	0.42 to 0.59
B-47	Camera	1	None	10	3	0.34 to 0.7
B-52	Cameras	2	None	5.3	4	0.34 to 0.7
B-66	Cameras	4 to 6 ^b	Spectroscopes	25 to 160	2	0.32 to 0.7

^a Aircraft incorporating spectroscopes in the tail instrumentation (B-57, B-66) had one red filtered and one blue filtered camera in this station (Station 1, Figure 2.1).

^b Of the additional six cameras on the B-66, located at Station 2, Figure 2.1, two were fitted with spectroscopes. The other four cameras were fitted with lenses and filters which were required to obtain the additional information possible because of geometry. This camera mount was oriented to the rear and 30 degrees off the vertical.

TABLE 2.4 CALIBRATION FACTORS

A random sample of radiometer and calorimeter calibration factors. The calibration unit is cal/cm²-sec-mv for the radiometer and cal/cm²-mv for the calorimeter.

Instrument	Designation	Factors		B - A B
		Precalibration (A)	Postcalibration (B)	
Radiometer	RF-10-56	1.72	1.54	-0.12
	RF-10-153	1.85	1.87	+0.01
	RF-10-162	1.80	1.75	-0.03
	RF-50-159	10.67	9.33	-0.14
	RF-50-160	7.04	9.12	+0.23
	RF-50-162	10.32	8.63	-0.20
Calorimeter	WH-162	0.564	0.595	+0.05
	WH-192	0.570	0.613	+0.07
	WH-193	0.582	0.577	-0.01
	BK-18	1.27	1.26	-0.01
	BK-57	0.470	0.434	-0.08
	BK-89	0.435	0.435	0
	BK-195	1.24	1.21	-0.02
	BK-230	1.20	1.18	-0.02
	BK-246	1.14	1.15	+0.01

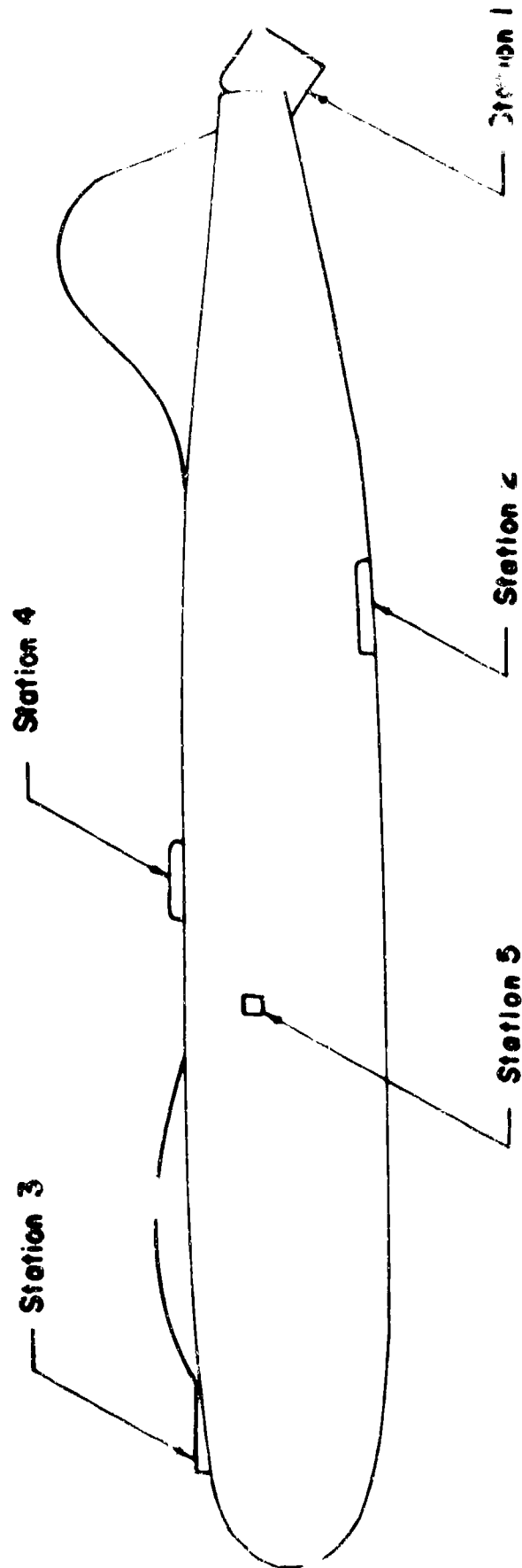


Figure 2.1 Typical locations of aircraft instrumentation.
The cameras are located at Station 1.

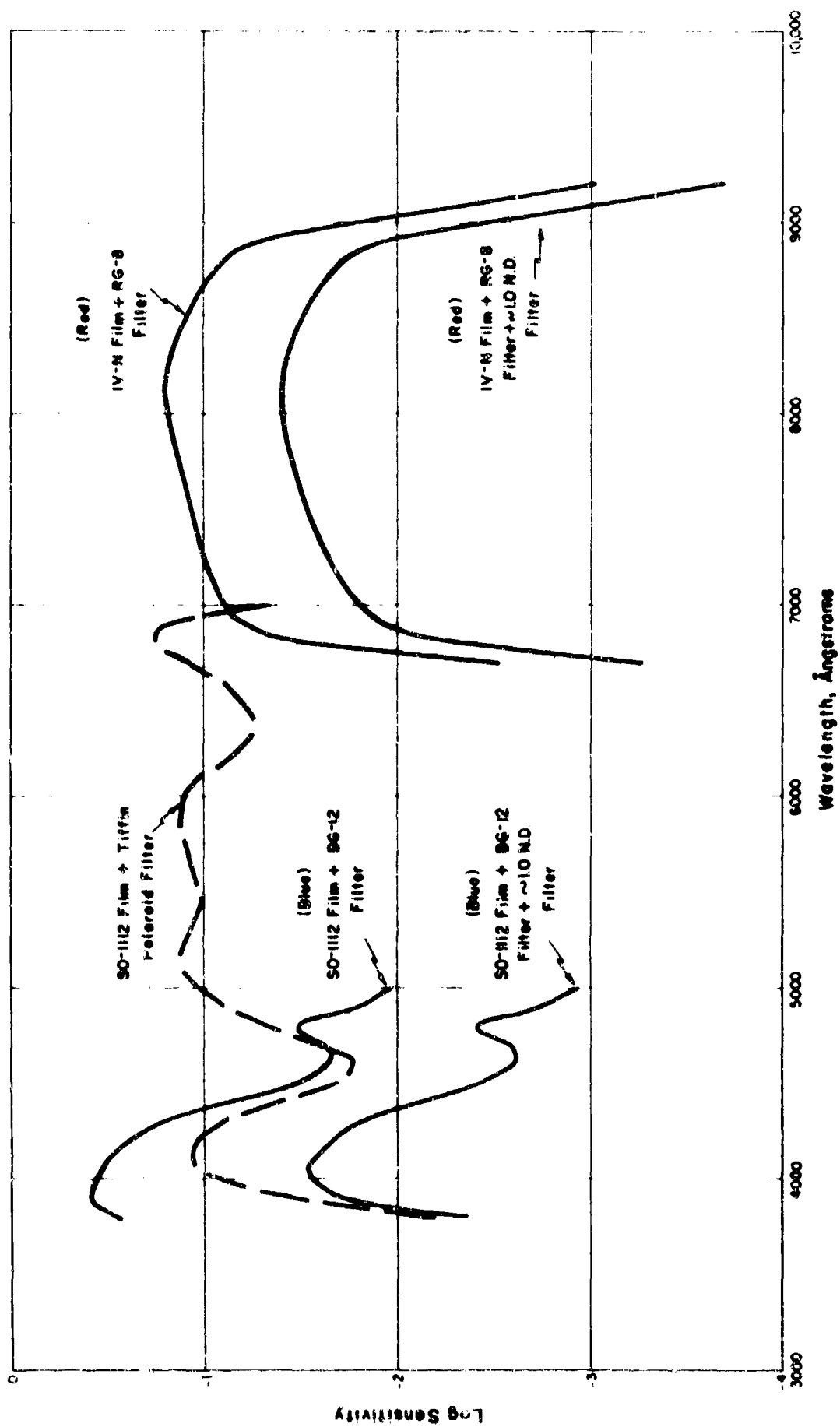


Figure 2.2 Sensitivity as a function of wavelength for the Red, Blue, and Polaroid systems. The units of sensitivity are $(\text{erg}/\text{cm}^2)^{-1}$ for film density 1.0, for the manufacturer's suggested development procedure. The ND-1 filter has attenuation higher than 10 in the Blue and lower in the Red.

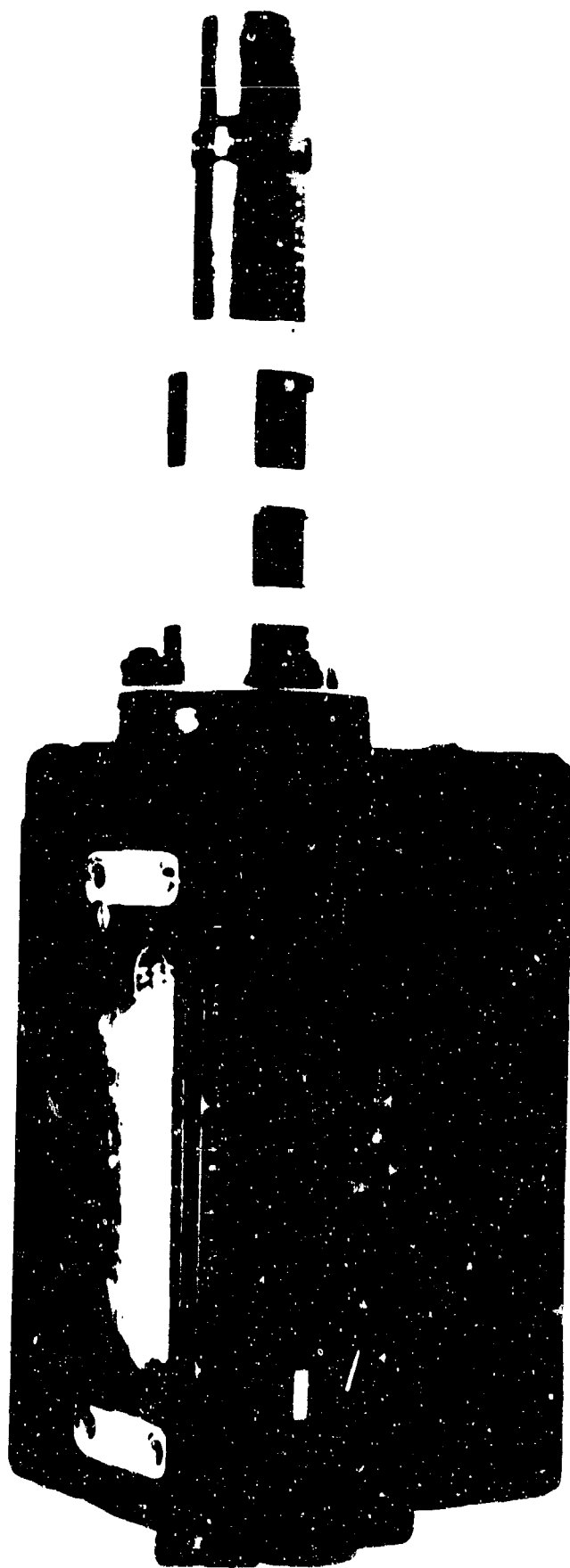


Figure 2.3 Complete assembly of N-9 camera with spectroscopic attachment.

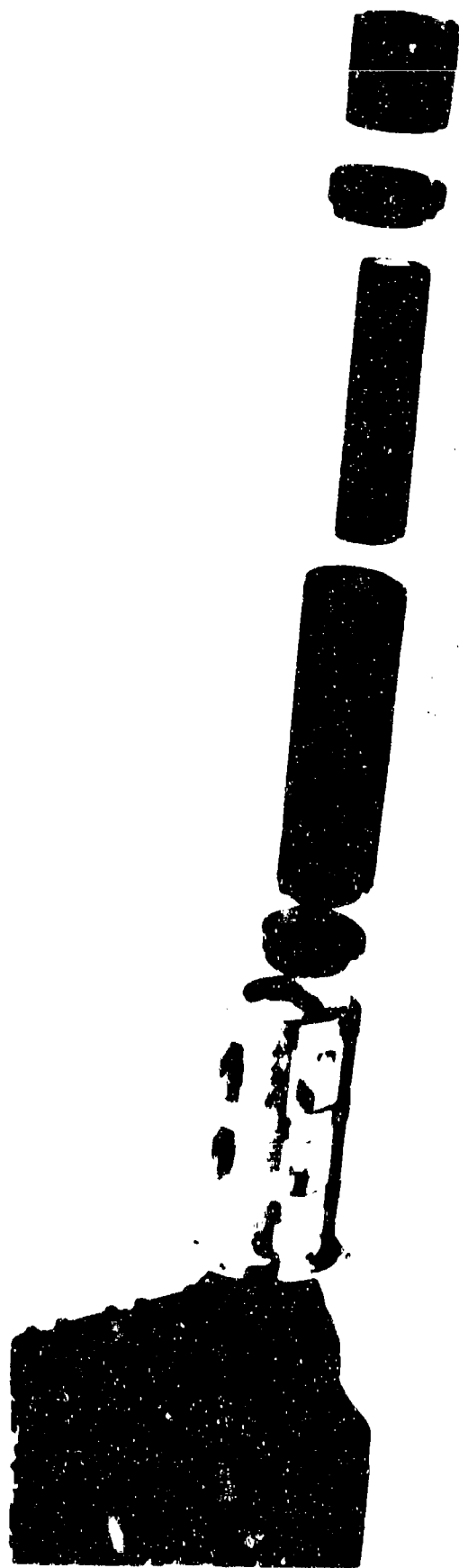


Figure 2.4 Exploded view of N-9 camera with spectroscopic attachment.

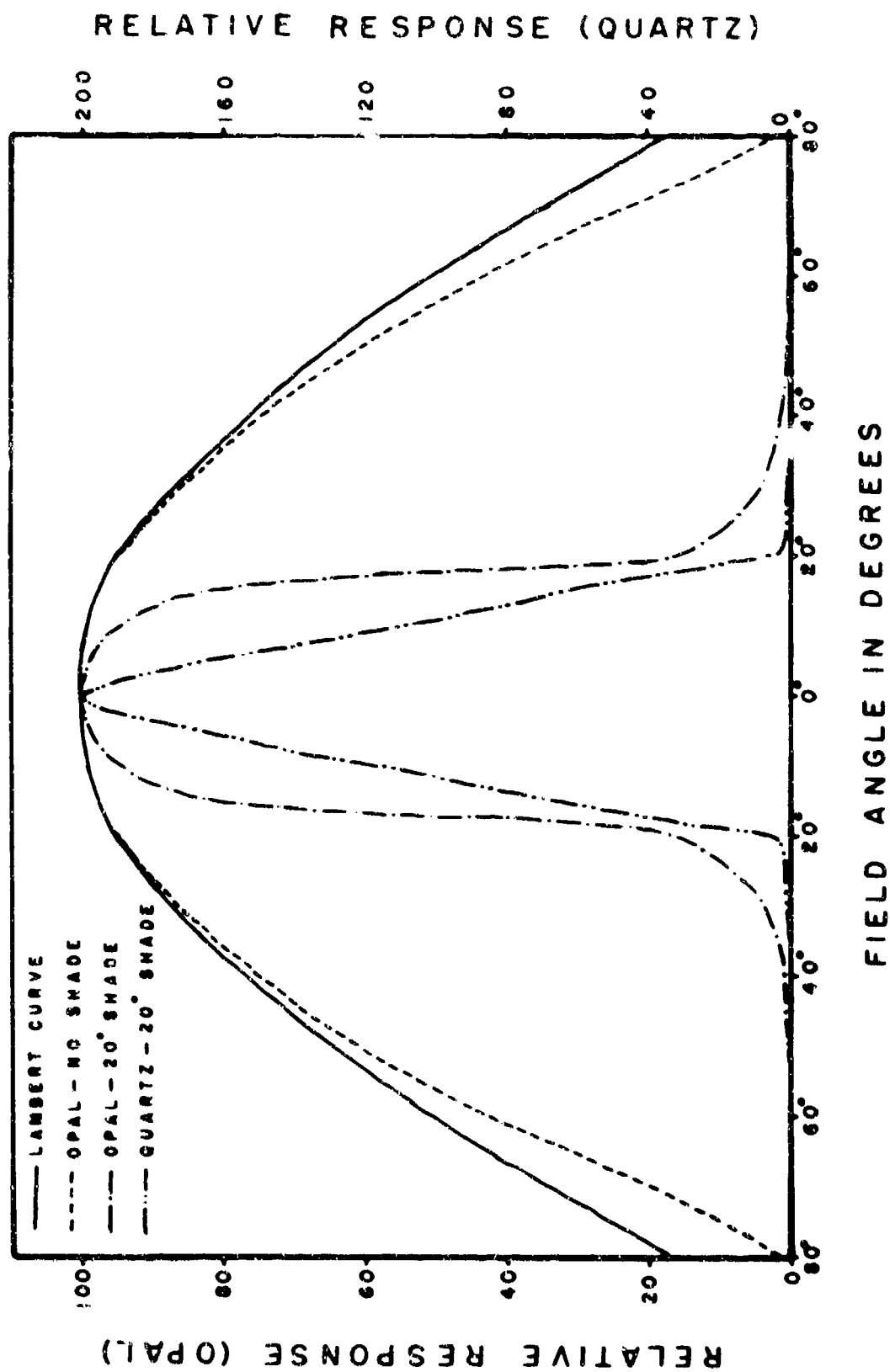


Figure 2.5 Response of spectrograph over various fields of view.

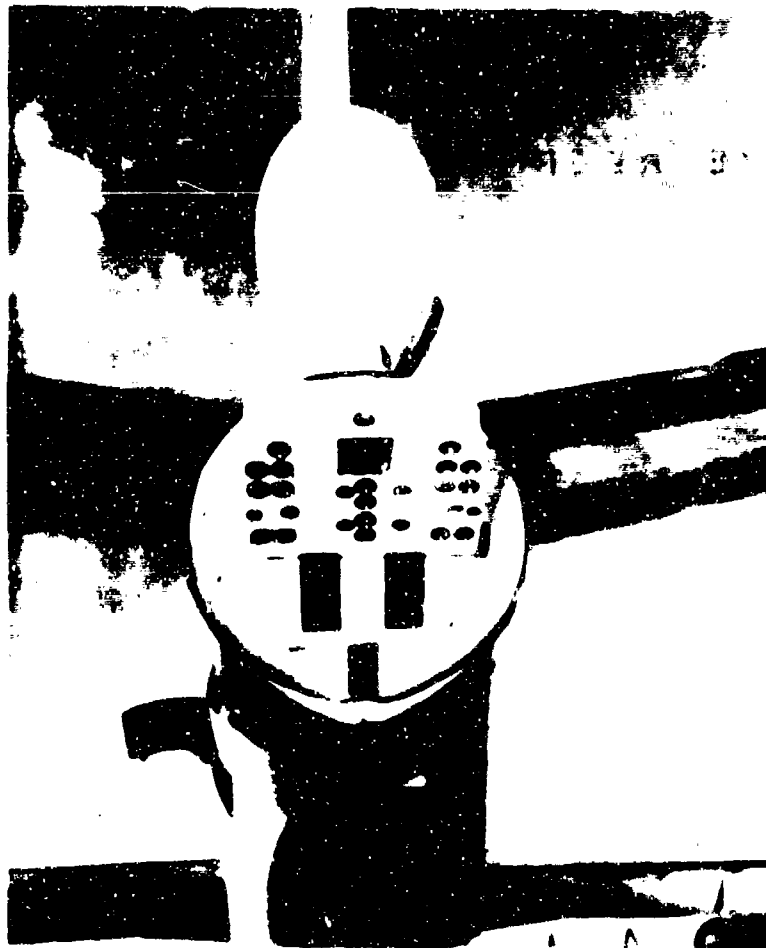


Figure 2.6 Tail instrumentation mount, B-47 (rear view).



Figure 2.7 Tail instrumentation mount, B-47 (side view).

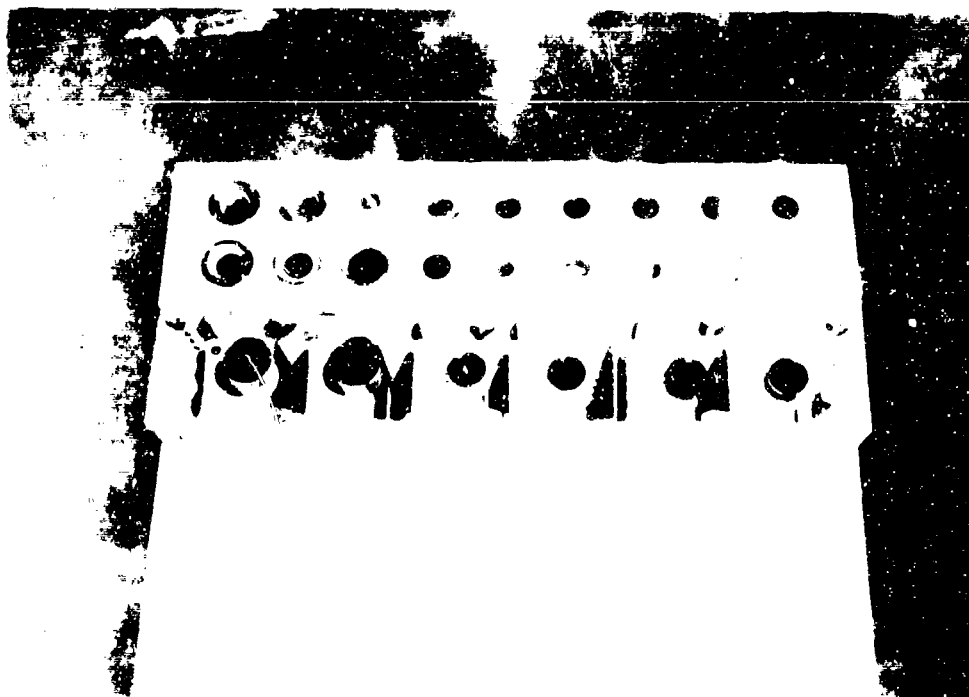


Figure 2.8 Tail instrumentation mount, B-52 (rear view). The camera cover plate is removed. Note the two different sizes of lenses on the four cameras on the left. This was an attempt to obtain a large fireball image, with a hedge against missing it entirely by use of the lens with a larger field of view on the second pair.



Figure 2.9 Tail instrumentation mount, B 52 (side view).

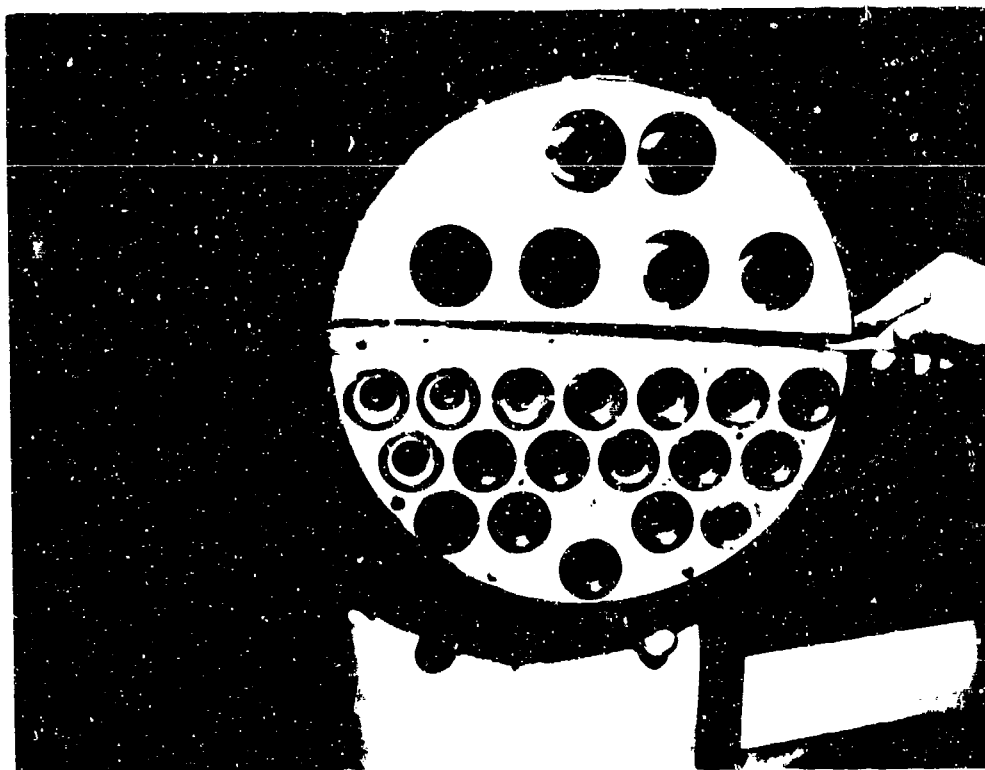


Figure 2.10 Tail instrumentation mount, B-57 (rear view). This picture shows a departure from the basic instrumentation in that two of the bottom four cameras were normally equipped with spectroscopic attachments. The configuration shown here was for maximum number of fireball records.

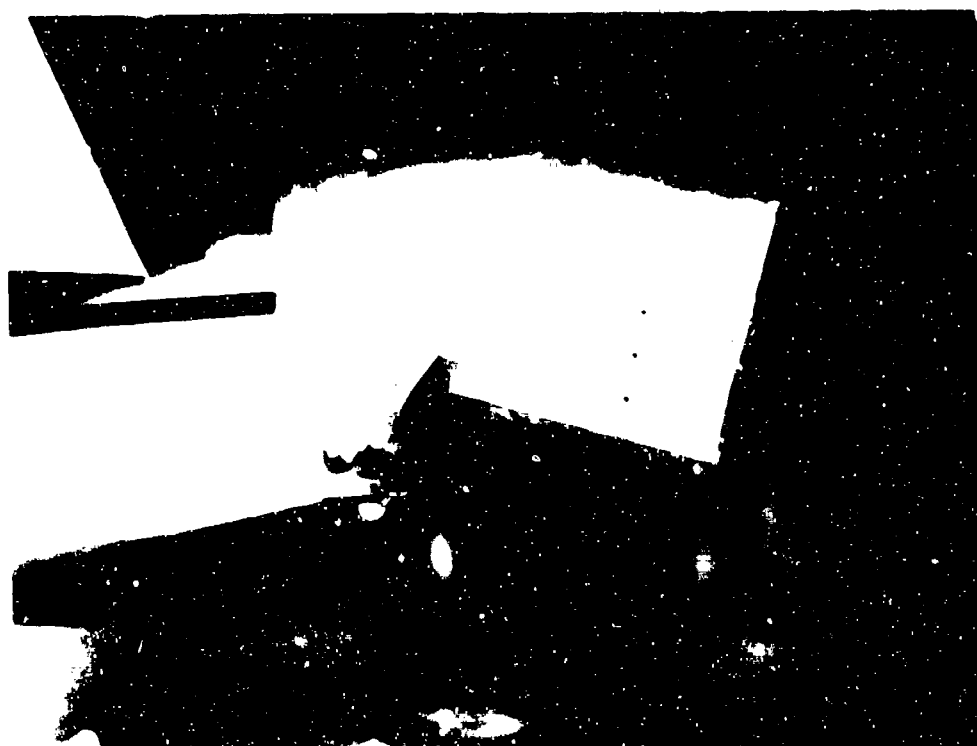


Figure 2.11 Tail instrumentation mount, B-57 (side view).

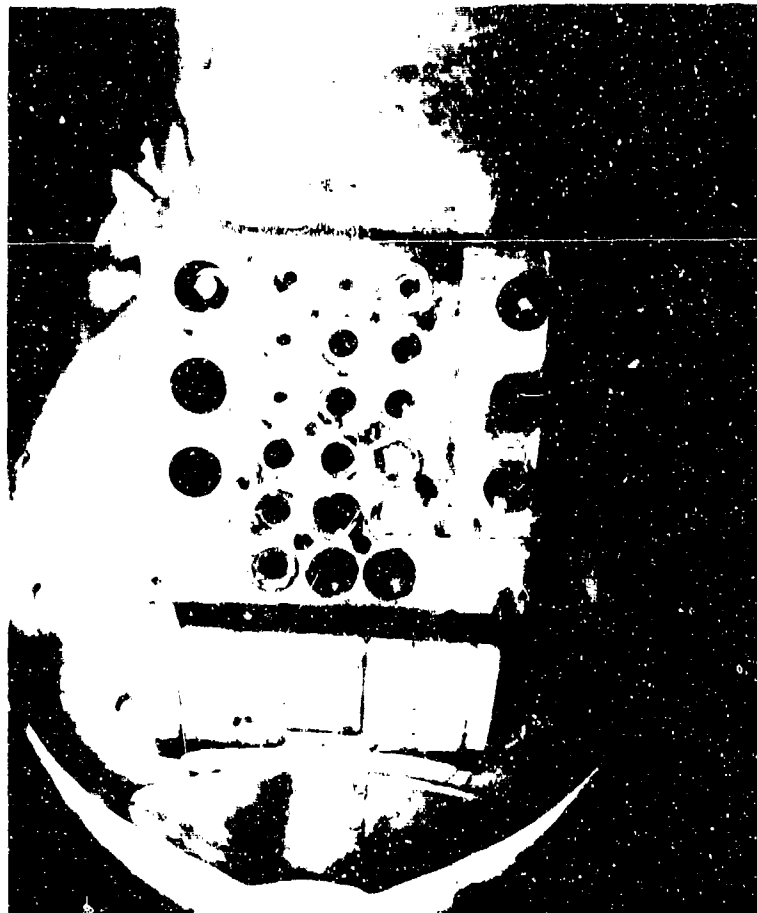


Figure 2.12 Tail instrumentation mount, B-66 (rear view). This photograph was taken after a mission on which the aircraft had developed a small hydraulic leak, but the dirt and moisture on the instrumentation was not unusual.

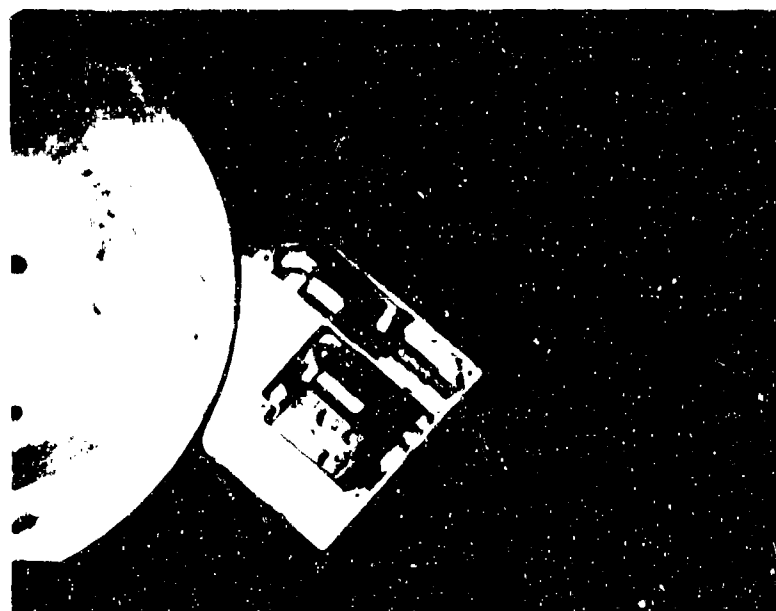


Figure 2.13 Tail instrumentation mount, B-66 (side view). The camera cover plate is removed. This was the basic configuration of instrumentation for this aircraft.

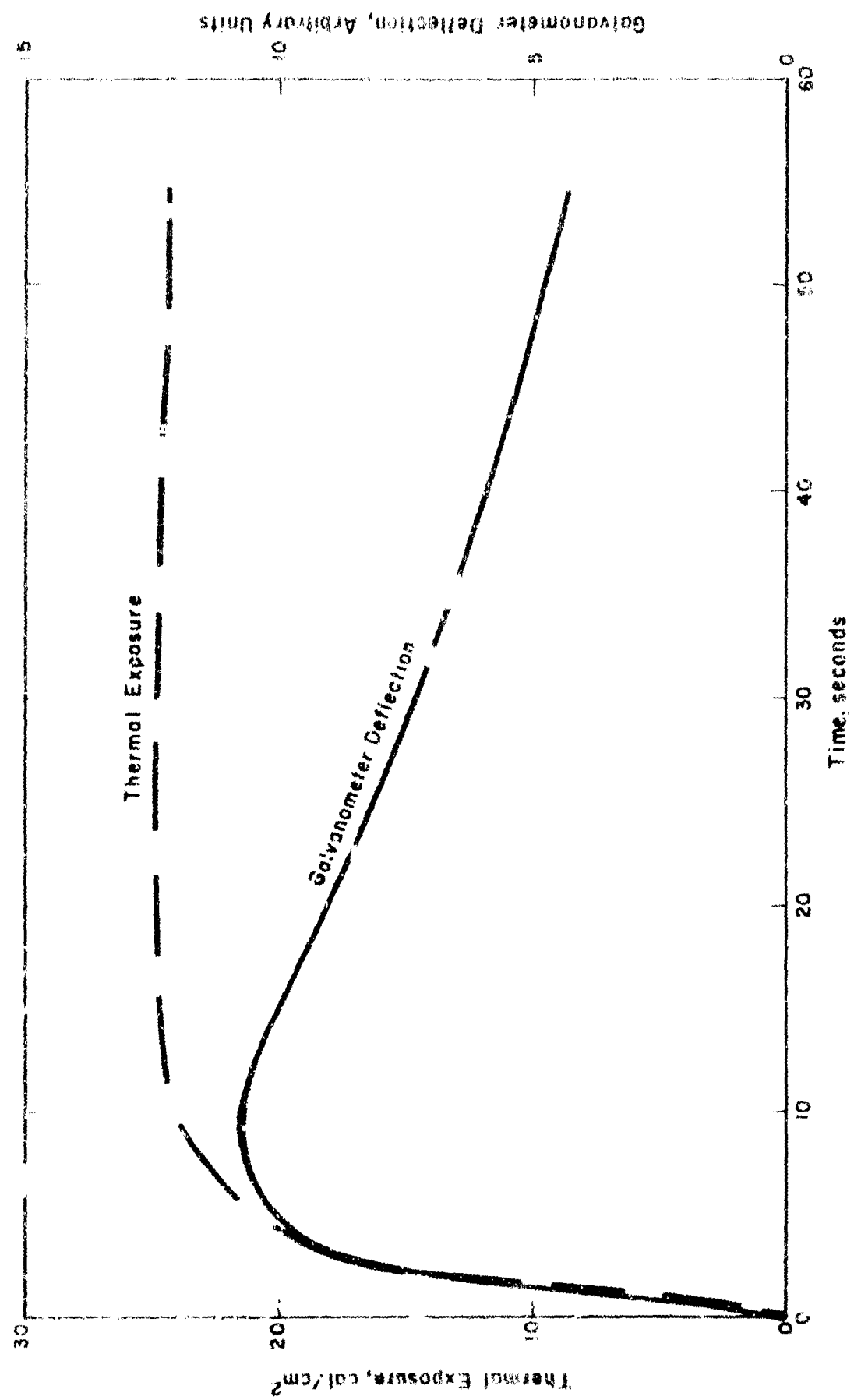


Figure 2.14 Radiant exposure as a function of time. The lower curve is the uncorrected data, i.e., galvanometer deflection as a function of time. When this curve is corrected for the rate of heat loss, the upper curve results.

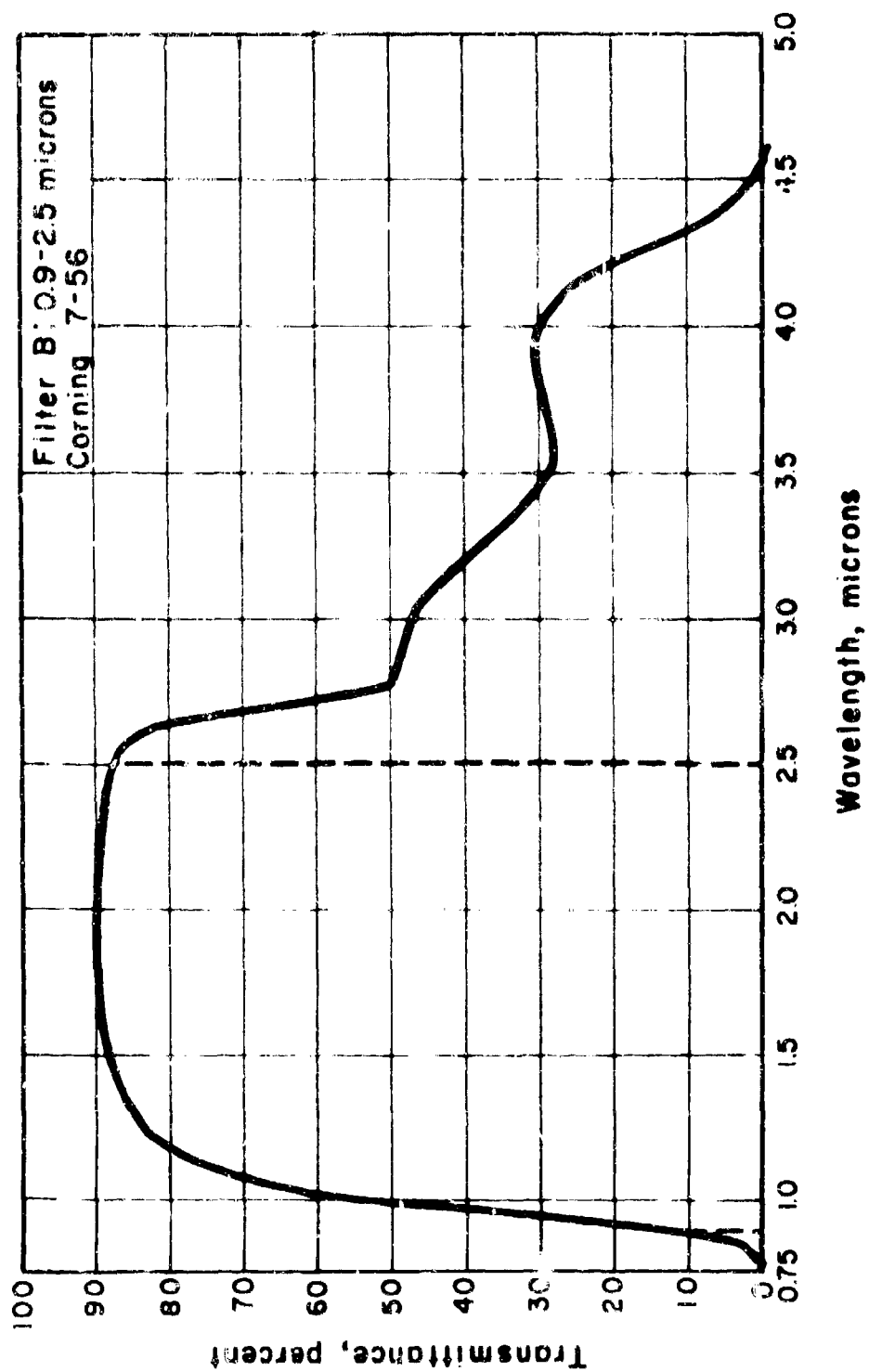
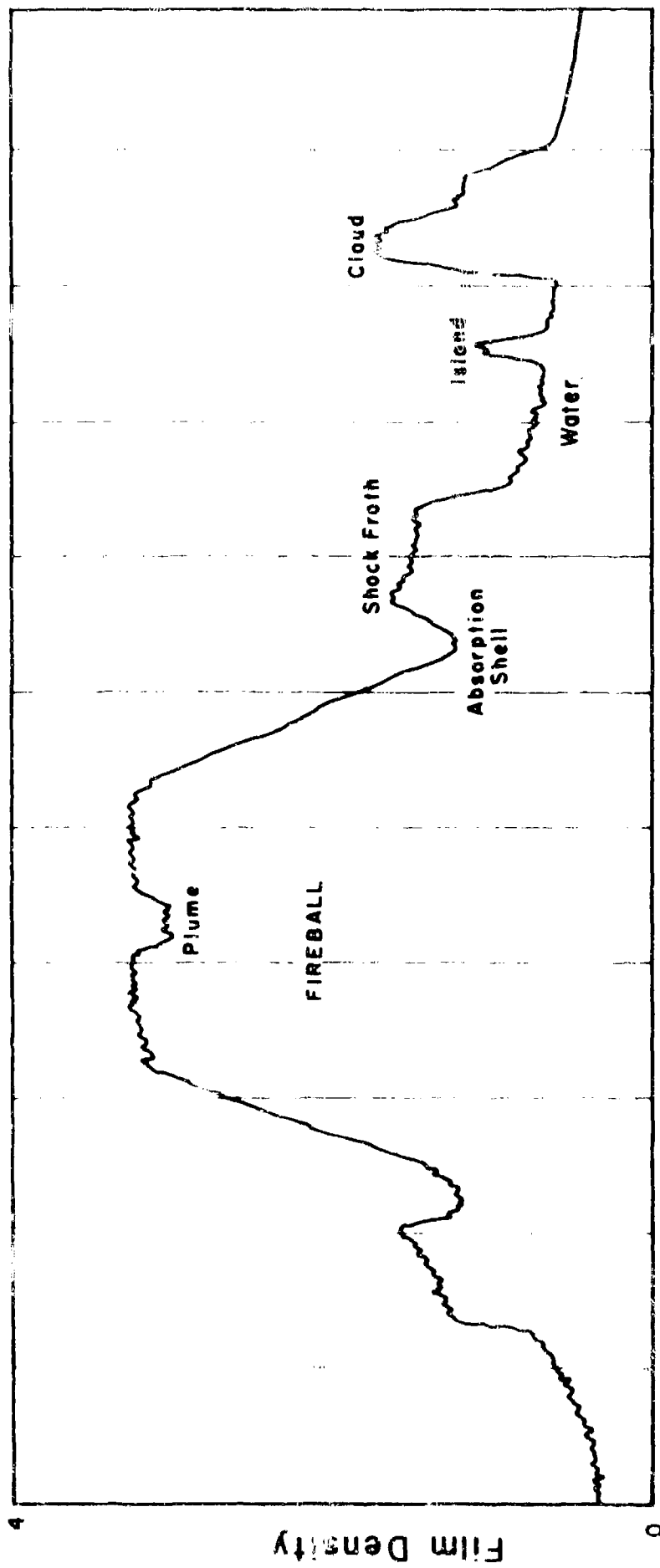


Figure 2.15 Transmittance of Filter B (Corning 7-56) as a function of wavelength. The dashed vertical lines indicate the transmission limits, 0.9 to 2.5 microns.



Distance Across Trace

Figure 2.16 Typical microdensitometer trace across the fireball and its associated albedo elements.

SECRET

Chapter 3

RESULTS

In all, there were 17 nuclear explosions, of which 11 had successful coverage by some or all of the airborne instrumentation installed in the four aircraft. The positions of the aircraft at time zero are listed in Table 3.1.

3.1 CALORIMETER AND RADIOMETER RESULTS

These results are presented in several tables and figures. Table 3.2 presents a summary of the effectiveness of the thermal measurement portion of the effort. Aircraft showing overall zero results either aborted the mission or had complete recorder failure.

Table 3.3 presents the thermal data, fully corrected for all instrumental calibrations. The figures show the radiant exposure and irradiance as a function of time for typical exposures of calorimeters and radiometers. B-52 results are not presented, because the required electrical calibration constants were not available prior to completion of data reduction. The tabulated results are considered final.

During five events (Seminole, Blackfoot, Kickapoo, Osage, and Yuma), no aircraft participated. During two events (Navajo and Tewa) three aircraft participated. During three events (Lacrosse, Erie, and Inca) two aircraft participated. During seven events (Cherokee, Zuni, Flathead, Dakota, Mohawk, Apache, and Huron), four aircraft participated. These figures (Table 3.2) include aircraft that subsequently aborted or had recorder failure. During Mohawk and Huron, the B-47 was positioned for side loads and so obtained minimal thermal records.

3.1.1 Summary of Cumulative Thermal Radiation Data. The data presented in Table 3.3 may be considered as a summary of the principal thermal effects of this series of tests. The columns give the following information.

Column I gives the Shot name and the approximate yield in kilotons.

Column II indicates the type of instrument used (C for calorimeter and R for radiometer), the field of view of the instrument (in general, either 90° or 160°), and the type of filter employed. The filters are described in Chapter 2. The filter designations and spectral characteristics are given in Table 3.4. For example, a calorimeter having a 90° field of view and transmitting in the wavelength region from 0.7 to 2.5 microns is listed in Column II of Table 3.3 as C-90-A. Similarly, a radiometer with a 90° field of view transmitting in the wavelength region of 0.2 to 4.5 microns is listed in the table as R-90-Q.

Column III gives the aircraft type less the bomber designation B, the position (station) of the instrument in the aircraft, and a letter expressing the orientation of the instrument. The letter F indicates an instrument pointing directly at the fireball, whereas the letter V (vertical) indicates an instrument whose receiving surface was parallel to and viewing the surface of the earth. The letters BS (representing backscatter) denote a calorimeter in front of either the pilot's canopy or the rear upper dome (Stations 3 or 4). Thus in Column III, an instrument located in the tail of a B-57 (Station 1) pointing directly at the fireball would be described by the symbols 57-1-F. Similarly an instrument located on the underside of the fuselage of a B-47 (Station 2) directed to view the water surface beneath the aircraft would be coded as 47-2-V.

The range at the time of maximum irradiance given in Column IV was chosen as the representative range to describe the event. Because the speed and course of the aircraft (outbound

from the events in virtually all cases) are known, the position of the aircraft at time of maximum irradiance is known. A numerical integration of the model irradiance curve as a function of time, given in Figure 6 of Reference 1, shows that about 25 percent of the total radiant exposure has been received by the aircraft at this time. The change in range during the fraction of a minute that thermal radiation is being received by the aircraft's instruments is small compared to the distance of the aircraft from the event. As a result, it is possible to consider the aircraft's range constant during the entire period in which significant amounts of thermal radiation were being received. Using this assumption, the error made in the determination of Q due to the divergence of the thermal radiation as the aircraft moved away from the source is small and can be neglected. The radiant exposure Q need not be and is not corrected for the small change in range that occurred.

Column V expresses the best estimate of the total radiant exposure experienced by an aircraft in terms of calories per square centimeter of calorimeter detecting surface.

Column VI expresses the best estimate of the maximum rate at which each square centimeter of radiometer detecting surface was accepting the thermal energy from the device.

Columns VII, VIII, and IX have been added for comparison and analysis purposes. Column VII expresses the quantity QD^2/W where Q is the radiant exposure in cal/cm², D is the range of the aircraft at the time of maximum irradiance in units of kilometers, and W is the yield in kilotons. This parametric form of presentation was chosen because this parameter admits of ready comparison with the scaling data given in Reference 1. From elementary physical arguments, it is expected that this parameter will be relatively constant. For convenience, the specific thermal energy is defined as

$$E = \frac{QD^2}{W} \quad \frac{\text{cal-km}^2}{\text{cm}^2\text{-kt}} \quad (3.1)$$

Column VIII is the total radiant exposure of the vertically oriented receivers of Column V multiplied by the secant of the angle θ as defined in Figure 3.1. This is done to remove the obliquity factor tending to decrease the radiant flux received by a vertically oriented receiver over one viewing the fireball directly.

Column IX shows the effective value of E obtained from the vertically pointing calorimeters. A comparison of Column IX with Column VII will help to decide whether or not the albedo of the surface can be determined.

3.1.2 Time History of Thermal Radiation Measurements. A large amount of thermal data was taken in the course of the project, all of which was time-dependent. In the preceding section, this time-dependency was effectively eliminated in order to show total or cumulative thermal effects. This data is probably in the most useful form from the old operational point of view. The scientific value of the data is enhanced by knowing the time rate of change of both the radiant exposure and the irradiance. In this section, the data obtained by certain calorimeters and radiometers as a function of time is presented for familiarization purposes. The data is judged to be typical. Shot Dakota was selected as the thermonuclear event to be presented when possible. It was in the megaton range and was the most completely documented shot photographically. Unfortunately, the backscattered radiation was not successfully measured for this event. Instead, the backscattered radiation observed during Shot Tewa has been substituted. A description of this selected data follows.

Figures 3.2 and 3.3 show the time-dependence of the radiant exposure and the irradiance as observed from a B-57 whose altitude and horizontal range at time zero were 17,650 and 25,020 feet, respectively. The aircraft was on an outbound track. Figures 3.4 and 3.5 similarly show the time sequence of radiant exposure and the irradiance as observed from a B-66. The B-66 was flying an outbound track at an altitude of 16,000 feet and horizontal range of 13,100 feet at time zero. Because both aircraft were simultaneously observing the fireball in Shot Dakota, the difference in values of thermal exposure and irradiance are due to the different slant ranges of the two aircraft. Apart from the range effect, and the internal inconsistencies mentioned

earlier, the two sets of figures should present identical values.

Figure 3.2 is typical of the data obtained from the calorimeters. Time is plotted on a logarithmic basis to compress the scale at the highest values. It will be noticed that very few seconds are required to receive all the thermal energy possible from the event. This effect is shown by the flattening out of the radiant exposure at times in excess of a few seconds. The same trend is shown for the filtered calorimeters also. In addition, the total radiant exposure is a function of the spectral limits of the filter and the transmissivities of filter and atmosphere in the transmitted spectral range.

Figure 3.3 points up the variation with time of the rate at which the energy is received. A logarithmic time scale has been used, because it is felt that this plot emphasizes the time-dependence better. In a conventional plot of irradiance versus time, the area under the curve is proportional to radiant exposure. In Figure 3.3 this relationship is implied only.

Figure 3.6 presents plots of radiant exposure versus time as viewed by three calorimeters at the same station during Shot Apache. A discussion of variations in this data is presented in Chapter 4.

3.1.3 Backscattered Radiation. Another important phase of the thermal program was the investigation of the amount of energy scattered into the aircrew space by the clouds and air in the half hemisphere ahead of the aircraft. Because of the orientation and the aperture of the instruments, scattered radiation from a considerable portion of the sky ahead of the aircraft was received. This radiation will be referred to as backscattered radiation or simply backscatter. The total backscattered radiant exposure for those events where this parameter was successfully observed is given in Table 3.5. In general, the radiant exposure is of the order of a few tenths of 1 percent of the radiant exposure received directly from the fireball.

Table 3.5 gives all of the data that has been received on the backscattered radiation. The range and approximate device size have been included for the convenience of the reader. The most important information is obtained from the last column, which gives the ratio of the average backscattered radiant exposure \bar{Q}_{BS} to the average radiant exposure received from the fireball \bar{Q}_F . Except for Flathead where the ratio appears to be abnormally high, the remaining ratios are of the same order of magnitude, i.e., 1×10^{-3} to 5×10^{-3} . Although there appears to be some trend showing a decrease of the ratio \bar{Q}_{BS}/\bar{Q}_F as the device size increases, consideration should be given to the third and fifth columns before any conclusions are drawn. These two columns are the individual values of the radiant exposure from which the ratio in the last column is constructed. There is large variability in the data.

Further refinement in the analysis of the backscattered data does not seem justified because of the paucity of the data and the lack of knowledge of the details of the environment under which the data was collected. For example, the cloud cover is known only by conventional meteorological description. As the purpose of this experiment was to measure typical thermal exposures experienced by the aircrew under the conditions of the test, the mission is accomplished if the measured values given in Table 3.5 are interpreted as order of magnitude results.

3.2 PHOTOGRAPHIC RESULTS

In this section a description of representative series of photographs of each of the detonations, is presented. Shot Mohawk, however, is not presented, because the thick cloud layers obscured detail; nor are Yuma, Seminole, Blackfoot, Kickapoo, and Osage, which did not have photographic coverage. Each series was chosen on the basis of the quality of its photographs and its pointing up the principal features of the detonation. Furthermore, a representative group of pictures are described, in that Red and Blue and Polaroid photographs taken from several altitude angles under conditions in which the fireball itself covers various fractions of the field of view (that is, the cameras used lenses of various focal length) were chosen for display. The photographs are presented as Appendix A. Field coverage of the various detonations, and the film records successfully obtained, are listed in Table 3.6. Not all the photographic records obtained are of high enough quality for analysis; for example, none of the Inca series yield useful information

about this detonation. The backscatter and albedo records have not been reduced.

The photographic parameters of the several series are shown in Table 3.7. Distance scales, shown in the last column, were calculated by normalizing to the shock wave size. The frames shown are scaled by the square-root-of-yield law to the times of those shown for Shot Dakota: Frame Zero, 7 (minimum), 15, 30, 45, 66 (second maximum), 90, 115, 150, 200, 250, 325, 375, 425; and even farther if anything of interest shows on the photograph. Occasionally other frames are shown also.

The photographs, presented as Appendix A, are reproductions of enlargements of negatives taken with the Polaroid camera, of the projection of the original film on the ground glass screen of the microdensitometer (Chapter 2). Consequently, at least four reproductions are involved, and some detail is necessarily lost. Furthermore, the latitude of the prints is low, and occasionally, detail of the brighter features has been sacrificed in order to show up the dimmer ones, such as clouds, air shock, and islands.

3.2.1 Qualitative Picture of a Detonation. For orientation purposes there is presented here a short description of the various facets of nuclear detonation contributing to the thermal flux, as observed in the several series of photographs; a more detailed discussion is given in the next chapter. The aircraft are typically at elevation angles ranging from 19° to 85° , (as seen from ground zero) in level flight radially away from the explosion site. The slant ranges vary from 11,000 feet for the lowest yield devices (15.5 kilotons) to about 50,000 feet for the largest (5 megatons). The detonations are water or low tower shots, with the exception of Cherokee which was an air burst, and Lacrosse (17 feet above ground surface).

Frame Zero. The camera shutter operating at 64 frames per second is alternately open for 1 msec and closed for 15 msec. The cameras are not synchronized with time zero, nor with one another; consequently Frame Zero will occur at a different time on each camera and at any time extending from time zero (the detonation occurring just as the shutter is closing) up to about zero + 15 msec. Actually during the 1-msec shutter time, there is considerable fireball development for small bombs and/or very early times. For example, for Dakota the fireball radius grows to 250 feet in the first millisecond, and to 330 feet in the second millisecond time interval.

Red Frame Zeros are characterized by a bright, symmetric fireball, which illuminates the clouds, islands, and air in the field of view. The corresponding blue frames are far less bright, and in fact are often missed altogether. In no case is the blue light from the fireball surroundings intense enough for its angular distribution to be measurable with high accuracy.

Dip to Minimum. The frames immediately following Frame Zero show a fireball of larger radius and diminished surface brightness. No outside structure is yet apparent. Generally the blue flux is below the threshold of the film, and the blue image disappears. During this period, individual hot spots—local areas of brightness—appear; their motion, outward with the expanding fireball, can be observed, although the blue fireball continuum completely disappears (Section 4.4.1). Thermal flux minimum occurs at roughly $0.0031/W$ second; where W is the yield of the weapon in kilotons; this is at about Frame 1 for Erie (14.9 kt) and Frame 14 for Navajo (4,500 kt). After minimum, the surface brightness of the fireball increases again.

Development of Shock Froth, Absorption Shell, and Plume. At minimum, the shock wave separates from the fireball (breakaway), and advances ahead of it, roughing up the water surface and making it a rather good diffuse reflector (shock froth). An absorbing, dark concentric envelope (absorption shell) appears about the fireball in slightly later frames. The outlines of the fireball itself are somewhat fuzzy; the apparent radius of the luminous fireball often appears to decrease just after minimum.

At the top of the fireball is observed a small bright area (the plume) which darkens and grows in succeeding frames. This plume obscures in late frames an appreciable fraction of the thermal radiation going upward from the bright fireball. These features of the fireball are shown schematically in Figure 3.7.

At about $t = 0.032 \sqrt{W}$ second (henceforth referred to as $t_{\max II}$) the fireball reaches maximum thermal flux output.

Late Times. The fireball grows only slowly after this second thermal maximum is reached; the absorption shell thickens and its light attenuation appears to decrease. The fireball starts to lose its hemispherical shape as it rises from the detonation site. The plume becomes almost as large as the fireball itself. The air shock striking nearby clouds causes them to evaporate; this has the effect of reducing the fraction of the thermal flux that is scattered from clouds (cloud albedo). At very late times, the lowered pressure behind the shock front causes clouds to re-form (Wilson cloud effect); a ring (like a circular amphitheater) of these clouds is seen around the now-dim fireball, the risen fireball remaining unobscured from most aircraft viewing angles. In general, dense clouds can reduce (by absorption) the thermal flux from the fireball, or (by reflection) increase the flux by a considerable amount.

3.2.2 Shot Erie. A photographic series of this 14.9-kt shot is presented in Figures A.1 through A.15. This detonation was on a 300-foot tower. The island (Yvonne) and nearby reefs show clearly from the 70° altitude angle. Frame Zero is found by application of the shock theory to occur at 10 msec after detonation; this is 2 msec before breakaway, which occurs between Frame Zero and Frame 1. The absorption shell shows clearly in Frames 1 through 5, and less clearly thereafter. Note the jagged shape of the fireball and the variable thickness of the absorption shell, the exterior outline of which is more regular; the absorption shell does not follow the shape of the surface of the luminous region. In Frame 1 the thickness of this ring is about 50 feet, and it is quite opaque; no island features are visible through it. The fireball is then some 350 feet in radius and touches the ground.

By Frame 2 some of the details of the "feet" of the island are visible through the absorption shell (this is not obvious on the print) and in Frames 3, 4, and 5 the absorption shell becomes increasingly transparent. This decrease in opacity of the absorption shell is thus observed for surface bursts of all yields from nominal kiloton to at least 5 Mt.

The shock froth is definitely brighter than are the "legs" of the island; this is observed also in Shots Flathead (Section 3.2.5) and Dakota (Section 3.2.11).

The air shock shows faintly in Frame 5 and in Frame 8 at second thermal flux maximum. Puffs of dust kicked up on the island are clearly visible; they give the shock froth its apparently rough front in frames near second maximum. The fireball of this particular relatively small weapon evolves into a diamond shape (Frame 18 et seq); no plume is seen. Note the shadow cast by the dust cloud on the shock froth (Frame 24). The dust cloud itself has high albedo; note the bright puffs on the reef at 3.0, 38.5 in Frame 30. By Frame 39, however, it appears that the shock wave is raising very little more dust from the coral reef.

The plume of this tower shot (during which the fireball did not touch the ground until about second thermal flux maximum) is conspicuously absent.

3.2.3 Shot Lacrosse. The photographic series of this 39.5-kt shot is presented in Figures A.16 through A.28. These Blue photographs of a land-water (shoreline) detonation are taken from an altitude angle of about 65°. The detonation took place 17 feet above ground level.

Two Frames Zero are shown, to illustrate the criticality of the photographic reproduction. Rocket trails show clearly, to the right of the detonation site. The fireball is seen to be quite asymmetric. It is understood that, in this test detonation, a considerable amount of matter was around the weapon, and presumably, the detonation is perturbed by the asymmetry of the site. In Frame 1 some structure is still apparent, but the outside rim of the fireball is quite symmetric; note the hot spots and the large dark central area which has a thin bright rim.

Minimum occurs between Frames 1 and 3. In Frame 2, this central area shows bright, as it does in Frame 3, where a considerable structure is again apparent. The bright knot has a ring around it resembling a miniature absorption shell. By Frame 13, second thermal maximum, the plume is already covering almost half of this projected area of the fireball.

The lack of illumination of the near side of the shock froth is peculiar and may be due to

possible shock passage over land or shoal not seen on the photographs. No cloud appears in this region on a close examination of Frame Zero. The time history of this darkening suggests that it is caused by the variation in fireball surface brightness, possibly due to land-water asymmetry and/or experimental structures. This variation does not show on the photographs, nor is it well resolved on a test microdensitometric trace; but its existence is indicated by the very bright right-hand shock froth in Frame 9, and the general fluctuations in shock froth brightness seen throughout the series. Another noteworthy feature is the group of horizontal dark lines in the left-hand shock froth, in Frames 13, 18, and 23; these may be shadows of structures nearby. In later frames the 45° streak on the left side of the fireball, which first shows in Frame 3, is still visible.

It is noteworthy that the characteristic blue air shock attenuation, seen in all other Blue series, does not show in these photographs.

3.2.4 Shot Huron. The photographic series of this 250-lb shot is presented in Figures A.29 through A.41. This series shows the routine Blue behavior: a dim Frame Zero (which shows considerable limb darkening in a densitometer trace), hot and dark spots, the horizontal fireball belt line, and obscuration behind the fireball. At this somewhat low angle (49°) the intensity minimum in the shock froth is not pronounced, especially in the foreground (compare Flathead, next section). As was observed with Dakota and Flathead, the Blue island albedo is well less than the shock froth albedo. The Blue obscuration by the plume is clearly less than for Lacrosse.

3.2.5 Shot Flathead. The Blue series for this 365-kt shot is viewed from only 5° from the vertical (Figures A.42 through A.56). The hot spots in Frame 4 (minimum) seem to be concentrated near the fireball limbs, away from the center. In Frame 18 the shock froth and its mid-line brightness minimum are visible; note how this ring of minimum brightness within the shock froth brightens with increasing time. This is one of the series that gives evidence for the Blue absorption of the air shock (Section 4.4.5). A bright ring (tidal wave albedo?) appears within the absorption shell. The shock froth albedo at this geometry, calculated with the 85 percent subtraction as described in Section 3.2.11, is 1.8 times as great as the island albedo. This again is in contrast to what is observed in the complementary Red photographs (not shown). In the Red, the island outside the shock froth has the same albedo as the shock froth, to within about 7 percent; but when the island is inside the shock front, its corrected albedo falls to about (1/1.6) of the shock froth value.

From this similar high angle of view the obscuration by the plume is signally less than for Lacrosse.

3.2.6 Shot Apache. The photographic series of this 1.9-Mt shot is presented in Figures A.57 through A.79. Three series of photographs of this water detonation are shown, a Red series and a Polaroid pair.

Red Series. This group of pictures is of interest because the camera was fitted with a neutral density 2 filter. Consequently, the brightnesses are reduced by roughly a factor 10 below the other Red series shown, and certain features are optically resolved on the film. The fireball is only faintly visible on the original negative at minimum; the dark belt shows in Frames 19 and 39. A scan across this belt shows it to be some 20 percent less bright than the surrounding region (such a difference in a line is easily missed on the densitometer trace, without a guiding visual identification); the lower segment of the fireball is generally less bright than the upper, and this vertical effect is also observed in the other Red traces. Another feature observed in the Blue photographs, and only rarely in the other, more dense, Red ones, is the fireball puffiness at late frames. Scans of Frames 38 and 88 (second thermal flux maximum) show that the fireball has very little limb darkening; this is the same behavior as that observed on the Dakota Red films, with both neutral density 1 and with no neutral filter. This indicates that the characteristic flat top of the Red microdensitometer trace is not an effect of instrumental or photographic saturation.

This series serves to illustrate the point that casual photographs of detonations must be interpreted with caution because of film latitude and saturation effects. With a factor-of-10 attenuation, the horizontal belt and the late-frame structure of the fireball are visually resolvable, as they are in the several Blue series; the fireball is barely visible (perhaps not at all in the reproduction) at minimum. Other Red features, however, are similar to those observed in less filtered L. photographs.

Polaroid Series. In this low angle ($\sim 19^\circ$) series, the horizontally polarized Frame Zero (37219) occurs a few milliseconds before the vertically polarized Frame Zero. The photographs have less exposure than the Dakota polarized pair, since the lens was stopped to f/16 instead of f/5.6 and a neutral density 1 filter was used.

In Frame Zero the light specularly reflected from the water surface is clearly visible. At these angles between the aircraft and the (extended) fireball, Fresnel's laws predict roughly 20 percent specular reflection for θ and 5 percent reflection for ϕ ; this is qualitatively borne out by the photographs. The total albedo drops off quite sharply at the sides of the reflected image of the fireball. This points up the fact that, at this low angle at least, the Lambert water albedo is small compared to the specular albedo.

In Frame 19 no difference between the two planes of polarization is resolvable. Evidence of the absorption shell appears, and above this dark region is a bright topknot some 600 feet across, which is destined to become part of the plume (Frame 39). The horizontal belt and a lens structure of the fireball, show clearly on these photographs. The specular reflection from the water, of the light from the θ fireball, shows up to Frame 148; in the ϕ photographs, it is barely resolvable in Frames 58 through 106. The specular nature of this reflection is emphasized by the sharpness of the shadow at 3.7, 35.7 of the cloud above it on the photographs. What appears to be a reef (off island Gene) is illuminated on the lower right of these θ photographs.

Note that the specularly reflected light from the unshocked water surface, is more intense than the adjacent shock froth albedo at this low angle. In this forward direction, there appears to be a diminution of the shock froth brightness (compared to the brightness on the side). This is in contrast to the higher angle Polaroid observations of Dakota (Section 3.2.11). Presumably this darkening in the line of sight is due to self-shadowing by the roughness of the shocked water, which is here seen at nearly grazing incidence.

Another feature of these photographs is the narrow bright ring on the water surface inside the absorption shell, which is visible in both polarizations as well as in the Apache Red photographs. In Frame 148 a (spurious) streak has developed on the upper right of the ϕ series. A separation and rise of the fireball is visible in late frames.

3.2.7 Shot Zuni. The photographic series of this 3.38-Mt shot is presented as Figures A.80 through A.92. This Red series is taken from an observation angle of 25° , which is 6° higher than the Apache Polaroids.

In Frame Zero the relatively large number of local clouds is brightly illuminated; the fireball is not well reproduced, but it shows clearly in the original negative. Frame 12 (minimum) shows rather large hot spots and the horizontal dark belt, as well as the structure effects only occasionally resolved in the Red. The limb darkening here is quite apparent. In Frame 27 the absorption shell is seen to obscure light from the upper-right cloud, which is unusual in acting as an excellent viewing screen. The plume has a bright, luminous crown about 500 feet across, which has evolved from the large hot spot at 3.1, 38.2 in Frame 12. By Frames 55 and 83 this bright area has cooled to such a degree that it is no longer distinct from the rest of the plume.

The obscuration of the cloud by the absorption shell is even more clearly shown on Frame 55. Frames 83 and 121 have been printed to show the inner absorption shell, which is bright but still transparent to the light from the shock froth on the side of the fireball. In Frame 121 (second thermal flux maximum) the narrow (~ 150 -foot) bright ring on the water at 6.0, 37.0 shows inside the absorption shell. This ring appears to evolve into the water wave which appears in Frames 165 et seq. and which is a dominating feature in Frame 459. By Frame 212 there is evidence of the rising of the fireball; it is quite well separated from its base by Frame 368. Note that the dim inner absorption shell fills up this cleavage (Frames 286 through 459). The outer absorbing region is resolvable on all the original photographic frames.

3.2.8 Shot Cherokee. There was no successful photometric photography, of the type described in this report, for this 3.8-Mt detonation. The reproductions show only some Kodachrome frames, made at 32 frames/sec from an F-84 fighter plane at the great range of about 131,000 feet. These are negative prints, making bright areas appear dark in the reproductions. Very little detail is resolved even on the original film; the photographs are included for the sake of completeness and in the interest of showing some of the qualitative facets on the only megaton-range air detonation in the series (Figures A.93 through A.108).

The situation of poor resolution is complicated by the large number of cumulus and cirrus clouds in the field of view of the camera. The fireball at first appears like a bright orange sun (the colors shown by the Kodachrome are not to be taken too seriously because of possible saturation effects) which has a specular reflection in the water, similar to that of the Apache Polaroids except for the effect of the 5,000-foot altitude of burst; this reflection is visible up to Frame 239. The fireball appears white in the Kodachromes in frames near second thermal maximum. The air shock touches the water at about Frame 38; however, neither shock froth nor any absorption shell are resolved in the Kodachrome pictures. The fireball should touch the water surface at maturity, about Frame 100; this also is not observed. In Frames 311 et seq. the old fireball appears to start to split in two about a horizontal centerline. Wilson clouds, not clearly indicated in the reproductions, enclose the fireball at late times (\geq Frame 200).

3.2.9 Shot Navajo. This is a rather routine Red series for this 4.5-Mt detonation (Figures A.109 through A.127). The bright area that is to become the plume shows a dark ring around it in Frames 11 through 32, much like an absorption shell; however, part of this may well be the dark smoke of the developing plume underneath the bright topknot (note the low-angle Apache and Zuni views showing the topknot above the plume); but the local absorption shell is larger than the plume at this time (see, for example, Frame 24), and this cannot be the full explanation.

A flaw in the optical system shows as a dark streak in the lower right from Frame 15 on; and there is lens fogging from Frames 141 through 321. Wilson cloud is visible in Frames 650 et seq. One feature that does not show in the reproductions, is that the absorption shell is noticeable up to Frame 950.

3.2.10 Shot Tewa. This is also a routine Red series, albeit a rather dim one, for this 4.6-Mt shot (Figures A.128 through A.140). Note that the air light in Frame Zero is not very intense, and that the horizontal bifurcation of the fireball shows up through Frame 66 (half the time to second thermal maximum). It is hard to reconcile this loss in surface brightness of the bottom part of the fireball with the photogrammetric parameters; the slant range of 50,000 feet is not anywhere near large enough to explain the loss as being due to increased attenuation (Chapter 4). The fireball surface structure shows clearly in late frames.

3.2.11 Shot Dakota. In this section are presented commentary pertinent to eleven series of photographs from this 1.1-Mt shot (Figures A.141 through A.256). The photographs serve to point out the important features to be discussed in Chapter 4, as well as the less critical ones that merit only a passing notice because of their small influence on the thermal flux.

The photographs include one Red-Blue pair from each of the four aircraft; one Polaroid pair; and a single Blue telephoto series complementary to a Red-Blue pair (some of the other Red-Blue pairs are telephoto also). The details of the photography are given in Table 3.7. Not all the series show the same frames, as there were some cases of lens fogging or other malfunction; and some of the Blue photographs are so underexposed that frames before $2/3 t_{\max II}$ are not shown. In general, however, an attempt was made to show Frames Zero, 7 (minimum), 15, 30, 45, 66, 90, 115, 150, 200, 250, 305, 375, and 425, (at which time 95 percent of the integrated thermal flux has been emitted), as being representative of the course of the thermal pulse from the detonation. Other photographs appear in some of the series.

Red-Blue Pair (Figures A.233 through A.256). This is a typical pair, with good Red-Blue comparison; the two frames at second thermal maximum will be discussed in detail in Section 4.5.2. The Blue fireball is not visible at thermal minimum. In Frame 20 the plume has a bright crown.

Note the bright spots in the Blue at Frame 30. There are also short dark lines, which show at Blue Frames 20, 30, and 40. These dark regions appear as the shadows cast by bright areas contiguous to the dark ones, between them and the fireball center. That is to say, each dark line has a bright spot at its end near the fireball center (Section 4.4.1). In Frames 20, 30, and 40 the Blue fireball is cut horizontally by a dark belt about a third of a fireball diameter up from the water surface. The explanation of this phenomenon is not clear; the belt may be related to a shock wave reflected from the water surface (Mach front). The photographs do not allow any upward motion to be resolved. This belt is resolvable densitometrically up to Frame 80 (it is noticeable at the limbs of the fireball in the photographs). It is about 300 feet in width (in the vertical direction), and in Frames 30, 40, and 50 its apparent brightness (uncorrected for air-light) is about half that of its neighboring fireball points. This belt is usually visible in the Blue and Polaroid photographs; it is not seen in 36300 Red, but it is visible in many of the other Red series.

The bifurcation of the shock froth and the obscuration by the shocked air show very well in the Blue. In particular, in Frames 50 through 70, the light from the island to the right of the fireball is strongly attenuated as it passes through the air shock.

In late frames the Blue fireball again appears highly structured, or puffy. This roughness is of course seen on the microdensitometer traces. The vertical streaks on Frame 57 and on some other Red frames are due to faulty photographic printing.

Red-Blue Pair (Figures A.205 through A.215). The shutter of the Red Frame Zero opens at Time Zero plus 0.003 second; the actual fireball subtends only $1\frac{1}{2}^\circ$ on the film, although it appears much larger in the reproduction because of the short density scale of the photographic paper. The Red air shock is visible in Frames 30 and 45 (after this the lens system becomes clouded). The original Blue negative was scratched, and the photographic densities rather low. Note the dark belt on the Blue fireball in Frames 35 and 45.

Red-Blue Pair (Figures A.141 through A.158, and A.172 through A.182). The qualitative view of the general behavior of the air-light before it is masked by the shock froth after breakaway, appears in Frames 0 through 4 of the Red series. The growth of the fireball up through Frame 10 is clearly shown. Note the hot spots in Frames 5 through 10. Limb darkening is quite apparent, and seems to increase, in Frames 6 through 10. Breakaway occurs before Frame 8, when the shock froth is just visible. A hint of the horizontal fireball dark belt, which is more easily observed in the Blue, appears in Frames 8 and 9; however, it is not resolvable in Frames 15, et seq. Note that the darkened limb develops into the absorption shell (Frames 9, 10, 15), which appears quite opaque in all frames. These pictures show the difficulty of calculating the absorption coefficient of this shell; there is considerable scattered light from both the shocked and unshocked air.

The island (Dog) appears to have a small cloud over it (this may be some local imperfection in the camera or filter system; it appears in later frames but it is not observed in the Blue). The ratio of shock froth to average island albedo, corrected for air-light by subtraction of 85 percent of the neighboring water contribution (Section 4.5.2), is about 1.25 to 1 (1.25). Since the microdensitometer trace shows the unevenness and graininess evident on the photographs, this ratio cannot be found with good accuracy.

The Blue photographs show the characteristic dimness of the fireball in the neighborhood of thermal flux minimum. In Frame 13 several hot spots are visible, for example, the diagonal pair near 6.8, 38.2; by Frame 15 the fireball continuum shows dimly. Near 38.5, 7.5 is a relatively large structured bright region on frames 13, 14, and 15 that is associated with the plume. On the original negatives the plume is seen to begin to form earlier and over a very much larger area than this bright region. The latter region tends to remain at or near the top of the plume; eventually it darkens and disappears.

In Blue Frames 66, 90, 115, and 150 the island is within the shock froth and albedos can be compared. Again, a camera malfunction, which produced the broad horizontal streak across part of the island, interfered somewhat with the measurements. The ratios (uncorrected for air-scattered light) of the shock froth albedos to the average shocked island albedos, measured in three frames, all lie within 10 percent of 1.2. Any correction of this figure for air-scattered

light, is necessarily uncertain. Because of the absorption by the shocked air, the shock-covered area is darkened and it is unsafe to subtract the large (85 percent) fraction of the brightness of the unshocked water just outside the shock froth. If, however, such a correction is made, the ratio of albedos goes up to about 1.5; and if an adjustment is made by subtracting only 50 percent of the outside brightness the ratio is 1.3. These data should be regarded as restricted to the observation angle (about 60°) and azimuth and angle of incidence (see photograph of this observation. Note that the Blue albedo ratio appears somewhat higher than the Red (but see the following section).

Red-Blue Pair (Figures A.183 through A.204) and Complementary Blue Telephoto (Figures A.159 through A.171). The Blue telephoto series shows the hot and dark spots, the horizontal belt (albeit poorly: Frame 30), and the billowed surface and crescent shape of the luminous area in late ($\approx 3 \times t_{\text{maxII}}$) frames. While this Blue air shock is generally absorbing (bifurcation of shock froth, darkness of area behind fireball), it appears faintly bright to the upper left and upper right of the fireball in Frames 66, 90, and 115.

The ratio of the uncorrected shock froth albedo to the island albedo, in Frames 90 and 115 of Series 35923, is close to 1.3. If this ratio is corrected by the usual subtraction of 85 percent of the brightness just outside the shock froth (see the discussion in the last section), it jumps to 1.6; if 50 percent of this brightness is subtracted, the ratio is between 1.3 and 1.5. The same reservations apply as in Section 9.6.3. In Frame 90, attenuation of the albedo from the reef, as it passes through the air shock (near coordinates 1.5, 39.0), is detectable.

Series 36233 and 36236 will be discussed in detail in Section 4.5.2. The Blue fireball belt does not show in Frame 45. The Red photographs show the shock froth passing over the island.

This pair of photographs gives a good comparison of the plume properties. The Blue plume is about 35 percent wider than the Red at thermal flux maximum (Table 4.18), and 50 percent wider at $4t_{\text{maxII}}$. The Blue plume is dark, while the Red plume has a bright central area, which is particularly apparent in the reproductions of late (≈ 250) frames. The Red plume appears, in fact, reasonably bright throughout, as Table 4.18 indicates.

The ratios of the Red shock froth to the island albedos, corrected for air-light as indicated and measured in Frames 66, 90, and 115, are all within 5 percent of 1.25. It appears from these results, and from those of Flathead (Section 3.2.5) that the Red albedo ratio is somewhat less than the Blue albedo ratio; since the shock froth should be white (Section 4.5.2), this points up the observation that the island albedo is higher at longer wavelengths, which is a rather common property of powdery surfaces.

Polaroid Pair (Figures A.216 through A.232). These photographs will be discussed in detail in Section 4.5.4. They show the fireball belt, and the hot spots out to the fireball edge; the absorption shell appears also at these wavelengths. As is indicated in Section 4.5.4, gross differences between the two polarizations do not show in the microdensitometer traces, so none appear in the photographs. Since both shutter opening time and reproduction exposure differ among frames, even within a series, the appearance of bright features in the photographs—particularly the air scattering—should not be taken as a quantitative measure of the brightness.

3.3 SPECTROGRAPHIC RESULTS

Microdensitometer curves of selected spectral frames are presented in Figures 3.8 through 3.19. The curves presented in each figure are arranged to give a chronological spectral history of the event being considered. These are curves of film density versus wavelength. The spectral resolution is 40 \AA at 5790 \AA . Because there was no provision for timing signals on the film, all times are related to the first exposed frame, which is taken to be zero time. At a framing rate of 64 frames/sec, this means that the times quoted here could be in error by as much as 16 msec.

From examination of Figures 3.8 through 3.19 it can be seen that all events spectrally appear quite similar. The early spectra prior to the minimum are characterized by much structure, indicating that molecular and/or atomic emission and/or absorption processes are the dominating

factors. As the thermal pulse approaches its second maximum, the spectrum becomes that of a continuum with only slight hints of structure. This general appearance continues throughout the remainder of the thermal pulse.

The similarity of spectral details from shot to shot can be seen in Figure 3.20. This is a composite of densitometer traces of zero time spectra for several shots. Here it is apparent that the principal structure is identical in all the spectra.

TABLE 3.1 AIRCRAFT POSITIONS AT TIME ZERO

Shot and Aircraft	Horizontal Range GZ to Aircraft	Absolute Altitude	Ground Speed	Aircraft Course	Azimuth from GZ
	ft	ft	ft/sec	degree	degree
Eric					
B-57	3,829	10,150	681	050	071
Macrosse					
B-57	6,751	13,700	817	137	136
Huron					
B-47	45,974	22,150	744	003	123
B-52	5,700	20,000	753	110	116
B-57	10,223	16,290	775	051	048
B-66	8,768	9,894	771	040	040
Mohawk					
B-47	51,000	37,000	786	021	155
B-52	8,200	25,000	765	136	136
Flathead					
B-47	3,410	38,000	716	306	290
B-57	13,462	25,700	754	119	128
B-66	17,801	16,000	819	118	118
Dakota					
B-47	10,382	24,100	724	272	270
B-52	11,550	22,000	776	282	285
B-57	16,955	17,650	761	119	126
B-66	13,101	16,000	781	127	127
Apache					
B-47	29,000	30,050	745	325	322
B-52	18,550	34,000	746	111	120
B-57	28,517	10,200	492	050	051
B-66	23,500	8,000	748	080	080
Zuni					
B-47	32,500	31,000	750	258	250
B-52	23,850	32,000	764	244	263
B-57	35,460	16,900	807	073	073
B-66	21,900	19,000	843	070	070
Tewa					
B-47	25,640	34,200	736	269	270
B-52	26,700	41,000	760	106	102
B-66	27,243	19,000	779	121	121
Navajo					
B-47	33,342	33,600	758	264	263
B-52	18,300	38,000	758	283	281
B-66	57,552	21,000	770	254	254
Cherokee					
B-47	53,765	38,000	752	296	270
B-52	35,850	31,000	723	282	249
B-66	47,758 + 560	34,000	771	223	184

TABLE 3.2 EFFECTIVENESS OF THERMAL INSTRUMENTATION

Event	Participation	Sensors Pointed at Ground Zero		Sensors Pointed Vertically Down		Sensors Oriented for Back-scatter		Total Number of Sensors		Percent Effective
		Number Operated	Usable Records Obtained	Number Operated	Usable Records Obtained	Number Operated	Usable Records Obtained	Number Operated	Usable Records Obtained	
Lacrosse	B-47	18	15	3	3	0	0	21	18	85
	B-66	18	0	3	0	0	0	21	0	0
	Total	36	15	6	3	0	0	42	18	43
Cherokee	B-47	18	18	3	3	6	1	27	22	81
	B-52	18	17	3	3	2	2	23	22	96
	B-57	18	0	3	0	0	0	21	0	0
	B-66	18	12	3	3	0	0	21	15	80
	Total	72	47	12	9	8	3	92	59	64
Zuni	B-47	18	18	3	3	6	2	27	23	85
	B-52	18	16	3	3	2	2	23	21	91
	B-57	18	16	3	2	0	0	21	18	86
	B-66	18	18	3	3	0	0	21	21	100
	Total	72	68	12	11	8	4	92	83	90
Erie	B-57	18	15	3	3	0	0	21	18	85
	B-66	18	0	3	0	0	0	21	0	0
	Total	36	15	6	3	0	0	42	18	43
Flathead	B-47	18	18	3	3	6	6	27	27	100
	B-52	18	0	3	0	2	0	23	0	0
	B-57	18	17	4	4	0	0	22	21	95
	B-66	18	18	3	3	0	0	21	21	100
	Total	72	53	13	10	8	6	93	69	74
Inca	B-57	18	0	4	0	0	0	22	0	0
	B-66	18	0	3	0	0	0	21	0	0
	Total	36	0	7	0	0	0	43	0	0
Dakota	B-47	18	15	3	3	6	5	27	23	85
	B-52	18	14	3	2	2	2	23	19	82
	B-57	18	16	4	4	0	0	22	20	91
	B-66	18	14	3	2	0	0	21	16	76
	Total	72	59	13	12	8	7	93	78	84
Mohawk	B-47	a	a	3	1	6	6	9	7	78
	B-52	18	17	3	3	2	2	23	22	95
	B-57	18	0	4	0	0	0	22	0	0
	B-66	18	0	3	0	0	0	21	0	0
	Total	54	17	13	4	8	8	75	29	39
Apache	B-47	18	17	3	3	6	6	27	23	85
	B-52	18	18	3	3	2	2	23	23	100
	B-57	18	17	4	4	0	0	22	21	95
	B-66	18	14	3	3	0	0	21	17	78
	Total	72	66	13	13	8	8	93	84	90
Navajo	B-47	18	18	3	3	6	5	27	26	96
	B-52	18	17	3	3	2	2	23	22	96
	B-66	18	0	3	0	0	0	21	0	0
	Total	54	35	9	6	8	7	71	48	68
Tewa	B-47	18	18	3	3	5	4	26	25	96
	B-52	18	17	3	3	2	2	23	22	96
	B-66	18	14	3	3	0	0	21	17	81
	Total	54	49	9	9	7	6	70	64	91
Huron	B-47	b	b	3	2	6	6	9	8	89
	B-52	18	18	3	3	2	2	23	23	100
	B-57	18	18	4	4	0	0	22	22	100
	B-66	18	14	3	3	0	0	21	17	81
	Total	54	50	13	13	8	8	75	70	92

^a In this event, the B-47 was positioned for side loads. None of the tail instrumentation (Station 1, Figure 2.1) was operated.

^b In this event, the B-47 was positioned for side loads. Only one very sensitive instrument was operated in the tail instrument position (Station 1, Figure 2.1) and was a back-scatter instrument. The output of this instrument was simultaneously recorded on an oscillograph and on frequency-modulated magnetic tape.

TABLE 3.3 THERMAL EXPOSURE AND MAXIMUM IRRADIANCE

Site	Instrument, Field of View - Filter	Aircraft, Station, Orientation	Slant Range, D km	Radiant Exposure, Q cal/cm ²	Maximum Irradiance, H cal/cm ² -sec	$E = \frac{QD^2}{W}$ cal-km ² cm ² -kt	$\frac{D}{QVA}$ cal/cm ²	$E = \frac{Q_0 D^3}{WA}$ cal-km ³ cm ² -kt
Lacrosse	C-90-Q	57-1-F	4.68	1.42		0.78		
	C-160-A	57-2-V		0.84				
	C-160-Q	57-1-F	(15,350 ft)	1.34		0.75	0.94	0.50
	C-160-Q	57-2-V		1.21				
	C-90-A	57-1-F		1.03				
	C-90-B	57-1-F		0.50				
	C-90-E	57-1-F		1.17				
	R-90-Q	57-1-F		1.42				
	R-90-Q	57-1-F		1.57				
	B-47 No results							
	B-46 No results							
Cherokee	C-90-B	47-1-P	19.64	10.2			9.15	0.51
	C-160-A	47-2-V		4.69				
	C-90-A	47-1-F	(64,420 ft)	8.86		1.54		
	C-160-Q	47-1-F		15.2				
	C-90-D	47-1-F		12.0				
	C-90-E	47-1-F		10.6				
	R-90-Q	47-1-F		6.62				
	R-90-Q	47-1-F		16.2				
	R-90-Q	47-1-F		1.64*				
	B-57 No results							
	C-160-Q	66-1-F	17.44	18.8				
	C-90-Q	66-1-F		14.8				
	C-45-Q	66-1-F	(57,200 ft)	6.01		0.48	22.6	0.92
	C-160-Q	66-2-V		11.5				
	C-160-B	66-1-F		5.72				
	R-90-Q	66-1-F		10.3				
	R-90-Q	66-1-F		4.50				
	R-90-Q	66-1-F		5.70				

TABLE 3.4 CONTINUED

Shy	Instrument Field of View - Filter	Aircraft, Station, Orientation	Slant Range, D km	Radiant Exposure, Q cal cm ²	Maximum Irradiance, H cal cm ² -sec	E = $\frac{QD^2}{W}$ cal-km ² cm ² -kt	D $\frac{Q_0}{A}$ cal cm ²	E = $\frac{Q_0 D^2}{WA}$ cal-km ² cm ² -kt
Zoo.	C-160-Q	47-2-V	13.99	18.6			27.6	1.54
	C-160-A	47-2-V		13.0			14.3	1.05
	C-90-Q	47-1-F	(45,910 ft)	27.3		1.53		
	C-90-D	47-1-F		26.6				
	C-90-E	47-1-F		23.5				
	C-90-F	47-1-F		23.8				
	C-90-B	47-1-F		21.7				
	C-90-B-Ge	47-1-F		9.76				
	C-90-Q	47-1-F		29.5		1.64		
	R-90-Q	47-1-F		26.1	5.13	1.13		
	R-90-Q	47-1-F		35.5	8.62	1.99		
	R-90-Q	47-1-F		35.7	9.65	1.99		
	E-57 No results							
	C-90-A	66-1-F	11.97	21.3				
	C-90-Q	66-1-F		29.9		1.23		
	C-160-Q	66-2-V	(39,260 ft)	18.7			38.8	1.55
	C-90-Q	66-1-F		30.3		1.24		
	C-90-F	66-1-F		23.7				
	C-45-Q	66-1-F		28.8		1.15		
	C-160-A	66-2-V		10.9			22.5	0.92
	C-21-Q	66-1-F		14.6		0.55		
	C-90-B	66-1-F		9.90				
	C-90-D	66-1-F		27.1				
	C-90-E	66-1-F		3.31				
	C-90-A	66-1-F		21.2				
	C-90-D	66-1-F		27.1				
	R-90-Q	66-1-F		15.0	4.57	0.61		
	R-90-Q	66-1-F		29.5	7.75	1.21		
Eric	E-47 No results							
	C-90-Q	57-1-F	3.41	4.04				
	C-160-Q	57-2-V	(11,170 ft)	3.47		3.03	3.77	2.79
	C-90-B	57-1-F		1.56				
	C-90-Q	57-1-F		4.34		3.26		
	C-160-A	57-2-F		2.50			3.26	1.73
	C-90-A	57-2-V		3.03				
	C-90-B	57-1-F		1.47				
	C-90-E	57-1-F		5.35				
	C-90-Q	57-1-F		9.20				
	R-90-Q	57-1-F		5.12	10.3	3.55		
	R-90-Q	57-1-F		4.90	10.4	3.55		

TABLE 3.3 CONTINUED

Boat	Instrument Field of View - Filter	Altitude Sighting Orientation	Start Range, D	Radiant Exposure, Q	Maximum Irradiance, A	$E = \frac{QD^2}{A}$	$\frac{D}{QV_A}$	$E = \frac{QVD^2}{A}$
			km	cal/cm ²	cal/cm ² -sec	cal-km ² /cm ² -kt	cal/cm ²	cal-km ² /cm ² -kt
B-66 N. Results								
Flathead	C-160-Q	47-1-F	11.64	1.39		1.21		
	C-160-Q	47-2-V		1.48			3.31	1.26
	C-160-A	47-1-V	08.190 R	2.79			2.92	1.00
	C-160-Q	47-1-F		4.04		1.43		
	C-160-D	47-1-F		2.90				
	C-160-F	47-1-F		2.71				
	C-160-F	47-1-F		2.77				
	C-160-B	47-1-F		1.21				
	C-160-B	47-1-F		1.80				
	C-160-A	47-1-F		2.54				
	C-160-A	47-1-F		2.81				
	C-160-Q	47-1-F		2.59		3.92		
	C-160-Q	47-1-F		2.33		3.82		
	C-160-Q	47-1-F		2.39		3.77		
	C-160-E	47-1-F		2.31		1.23		
	C-160-Q	47-1-F		4.75	3.13			
	C-160-Q	47-1-F		3.62		1.19		
	C-160-Q	47-1-F	4.31	4.32			7.14	1.35
	C-160-Q	47-1-F	29.140 R	3.55		1.14		
	C-160-A	47-1-F		3.46			0.97	1.43
	C-160-Q	47-1-F		7.13		1.11		
	C-160-A	47-1-F		4.14				
	C-160-B	47-1-F		3.02				
	C-160-B	47-1-F		1.84				
	C-160-A	47-1-F		4.24				
	C-160-Q	47-1-F		3.53	3.19	1.13		
	C-160-Q	47-1-F		3.66	3.70	1.13		
	C-160-A	47-1-F	7.41	1.13				
	C-160-Q	47-1-F		1.13			25.4	1.47
	C-160-Q	47-1-F	24.310 R	3.13		1.13		
	C-160-Q	47-1-F		1.95				
	C-160-Q	47-1-F		3.42		1.33		
	C-160-B	47-1-F		2.50				
	C-160-Q	47-1-F		3.45		1.17		
	C-160-A	47-1-F		1.57			3.43	1.43
	C-160-F	47-1-F		1.44				
	C-160-Q	47-1-F		34.97	6.33	1.13		
	C-160-Q	47-1-F		4.13	6.61	1.13		
	C-160-Q	47-1-F	3.94	20.8		1.16		
	C-160-Q	47-1-F		20.0				
	C-160-Q	47-1-F	24.500 R	22.3			1.17	1.47

TABLE 3.3 CONTINUED

Site	Instrument Field of View - Filter	Aircraft Station Orientation	Slant Range, D km	Radist Exposure, Q cal/cm ² -sec	Maximum Irradiance, M cal/cm ² -sec	$E = \frac{QD^2}{4r^2}$ cal/cm ² -sec	$\frac{D}{Q\sqrt{A}}$ cal/cm ²	$E = \frac{D^2}{4r^2}$ cal/cm ² -sec
JAGG	C-160-A	47-2-V		18.1			18.1	
	C-90-Q	47-1-F		1.84				
	C-90-Q	47-1-F		21.6		1.01		
	C-90-Q	47-1-F		30.2		1.55		
	C-90-D	47-1-F		28.0		1.53		
	C-90-E	47-1-F		22.1				
	C-90-A	47-1-F		18.5				
	C-9	47-1-F		19.6				
	C-90-B	47-1-F		5.72				
	C-160-Q	47-1-F		27.2		2.20		
	C-45-Q	47-1-F		24.5		1.40		
	C-90-B-Ce	47-1-F		8.80				
	C-21-Q	47-1-F		21.7		1.24		
	C-90-Q	47-1-F		24.5		1.40		
	R-90-Q	47-1-F		33.4	12.9	1.89		
	R-90-Q	47-1-F		42.1	13.7	2.40		
	C-90-Q	57-1-F	7.63	27.7		1.40		
	C-90-C	57-1-F		0.92				
	C-90-Q	57-2-V	(25,020 ft)	18.1			23.7	1.31
	C-160-Q	57-2-V		18.1			25.1	1.31
	C-180-A	57-2-V		14.2			20.1	1.01
	C-90-A	57-1-F		15.7				
	C-90-B	57-1-F		9.08				
	C-90-D	57-1-F		24.0				
	C-90-E	57-1-F		23.4				
	R-90-Q	57-1-F		30.8	13.5	1.54		
	R-90-Q	57-1-F		30.5	13.1	1.54		
	C-90-A	66-1-F	6.47	21.0				
	C-160-Q	66-2-V		32.3			43.0	1.55
	C-160-Q	66-1-F	(21,210 ft)	28.0		1.04		
	C-90-E	66-1-F		27.3				
	C-90-Q	66-1-F		32.2		1.21		
	C-90-B	66-1-F		9.52				
	C-21-Q	66-1-F		15.1		0.70		
	C-160-A	66-2-V		14.7			10.6	0.72
	C-90-D	66-1-F		31.0				
	R-90-Q	66-1-F		37.2	17.3	1.37		
	R-90-Q	66-1-F		35.1	15.4	1.29		

TABLE 3.3 CONTINUED

Shot	Instrument, Field of View-Filter	Aircraft, Station, Orientation	Slant Range, D km	Radiant Exposure, Q cal/cm ²	Maximum Irradiance, H cal cm ² -sec	$\frac{QD^2}{A}$ cal-km ² cm ² -kt	$\frac{D}{Q\sqrt{A}}$ cal. cm ²	$\frac{Q_v D^3}{WA}$ cal-km ³ cm ² -kt
Apache	C-160-Q	47-1-F	12.95	10.2		0.91		
	C-160-Q	47-2-V		10.5			14.8	1.81
	C-90-Q	47-2-V	(42,490 ft)	7.87			11.1	0.99
	C-90-Q	47-1-F		12.8		1.13		
	C-90-F	47-1-F		11.0				
	C-90-E	47-1-F		11.6				
	C-90-F	47-1-F						
	C-90-A	47-1-F		9.52				
	C-160-Q	47-1-F		12.7		1.13		
	C-90-Q	47-1-F		15.9		1.40		
	C-90-B	47-1-F		11.9				
	C-90-D	47-1-F		4.50		1.50		
	R-90-Q	47-1-F		17.0	6.11			
	C-90-C	57-1-F	9.43	0.60			21.7	1.02
	C-160-Q	57-2-V		7.15				
	C-150-Q	57-1-F	(30,340 ft)	20.4		0.96		
	C-160-A	57-2-V		4.69		1.02		0.67
	C-90-Q	57-1-F		21.5				
	C-90-A	57-1-F		15.9				
	C-90-D	57-1-F		16.7				
	C-90-E	57-1-F		6.21				
	R-90-Q	57-1-F		18.5	8.40	0.88		
	R-90-Q	57-1-F		19.5	7.30	0.92		
	C-160-Q	66-1-F	7.87	23.4		0.76		
	C-90-Q	66-1-F		23.3		0.76		
	C-90-B	66-1-F	(25,820 ft)	25.2				
	C-45-Q	66-1-F		7.31		0.25		
	C-160-Q	66-2-V		6.09			19.7	0.64
	C-160-A	66-2-V		5.96			19.3	0.64
	C-21-Q	66-1-F		5.06		0.16		
	C-90-D	66-1-F		20.7				
	R-90-Q	66-1-F		31.1	9.47	1.02		
Navajo	C-160-Q	47-1-F	14.62	23.0		1.03		
	C-160-Q	47-2-V		24.7			35.5	1.62
	C-90-Q	47-2-V	(48,610 ft)	17.4			25.1	1.15
	C-160-A	47-2-V		20.0			28.8	1.32
	C-90-Q	47-1-F		32.1		1.48		
	C-90-F	47-1-F		24.3				
	C-160-Q	47-1-F		29.7		1.32		
	C-45-Q	47-1-F		26.5		1.18		
	C-21-Q	47-1-F		8.22		0.37		
	C-90-Q	47-1-F		34.5		1.58		

TABLE 3.3 CONTINUED

Shot	Instrument, Field of View - Filter	Aircraft, Station, Orientation	Sight Range, D	Radiant Exposure, Q	Maximum Irradiance, H	$E = \frac{QD^2}{W}$	$\frac{QD^2}{WA}$	$E = \frac{Q_1 D^2}{W_1 A_1}$
			km	cal/cm ²	cal/cm ² -sec	cal km ² /cm ² -kt	cal cm ²	cal-km ² /cm ² -kt
Towa	C-90-A	47-1-F		28.2				
	C-90-D	47-1-F		26.4				
	C-90-E	47-1-F		22.6				
	C-90-B	47-1-F		10.5				
	R-90-Q	47-1-F		37.5	8.34	1.74		
	R-90-Q	47-1-F		25.8	6.18	1.19		
	B-57 No results							
	B-66 No results							
	C-160-Q	47-1-F	13.30	21.8		0.78		
	C-160-Q	47-2-V		25.5			32.7	1.24
	C-160-A	47-2-V	(43,640 ft)	20.2			25.9	0.92
	C-90-Q	47-1-F		29.5		1.05		
	C-90-D	47-1-F		29.0				
	C-90-E	47-1-F		29.2				
	C-90-F	47-1-F		27.6				
	C-90-F	47-1-F		24.3				
	C-90-A	47-1-F		12.7				
	C-160-Q	47-1-F		32.6		1.14		
	R-90-Q	47-1-F		35.6	8.63	1.26		
	R-90-Q	47-1-F		35.0	9.34	1.23		
Huron	B-57 No results							
	C-160-Q	66-1-F	10.52	40.9		0.91		
	C-90-Q	66-2-V		5.92			10.8	
	C-90-Q	66-1-F	(34,500 ft)	42.3		0.94		
	C-90-D	66-1-F		38.1				
	C-46-Q	66-1-F		37.4		0.84		
	C-160-Q	66-1-F		26.3		0.59		
	C-160-A	66-2-V		17.9			32.51	0.73
	C-21-Q	66-1-F		20.3		0.45		
	R-90-Q	66-1-F		50.1	11.2	1.11		
	R-90-Q	66-1-F		54.5	12.9	1.21		
	B-47 No results							
	C-160-Q	57-2-V	5.92	8.63			10.6	1.37
	C-90-Q	57-1-F		11.5		1.50		
	C-90-C	57-1-F	(19,410 ft)	0.33				
	C-90-Q	57-2-V		9.48			11.4	1.56
	C-160-Q	57-1-F		11.3		1.46		
	C-160-A	57-2-V		6.45			7.74	1.00

TABLE 3.3 CONTINUED

Shot	Instrument, Field of View - Filter	Aircraft, Station, Orientation	Slant Range, D km	Radiant Exposure, Q cal/cm ²	Maximum Irradiance, H cal/cm ² sec	$\frac{QD^2}{W}$ cal/cm ² cm ² -kt	$\frac{D}{Q \sqrt{A}}$ cal/cm ²	$\frac{Q \sqrt{D^2}}{E} = \frac{Q \sqrt{A}}{WA}$ cal-km ² cm ² -kt
	C-90-Q	57-1-F		11.1		1.53		
	C-90-Q	57-1-F		7.01				
	C-90-B	57-1-F		34				
	C-90-D	57-1-F		9.08				
	C-90-E	57-1-F		5.43				
	R-90-Q	57-1-F		13.5	11.9	1.78		
	R-90-Q	57-1-F		13.6	9.91	1.70		
	C-160-Q		4.12	19.3		1.21		
	C-90-A			14.0				
	C-90-Q		(13,520 ft)	21.6		1.37		
	C-10-F			14.0				
	C-45-Q			18.2		1.15		
	C-90-B			6.12				
	C-90-D			17.1				
	R-90-Q			135.71	17.4	8.64		
	R-90-Q			25.8	20.2	1.62		

* Radiometer data inconsistent. † Large contribution from the tail of the radiometer trace. ‡ Radiometer trace fell off very slowly after second maximum.

TABLE 3.4 FILTER NOMENCLATURE

Identification	Transmission Interval micron
Q	0.2 to 2.5
A	0.7 to 2.5
B	0.9 to 2.5
C	2.0 to 2.5
D	0.5 to 2.5
E	0.57 to 2.5
F	0.63 to 2.5

TABLE 3.5 RATIO OF BACKSCATTERED RADIANT EXPOSURE TO DIRECT RADIANT EXPOSURE AS OBSERVED AT B-47

Shot and Yield (kt)	Range	Q_{BS}	\bar{Q}_{BS}	Q_F	\bar{Q}_F	Q_{BS}/\bar{Q}_F
	km	mcal/cm ²	mcal/cm ²	cal/cm ²	cal/cm ²	
Cherokee 3,800	12.75	31.0	31.0	6.62 15.2 16.2 1.64*	12.7	2.45×10^{-3}
Zuni 3,380	13.99	98.9 102.	100	27.3 29.5 30.1 35.3 35.7	29.6	3.38×10^{-3}
Flathead 365	11.64	75.8 69.0 75.8 77.5 69.7 65.9	72.3	1.94 2.38 2.32 2.99 4.76	3.34	21.7×10^{-3}
Dakota 1,100	8.09	156. 191. 150. 180. 116	164	1.84* 27.6 36.2 27.2 21.3 33.4 32.3	30.8	5.35×10^{-3}
Apache 1,900	12.95	24.5 21.3 19.7	21.8	10.3 12.8 12.7 15.9 17.0	13.7	1.55×10^{-3}
Navajo 1,500	11.82	34.2 37.0 41.9 33.9 39.4	36.9	23.0 32.1 20.7 34.6 47.5 25.0	30.1	1.21×10^{-3}
Tewa 1,500	11.53	37.6 33.2 30.2 31.4	37.1	31.6 29.6 32.3 35.4 38.0	30.3	9.80×10^{-3}

* These readings were omitted from the averaging.

TABLE 3.6 EFFECTIVENESS OF PHOTOGRAPHIC INSTRUMENTATION

Shot	Participation	Backscatter			Albedo			Red Filtered Fireball			Blue Filtered Fireball			Polaroid			Total	
		Number Operated	Records Obtained	Number Operated	Records Obtained	Number Operated	Records Obtained	Number Operated	Records Obtained	Number Operated	Records Obtained	Number Operated	Records Obtained	Number Operated	Records Obtained	Number Operated	Records Obtained	
Eric	B-57	0	0	2	2	1	1	1	0	0	0	0	0	0	0	4	3	
	B-66	0	0	0	0	2	0	2	0	0	0	0	0	2	0	8	0	
	Total	0	0	2	2	3	1	3	0	0	0	0	0	2	0	12	3	
Lacrosse	B-57	0	0	2	2	1	0	1	1	1	1	0	0	0	0	4	3	
	B-66	0	0	2	0	2	0	4	0	0	0	0	0	0	0	8	0	
	Total	0	0	4	2	3	0	5	1	1	1	0	0	0	0	12	3	
Huron	B-47	1	1	2	2	0	0	0	0	0	0	0	0	0	0	3	3	
	B-52	1	1	1	1	2	2	1	1	1	0	0	0	0	0	5	5	
	B-57	0	0	2	2	2	2	2	2	2	0	0	0	0	0	6	6	
Mohawk	B-66	0	0	4	3	1	1	1	1	1	1	0	0	0	0	6	5	
	Total	2	2	9	8	5	5	4	4	4	0	0	0	0	0	20	19	
	B-47	1	1	2	0	0	0	0	0	0	0	0	0	0	0	3	1	
Flathead	B-52	2	1	2	2	2	2	2	1	1	1	0	0	0	0	8	5	
	B-57	0	0	2	2	1	0	1	0	0	0	0	0	0	0	4	0	
	B-66	0	0	4	4	1	1	1	1	1	1	0	0	0	0	6	6	
Delaware	Total	3	2	10	6	4	2	4	2	2	2	0	0	0	0	21	12	
	B-47	1	1	2	1	2	1	2	2	2	0	0	0	0	0	7	5	
	B-52	2	2	2	2	2	2	2	1	1	1	0	0	0	0	8	6	
Apache	B-57	0	0	2	2	1	1	1	1	1	1	0	0	0	0	4	4	
	B-66	0	0	6	6	1	1	1	1	1	1	0	0	0	0	8	7	
	Total	3	3	8	6	7	6	7	3	4	4	2	2	2	2	27	23	
Zuni	B-47	1	0	2	2	2	2	2	1	1	0	0	0	0	0	7	5	
	B-52	2	0	2	2	2	2	2	1	1	0	0	0	0	0	8	5	
	B-57	0	0	2	2	0	0	0	0	0	2	2	2	2	4	4	4	
Cherokee	B-66	0	0	6	6	1	1	1	1	1	1	0	0	0	0	8	8	
	Total	3	0	12	12	5	5	3	3	3	2	2	2	2	27	22	22	
	B-47	1	1	2	2	2	2	2	2	2	0	0	0	0	0	7	7	
Tewa	B-52	2	1	2	2	2	2	2	2	2	0	0	0	0	0	8	7	
	B-57	0	0	2	2	1	1	1	1	1	0	0	0	0	4	4	4	
	B-66	0	0	6	6	1	1	1	1	1	1	0	0	0	0	8	8	
Navajo	Total	3	1	12	8	4	2	4	1	1	6	3	3	29	15	20	20	
	B-47	1	1	2	2	2	2	2	2	2	0	0	0	0	7	7	7	
	B-52	1	1	1	1	2	2	1	1	1	0	0	0	0	5	5	5	
Inup	B-66	0	0	6	6	1	1	1	1	1	0	0	0	0	8	8	8	
	Total	2	2	9	9	5	5	4	4	4	0	0	0	0	20	20	20	
	B-47	1	1	2	1	2	2	2	2	2	0	0	0	0	7	7	6	
Total	B-52	1	0	2	2	2	1	2	2	2	0	0	0	0	7	7	3	
	B-66	0	0	4	4	1	1	1	1	1	0	0	0	0	7	7	5	
	Total	2	1	9	7	5	3	5	3	3	0	0	0	0	21	21	14	
Total	B-57	0	0	2	2	2	1	1	1	1	0	0	0	0	4	4	4	
	B-66	0	0	2	0	2	0	2	0	0	2	2	0	0	6	0	0	
	Total	0	0	4	2	3	1	3	1	1	2	2	0	0	12	12	4	

TABLE 3.7 PHOTOGRAPHIC PARAMETERS

See also Tables 4.2 and 4.3 for transmission data

Spot	Aircraft	Absolute Altitude	Initial		Ground Speed	Initial		Aircraft Azimuth Direction	Initial Aircraft Azimuth Altitude	Film Number	Camera Number	Type Film	Filter	Focal Length of Lens		Aperture	Scale of Photograph
			Horizontal Range	Slant Range		Aircraft Position	Aircraft Altitude							mm	f/		
Erie	B-57	10,450	3,829	11,130	681	050	69.9	2	69.9	34565	49	SI	ND 1 + red	25	11	11	400
Lacrosse	B-57	13,700	6,751	15,260	817	137	63.8	136	63.8	31587	1	MF	ND 1 + blue	25	11	11	560
Huron	B-66	9,894	8,768	13,210	771	040	48.8	040	48.8	37505	29	MF	Blue	17	16	16	730
Flathead	B-47	38,000	3,410	38,150	716	306	85.0	280	85.0	35157	46	MF	Blue	25	8	8	1500
Apache	B-47	30,050	29,000	41,750	745	325	46.1	322	46.1	37214	43	SI	NND 2 + red	17	16	16	2300
	B-57	10,200	28,517	30,290	492	050	19.6	051	19.6	37218	49	MF	NND 1 + Pola ϕ	17	16	16	1800
Zuni	B-57	16,900	35,460	39,280	807	073	25.5	073	25.5	37219	1	MF	NND 1 + Pola θ	17	16	16	1600
Cherokee	F-84	approx. 28,000								34383	49	SI	ND 1 + red	25	16	16	1450
Navajo	B-52	32,000	18,300	42,180	758	283	64.2	281	64.2	36808	36	SI	ND 1 + red	10	16	16	4000
Tewa	B-52	41,000	26,700	48,930	760	106	57.0	102	57.0	37477	36	SI	ND 1 + red	17	16	16	2700
Dakota	B-52	22,000	11,550	24,850	776	282	62.2	285	62.2	36231	5	MF	Blue	17	8	8	1370
	B-66	16,000	13,101	20,680	781	127	50.6	127	50.6	34377	12	SI	Red	17	16	16	1370
										36241	29	MF	Blue	10	16	16	2140
										36242	13	SI	Red	10	16	16	2140
										36249	24	MF	Pola θ	17	5.6	5.6	1300
										36250	27	MF	Pola ϕ	17	5.6	5.6	1300
B-57		17,650	16,955	24,480	761	119	46.1	126	46.1	36299	49	MF	ND 1 + blue	17	11	11	1330
										36300	1	SI	ND 1 + red	17	11	11	1330
B-47		24,100	10,382	26,240	724	272	66.6	270	66.6	36236	46	SI	ND 1 + red	10	11	11	2650
										36233	17	MF	ND 1 + blue	10	11	11	2650
										35923	44	MF	Blue	17	8	8	1470

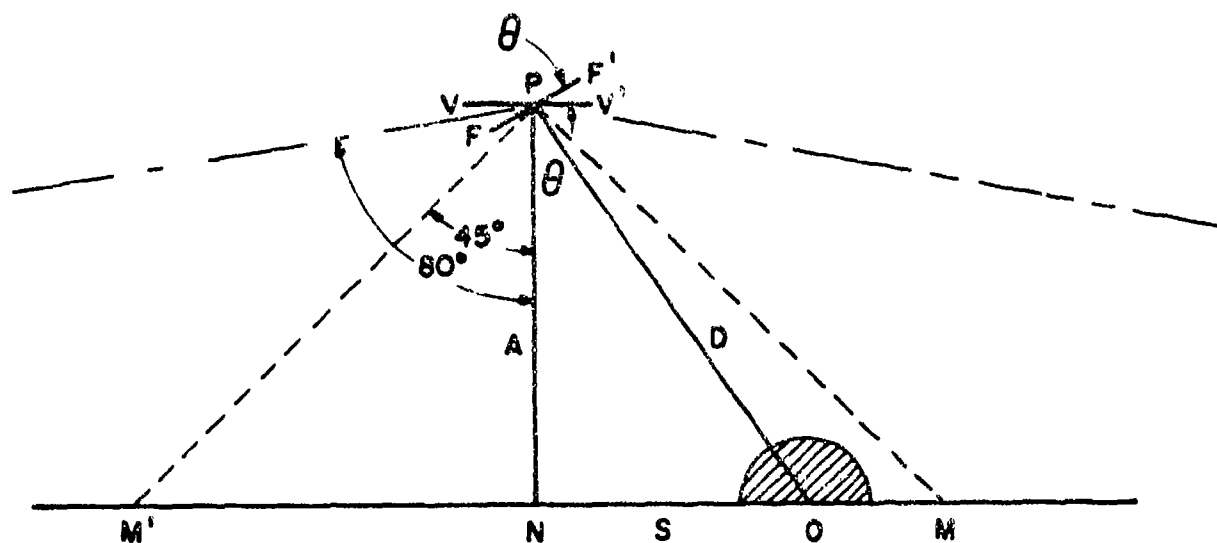


Figure 3.1 Geometry of a vertically oriented receiver. This shows the combined influence of the obliquity factor, $\sec \theta$, and field of view of a detector on the energy received by a vertically oriented receiver. The receiver VPV' located at P views the fireball D units away at O. The fireball size is given by the shaded hemisphere about O. The acceptance angle M'PM is so large that the direct radiation from O reaches VPV'.

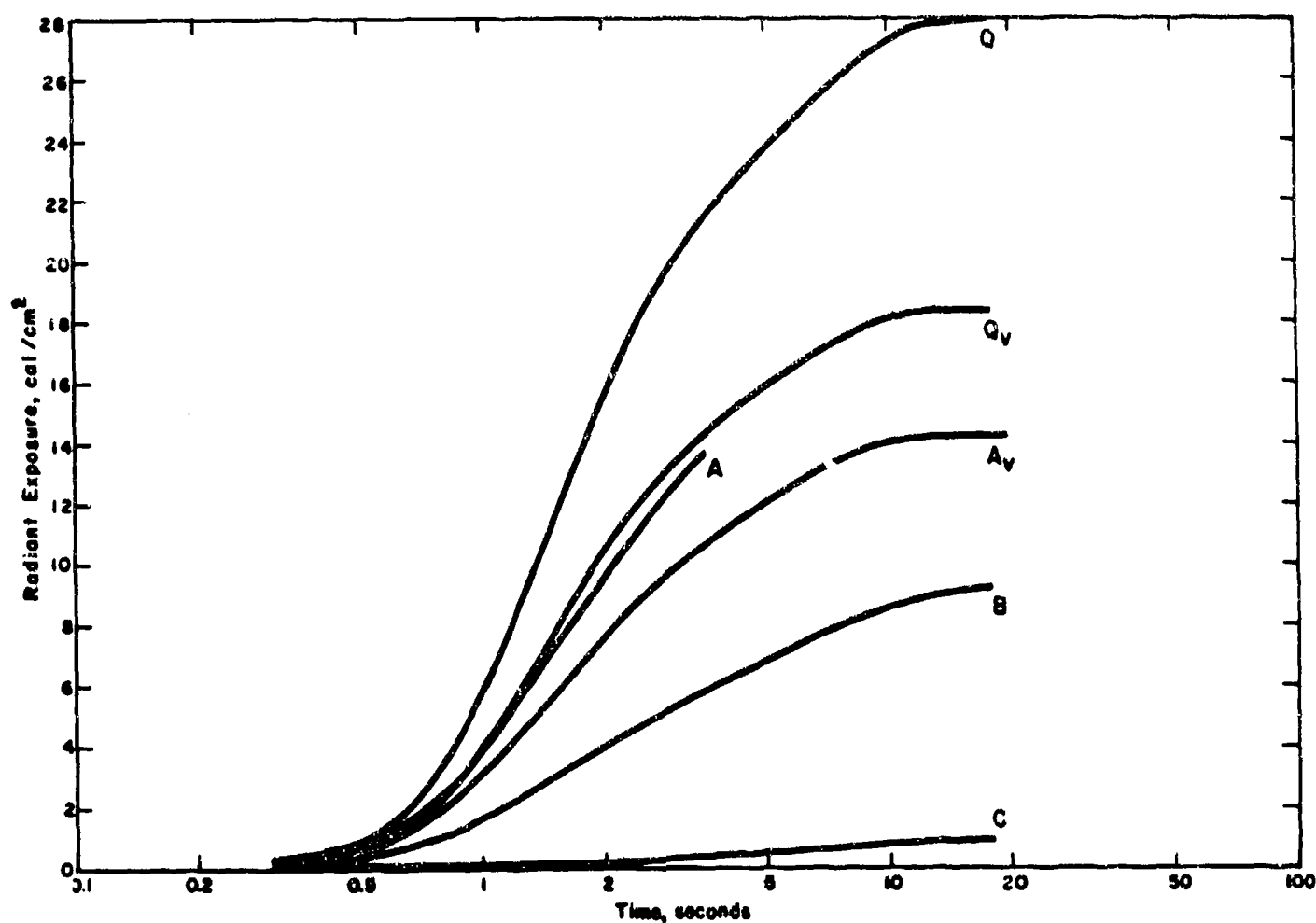


Figure 3.2 Radiant exposure as a function of time for Shot Dakota as measured by calorimeters from B-57. The letters indicate the filters used, and the subscript V indicates vertical (down) orientation. Filter A range: 0.7 to 2.5 microns; B: 0.9 to 2.5 microns; C: 2.0 to 2.5 microns.

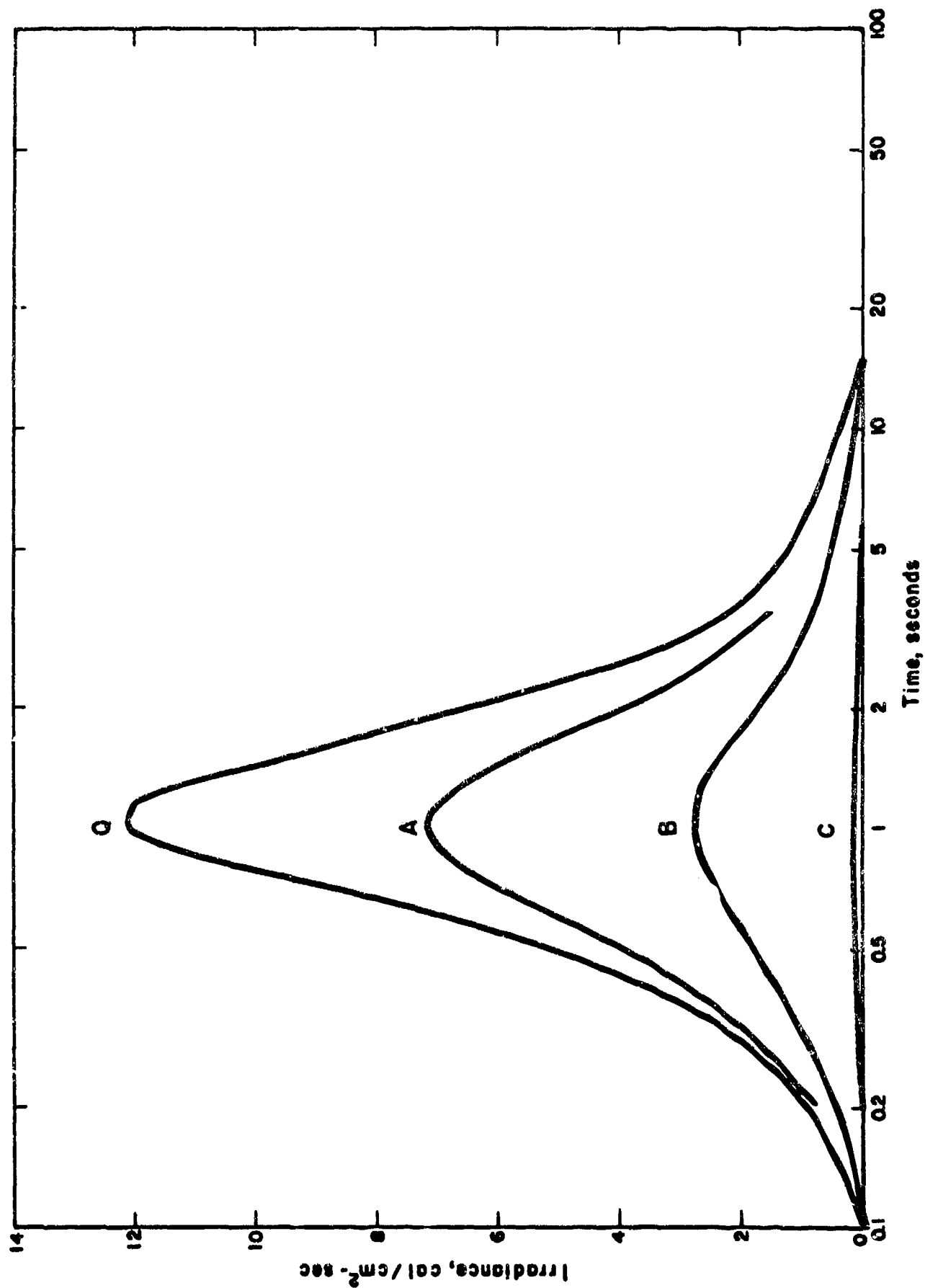


Figure 3.3 Irradiance as a function of time for Shot Dakota as measured from B-57. The thermal exposure was differentiated to obtain the irradiance. The filters are the same as used for Figure 2.5.

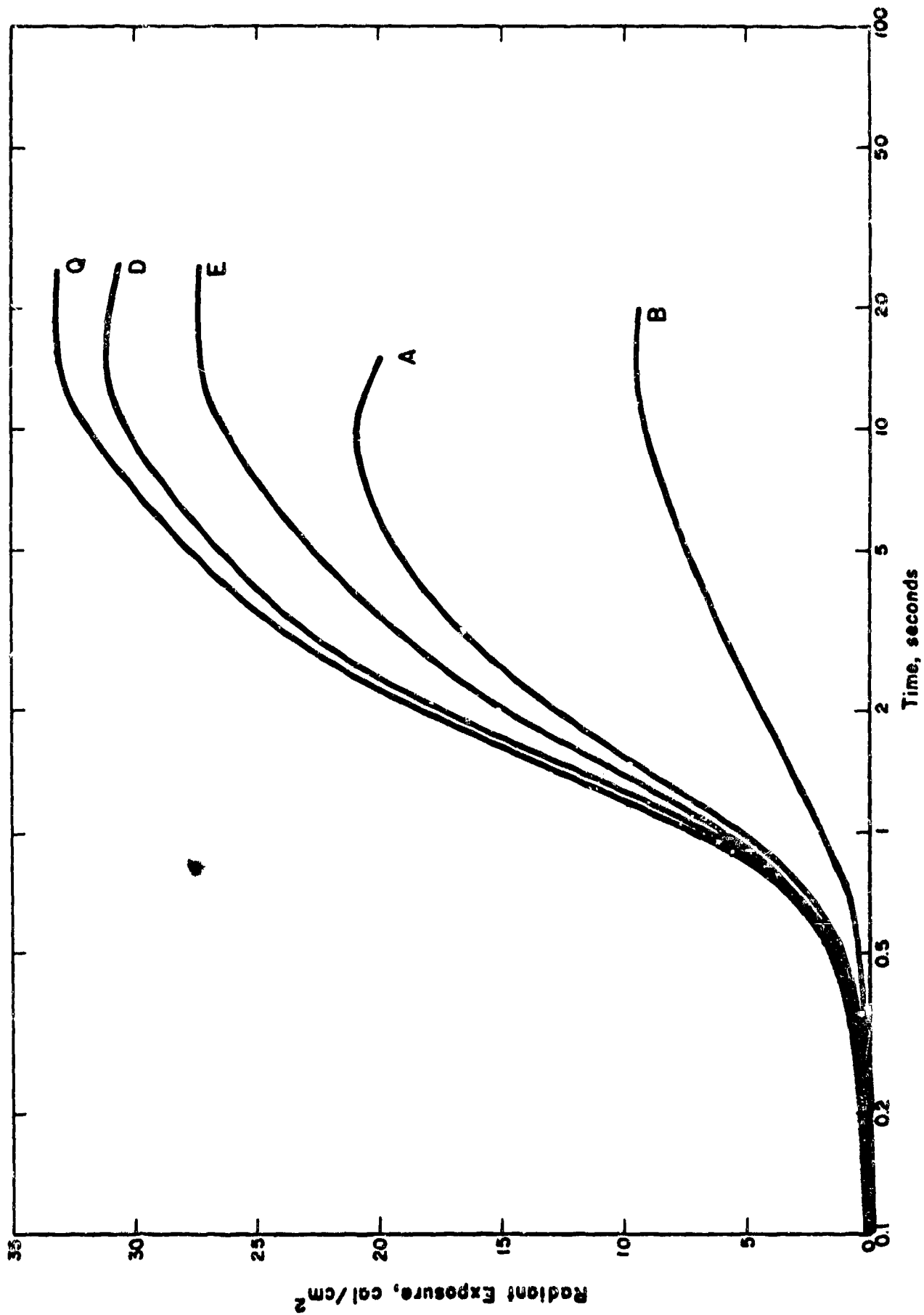


Figure 3.4 Radiant exposure as a function of time for Shot Dakota as measured by calorimeters installed on B-66. The filters have the following ranges: A: 0.7 to 2.5 microns; B: 0.9 to 2.5 microns; D: 0.5 to 2.5 microns; E: 0.57 to 2.5 microns.

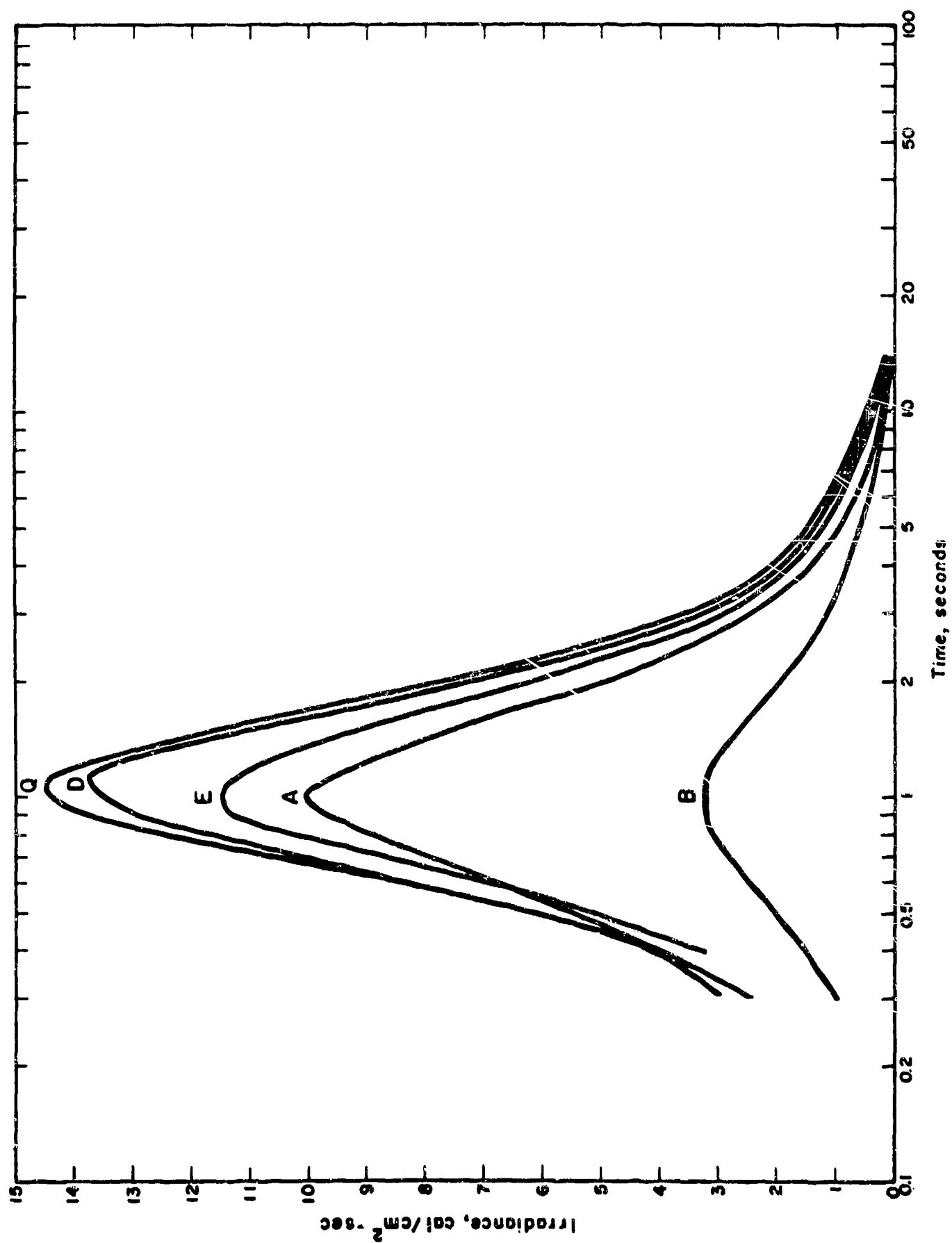


Figure 3.5 Irradiance as a function of time for Shot Dakota as measured from B-66. The thermal exposure was differentiated to obtain the irradiance. The filters are the same as used for Figure 3.4.

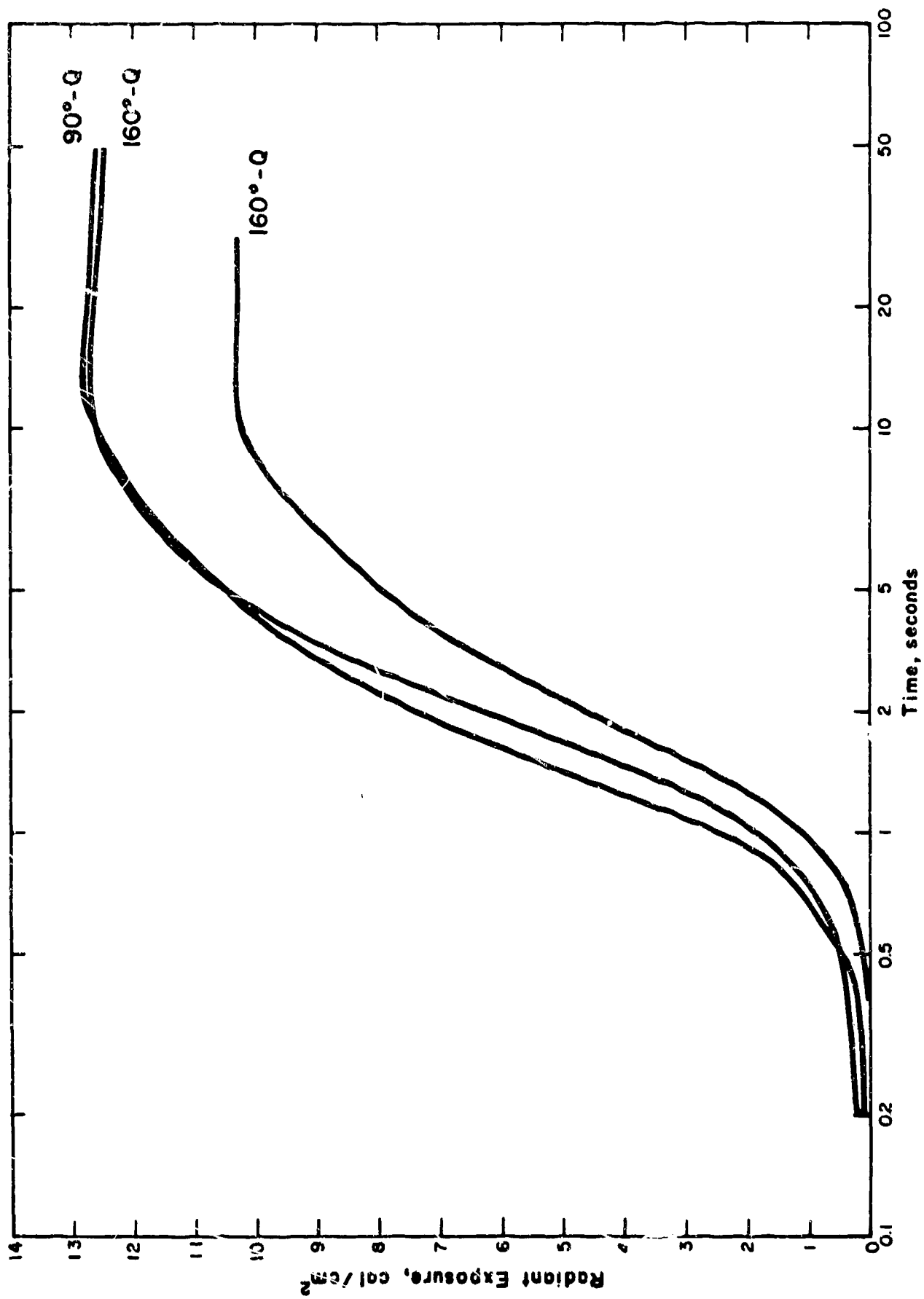


Figure 3.6 Radiant exposure as a function of time for Shot Apache, measured by three calorimeters on the same aircraft. The calorimeters, whose angular field of view was either 90° or 160°, viewed through quartz windows.

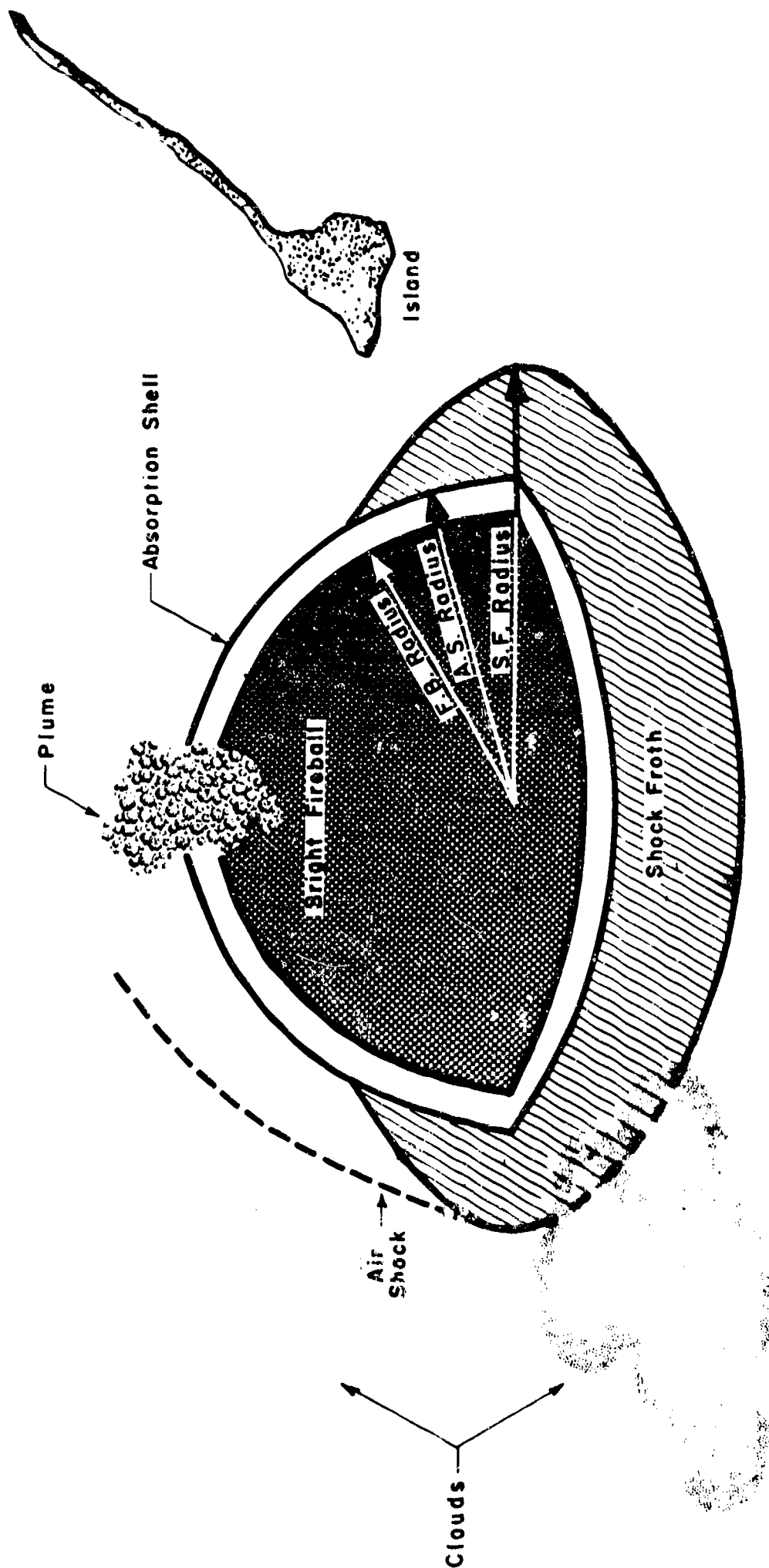


Figure 3.7 Schematic diagram of a surface detonation.

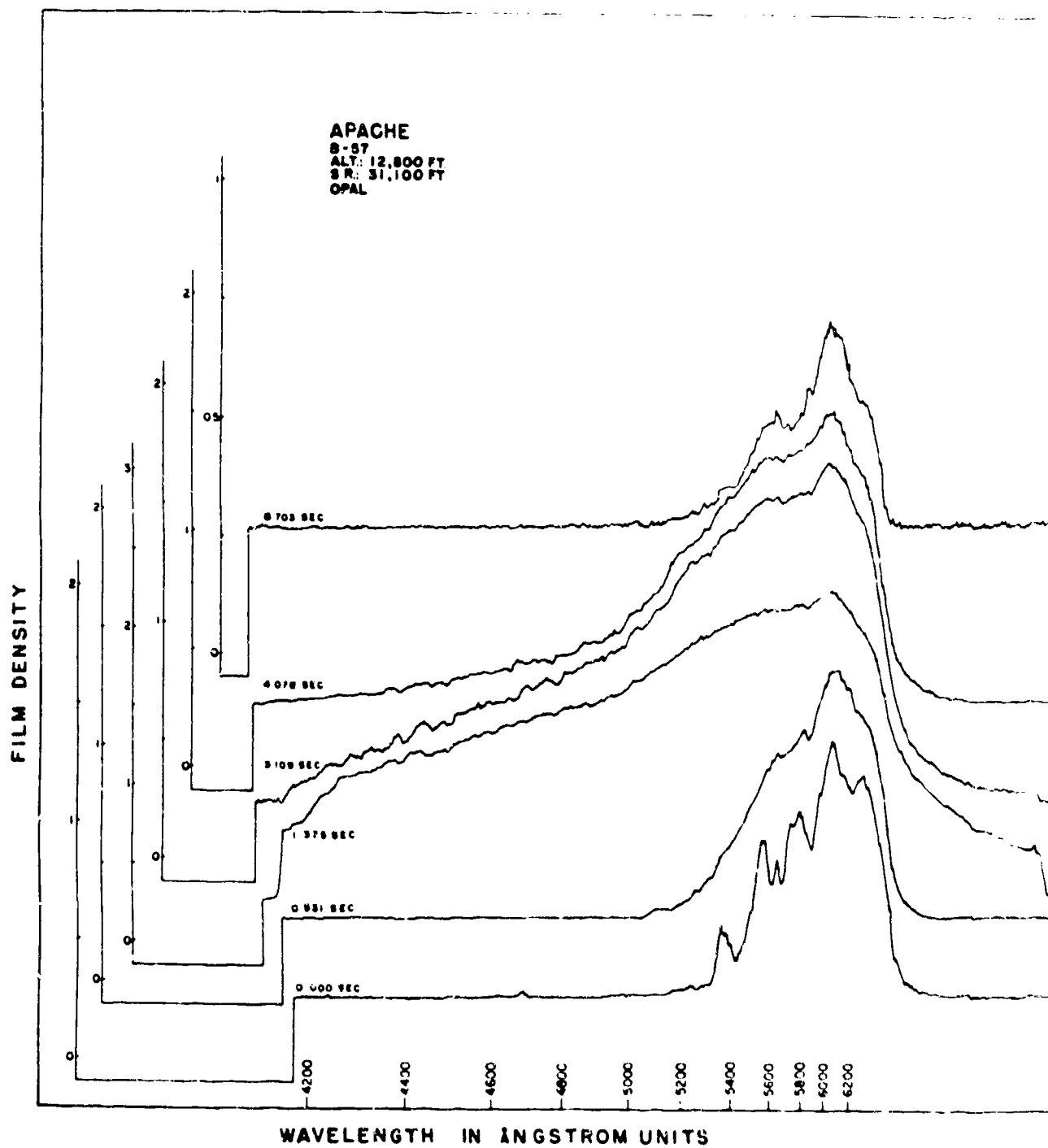


Figure 3.8 Chronological spectral history, Shot Apache.

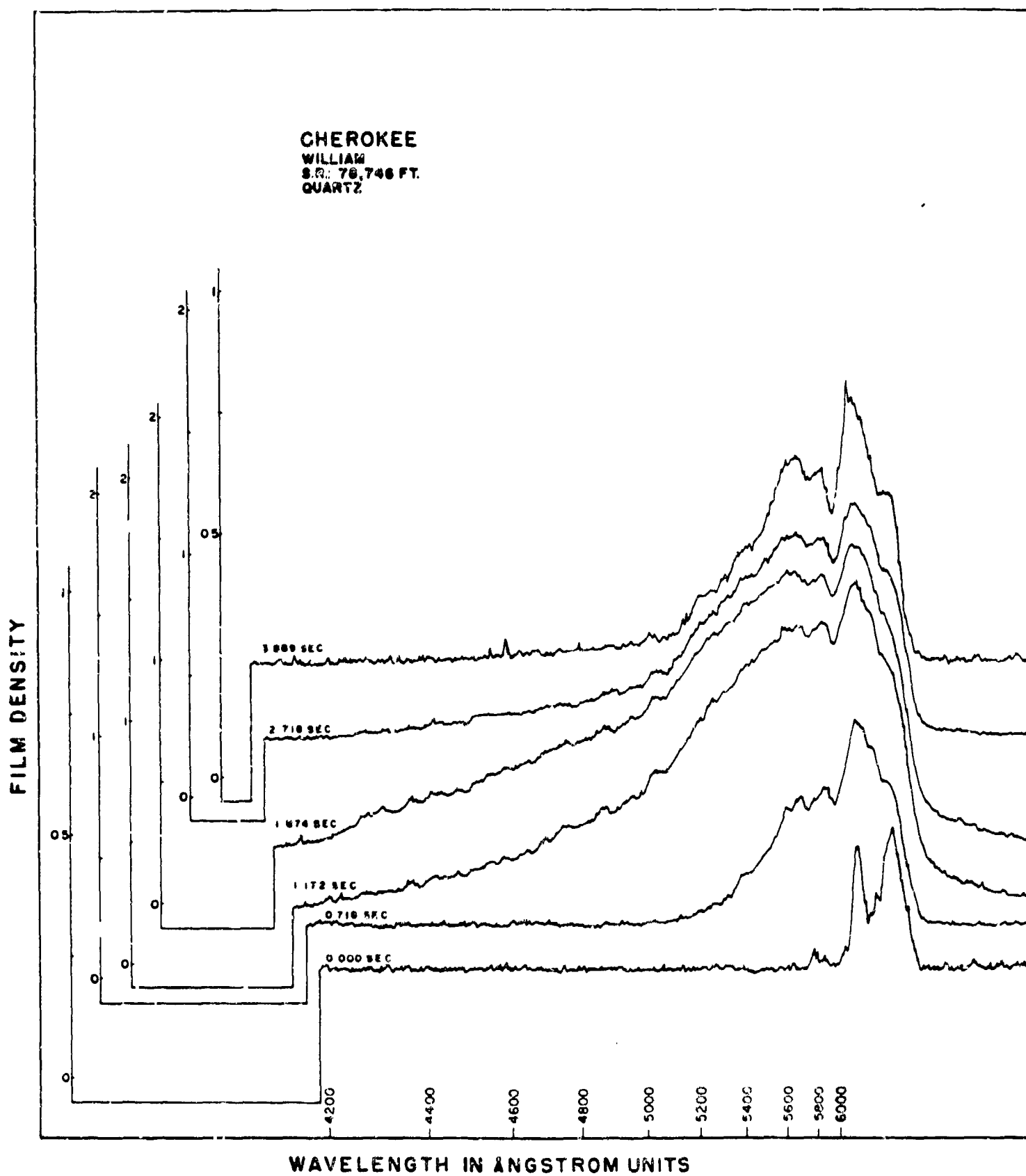


Figure 3.9 Chronological spectral history, Shot Cherokee.

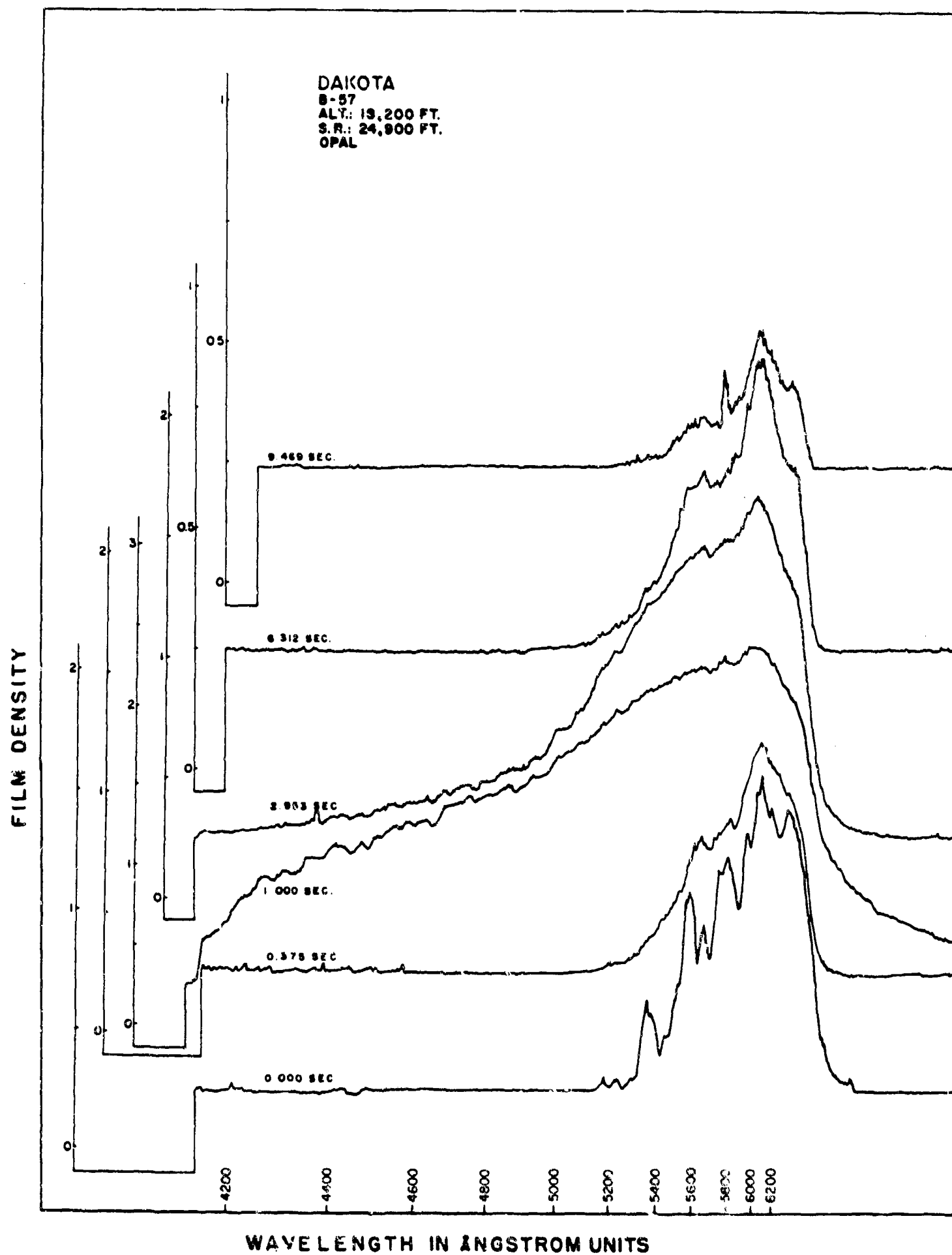


Figure 3.10 Chronological spectral history, Shot Dakota.

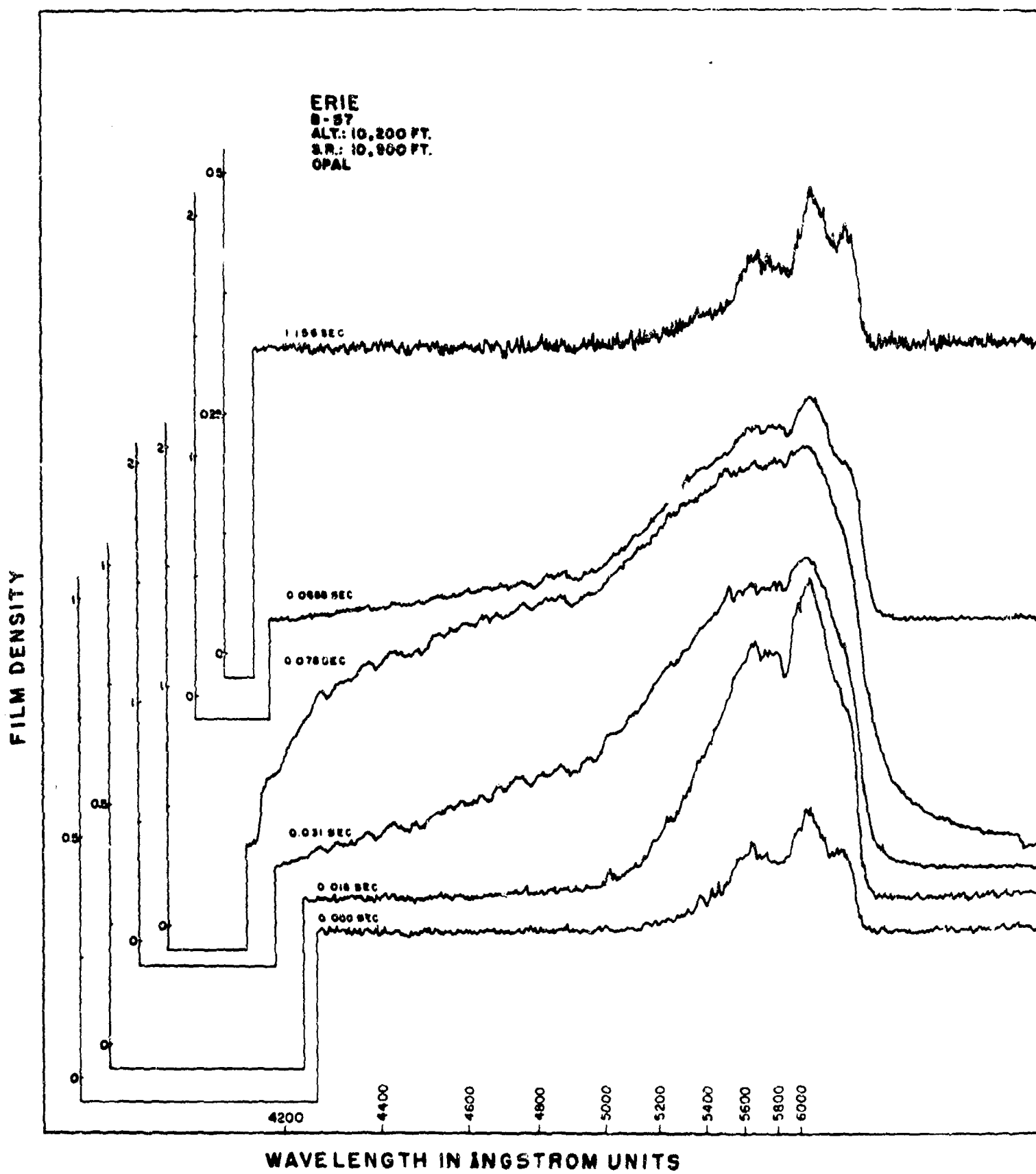


Figure 3.11 Chronological spectral history, Shot Eerie.

FILM DENSITY

FLATHEAD
B-57
ALT: 25,900 FT.
SR: 28,900 FT.
OPAL

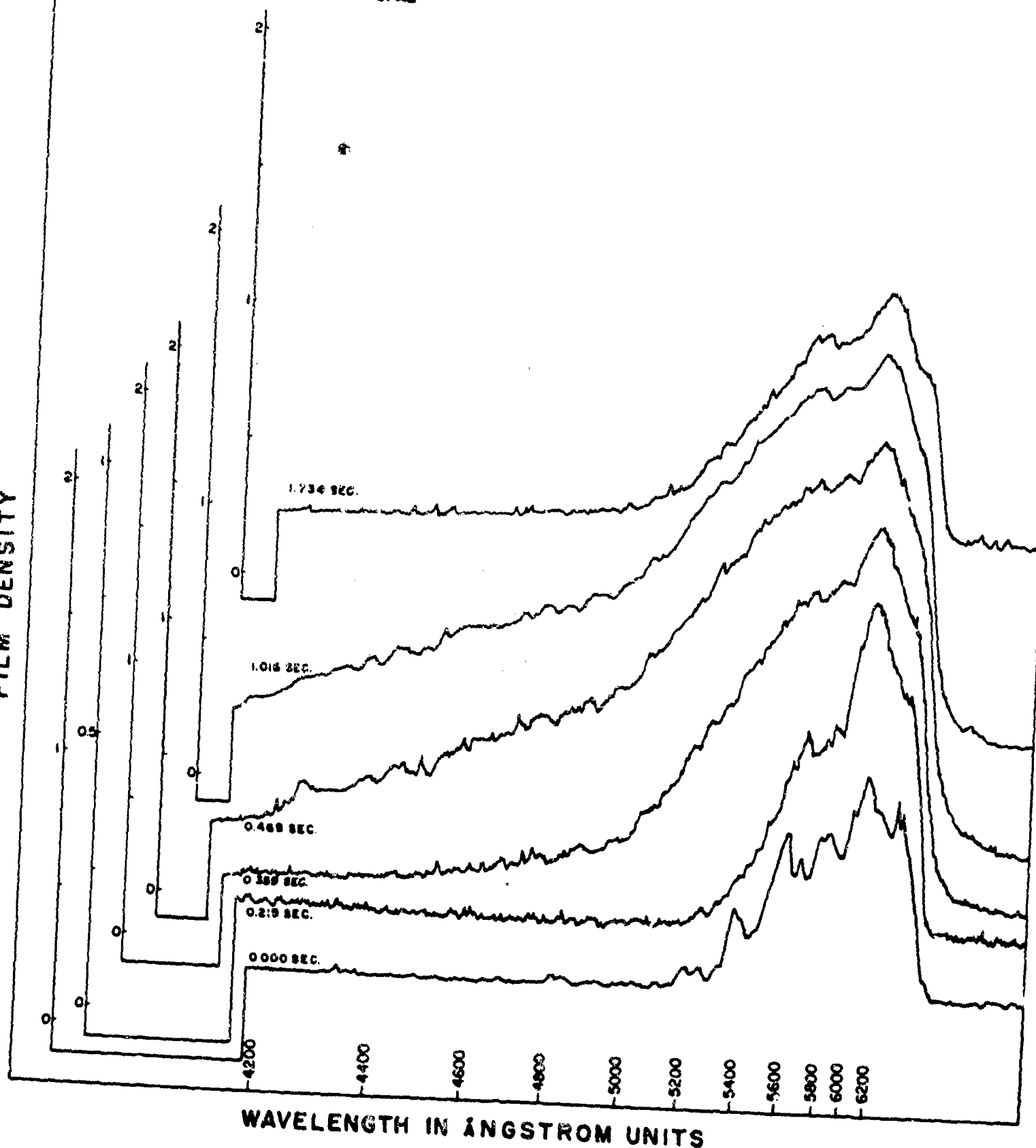


Figure 3.12 Chronological spectral history, Shot Flathead.

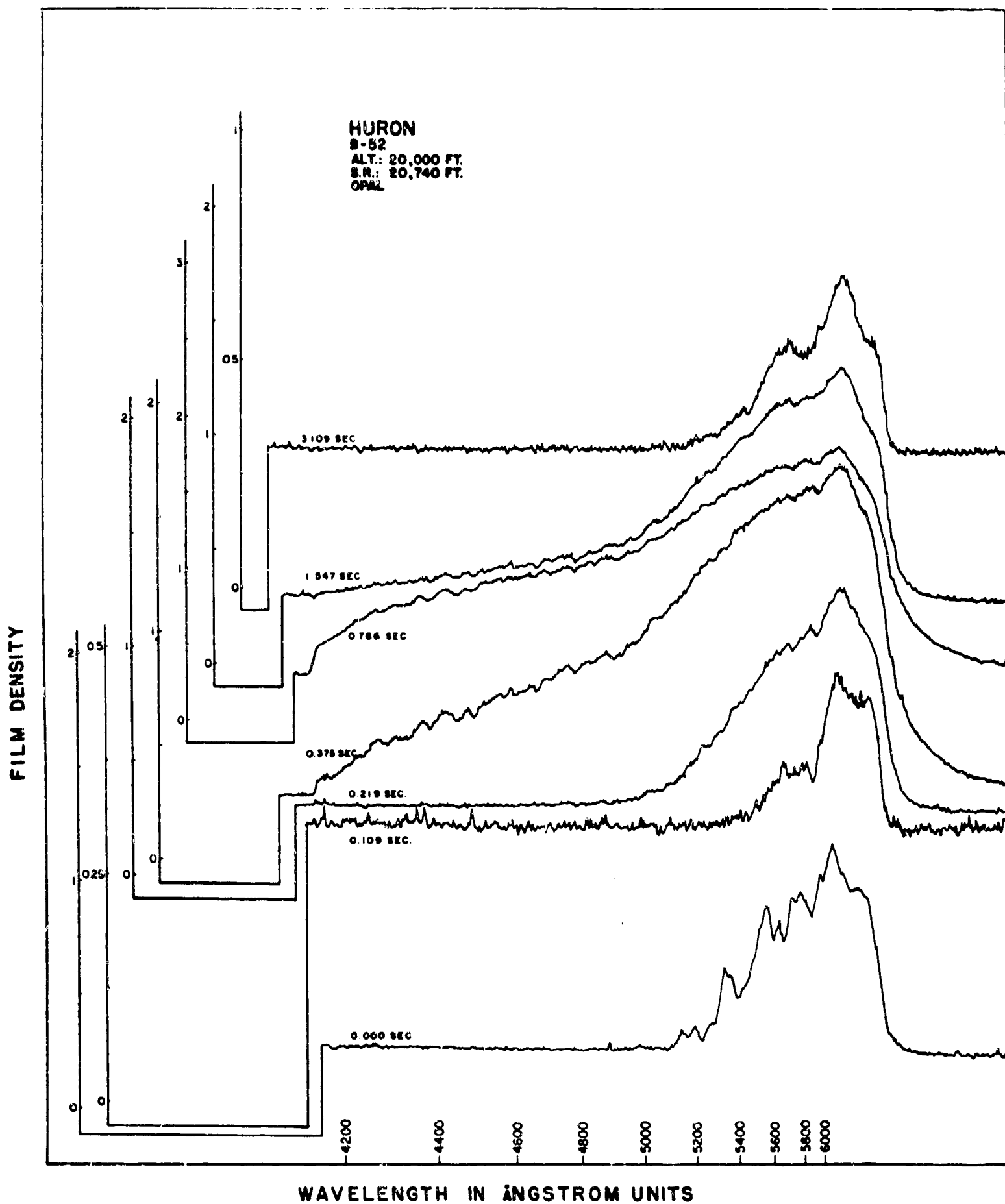


Figure 3.13 Chronological spectral history, Shot Huron.

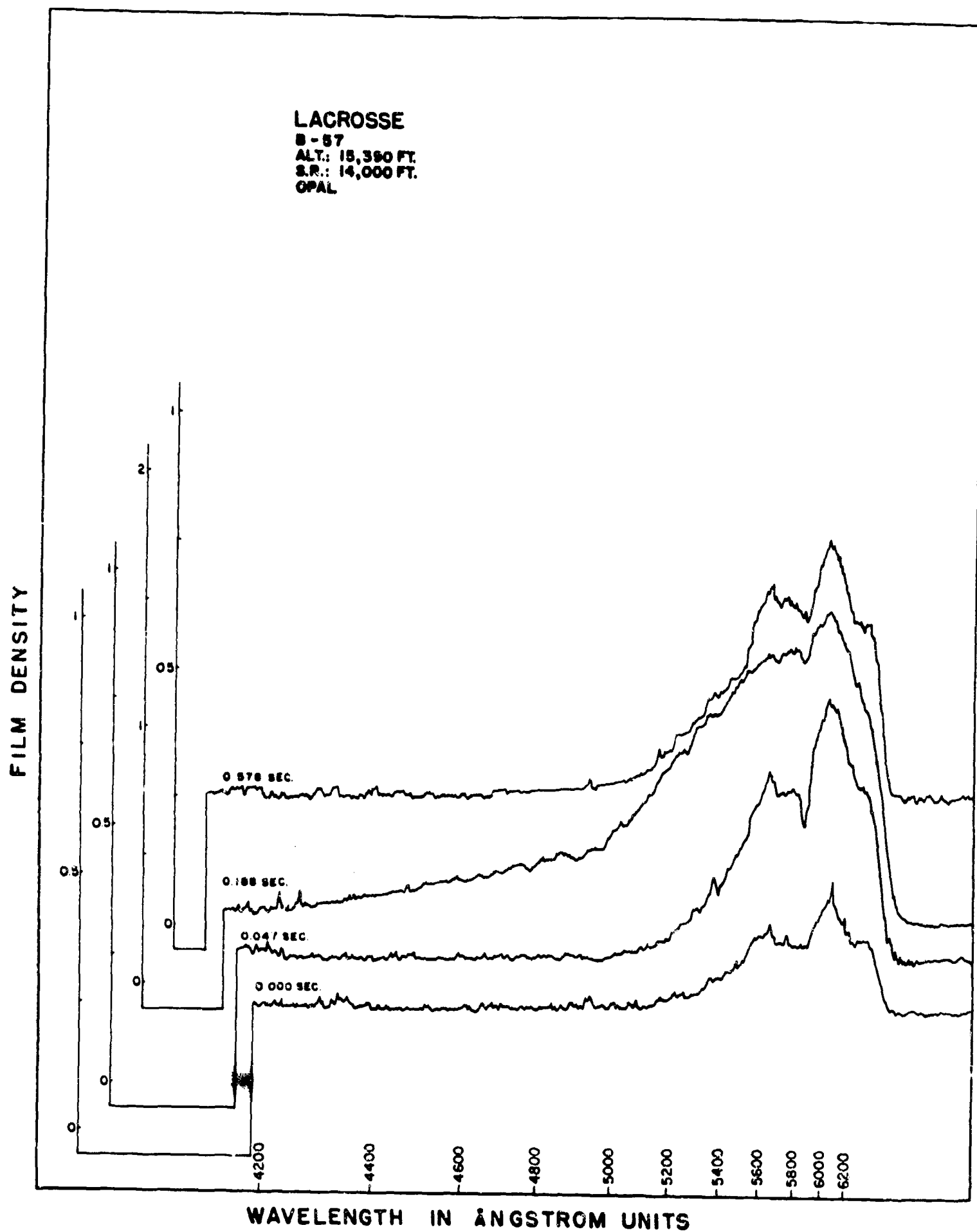


Figure 3.14 Chronological spectral history, Shot Lacrosse.

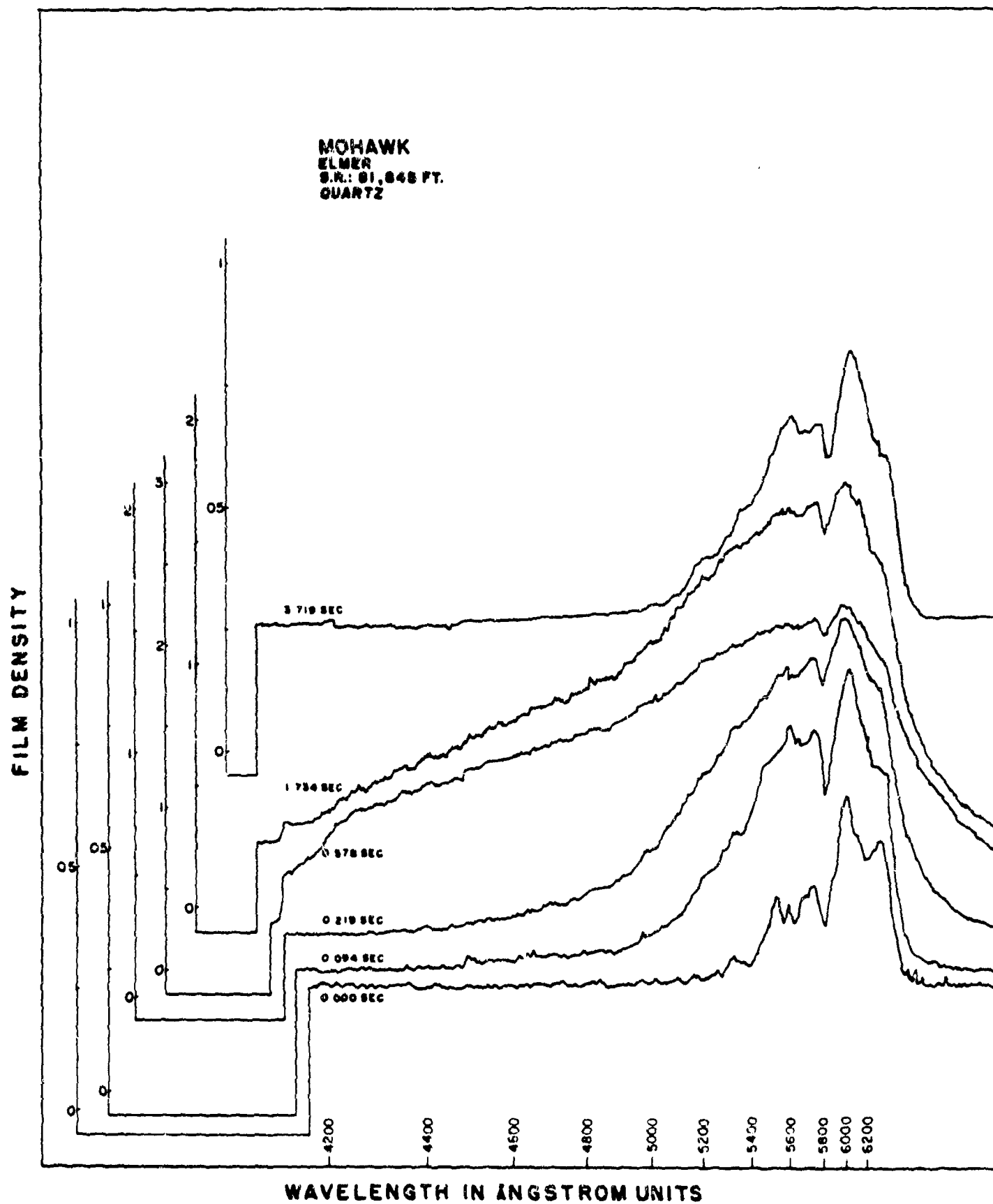


Figure 3.15 Chronological spectral history, Shot Mohawk.

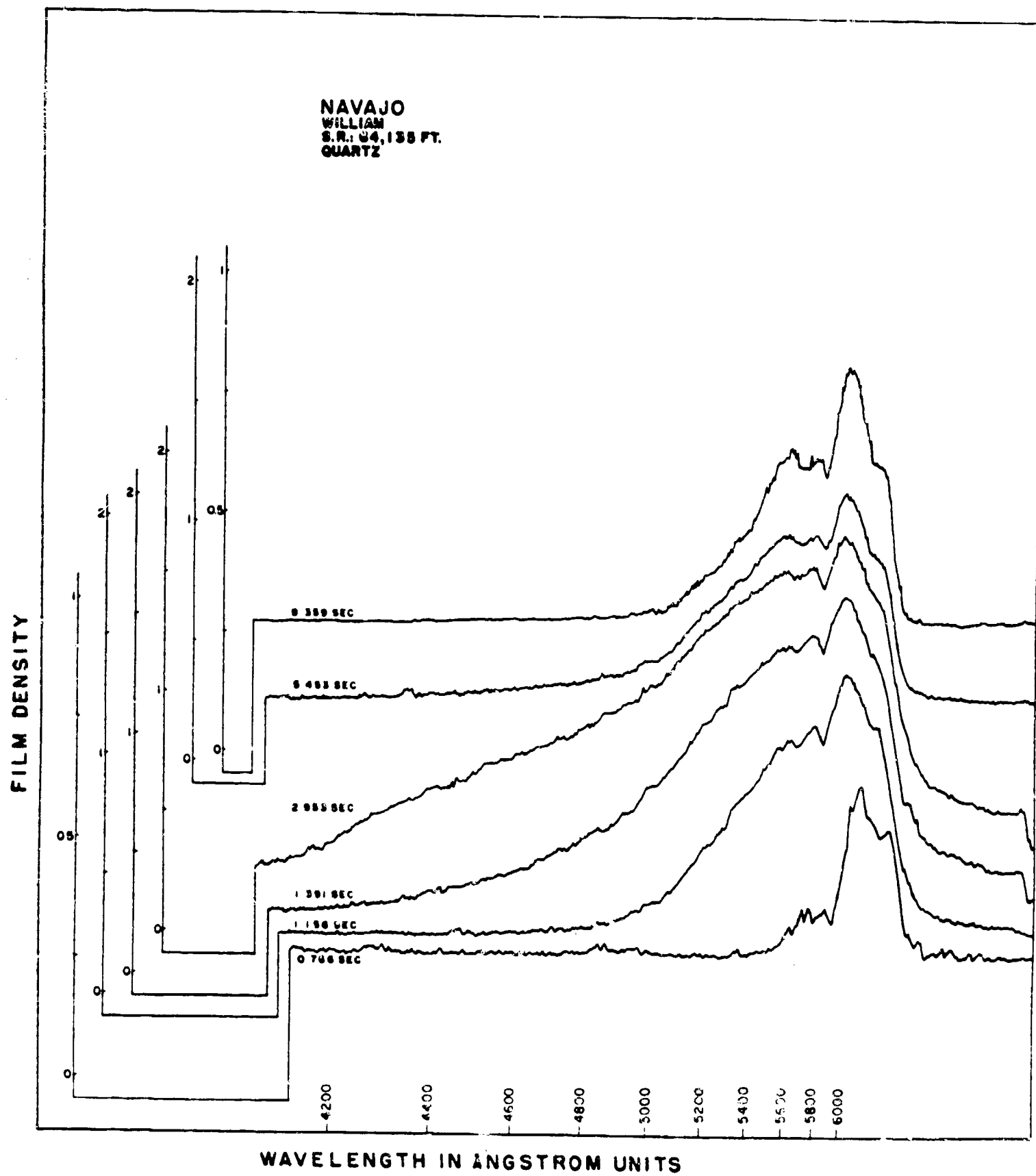
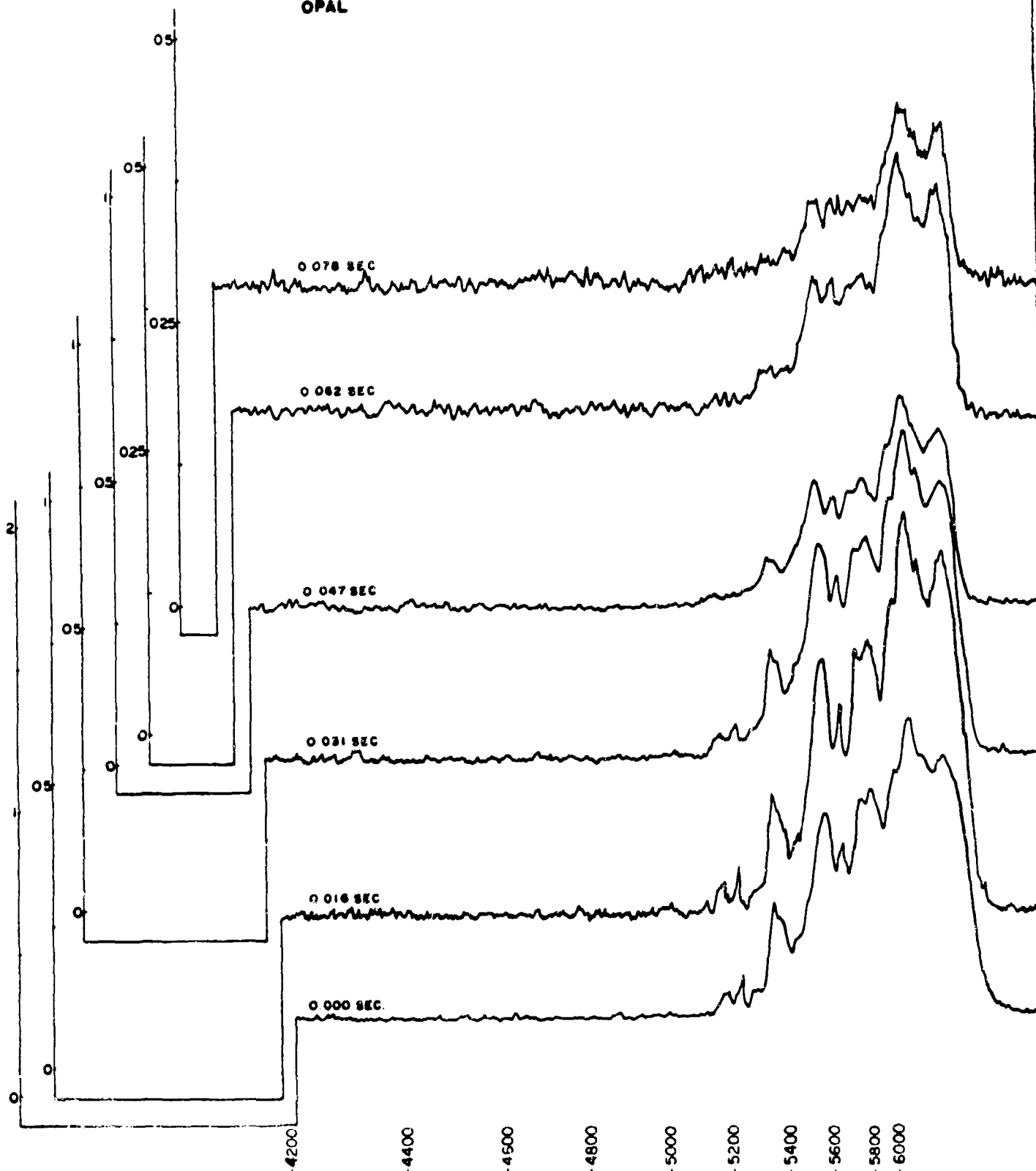


Figure 3.16 Chronological spectral history, Shot Navajo.

FILM DENSITY

TEWA
B-66
ALT: 19,000 FT.
S.R. 33,000 FT.
OPAL



WAVELENGTH IN ÅNGSTROM UNITS

Figure 3.17 Early time spectra, Shot Tewa.

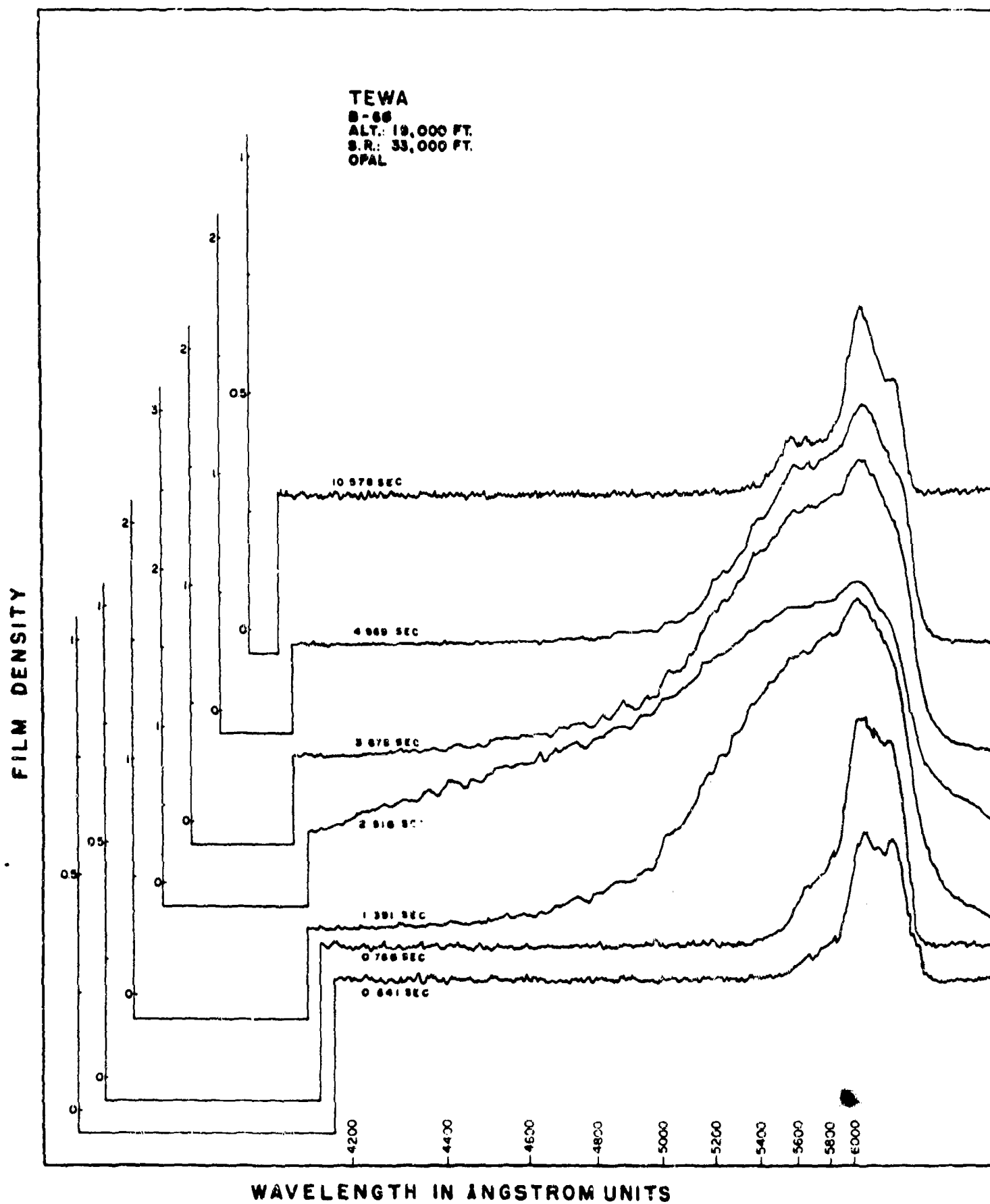


Figure 3.18 Chronological spectral history, Shot Tewa.

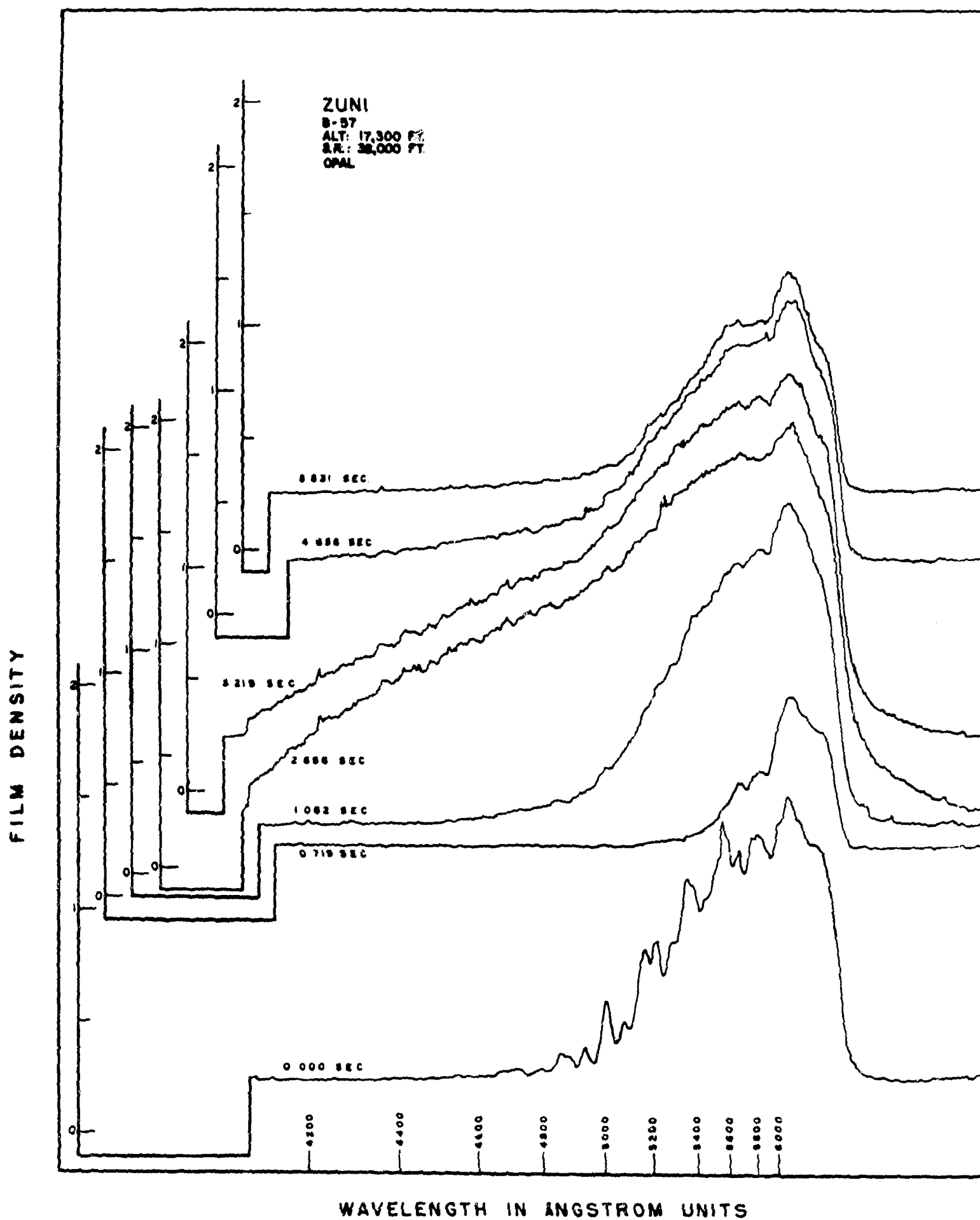


Figure 3.19 Chronological spectral history, Shot Zuni.

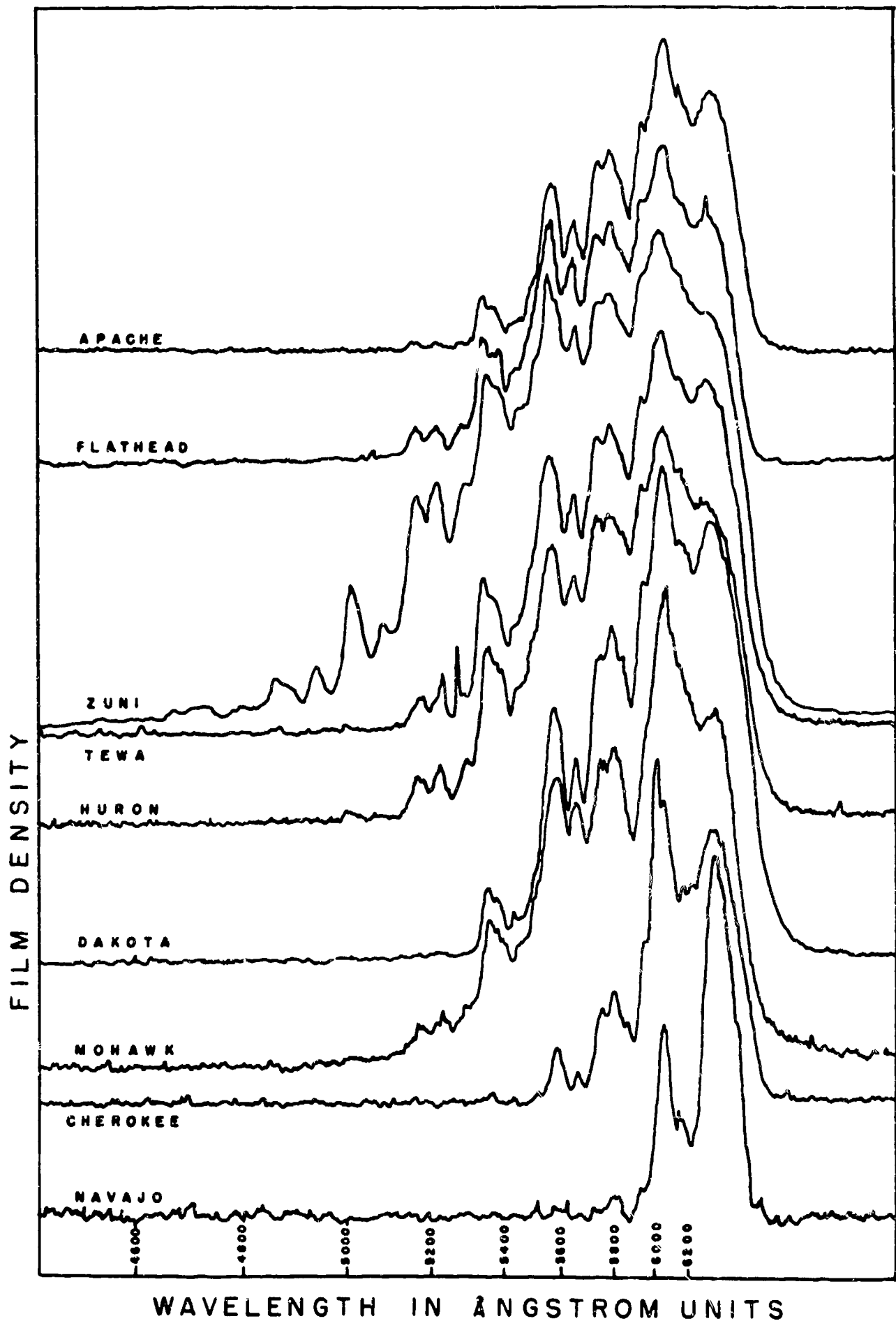


Figure 3.20 Comparison of zero time spectra.

Chapter 4

DISCUSSION

4.1 ATMOSPHERIC ATTENUATION

4.1.1 Absorption by the Atmosphere. Much work has been done on the absorption properties of atmospheric water vapor and carbon dioxide. Perhaps the most complete investigation from the point of view of radiometry is in Reference 9. That report plus Reference 10 effectively gives the transmissivity of air from the long wave end of the visible region to beyond the 6.4-micron band of water vapor. To the precision required in these tests, there is no significant absorption by any of the other permanent gases in the range 0.2 to 4.5 microns except for some oxygen absorption near 0.7 micron. Figure 4.1 shows the absorption spectrum constructed for the permanent atmospheric gases and water vapor. This spectrum is constructed under the assumption of 60 mm of precipitable water and is of the magnitude and type used in analyzing data recorded by B-57 calorimeters for Shot Dakota. The figure is schematic only and absorption values can be obtained from the references cited. Subsequent checking has shown that there is no significant difference in the absorption spectrum of 60 mm of precipitable water as compared to the ambient 54 mm of precipitable water for Dakota at time zero. Also the precipitable water path increased as the aircraft moved away from ground zero.

In the vicinity of the event, the temperatures and pressures are suitable for the formation of oxides of nitrogen. Of these oxides, NO_2 and N_2O_4 show strong absorption properties in the visible. The absorption spectrum of the other oxides of nitrogen are in the infrared beyond 4 microns. The NO_2 and N_2O_4 absorption spectra are given as Figure 4.2. This curve has been constructed as a composite from data obtained from several sources (References 11 through 15).

Although there may be other absorption gases in the path, the above is a summary of the absorption characteristics of those gases that are known or suspected to exist in the atmosphere surrounding the detonation.

Table 4.1 presents tabulated values for the transmission of thermal energy through Pacific air for the detonations analyzed in this report. A temperature of $3,000^\circ\text{K}$ is assumed for all events except Erie ($4,000^\circ\text{K}$) and Cherokee ($6,000^\circ\text{K}$). The transmissivities (T) are taken from Figure 11 of Reference 1. $T = F_v + T_w F_{IR}$ where F_v , T_w , and F_{IR} are defined in Chapter 1. The water vapor content w is expressed as millimeters of precipitable water.

4.1.2 Climatological Conditions and Atmospheric Optical Effects. Table 4.2 contains the relevant climatological data for the series of detonations. It is noteworthy that the conditions are sensibly the same for all detonations. A typical figure for the sea-level water vapor density can be taken from the Dakota data; it is 21.6 gm/m^3 . ($P_0 = 22.4 \text{ mm of mercury}$.)

Dependence of atmospheric attenuation of the thermal radiation on local meteorological conditions, as well as the general behavior of this phenomenon, is discussed in some detail in Reference 1. Some further treatment is given in Reference 16. In what follows, it is necessary to make the usual distinction between narrow-beam (collimated) and broad-beam detection and attenuation. The camera acts as a narrow-beam detecting instrument when it looks at small, sharp-edged features, for multiple-scattered photons originating in such regions must have both fortuitous direction and orientation to appear to come from a point on the object. On the other hand, in the case of extended sources (fireball, shock froth, air scatter) there should be considerable crosstalk among neighboring local areas because of scattering, and a buildup factor of the type discussed in Reference 1 should be used. Furthermore, this scattered component may interfere with the interpretation of small-area data, and in fact this will be shown to be the case in several circumstances.

Blue and Polaroid Attenuation. Reference 16 contains data for the attenuation of Blue light in the Marshall Islands, where the climatological conditions are expected to be closely the same as at Bikini and Eniwetok. The night sea-level (exponential) narrow-beam attenuation coefficient at 4,000 Å varies between 0.17 and 0.25 km⁻¹. Note that the Rayleigh coefficient here is 0.04 km⁻¹. (Since the measured attenuation was found to be relatively wavelength-insensitive, the author concluded that it included a large contribution from sea spray.) This figure should be compared with that derived from Equation 12 in Reference 1, which is germane to the present situation. This gives the usual relationship between attenuation and visibility (in miles), (attenuation coefficient) = 2.5/visibility per kilometer. This formula gives a sea-level attenuation of 0.25/km for the nominal visibilities of Table 4.2, in reasonable agreement with Reference 16. Now the observation points (that is, the aircraft) are of course not at sea level, but at a range of altitude angles greater than 19°; therefore, it is necessary to use the methods of Reference 1 to take account of this effect for calculating the attenuation of the light reaching the cameras.

The results of such a calculation for Dakota, assuming the sea-level narrow-beam attenuation coefficient to be 5.0×10^{-6} ft⁻¹ (visibility 15 miles) are shown in Table 4.3. (The calculation also makes the tacit assumption that the scattering particles have the same (exponential) altitude dependence as the air density.) The Blue is attenuated by about a factor 2 1/2 under these typical conditions. The calculation should be valid for the Polaroid photographs also, that is, up to wavelengths 7,000 Å. These calculations assume that all features are at ground zero, and so are only approximate; in particular, the fireball surface extends a considerable distance along the line of sight. Furthermore, because of the aforementioned buildup effect, the flux from the extended source regions will be attenuated by a far lower factor than that shown in the table.

Red Attenuation. In the near-infrared band of wavelengths passed by the Red filter, 6,800 to 9,000 Å, there is some absorption by water vapor but a reduced attenuation by scattering from molecules and aerosol particles. Fortunately this wavelength band is closely matched to one of the windows treated in detail in Reference 17, 7,000 to 9,000 Å. For an atmosphere that is very clear in the visible, it is found that in this window the (collimated) selective transmission $T_{c,s}$ fits the formula

$$T_{c,s} = (0.998)^w (1.063 - 0.151 \log_{10} w), \quad (4.1)$$

where w is the water path in precipitable millimeters. A straightforward argument, following a recipe for w quoted in Equation 19 of Reference 1, gives

$$w = 2.3P_0 \csc \theta (1 - e^{-A/7.12 \times 10^3}) \quad (4.2)$$

where P_0 is the sea-level vapor pressure of water in millimeters of mercury, and A and θ the altitude (in feet) and altitude angle of the point of observation. Values of w for Dakota are given in Table 4.3, as are the transmissions. (Again all surfaces are assumed to be at ground zero.) Note that the selective transmission is quite insensitive to the water path (as the form of the equation verifies).

To find the total window transmission, it is necessary to multiply this selective transmission by a transmission factor appropriate to the visibility, that is, a factor that accounts for the scattering by molecular and miscellaneous airborne particles. This requires a rather bold interpolation of some badly scattered data in Figure 14 of Reference 17; this air-scatter factor, and the overall Red transmission, are given in the last column of Table 4.3. It can be seen that the increased water absorption and decreased scattering roughly compensate one another, and that the narrow-beam attenuation of these atmospheres for the Red and Blue systems will be, sensibly, about the same. Furthermore, the buildup in the Red will be but little different from that in the Blue, and so the uncollimated atmospheric attenuation will be very close also (Reference 16).

4.1.3 Spectrographic Scattering Experiment. In order to determine the scattering corrections to be applied to the spectrographic data, solar spectra were recorded on Eniwetok during the operation. Spectra, as a function of solar elevation and instrument field of view, were obtained with the N-9 camera fitted with the spectroscopic attachment. The reduced intensities were then plotted as a function of air mass (ratio of the path length of radiation through the atmosphere, at any given angle, to the path length toward the zenith). It was found that over the range of 1.04 to 7.01 air masses, the following held to within the experimental error: (1) intensities recorded as a function of wavelength for the 40° field of view quartz diffuser varied with air mass in a manner consistent with the Rayleigh scattering calculations of Reference 18, and (2) intensities recorded as a function of wavelength for the 160° field of view opal diffuser showed no variation with air mass. This is in agreement with the wide angle scattering calculations of Reference 19.

The solar intensities measured with the quartz diffuser were corrected using the data of Reference 18 and fitted to Wien's approximation to Planck's law. The intensities measured with the opal diffuser were fit directly to Wien's law with no correction for atmospheric scattering. From the data, a series of solar color temperatures were obtained. Table 4.4 presents a tabulation of these results, together with the color temperatures determined from a similar treatment of the data in References 18, 20 and 21.

The average solar spectral intensities extrapolated to zero air mass as measured on Eniwetok agree in absolute value to within ± 21 percent with those given in Reference 20. It is felt that this is an indication of the highest degree of accuracy that can be expected from any field measurements made with the spectrograph described in Chapter 2; in general, the errors will be greater.

As a result of this transmission study, all data taken with the quartz diffuser was corrected using the scattering coefficients of Reference 18, and no corrections were applied to the data taken with the 160° opal diffuser.

4.2 ANALYSIS OF CALORIMETER AND RADIOMETER DATA

4.2.1 Data Reliability. A close inspection of Table 3.3 indicates that the data is not as homogeneous as might be desired or expected. This lack of homogeneity can best be illustrated by plotting some of the data given in Column VII as a function of the slant range for the instant when maximum irradiance was recorded. This plot of E versus D is given as Figure 4.3.

In Figure 4.3 data from three different aircraft—B-47, B-57, and B-66—are plotted for those devices that were positioned on barges, which were of the largest yield, and for two lower yield towar detonations. All instruments viewed the fireball directly through quartz windows. A preliminary investigation showed no significant difference between the instruments with a 90° field of view and those with a 160° field of view. From Figure 4.3 several statements can be made.

1. A large amount of variability exists among the various instruments on the same aircraft purporting to be recording the same event. An inspection of the original records and processed data indicates that in many cases saturation effects occurred, which caused the readings to be low. A verification of this point can be obtained through a comparison of some of the data where filters were used with the calorimeters and the data where filters were not used. In some cases, the filter data shows radiant exposures greater than those recorded by the unfiltered calorimeters. From Table 3.3, for example, in Shot Dakota, under the B-47 aircraft, a comparison of the sixth entry with the eighth entry shows that the energy in the wavelength region from 0.5 to 2.5 microns is greater than that over the entire spectral region from 0.2 to 4.5 microns. In other cases, the integrated radiometer data shows values of the radiant exposure comparable to the highest values of the unfiltered calorimeters. The radiometers in every case had a quartz window, so that the integrated radiometer data should be comparable with the unfiltered calorimeters.

In explanation of these effects it is noted that thermal damage to the filters and windows is common and can change the transmission characteristics of the windows during the period of the

most intense irradiance. Also the windows and filters of the instruments used in the test were exposed to the environment during the entire operational phase of the aircraft, which included takeoffs and landings from an airfield. The dust raised during the takeoff phase may settle on instrument windows and cause, by scattering, a reduction in the energy incident on the detector. Although the possibility exists that some instruments may indicate high and that this error is not removed by calibration, the weight of the evidence indicates that the low values are in error. Using these highest values, there is in many cases good agreement between calorimeters and radiometers for a given event and aircraft.

Typical calorimeter data is shown in Figure 3.6. A common problem is illustrated here. Three calorimeters located in the same aircraft at the same station simultaneously receive radiant energy from Shot Apache. As indicated on the diagram, the three calorimeters had quartz windows and either 90° or 60° fields of view. The differences between curves cannot be ascribed to variations in field of view; a general analysis of the results shows no correlation here. Although it appears that the lowest curve can be brought into reasonable coincidence with the two upper curves through multiplication by a constant (in effect a new calibration factor), no nonsubjective evidence that is available permits doing this. These instruments are presumed to be calibrated in absolute units and in the absence of evidence to the contrary, this calibration must be accepted.

2. The average value of the specific thermal energy from barge shots is shown as the solid horizontal line of Figure 4.3. This figure indicates a reasonable assumption for the specific thermal energy under these conditions is $E = 1.3\text{-km}^2/\text{cm}^2\text{-kt}$. The slant range is restricted to be in excess of 5 km. If additional data from two tower shots is averaged in with the barge data, the average value of E becomes $1.4\text{ cal-km}^2/\text{cm}^2\text{-kt}$. This independence of range is expected, because a consideration of the water vapor spectrum and the high water vapor content of tropical Pacific air leads to the conclusion that only a short distance is required to remove nearly all of the energy falling within the water vapor absorption bands. An inspection of the last column of Table 4.1 illustrates the magnitude of the variation in total transmission that occurs in moist Pacific air. No haze correction has been made nor has a correction been made for atmospheric gases other than water vapor. With the exception of nitrogen dioxide whose concentration is unknown, carbon dioxide and haze are assumed to give small but constant attenuation, a not unreasonable assumption. The tests were conducted under conditions of good visibility, i.e., little haze. Visibilities were reported as 10 miles or more for all events listed in Table 3.3 with the exception of Shot Zuni; a visibility of 8 miles was reported for this event.

No correction for transmission differences has been made to the data used in constructing Figure 4.3, because the scatter of data obscures any effect arising from these differences.

Although the scatter of individual data masks the effect, close inspection indicates that the radiant exposure may have an angular dependence of the form discussed in Reference 1. The angular dependence can be best described by reference to Figure 3.1. This figure shows that an aircraft at a small angle θ (nearly over the fireball) will see more of the fireball surface than will an aircraft flying at a large angle θ . In Reference 1, consideration of the fireball brightness and projected area led to the postulation of a $\cos^{2/3} \theta$ dependence for surface bursts. To test this postulate, Figure 4.4 is presented.

Figure 4.4 includes all of the pertinent data from surface shots—Zuni, Flathead, Dakota, Apache, Navajo, Tewa, and Huron. The values of E were taken from Column VII of Table 3.3. Figure 4.4 is in two parts, the upper graph showing E as a function of θ , while the lower shows $E/\cos^{2/3} \theta$ as a function of θ .

The spread in the individual points is considerable, but it appears that

$$\frac{E}{\cos^{2/3} \theta} = 1.45 \quad (\text{Curve A or C}) \quad (4.3)$$

is a better fit to the data than

$$E = 1.28 \quad (\text{Curve B}) \quad (4.4)$$

In the angular range $0^\circ < \theta < 60^\circ$, either expression fairly represents the data.

3. Because of the variability that has been shown to exist in the unfiltered calorimeter data and because of the lack of data to compare several sets of filtered calorimeter values under the same ambient conditions, large absolute errors may exist in the calorimeters equipped with filters.

4. In the planning stages of the project, it was hoped that some information on the effective albedo of the water surface could be obtained by placing calorimeters in the underside of the fuselage with the detector surface parallel to and viewing the mean water surface. Calorimeters oriented to this geometry have been designated as vertical calorimeters. Unfortunately, as Figure 3.1 suggests and Column IX of Table 3.3 verifies, the vertical calorimeters see the entire fireball and its immediate surroundings. As a result, no information can be gained concerning the relatively small flux reflected from water areas far from the fireball.

4.2.2 Comparison of Observed Data with Predictions. One of the most important results that emerges from this study is the verification, or lack of same, of equations, graphs, or nomograms that were used for predictive purposes. A method which is used to predict the radiant exposure is described in Reference 22. In this reference, the yield of the burst, the height of the burst and the distance of the receiver from the source, the velocity of the aircraft, the moisture content in the atmospheric path, the height of the haze layer, and the visibility are parameters used in arriving at a forecast of the radiant exposure. Of these parameters, the forecast radiant exposure is least sensitive to the ratio of the visibility to the height of the haze layer and most sensitive to the range effect. These conclusions, which seem to be nearly self-evident, were reaffirmed when recalculating the predicted Q , the radiant exposure, using observed values of the parameters. It was found that the predicted Q on recalculation was in general within a few percent of the Q predicted on the basis of planning data. That this occurred depended overwhelmingly on the fact that the planning data on the yield of the weapon and the positioning of the aircraft was that subsequently measured in the test. As these tests are always carried out in relatively clear air so moisture laden that water vapor absorption is near maximum, the weather parameters are essentially constants in the predictive equations. This point can be illustrated as follows.

Figure 4.5 is a plot of the observed radiant exposure Q_{obs} , versus the calculated radiant exposure Q_{rec} . The planning data, computed from the nomograms of Reference 22, refer to the radiant exposure on a horizontal detector. The bulk of the data has been taken with the detector surface oriented toward the fireball rather than being parallel to the earth's surface, thus a $\sec \theta$ correction factor (Figure 3.1) has been incorporated in calculating Q_{rec} , approximately correcting a horizontal receiver to one oriented toward the fireball. The scattering of the observed data is large, but the trend is correct. The data scatters approximately evenly about the verification line, the solid line at 45° inclination. It is reasonable to state that on the average, the methods used to predict the radiant exposure Q_{obs} are good. The unfortunate situation exists, however, that the spread in the observed data is so large that detailed verification cannot be made. The spread in the observed data at any one predicted radiant exposure is as large as, for example, the difference between 21 and 42 cal/cm² for a predicted value of 27 cal/cm².

Because the scatter in observed data is so large, a rather simple picture of the thermal radiation process might be visualized. Figure 4.4 indicates that the value $QD^2/W \cos^2 \theta$ is, to within the confidence that can be placed in the data, equal to a constant independent of range. The value of the constant is 1.45 cal-km²/cm²-kt. Using this value, Q_{rec} is found for each burst from

$$Q_{rec} = 1.45 \frac{W}{D^2} \cos^2 \theta \quad (4.5)$$

The equivalent yield W , the slant range D , and the zenith angle θ are known. In this formula, W must be expressed in kilotons and D in kilometers. The resulting Q_{rec} is in units of cal/cm². The measured radiant exposure, Q_{obs} , is plotted against Q_{rec} in the manner of Figure 4.5 to construct Figure 4.6.

There is about the same scatter of data points about the predicted Q in Figure 4.6 as there is in Figure 4.5. This fact points out that the simpler formulation derived from this data and used in constructing Figure 4.6 results in predictions for these specific events as trustworthy as the more elaborate method used to construct Figure 4.5. The tower shots and the single airburst have been included in Figure 4.6 as well as the barge shots from which the prediction equation was constructed. The conclusion that can be drawn from these two figures is that refined prediction techniques are unnecessary and perhaps misleading as long as the data from which these prognostic techniques are developed have the present lack of precision.

4.2.3 Comparison of Thermal Yield from Air Drop and Barge Shot. Shot Cherokee was the only air drop. The aircraft data is meager so that a comparison of the thermal yield for this air drop with the thermal yield from a barge shot could only be made in a few instances. The barge shot selected for comparison was Shot Zuni. The only usable data was that from the B-47 aircraft. Comparison could be made between three sets of calorimeters and three sets of radiometers.

Since the range at the second maximum for Cherokee was 64,420 feet, and that of Zuni only 45,910 feet, while the weapon yields were similar, the thermal exposure and irradiance data were normalized by multiplying by D^2/W , the ratio of the square of the slant range by the yield. The normalized data was used in the following way to construct Figure 4.7.

Three calorimeters were found for Cherokee that had thermal records that extended to at least 18 seconds. Each of the three calorimeters had a different filter. The first had just the quartz window, symbol Q , the second filter A , and the third filter B . The transmission intervals measured in microns are respectively 0.2 to 4.5, 0.7 to 2.5, and 0.9 to 2.5. In investigating the Zuni data from the same aircraft, it was found that the same instruments in the Zuni and Cherokee events were equipped with the same filters. This fortunate state of affairs enabled the comparison to be made with the same instruments equipped with the same filters for both Zuni and Cherokee. The ratio of the specific thermal yield $E_{\text{Cherokee}}/E_{\text{Zuni}}$ was taken as a function of time where E is defined by Equation 3.1. This gives the first three curves of Figure 4.7. The filter is the constant parameter for each curve.

The fourth through sixth curves of Figure 4.7 are constructed in the same manner as the first three curves, except that the sensing instruments were radiometers instead of calorimeters. No filters were used, only quartz windows. In this set of measurements, comparison could also be made between the same three instruments for both Cherokee and Zuni. Here the comparison is between rates at which energy is received, rather than cumulative amounts of energy.

The evidence supplied by Figure 4.7 (excluding the third curve from the top) and the data from Column VII of Table 3.3 show that the specific thermal yield of Cherokee is of the order of 0.8 the specific thermal yield of Zuni. Stated a bit differently, it appears from this one set of data that an aircraft will receive at least as much and perhaps more thermal exposure from a surface burst than it will under comparable conditions from an airburst. Several factors may contribute to this effect, and these more than compensate for the reduced fireball area presented to an aircraft flying at a low elevation angle in respect to the fireball. These factors include an enlargement of the hemispherical radius of a ground burst over an equivalent airburst, the high albedo of the shock froth, and the scattering by the air and clouds. All of these effects tend to increase the thermal flux. A discussion of these effects is presented later.

Using the equation for the thermal exposure Q_E given in Reference 1 and using the available data on the characteristics of the device, the positions of the aircraft, and ambient weather conditions, it was calculated that the total radiant exposure that would be received on a horizontal detector in the B-47 aircraft for Cherokee was 13.8 cal/cm² distributed such that 8.1 cal/cm² were received in the visible and 5.7 cal/cm² were received in the infrared. Corresponding values as calculated for Zuni gave respectively, 13.9, 1.6, and 12.3 cal/cm². A surface albedo was chosen as $\rho = 0.6$.

The only available data from Table 3.3 to check these calculations were the second entry under Cherokee and the first and second entries under Zuni. The Cherokee value was 4.69 cal/cm² received in the infrared. The Zuni values were 18.6 cal/cm² total and 13.0 cal/cm² in

the infrared. The only direct check that can be made, therefore, is in the infrared where the calculated values of 5.7 and 12.3 cal/cm² can be compared with the measured values of 4.69 and 13.0 cal/cm², respectively. The ratios 5.7/12.3 and 4.69/13.0 are respectively, 0.46 and 0.36. The agreement is reasonable when considered in terms of the large variability that is known to exist in the data.

A comparison between theoretical and experimental thermal exposures for calorimeters pointed directly at the fireball is not so straightforward, mainly because of the approximate correction made to Q_E in order to estimate the direct radiant exposure. The correction is geometrical, and rotates the horizontal receiver to a position where the normal to the receiver surface points directly at the fireball. This rotation, of course, maximizes the direct flux incident on the receiver, but is not a rigorous correction for the scattered and reflected fluxes. However, as the theory is relatively insensitive to the indirect as compared with the direct flux, the orientation of the receiver in respect to the direct flux is a factor of primary magnitude. In terms of the angle θ of Figure 3.1, $Q_E \sec \theta$ is an estimate of the direct flux. For Cherokee, this increases the total radiant exposure from 13.8 to 24.0 cal/cm², and for Zuni the corresponding value increases from 13.9 to 20.0 cal/cm². The ratio 24.0/20.0 = 1.2 is 50 percent higher than the 0.8 estimated from Figure 4.7.

4.2.4 Determination of Irradiance from Calorimeter Data for Shot Dakota. Since Shot Dakota has been selected to receive a detailed photographic analysis (Section 4.5), an attempt will be made to extract more information from the calorimetric data that has already been presented in Table 3.3. The method to be used, though basically sound, leads to results of limited value. This statement is made for two reasons. First, there is a relatively large uncertainty in the accuracy of the stated experimental values. Second, the stated wavelength interval is only approximate because of the specific transmission characteristics of the filters mentioned earlier. With these limitations in mind, Figure 4.8 has been constructed.

Figure 4.6 is a plot of the irradiance in several narrow wavelength intervals as a function of the logarithm of time. The direct energy from the fireball of Shot Dakota was measured. This curve is a derived curve, constructed from filtered calorimeter data. In theory, the slope of the time-dependent radiant exposure curves (calorimeter data) yields irradiance. The difference in two irradiances, each filtered differently, that view the same thermal event for the position in space is used. This difference is just the irradiance that would be received by a calorimeter having a filter whose transmission was the difference of the two filters used. By this differencing technique, it is possible to estimate the irradiances for the wavelength intervals listed in Table 4.5.

Figure 4.9 is similar to Figure 4.8. In this figure, the irradiance from Dakota measured by calorimeters pointing vertically downward is presented. Because of the obliquity factor discussed in Chapter 3, the irradiance in Figure 4.9 is less at any instant of time than the irradiance given by Figure 4.8. Like plots for other events showed similar characteristics.

No particular inferences should be drawn from the fact that the time to maximum irradiance of curve Q-A in Figure 4.8 is greater than times shown by the other curves. The smoothing of the data and subsequent numerical differentiation does not lead to curves of sufficient accuracy for evaluating such fine detail.

In constructing these curves, smoothing of the data is necessary. This precaution is especially pertinent when large amounts of data are processed by machine methods without the inclusion in the program of a smoothing routine. Otherwise, the slopes, and hence the irradiance, are extremely sensitive to small errors in the calorimeter data. The smoothing of these curves was accomplished by using a running mean of five points, where each point was of the order of 0.05 second apart.

4.2.5 Radiometric Determination of the Source Color Temperature. An indirect product of these thermal measurements is an estimate of the effective black body temperature of the source. For this section of the report, the color temperature of the source will be defined as that temp-

erature used to construct a black body curve that best fits the observed data, when corrected for all known absorptions. From a consideration of the uncertainty in the accuracy of the data used to arrive at the final answer, it is estimated that the error in a temperature determination may be of the order of $\pm 1,000^\circ\text{K}$. Only Shot Dakota was analyzed, using data supplied from the B-57. The results of this analysis is a curve of temperature as a function of time (Figure 4.10). This figure indicates that the highest temperature attained was of the order of $6,000^\circ\text{K}$. This peak temperature occurred at the instant when maximum irradiance was measured. This high temperature is about a factor of 2 greater than the $3,000^\circ\text{K}$ temperature assumed for surface bursts in Reference 1.

To derive the data from which Figure 4.10 was constructed, it was assumed that the ratio of the irradiances measured in two different filter regions was just the ratio of the black body energy leaving the source corrected for the known absorptions. The known absorptions for the regions selected are due to water vapor, carbon dioxide, and the filter absorptions. The visible region was not used because of the unknown transmissivity of NO_2 and N_2O_4 . Figure 4.2 gives the absorption per unit length at standard temperature and pressure for these two gases, but as the concentration, temperature, and distance from the fireball of the gases was unknown, no transmissivity could be determined. In the vicinity of the fireball, absorption and re-emission of radiation is a complex phenomena for which Figure 4.2 is of limited validity.

Radiosonde balloons launched just before the event indicated that 54 mm of precipitable water occupied the path the radiation subsequently traversed between source and receiver at time zero. The carbon dioxide content of the atmosphere is relatively constant and known. Thus, it was possible to estimate the transmissivities of water vapor, carbon dioxide, and the filters as functions of wavelength. These transmissivities will be indicated as τ_1 , τ_2 , and τ_i , respectively. The subscript i is a general filter index, where the index system is the same as used earlier in Chapter 3 (Table 3.4). Using symbols, it is expected that two instruments on the same aircraft which review the same event, will show the following ratio of irradiances.

$$\frac{H_{A-B}}{H_{B-C}} = \frac{\int_0^\infty \tau_1 \tau_2 \tau_{A-B} \epsilon(T) d\lambda}{\int_0^\infty \tau_1 \tau_2 \tau_{B-C} \epsilon(T) d\lambda} \quad (4.6)$$

In the above equation

$$\epsilon(T) = \frac{c_1 \lambda^{-5}}{e^{\frac{c_2}{\lambda T}} - 1} \quad (4.7)$$

the black body intensity function expressed in conventional symbols. This function is temperature as well as wavelength dependent. Tables of this function exist in a form suitable for computation. If small and uniform intervals $\Delta\lambda$ are chosen and the τ 's and $\epsilon(T)$ are replaced by their mean values over the interval, Equation 4.6 takes the simple form

$$\frac{H_{A-B}}{H_{B-C}} = \frac{\sum \tau_1 \tau_2 \tau_{A-B} \epsilon(T)}{\sum \tau_1 \tau_2 \tau_{B-C} \epsilon(T)} = \frac{\sum h_{A-B}(T)}{\sum h_{B-C}(T)} \quad (4.8)$$

In practice, the summation is taken over all intervals where τ_{A-B} or τ_{B-C} has a value other than zero.

The ratio $\sum h_{A-B}(T)/\sum h_{B-C}(T)$ can be found from available data using several arbitrary temperatures and the results plotted as functions of the temperature. This procedure leads to Figure 4.11, constructed for the following parameters

Water vapor	60 mm of precipitable water
Carbon dioxide	250 atmosphere-cm
Filter A-B	0.7 to 0.9 micron
Filter B-C	0.9 to 2.0 microns

These parameters describe Shot Dakota as viewed from the B-57.

To construct Figure 4.10, the irradiance data as derived from the filtered calorimeters to

form the ratio H_{A-B}/H_{B-C} is used. From the original data

$$H_{A-B} = H_A - H_B \quad (4.9)$$

$$H_{B-C} = H_B - H_C \quad (4.10)$$

where the letter subscripts represent the filters described earlier. The ratio of irradiances changes with time. Assuming the equality specified by Equation 4.8, Figure 4.11 can be entered to find a temperature consistent with the observed ratio H_{A-B}/H_{B-C} . This temperature plotted at the time this ratio was measured is a point on the graph, Figure 4.10.

It is unfortunate that more spectral regions are not available for analysis, so that these results can be checked. Data from the region 2.0 to 2.5 microns was not used because of the low signal-to-noise ratio and the low signal level exhibited by the data. The region from 0.2 to 0.7 micron could not be used because of the lack of information concerning the transmissivity of NO_2 and N_2O_4 . In principle, the average transmissivity of the combination of these two gases could be determined if the validity of Figure 4.10 is accepted. An equation of the form of Equation 4.7 would be used, except that T is now known and one average $\bar{\tau}_1$ is unknown. Here $\bar{\tau}$ is defined from

$$\bar{\tau}_1 \sum \tau_1 \tau_2 \epsilon(T) = \sum \tau_1 \tau_2 \tau_1 \epsilon(T) \quad (4.11)$$

The crudeness of the data does not merit this additional refinement.

4.3 ANALYSIS OF LOW-RESOLUTION SPECTROGRAPHIC DATA

4.3.1 Structure Identification. Considerable effort was spent in trying to identify the absorption structure shown in the spectrographic traces (Figures 3.8 through 3.20). The results of this investigation are shown in Figures 4.12 and 4.13. Figure 4.12 is a composite of laboratory absorption spectra of NO_2 taken at various amounts of absorber concentration. Figure 4.13 presents a comparison of the laboratory absorption spectra with two frames from a typical shot. It is evident, from data of this type, that in the spectral region considered nearly all of the spectral structure can be attributed to the absorption of radiation by NO_2 .

The amount of absorber present was determined by the method described in Reference 23. This involves the use of differential absorption coefficients based upon the values of the absorption coefficient of NO_2 measured at room temperature. The results of this analysis are summarized in Table 4.6. It is felt that these amounts represent lower limits to the absorber concentrations present. Errors due to slit width corrections could increase these values by as much as 20 percent, although these errors are probably small as compared to the errors introduced through the use of room temperature absorption coefficients.

Examination of the last column of Table 4.6 reveals that the NO_2 concentration at the time of the second maximum is roughly independent of the device yield. This implies that the absolute amount of NO_2 present at this time varies in direct proportion to the square of the fireball radius. This in turn implies that the concentration varies approximately with the yield raised to the two-thirds power.

Thus, at least in the visible portion of the spectrum, the spectral histories of all events appear quite similar, regardless of the yield. A large amount of NO_2 is formed quite early in the bomb history and persists throughout the entire event. The actual amount of NO_2 formed, the mechanisms of formation, and the role it plays in thermal radiation cannot be precisely determined until absorption coefficients for NO_2 are known for the temperatures involved.

4.3.2 Spectrographic Determination of Color Temperature. To simplify thermal radiation flux calculations, it is desirable to represent the spectral distribution of the radiation by a single number. This leads to the concept of spectral temperatures. Attempts were made to find a color temperature that would represent the data during a major portion of the thermal pulse. When the relative spectral intensities were reduced to plots of Wien's law, it was found that they deviated considerably from a gray-body distribution. This is due to the tenuous nature of the fireball as well as the large absorptions by NO_2 . Since temperatures determined from the

Wien plots would have been quite low and clearly not representative of the fireball surface temperature, it was decided to obtain a temperature for each wavelength interval defined by the surface brightness of the fireball in that interval. Thus, it would be possible to obtain a set of temperatures as a function of wavelength as well as a function of time.

This method involved the measurement of absolute spectral intensities, correction for aircraft position as a function of time, corrections for the nonspherical shape of the fireball, and assumptions as to the effective fireball emissivity. For the purpose of these calculations the fireball was assumed to have an emissivity of 0.63 and the shape correction was that recommended in Reference 1, for a hemispherical surface burst.

The results of this calculation are summarized in Table 4.7. The temperatures presented here are for the wavelength region from 4,400 to 6,000 Å, the higher values of temperature corresponding to the longer wavelength. In nearly all cases considered, the temperature at any time during the pulse increased with increasing wavelength. Also, in general, the spread of temperature values decreased with increasing time after the second maximum.

If the logarithm of the temperature is plotted as a function of the logarithm of time, it is seen that the average values of the temperatures fall along a straight line, the slope of which is minus $\frac{1}{3}$, as suggested by Reference 24. The data was reduced by this slope, and the resulting intercepts were plotted as a function of the weapon yield. This resulted in the empirical equation,

$$T = 2570 W^{0.12} t^{-1/3}, \quad (4.12)$$

Where: T = temperature in °K

W = weapon yield, kilotons

t = time, seconds.

This equation holds only for times greater than the time of the second thermal maximum. At the second maximum, Equation 4.12 reduces to

$$T = 8690 W^{-0.047} \quad (4.13)$$

In order to facilitate comparison of the spectral data with that obtained from calorimeters and radiometers, it seemed desirable to obtain an average color temperature for the entire thermal pulse. This was accomplished by plotting the relative spectral intensities as a function of time. The resulting power-time curves were graphically integrated, and the values of the integral fitted to Wien's law. This resulted in an effective integrated color temperature for the visible region. The results are presented in Table 4.8. The type of temperature presented here is equivalent to that determined from measurements made with filtered calorimeters, the main difference being that the calorimetric temperatures are essentially measures of the color temperature in the infrared.

Thus, due to the variation of the fireball absorption coefficient with wavelength, it is impossible to represent accurately the spectral distribution of the radiation in the visible region. Approximate values for the spectral temperature for times greater than the second maximum can be estimated from Equation 4.12.

4.3.3 Time to Second Maximum Spectral Dependence. In examination of the spectral power-time curves, it was noticed that the curves for different wavelengths peaked at different times. Time to the peak was determined from the peak of the smooth curve through the data points for each wavelength. The resulting times were then fitted by the method of least squares to an equation of the form

$$t_{\max} = K W^b \quad (4.14)$$

Where: t_{\max} = time, seconds to the second maximum

W = yield, kilotons.

The values of b obtained from the above relation scattered in a random fashion from 0.45 to

0.52. It was decided to fix b at 0.50 and solve for K as a function of wavelength. Thus,

$$t_{\max} = K(\lambda) W^{1/2} \quad (4.15)$$

When plotted versus wavelength, values of K determined in this manner resulted in a band of data points indicating a general trend. For each wavelength the rms value of K was calculated and a smooth curve fit to the points. The results are summarized in the table of $K(\lambda)$ coefficients (Table 4.9). Table 4.10 presents a comparison of the measured t_{\max} values with the ones calculated from Equation 4.15, using the coefficients in Table 4.9.

Variations in the time to the second maximum with wavelength have been found. These variations are most probably the result of the varying transparency of the fireball as a function of wavelength and time. That is, as the fireball becomes more transparent radiation is measured from regions of higher temperature. This interpretation is consistent with the behavior of the NO_2 absorption coefficient.

4.3.4 Fireball Diameter Correlation. In the process of determining spectral temperatures, it was necessary to measure the fireball radius as a function of time. This was accomplished by measuring the image diameters photographed with cameras adjacent to the spectrographs. These image diameters were related to fireball diameters through knowledge of the aircraft position and camera focal length. As a byproduct, these data were analyzed with respect to the scaling laws.

It was found through the method of least squares that the maximum fireball radius R_{\max} obeyed the relation

$$R_{\max} = 330 W^{0.22} \text{ (feet), } W = \text{yield (kt)} \quad (4.16)$$

and the radius, R_t , at $t = t_{\max}$ varied as

$$R_{t_{\max}} = 266 W^{0.24} \text{ (feet), } W = \text{yield (kt)} \quad (4.17)$$

These results are summarized in Tables 4.11 and 4.12.

4.4 ANALYSIS OF PHOTOGRAPHIC DATA

The remainder of this chapter is concerned with the interpretation of the photographic records taken from the four aircraft. The phenomena of interest were those of significance in the prediction of the thermal radiant exposure and irradiance at a point in space as a result of the nuclear explosion. To this end, the time history of the fireball and its associated reflecting, absorbing, and scattering elements have been studied over the complete thermal development time of the detonation.

This section treats several of the ancillary features which are observed in each detonation, and serves as a further introduction to the more complete analysis of Shot Dakota (Section 4.5) and of the absorption shell phenomenon (Section 4.6).

4.4.1 Hot Spots. Good examples of this effect are shown in the reproductions of the two Dakota Polaroid shots and in most other series as well (see Appendix). The bright areas appear to be fairly randomly interspersed in the outer regions of the fireball; they are of course not as easily detectable against the bright background of the central portions. Spots are observed up to the very edge of the fireball or absorption shell, but not outside. The spots have a size distribution ranging from just resolvable specks up to areas subtending such large angles that they appear to be 100 feet across. (Resolution of the Microfilm film is, typically, 5 feet in these photographs; the lens system decreases this resolution to two or three times this figure for the f -numbers used.) However, irradiation (image growth by diffusion in the emulsion) could account for all or part of the image size. (But see below.)

In the Polaroid photographs shown, the spots appear at about half the time to minimum and gradually become undetectable, first visually and then densitometrically, as the fireball brightens.

Those in the absorption field are still detectable up to about $3 \times$ minimum, after which time they fade into the background. This same behavior is observed in the Red photographs. In the Blue frames, the hot spots first appear on the film and expand with time (expanding star cluster) when there is no visible continuous fireball; consequently, all the blue flux affecting the film for a few frames is from the hot spots. The individual spots are distinguishable against the dimmer background up to about $6 \times$ minimum. Only 1 percent of the integrated thermal flux has been emitted at $3 \times$ minimum, and about 8 percent at $6 \times$ minimum, so that the contribution of the hot spots to thermal damage is in any case small.

A microscopic examination of the Red image of the spots fails to show any structure resolved by the camera system. The spots appear circular, or, occasionally, oval with the short axis radial from the fireball center. Since they are smaller than the slit, no density profile can be made. Consequently, it is not possible to decide from the Red data whether they are as large as they appear (which is very large indeed), or whether the extended bright spot is due to light diffusion effects in the emulsion. There are, however, no noticeable diffusion effects at other sharp demarcation lines, such as the fireball edge in Frame Zero.

Most of the Blue series show a dark tail on the bright hot spots. An example is Dakota Series 36299, shown in the Appendix. These tails appear to extend radially out from the fireball center; their length generally increase with projected distance from the center. Thus the tail gives the appearance of being the shadow of the bright area. Since no question of image diffusion is involved with these dark streaks, and since the streak width is the same as the width of the hot spots, the hot spots must have essentially the finite extent measured on the film.

The finite slit size makes the relative light contribution of the spots difficult to evaluate. Near minimum in blue light this figure is approximately 100 percent as noted above. For the red between minimum and $3 \times$ minimum a crude value of 10 percent may be assigned by estimating the fractional area of the fireball covered by the spots as 1 percent, and the ratio of spot brightness to brightness of surroundings as 10.

It is possible to identify the same hot spots in the various series of photographs of detonation, and to trace individual histories. The bright local areas appear to move out with the expanding fireball; their relative positions therefore change only slowly.

4.4.2 Plume. This large topknot appears to be a billowy cloud of opaque gas, developing at about the time of minimum. A plume is visible on all the ground, water, and barge detonations, but none is detectable on Erie or Mohawk, the two tower shots; and none is resolvable on airburst Cherokee (which has extremely poor photographic coverage). Presumably, then, the plume is associated with an interference effect of the early shock wave reflected from the surface.

The genesis of the plume appears to be as follows. A large hot spot, or group of hot spots, generally less bright than the other hot spots, develops near the crown of the fireball at about the time of minimum (it is first observed somewhat later on the blue films). An enlarged view of the hot spot on Dakota, in the Blue, shows it to consist of four resolvable bright spots, arranged in a rough square. This spot brightens and then darkens, growing into a large dark volume extending in later frames well above the fireball. The limb of this plume, and particularly its very top in early frames, may be luminous in the Red; however, the plume is always quite opaque in the Blue.

The plume appears to develop earlier in scaled time for low-yield devices (compare, for example, the Lacrosse, Flathead, and Zuni photographs in the Appendix). Consequently, its effect on the thermal flux from low-yield weapons, should be relatively larger than its effect on larger ones.

A detailed analysis of the thermal flux obscured by the plume has not been made. However, estimates of the obscuration of the thermal flux from a megaton-yield device such as Dakota can be made from the several series of pictures in the Appendix. In general, the plume appears to obscure about twice as much of the fireball in the Blue photographs as in the Red ones. Keep in mind that the fraction of thermal flux coming from the fireball proper is roughly 50 to 60 percent (Section 4.5.3), the photographs (Appendix) show that in late frames (say 3 to $5 t_{\max}$) the plume

can block as much as 50 percent of the direct thermal flux reaching a detector above surface zero. (The plume, of course, reduces the albedo also.) The flux to lower angle detectors is reduced by a much smaller factor, as the pictures indicate. At times near fireball maximum, where the flux rate is some seven times as great as at t_{maxII} , the plume covers no more than a tenth of the (Dakota) fireball area viewed from the vertical. An overall estimate of the total integrated thermal flux obscured by the plume in all its stages of development, is 5 percent. This figure is higher for small devices and lower for large ones.

4.4.3 Wilson Cloud. At late stages in the shock development, the air temperature somewhat behind the shock front falls below ambient; this causes condensation of atmospheric water vapor into droplets (Wilson cloud effect). A cloud starts to form near the inside edge of the shock wave, and then grows inward, appearing to take on the shape of an amphitheatre; it extends in, typically, to about one fireball radius from the fireball surface. In passing it may be noted that, when the Wilson cloud first begins to form, it appears to re-condense the same trade wind cumulus clouds that had been evaporated by the expanding shock wave a second or so earlier; in fact, cases are observed in which only the side of a cloud near the fireball is evaporated, and then appears to re-form almost immediately. This behavior is of course expected, as supersaturation is first reached in those regions in which there is a local water vapor surplus: the vapor from the clouds and the condensation nuclei have not had time to diffuse away before the conditions for cloud re-formation are reached. Then, as the temperature is lowered further, atmospheric vapor condenses into the larger, bowl-shaped cloud.

The time (in units of frames or 1/4th second) at which the first sections of Wilson cloud is seen, is shown in Table 4.13. These figures are not to be taken as extremely accurate, because an early cloud formation may be engendered by fortuitous local conditions (such as the presence of water vapor from a recently shock evaporated cumulus cloud). Nevertheless, there is evidence that the onset of Wilson cloud formation does not scale with the thermal effects, that is, as $(\text{yield})^{1/2}$. This is shown by the late (in terms of units of time to maximum thermal output) formation of the Wilson cloud in Mohawk; the relatively late formation in Dakota (which was observed from several aircraft stations) and Apache; and the observation that the thermal flux from the fireball was not great enough to show the Wilson cloud (if it indeed was formed) in the three lowest yield detonations. The time for Wilson cloud formation appears to scale with the other hydrodynamic phenomena, that is, as $(\text{yield})^{1/3}$; see the last column in Table 4.13. (Note again that a higher detection efficiency works in the direction of making the Wilson cloud of Dakota appear early.)

In any event the Wilson cloud does not obscure an appreciable fraction of the fireball or shock froth until 5 to 6 t_{maxII} , when about 90 percent of the thermal flux has already been emitted from the device and the rate of emission is only 10 percent as high as it is at t_{maxII} . Consequently, the importance of the obscuration by the Wilson cloud, from a thermal viewpoint, is reasonably small. The cloud obscures the scattered light from the shock froth, which contributes almost half the thermal flux in these very late frames, and it obscures most of the fireball for low-angle observers. On the other hand, the cloud does not block the flux from the fireball to near-vertical observers, and there is an appreciable albedo contribution from the illuminated cloud interior into such angles. A crude estimate of the fraction of the total thermal flux obscured by the Wilson cloud is 7 percent. It appears that, by the time the Wilson cloud evaporates, the thermal blast is over. (The irreversible shock-heating makes the final ambient air temperature higher than before the blast.)

4.4.4 Air and Water Scattering. In addition to the albedo contribution from shock froth, clouds, and islands, some light appears to come from the water surface. Presumably this light is scattered both from the water, which has a nominal albedo of 10 percent (Reference 1 and later discussion here) and from the air and aerosol particles. Essentially specular reflection from the water surface is observed at low observation angles (see Apache photographs in Appendix), but in general it appears that the major fraction of this part of the albedo comes from

air-scattered light. This air-scattering extends as a background over other features of the photographs and must be subtracted to determine the quantitative surface brightnesses of objects.

Scattering Function. The intensity of this albedo light as a function of (angular) distance from the fireball must be measured at frames before the breakaway of the shock wave. This is necessary because the shock froth, air shock, and absorption shell that develop then make interpretation of the close-in brightness pattern impossible; the far-out brightness is not far enough above film background for proper analysis. The early fireball has a very sharp edge and, in the Red, is bright enough to illuminate strongly the surrounding area. However, the Blue, even at Frame Zero, is not intense enough to permit very good brightness profiles to be made.

Such brightness plots are given in Figures 4.14 through 4.16, the brightness being registered at angles measured from the apparent fireball edge. More such brightness plots are given in Section 4.5.4, along with further discussion. These graphs show that the scattering from angular regions to the front and rear of the fireball is about as great as that from the sides. This near-isotropy gives some implication that the scattering is from the air, because in the photogrammetry, equal angles measured vertically and horizontally do not extend over equal water distances. Furthermore, because of the finite size of the fireball the front and rear angles do not measure symmetric water distances. Another critical point is that the scattering does not fall off as rapidly as $1/(\text{angle})^2$ (an upper limit to what would be expected from a Lambert plane illuminated by a point source), even at angles several times as large as that subtended by the fireball. This point is examined in detail in what follows. A third point is that if the scattering were mainly from the water surface, the light (which has a low-angle source in the fireball) coming from the rear would be expected to be much less intense, unless the water were a very good Lambert plane indeed. An additional observation against water reflection is that the Red albedo is observed to be greater than the Blue, while Reference 25 indicates that the Blue water albedo should be many times greater than the Red. Further evidence that the luminous region about the fireball is the result of air scatter follows.

Scattering by Atmospheric Haze — Fireball Aureole. An examination of the brightness traces made on a horizontal line across the center of the fireball in the first few hundredths of a second after detonation shows a remarkable likeness to similar scans made across the face of the sun and into the adjacent environment. The bright ring surrounding the sun that is observed even on the clearest days is called the aureole, and this same nomenclature will be adopted for the bright ring that surrounds the fireball in its early stages of development. Figure 4.17 illustrates the brightness as a function of angle for several situations. In this figure, the Curves R, J, and D are taken from Figure 28 in Reference 26. These curves are experimental curves of the angular distribution of brightness extending radially from the limb (edge) of the sun taken at ground level at Tübingen (R), Davos (D), and Utrecht (J). The curves have been normalized to a solar disk brightness of 10^6 (log brightness = 6 on the scale that has been adopted for Figure 4.17). It will be noted that the brightness at 0.3° from the edge of the solar disk is of the order of 500 and that it decreases to about 10 at 7° from the sun's limb. The detectors used in these measurements were sensitive to the blue-green region of the spectrum.

Superimposed on these curves are the aureoles observed from three different photographs of Shot Dakota immediately after detonation. Curve 36242 (Red filter) is taken 16 msec after time zero. In order to make a comparison with the sun's aureole, this curve was normalized to Curve D at a point 0.33° from the limb of the luminary. (With this normalization, the brightness across the fireball disk is 3.2×10^3 , as compared with 10^6 for the sun; the angle subtended by the fireball is 2.6° , compared with the 0.5° subtended by the sun.)

Curves 36300 Red and 35925 Blue are derived from photographs of the same event (Figures 4.14 and 4.15). No particular normalization point has been chosen for these curves. These frames were exposed nominally at time zero, i.e., at a time that did not exceed 16 msec after time zero.

Curves A and B are taken from Reference 27. These curves are experimentally measured aureoles about a spherically symmetric array of photoflash bulbs set off in light haze. The

angular subtense of the source was of the order of $1'$ to $2'$ of arc. The curves are unnormalized. In addition, a curve of $1/(\text{angle})^2$ is shown.

These several curves of Figure 4.17 are presented to reinforce the position that the aureole about the fireball is primarily the result of light scattering by the haze in the atmosphere and that water reflection is relatively unimportant. Qualitatively, the slopes of the curves are pertinent to the discussion at this stage of understanding of the phenomena.

A solar aureole is "explained" by the highly directed scattering pattern of particles of the size of haze, i.e., particles having diameters of the order of $\frac{1}{2}$ to 1 micron or larger (Reference 26). The predominance of forward scatter can be illustrated by considering the Mie theory of scattering by spherical particles. Assuming a haze particle to have an index of refraction of $4/3$ and a diameter of 1 micron, the Mie theory indicates that the scattering at angles of 0° , 10° , 30° , and 60° measured to the forward direction, is in the ratio of $1:0.74:0.04:<0.01$. For a 2-micron particle, the forward directivity is even more pronounced, being in the ratios of $1:0.18:0.05:<0.01$. In general, when a qualitative model is discussed, the significant part of the scattering pattern is given by the Fraunhofer diffraction pattern from an opaque circular disk of the same cross-sectioned area as the haze particle. Sideward and backward scattering can be assumed to be small. Its effect is to increase by a small amount the background brightness. With this highly directed scattering pattern and the parallel rays from the sun incident upon the haze, it follows that the light scattered by the haze should rapidly diminish in intensity as the angle from the direct solar rays is increased. Single scattering dominates because of the relatively long mean free path of the photons in haze, and the observed large decrease in the flux when scattered at large angles. These considerations lead to scattering patterns such as Curves D, R, and J. The details of the curves such as brightness and the relatively slight changes in slope depend on the concentration and distribution of particle size in the haze.

The aureole about the fireball and other sources imbedded in the hazy atmosphere may be described by invoking the same argument, which is based on the directivity of the scattering pattern used to explain the solar aureole. The fact that the rays going into the scattering volume from the fireball are more divergent than those from the sun (the sun is effectively a source at infinity) does not decrease the effectiveness of the model, because the directivity of the model requires only that part of the atmosphere between the fireball and detector to be the scattering medium. The atmosphere to the side and to the rear does not materially contribute to the brightness of the aureole because of the strong forward directivity of the scattering pattern. Note also that the fireball is about one scattering mean free path from the observer (Section 4.1.2), a fact that contributes to the validity of this single-forward-scattering (as opposed to multiple-scattering, diffusion-theory) picture.

However, as the air light is backed by a water surface illuminated by the fireball, some of the brightness of the aureole may be due to this background, which has a small smearing effect. This effect is not of major importance in the formation of aureole and is estimated to contribute the order of 15 percent to the brightness (Section 4.5.3).

A further critical observation to support the theory of air scattering is shown in the case of Shot Zuni (Figure 4.16). Here the observation angle is only 27° and the rear water surface is about one fireball radius from the fireball edge. Even under this geometry, the shape of the scattering function is little different from that of the higher angle observations.

One additional observation may be invoked to test the consistency of the theory that air scatter is responsible for the aureole's appearance. The observation is that the aureole is essentially unpolarized (Section 4.5.4). An inspection of Figure 4.31 confirms this. In this figure the ϕ and θ polarizations are not coincident in time. An interpolation must be made to determine the ϕ and θ polarizations at the same instant. When this is done, the total light is unpolarized. The lack of polarization is expected when haze is the scattering agent. The Mie theory predicts no polarization of the scattered light at 0° (unpolarized source assumed) and no significant polarization effect for small angle scattering.

In summary, the weight of evidence suggests that the aureole about the fireball is a result of scattering by the haze in the atmosphere. Although there may be small differences in the aureole when observed through red, blue, or Polaroid filters, these differences are small and

difficult to detect because of the precision required. A representative picture of the aureole is that it is white, unpolarized, and arises because of the directivity and the non-color-selectivity of haze scattering.

4.4.5 Hydrodynamics—Air Shock and Shock Froth Phenomenon. In Figures 4.18 through 4.20 are plotted the radii of the fireball, absorption shell, and shock froth of Zuni (about 3,380 kt), Huron (about 250 kt) and Lacrosse (about 38.5 kt). These three detonations cover a factor of 100 in weapon yield. Complete data for Dakota will be presented separately, along with a more thorough discussion of the features touched on in this section. It should be kept in mind that the hydrodynamic phenomena scale more slowly with device size than do the strictly thermal ones. No attempt was made to compare the horizontal and vertical sizes, because of the photogrammetric uncertainties; no gross differences between these radii appear on the photographs.

The radii of the fireball and absorption shell were measured visually, that is, they are the radii of the apparently bright central hemisphere and the dark absorbing ring, respectively. In light of the known nonlinear behavior of photographic film, this is a rather arbitrary procedure. However, there are practical difficulties that make the densitometric measurement of these radii time-consuming and not particularly accurate. No attempt was made to use landmarks as fiducial points; experience with Dakota showed that such cartographic calibrations can be quite inaccurate, since landmarks corresponding to those seen on the photographs were not clearly indicated on available charts. Furthermore, landmarks were missing on some of the series. Instead, the shock froth data was fitted to that of Reference 28, and the other hydrodynamic data fitted in turn to that. In addition, the data was adjusted for the motion of the aircraft (the apparent sizes get smaller as the aircraft moves away from the detonation site).

Also shown on the graphs is the thickness of the absorption shell. Since this is the difference of two nearly equal radii, the smaller being the fuzzy fireball edge, only the general trend of its time dependence is significant. An inner absorption shell radius is given for Zuni; this will be discussed in Section 4.6.

Fireball. The bright central fireball appears to grow quite slowly after breakaway; this is a well-known optical phenomenon and will not be treated here. At times greater than about $3t_{\max II}$, it appears to decrease slightly in size and becomes very poorly defined.

A correction to the time time zero can be straightforwardly made. From the data of Reference 28 the corrected time at which the Frame One fireball (then coincident with the shock front) has its measured size can be found. In all cases, this adjustment was found to fit smoothly onto the measurements for Frames 0, 2, and 3. All of the data has been corrected by this method.

Absorption Shell. This phenomenon will be discussed in detail in Section 4.6. Note that its radius fits smoothly onto that of the fireball-shock front at times just after thermal flux minimum, where the luminous fireball has a discontinuity in its growth. This implies that the absorption shell is intimately connected with the early history of the expanding luminous volume.

Air Shock and Shock Froth. The problem of growth of the shock wave has been treated by several authors, and to date theory and experiment appear to be in good agreement. Because of the paucity of good fiducial data, no attempt has been made to compare the absolute shock froth data to the predicted values, except in the case of Dakota (Section 4.5). However, the shape and slope of the radius-time curve is found to conform very closely to that predicted in Reference 28.

The shock froth appears to have an extremely high albedo, and at late ($> 5t_{\max II}$) frames about half of the thermal flux comes from it and the air between it and the camera lens. The flux from the outside edge of the shock froth is always two to four times brighter than that from the neighboring unshocked water. This figure is smeared by the air light. Further details of the scattering properties of the shock froth, including the ratio (shock froth albedo)/(unshocked water albedo), will be presented in Section 4.5.

The shock wave, as it heats the air, evaporates the local clouds; this has the effect of reducing cloud albedo, or, in certain cases, increasing the direct flux from the fireball. A discussion of one case of cloud dispersal is given in Section 4.5.3.

The air shock itself is visible on some of the Red films at times near thermal flux maximum (Dakota 36236 and 36300, among others). This is presumably not self-luminescence. If it were, the shock would be brightest right after breakaway, when its amplitude is highest. Furthermore, the expected temperature of the shocked air near thermal maximum is too low for self-luminescence (Reference 29). Rather, the brightness pattern is consistent with scattering from the denser air, which extends about a tenth of the shock radius behind the shock front. Some semi-quantitative data on this contribution to the thermal flux will be given in Section 4.5.

However, in the Blue this air shock is definitely absorbing, obscuring the region behind it; this behavior is evident on all Blue photographs, in striking contrast to what is observed in the Red. Specific examples of this effect are shown in the photographs reproduced in the Appendix. The quantitative effect of this absorption on the thermal flux is not easy to evaluate. The region behind the fireball is, effectively, obscured; some of the light from the shock froth is absorbed; and the fireball itself is darkened.

This absorption by the air shock probably accounts for the structure in the brightness of the Blue shock froth. The froth is bright on the inside and outside edges, with a minimum between; the illumination by the fireball falls off with distance, while the absorption of the scattered light increases with the thickness of the shocked air traversed. The Red shows no minimum in the shock froth, and the Polaroid shows a small, but definitely detectable minimum. This absorption may cause some of the limb darkening of the Blue fireball discussed in Section 4.6 and so interfere with the analysis of the absorption shell (not to be confused with the absorption of the shocked air).

It is tempting to explain this Blue-Red difference by postulating that a small amount of NO_2 is present in the shock-heated air. The absorption coefficient of NO_2 is some 500 times as high in the Blue as in the Red, so the Red light will not be measurably attenuated by the shock-heated air. An alternative explanation, that multiple Rayleigh scattering makes the region dark in the Blue—the Blue Rayleigh scattering cross section some sixteen times the Red cross section—is also not implausible. (It will be recalled that the sky around a red setting sun is red also.) The argument that the shocked air is warm enough to radiate only in the Red is not borne out by the above-mentioned properties of the Red scattering. Unfortunately, the Polaroid data (Section 4.5.4) does not permit accurate analysis of the light from this region to help further in resolving the scattering-absorption question. Furthermore, it is difficult to arrive at a figure for the fractional absorption of the shocked air, as no convenient viewing screen is available. Also the data are beclouded by the contribution of the scattering from the unshocked air, and in any case the Blue film densities in the region above the fireball are always close to the fog background. A very crude estimate is 50 percent transmission for Dakota (1.1 Mt) at thermal maximum, where the air shock is 2,000 feet thick. (This would correspond to an NO_2 pressure of 5×10^{-4} mm Hg, or one molecule in 10^6 .) This is an extremely rough figure, and the shocked-air absorption of the Blue light may be a relatively important factor in the thermal pulse from a nuclear detonation. For further discussion, see Section 4.6.

Fireball Radius and Yield. In Figure 4.21 is shown the radius of the mature fireball as a function of the bomb yield. Characteristically, the bright central fireball, measured as described in the preceding section, grows slowly near and after second thermal maximum, its radius reaching a very flat maximum near $2t_{\text{maxII}}$ (note again that thermal and hydrodynamic phenomena scale differently: the maximum radius comes somewhat later for the smaller weapons in the series) after which it appears to decrease slowly. See Figures 4.18 through 4.20. The datum for Dakota is the average of the several sets of measurements shown in Section 4.5; two points corresponding to two series, are shown for Huron and Zuni; and the other maximum radii are the results of measurements on a single series of photographs of the detonation. The radii are all normalized to the shock froth radii, as described in the last section.

In light of the arbitrariness of this fireball radius measurement procedure (which is evidenced by the spread of the Huron and Zuni points, as well as that of the Dakota points, Figure 4.23) no

least squares fit to the data was attempted. Two straight lines have been drawn through the Dakota point, one having slope $\frac{1}{3}$ (Reference 1) and the other, which makes a rather better fit, having slope 0.258. All points lie within 12 percent of these lines. The tower shots fit about as well as the ground and water shots. The coefficient of the (yield) $^{1/3}$ law is about 20 percent higher than that given for yields up to 500 kt in Reference 1; that is to say, the luminous (in the sense of the film blackening; note again the reservations of the last section) area of the fireball is some 40 percent larger.

In summation, the maximum radii of the fireballs of the 10 detonations ranging in yield from 15 to 5,000 kt can be fit to a power-law dependence on yield, with a relative average deviation of about 5 percent.

Asymmetry. A discussion of the asymmetry of the smaller fireballs, as well as a more detailed discussion of the asymmetry of Dakota, is given in Section 4.5.5.

4.5 ANALYSIS OF SHOT DAKOTA

Since the photography of Dakota was the most successful, this detonation was chosen for detailed analysis. Such a study can also serve as a check on the internal consistency of the data and the reduction methods. In all, 13 series of photographs, taken from four aircraft, were readily analyzable. There are several good matched pairs. Selected frames from these reels are shown in the Appendix. Dakota is an "average" water shot; it is reasonably symmetric (but see Section 4.5.5), shows all the features discussed in Section 4.4, and has a normal complement of cumulus clouds. Atmospheric data are given in Tables 4.2 and 4.3. The locations of surface zero, the islands, and the aircraft are shown in Figure 4.22.

4.5.1 Hydrodynamics. The time dependence of the radii of the fireball, absorption shell, and shock froth, as well as the shell thickness, are shown in Figures 4.23 through 4.25. The film measurements, and the reservations pertaining to them, are described in Section 4.4.5. However, these radii have all been measured absolutely, in that the horizontal distances from surface zero to features on the islands Easy and Dog have been used as fiducials. Alternatively, the time for the shock froth to reach an island point a known distance away, was used for calibration; this enabled more clearly indicated points at all orientations to be used. All of the data has been corrected for motion of the aircraft but not for the Frame Zero shift.

The internal consistency of the data is seen to be very good. Deviations at early times are due to the failure of Frame Zero to coincide with time zero; note that on a logarithmic scale this effect makes points very far separated at early times. These early fireball points (Figure 4.23) lie to the left of the Haskell (Reference 28) line, as expected. The differences among the several series are most likely caused by errors in the measurement of the distances to the fiducial island points. This is borne out by the observation that the coincidence between camera Red-Blue pairs is better than that between the three sets of pairs. Furthermore, the order of sizes is the same on each of the three graphs. Since the shock froth should have the same radius to observers at all angles, this last indicates that the radius of fireball and absorption shell does not vary appreciably with observation angle.

There is no significant difference between Red and Blue absorption shell radii; nor between Red and Blue fireball radii, except at times between thermal minimum and maximum. During this time, the isothermal sphere becomes less and less obscured; the Red fireball appears appreciably larger than the Blue, which has a sharp discontinuity in size. This behavior is, as stated above, to be expected. The scatter of the fireball data is greater than that of the absorption shell radius; this also is expected since the absorption shell is relatively sharp edged.

The check with the shock radius theory (Reference 28) is seen to be very good. This lends credence to the procedure of Section 4.4.5, in which shock radii were used as calibration points for the radii of the other features of the other detonations. The radii of Dakota are seen to have the same general properties as those of Shots Lacrosse, Huron, and Zuni.

The internal consistency of these measurements indicates that the timing of the six cameras was sensibly the same and suggests that it is reasonably safe to assume that the GSAP cameras may be used as clocks for the detonations.

4.5.2 Partition of Light; Relative Albedo Contribution. In this section are determined the fractions of the thermal flux coming directly from the fireball, and as albedo contribution from the shock froth, islands, clouds, and unshocked water; and the variation with time of these fractions.

Optics; Method of Measurement. Photographs in Series 36233 and 36236, a Blue-Red pair, were analyzed. In addition, two telephoto frames (at second thermal flux maximum) from the Blue-Red paired series 36299 and 36300 were compared. The fireball is very well centered in these photographs. The results are, of course, valid only for the particular observation angles. The optical parameters of the two sets of lenses and the aircraft ranges and altitudes are given in Table 4.14. Note that the fields of view are considerably smaller than those normally associated with radiometers and calorimeters. In consequence the relative and absolute contributions of the albedo will be underestimated, perhaps severely. Furthermore, the camera and film system must, for the usual photographic reasons, be regarded as a receptor whose sensitivity varies as $\cos^4 \theta$, where θ is the angle between the incoming ray and the optic axis. EG&G have stated that vignetting and aberrations are small for the small entrance pupils used. ($\cos^4 \theta_{\text{extreme}}$ is shown in Table 4.14). This falloff has the effect of reducing slightly the apparent albedo contribution, but since the effect is small no correction has been made. The scattering of light out of the longer paths to off-axial points is another factor in lowering apparent surface brightnesses. However, points on the fireball are always within 10° ($= \arccos 0.94$). Note also the caveat of Section 2.6.3, which tends to make the albedo somewhat high.

The optical densities of the film, measured along several scan lines, were copied onto an enlargement of the frame. Then the brightnesses, as taken from the H and D curves, were copied onto another enlargement. An example of such a brightness plot is given in Figure 4.26. It was found impractical to attempt to trace isophot lines; this would have required an inordinate number of points, of considerably higher accuracy than those that could be actually measured. Instead, areas of essentially constant brightness were blocked out by tracing over the photographs with thin cross-section paper. The total light flux appearing to emanate from fireball, shock froth, unshocked water, and clouds was computed by counting the number of squares inside each constant-brightness area, multiplying by this brightness, and adding. This procedure is necessarily subjective, especially in assignment of brightnesses to the rapidly varying clouds. The measurements were made by one observer, even though considerable labor was needed to analyze a single frame. It is estimated that the results are accurate only to about 20 percent.

The thermal contributions from the various elements have not been corrected for background air-scattered light. Consequently for shock froth, read shock froth plus air-light, and so forth. There seems to be no way of making this correction without seriously prejudicing the results; in one case, however, an attempt in this direction has been made. The data is also uncorrected for the loss of apparent brightness of off-axial points, described above.

Series 36236 and 36233 were chosen because they are exposed to relatively high density, which affords the wide latitudes needed to get accurate results on the low-brightness albedo points. Even so, the Blue is so dim that only a few scans near thermal flux maximum are useable. The Red is so bright as to have a lens flare near the center and a bright rim around the edge of frames near thermal maximum. Unfortunately, 36236 has large variations in the shutter opening time (Section 4.5.3), and so frame-to-frame comparisons cannot be made with complete safety.

Note also that the angle of observation (as measured to surface zero) decreases from 66.7° to 58.5° from Frame 15 to Frame 375 of 36236 and 36233. It should again be stressed that the results presented in the next section are applicable only to this range of angles; that estimates of contributions of nonparaxial flux will be too low; that air-scattered light is smeared over the results; and that this method of analysis of the microdensitometer data is necessarily somewhat arbitrary and inexact.

Results. The results for the two sets of series are shown in Tables 4.15 to 4.18; some of the values from Table 4.15 giving the thermal flux partition, are plotted in Figure 4.27. Although the information is, as noted above, not particularly accurate, it serves to illustrate, in

a semiquantitative way, a large number of features of the thermal pulse.

Partition of Thermal Flux. The series 36236 (Red) was analyzed from Frame 15 ($\frac{1}{2}t_{\text{maxII}}$) to Frame 375 ($6t_{\text{maxII}}$). This spans the thermal pulse from a time at which less than 1 percent of the integrated flux has been emitted to where more than 90 percent has already escaped. Over this time the fraction of the flux coming directly from the fireball to the observation point decreases monotonically from 60 percent to 30 percent, even though the fireball is growing by about a factor 7 in area. The reason for this decrease is the increased importance of the albedo of the shock froth, from which appears to emanate over 40 percent of the Red radiation in the late frames. Meanwhile the fraction of the light appearing to come from the water surface (mostly air-scattering; see above discussions) decreases markedly, which is hardly surprising in that in late frames very little unshocked water appears in the narrow field of view of the photograph. A normal complement of trade wind cumulus clouds are in the field of view; the closest, most important of these is evaporated between Frames 65 and 150, lowering the cloud albedo markedly. The cloud contribution is seen to increase again as the Wilson cloud is formed (between 4 and 6 seconds).

Clearly the fireball proper and developing shock froth dominate the thermal flux (within the stringent conditions mentioned above) for a flat detector pointed at surface zero. It would be desirable to estimate the air-light contribution to the flux appearing to come from the shock froth. Note that the ratio of apparent brightness just inside the shock froth to that just outside does not vary with size of the shock froth, and has an average value of 3.3 (D/E and G/H in Table 4.17). This would indicate that the fraction of air-light in the shock-froth albedo is constant at all distances from the fireball. If it is assumed that 85 percent (a reasonable figure, but see below) of the flux appearing to come from the unshocked water is in reality air-light, then 26 percent ($= 1.00 - (3.3 - 0.85)/3.3$) of the light appearing to come from the shock froth is air-scattered light. The raw data has been corrected under this assumption and is shown as dashed lines in the graph of Figure 4.27. The fraction of air-scattered light is seen to decrease linearly with time on this semilogarithmic plot, and the relative shock froth contribution increases less rapidly than when uncorrected but still fast enough to drive the fractional air contribution down. The unshocked water-light, 15 percent of the uncorrected air-light, has been subtracted from the corrected air-light but is itself not shown in the figure.

Considering the total illumination, it should be noted that the high-albedo, growing shock froth should make for an increase in the thermal flux; the shock wave is conditioning the water surface, so to speak, for increased albedo. However, because of the serious frame-to-frame brightness fluctuations, the total absolute shock froth contributions cannot be safely evaluated. Note, for example, that the total flux from Frame 45 is higher than that at maximum, in Frame 65. (This correlates with the results of Figure 4.29.) Note also that the evaporation of the nearby cloud reduces the cloud albedo from 10,000 to 2,000 units from Frame 65 to Frame 150, while the fireball itself is going from 43,000 to 16,000 units. For the typical atmospheric conditions of Dakota, the loss in cloud albedo compensates in part for the growth of the shock froth (this is, of course, a fortuitous situation; shock-induced evaporation of a cloud on a line between the fireball and observer would increase the flux).

The Blue 36233 series is so underexposed that the percentage flux assignments in Table 4.15 should probably not be taken too seriously. For example, most of the flux from the air is undetectable, the illumination being down in the film background fog.

The 36300 Red-36299 Blue pair of photographs show a smaller field of view than the 36236-36233 series, and consequently the fireball appears to give a rather larger fractional contribution (Table 4.16) to the thermal flux. Since the angle of view is lower, the rear of the shock froth is obscured by the fireball and the shock froth contribution is lowered.

Brightness Ratios. The brightness at various points on the photographs and the corresponding fractions of maximum brightness, are shown in Tables 4.17 and 4.18 (it should be remembered that air-light is smeared over these brightnesses). The plume, as expected, gets more opaque with time; the cloud and island illuminations seem to vary with the fireball brightness (Section 4.5.3). Note that some points on the nearby right-hand cloud in 36236 are some 35 percent as bright as the brightest points on the fireball. These results, and those in the

other two tables as well, show the apparent Blue albedo to be consistently lower than the Red. The loss of apparent Blue albedo from the shock froth is consistent with the Blue absorption of the shocked air. The low cloud, air, and island albedos are probably explained by the observations that the total fireball brightness is lower in the Blue; and that the integrated flux lighting the albedo area must pass through longer, slant paths in the shocked air and is more attenuated than the direct beam from the fireball to the camera.

The shock froth, at its edge, appears to be about three times as bright as the unshocked water in the Red and twice as bright in the Blue. This holds over a large range of shock radii and varies little with the angle of observation; note the data for the sides and rear. Assume that the fraction of the apparent light that is true albedo of the unshocked water is ϵ . Then $1 - \epsilon$ is air-scattered light; the ratio η of the albedo of the shocked water to the unshocked water, is given by

$$\eta = \frac{3 - (1 - \epsilon)}{\epsilon} = \frac{2 + \epsilon}{\epsilon} \quad (\text{Red}) \quad (4.18)$$

$$= \frac{1 + \epsilon}{\epsilon} \quad (\text{Blue}), \quad (4.19)$$

or, in general

$$\eta = \frac{\xi - 1 + \epsilon}{\epsilon}, \quad (4.20)$$

Where ξ = apparent brightness ratio.

The ratio η is given as a function of ϵ for various ξ in Table 4.19. The experimental variations in ξ , coupled with the uncertainty of ϵ and the lack of specific data on the albedo of shocked and unshocked water makes assignment of correct albedo ratios (or, conversely of accurate ϵ 's) extremely uncertain. However, certain comments and a discussion of some of the albedo data found in the literature are in order. The shock froth is a water spray containing large droplets, hence is white; its albedo must lie near that of dense clouds or freshly fallen snow, 0.8 (Reference 30), since it is undoubtedly optically thick. The specular reflectance of water has been found to follow the Fresnel formula up to wind speeds of 9 knots (Reference 31); this formula predicts a reflectance of 0.03 at 45° from the normal, a typical angle of incidence for the light from surface detonations. A Lambert-type albedo, which is the phenomenon of interest in these experiments, has been measured (Reference 25) by pointing a spectrograph at a water surface and at an incidence angle of 45° , at 90° azimuth from the sun; the results were compared with those from a standard magnesium oxide powder surface. Albedos ranged from 0.15 at $4,000 \text{ \AA}$ monotonically down to 0.01 at $8,000 \text{ \AA}$ (this correlates with the blue-green color of water surfaces). While these values do not accurately fit the field situation, they indicate that for the Blue $\epsilon \approx 0.20$. For the Red, ϵ may well be lower; the higher measured values of ξ for Red systems are consistent with the low unshocked water albedos of Reference 25. In general, a value of $\epsilon = 0.15$ has been adopted for use in other sections of this report.

The brightness at the inner edge of the shock froth is compared with that at its neighboring point just within the absorption shell in Table 4.18. There is considerable scatter of points here; clearcut Red-Blue differences, if any, are not resolved. Presumably, the view is through the absorbing shell at the shock froth in these photographs; the data gives some idea of the transmission of the absorption shell. The smearing effect of the air-light helps mask any Red-Blue differences. The absorption shell will be treated in more detail in Section 4.6.

Other Contouring Features. The Blue fireball surfaces appear to be randomly lumpy, especially in frames before second thermal maximum. This shows, qualitatively, in the Dakota photographs. The brightness of these excursions is often half as great as that of neighboring points. The Red microdensitometer traces do not show these oscillations. In addition, the mature Blue fireball shows limb darkening, being dimmer at its edges than at the center; the Red shows far less limb darkening. A measure of this is the ratio B/A of Table 4.18, an effective fireball area which for the Red is 3 to 4 times as high as the Blue. This point will be discussed in the next section.

In Frame 65 of Red Series 36236, the air shock is clearly visible against air and unshocked water and at its edge is 10 to 15 percent brighter than the neighboring air. The contribution to the total thermal flux, however, of the light scattered from the air shock, is well less than 1 percent. Note that this mantle (Section 4.6.4) should out-scatter some of the light coming directly from the fireball and absorption shell; this effect appears to be quite small also.

4.5.3 Time Variation of Fireball Brightness. The fireball luminous surface is the ultimate source of all the thermal flux, including the large albedo contribution discussed in Section 4.5.2. Consequently, the fireball output is a reasonably good measure of the time variation of the thermal pulse amplitude. The brightness varies only relatively slowly over the fireball surface (Section 4.6.4), especially in the Red, and the fireball area grows slowly also; therefore, the maximum brightness found on the several microdensitometer traces may be used as an indicator of this time variation. It should be emphasized, however, that this procedure gives a less than perfect measurement of the true total thermal flux time variation, and the data should be taken as secondary to the radiometer and calorimeter data. However, the results are of some interest from the point of view of fireball physics.

Such maximum brightnesses for Dakota are shown in Figure 4.28. These are the maxima of the smoothed traces; the erratic hot spots are excluded. The times have been corrected for zero-shift. It should be noted that differences in filter and film system bandwidths, and aircraft slant ranges, make intercomparison of the absolute values of points on these several curves difficult.

Time to Minimum. There is evidence that the minimum in the Red comes earlier than in the Polaroid (which has a wavelength-sensitivity as shown in Figure 2.2). This is borne out by the data from the two Polaroids and three Red series. Note that the Polaroids, which are paired, check quite well with one another, as expected. (The light from fireball surface is not expected to be polarized.) This time difference is of the order of 1/10 the (average) time to minimum. Unfortunately none of the Blue photographs resolve the fireball from the background film fog for about 10 frames near the minimum, and an interpolation of the data in this region is very uncertain (as the graph shows). Consequently, a narrow-band comparison is not possible, and the Red can only be compared to the wide-band (4,000 to 7,000 Å) Polaroid. The direction of the effect is in the same direction as that observed with spectrometers (Reference 32) and is to be expected on theoretical grounds (Reference 33).

Time to Second Maximum. The scaling laws predict a brightness maximum at a time very close to 1.0 second. This also appears to be the time at which a broad maximum in the maximum brightness of the fireball is observed. The fireball grows very slowly near t_{maxII} , so this effect is expected. The measurements do not resolve any differences in the maximum-brightness time among the Red, Blue, and Polaroid photographs. Note the severe fluctuations in the 36236 data; this phenomenon is thought to be due to variations in the shutter opening time, and is discussed later.

Maximum-Minimum Ratios. The ratio of the brightness at second thermal flux maximum to the brightness at minimum, appears to increase with decreasing wavelength. For the three Red series shown, this ratio lies between 10 and 20; for the Polaroids, it is 650; and for the two Blue series an interpolation shows it to be of the order of 2,000. (It should be noted in passing that the fireball surface area goes up by about a factor 2.4 in that time, so the total thermal flux ratios will be still larger.)

Curve Shape Comparisons. The shape of the falloff after maximum is closely the same in the Red and Blue photographs (this effect shows more clearly in a semilogarithmic plot) but the Polaroids have an apparently steeper falloff.

After minimum, the rate of climb of the brightness curve for the Red fireball is slower than that of the Blue; the Polaroid is intermediate. This is, of course, connected with the lower intensity of the Polaroid and Blue fireball. The effect of the faster rise and similar falloff, is to make the Blue maximum-pulse narrower than the Red; this holds for the Polaroid also.

The maximum brightness at first maximum in the Blue is very low compared to that in the Red and Polaroid. For these latter the fireball brightness then is as high as, or higher than,

the maximum brightness at second maximum; for the Blue wavelength band this brightness is only about one thousandth as great. This behavior is observed in all the Blue photographs and is not due to the true first maximum being missed. The early brightness is seen to extend below the 6,800 Å cutoff of the Red and into the Polaroid sensitivity, which ends at about 7,000 Å, but it does not reach as far as the Blue (~4,500 Å). Consequently, it appears that the viewer sees a relatively cool surface.

Another feature of some interest here is the (logarithmic) rate of change of brightness in these very early times; this is greater for the Blues and Polaroids than it is for the Red. For example, both Reds lose in brightness by only a factor of 1.2 in the 1/64-second time interval centered at about 0.01 sec, while the Blue and Polaroid are changing by about a factor 2.

Cloud Brightness; Shutter Opening Variations. The albedo brightness of a point on a cloud several fireball radii from surface zero should also be a measure of the integrated fireball brightness. The V-shaped cloud to the upper right in Series 36236 was scanned along a horizontal line intercepting the second little spur from the bottom on its left side, which appears as 39.0 in Frame 0 (Section 4.5.4). The brightest cloud point in this vicinity—at 6.3, 39.0 in Frame 0—was found, and its brightness plotted as a function of frame number (Figure 4.29). Also shown is the water-background point along this line, taken just before the slit starts to pass over the cloud. Repeated vertical positioning of the slit showed the individual readings to be reproducible to better than 5 percent.

The readings show severe uncorrelated frame-to-frame fluctuations, neighboring points differing by as much as a factor of 2. There is some indication that these start at about Frame 15, but since only 1 percent of the total thermal flux has been emitted by that time, it is doubtful that the cause of the fluctuations could be thermal damage. Note that high cloud brightness is always correlated with high water background brightness. Presumably this overall frame brightness variation is due to variations in the (nominally 1 msec) opening time of the camera shutter. While it is believed that the camera used in Series 36236 gives extraordinarily bad results, it appears from a closer examination of Figure 4.28 that this failure is endemic to GSAP-type cameras. Consequently, caution must be exercised in making comparisons of brightness among frames.

Over and above these fluctuations, Figure 4.29 has the general shape of a thermal-irradiance curve. Such a curve for Dakota, taken from the B-57 with 90°-field-of-view calorimeters for a passband 7,000 to 9,000 Å (that is, virtually the same as the Red response) is also shown in the figure; the fit is seen to be rather good. (The radiometer curve is arbitrarily normalized at its maximum point.) However, the cloud brightnesses at the two thermal maxima do not mirror the situation in Figure 4.28, which shows the fireball to have essentially the same brightness at the two maxima. This effect is probably caused by the increase in fireball area, which grows by about a factor 7 in this time; and by the lessening of the distance from the fireball surface to the cloud. The projected distance to the cloud from the fireball edge decreases from about 4 to 1.5 fireball radii during this time (densitometer traces show the fireball to be only half its apparent size in the necessarily poor reproduction of Frame 0). The actual distance to the cloud is somewhat closer than this projected distance; the air shock has already reached it by Frame 150, while the shock front has not.

Also shown in Figure 4.29, is the maximum-brightness curve for 36300, replotted from Figure 4.28 and normalized to the radiometer curve at thermal maximum. The maximum-brightness curve lies above the radiometer curve, both before and after maximum; this may be partly due to the normalization procedure (note the scatter of the points near maximum). This effect is rather difficult to correlate with the other observations of this study.

It may be concluded that the results of this maximum-brightness approach, both for the fireball and the albedo of nearby objects, must be interpreted with considerable caution; results as described in this section are only indicative of the total thermal flux pattern.

4.5.4 Comparison of Polaroid Pictures of Shot Dakota. Series 36249 and 36250 are complementary Polaroid telephoto photographs, taken on Microfilm film. They are shown in the Appendix. These series will be referred to as θ (horizontal polarization) and ϕ , respectively.

The B-47 is at 20,680-foot slant range, 50.7° altitude and 127° azimuth at time zero; by frame 65 (1 second) its slant range has increased to 21,000 feet, angle 49.5°. A complete description of the photogrammetry is given in Table 3.7.

Complete fireball diameter measurements on the first 10 frames indicate that time zero for θ is 0.008 second before Frame Zero; for ϕ it is 0.002 second. This makes for an important difference in early (\approx Frame 8) photographs but only a negligible difference in later ones. The photographs show the whole fireball up to about Frame 8 but only about two-thirds of it, on the average, thereafter; no island fiducial marks appear; there is a small cloud at the left of the fireball appearing at a projected distance of about 3,500 feet from surface zero, and a rather large cloud system appearing under and to the lower right of the fireball in the photographs, also at about 3,500 feet from surface zero. Unfortunately, the cameras suffer somewhat from the drawback of variable shutter speeds (Section 4.5.3). This effect is apparent in Figure 4.28; it is evidenced by the greater fireball brightness shown there (the light from the fireball is not expected to be polarized).

The following pairs of photographs were compared:

- A. Frames 0, θ and ϕ
- B. Horizontal scans only, through fireball center, on Frames 1, 2, 3, 4, θ and ϕ
- C. Frames 7, θ and ϕ
- D. Frames 9, θ and ϕ
- E. Frames 24, θ and ϕ . These were rejected out of hand because the shutter opening variation was too great; points on ϕ were all about 50 percent higher than corresponding points on θ .
- F. Frames 64, θ and ϕ
- G. Frames 34 and 44, θ and 39, ϕ . These too were rejected for brightness-difference reasons.

Results of Frame Comparisons. **Frames Zero.** As expected, since ϕ is 0.006 second younger than θ , corresponding points on the photographs are considerably brighter except in the immediate neighborhood of the smaller fireball. This makes absolute comparison of the scattering and reflection rather difficult. The angular distributions of the air plus water albedos are shown in Figure 4.30. Note that for both polarizations the brightnesses to the right and left of the fireball correspond closely to those in front. This effect is observed in the Red and Blue series also, and suggests that scattering from the water surface, at least at these angles, is small compared to air scattering; there is no special forward scattering (from a water surface). The few points behind the bright hemisphere show a somewhat more complicated behavior. The vertically polarized light appears to fall off more steeply than the horizontally polarized; the slopes on the loglog plot being -1.7 and -1.1 . This somewhat unexpected behavior of the albedo light is explained by the observations on succeeding frames.

Frames 1, 2, 3, 4. The brightnesses as a function of angle from fireball edge, measured on a horizontal scan to the right and through the center of the fireball are shown in Figure 4.31. The shutters appear to be quite well behaved, but the differences in time zero again make absolute intercomparison impossible. The slopes of such loglog plots appear to decrease as the fireball gets larger and less bright; larger luminaries result in flatter aureoles. This is plausible from a superposition-of-point-sources viewpoint. This same behavior is observed in the Red photographs of Zuni (Figure 4.16); however, there is some indication of steeper slopes for ϕ . Note that even at three or four fireball diameters, where the fireball should appear as a reasonable point source, the slopes in Frames Zero and 1 do not coincide. (This nonlinearity suggests an admixture of scattering from the water surface for the taller fireball.)

Graphs of brightness of points as measured from the fireball center are steeper near the fireball edge; the slopes of the curves comparable to those in Figure 4.31 are about -3 .

Frames 7. These photographs are somewhat past thermal minimum. The radius of θ is by now only about 2 percent greater than that of ϕ , and its peak brightness appears 50 percent higher. However, the older θ shows more limb darkening (that is, the microdensitometer trace across the fireball center is more bowed; (see Section 4.6) and at about two thirds fireball radius from the center of the two fireball surfaces have equal brightness. This is an intrinsic property of the fireball and its surrounding absorbing medium which does not appear to be polarization-dependent (see below).

Frames 9. A good intercomparison is available here. Horizontal traces through the fireball center are by now identical, within an experimental error of about 0.04 density unit. The peak brightnesses, shape of curve (a measure of limb absorption) and water albedo just at the sides, are the same. A vertical trace through the fireball center shows that the light scattered from the area directly in front of the shock froth is about 10 percent more intense for θ than ϕ ; the intensity is not great enough to permit a proper scattering function to be measured. The brighter θ is consonant with greater θ water scattering or air scattering. The shock froth has not yet developed sufficiently to be useful for scattering measurements.

Frames 24. Since the shutter time variation here makes points on ϕ all about 50 percent brighter than corresponding points on θ , these photographs were not analyzed.

Frames 64; Thermal Maximum. The fireball is mature, and the differences in times zero should have a negligible effect. The maximum brightnesses in the fireball here are about 10 to 15 percent higher for ϕ ; this holds for five separate pairs of scans over the now-large fireball. However, in spite of this difference in fireball center brightness, θ is generally 20 to 30 percent brighter than ϕ on scattering surfaces: this obtains for water and shock froth surfaces to the right and left of the fireball, as well as those in front of the fireball. In other words, in each of the scans the optical density of ϕ photographs is larger at corresponding points in the fireball, crosses the trace of θ somewhere in the absorption shell, and then is lower than the θ -optical density outside of the self-luminous area. This indicates that the θ albedo is of the order of 30 percent greater than the ϕ albedo, in all directions.

Frames 39 and 44 θ and 39 ϕ . Again, no comparison was possible.

Polarization of the Shock Froth. A series of density and brightness measurements was made at adjacent points on the shock froth boundary, one point lying within the shock froth and the other just outside. This was done on θ Frames 10, 25, 35, 45, and 65, and ϕ Frames 10, 17, 25, 40, and 65. The brightness just inside is two to four times as great as the outside brightness, as is observed with the Red and Blue photographs (Section 4.5.2). Also measured was the brightness of the shock froth, on its inside (fireball) edge. In these measurements, no difference between the scattering patterns of θ and ϕ was resolvable. As was pointed out above, the differences in shutter times makes absolute comparisons difficult; the evidence of Frames 64, however, suggests that θ -albedo, uncorrected for air-light, is in general some 30 percent higher than ϕ -albedo.

The shock froth brightness decreases from the front of the fireball around to the sides. The brightness at the sides of the shock froth is only 60 percent as high as at the front. The shock ring appears symmetric about a center line, as expected. The decrease may be due to the absorption of light by the shocked air (Section 4.4.5); the polarized light from the shock froth shows the characteristic minimum (sag) shown more strikingly in the Blue photographs. This lends credence to the argument given in Section 4.4.5 that the shocked air is absorbing because of NO_2 absorption: the sag in the shock froth is less in the Polaroid wavelengths as expected, but nonetheless it is definitely detectable.

Summary. In general, the overall thermal flux is not strongly polarization-dependent. The θ -albedo appears in Frames 64 to be some 30 percent higher than the ϕ -albedo; there is evidence in Frames 9 to support this; since the albedo contributes roughly half of the flux, the total θ flux would be about 15 percent greater than the ϕ -flux. Furthermore, there is a very weak indication that the vertically polarized air-cum-water albedo has a slightly faster falloff with angle from the fireball, than does the horizontally polarized albedo.

In light of the shutter variations and the time zero difference, firm upper limits to the polarization of the light from the various features in the photographs cannot be safely given. Differences in the fireball peak brightness, limb darkening, and absorption shell brightnesses are not resolved. This implies that the absorption shell and air shock attenuate by absorption rather than scattering. In short, no striking differences between the two polarizations is seen.

4.5.5 Asymmetry. In general, the thermal emission of the fireballs and their reflecting elements appears to be symmetric about a vertical central axis, as the photographs in the Appendix show. However, for smaller weapons, there may be considerable asymmetry; and a

microdensitometric examination of Dakota has shown that its fireball is not symmetric.

Erie and Lacrosse Asymmetry. For these small devices, the photographs show a large asymmetry in the fireball shape; Lacrosse appears to show a surface-brightness asymmetry. This may be because smaller detonations are more sensitive to local material and less stable against fluctuations causing breakup.

The Erie fireball begins to assume a square shape shortly after $t_{\max II}$; the square is quite well developed at $2t_{\max II}$. During this time about a third of the total thermal flux is emitted. Somewhat similar features are noted for Lacrosse, which has a very rough surface. From the high (66°) observation angle, the Lacrosse plume (itself asymmetric) obscures almost half the fireball at second thermal flux maximum; this phenomenon is discussed in Section 4.4.2. The asymmetry of the Lacrosse fireball is further evidenced by the variation in illumination of the shock froth (Section 3.2.3). Calorimeter-radiometer results on Lacrosse show definite differences in the thermal flux history of the land and water sides of the detonation (Reference 34).

Dakota Asymmetry. The asymmetry of this device is not, as mentioned initially, evident from a visual examination of the photographic record. It requires a very large number of scans across a large number of frames to properly characterize it; for this reason, only Dakota has been thus analyzed.

The brightnesses and brightness ratios (asymmetry) are shown in Figure 4.32 for the Red and Blue scans of Table 3.7; the figure also shows at what points on the microdensitometer scans they are taken. The time at second thermal flux maximum was chosen for observation; as will be shown later, qualitatively similar results are obtained at other times.

Attempts were made to reduce all of the brightness figures to a common base, but owing to the fact that the film calibrations did not reflect the actual conditions of use, this was not possible. As a result, the brightness figures must not be intercompared; the ratios however describe in a semiquantitative way the thermal picture of the fireball at second maximum.

The B-57 and B-66 records are taken from the same side of the fireball, and they are in essential accord; on this side the fireball is thermally symmetric in the Red photographs. With the Blue film-filter combination, there is definite evidence of asymmetry; the ratio of the brightness on the right side to that on the left side is 1.7 for the B-57 and 2.45 for the B-66. The microdensitometer traces show a definite uniform sag, which is not attributable to cloud effects. These scans were taken across the fireball at the same level; as closely as could be determined, they were made about a third of the distance from the top of the luminous hemisphere to the bottom. The correspondence of the scan lines is most exact with the film records (Red and Blue) from an individual aircraft; it is less exact with the records from different aircraft.

The third and fourth aircraft, the B-52 and the B-47, observed Dakota from higher angular altitudes than the others (62° and 67° as contrasted with 45° and 50°), and from azimuthal directions about 160° away from the other two aircraft. Thus they were observing the back of the fireball, and it might therefore be expected that the sense of the asymmetry observed by the B-57 and B-66 would here be reversed. For the Blue pictures, that is the observation: values of 0.57 and 0.46 (that is, about 1:2) are obtained for the ratio of the brightness of the right side to the left side. The pictures taken in the Red, however, exhibit ratios of 0.93 and 1.23. This effect was checked by examining other frames; for example, the same ratios are obtained from Frames 150, Red and Blue, in the case of the B-47. These results suggest the presence of what may be called a cool spot in the fireball: the Blue asymmetry is greater than the Red. Although the plume is invariably larger in the Blue than in the Red and might, at least in part, be responsible for the asymmetry, traces lower down and therefore farther away from the plume still exhibit this same behavior. It was found that in both the Red and Blue records, the asymmetry increased as the traces were made higher and higher on the fireball. On some of the views the lowest traces show no detectable asymmetry. The asymmetry of the highest traces is somewhat uncertain because of interference by the plume (see Figure 4.32, showing the criteria of the measurement). This is more important in the high angular-altitude photography, where the plume occupies a greater proportion of the field of view relative to the fireball. Since the plume is smaller in the Red photographs than in the Blue, this decrease in the asymmetry of the

highest traces would be expected to be smaller here than in the Blue. This effect can be observed qualitatively in the densitometer traces.

The question naturally arises as to whether there is a time variation in this asymmetry. In order to answer this question, scans were made on a sequence of Blue pictures from the B-57. These ranged from $0.6 t_{\max II}$ to $2.2 t_{\max II}$. The ratios of brightness of the right side to the left side of the fireball were found to be scattered throughout a range of 1.6 to 2.2. The spread of the data is somewhat greater than might be desired; the scatter of the points precludes a decision on whether a trend is present.

The inference of these results is that Dakota did not emit thermal radiation symmetrically; parts of the fireball surface appear to have lower brightnesses than others (over and above limb-darkening effects). That is to say, from different aspects the weapon may appear to have different (thermal) yields. This may well be an important factor in the thermal damage caused by such devices.

4.6 ABSORPTION SHELL PHENOMENON

This section deals with the properties of the dark attenuating ring that is seen to encircle the luminous fireball in each set of photographs (except the poorly resolved Cherokee series). The absorption shell has been rather poorly seen on previous tests because of the lack of shock froth (air and land bursts) and/or the lack of detailed photography from above to utilize the shock froth as a viewing screen for the absorption shell. However, in the Erie Red Series 34565, Frames 1 through 5 show that the absorption shell of a 14.9-kt tower shot can be seen nearly as well against a land background as against a shock froth background, when seen from directly above. Also, in Zuni Series 34383, Frames 55 through 212 show that under the proper circumstances background clouds can make the absorption shell of a megaton-range burst spectacularly visible.

The absorption shell, first seen at the Trinity test, was measured on Shot Easy and discussed in the Operation Greenhouse report (Reference 35).

4.6.1 General Properties. Clearcut absorption shells are visible on all the reproductions shown in the Appendix, with the exception of the photographs of Cherokee. These include surface and land, and low-tower bursts. The resolution on the Cherokee series is very low (the range is some 131,000 feet), and no shock froth appears in this airburst as a viewing screen for the absorption shell. This absence of the shock froth, a feature which is always strongly in evidence in the other photographs, points up the idea that the less easily seen absorption shell is simply missed. The quality of the Mohawk pictures is very low; the detonation is viewed through a thick haze; and the absorption shell is only dimly seen in some of the series (not reproduced).

The attenuating properties of the shell are sensibly the same in Red, Blue, and Polaroid (of this more later; see also Section 4.5.2); no polarization difference is resolved. The shell is observable as a highly attenuating ring obscuring the shock froth, right after breakaway, as the limb darkening of the fireball increases (Section 3.2.11 and the photographs described in that section). The thickness of the absorption shell increases with time; at second thermal flux maximum it is, typically, a quarter of the fireball radius. The attenuation of the shell decreases with time (details later). The limitation on the resolvability of the shell at very late times is the lack of illumination from the fireball. In one extreme case, Navajo (about 4.5 Mt) it is still visible at $5.8 t_{\max II}$.

4.6.2 Hydrodynamics. The time dependence of the shell radius, for Lacrosse (about 39.5 kt), Huron (about 250 kt) and Zuni (about 0.38 Mt), is given in Figures 4.18 through 4.20; for Dakota, it is given in Figure 4.24. This radius is quite sharply indicated on the densitometer traces; the demarcation is less than a slit width at all magnifications, except after the fireball begins to rise and lose its hemispherical shape. The measurement, however, was made visually on the

frame image on the microdensitometer viewing screen. The absorption shell edge has smaller deviations from circularity (see the photographs of Erie, Lacrosse, and Flathead) than the fireball edge, and does not particularly follow the luminous fireball.

After breakaway, the absorption shell radius fits smoothly on to the single radius versus time curve describing the shock and radiation front, while there is a discontinuity in the apparent fireball size. This well-known effect occurs as the shock front becomes transparent and it becomes possible to look deeper into the fireball; it points up the observation of the last section that the outer edge of the absorption shell is a continuation of the once-luminous limb of the fireball. The absorption shell appears to scale hydrodynamically with device yield and time. In the four detonations for which data are presented, the absorption shell radius is 1.25 ± 0.05 times the mature (in the sense of Section 4.4.5) fireball radius; consequently the absorption shell radius scales with device yield just as the fireball radius does. It is difficult to set up better scaling parameters, and in particular, a proper time-scaling, for these relatively late-time phenomena.

The thickness of the absorption shell varies over a very wide range. At times $> 2t_{\text{maxII}}$, when the luminous fireball decreases in size, the absorption shell keeps on growing. At fireball maturity, this thickness is given by

$$\Theta \approx 0.25 R \approx 70 W^{1/3} \quad (4.21)$$

where the thickness Θ is in feet and the device yield W is in kilotons. This point will be brought up in the discussion of the attenuation of the absorption shell.

The velocity of growth of the fireball and the absorption shell is shown in Figure 4.33. Considerable experimental inaccuracy in the data is introduced by the subtraction of neighboring points. The fireball growth velocity is not particularly meaningful at times after breakaway and at late times (it appears negative in some of the film series). On this somewhat inchoate figure, the growth speeds appear to go about as $1/(\text{time})$; there is no marked difference in this slope among the several detonations. (In the Taylor shock region, the air shock velocity should go as $t^{-3/5}$; the shock is rapidly outdistancing the fireball and absorption shell.) The velocity of the absorption shell outer edge through the air that has been preheated by the shock wave, becomes subsonic at times that do not scale with the time to thermal flux minimum; this is of course expected for a hydrodynamic phenomenon. These subsonic speeds suggest that the absorption shell propagates by other than air-shock mechanisms.

4.6.3 Absorption Coefficient. Part of the shock froth is typically obscured by the absorption shell; it is possible to compare the brightness of the unobscured froth to the obscured region, and so calculate the absorption. The apparent brightnesses must be corrected for the aureole light, a difficult correction that often entails a subtraction of two numbers that are very close to one another. In practice, only a single absorption measurement can be made on any one scan; this is the attenuation at the outer edge of the absorption shell. The edge is extremely sharp, and it is difficult to assign a path length to the light passing through the absorbing region. For these and other reasons that will become apparent in the following discussion, accurate measurement of the attenuation coefficient of the absorption shell is not possible; only approximate figures, and trends, can be given.

Zuni. The series of (Red) frames of Zuni shown and described qualitatively in Section 3.2.7, show the absorption shell attenuating the light from the shock froth as well as from the clouds behind the fireball. Unfortunately, the complementary Blue photographs are of such poor quality as to be unanalyzable. Qualitatively, it can be seen that the Red attenuation decreases with time; in Frames 27 and 55 the shock froth edge is not visible through the absorption shell, but by Frame 121 (second thermal maximum) this edge shows through quite clearly; even the inner absorption shell is partially transparent. The same general behavior is observed for the clouds above the fireball and shell. After Frame 286, no absorption is apparent in the reproductions, but on the original photographs it can be seen to Frame 689. The inner band—further justification for which will be given later in this section—persists also and appears to

be present even in Frame 689 ($\sim 5t_{\text{maxII}}$), when the fireball has lost its hemispherical shape and started to rise from the water surface.

Radii of the shock froth, inner and outer absorption shell, and fireball are presented in Figure 4.20, along with the absorption shell thickness.

A horizontal scan along the fireball, such as Scan Line A in Figure 4.34, was taken; this scan intercepts the absorption shell where it obscures the shock froth and the unobscured shock froth as well. The air-scattering contribution is evaluated from Scan Line B, which just clears the frothed ring. Eighty-five percent of the brightness measured just outside the edge of the absorption shell is subtracted from each of the two shock froth brightnesses; this assumes that 85 percent of the apparent albedo from the unshocked water is air-light, an assumption that is discussed in Section 4.5.2. The absorption shell attenuation, then, depends on the interpretation of the air-scattering measurements.

A typical microdensitometer Scan Line A, 37.3 on Frame 83, is shown in Figure 4.35. The densities are proportional to logarithms of the light intensities. The (air + water) background gets brighter near the fireball, as does the shock froth. The slowness of the rise and fall of these brightnesses is principally an instrumental effect, due to the finite-sized slit passing over the obliquely oriented demarcation line. Transition from dark to light sections of the absorption shell is marked by a small change in the slope of the brightness-distance curve, rather than a step function in brightness. The transition from the inner (bright) absorption shell to the fireball proper is easily found by the sharp change in slope, as is indicated in the diagram. The absorption of light from the shock froth appears to be highest at the outer edge of the (dark) absorption shell in all such scans; apparently the lowering of illumination with increasing distance from the fireball overcomes any increase in absorption due to greater thickness of shell traversed. An upper limit to the transition region at the edge of the shell is 100 feet; it may very well be much less.

Note that the details of the inner and outer absorption shells are masked by noise. The shock froth is brightest, and the absorption shell region least bright, at adjoining points. These two brightnesses are chosen for the attenuation measurement. The corrected ratios of these brightnesses are given in Table 4.20 (which also presents the raw data) and in Figure 4.36. Also presented in Figure 4.36 is the function

$$\mu' = -\frac{1}{\Theta} \log_e \frac{(\text{inside brightness})}{(\text{outside brightness})} \quad (4.22)$$

Where: μ' = rough measure of the absorption coefficient of the absorption shell
 Θ = shell thickness, centimeters.

This crude procedure assumes that the light path is one shell thickness and that the attenuating properties of the absorption shell are the same throughout its volume, an even more presumptuous assumption. Furthermore, only the most trivial type of radiation transport—pure experimental attenuation—is assumed. Consequently, μ' should not be regarded as a proper absorption coefficient.

While there is considerable scatter in these points, especially at early and late times when the illumination is low and one is working on the toe of the H and D curve, the trend of the results is quite clear: the attenuation of the absorption shell decreases with time, μ' going about as $t^{-3/2}$.

A rough check on these results was provided by measurements of the attenuation of the light from the cloud to the right of the plume. Because of the rapid point-to-point fluctuation of the light from such a viewing screen, consistent frame-to-frame variations were not observed. The transmission, however, turned out to be in the same range as that observed with the shock froth as viewing screen.

These necessarily crude measurements indicate that the absorption shell is attenuating the red thermal flux by about a factor of 2 at times near second maximum. In light of the approximations in the procedure, further interpretation of these data should be made with caution.

Flathead. Upon examination of the several film series available, it was found that the

Red-Blue pair best suited for an absorption shell analysis of the type described in the last section included Flathead Series 35455 and 35456. In these series the camera lenses were set at $f/16$, and no neutral density filter was used; this made the Blue exposure high enough to allow readings to be made in spite of the attenuation of the air shock. However, the slant range of 24,000 feet and focal length of 10 mm resulted in a small image and low resolution; and the observation (altitude) angle of 42° is not as satisfactory as the lower angle of the Zuni observations. At this high angle, Scan Line B is at a considerable angle from Scan Line A (Figure 4.34) and the location of the proper air-light point on the rapidly rising brightness curve of Scan Line B is extremely uncertain. Furthermore, the Blue Scan Line B is taken through a greater thickness of absorbing shocked air, making the apparent air light too low.

Consequently even these optimum series give results of considerably lower accuracy than those taken on Zuni; these results permit only rough inferences about the absorption shell to be made. The attenuation of the absorption shell appears to decrease with time in both Blue and Red; indeed, this behavior can be observed qualitatively in all the series shown in the Appendix. The Blue light is attenuated by about a factor of 3 at half the time to second thermal flux maximum; the attenuation factor has decreased to about 2 at $2t_{\text{maxII}}$. This attenuation may be too low because of the failure to subtract a high enough air-light contribution. The Red attenuation decreased from about 2 to $1\frac{1}{4}$ in this time. The attenuation coefficient μ' is 4×10^{-6} in the Red and 8×10^{-6} in the Blue at t_{maxII} . It appears then that the Blue attenuation is rather higher than the Red, and that the Flathead (about 365 kt) Red attenuation is not as great as is that of Zuni (about 3,380 kt), Red. However, the Red attenuation coefficients ($\mu' s'$) are about the same for these two detonations. These should be considered as inferences from rather poor data, rather than as firm conclusions. A principal implication of the Flathead measurements is that the absorption coefficient of the absorption shell—if such a parameter may be properly defined—is the same, within a factor of 3, for the Blue and the Red.

4.6.4 Limb Darkening. It was early noticed that the fireball photographs, both in the Red and in the Blue, exhibited the phenomenon of limb darkening, that is, a decrease of the image brightness toward the fireball sides on an equatorial scan.

Dakota. The Dakota films were carefully examined in order to obtain a qualitative description of this feature. In addition, the log relative brightness scans of a matching pair of Dakota Red-Blue films up to t_{maxII} were measured; these are shown in Figures 4.37 through 4.39. These typify the general features which are observed in the eight Dakota records examined and which are described below. In the Red, although Frame Zero shows no detectable limb darkening, (the fireball is flat) some limb darkening appears almost immediately thereafter, sometimes as early as Frame 1. This Red limb darkening then increases, the bowing of the fireball getting more pronounced. At a time before t_{maxII} , but apparently well after t_{min} , the limb darkening decreases and the fireball surface brightness becomes flat over most of its extent. It is not possible to pinpoint the time of reversal (Figure 4.39). Finally, as well as can be observed through the breakup of the fireball, the limb darkening appears to be gradually increasing again.

The Blue limb darkening, on the other hand, is initially present in Frame Zero, appears to increase in degree with time, and is still present at well after t_{maxII} . Qualitatively, the microdensitometer traces showing limb darkening in the Blue are different from those in the Red. The Blue fireball brightness contour is rounded, whereas the Red has a rather flat top extending into a sharply rounded corner and steep sides.

Quantitative Analysis of a Typical Pair of Red-Blue Pictures. A concentric absorbing layer around the fireball—whether air shock or absorption shell—should produce limb darkening. A crude analysis of this limb darkening has been performed. In this analysis it is assumed to be due to the variable thickness of material that the viewer must look through to see different parts of the luminous fireball. The following simplifying assumptions have been made: (1) the luminous fireball itself has no intrinsic limb darkening, (2) the absorbing material is uniformly concentrated in a spherical shell whose inner radius is the fireball radius and whose outer radius is either the absorption shell or shock froth radius (both cases

have been tried), (3) the attenuation is characterized by a single extinction coefficient γ , and (4) there is no buildup or other radiation transport. The limb darkening across the luminous fireball is thus considered to be due to the light passing through different thicknesses of the spherical absorbing shell and can be calculated straightforwardly. The result is

$$\frac{I_{\lambda}(a)}{I_{\lambda}(0)} = \exp \left[-\gamma R_1 \left(\sqrt{\left(\frac{R_2}{R_1}\right)^2 - \left(\frac{a}{R_1}\right)^2} - \sqrt{1 - \left(\frac{a}{R_1}\right)^2} \right) - \gamma (R_2 - R_1) \right] \quad (4.23)$$

or

$$I_{\lambda}(a) = \log_e \frac{I_{\lambda}(a)}{I_{\lambda}(0)} = -\gamma \left[R_1 \left(\sqrt{\left(\frac{R_2}{R_1}\right)^2 - \left(\frac{a}{R_1}\right)^2} - \sqrt{1 - \left(\frac{a}{R_1}\right)^2} \right) - (R_2 - R_1) \right] \quad (4.24)$$

Where: I_{λ} = apparent surface brightness in a wavelength range centered at λ

a = distance of the surface point from the center of the fireball, measured in the plane of the photograph

R_1 = radius of the fireball

R_2 = outer absorbing shell radius

γ = extinction coefficient (base e).

This theoretical limb darkening formula is a one-parameter formula, the parameter being γ . The theoretical formula was fitted to the experimental plot of the log of intensity versus (projected) radius by fitting the point a_{μ} at which the log of the intensity ratio $I_{\lambda}(a_{\mu})$ has the average of its values at the center and the edge of the fireball. It is necessary to choose a great circle (central) fireball microdensitometer scan. This fit then determines γ . The point at which the fit is made is near the edge of the fireball where there is a relatively large length of absorbing path.

The results of this analysis, performed on the Red and Blue pictures, Frame 45, Series 36241 and 36242, central scan of Dakota, are shown in Table 4.21. The remainder of this section is concerned with this pair of pictures. This fit to the data is plotted in Figure 4.40. The fit to the Blue data is excellent, indicating that, for the Blue absorption, the assumptions made are probably valid; however, the fit to the Red data is not very good, which indicates that the model is not a good one for the absorption in the Red. There is no marked difference in the γ obtained for different absorbing shell radii.

It should be noted that the fit to the data is not markedly sensitive to the distance chosen as the outer radius of the attenuating shell. The crucial distance in this extinction coefficient calculation is the difference between the path lengths of absorbing material traversed looking at the point at distance a from the center, and at the center of the fireball. When the outer radius of the absorbing shell is increased, both of these path lengths increase, but their difference, which is the important distance here, increases only slightly, and thus the extinction coefficient decreases only slightly. This brings about the closeness of the calculated γ 's for the different outer shell radii.

A second fact which should be noted about fitting the data is that changing the extinction coefficient does not change the shape of the curve, but only multiplies the whole curve (on this log plot) by a scale factor; in addition, changing the values of the absorption shell radii also does not greatly change the shape of the curve. In particular, the sharp corner of the Red limb

darkening curve cannot be fit by such adjustments. For example, a plot of the Red theoretical limb darkening with $\gamma = 10^{-5} \text{ cm}^{-1}$ is also shown in Figure 4.40; while it fits the top of the brightness curve, it does not go down steeply enough to fit the edge.

In making these fits to the data, there are uncertainties, partly due to the inexactness of the initial data. The slit width of the microdensitometer scanning unit in this particular case corresponded to 37 meters in the actual burst geometry. The microdensitometer trace is usually very jagged; furthermore, it is small in size, and there is difficulty in reading points from it numerically. The numerical values of density are probably accurate to 1 part in 20. These density values must now be converted to intensity values using the H and D curve; this operation is relatively accurate, but it still involves another numerical-graphical operation with some attendant error. Finally, in analyzing the limb darkening, the fireball radius, to which the extinction coefficient (in this analysis) is sensitive, is chosen by inspection. An error in the fireball radius equal to the slit width can change the extinction coefficient by 1 part in 8. The accuracy of the number obtained for the extinction coefficient (over and above the failure of the assumptions mentioned in the second paragraph) is probably no better than 1 in 5.

Further Darkening Analysis. Several simple attempts were made to refine the limb darkening discussion. One of these is an attempt to correct for background air-light. In making this correction, the background air-light as measured in the microdensitometer was smoothed off and extrapolated through the center of the fireball. This affects the brightness at the fireball edges markedly, but the central brightness is virtually unchanged. (Actually, this is a somewhat arbitrary correction; the extrapolation is quite subjective, but the Frame-Zero and other flat-top evidence shows the air-light must be flat across the fireball center.) The log of the corrected fireball intensity was then plotted and the limb darkening analysis carried out for the corrected curve. These results, which give an extinction coefficient differing by about 20 percent from the uncorrected extinction coefficient, are listed in Table 4.21. This procedure did not affect the fit to the curves.

Another simple attempt to refine the discussion without making detailed calculations was the removal of the intrinsic limb darkening due to the luminous fireball itself. A simple hypothesis to investigate is that the intrinsic fireball limb darkening is similar to that of the sun. An attempt based on this hypothesis, in which the fireball intensity was increased so as to remove the sun's limb darkening (Reference 36), led to a corrected fireball intensity that has a maximum at some distance from the center rather than at the center. Such a fireball intensity profile is unreasonable, and so no further limb darkening analysis was performed on these curves. This result, shown in Figures 4.41 and 4.42, shows that the fireball has less intrinsic limb darkening than the sun.

Discussion. Returning to the discussion of the extinction coefficient found from this limb darkening analysis, it may be concluded that the results from this alone (Table 4.21) cannot determine the location of the absorbing material. However, the direct photographic evidence shows that the absorbing material for the Blue radiation extends from the fireball to the shock front with additional attenuation in the absorption shell. For the Red radiation, it extends from the fireball only to the outer absorption shell radius; the air shock shows no apparent absorption and only slight scattering of the radiation. The extinction coefficients calculated from this limb darkening discussion are higher than from the chord data (Section 4.6.3), but in light of the approximations made in the two sets of calculations the check is reasonably good.

The poor theoretical fit to the Red data indicates that the absorbing layer around the fireball does not cause the limb darkening in the simple fashion described here. Presumably limb darkening inside the fireball, which requires a more detailed radiation transport analysis for its explanation, is an important factor in the Red limb darkening. (See Section 4.6.5 for an outline of a more detailed radiative transfer analysis.) Furthermore, the presence of the bright inner absorption shell indicates that the close-in layers of this mantle are not enough to be self-luminous.

The good fit to the Blue data is partly fortuitous and should not obscure the fact that the internal structure of the luminous fireball also contributes to the limb darkening. The required attenuation of $20 \times 10^{-5} \text{ cm}^{-1}$ would cause over 90 percent of the fireball light to be absorbed by the absorption shell alone. This model gives too high an attenuation in the Blue.

4.6.5 Discussion. Certain other aspects of the absorption shell are discussed in this section, first in a simple manner, then in a more realistic manner involving the equation of radiative transport and the detailed physics of the fireball.

Scaling Laws. The absorption shell radius and thickness appear to scale with yield. Data presented earlier in this chapter and qualitative examination of the photographs fail to resolve any significant differences in the attenuating properties of the shells of different yield (but see Section 4.6.3). A further point of importance is that radiometer and calorimeter results do not indicate any great deviation of the total thermal flux from a first-power-of-yield law; consequently, the attenuation of the absorption shell cannot vary sharply with yield.

This constancy of the gross properties of the absorption shell implies that the number of attenuating centers produced varies as the surface area of the fireball, as the following argument shows.

It is possible to write (following Sections 4.4.5 and 4.6.2)

$$R_2 = K_R W^{1/3} \quad (4.25)$$

and

$$\Theta = K_\Theta W^{1/3}, \quad (4.26)$$

where R_2 and Θ are the radius and thickness of the absorption shell of a weapon having yield W , and the K 's are appropriate constants. Then the shell volume V is given by

$$V = 2\pi R_2^2 \Theta = 2\pi K_R^2 K_\Theta W \quad (4.27)$$

Let $N (=K_N W^n)$ be the total number of attenuating centers produced. If the total attenuation factor is the same for all devices, then, assuming a simple attenuation law to hold

$$\exp - \left(M \frac{N}{V} \Theta \right) = \text{constant}' \quad (4.28)$$

(where M is an absorption cross section) and

$$\frac{N}{V} \Theta = \text{constant} = \frac{K_N W^n}{2\pi K_R^2 W^{2/3}} \quad (4.29)$$

Thus

$$W^n \sim W^{2/3} \quad \text{and} \quad n = 2/3. \quad (4.30)$$

The area of the emitting surface varies as $W^{2/3}$ also. This effect indicates a further connection between the absorption shell and the thermal output. However, acceptance of this result means a rejection of the usual (that is, hydrodynamical) scaling laws for detonations at a given scaled radius and scaled time, the temperature, pressure, and density (and thus presumably the chemical composition) have fixed values. Nonetheless, this accepted scaling does not give the observed attenuating properties of the absorption shell, in that the attenuation does not scale with the shell thickness; it predicts that larger devices should have thicker absorbing mantles and consequently lower brightness and total thermal flux. Presumably the resolution of this paradox lies in a more realistic study of the radiation transport through the absorption shell. The existence of a temperature (and therefore an absorber concentration) gradient is certainly to be expected on theoretical grounds and is further inferred by the bright inner section of the absorption shell.

Temperature Rise. Another check on the properties of this attenuating mantle may be made by calculating its temperature increase ΔT on absorption of half (see Section 4.6.3) of the thermal flux. Since $K_\Theta = 70$ and $K_R = 290$ (W in kilotons, distances in feet), $V = 4 \times 10^7 W \text{ ft}^3$. In lieu of a detailed calculation taking into account the details of fireball brightness and absorption shell properties, assume that all the thermal flux is emitted at second maximum,

and that half of it is absorbed in a shell of this volume. Then

$$\Delta T = \frac{(1/2) \lambda W \times 10^{12} \text{ calories}}{4 \times 10^7 W \times 8.5 (\rho/\rho_0) \text{ calories/}^\circ\text{K}}$$

$$= 1.5 \times 10^3 \frac{\lambda}{(\rho/\rho_0)} ^\circ\text{K} \quad (4.31)$$

where λ is the fraction of W leaving the fireball as thermal flux and ρ/ρ_0 is the (normalized, average) density of the air in the absorption shell. If $\lambda \approx 0.4$ (Reference 1) and $\rho/\rho_0 \approx 0.25$ (Reference 29; this is actually a very crude figure, but it does not appreciably affect the conclusion below) then $\Delta T \approx 2,400^\circ\text{K}$. Now, in actuality the temperature rise takes place over the whole thermal history of the detonation, and in light of the possibility of the reradiation of this absorbed energy at longer wavelengths this figure should not be regarded as making the absorption shell hotter than is experimentally observed. In fact, it is possible to conclude from this argument that the absorption shell can very well absorb half of the thermal flux (in the crude sense of this argument, that is, regard it as a simple filter) with unresolved temperature increase, which is consistent with that observed in this experiment.

Origin. Considerable effort has been expended in an attempt to find the molecular species (or other absorber) responsible for the attenuation of the shell. It is not possible, out of hand, to reconcile the properties of NO_2 with the absorption, as its attenuation coefficient in the Blue is at least 200 times as great as in the Red at laboratory ($\sim 300^\circ\text{K}$) temperatures (Figure 4.2). While some wavelength flattening of this coefficient is expected at high temperatures—the Red absorption coefficient increases up to 500°K (References 37 and 38)—considerably more change than has been observed in analogous cases would be needed to explain the near-similarity of the Red and Blue attenuations at the absorption shell temperatures ($1,500$ to $2,000^\circ\text{K}$). Calculation of the population of excited states of triatomic molecules at these temperatures is extremely difficult. In passing it should be remarked that, if other experiments can be devised to show the absorber is indeed NO_2 , the high-temperature absorption coefficients and population states of this gas become experimentally accessible in observations of detonations.

Clearcut NO_2 absorption bands are in fact spectroscopically observed in the early stages of the detonation; the apparent absorption increases to a maximum at breakaway, thermal flux minimum (recall apparent extinction of the Blue fireball), and then starts to decrease (Chapter 3). This behavior is consistent with the early NO_2 in the shock-radiation front being pushed out into the shocked air where it is metastable at the lower temperature (freezing-in); the air shock is attenuating in the Blue. Presumably conditions for further NO_2 formation still exist after breakaway.

It is expected that details of the Red and Blue radiation transport phenomena should be quite different; for example, the Red absorption shell appears in part luminous, as is evidenced by the inner bright section. Further analysis of this question may aid in explaining the lack of pronounced attenuation differences.

A second hypothesis that was considered briefly is that the absorption shell attenuation is due to the scattering by iron particles, the order of 1 micron in size. Enough such particles can be made to give the observed attenuation, from about 5 tons of iron per megaton yield; furthermore, any Red-Blue attenuation difference can be fitted by small adjustments in the (average) size of the particles. However, this attempt was abandoned when it was realized that such materials travel only a few meters, the fireball growing by engulfing air.

Discussion of Theoretical Model. This section is devoted to theoretical considerations for finding a mechanism to account for the absorption shell.

Temperatures, Densities. To explain the shell, it is necessary to have some idea of the temperatures and densities throughout the blast and the absorption coefficients for the various chemical constituents as functions of the temperature and density of air.

The temperatures and densities throughout the blast were determined from Reference 29. That report assumes an early phase during which radiation spreads the thermal energy evenly

into an isothermal sphere of hot air. This isothermal sphere provides the initial condition for a purely hydrodynamic calculation in which no attempt is made to account for the effects of thermal radiation. It was necessary to ascertain whether the data from Reference 29 could be scaled to the yield of the detonations encompassed. The shock front data in the report was scaled hydrodynamically (radii and time multiplied by the cubic root of the yield ratio), and the shock fronts were found to scale fairly accurately. The fireball temperatures in the report, however, are somewhat too high because of the neglect of thermal radiation. A more recent report (Reference 38) approximately accounts for radiative losses in the vicinity of the fireball and results in lower fireball temperatures. Except for very early and late times, the two reports differ only in details. In the region of concern, both are in substantial agreement.

Absorption by NO_2 . There has been much speculation as to which process is responsible for the absorption of radiation in the absorption shell. It is believed that the NO_2 molecule is responsible for most of the absorption in the absorption shell. Reference 40 reports substantial absorption spectra of NO_2 in the fireball of a 20-kt blast for times between breakaway and second thermal maximum. This observation has been confirmed for kiloton and megaton yields during Operation Redwing. Since these are the times of concern in this analysis, NO_2 absorption should be an important factor. There is very little theoretical information on the NO_2 molecule, nor is there much experimental radiation absorption data—none over $1,000^\circ \text{K}$.

The one piece of quantitative information on the magnitude of the absorption is contained in Figure 4.35. This indicates that approximately 40 percent of the light from the shock front is absorbed by the absorption shell at this particular time. Figure 4.35 is based on data taken through a red filter, a spectrum approximately in the 1.50- to 1.75-ev interval. The only band spectrum in this interval is the $\text{N}_2(1_+)$ spectrum, but this becomes significant only above $4,000^\circ \text{K}$. The continuum absorption is unimportant below $6,000^\circ \text{K}$. Thus, NO_2 data in this region is essential.

The best data on NO_2 absorption goes up to $1,000^\circ \text{K}$ in the blue and 500°K in the red and infrared (Reference 38). In order to make some estimate of the absorption coefficients at higher temperatures in the red, it is assumed that the temperature does no more than increase the population of the first excited state of the NO_2 molecule, i.e., the increased absorption is due to the increased number of transitions arising from the first excited state. This simple model gives a good fit to the referenced data above 400°K . The 300°K data is complicated by the presence of N_2O_4 . However, the model is simple and cannot be expected to be valid over a wide range of temperature and frequency. The model seems to be valid in the red portion of the referenced data and invalid in the blue and infrared. Using this approach, the NO_2 absorption cross section was then arbitrarily taken to hold at all temperatures above $1,000^\circ \text{K}$ in the calculation and was used to determine the NO_2 absorption coefficients.

Radiation Transport Through Air Containing Equilibrium Concentration of NO_2 . The Zuni detonation at the time of Figure 4.35 was chosen for detailed study. Temperatures and densities were scaled from Reference 29. Several parallel sea-level chords were chosen through and beyond the absorption shell. Temperatures and densities were established along the chords. (These differ from the temperatures and densities in Reference 29 which are along radii.) The intensity I_ν of the observed light is calculated from the radiation transport equation:

$$I_\nu(s) = I_\nu(0) e^{-\tau(0,s)} + \int_0^s \mu_\nu(T', \rho') B_\nu(T') e^{-\tau(s',s)} ds'$$

Where: s = thickness of the absorption shell

$I_\nu(0)$ = intensity at the fireball edge

$\mu_\nu(T, \rho)$ = absorption coefficient

$B_\nu(T)$ = intensity of light coming from a black body of temperature T

$$\tau(s', s) = \int_{s'}^s \mu_\nu(T'', \rho'') ds''$$

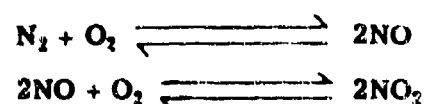
Such calculations carried out numerically along chords through the absorption shell indicate that any incident intensity of light (such as the shock front) would be eliminated approximately 48 percent by a chord through the absorption shell, i.e., the exponential factor of $I_p(0)$ in the equation above is approximately equal to 0.52. This is to be compared to a factor of approximately 0.60 from experiment. The contribution from the sources in the air (the integral term) appears to be negligible. The absorption shell should then be nonluminous. However, it will require further work to establish whether the intensity obtained from the integral term of the calculation would register on the film of the observation aircraft.

In the foregoing calculation, local thermodynamic equilibrium is assumed to prevail throughout the blast, and consequently, the equilibrium concentrations given by Reference 41 are used in the determination of the absorption coefficients from the various components of air. The various chords have the behavior that would be anticipated from the smooth variation of temperature and density. The contribution of the source term increases in going from the cooler shock front toward the fireball. Similarly, the optical depth increases as chords are taken nearer the fireball, so that absorption of incident radiation increases markedly. There is no discontinuity in absorption that could be labeled an absorption shell. The only indication is that, at the radial distance for the absorption shell as given by the data, there seems to exist an amount of absorption indicated in Figure 4.35.

Freezing-in Mechanism for NO_2 . The front of the absorption shell is observed to be very sharp, and the calculations of the previous section give no account of that.

A possible solution to this difficulty lies in the formation of nonequilibrium and higher concentrations of NO_2 .

The chemical reactions of interest are:



The rate of the first of these reactions can be obtained from Reference 42. The rate in either direction is very sensitive to temperature. If a fraction of air is heated to a high enough temperature and then cooled rapidly enough, the equilibrium concentration of NO at the higher temperature will be found at the lower value. The gas has been frozen in. Rapid oxidation follows, and a value for the concentration of NO_2 higher than that which would be obtained for this gas in air at these same values of temperature and density would be found. It has been estimated (Reference 43) that heating the air to 2,400° K and cooling it to 1,800° at the rate of 20,000° K/sec will produce significant amounts of NO.

These particulars of the chemical formation of NO_2 suggest the following description of the formation of the absorption shell. The shock front raises the temperature of the air through which it passes. The air, thus heated, cools rapidly and generates NO_2 in the manner already described. As the shock front progresses, the temperature to which the encountered air is raised lessens until such a point is reached where no further nonequilibrium NO_2 is produced. The NO_2 proceeds with particle velocity and the region expands but at a velocity less than that of the shock front.

The qualitative features of the absorption shell are thus accounted for; however, some important data is missing. The description cannot, therefore, be supported quantitatively. The chemical kinetics of the formation of NO_2 are in dispute. There is general agreement of the qualitative aspects of the reaction, but the situation is completely reversed when the quantitative results are considered. The pertinent absorption cross sections for NO_2 at the temperatures and densities of interest are also among the vital data needed for a quantitative description of the absorption shell. Finally, a more detailed analysis that would describe the life history of a particle subjected to shock is necessary.

A rough quantitative check of the consistency of the model can be obtained from Figures 4.18 through 4.20, which present the radius-time curves of the shock front as well as of the absorption shell. According to the model, the front of the absorption shell should coincide with

with the path of those particles that have been shocked to the critical temperature of 2,400° K. The time at which this path intercepts the shock curve (Reference 28) is read off the graphs, scaled to the yield of the calculations (References 29 and 39), and used to find the calculated shock temperature. These temperatures are somewhat lower than expected, but the margin of error in locating the time of the intercept is wide enough to include the aforementioned 2,400° K.

Hydrodynamics Basis for Sharp Absorption Front. Inspection of the temperature profiles of Reference 39 has revealed an isothermal region that trails behind the shock front. The radius of the edge of this plateau as a function of time was compared to the outer radius of the absorption shell for Shot Zuni, and the curves were practically identical. If it can be shown that the isothermal region is not just an accident of the method of calculation but represents a true hydrodynamic phenomenon, such a region may well be related to the observed absorption shell, e.g., by accentuating the mechanism discussed above or by introducing the discontinuity missing in the mechanism.

The remarks made earlier concerning a quantitative description apply even more so for this model. In particular, the reality of the temperature plateau should be studied. It has been suggested that the front edge may be a contact discontinuity. In any case, the temperature history of particles in that region should be studied in some detail.

TABLE 4.1 TRANSMISSION OF THERMAL ENERGY
THROUGH PACIFIC AIR

Shot	Aircraft	w mm	T _w	T
Lacrosse	B-57	14	0.68	0.71
Cherokee	B-47	45	0.65	0.83
Zuni	B-47	22	0.64	0.67
	B-66	15	0.63	0.64
Erie	B-57	17	0.71	0.78
Flathead	B-57	17	0.67	0.70
	B-66	18	0.66	0.69
Dakota	B-47	44	0.57	0.60
	B-57	54	0.55	0.59
	B-66	48	0.56	0.60
Apache	B-47	30	0.61	0.64
	B-57	48	0.56	0.60
	B-66	49	0.56	0.60
Navajo	B-47	31	0.61	0.64
Tewa	B-47	28	0.62	0.64
	B-66	35	0.60	0.63
Huron	B-57	19	0.65	0.68
	B-66	17	0.67	0.70

TABLE 4.2 METEOROLOGICAL DATA

Shot	Surface Air Temperature	Sea Level Barometric Pressure	Surface Relative Humidity	Vapor Pressure P ₀	Surface Wind Speed	Wind Direction	Surface Visibility	Inversion Layer Height
	°F	mb		mm Hg	knot	degree	mile	ft
Erie	80.3	1,009.1	80.2	21.2	12	100	10	~ 10,500
Lacrosse	81.0	1,008.5	81	22.8	16	80	10	~ 7,000
Huron	81.4	1,007.8	84	23.0	17	90	10	—
Mohawk	79.6	1,010.2	81	21.0	16	100	10	—
Flathead	82.0	1,012.9	82	23.0	10	50	10	17,000
Dakota	82.0	1,009.1	80	22.4	14	50	10	—
Apache	80.3	1,010.5	84	22.3	15	30	10	~ 10,000
Zuni	81.0	1,010.5	80	21.7	12	90	8	~ 10,000
Cherokee	81.0	1,009.0	76	20.6	10	140	10	~ 6,000
Navajo	81.2	1,010.2	80	21.8	8	90	10	—
Tewa	82.0	1,009.3	85	23.8	8	140	10	—

TABLE 4.3 ATMOSPHERIC TRANSMISSION FOR AIRCRAFT POSITIONS, SHOT DAKOTA
For definitions of the column heads, see Section 4.1.2.

Aircraft	Blue Total Transmission	w cm H ₂ O	Red Selective Transmission	Air-Scatter Transmission Factor	Red Total Transmission
B-47	0.36	54.8	0.79	0.43	0.30
B-57	0.42	66.7	0.79	0.46	0.33
B-66	0.45	61.2	0.80	0.51	0.36

TABLE 4.4 SOLAR COLOR TEMPERATURES EXTRAPOLATED
TO ZERO AIR MASS

Data Source	Air Mass	Method	Temperature K
Stair	1.00	Experimental	5,700
Johnson	1.00	Experimental	5,750
Sekera	All	Calculated	5,600
Opal	1.76	Direct measure	5,800
Opal	2.55	Direct measure	5,500
Opal	3.21	Direct measure	5,450
Opal	4.07	Direct measure	5,400
Opal	5.13	Direct measure	5,470
Quartz	2.28	Reference 18	5,500
Quartz	3.82	Reference 18	5,600
Quartz	8.02	Reference 18	5,850
Quartz	7.91	Reference 18	5,800

TABLE 4.5 EFFECT OF COMBINING DATA FROM
VARIOUS FILTERED DETECTORS

0.2 to 4.5 microns; Quartz Window Q
0.2 to 0.7 microns; Filter Q minus Filter A*
0.7 to 0.9 microns; Filter A minus Filter B
0.9 to 2.0 microns; Filter B minus Filter C
2.0 to 2.5 microns; Filter C

* The energy in the 2.5- to 4.5-micron region is nearly completely absorbed by water vapor. Furthermore, the energy in this interval is small compared to that in the 0.2 to 0.7 range.

TABLE 4.6 AMOUNTS OF NO₂

Shot	Time	Amount of NO ₂ in Atmo-cm
Apache	zero	0.687
	t _{max}	3.29×10^{-2}
Cherokee	zero	1.317
	t _{max}	3.42×10^{-2}
Dakota	zero	0.953
	t _{max}	2.89×10^{-2}
Erie	zero	—
	t _{max}	3.68×10^{-2}
Flathead	zero	0.561
	t _{max}	4.08×10^{-2}
Huron	zero	0.688
	t _{max}	2.50×10^{-2}
Lacrosse	zero	—
	t _{max}	4.21×10^{-2}
Mohawk	zero	0.364
	t _{max}	3.68×10^{-2}
Navajo	zero	—
	t _{max}	2.37×10^{-2}
Tewa	zero	0.798
	0.0156 sec	1.190
	0.0312 sec	0.378
	0.0468 sec	0.308
	0.0624 sec	0.196
	t _{max}	4.87×10^{-2}
Zuni	zero	0.46
	t _{max}	2.6×10^{-2}

TABLE 4.7 TEMPERATURE AT t_{max} FOR A RANGE
OF 4,400 TO 6,000 Å

Shot	Temperature °K
Apache	4,800 to 5,400
Cherokee	5,200 to 6,100
Dakota	4,900 to 5,700
Erie	6,800 to 9,500
Flathead	4,800 to 5,500
Huron	6,300 to 7,900
Lacrosse	4,600 to 5,400
Mohawk	5,700 to 7,900
Navajo	6,600 to 6,900
Tewa	4,200 to 4,800
Zuni	4,800 to 5,500

TABLE 4.8 INTEGRATED TEMPERATURES

Shot	Temperature	
	K	
Apache	3,825	
Cherokee	3,500	
Dakota	3,975	
Flathead	4,475	
Tewa	4,050	
Zuni	4,075	

TABLE 4.9 $K(\lambda)$ AS A FUNCTION OF WAVELENGTH

Wavelength	$K(\lambda)$
\AA	
4,400	0.0353
4,600	0.0337
4,800	0.0325
5,000	0.0315
5,200	0.0308
5,400	0.0305
5,600	0.0304
5,800	0.0307

TABLE 4.10 COMPARISON OF MEASURED AND CALCULATED VALUES OF t_{\max}

Shot	Wavelength	t_{\max} , Measured	t_{\max} , Calculated	Percent Error of t_{\max} , Calculated	Shot	Wavelength	t_{\max} , Measured	t_{\max} , Calculated	Percent Error of t_{\max} , Calculated
	\AA	second	second			\AA	second	second	
APACHE					DAKOTA				
	4,400	1.603	1.518	5.3		4,400	1.127	1.160	2.9
	4,600	1.442	1.449	0.000		4,600	1.035	1.107	7.0
	4,800	1.409	1.398	0.78		4,800	1.030	1.068	3.7
	5,000	1.271	1.355	6.6		5,000	1.059	1.035	2.3
	5,200	1.274	1.325	4.0		5,200	1.096	1.012	7.7
	5,400	1.318	1.312	0.46		5,400	0.933	1.002	7.4
	5,600	1.365	1.308	4.2		5,600	1.000	0.999	0.10
	5,800	1.259	1.320	4.8		5,800	0.971	1.009	3.9
CHEROKEE					FLATHEAD				
	4,400	1.968	2.118	7.6		4,400	0.697	0.683	1.9
	4,600	1.982	2.022	2.0		4,600	0.631	0.652	3.4
	4,800	1.958	1.950	5.0		4,800	0.659	0.628	4.6
	5,000	1.977	1.890	4.6		5,000	0.653	0.610	6.6
	5,200	1.799	1.848	2.7		5,200	0.649	0.596	8.1
	5,400	1.746	1.830	4.8		5,400	0.566	0.590	4.3
	5,600	1.802	1.824	1.2		5,600	0.581	0.588	1.3
	5,800	1.884	1.842	2.2		5,800	0.624	0.594	4.7
HURON					TEWA				
	4,400	0.564	0.580	2.8		4,400	2.884	2.409	15.4
	4,600	0.562	0.554	1.4		4,600	2.265	2.385	5.3
	4,800	0.524	0.534	1.9		4,800	2.089	2.300	10.1
	5,000	0.582	0.518	11.0		5,000	1.995	2.230	11.8
	5,200	0.512	0.506	1.2		5,200	2.018	2.180	8.0
	5,400	0.512	0.501	2.2		5,400	1.941	2.159	11.2
	5,600	0.526	0.499	5.1		5,600	1.950	2.157	10.7
	5,800	0.519	0.504	2.9		5,800	1.928	2.173	13.7
NAVAJO					ZUNI				
	4,400	2.213	2.420	9.6		4,400	2.051	2.089	1.8
	4,600	2.130	2.310	8.4		4,600	2.042	1.994	2.3
	4,800	2.004	2.228	11.2		4,800	2.051	1.923	6.2
	5,000	2.018	2.160	7.0		5,000	1.972	1.861	5.5
	5,200	2.018	2.112	4.7		5,200	1.694	1.822	7.6
	5,400	1.985	2.091	4.8		5,400	1.778	1.801	1.5
	5,600	2.018	2.081	3.3		5,600	1.445	1.708	16.6
	5,800	1.972	2.105	6.7		5,800	1.733	1.816	4.7

TABLE 4.11 FIREBALL DIAMETER AT t_{max} AS A FUNCTION OF YIELD

Listed yields were used in calculations. Later yields are given in Table 2.2.

Shot	Yield	Diameter Measured, D_m	Diameter Calculated, D_c	Error
	kt	ft	ft	$\frac{ D_m - D_c }{D_m}$
Apache	1,850	7,187	6,934	0.074
Cherokee	3,600	7,820	8,710	0.114
Dakota	1,080	6,010	5,768	0.040
Erie	15.5	1,294	1,358	0.049
Flathead	375	4,000	3,917	0.021
Huron	270	3,450	3,597	0.043
Lacrosse	38.5	2,100	1,849	0.120
Navajo	4,700	9,900	9,528	0.038
Tewa	5,010	10,000	9,750	0.025
Zuni	3,500	8,600	8,630	0.004

TABLE 4.12 MAXIMUM FIREBALL DIAMETER AS A FUNCTION OF YIELD

Listed yields were used in calculations. Later yields are given in Table 2.2.

Shot	Yield	Diameter Measured, D_m	Diameter Calculated, D_c	Error
	kt	ft	ft	$\frac{ D_m - D_c }{D_m}$
Apache	1,850	7,487	7,343	0.019
Cherokee	3,600	10,165	9,088	0.106
Dakota	1,080	6,169	6,180	0.002
Erie	15.5	1,724	1,588	0.079
Flathead	375	4,065	4,406	0.084
Huron	270	3,631	3,366	0.092
Lacrosse	38.5	2,228	2,125	0.046
Navajo	4,700	9,979	9,900	0.008
Tewa	5,010	10,032	10,100	0.007
Zuni	3,500	9,064	9,007	0.006

TABLE 4.13 WILSON CLOUD EFFECTS

Listed yields were used in calculations. Later yields are given in Table 2.2.

Detonation	Yield	Thermal Maximum Frame Number	First Wilson Cloud Observation, FN	Multiple of t_{max}	Wilson Cloud Appearance Time
					Yield $^{1/3}$
	kt				
Erie	15	—	Not seen	—	—
Lacrosse	38.5	—	—	—	—
Huron	270	—	—	—	—
Mohawk	350	33	265	7	38
Flathead	380	39	256	6.6	35
Dakota	1,150	67	320	4.8	34
Apache	1,900	86	426	4.9	35
Zuni	3,500	120	500	4.2	32
Navajo	4,800	141	550	3.9	32
Tewa	5,000	145	615	4.2	36

TABLE 4.14 OPTICS OF CONTOURED PHOTOGRAPHS

Series	Aperture	Filter	Focal Length of Lens	Field of View	\cos^4 Extreme Angle*	Range	Altitude
			mm	degree		ft	degree
36236	f/11	Red + ND1	10	61	0.39	26,240 to	66.7 to
36233		Blue + ND1		43 1/2		28,250	58.5
				(76 extreme)			
36300	f/11	Red + ND1	17	35 1/2	0.74	25,000	44.9
36299		Blue + ND1		25 1/2			
				(44 extreme)			

* As measured from the center of the frame.

TABLE 4.15 PARTITION OF THERMAL FLUX, FRAMES 15 THROUGH 375

Feature	Frame	36233 Blue Brightness x Area	Percent of Total	36236 Red Brightness x Area	Percent of Total
Fireball	15	—	—	10,700	60
	45	600	96	45,500	53
	65	4,300	87	43,000	53
	150	1,150	94	25,000	51
	250	—	—	13,200	53
	375	—	—	9,300	49
Shock froth	15	—	—	1,120	6.5
	45	20	3	17,000	19
	65	350	7	16,000	20
	150	65	6	20,200	40
	250	—	—	10,200	41
	375	—	—	8,900	44
Clouds	15	—	—	2,300	13
	45	6	1	10,000	12
	65	200	4.5	10,600	12
	150	—	—	2,300	4
	250	—	—	510	2
	375	—	—	980*	5*
Fv	15	—	—	3,600	20
	45	—	—	13,000	14
	65	65	1.5	11,000	15
	150	—	—	14,000	6
	250	—	—	1,000	4
	375	—	—	500	2.5
Total	15	—	—	17,800	—
	45	600	—	86,000	—
	65	5,000	—	80,000	—
	150	1,200	—	51,600	—
	250	—	—	24,500	—
	375	—	—	20,300	—

* About 80 percent of this is scattered from the Wilson cloud.

TABLE 4.16 PARTITION OF THERMAL FLUX, FRAME 65

These data are taken at second thermal maximum.

Feature	36200 Red		36209 Blue	
	Brightness	Area of Total	Brightness	Area of Total
Fireball	125,200	70	81,400	84
Shock froth	27,500	16	4,500	4.5
Clouds	15,600	7.2	5,600	5.7
Air	13,500	7.5	5,100	5.5
Total	181,900	—	97,000	—

TABLE 4.17 INTERCOMPARISON OF SERIES 36236 RED FRAMES

Feature	Brightness or Brightness Ratio At Frame Number					
	15	45	65	105	150	175
A. Brightest fireball point	543	1,550	1,470	907	570	664
B. Plume minimum	260	260	178	55	15	12
C. B/A	0.48	0.17	0.12	0.06	0.03	0.02
Shock froth:						
D. Near edge, in	172	262	140	28	7.6	—
E. Near edge, out	44	80	50	8	2.2	—
F. D/E	3.9	3.3	2.8	3.5	3.5	—
Shock froth:						
G. Far edge, in	—	386	235	34	9	—
H. Far edge, out	—	105	63	12	3	—
I. G/H	—	3.7	3.7	3.1	3	—
J. Brightest LH cloud point	125	590	535	64	—	—
K. Brightest RH cloud point	39	88	71	49	28	14
L. Island bulge	10	55	40	26	—	—

TABLE 4.18 COMPARISONS AT THERMAL FLUX MAXIMA

Feature	36236 Red	36232 Blue	36200 Red	36209 Blue
A. Maximum fireball brightness	1,470	430	1,500	1,800
B. Total fireball brightness & area	43,000	4,300	126,200	81,400
C. B/A	29	10	33	20
D. Apparent plume diameter, ft	1,500	2,000	1,300	2,500
E. Apparent fireball diameter, ft	5,600	5,400	5,800	5,300
Brightness and Percent of Maximum Brightness at:				
Plume minimum	178, 12%	5, 1%	28, 2%	13, 1%
SF front edge	145, 10%	5, 1%	100, 6%	30, 2%
SF rear edge	275, 19%	0	55, 3%	—
RH cloud maximum	535, 36%	16, 4%	Not applicable	—
LH cloud maximum	Not applicable	—	168, 11%	78, 5%
Bottom cloud maximum	Not applicable	—	250, 17%	78, 5%
Brightness at Absorption Shelf Edge/Brightness in Shock Froth				
LH side	0.73	0.47	0.52, 0.55, 0.78	0.85, 0.78
RH side	0.78, 0.61	0.73, 0.67	0.64, 0.62, 0.60, 0.74	0.80, 0.67, 0.73
Front	0.91	0.80	0.66	0.73, 0.74
Rear	0.90	—	—	—
Brightness Inside Shock Froth Edge/Brightness Outside Shock Froth Edge				
LH side	—	—	2.5	2.7
RH side	2.0	2.1	1.0, 1.1, 1.1	1.5
Front	2.4, 2.9, 3.0	3.1, 2.3, 1.9	—	1.8
Rear	3.0, 3.9, 3.9	—	—	—

TABLE 4.19 CORRECTED ALBEDO RATIOS

Albedo of shock froth Albedo of unshocked water η						
Apparent Albedo Ratio		0.05	0.10	0.15	0.20	0.30
1.5		11	6	4	4	3
2		21	11	8	6	4
3		41	21	14	11	8
4		61	31	21	16	11

TABLE 4.20 ABSORPTION SHELL (RED), SHOT ZUNI

Frame	Shock Froth Brightness		Air + Water Brightness	Corrected Brightness ratio
	Outside Absorption Shell	Inside Absorption Shell		
15	8	4	—	—
20	17	6	7	0.18
25	18	9	8	0.15
30	24	9	8	0.12
40	34	14	11	0.18
50	33	15	13.5	0.22
60	42	21	16	0.26
70	49	24	16.5	0.29
80	42	24	16	0.37
90	39	25	15	0.41
100	40	26	13	0.52
110	36	25	12	0.56
120	34	23	11.5	0.54
130	36	26	11	0.62
140	29	22	10.5	0.65
150	26	20	10	0.65
160	25	18	10	0.58
170	23	18	10	0.65
180	20	16	10	0.65
190	18	15	9.5	0.70
200	15	12	9.5	0.57

TABLE 4.21 LIMB DARKENING RESULTS, SHOT DAKOTA

Location of Absorber	Air-Light Correction Applied	γ_{Red} cm ⁻¹	γ_{Blue} cm ⁻¹	$\frac{\gamma_{\text{B}}}{\gamma_{\text{R}}}$
Absorption shell only	No Yes	6.7×10^{-4} 5.2×10^{-5}	22×10^{-5} 26×10^{-5}	3.3 4.9
Absorption shell + air shock	No	5.0×10^{-5}	21×10^{-5}	4.1
Chord measure- ments*	—	$\mu^{\text{r}}_{\text{Red}}$	$\mu^{\text{r}}_{\text{Blue}}$	—
Zuni	—	2×10^{-5}	—	—
Flathead	—	4×10^{-5}	8×10^{-5}	2

Fireball radius R_1 = 840 metersAbsorption shell radius 1R_2 = 980 metersAir shock radius 2R_2 = 1,250 meters* At t_{max} . See Section 4.6.3.

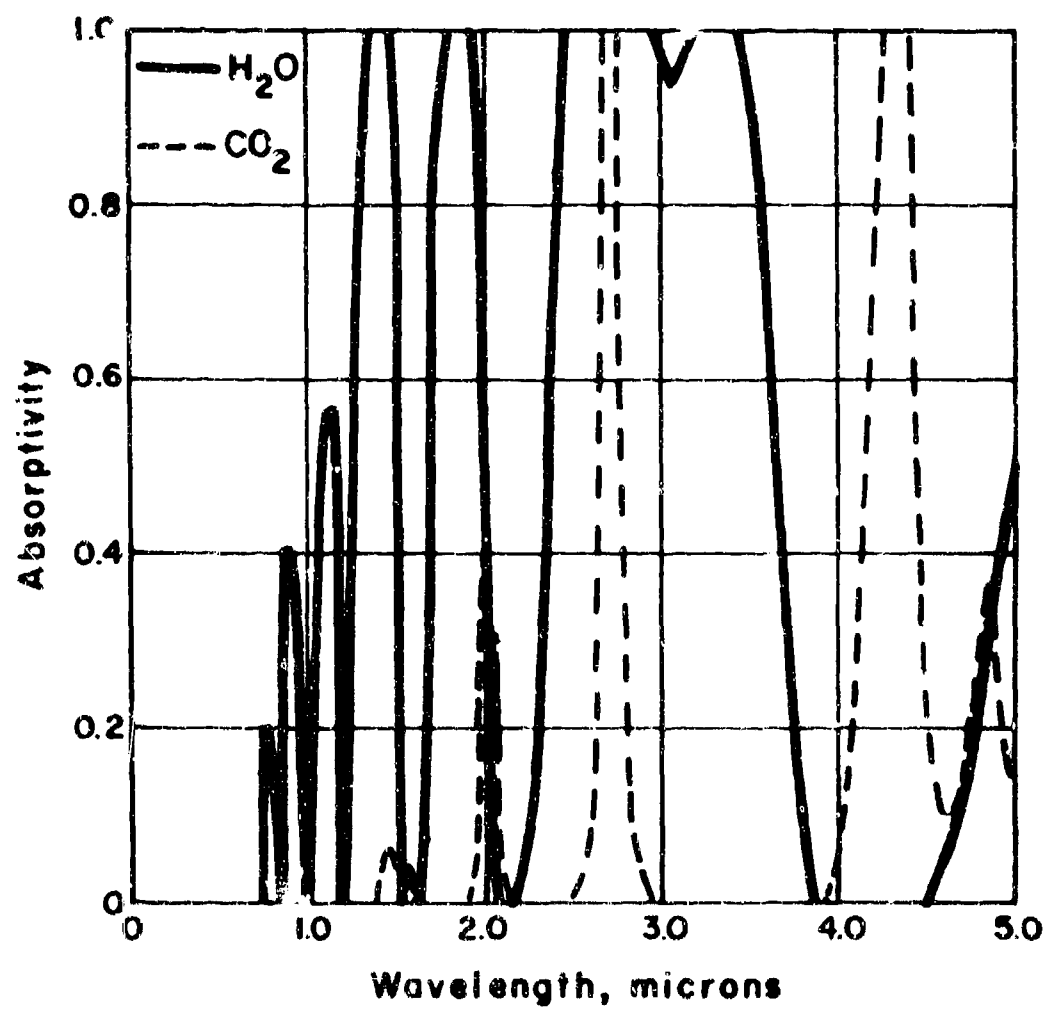


Figure 4.1 Infrared spectrum of water vapor and carbon dioxide.

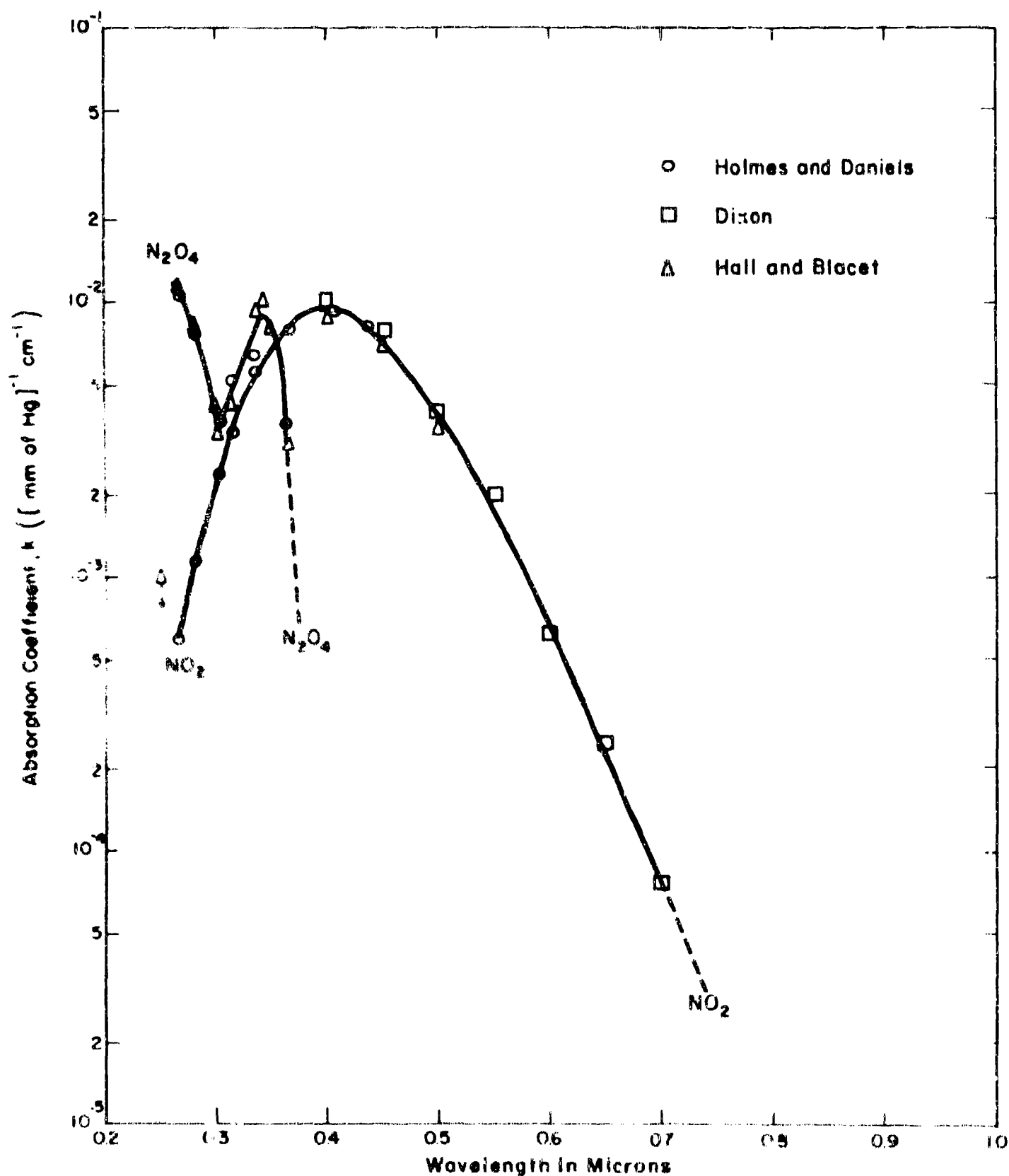


Figure 4.2 Absorption spectrum of NO_2 and N_2O_4 (per unit length at standard temperature and pressure). The absorption coefficient is $k = (pL)^{-1} \log_{10} (I_0/I)$, where p is the partial pressure of the gas in millimeters of mercury at 0°C , L is the path length through the gas in centimeters, and I_0/I is the ratio of the initial to the transmitted intensity. The absorption coefficient is less than $10^{-6} \text{ mm}^{-1} \text{cm}^{-1}$ between 0.8 and 4.4 microns wavelength.

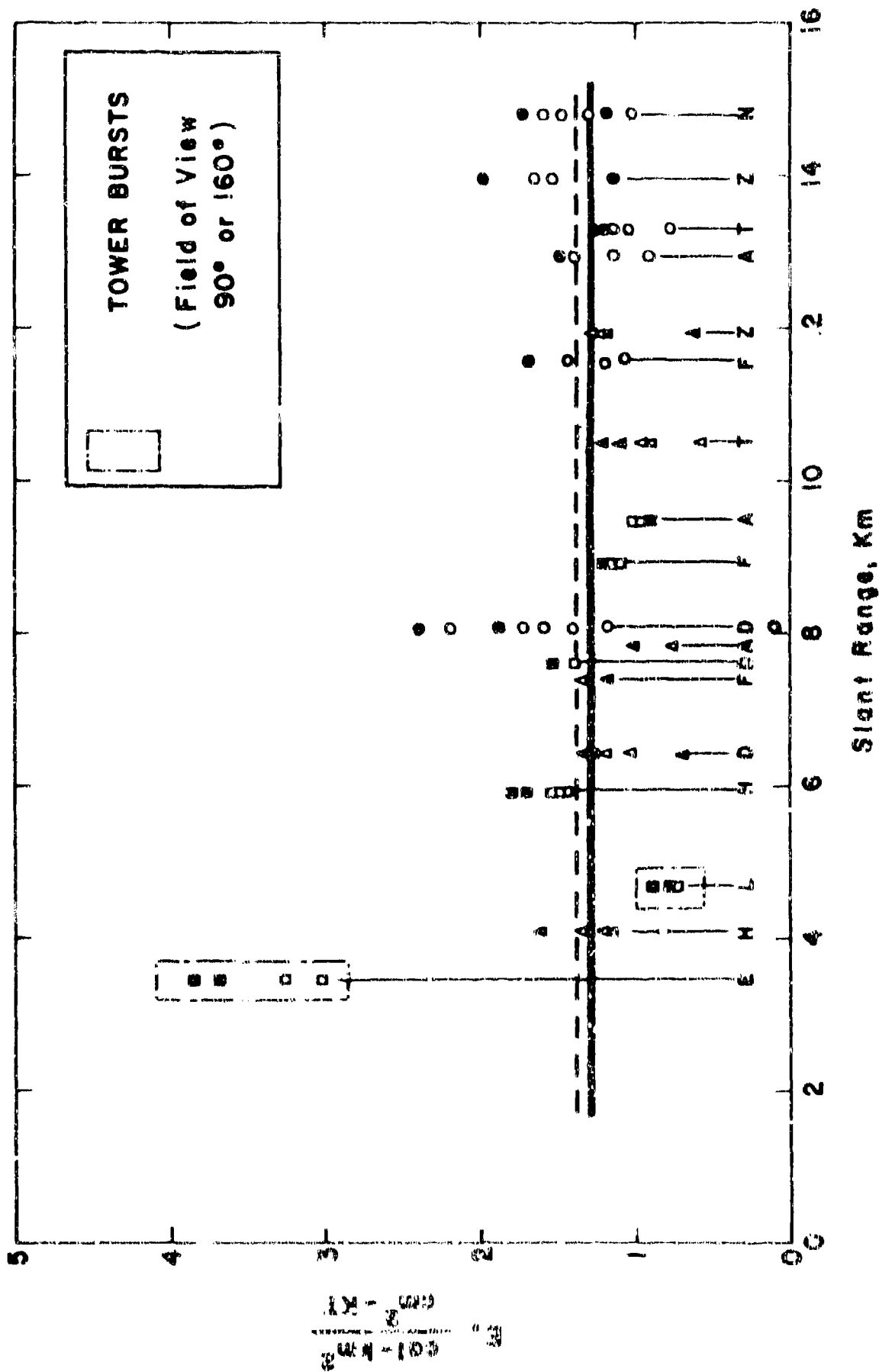


Figure 4.3 Specific thermal energy as a function of slant range. Quartz windows were used for all calorimeters. The results are reported according to aircraft: B (B-57); C (B-47); and L (B-66). An open symbol indicates a calorimeter, a filled symbol a radiometer, i.e., C (calorimeter) and ● (radiometer). The solid horizontal line is the mean value of the specific thermal energy for barge shots only and is independent of range; $E = 1.3 \text{ cal-cm}^2/\text{cm}^2\text{-kt}$. The dashed line is the average of all events; $E = 1.4 \text{ cal-cm}^2/\text{cm}^2\text{-kt}$. The letters are the initials of code names as given in Table 3.3.

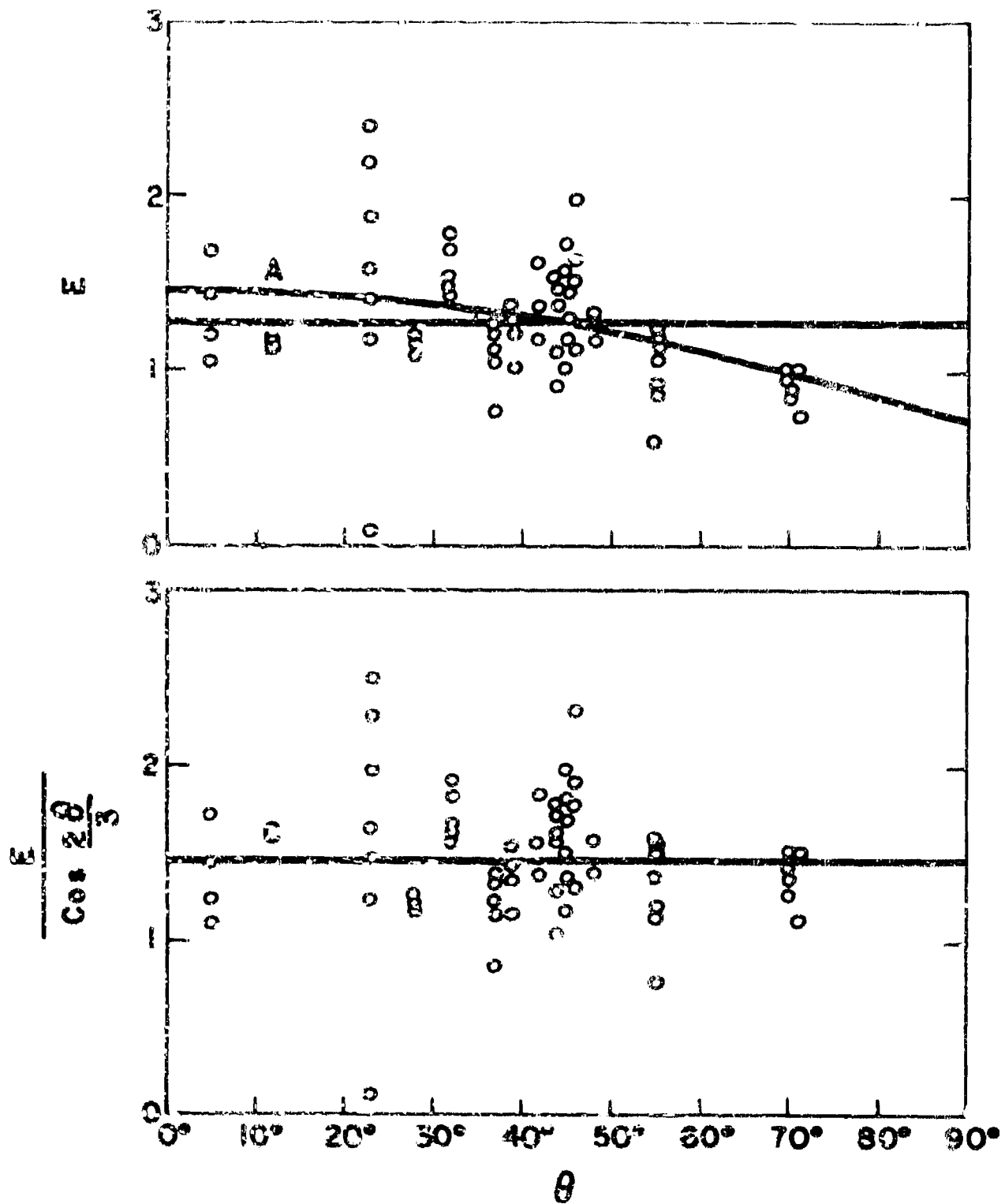


Figure 4.4 E as a function of θ and $E/\cos^{2/3} \theta$ as a function of θ . See Equation 3.1 for the definition of E , and Figure 3.1 for θ .

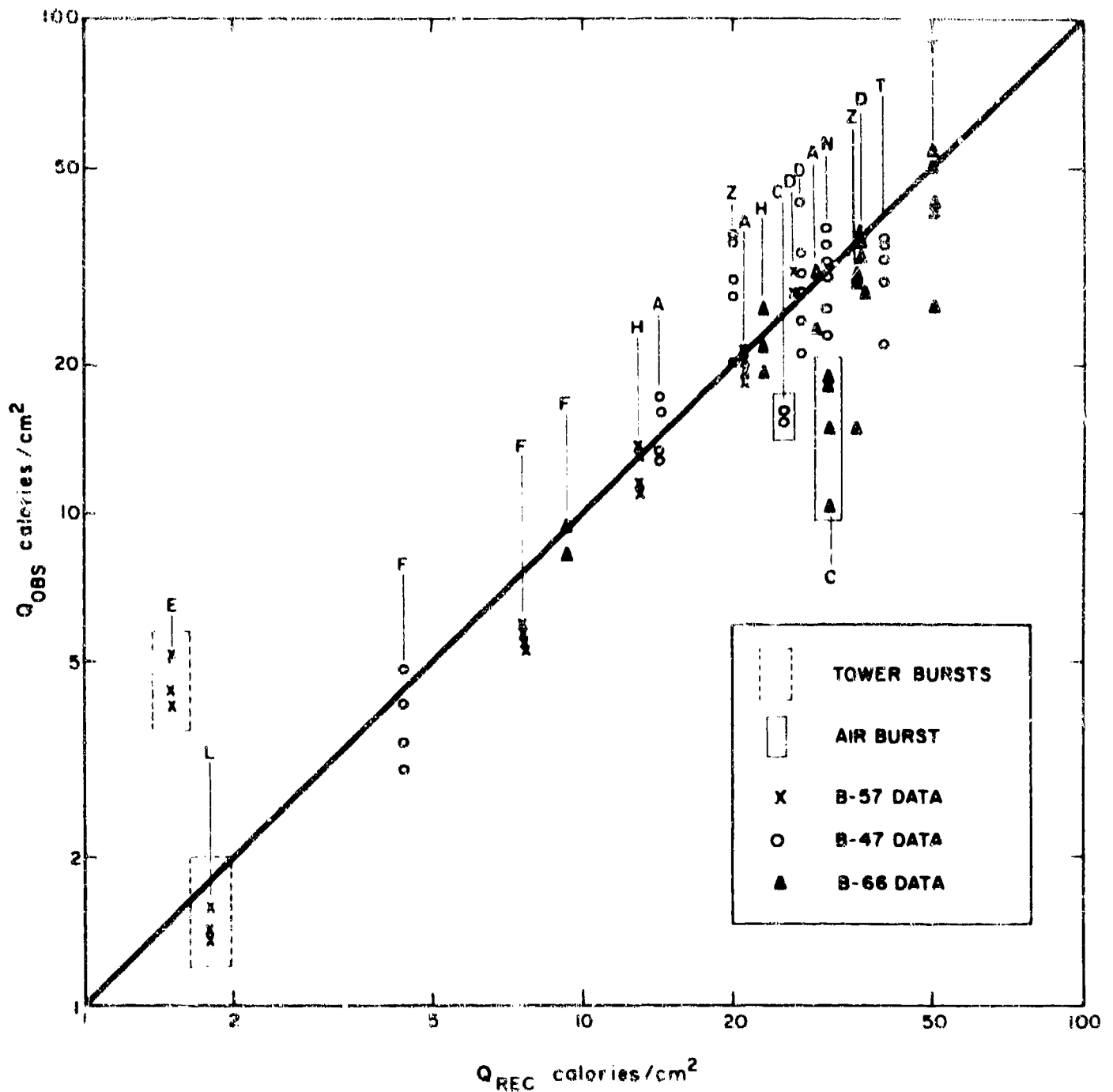


Figure 4.5 Correlation between predicted and observed radiant exposure Q_{REC} . The radiant exposure was predicted by the method described in Reference 22. The results are reported according to aircraft: X (B-57); (B-47); ▲ (B-66). The letters used to identify the events are the initials of the code name of Table 3.3, i.e., A for Apache, and so forth.

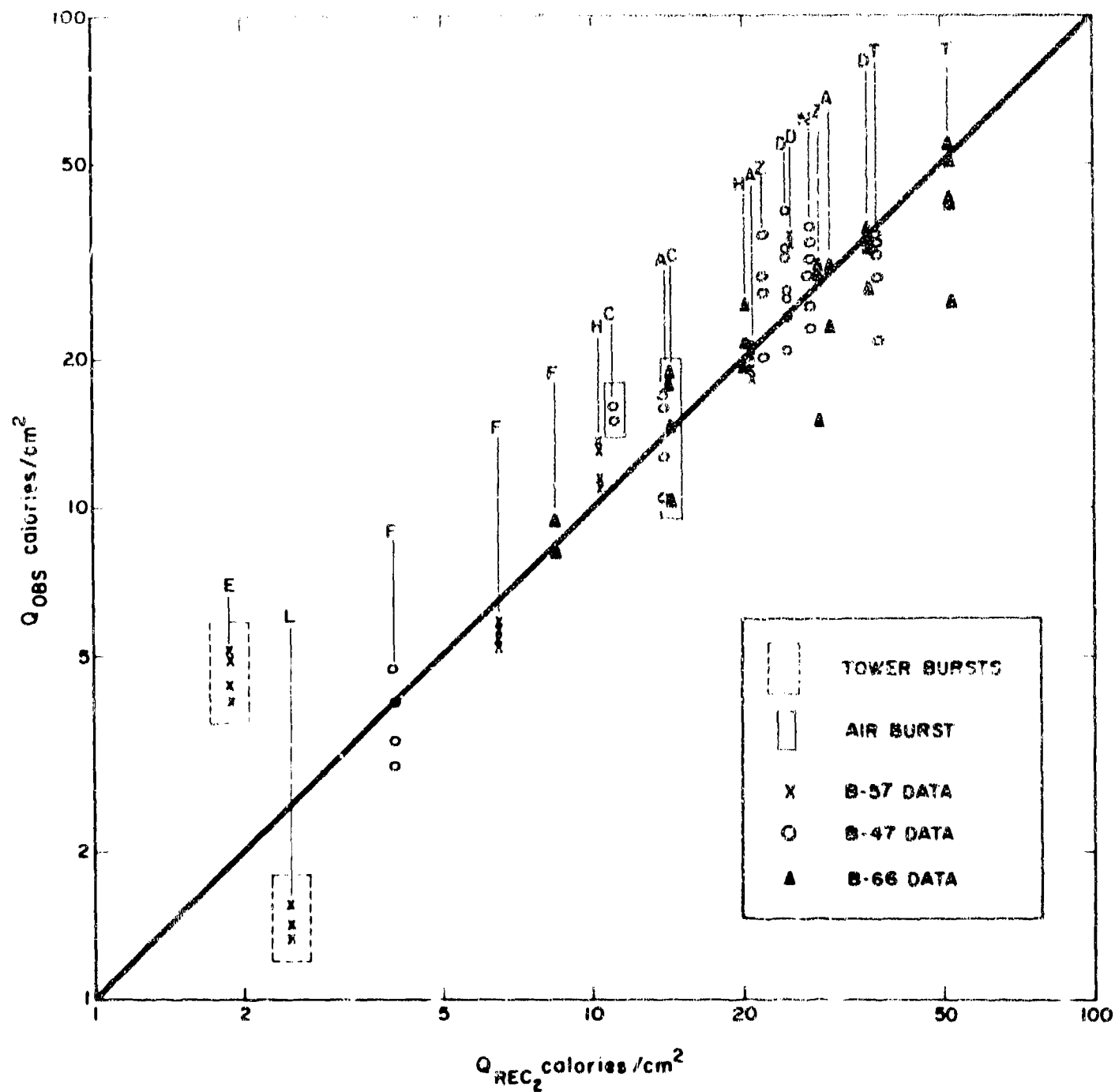


Figure 4.6 Correlation between predicted and observed radiant exposure. The radiant exposure was predicted through $Q_{rec} = 1.45 W \cos^2 \theta / D^2$. The results are reported according to aircraft: X (B-57); O (B-47); Δ (B-66). The letters are the initials of the code names of the events as given in Table 3.3.

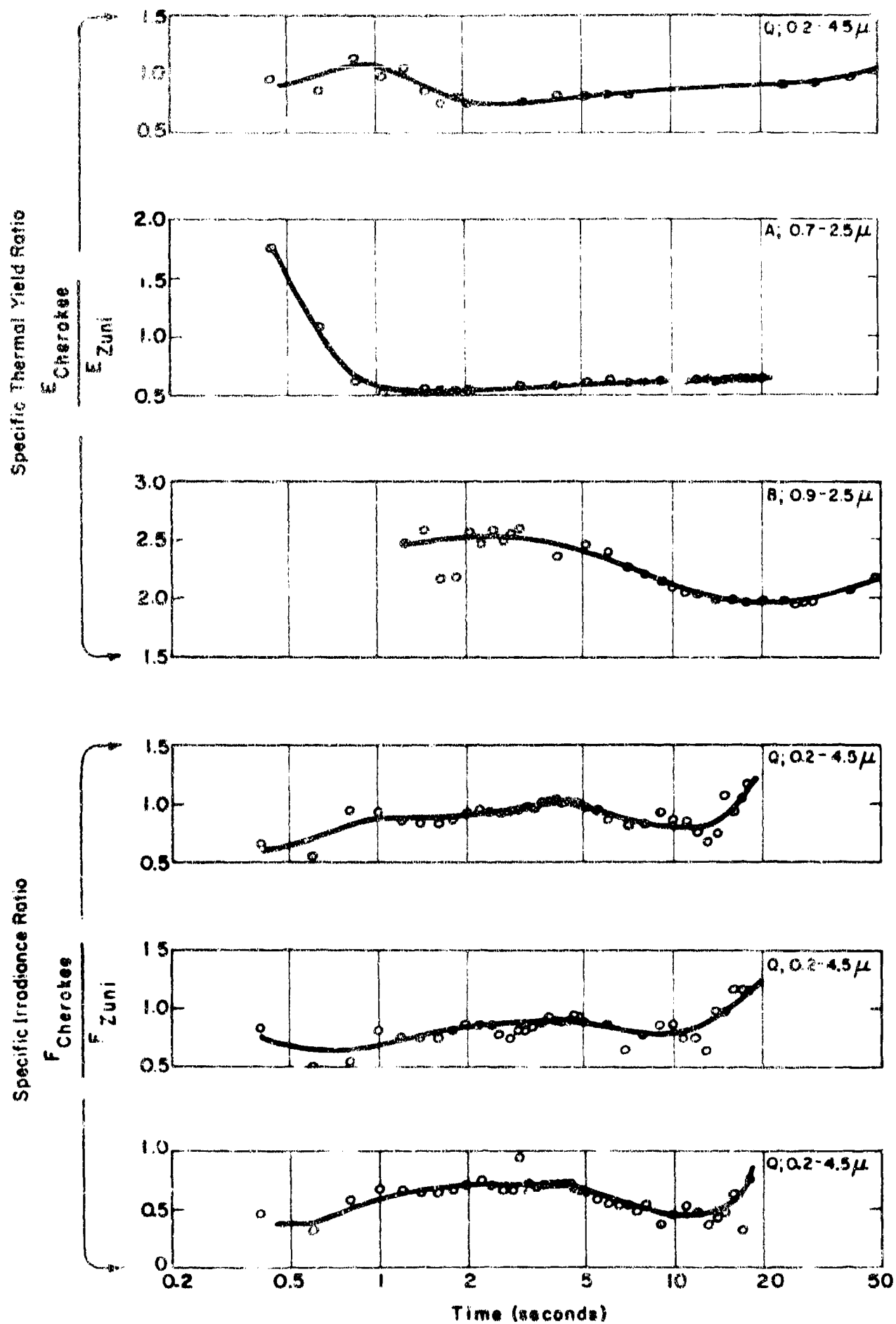


Figure 4.7 Ratio of specific thermal yield and the specific irradiance.
By definition, $E = QD^2/W$ and $F = HD^2/W$.

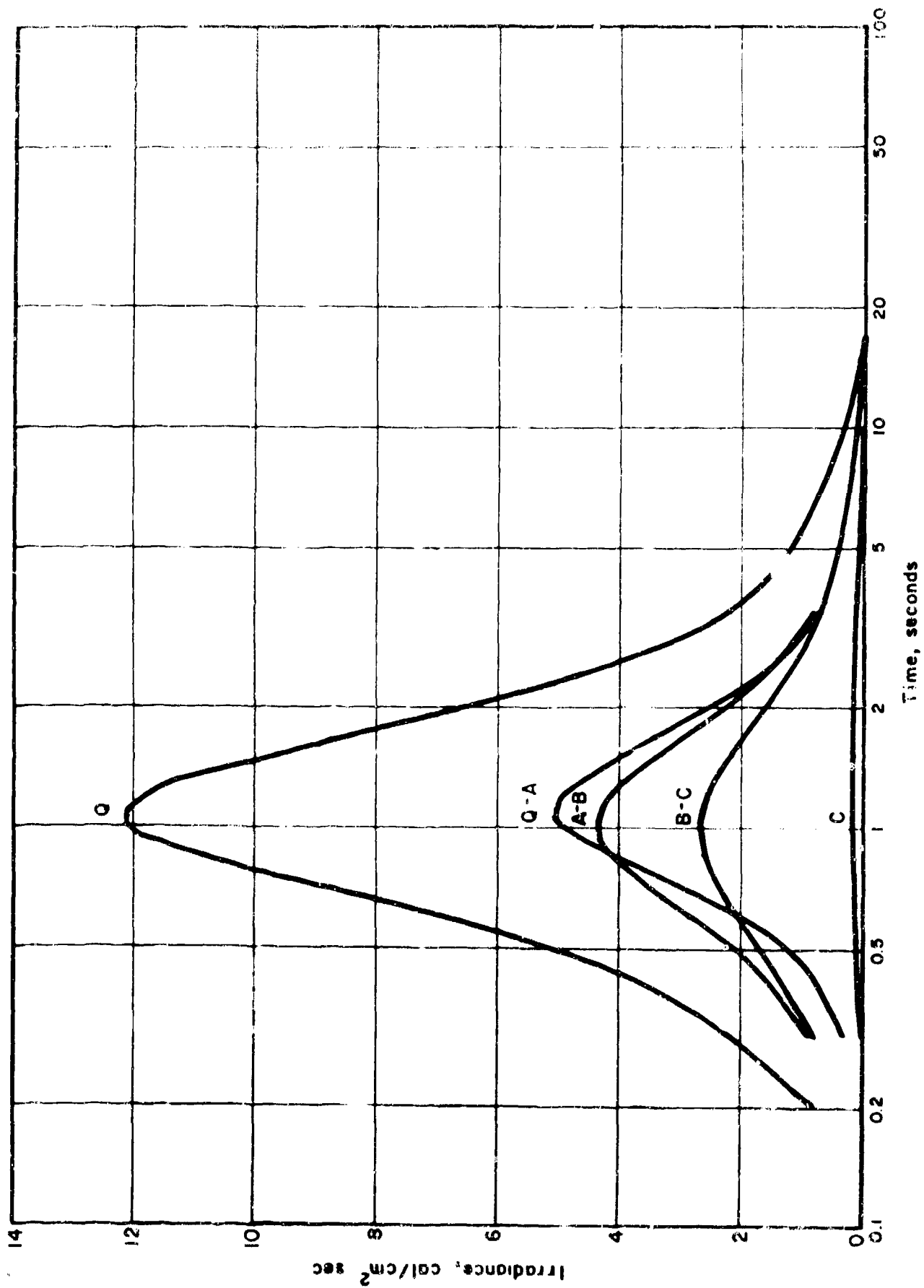


Figure 4.8 Irradiance as a function of time for narrow spectral regions, Shot Dakota. The letters identifying the various curves are explained in Table 4.5.

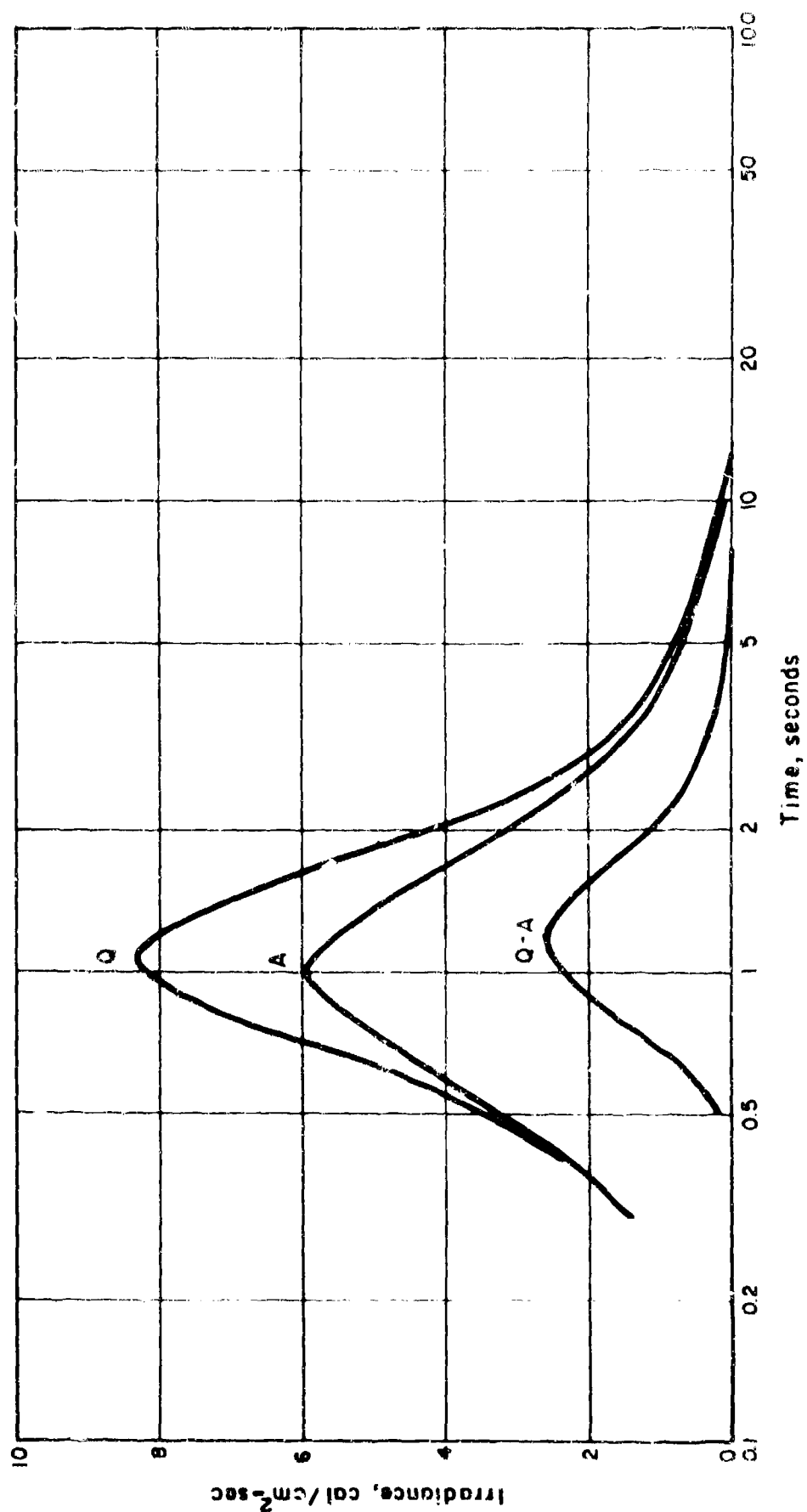


Figure 4.9 Irradiance as a function of time for instruments pointing downward, Shot Dakota. The curve lettered Q receives energy in the 0.2- to 4.5-micron range, A from 0.7 to 2.5 microns, and Q - A essentially in the 0.2- to 0.7-micron range of wavelengths.

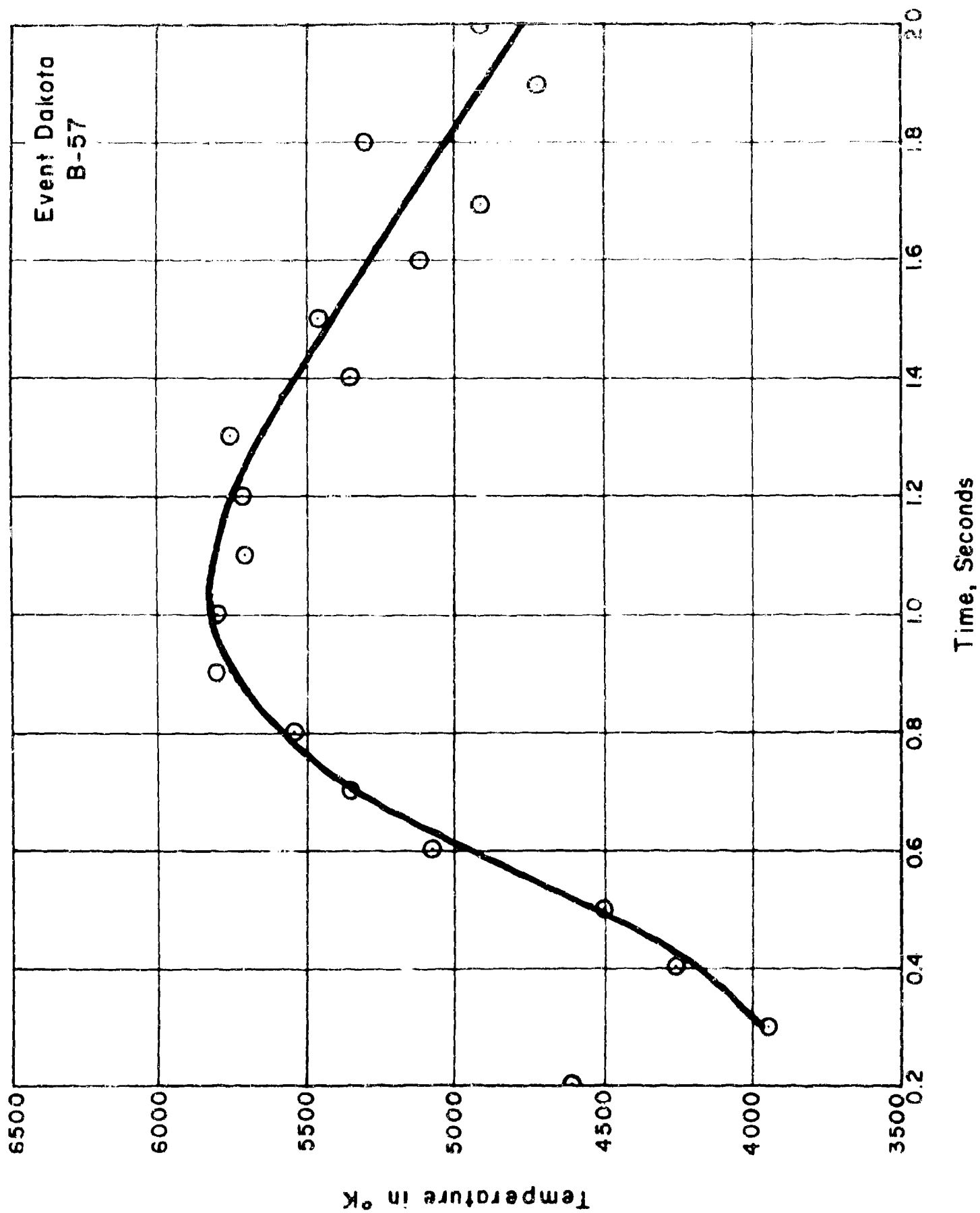


Figure 4.10 Color temperature as a function of time, Shot Dakota.

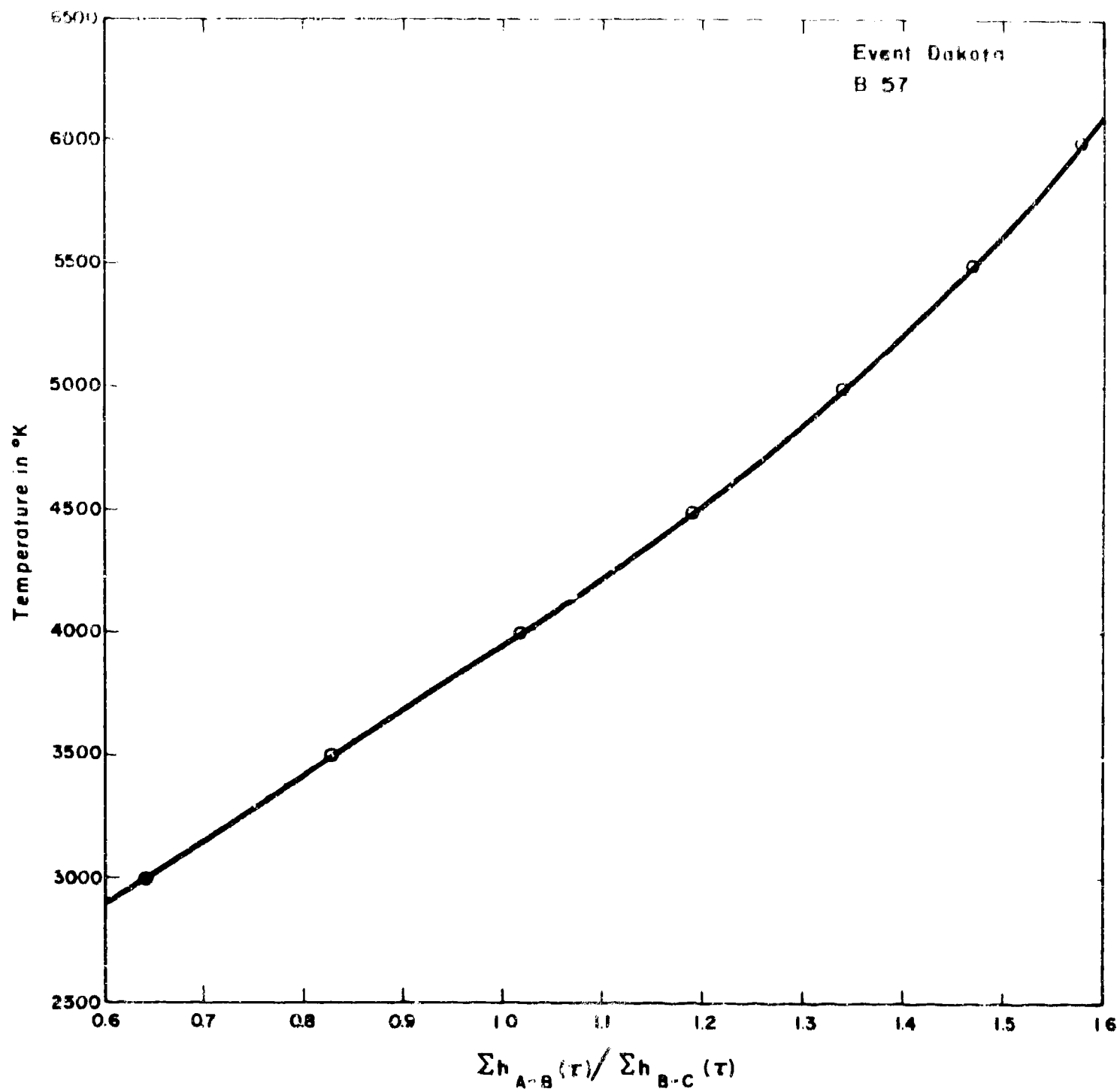


Figure 4.11 Black body temperature as a function of the ratio $\Sigma h_{A-B}(\tau) / \Sigma h_{B-C}(\tau)$.

SECRET

841

FILM DENSITY

ABSORPTION BY NO₂

① SOURCE

② 0.25 cm. Hg of NO₂

③ 1.00 cm. Hg of NO₂

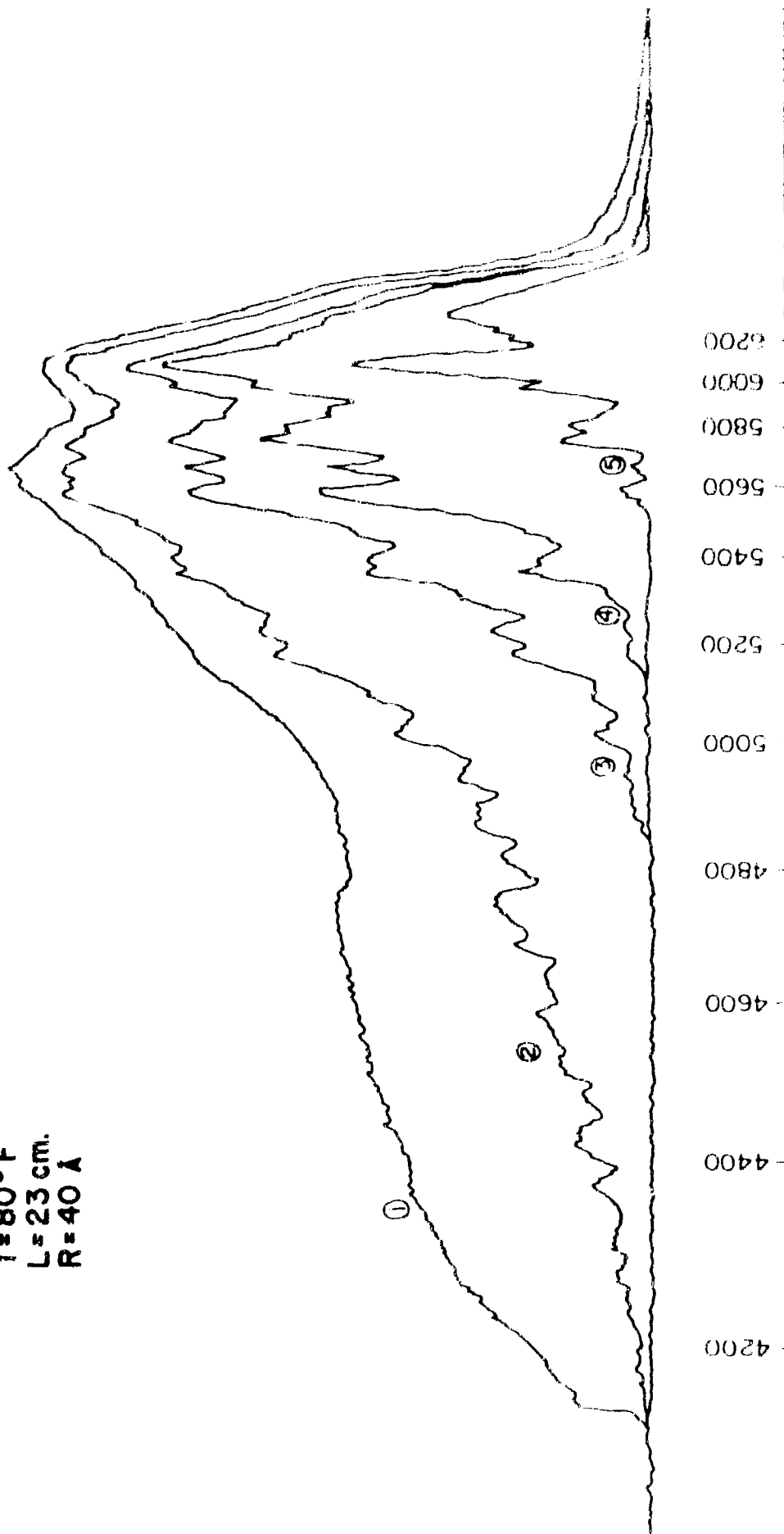
④ 2.50 cm. Hg of NO₂

⑤ 10.00 cm. Hg of NO₂

T=80°F

L=23 cm.

R=40 Å



WAVELENGTH IN ÅNGSTROM UNITS

Figure 4.12 Absorption spectrum of NO₂.

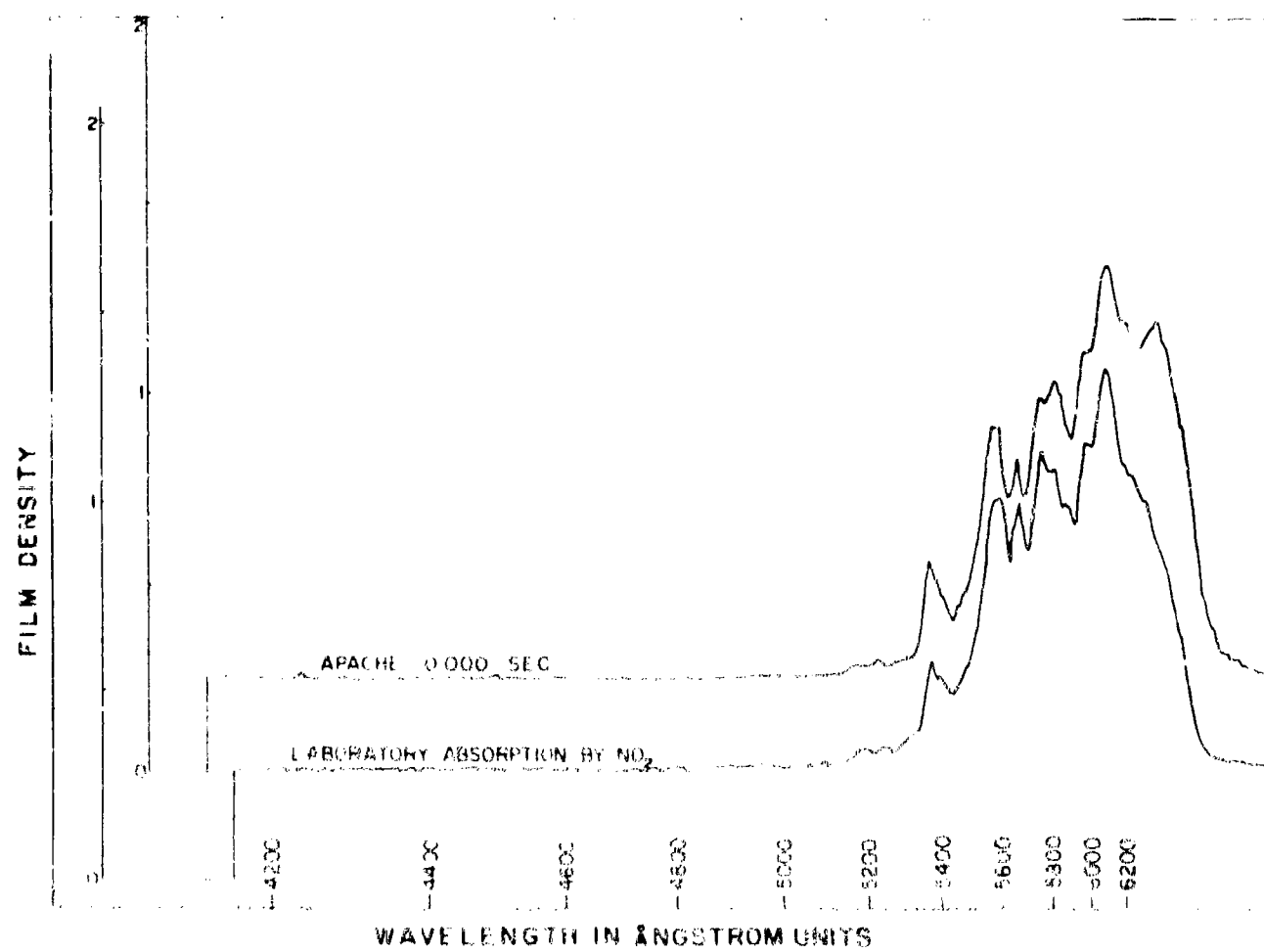
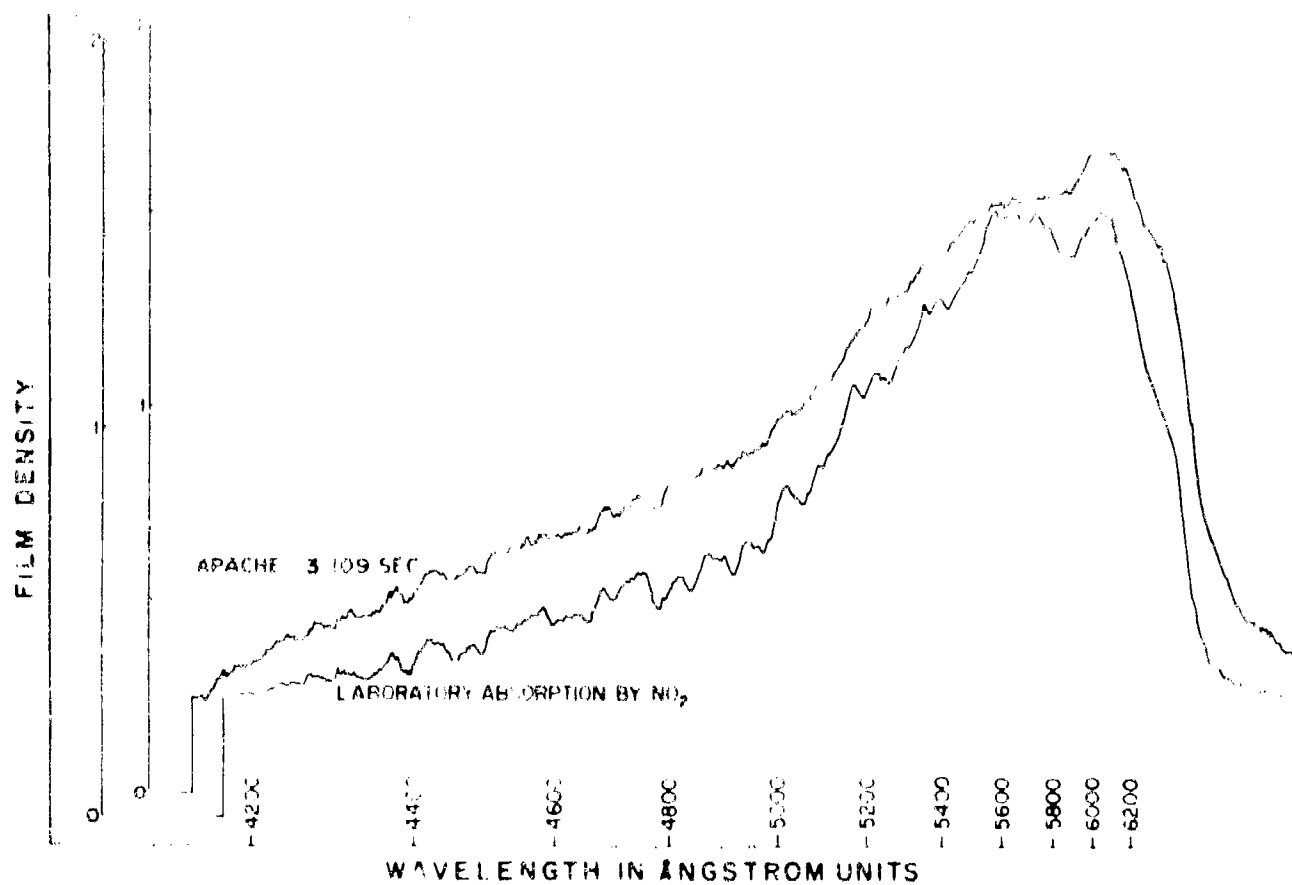


Figure 4.13 Comparison of NO₂ absorption spectrum with typical shot spectra.

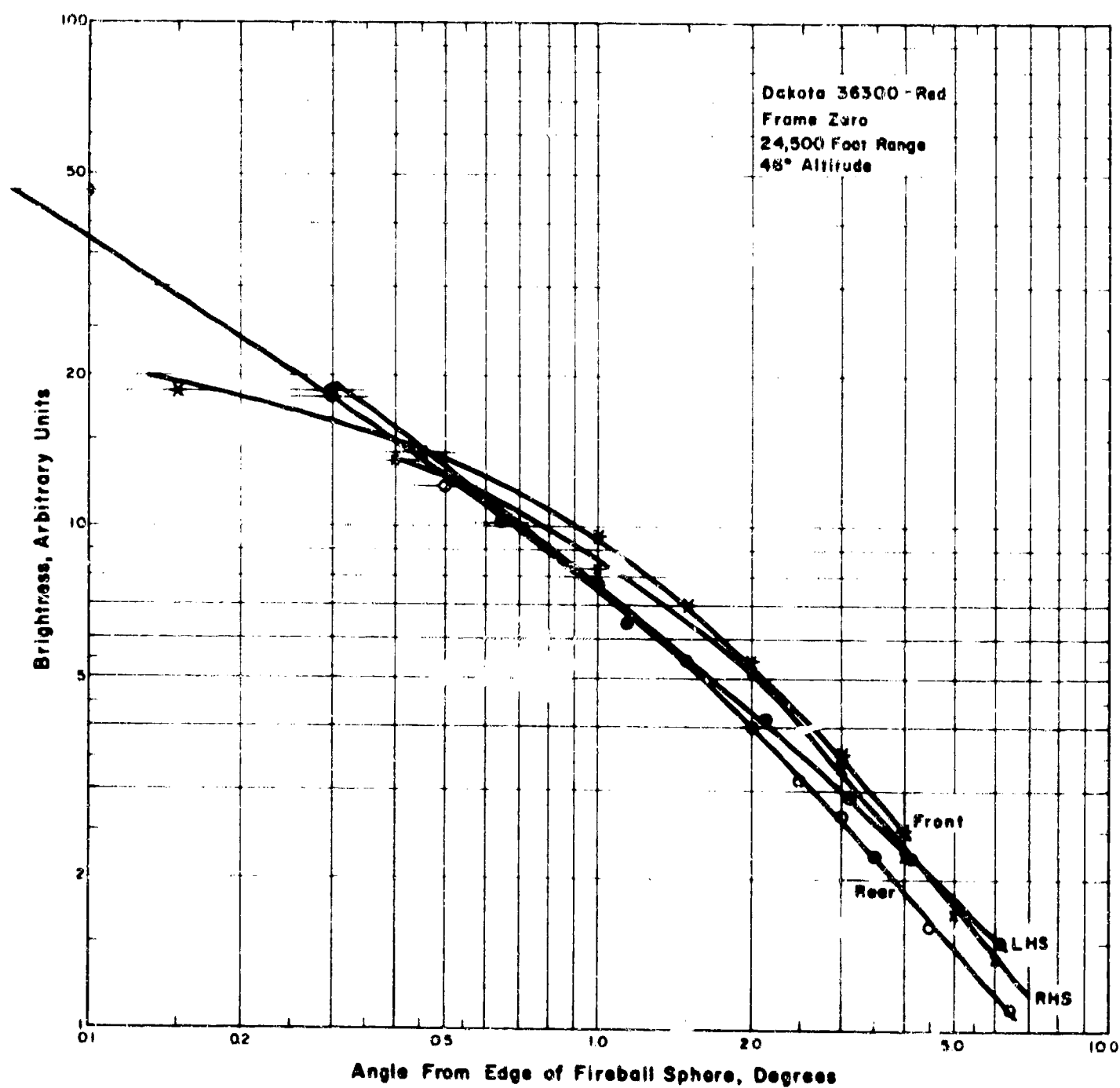
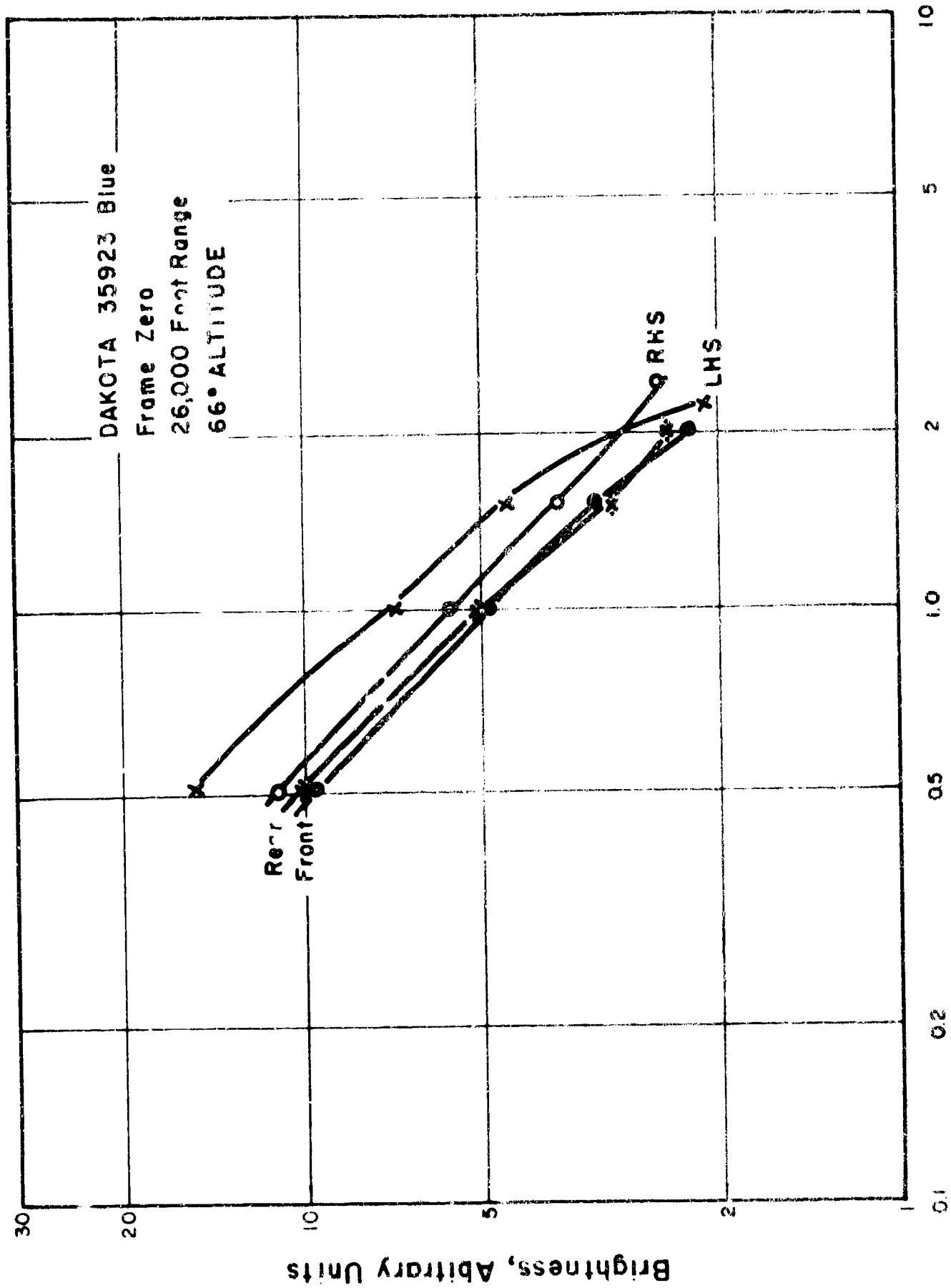


Figure 4.14 Scattering of light from region surrounding Shot Dakota, in red light. The scans are vertical (front and rear) and horizontal (LHS and RHS) through the fireball center.



Angle From Fireball Edge, Degrees

Figure 4.15 Scattering of light from region surrounding Shot Dakota, in Blue light. The scans are vertical (front and rear) and horizontal (LHS and RHS) through the fireball center.

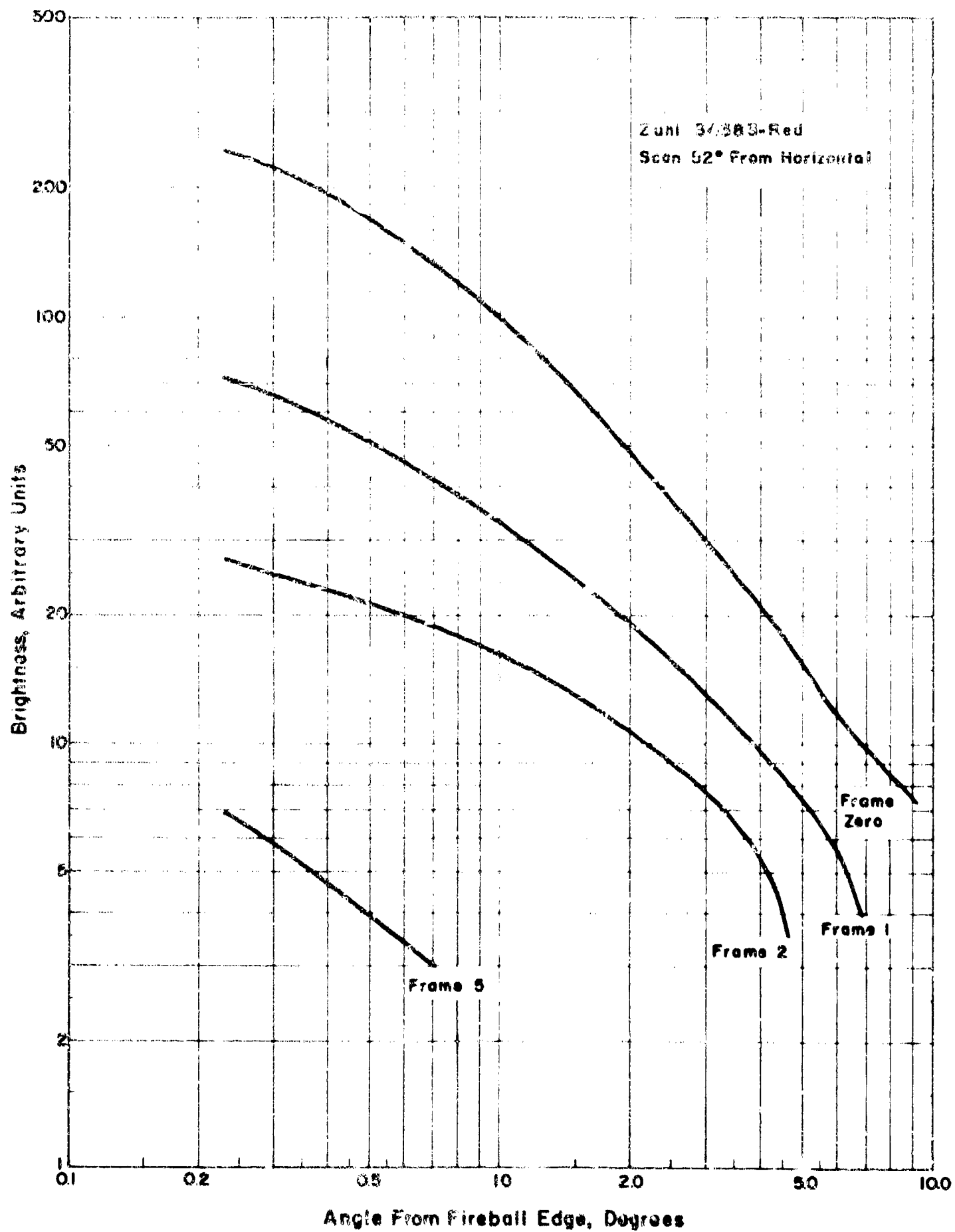


Figure 4.16 Scattering of light from the upper right section of the region surrounding Shot Zuni, in Red light.

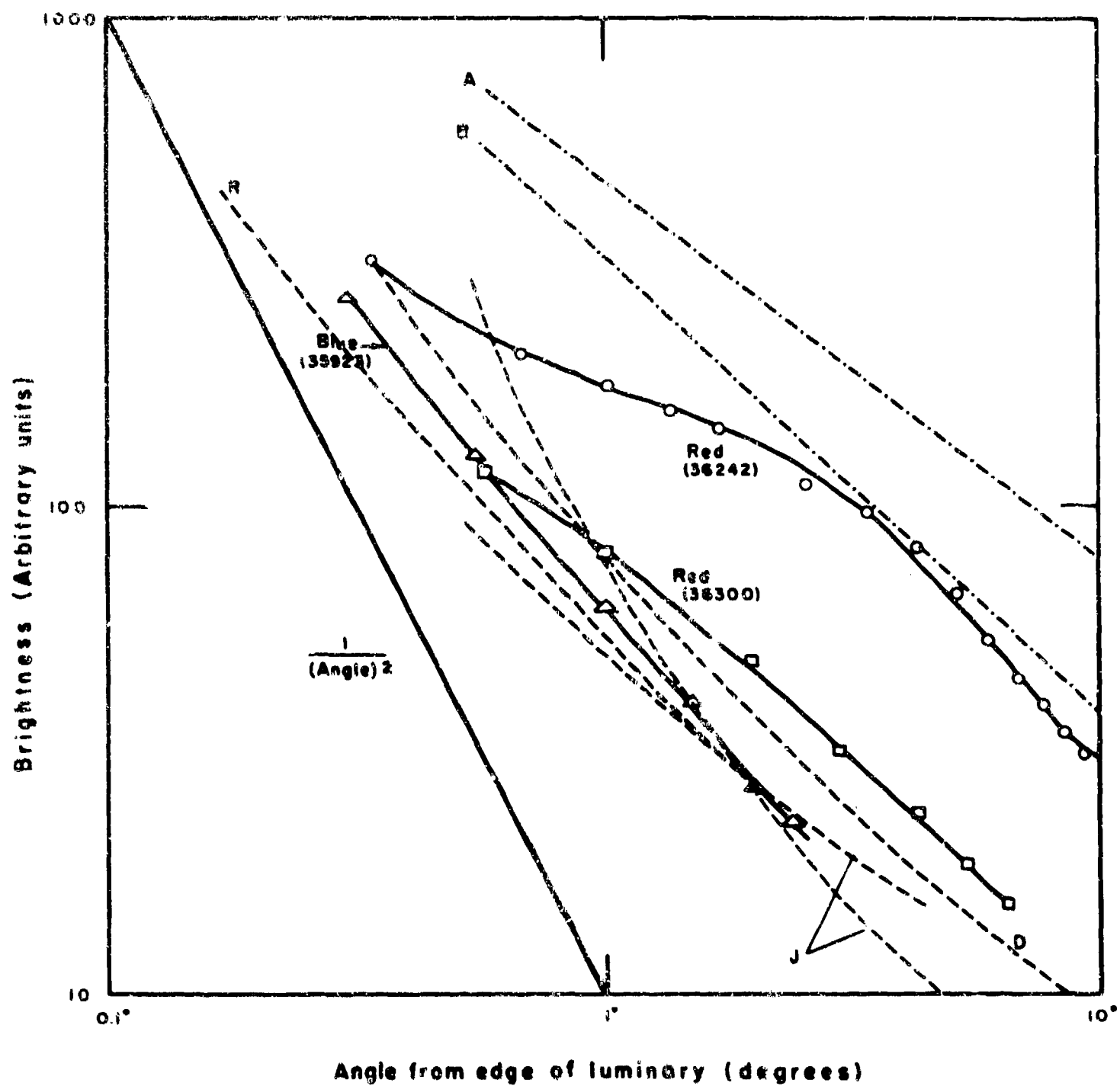


Figure 3.17 Comparison of fireball aureole to sun and flashbulb aureoles.

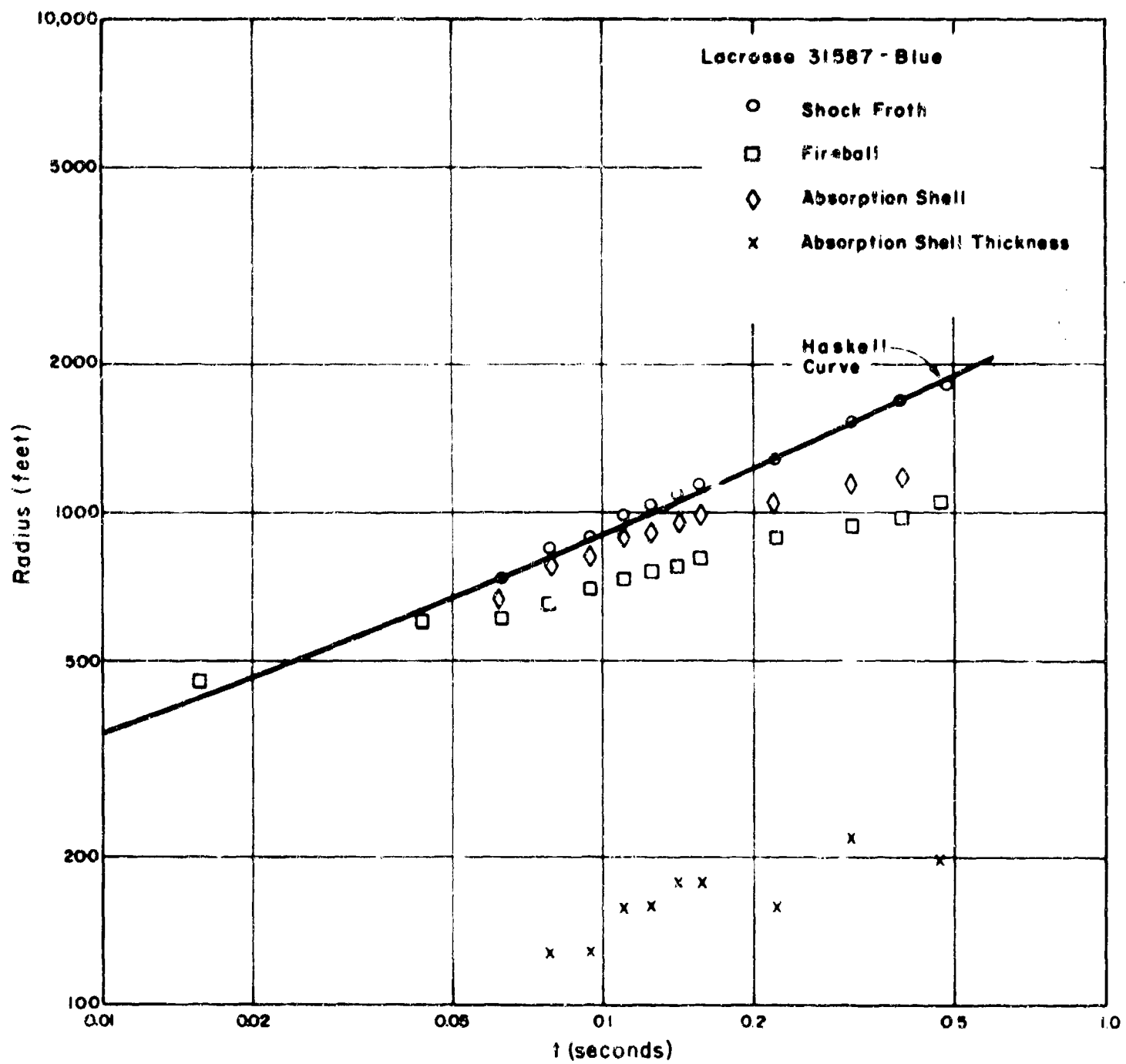


Figure 4.18 Hydrodynamic growth of Shot Lacrosse.

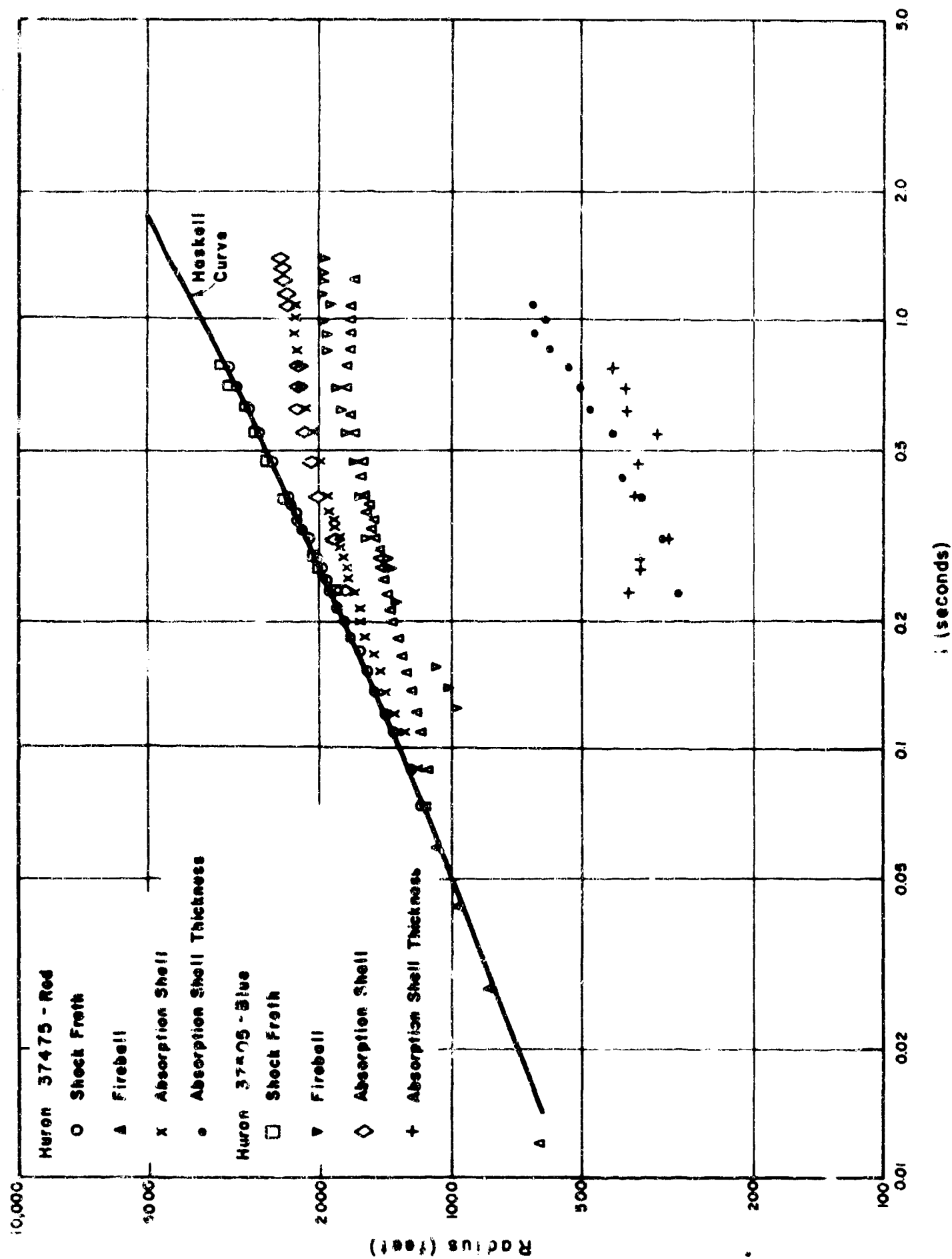


Figure 4.19 Hydrodynamic growth of Shot Huron.

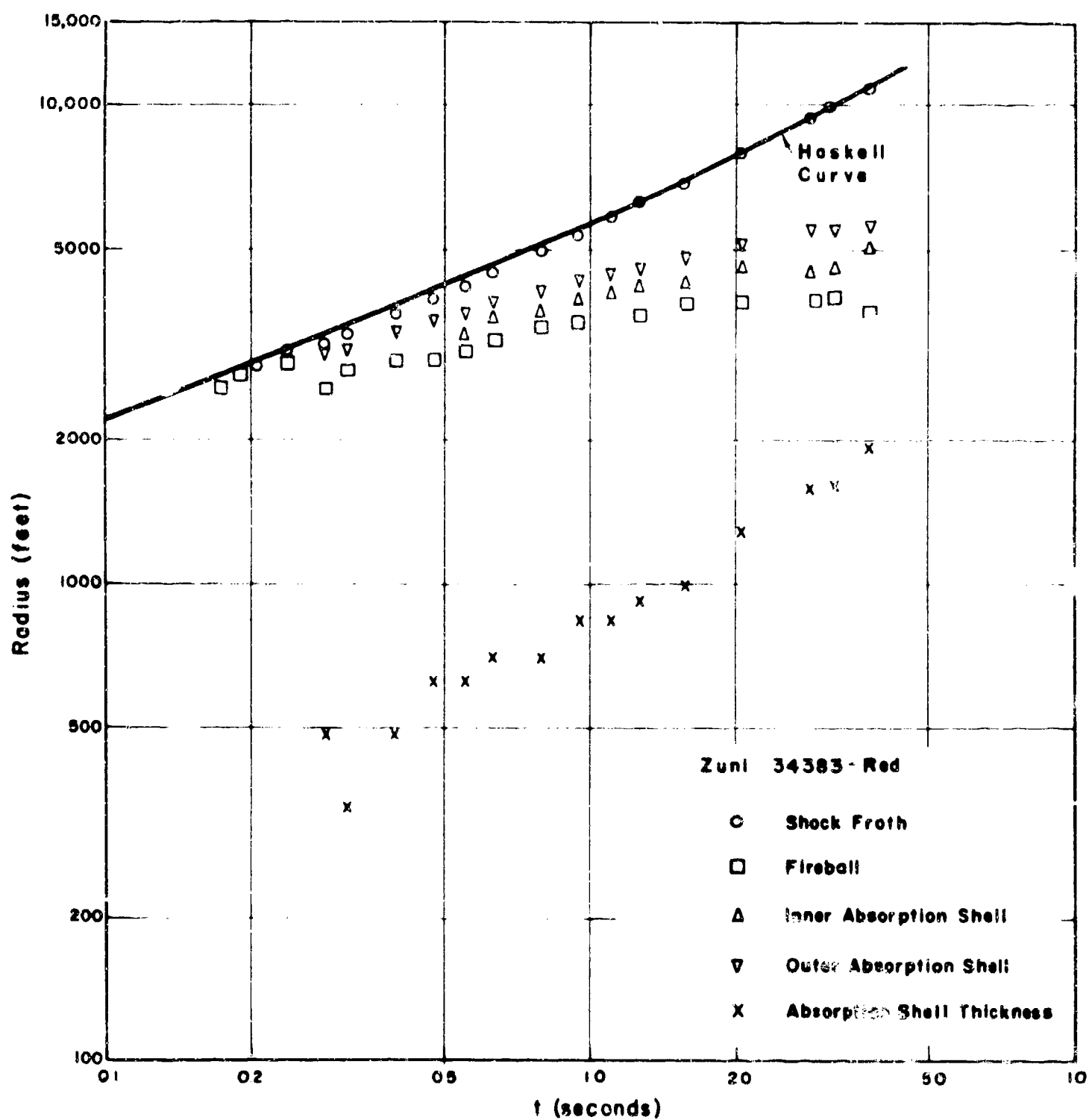


Figure 4.20 Hydrodynamic growth of Shot Zuni.

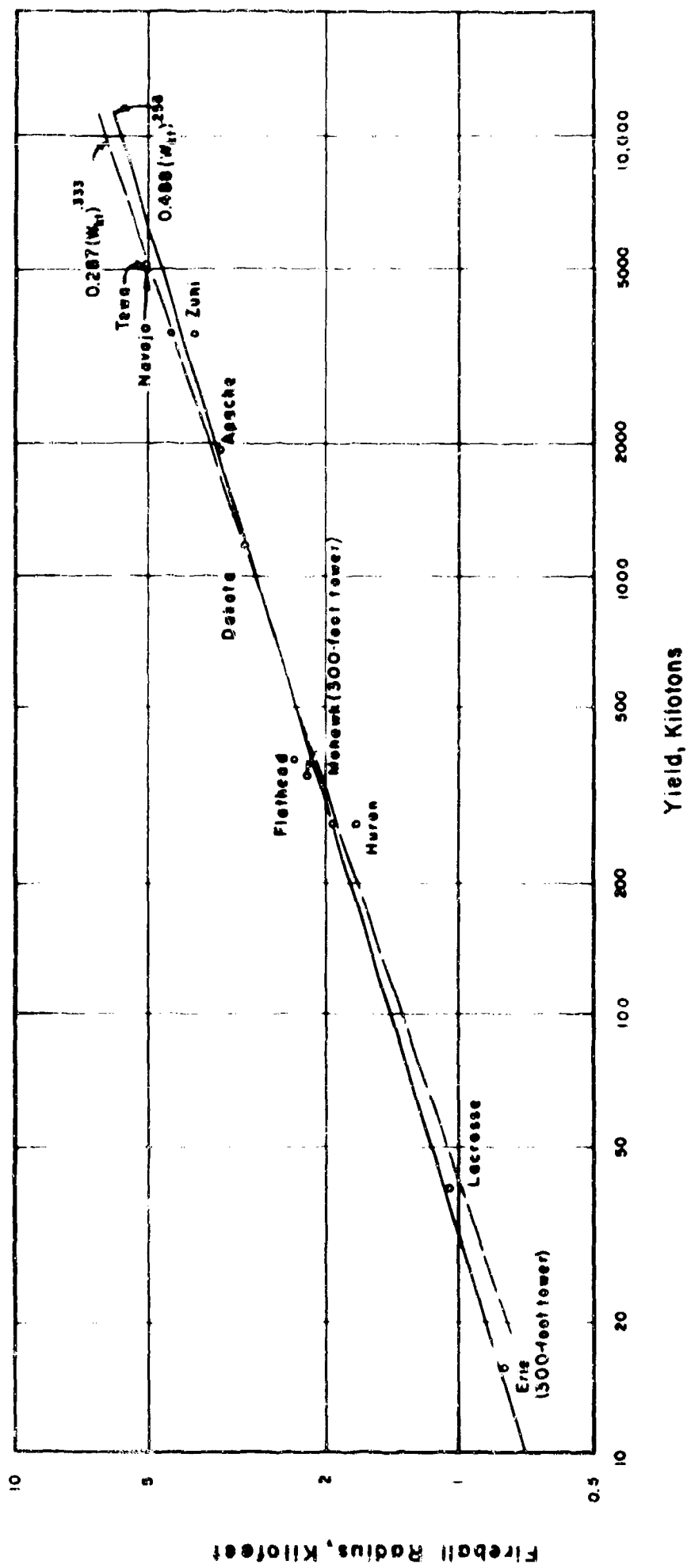
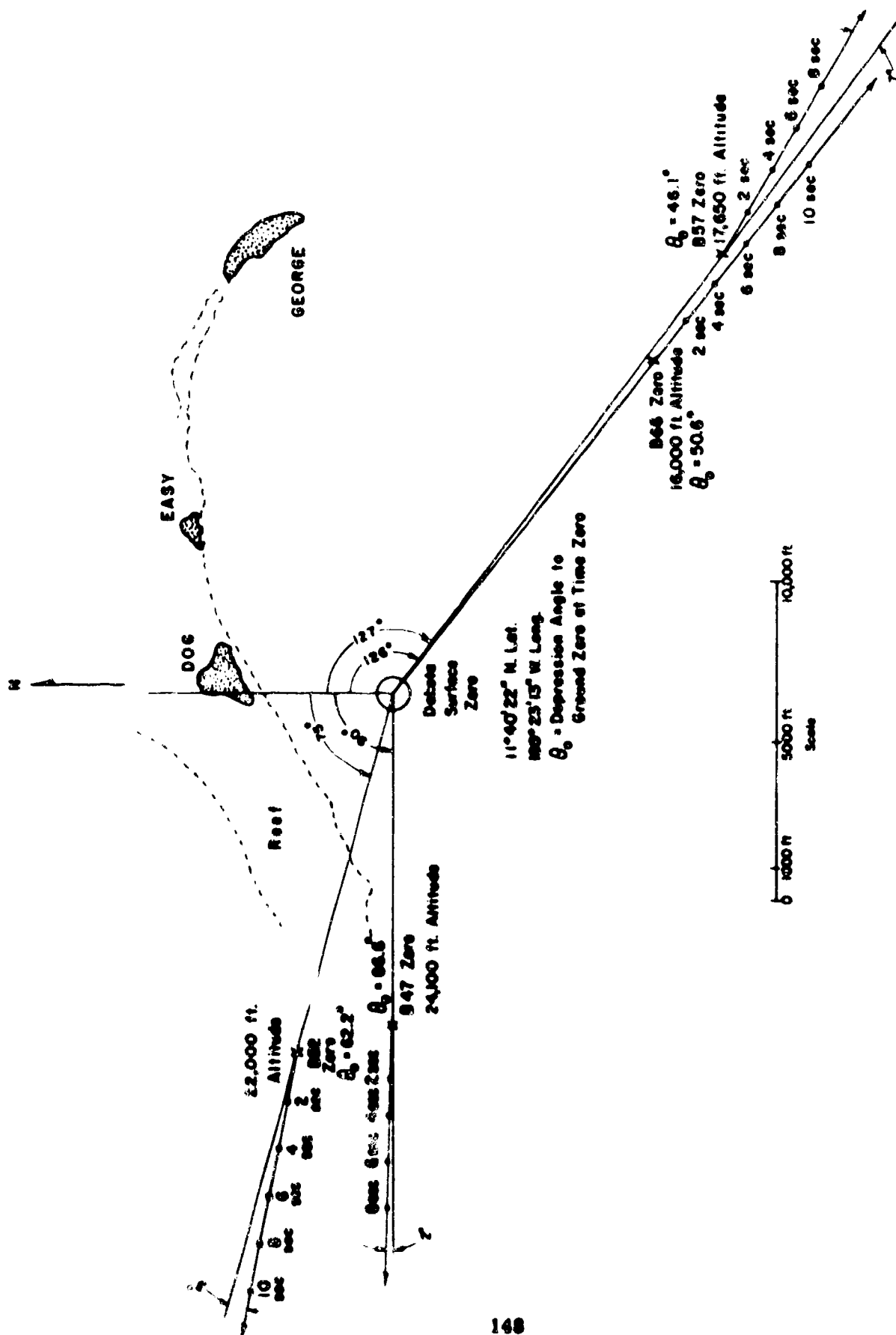


Figure 4.21 Mature fireball radius as a function of yield.



DAKOTA SITE - BIKINI ATOLL

Figure 4.22 Location of Dakota and its covering aircraft.

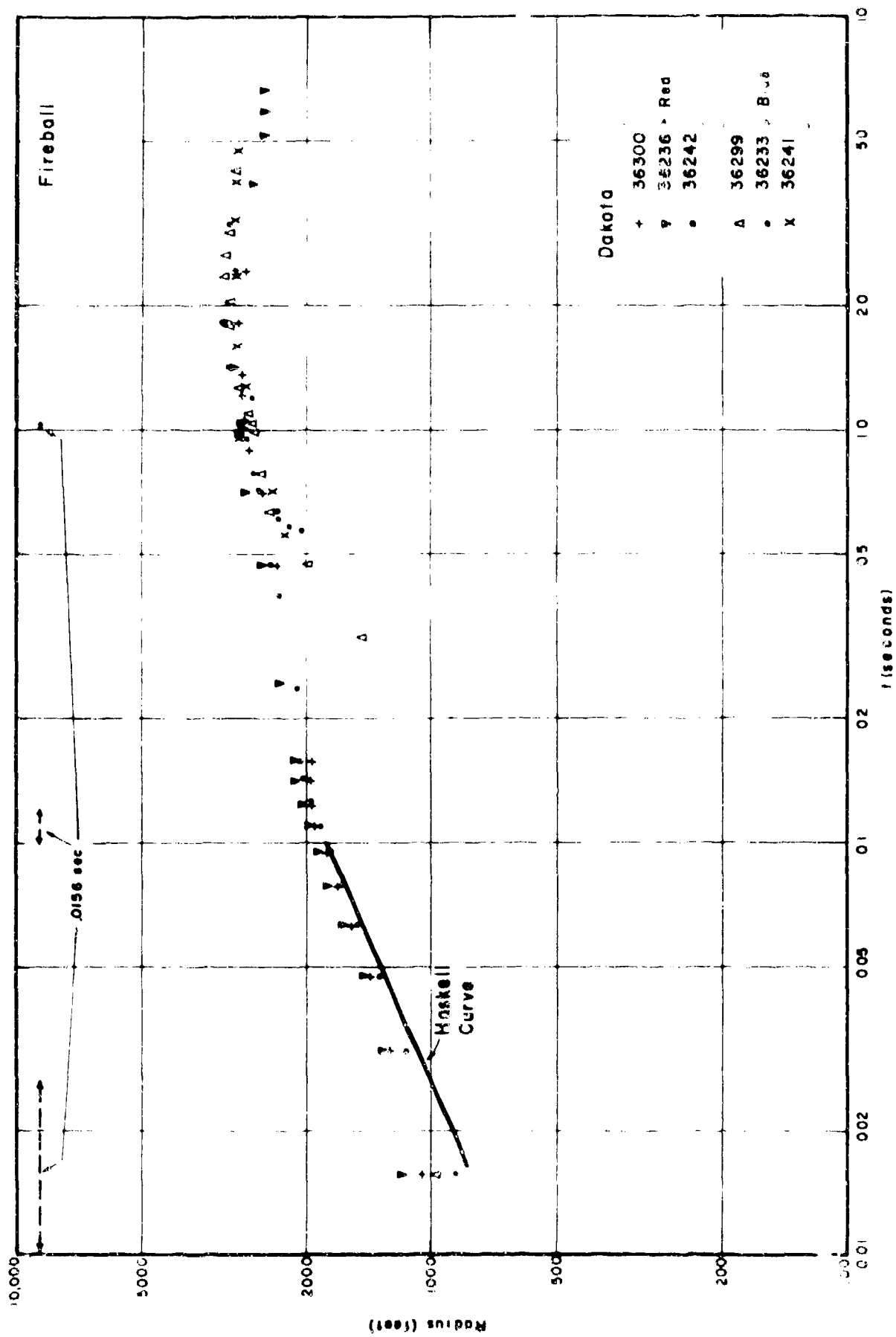


Figure 4.23 Growth of fireball, Shot Dakota.

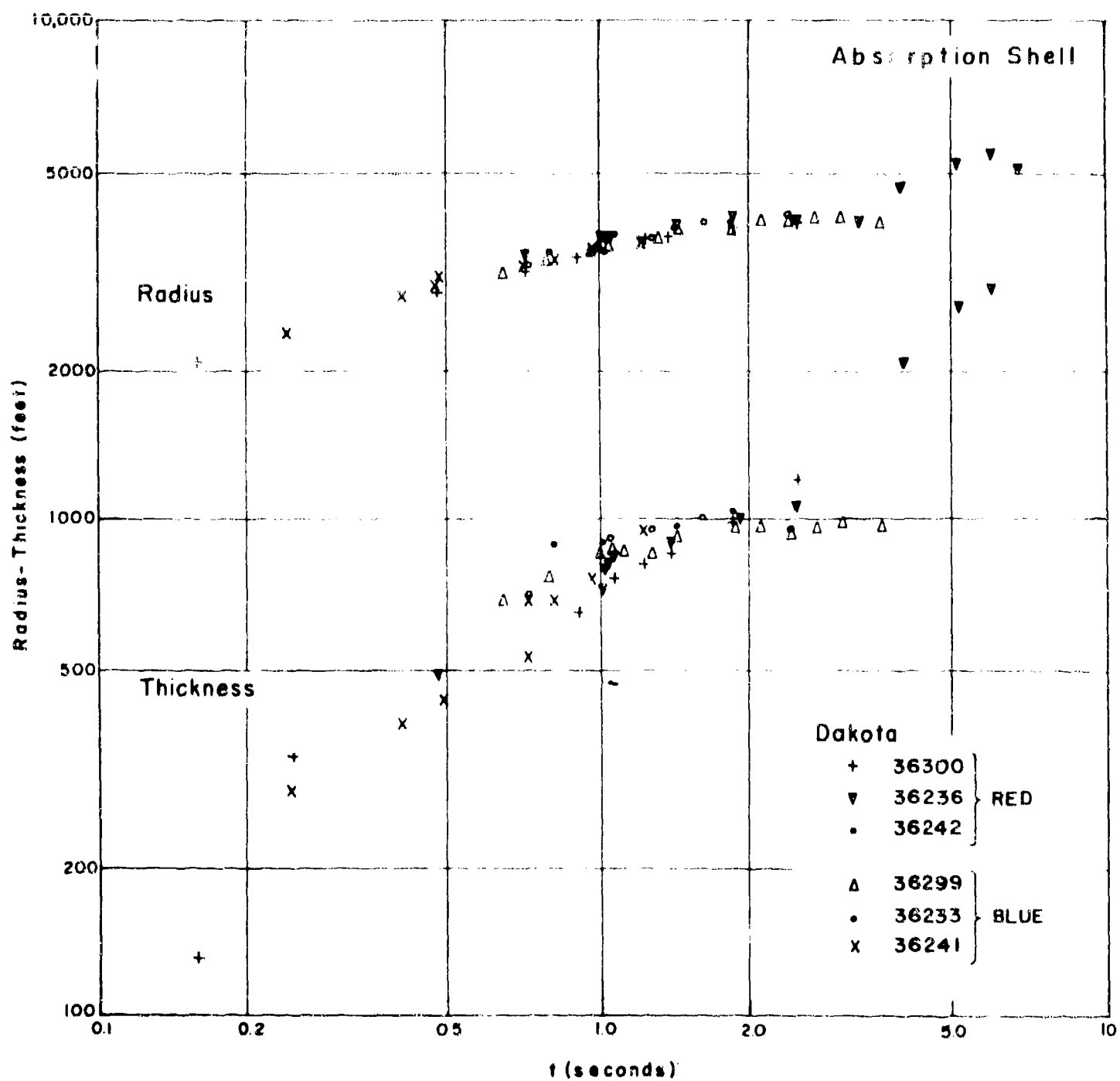


Figure 4.24 Growth of absorption shell, Shot Dakota.

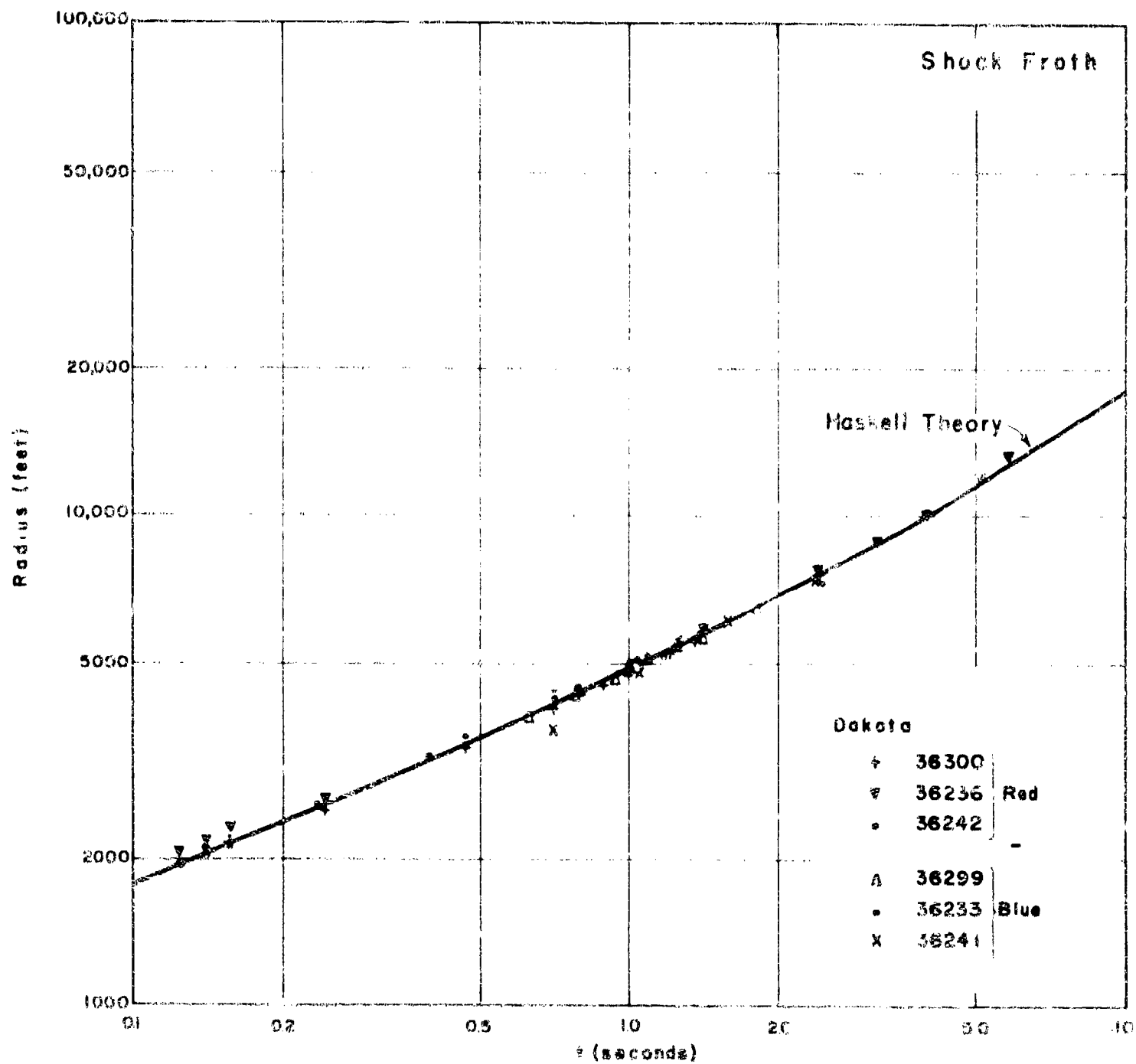


Figure 4.25 Growth of shock froth, Shot Dakota.

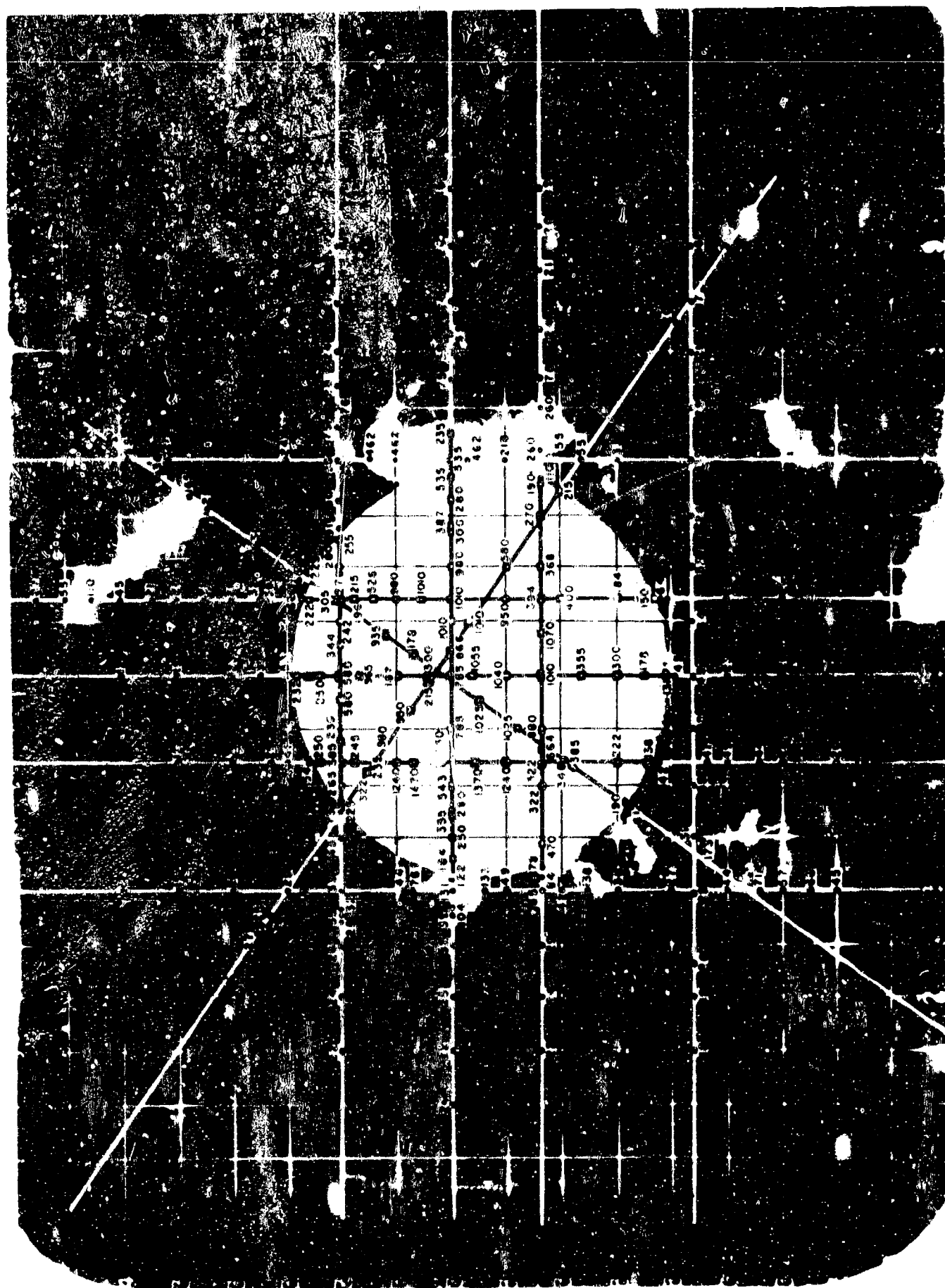


Figure 4.26 Typical brightness plot of fireball, Shot Dakota. This is frame 65 (second thermal flux maximum), Series 36236 Red. The fireball is somewhat overexposed in the reproduction and some of the contrast (for example, in the neighborhood of the absorption shell) is lost.

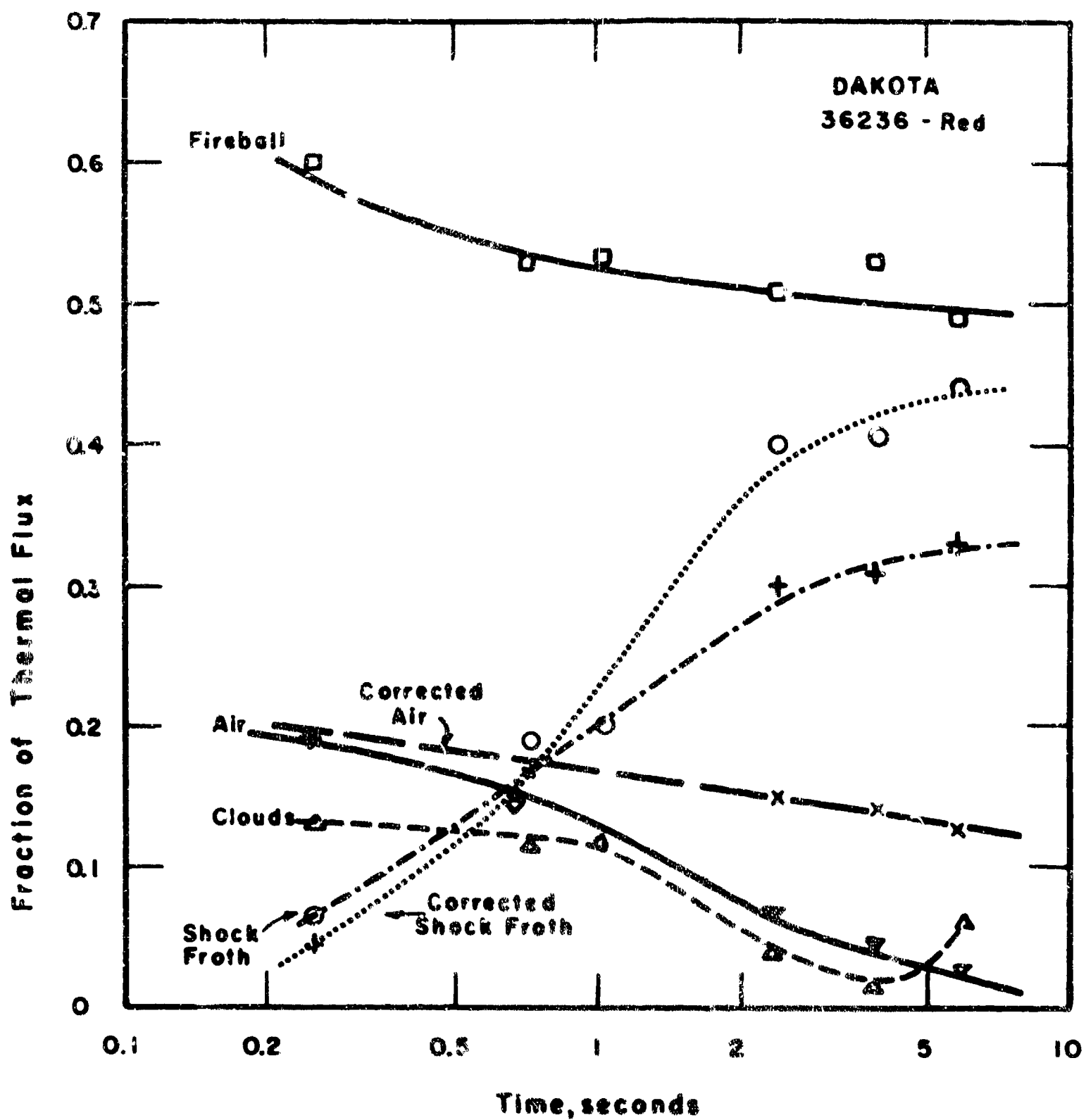


Figure 4.27 Partition of thermal flux from one Red photograph, Shot Dakota.

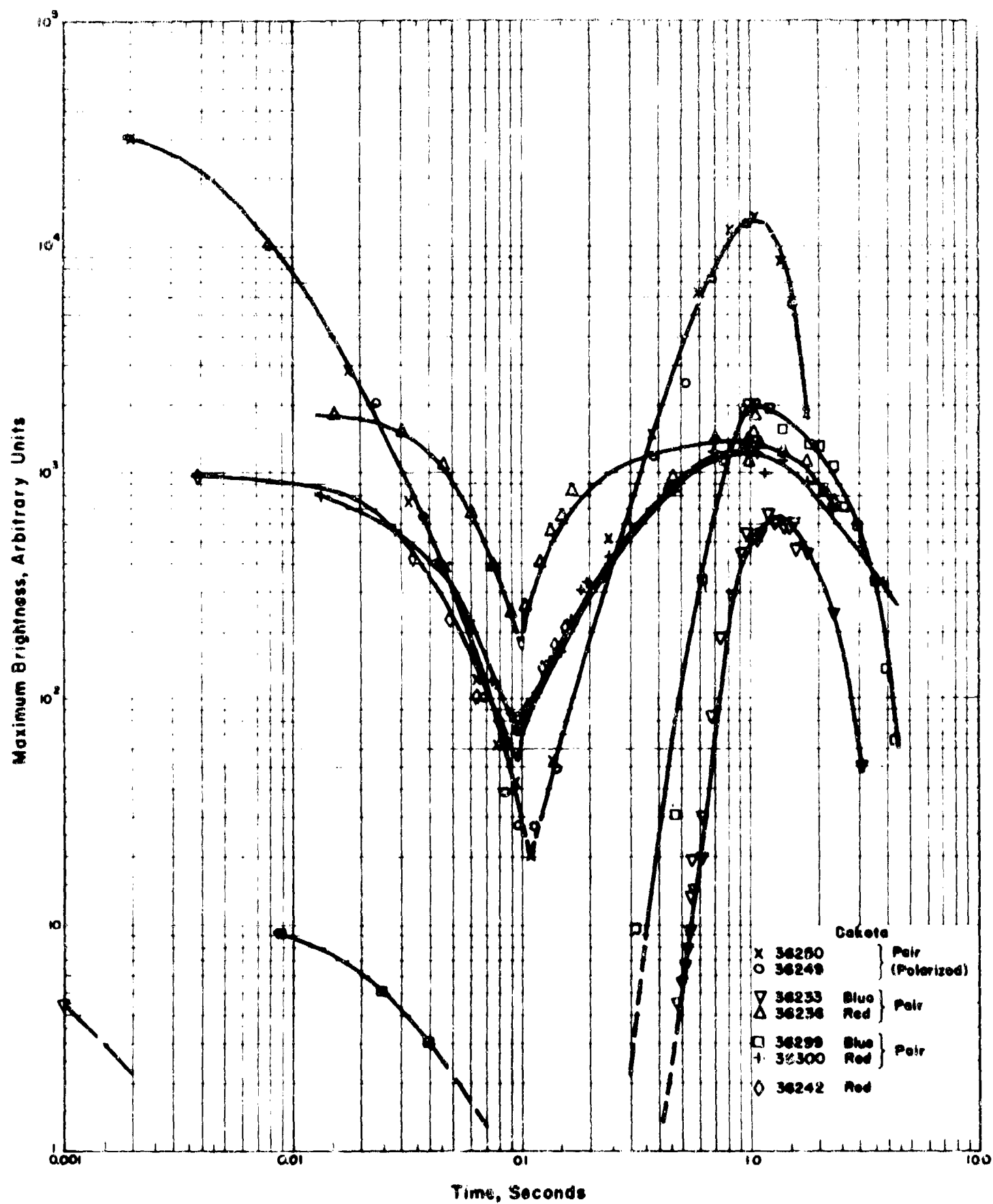


Figure 4.28 Maximum brightness history of fireball, Shot Dakota.

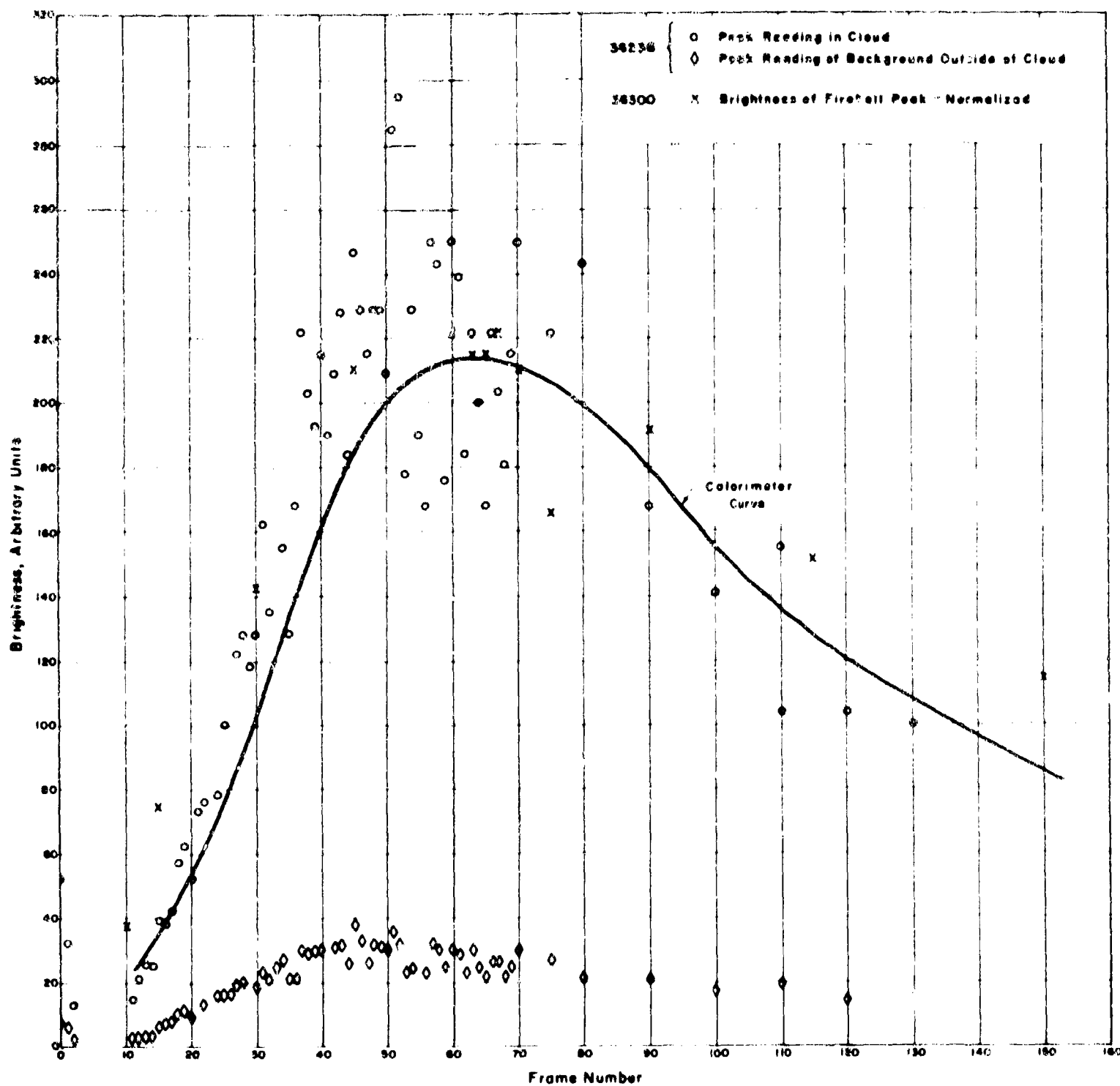


Figure 4.29 Cloud and water brightnesses in Red Series 36236, Shot Dakota. The solid line is a radiometer curve for Dakota for the region 7,000 to 9,000 Å.

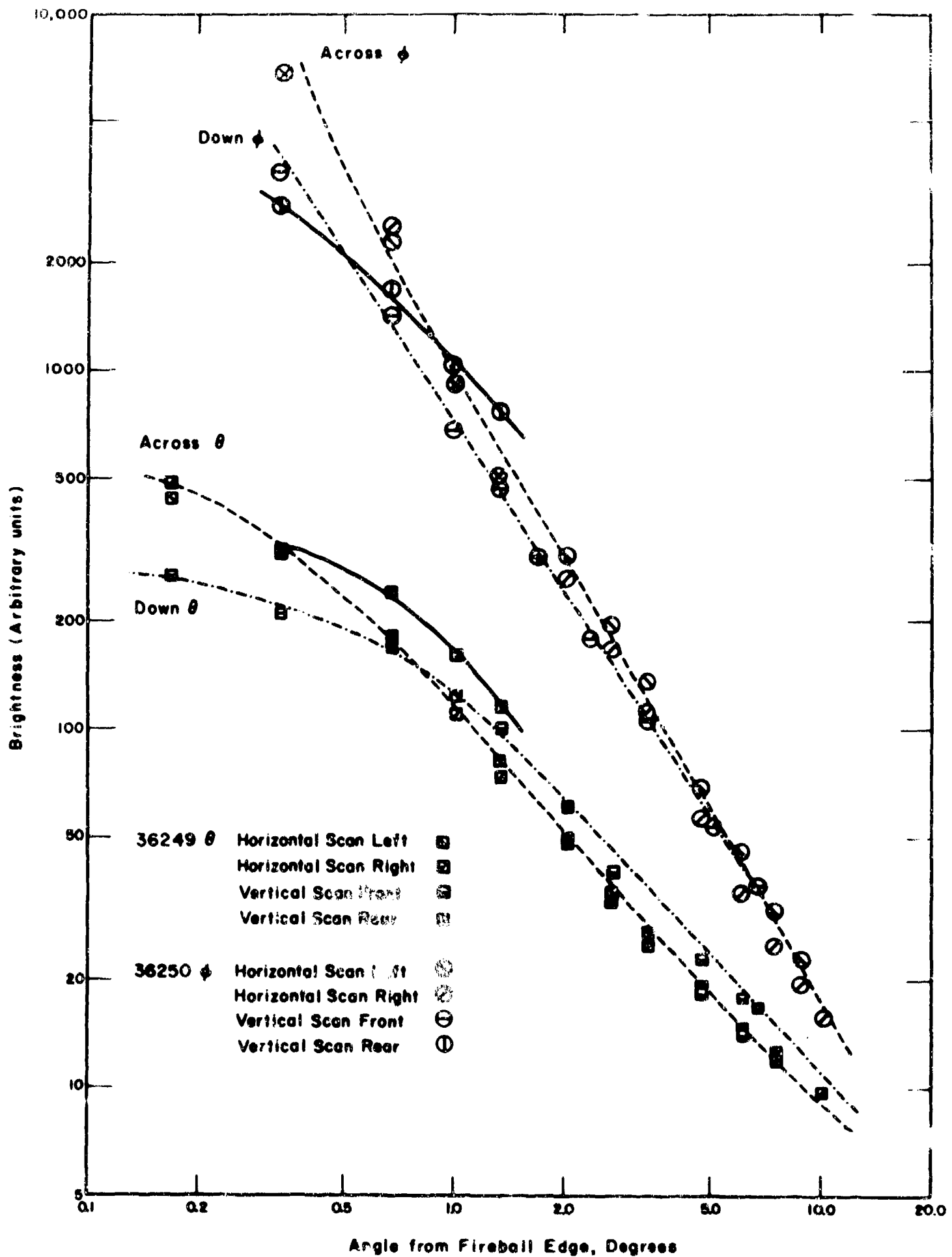


Figure 4.30 Aureole of Shot Dakota, Frame Zero, in two polarizations. See text for discussion.

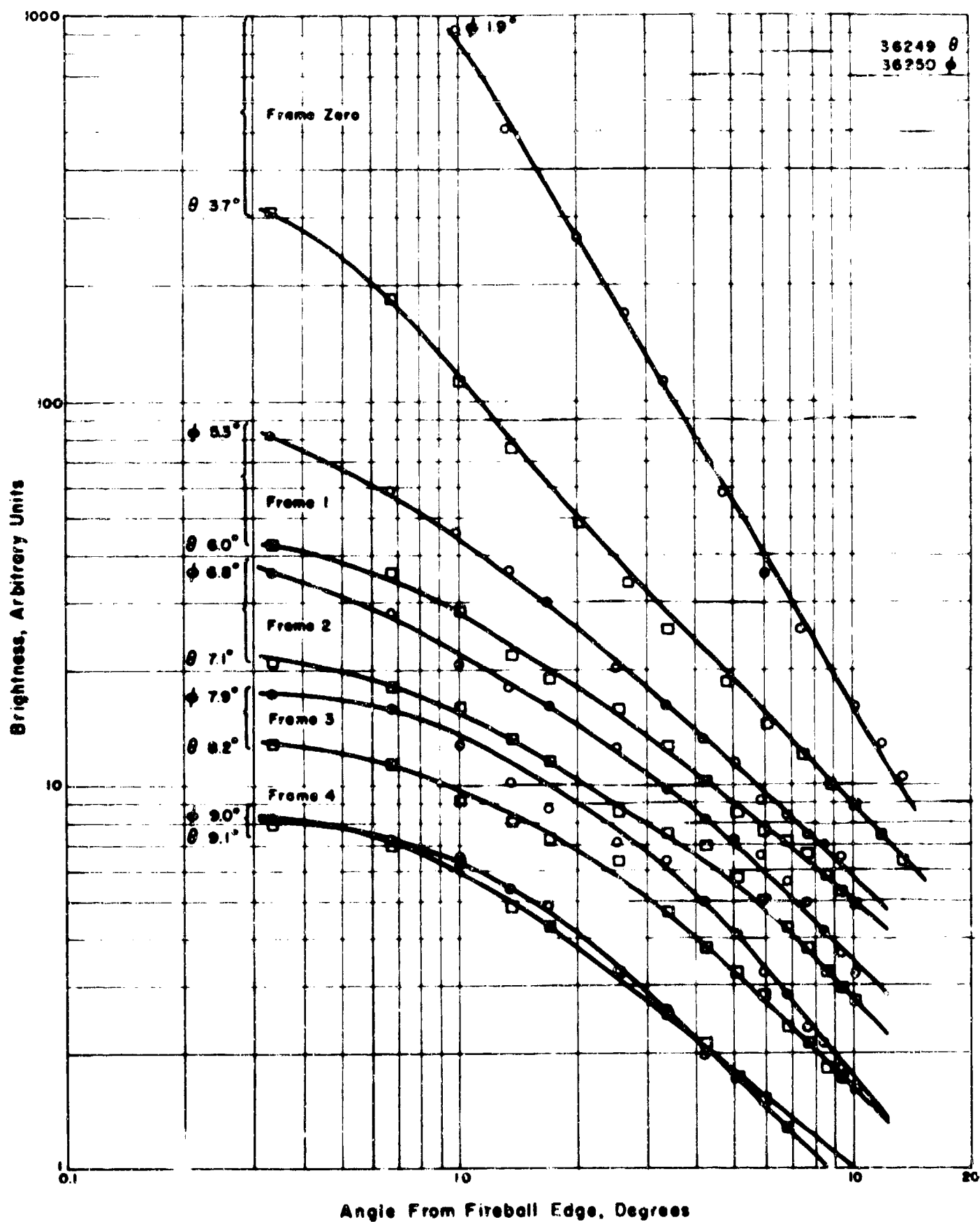


Figure 4.31 Aureole brightness on Frames 36249 (θ) and 36250 (ϕ), measured on a central scan to the right of the fireball, Shot Dakota. The (horizontal) angular extent of the fireball is shown to the left of each curve.

Brightness Figures for Dakota at $t_{\max II}$

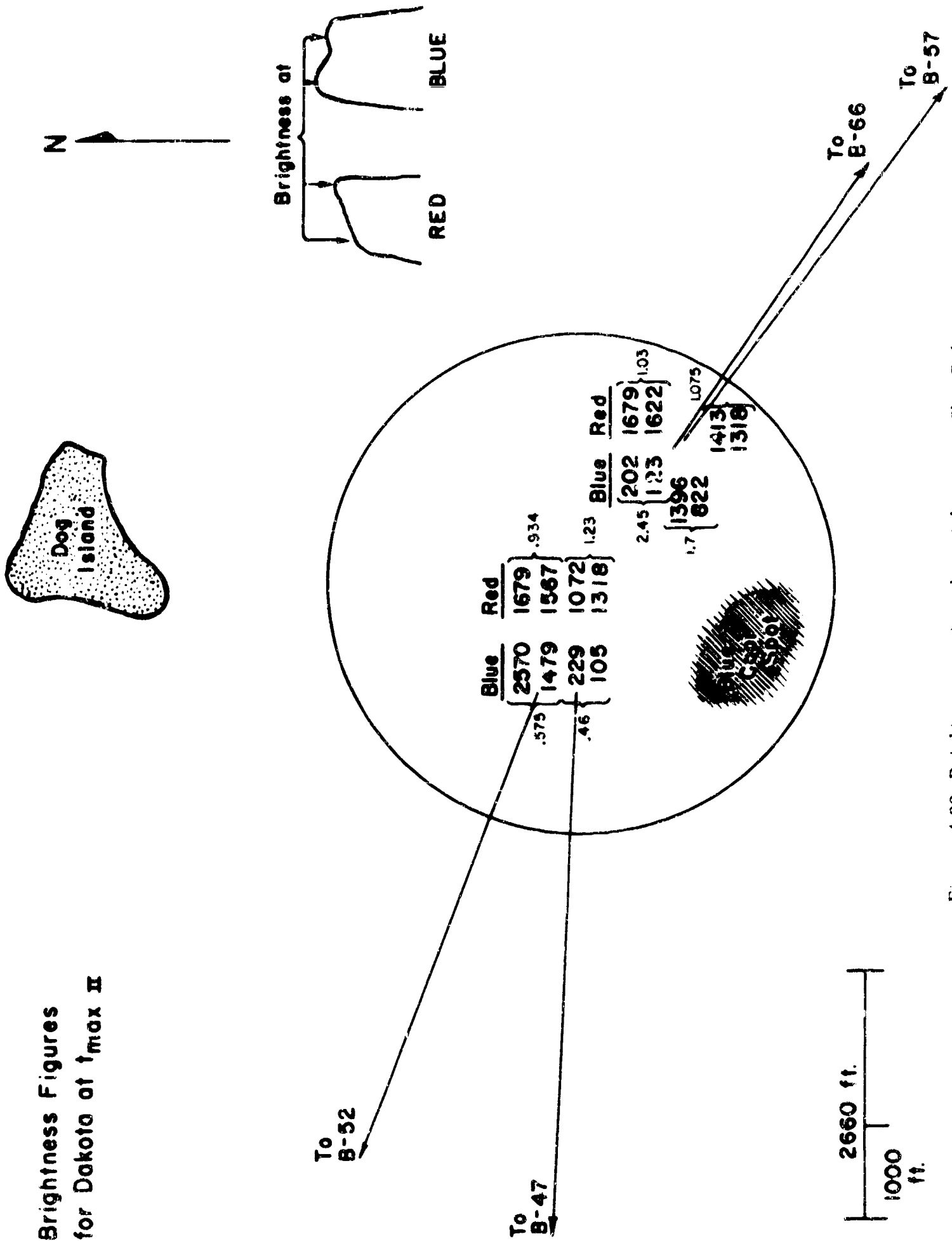


Figure 4.32 Brightness as viewed on eight scans, Shot Dakota.

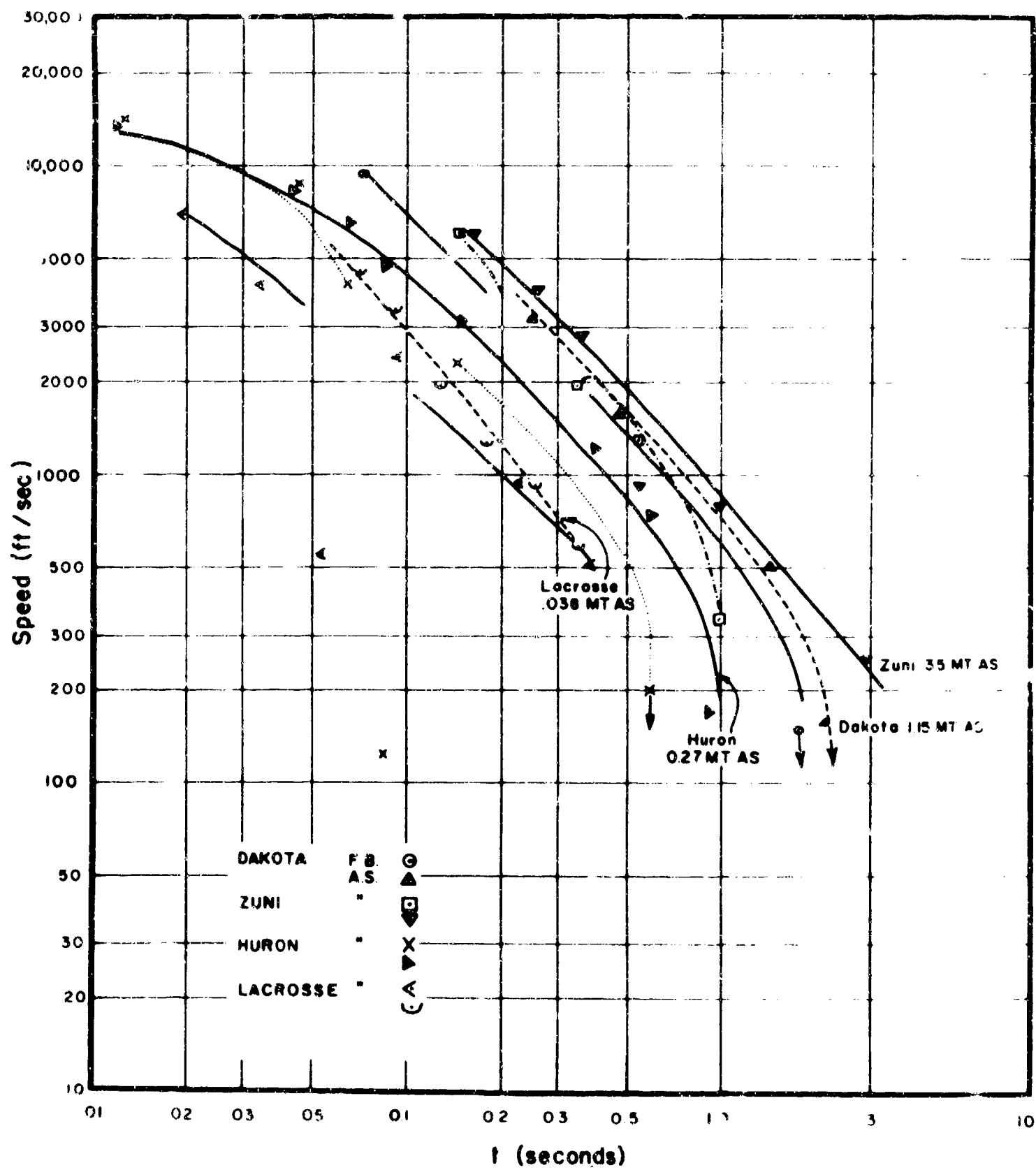


Figure 4.33 Speed of growth of fireball and shock froth radii.

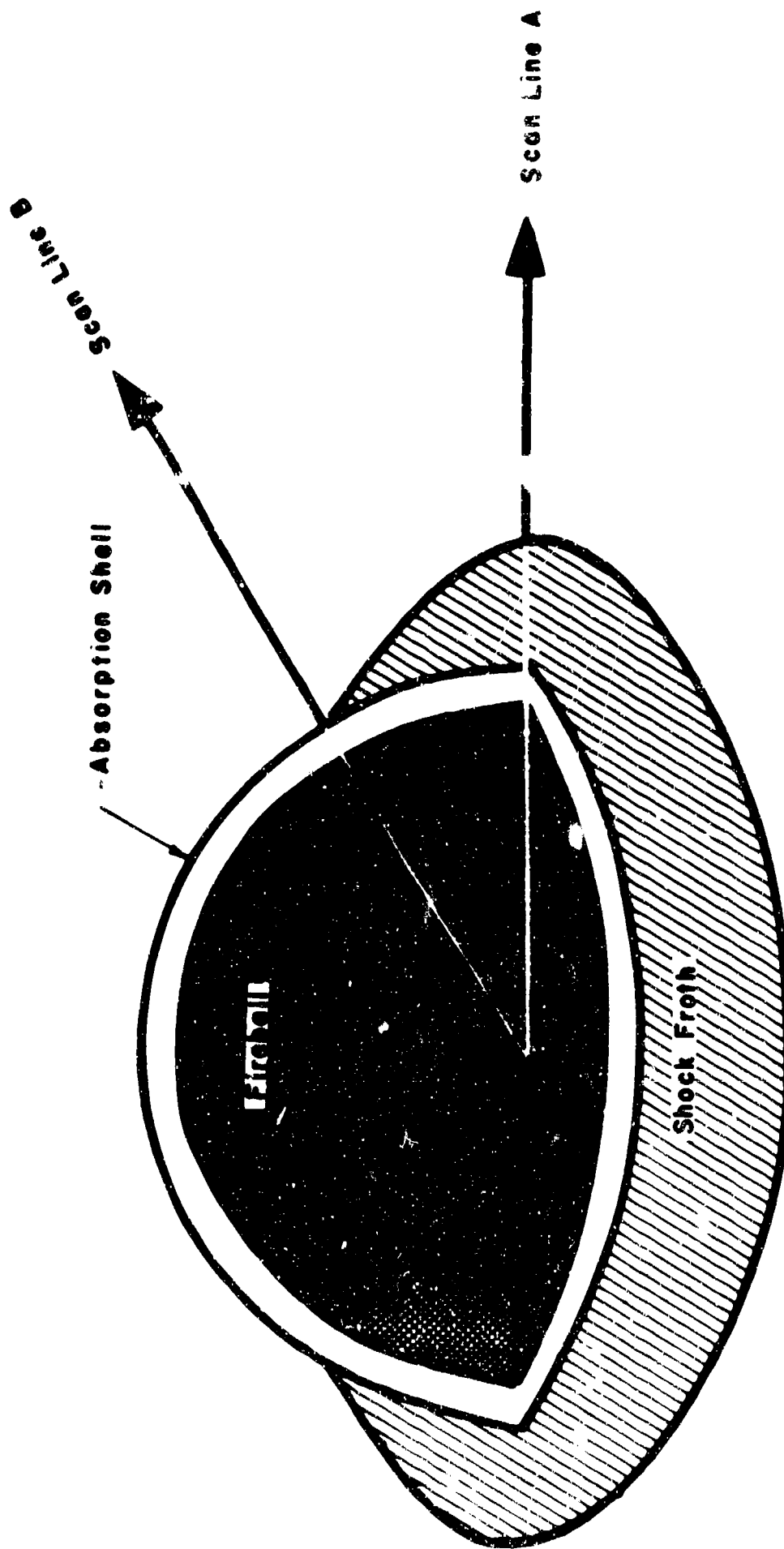
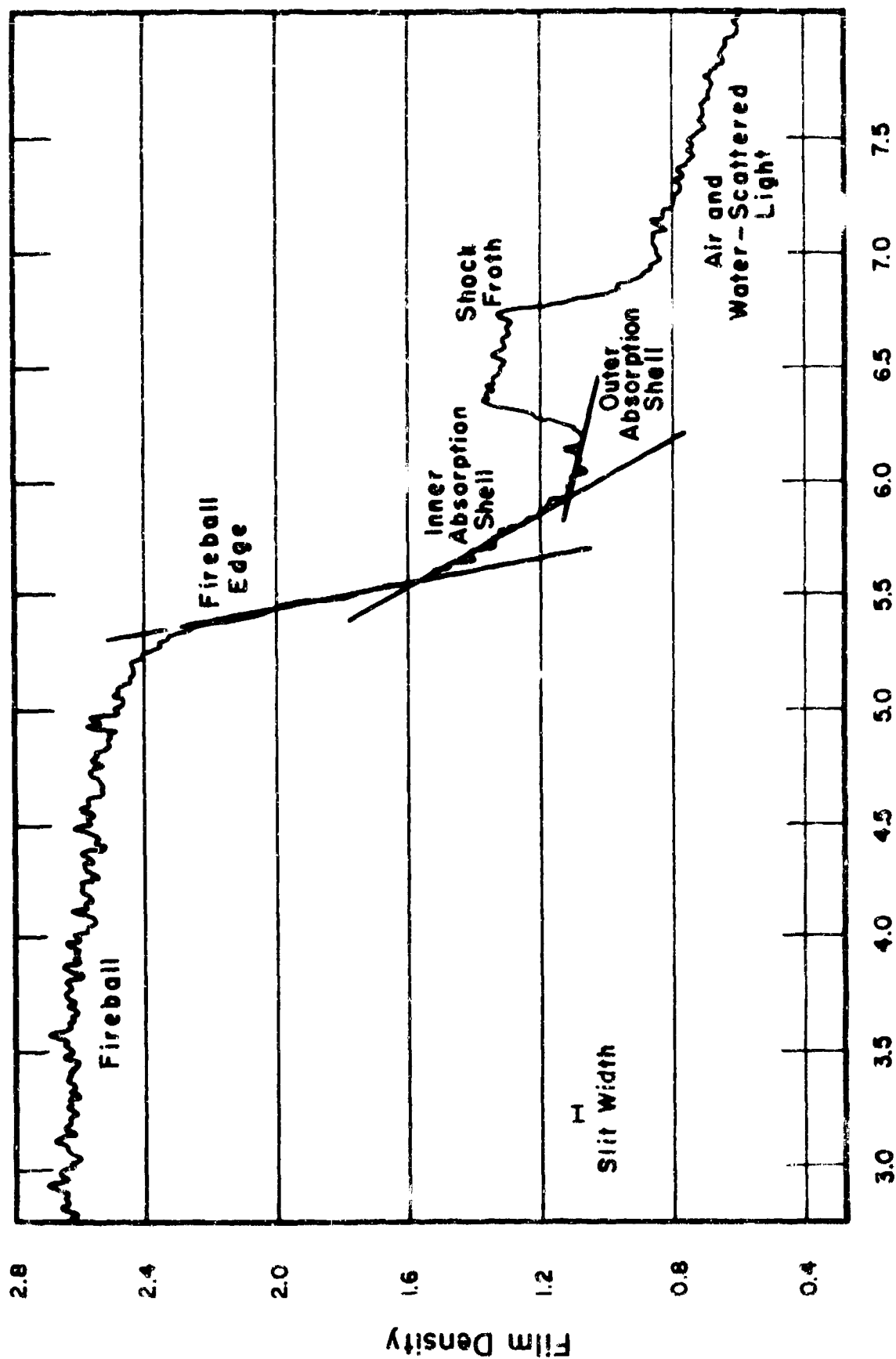


Figure 4.34 Location of scans for determining the attenuation of the absorption shell.



Horizontal Position on Film (Arbitrary Unit)

Figure 4.35 Scan Line A in Red Frame 83, Shot Zuni. The slit height is twice the slit width shown.

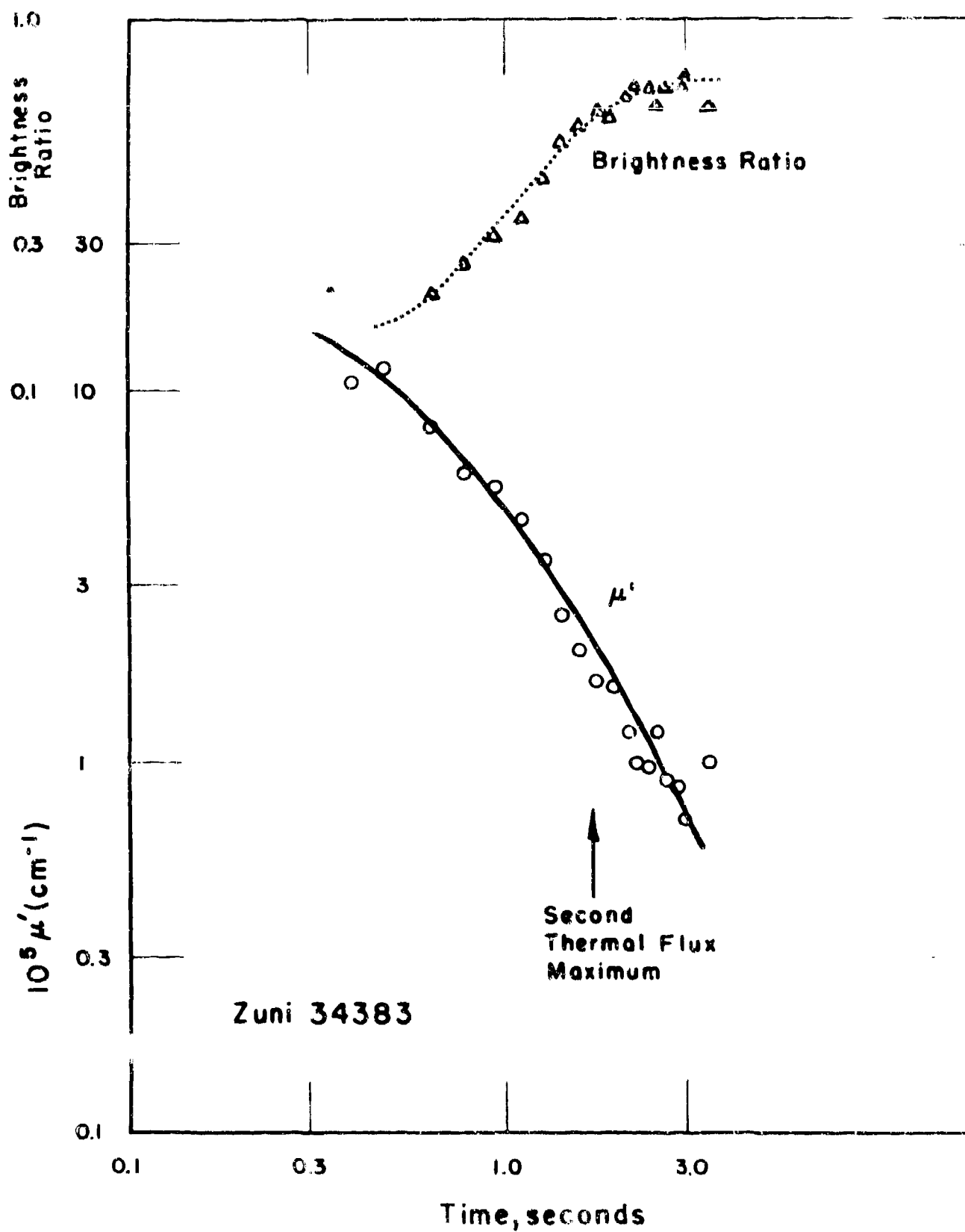


Figure 4.36 Red Brightness Ratio and μ' , Shot Zuni.

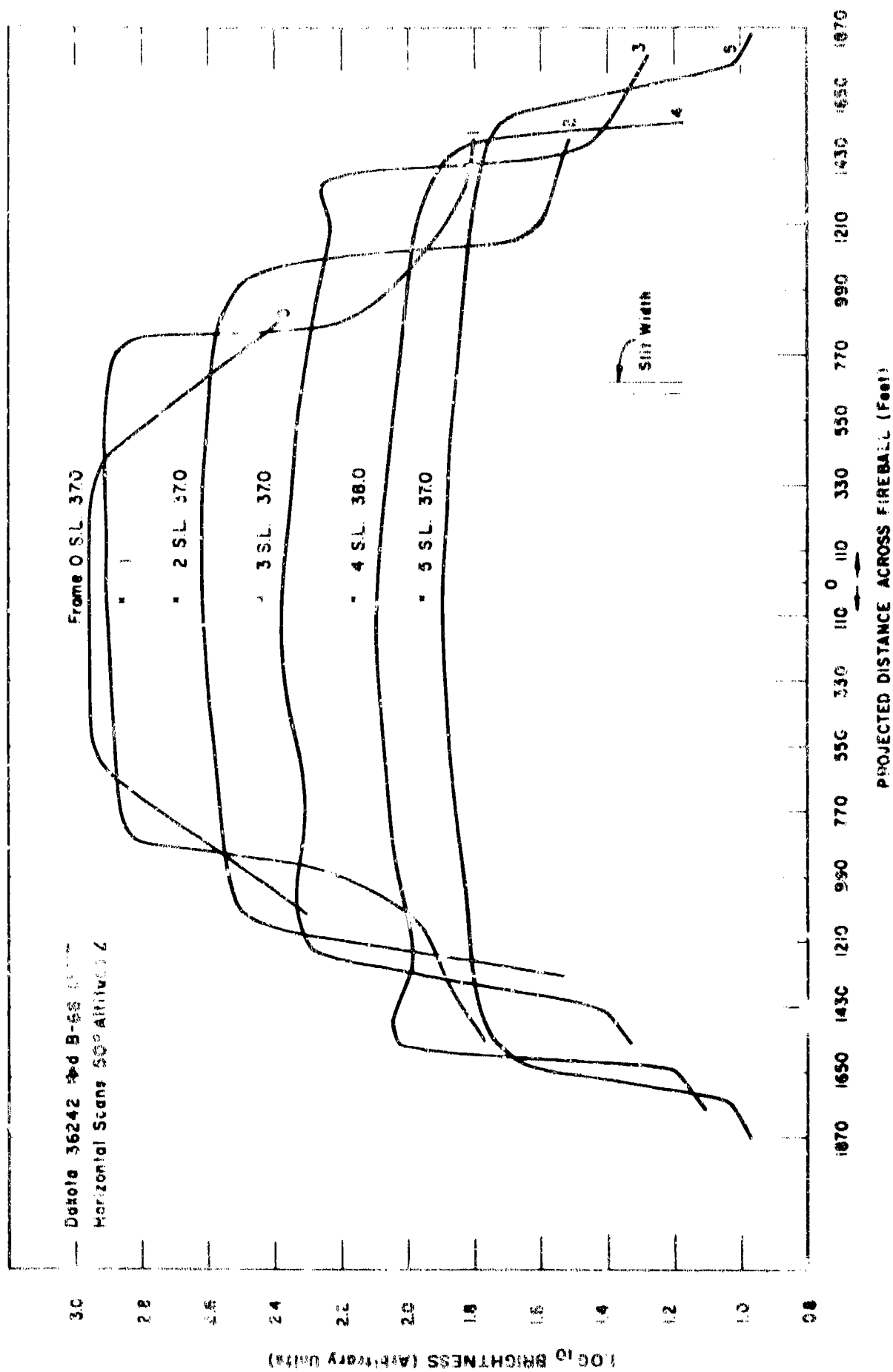


Figure 4.37 Red brightness profile of a central scan line, Shot Dakota. Frame Zero occurs at 4 msec past time zero. Note the increased bowing (limb darkening) in later scans

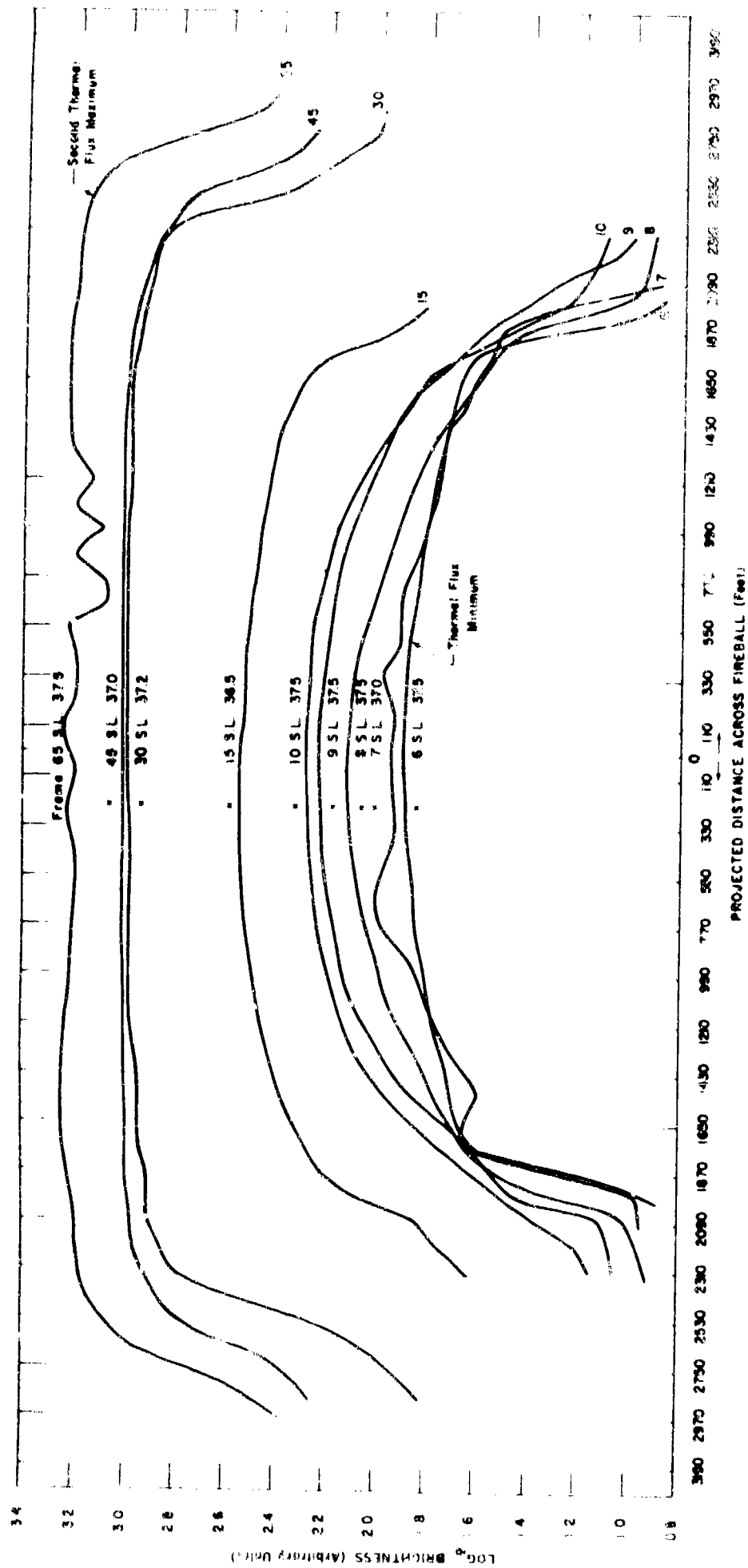


Figure 4.38 Red brightness profile of a central scan line, Shot Dakota (continued)
The limb darkening increases up to times past breakaway (Frame 8), then by
Frame 45 it has decreased until the fireball has a very flat contour.

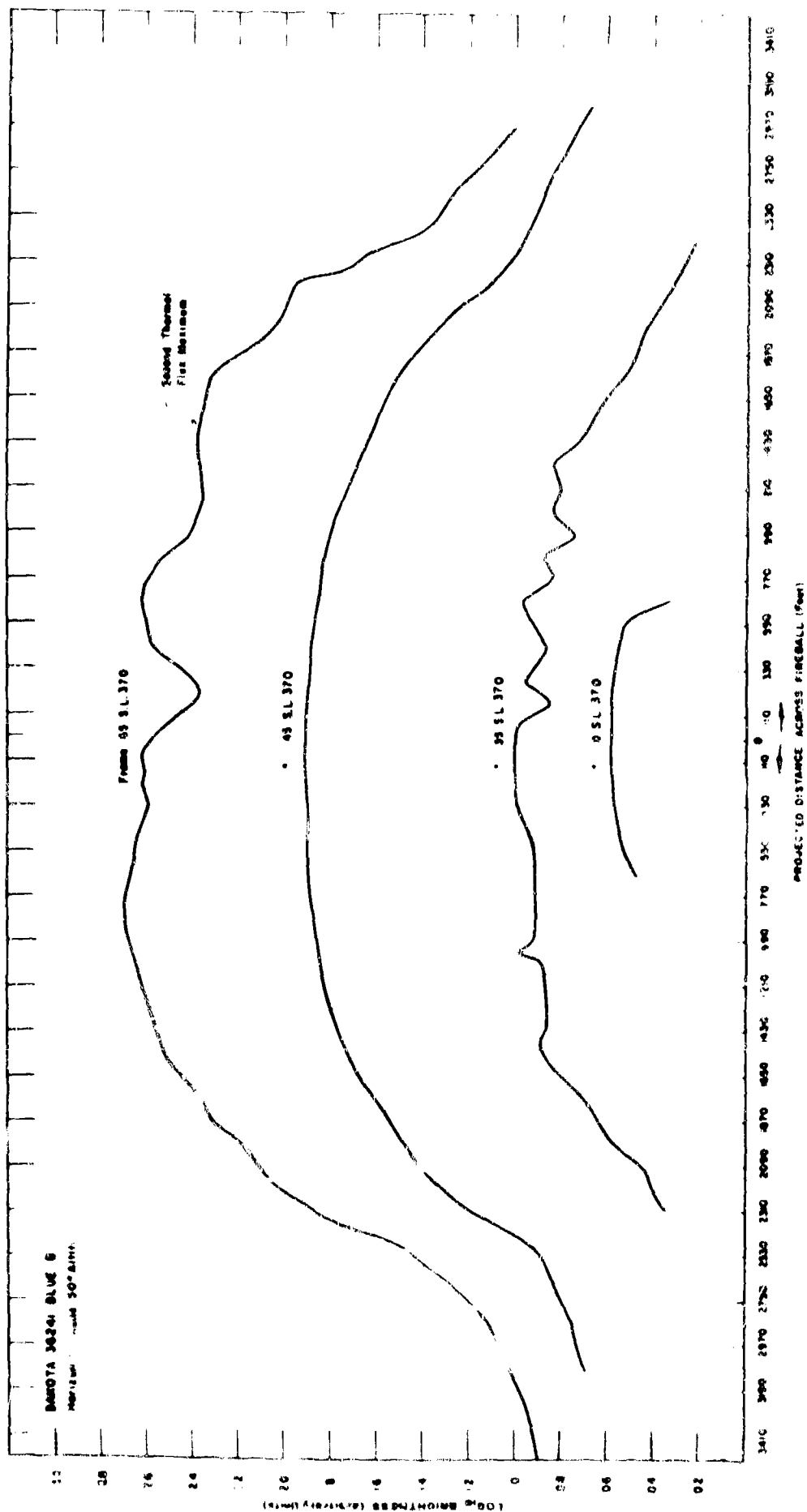


Figure 4.39 Blue brightness profile of a central scan line, Shot Dakota. Frame Zero occurs at 4 msec past time zero. Limb darkening is much more pronounced in the Blue.

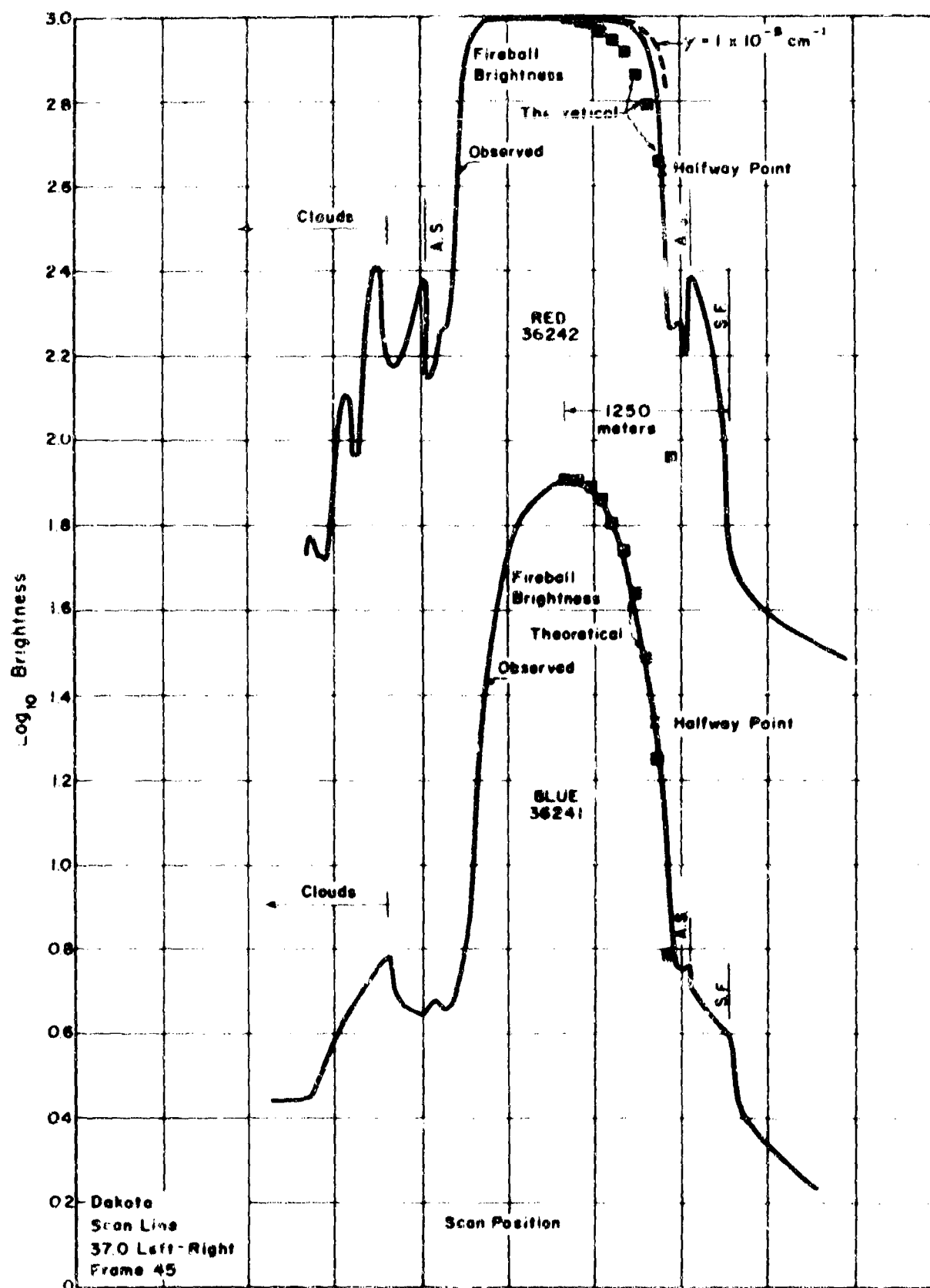


Figure 4.40 Observed and calculated limb darkening of fireball, Shot Dakota. For details, see text. A. S. and S. F. refer to the absorption shell and shock froth, respectively.

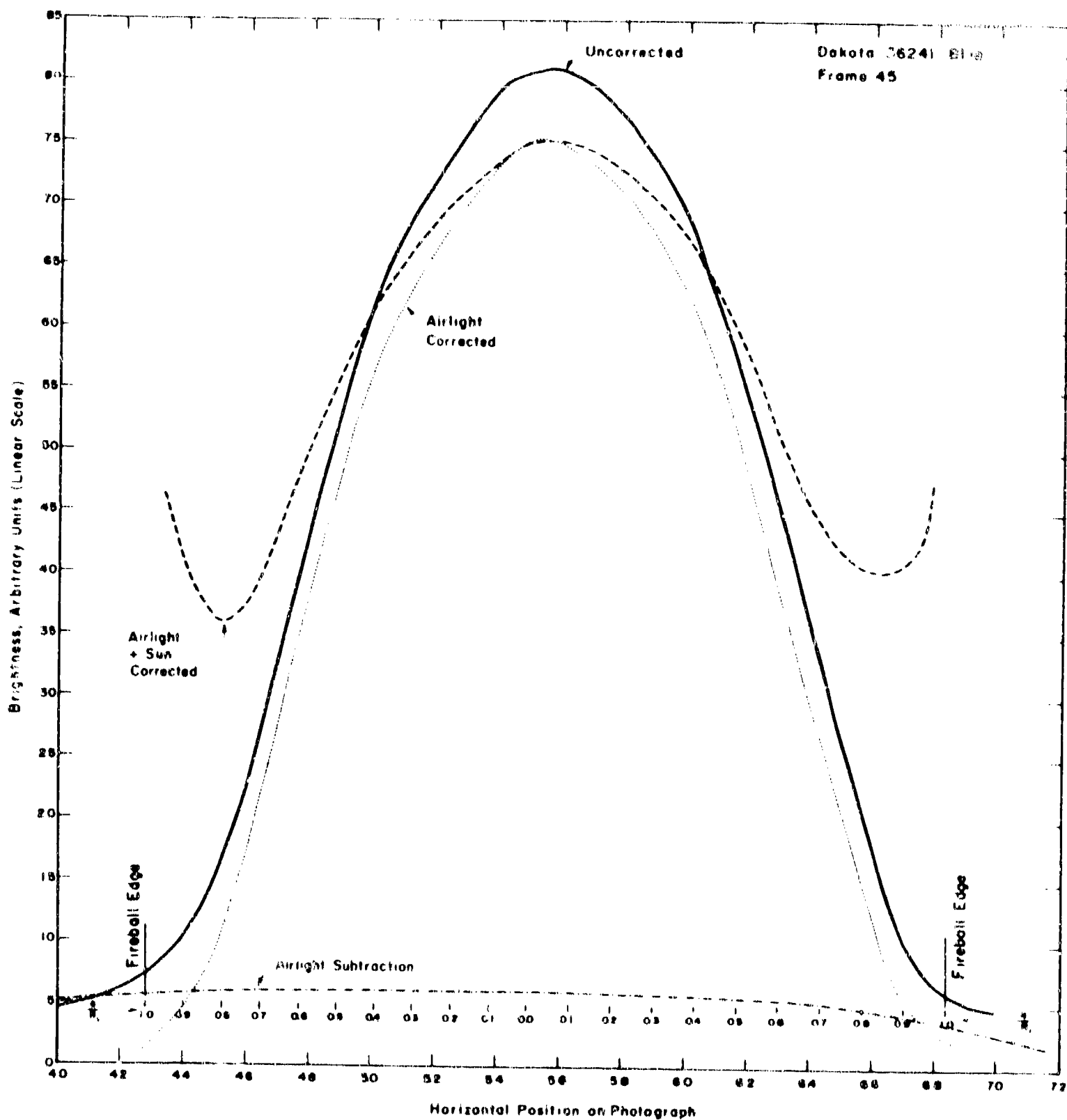


Figure 4.41 Blue fireball brightness contour, Shot Dakota. Contour corrected for air-scattered light and for intrinsic limb darkening, assuming that this darkening is the same as that of the sun (see text). This procedure results in an overcorrection.

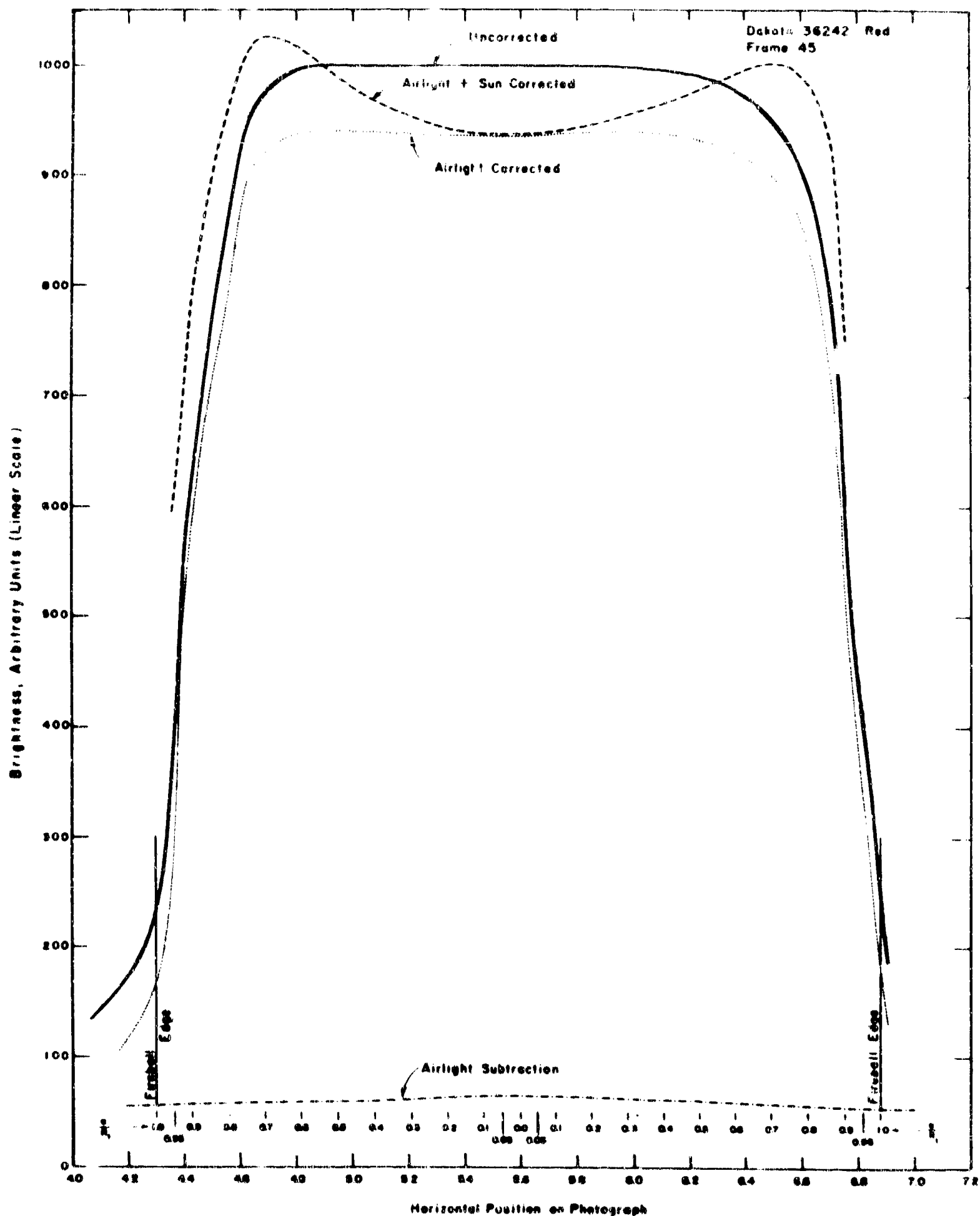


Figure 4.42 Red fireball brightness contour, Shot Dakota. Contour with the same corrections as in Figure 4.41. Again an overcorrection results (see text).

Chapter 5

CONCLUSIONS AND RECOMMENDATIONS

5.1 CONCLUSIONS

The large amount of data collected from aircraft indicates that the thermal yield can be predicted for the devices analyzed, i.e., for yields ranging from 15 kt to 4.6 Mt.

5.1.1 Thermal Exposure. Thermal measurements indicate that the formula evolved in Reference 1 in the analysis of the transfer of radiant energy from a nuclear device through the atmosphere may be unduly complicated when considered from the point of view of the present state of the art of the measurement of high thermal fluxes. As a comparison of Figure 4.3 with Figure 4.5 will show, it is possible to use a simpler empirical expression for predicting the thermal exposure encountered by aircraft in the Pacific area. In essence, the empirical formula,

$$Q = 1.45 (W/D^2) \cos^{1/2} \theta \cos \phi \quad (5.1)$$

is an approximate form of the more detailed formula of Reference 1 whose constant is a slowly varying function of the moisture content of the air, the albedo of the underlying surface, the scattering by haze, the height of the bomb burst, and the velocity of the aircraft where the measurement of Q , the thermal exposure, is made. In a particular climatic region and under the test configurations used, it appears that Equation 5.1 adequately predicts the test results. Additional requirements to equations of the form of Equation 5.1 will require more precise and consistent measurements of the thermal energy.

In Equation 5.1, the symbols are W , the weapon yield in kilotons; D , the slant range in kilometers; Q , the thermal exposure in cal/cm²; θ , the zenith angle indicated in Figure 3.1; and ϕ , the angle between the normal to the detector surface and the line joining this surface with the center of the fireball. For a detector pointing at the fireball $\phi = 0$ while for a horizontal detector $\phi = \theta$. The angle ϕ expresses the reduction in projected area of an arbitrarily oriented receiver when exposed to the direct thermal radiation of the fireball.

No evidence has been found in the analyzed thermal data that admits of including other factors such as weather or the albedo of the underlying surface to refine the prediction capabilities of Equation 5.1. The results exhibit too much fluctuation to support a more detailed predictive formula.

5.1.2 Backscattered Radiation. The measurements of backscattered radiation indicate that on the average the aircrew will suffer between $1/100$ and $1/1,000$ the radiant exposure from backscattered radiation as they would from being exposed to the direct thermal radiation. These measurements were made in the early morning when scattered clouds were reported. The evidence is that Equation 4.1 can be used to predict Q_{BS} if $\phi = 0$ and

$$10^{-2} Q > Q_{BS} > 10^{-3} Q$$

5.1.3 Thermal Exposure of Air Versus Ground Bursts. The evidence upon which the following conclusions are based is not extensive, being based on the airburst of Cherokee as compared with the barge shot Zuni and some additional information gained from Dakota.

It appears from a comparison of the Cherokee and Zuni data that devices of the same yield give about the same thermal exposure at a given point in the atmosphere, independent of the fact that one is an airburst and the other a surface burst. Unfortunately, as the measurements were restricted to zenith angles of $50 \pm 5^\circ$ and an albedo of the order of 0.6, these tests neither proved nor disproved the presence of a strong buildup factor for surface bursts backed by a surface whose albedo approaches unity.

Conflicting evidence exists for the radiation temperature of surface bursts versus airbursts. It appears from the infrared filter data (0.7 to 2.5-micron wavelength) that a $3,000^\circ \text{K}$ black body temperature used in Reference 1 for the surface burst and the $6,000^\circ \text{K}$ black body temperature used for the airburst predicts the division of energy in the infrared to suitable accuracy. However, this may be somewhat fortuitous because the theoretical predictions of Reference 1 are tested in this case with broad bandpass filters whose transmission characteristics are somewhat dependent on wavelength (Figure 2.15). An attempt was made to arrive at the color temperature of Dakota, a megaton-range surface burst, by correcting for all known absorptions in the wavelength interval over which radiation was received. From this analysis, it appears that a surface burst may reach a temperature as high as $5,000$ to $6,000^\circ \text{K}$.

5.1.4 Spectral Distribution of Thermal Radiation. Analysis of the measurements of the radiant exposure for several broad regions of the visible and near-infrared spectrum of Shon Dakota leads to the following conclusion. The spectral distribution of energy in a megaton-range surface burst is not inconsistent with that to be expected from a black body radiator at $5,000$ to $6,000^\circ \text{K}$, whose thermal irradiance is modified by water vapor and carbon dioxide absorption in the atmosphere. Effectively, little radiation is transmitted through long paths in Pacific air for wavelengths in excess of 1 micron, except in a few narrow bands particularly between 2.0 and 2.5 microns.

5.1.5 General Conclusions. The radiometers and calorimeters form a consistent set of thermal radiation receivers. By this it is meant that the integrated radiometer data gives the same value of radiant exposure as that measured by the calorimeter to within the limits of variability of the two types of instruments. As an alternate method of comparison, the differentiated calorimeter data agrees with the irradiance measured directly by the radiometers. This second method of comparison is not as satisfactory as the first from a technical standpoint because of the large amount of smoothing involved. If future tests are made that require filters to be used on the thermal detectors, the detectors should be radiometers instead of calorimeters. The filters used during Operation Redwing were broadband types. Information concerning the energy received in narrower bands, such as might be derived by subtracting the energy transmitted through two filters with overlapping transmission bands, requires that radiometer data be used if the source is changing in temperature. The radiometer data is then integrated over the time to give the thermal exposure. When filters are used on calorimeters, the equivalent of the above procedure should be done. It is for this reason that radiometers are to be preferred over calorimeters when filters are used.

The scaling laws in respect to time to maximum irradiance and the shape of the power curve seem to be in accord with those presented in Reference 1.

There is no detectable difference in the time at which maximum irradiance is reached for the various regions of the visible and infrared regions of the electromagnetic spectrum as selected by the various filters. The experiments were not designed to optimize these measurements, and these conclusions are drawn from derived rather than primary data. However, it seems justified to say that to within ± 10 percent of the time required for the unfiltered energy to reach maximum irradiance, no difference is noticed among the filtered irradiance curves in respect to t_{max} . In the case of the largest thermonuclear events, the 10 percent uncertainty in time is only of the order of $1/10$ second. These curves can be normalized in such a way that they show that the irradiance at longer wavelengths falls off less rapidly than the irradiance in

the visible. This point will not be labored here because there is relatively little transmitted energy at these long wavelengths. Furthermore, the data from which this conclusion is drawn contains large random errors.

5.2 RECOMMENDATIONS

5.2.1 Calorimetric and Radiometric Measurements. Analysis of the data used as a basis of this report shows that the usefulness of the data was limited primarily by the calibration procedure. It would not be overstating the case to suggest that little additional information is to be gained by amassing more data of a similar nature. On the other hand, if calibration techniques and schedules for field checking can be developed so that the calibration constants of each instrument for each event are known—including detectors, filters, and atmosphere as well—it may be that more meaningful prediction equations can be developed from new data. This would be especially true after instrumentation has been subjected to extreme thermal exposures.

It further appears that more information can be obtained through the use of radiometers as the basic measuring instrument instead of calorimeters. This recommendation is made with the realization that Table 2.4 indicates that, at the present stage of development, the calorimeters are apparently more stable than the radiometers. However, from the overall system point of view, there does not appear to be any significant difference between radiometers and calorimeters. Rate data such as given by the radiometers is of greater theoretical interest than integrated data given by the calorimeters. When necessary, the rate data can be summed to give radiant exposure.

Future instrumentation engineering should include methods to eliminate the problem of detector or filter exposure to adverse environment conditions during takeoff and low-altitude flight where moisture, dust, oil, fuel, and other foreign matter apparently obscure the viewing port.

A final comment is made with full realization that other overriding considerations, such as the safety of personnel, may preclude the suggestion from being seriously considered. It is suggested that more attention be given to maximizing the information content of these experiments through positioning of the aircraft and detectors. During Operation Redwing, it appears that too often aircraft were too closely bunched in range and elevation angle even though they were flying at different azimuths. All indications are that the range and elevation angle are the most sensitive parameters for the prediction of the radiant exposure, excluding of course the all-important device yield. If more detailed information is to be gained on the modifications introduced by surface and cloud albedos, and the atmosphere in general, a better experimental configuration is necessary.

5.2.2 Further Analysis of Photographic Data. In the necessarily limited effort of preparation of this report, it has been possible to consider only those topics which, a priori, appeared to have the most interest. The photographic coverage, while far from complete (and in fact, for some of the devices, quite scanty), still contains at least as much analyzable information about thermal effects as has been presented. Furthermore, the photographs contain valuable data on the physics of the growth of the detonation. Suggestions for further reduction of the data are given herein. In addition, there are presented suggestions for the improvement of the collection and analysis of future photographs of the type described in this report. Particularly, it should be noted that the thermal effects of nuclear devices could more easily be evaluated if the details of the particular test detonations (special shielding, experimental devices, and the like) were released.

Significant improvement in the microdensitometric analysis would result if the slit width and height could be reduced to about a third their present size. Further reduction would be of little help because of the granularity of the emulsions.

In general, the variation of the various thermal and physical phenomena with device yield has not been treated. Only generalized discussions of the aureole, thermal flux partition, hotspots,

plume, and absorption shell have been presented. (An exception is the Wilson cloud, for which the time of inception as a function of yield is given in Chapter 4.) It would be desirable to generate scaling laws for these effects.

In the following discussion the various phenomena are divided into those that have nonnegligible effect on the thermal flux and those that are of interest from a device-physics viewpoint only. In passing, it should be mentioned that future data analysis should be more strongly correlated with existing theoretical and experimental information, than was possible in the preparation of this report.

Thermally important phenomena, besides being of interest in the physics of the detonation, contribute measurably to the thermal flux. The plume appears to develop earlier for small surface-detonated devices. A hydrodynamical study of its development, as viewed from several observation angles, would be of interest.

There exists sufficient data to delineate further the intensity and angular distribution of the aureole as a function of fireball extent and surface brightness, in frames before breakaway. There is also data on these aureole properties as a function of angle of observation. However, such data exists only for Red and Polaroid photographs.

Asymmetry may be of considerable importance in that it may make the thermal flux azimuth-angle dependent. It would be desirable to scan all detonations to check on this effect, which appears to be definitely established for Dakota (Chapter 4).

In general, it is quite difficult and time-consuming to prepare isophot contours of the photographic frames, and in light of the inaccuracies involved, further efforts in this direction are not especially recommended. However, a consistent program of brightness comparisons would give important information on the albedos of islands and shock froth and especially of clouds. The contribution of the light scattered from clouds is, as has been indicated, a particularly ephemeral problem. The angular dependence of the shock froth albedo is as yet not understood; there is evidence that the direct albedo is smaller for low-angle observers (Section 3.2.6).

Further work should be done on the hydrodynamics of the absorption shell and on the limb darkening histories of the several fireballs. In particular, the scaling of surface contours is of interest. Another program of some importance is the correlation of absorption shell properties with the temperature, density, and pressure profiles of Reference 29. It is not recommended that further light-absorption measurements be made, as the best examples of this effect have already been analyzed and even these give indifferent results.

Physical effects have a direct perturbing effect on the thermal flux of less than 3 percent. Measurement of the time history of the position and brightness of the horizontal dark belt running across the fireball may aid in explaining this phenomenon.

The kinematics of hot spots (bright and dark areas in Red, Blue, and Polaroid) could be derived from the photographs. Speeds, number, space distribution, sizes, and brightness histories may be compared among the several detonations. The hot spots may aid in determining how far into the fireball the camera sees in early frames.

The Blue fireball shows considerable surface structure, appearing lumpy or puffy. This probably has a nontrivial effect on the Blue flux. Although it would be difficult to gather meaningful quantitative data on so diffuse a phenomenon as this, some study of it is indicated.

Although the Red-Blue intercomparison is made difficult by the sensitization and sensitivity differences of the receptors, the Polaroid pairs suffer from no such drawback. No gross differences between the two polarizations appeared in the analysis of the Dakota pair (Chapter 4), which were made with cameras having erratic shutters. However, the information content of these photographs is by no means exhausted, and a more thorough analysis of this pair and of the Apache pair is definitely indicated.

It should be mentioned that the problem has not been approached from a viewpoint of atmospheric transmission. In a qualitative sense no strong atmospheric attenuation differences among Red, Blue, and Polaroid are resolved. Nevertheless, it might be advantageous to review the results presented here, and any future results, from a standpoint of atmospheric scattering and attenuation.

5.2.3 Future Data. Analysis of the Redwing data has shown that great improvement could be made with small changes in receptors and sensitometry. More fundamental changes, involving serious overhaul of the apparatus without guarantee of commensurate improvement in the data, have also come to mind; these would include camera redesign to synchronize the Frames Zero and to lower flare light.

It was found in auxiliary experiments that the shape of the H and D curves varied with the filter used in the sensitometer. Consequently, there should be some inaccuracies in the H and D curves because the sensitizing lamp does not match the spectrum of the detonation. It should be a relatively straightforward matter to expose auxiliary strips of film through a step tablet and correct filters, to the detonation itself. Such a procedure has been used in the experiments of Reference 27. Enough exposures for the determination of the proper development procedure for $\gamma = 1$ can readily be made with the same camera.

Furthermore, standardized processing and further calibrating procedures should be developed to enable absolute brightness measurements to be made. With known absolute brightnesses and intercomparable cameras, atmospheric transmissions can be measured. Furthermore, observations from various angles will give information on the departure from Lambert scattering of various surfaces.

The surface of the detonation is sufficiently bright to allow narrower, sharper optical filters to be used. The spectral response of each filter should be routinely checked in the laboratory, before and after the test series.

The exposures in the Redwing series were generally too low; in no case was film saturation observed, but in one or two cases (notably Dakota Red 36236) there was a lens flare and a halo around each frame, presumably due to flare scattering. In particular, the Blue exposures were too low to show the albedo properly, especially near breakaway. Even an increase of a factor 100 in some Blue series should be considered, in spite of the burnout and increase in flare light that this may engender near second thermal flux maximum. Such exposures would provide data on the Blue aureole, on the attenuation of the Blue shocked air, and on the details of the Blue fireball near thermal flux minimum.

The films used are quite satisfactory, and the positions of the centers of the Red, Blue, and Polaroid passbands are well chosen. More Polaroid photographs should be taken, especially with telephoto lenses, for a closer examination of the absorption shell, hot spots, and other features. The shutter-opening fluctuations of the GSAP cameras must be corrected. A study of the falloff of apparent brightness of off-axial points would be useful. Every reasonable effort should be made to reduce spurious flare-light effects.

Although synchronized cameras opening at, say, 1 msec after time zero would be desirable, no critical questions have arisen that cannot be answered with present unsynchronized systems. Synchronized systems are of more importance in cameras with higher framing speeds running up to time of breakaway.

It appears that during Operation Redwing no consistent attempt was made to position the aircraft at uniform observation angles. There are no phenomena particular to any individual devices that are best viewed from a preferred angle; an improved device intercomparison would result if standard angles were chosen.

One viewing angle should be about 20° from the horizontal, to permit further measurements of the attenuation of the absorption shell (such as those described in Section 4.6.3). Ideally, islands and clouds should be behind the absorption shell and air shock, to act as viewing screens.

It has been noted that the data failed to give information on the scattering and attenuation of the atmosphere as separate from the proper thermal effects of the device. As mentioned earlier, absolute intercomparison among film series would throw light on this problem. However, for good results it is necessary that the aircraft be at ranges with extremes differing by at least a factor of 3. During Operation Redwing, the ranges rarely differed by more than a factor of 1.5.

Finally, there is the suggestion that the GSAP cameras photograph an artificial light source of known brightness at surface zero, at say, 1 second before time zero. However, practical

difficulties arise in designing a source so extended as to subtend an angle large compared to the film and lens resolution. The source must also be on for a time long enough to insure that the GSAP shutter will be open at least once (~ 15 msec). There is considerable effort involved in setting up any source at surface ~ 10 , but if this were done it would justify the relatively small further effort of using auxiliary defocused still cameras (or other photometric apparatus) for measuring the transmission and scattering of the atmosphere.

REFERENCES

1. R. M. Chapman and M. H. Seavey; "Report on the Attenuation of Thermal Radiation from Atomic or Thermonuclear Weapons"; AFRCRC-TN-54-25, November 1954; Air Force Cambridge Research Center, L. G. Hanscom Field, Massachusetts; Secret Restricted Data.
2. "Capabilities of Atomic Weapons"; Department of the Army Technical Manual TM 23-200, Department of the Navy OPNAV Instruction 03400.1B, Department of the Air Force AFL 136-1, Marine Corps Publications NAVMC 1104 Rev; Revised Edition, 1 June 1956; Prepared by Armed Forces Special Weapons Project, Washington, D. C.; Secret Restricted Data.
3. F. A. Guerrero and A. Grossman; "Operation Redding Handbook for Calculating Thermal Energy"; ARA-253; Allied Research Associates, Inc., Boston, Massachusetts.
4. "Handbook; Operation and Service Instructions, Gun Camera Type N-9"; Technical Order AN 10-10CB-25, 1 February 1954; Department of the Air Force and Department of the Navy.
5. "Illustrated Parts Breakdown, Gun Camera, Type N-9"; Technical Order AN 10-10CB-27, 20 May 1954; Department of the Air Force and Department of the Navy.
6. A. Broido and A. B. Willoughby; J. O. S. A., 48, 344-350; (1958).
7. "Corning Glass Filters"; 1946; Corning Glass Works, Corning, New York; Unclassified.
8. C. E. K. Mees; "The Theory of the Photographic Process"; 1954; The Macmillan Book Co., New York, N. Y.; Unclassified.
9. J. N. Howard, D. L. Burch, and D. Williams; "Near-Infrared Transmission Through Synthetic Atmospheres"; Geophysics Research Paper, No. 40, November 1955; Air Force Cambridge Research Center, L. G. Hanscom Field, Massachusetts; Unclassified.
10. F. E. Fowle; "The Transparency of Aqueous Vapor"; Astrophys. J., 42, 394-411 (1915); Unclassified.
11. H. H. Holmes and F. Daniels; "The Photolysis of Nitrogen Oxides: N_2O_5 , N_2O_4 and NO_2 "; J. Am. Chem. Soc., 56, 630-637 (1934); Unclassified.
12. J. K. Dixon; "The Absorption Coefficient of Nitrogen Dioxide in the Visible Spectrum"; J. Chem. Phys., 9, 157-160 (1940); Unclassified.
13. T. C. Hall, Jr. and F. E. Blacet; "Separation of the Absorption Spectra of NO_2 and N_2O_4 in the Range 2400-5000 Å"; J. Chem. Phys., 20, 1745-1749 (1952); Unclassified.
14. L. Harris and G. W. King; "The Infrared Absorption Spectra of Nitrogen Dioxide and Tetraoxide"; J. Chem. Phys., 2, 51-57 (1934); Unclassified.
15. R. E. Nightingale et al; "The Preparation and Infrared Spectra of the Oxides of Nitrogen"; J. Phys. Chem., 58, 1047-1050 (1954); Unclassified.
16. L. Dunkelmann; "Horizontal Attenuation of Ultraviolet and Visible Light by the Lower Atmosphere"; NRL Report 4031; Naval Research Laboratory, Washington, D. C.; Unclassified.
17. T. Elder and J. Strong; "Infrared Transmission of Infrared Windows"; Franklin Institute Journal, 255, 189 (1953); Unclassified.
18. H. Behndorf; "Tables of the Refractive Index for Standard Air and the Rayleigh Scattering Coefficient for the Spectral Region between 0.2 and 20.0 Microns and Their Application to

Atmospheric Optics"; J. Opt. Soc. Am. 47, 176, 1957.

19. D. Deirmendjian and Z. Sekera; "Global Radiation Resulting from Multiple Scattering in a Rayleigh Atmosphere"; TN-55-664, April 1954; Air Force Cambridge Research Center, L.G. Hanscom Field, Massachusetts.

20. R. Stair and R. G. Johnston; "Preliminary Measurements of the Solar Constant"; J. Res. of Nat. Bur. Standards, Vol. 57, No. 4, October 1956.

21. F. S. Johnson; "The Solar Constant"; J. Met. 11 (6), 431-439, December 1954.

22. F. A. Guerrero and A. Grossman; "Operation Redwing Handbook for Calculating Thermal Energy"; ARA-253; Allied Research Associates, Inc., Boston, Massachusetts; Secret.

23. J. A. Curcio et al; "Operation Upshot-Knothole-Part II. Low Resolution Spectroscopy"; NRL 4573 RD 543, September 1955; Naval Research Laboratory, Washington, D. C.; Secret.

24. R. Hillendahl; private communication, U.S. Naval Radiological Defense Laboratories, San Francisco, California.

25. E. L. Krinov; "Spectral Reflectance Properties of Natural Formations"; Technical Translation TT 439, 1953; National Research Council of Canada, Ottawa, Canada; Unclassified.

26. H. C. VandeHulst; "Scattering in the Atmospheres of the Earth and the Planets", in "The Atmospheres of the Earth and Planets", Kuiper, G. P., ed; University of Chicago Press, Chicago, Illinois; 1949 (Supp. 49-112); Unclassified.

27. R. Eldridge; Unpublished data; Technical Operations, Inc., Burlington, Massachusetts; Unclassified.

28. N. Haskell; internal report; Air Force Cambridge Research Center, L.G. Hanscom Field, Massachusetts; Secret.

29. H. L. Brode and R. E. Meyerott; "Thermal Radiation from Atomic Detonations at Times Near Breakaway"; RM-1851, August 1956; The RAND Corporation, Santa Monica, California; Secret Restricted Data.

30. S. Fritz; "Solar Radiation and Its Modification by the Earth and Its Atmosphere"; in "Compendium of Meteorology"; American Meteorological Society; 1951; p. 27; Boston, Massachusetts; Unclassified.

31. A. Angstrom; "On the Albedo of Various Surfaces of Ground"; Geographical Ann., 7, 323-342 (1925); Stockholm, Sweden; Unclassified.

32. "Summary Report of the Commander, Task Unit 3, Military Effects Programs 1-9"; Operation Redwing, ITR 1344, November 1956; Office of the Deputy Chief of Staff, Weapons Effects Tests, Field Command, AFSWP, Sandia Base, Albuquerque, New Mexico; Secret Restricted Data.

33. H. K. Sen; private communication; Air Force Cambridge Research Center, L.G. Hanscom Field, Massachusetts; Confidential.

34. R. Hillendahl; private communication; U. S. Naval Radiological Defense Laboratories, San Francisco, California; Confidential.

35. J. F. Moulton, Jr., and B. T. Simonds; "Blast Measurements, Part II Free-air Peak Pressure Measurements, Section 1"; Scientific Directors Report of Atomic Weapon Tests at Eniwetok, 1951, Annex 1.6, July 1951; Naval Ordnance Laboratory, White Oak, Maryland.

36. G. P. Kuiper, ed.; The Sun (Solar System I); 1953; p. 89; University of Chicago Press, Chicago, Illinois; Unclassified.

37. R. Walker; private communication; Air Force Cambridge Research Center, I. G. Hanscom Field, Massachusetts; Secret.
38. G. H. Dieke; private communication; The Johns Hopkins University, Baltimore, Maryland.
39. H. L. Brode; "Nuclear Blast Wave Calculations Including Thermal Losses"; RM-2076, December 1957; The RAND Corporation, Santa Monica, California; Secret.
40. Hugh E. DeWitt; "A Compilation of Spectroscopic Observations of Air Around Atomic Bomb Explosions"; LAMS-1935, June 1955; Los Alamos Scientific Laboratory, Los Alamos, New Mexico; Secret Restricted Data.
41. F. R. Gilmore; "Equilibrium Composition and Thermodynamic Properties of Air to 24,000° K"; RM-1543, August 1955; The RAND Corporation, Santa Monica, California.
42. N. Davidson; "Rates of Selected Reactions Involving Nitrogen and Oxygen"; AVCO Res. Rep. 32, June, 1958.
43. F. Daniels; Chem. and Engin. News 33, 2370, 1955.

APPENDIX
PHOTOGRAPHS

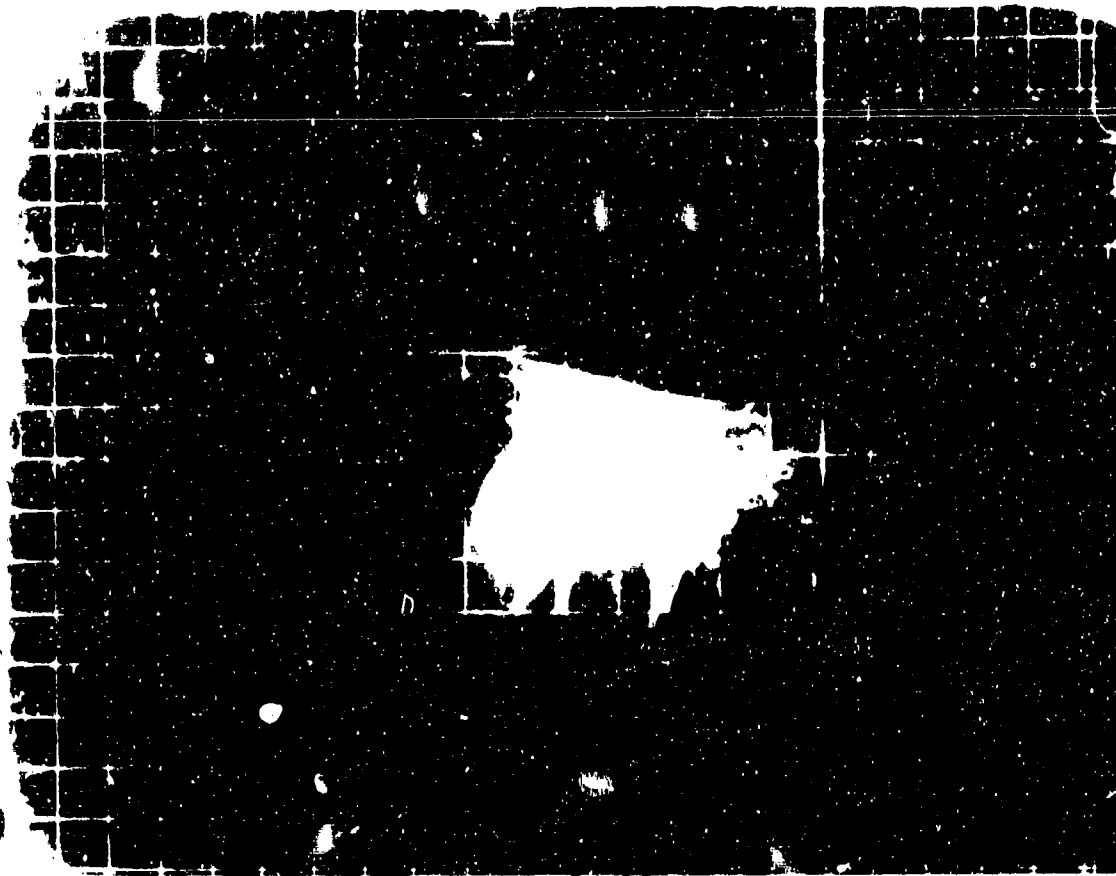


Figure A.1 Shot Erie, Series 34565, Frame Zero, Red, 25 mm, B-57.

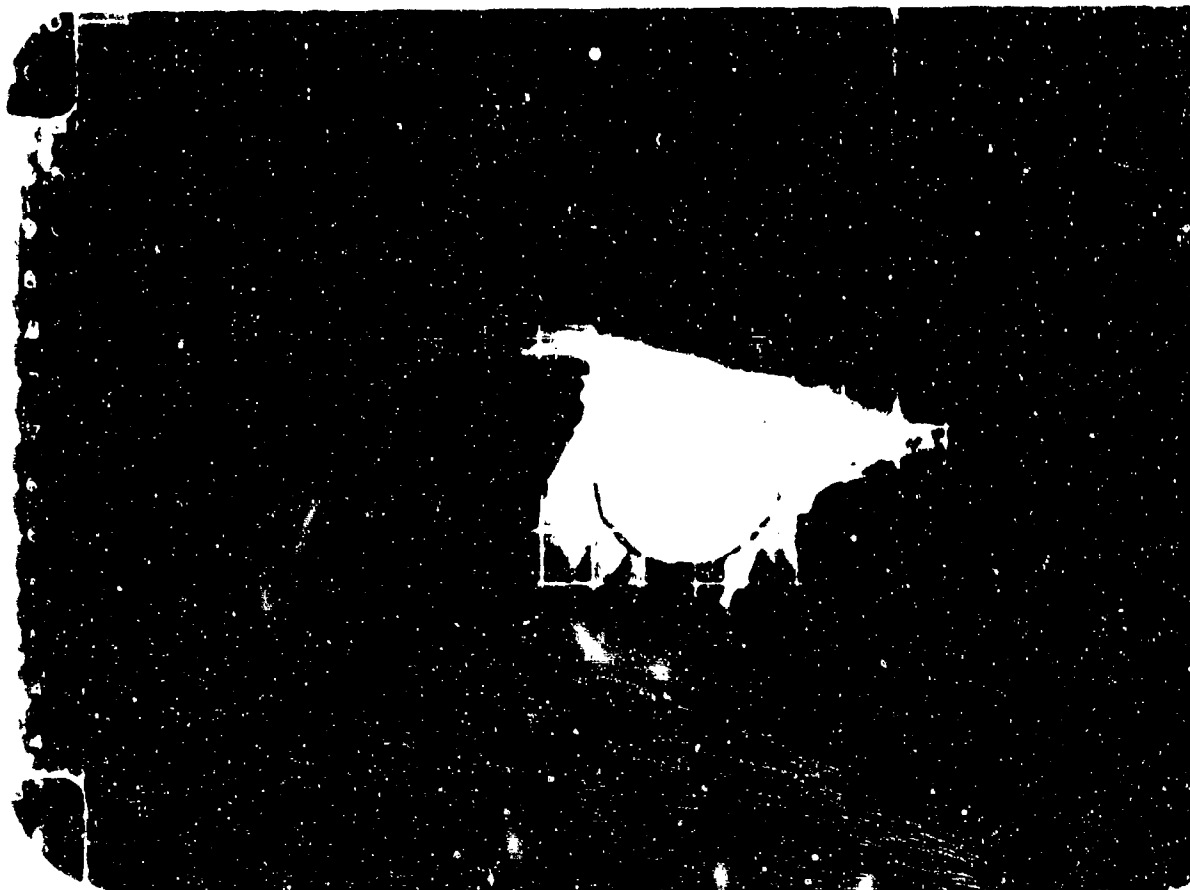


Figure A.2 Shot Erie, Series 34565, Frame 1, Red, 25 mm, B-57.

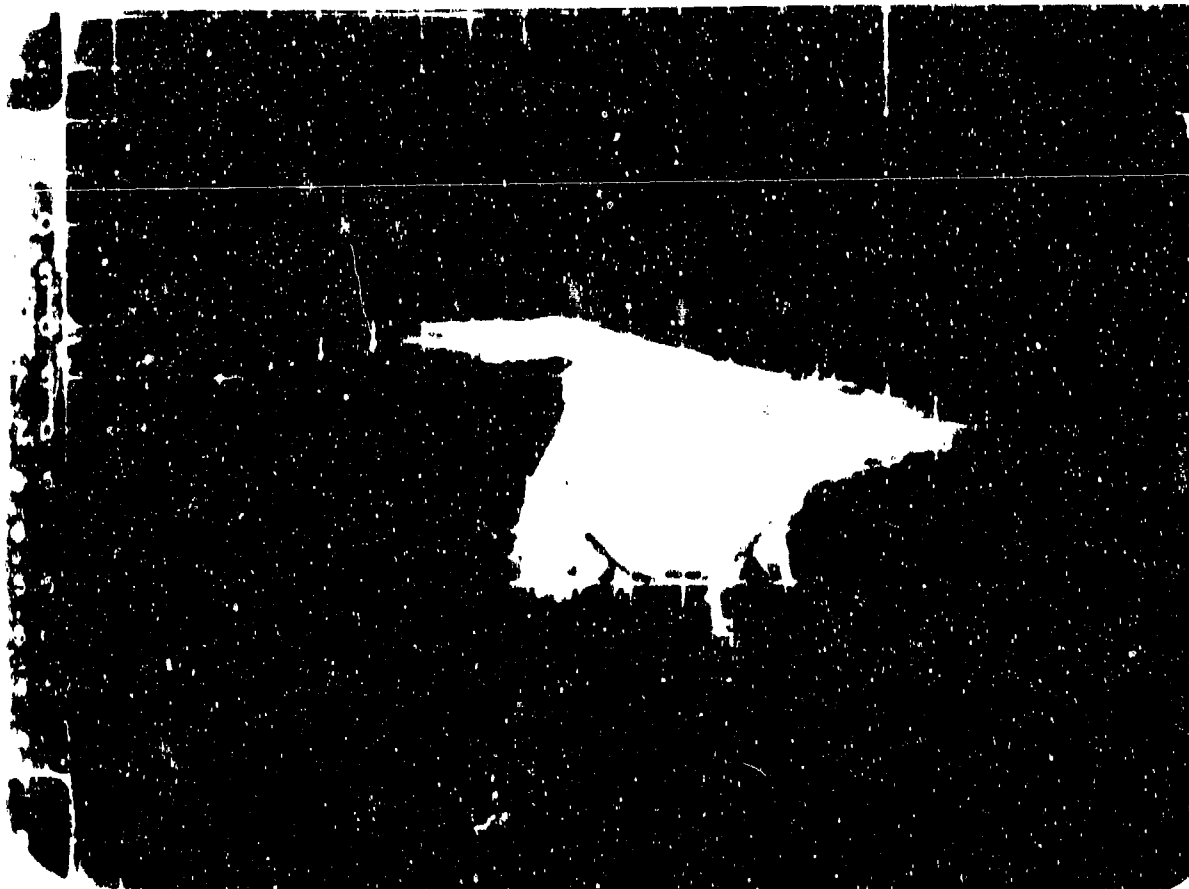


Figure A.3 Shot Erie, Series 34565, Frame 2, Red, 25 mm, B-57.

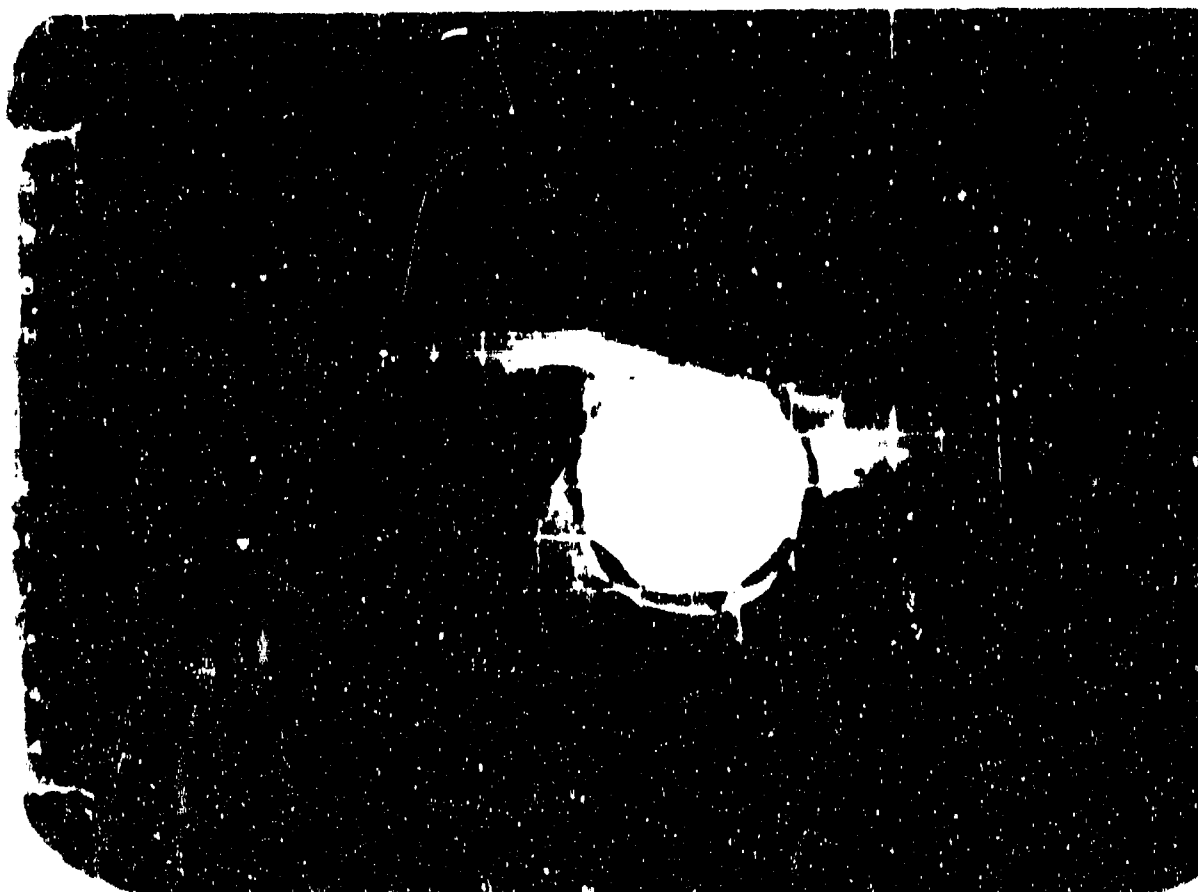


Figure A.4 Shot Erie, Series 34565, Frame 3, Red, 25 mm, B-57.

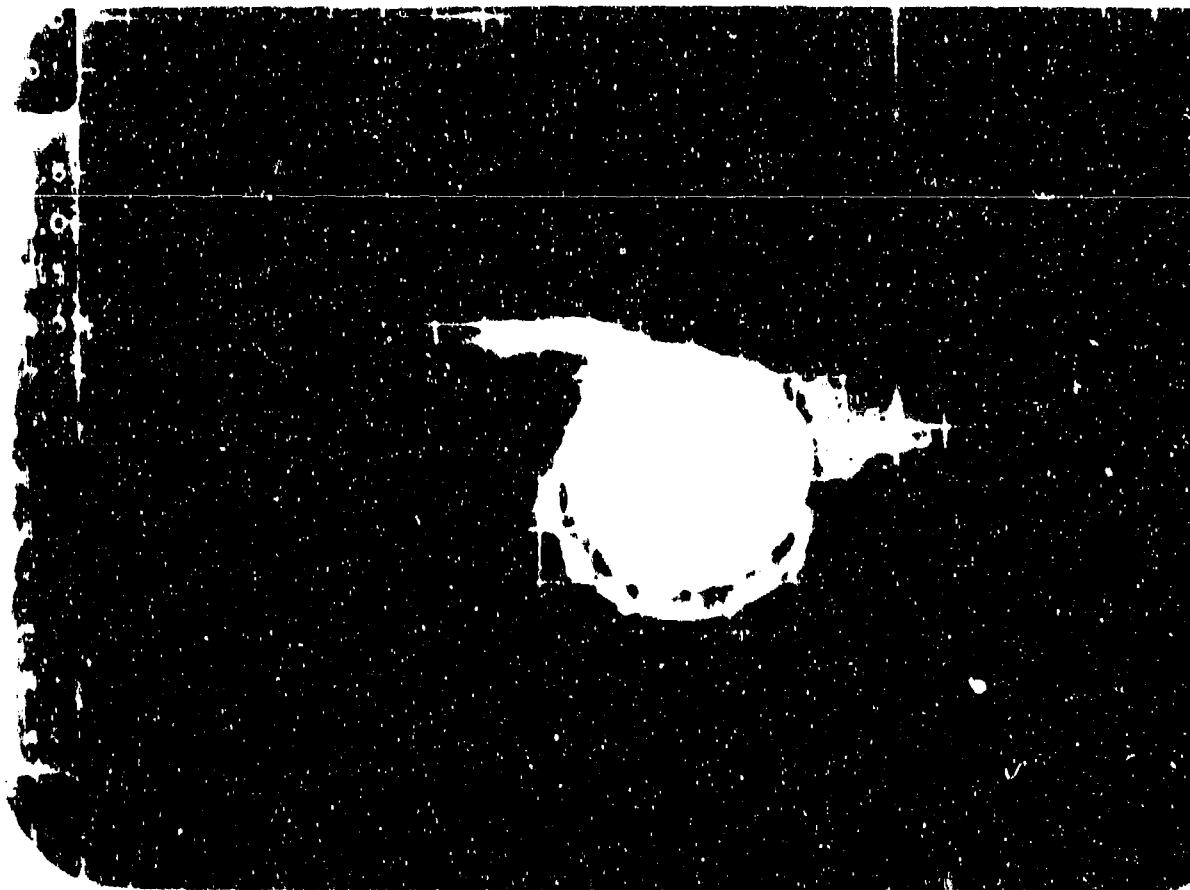


Figure A.5 Shot Erie, Series 34565, Frame 4, Red, 25 mm, B-57.

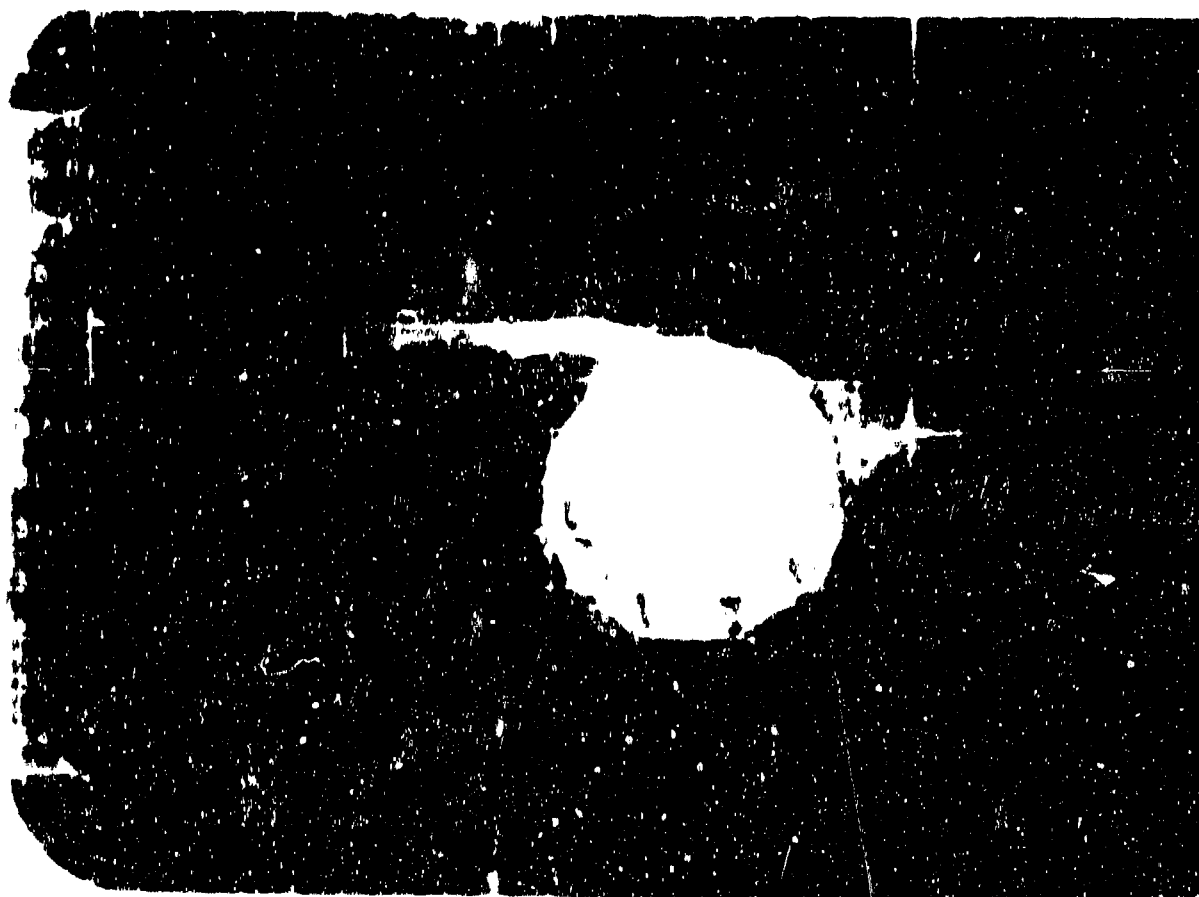


Figure A.6 Shot Erie, Series 34565, Frame 5, Red, 25 mm, B-57.

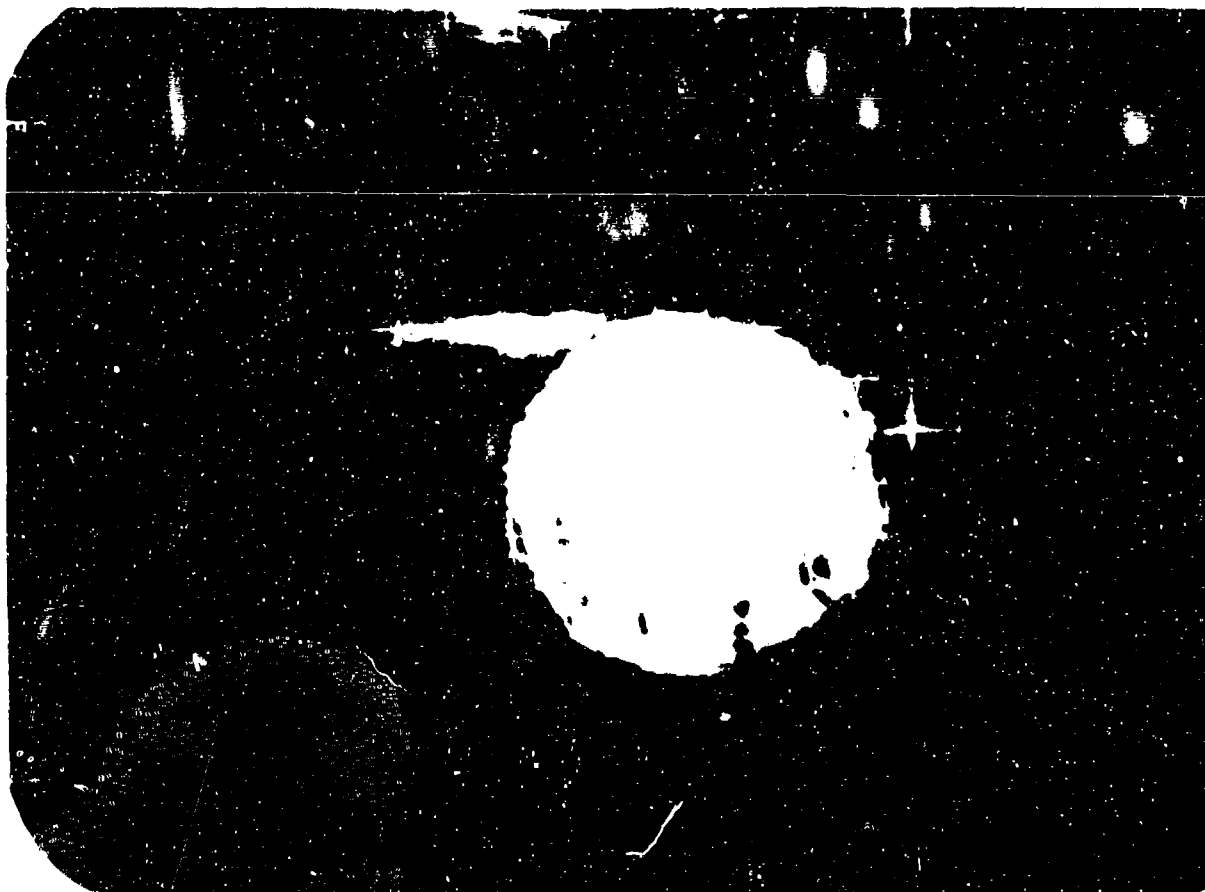


Figure A.7 Shot Erie, Series 34565, Frame 8. Red. 25 mm. B-57.

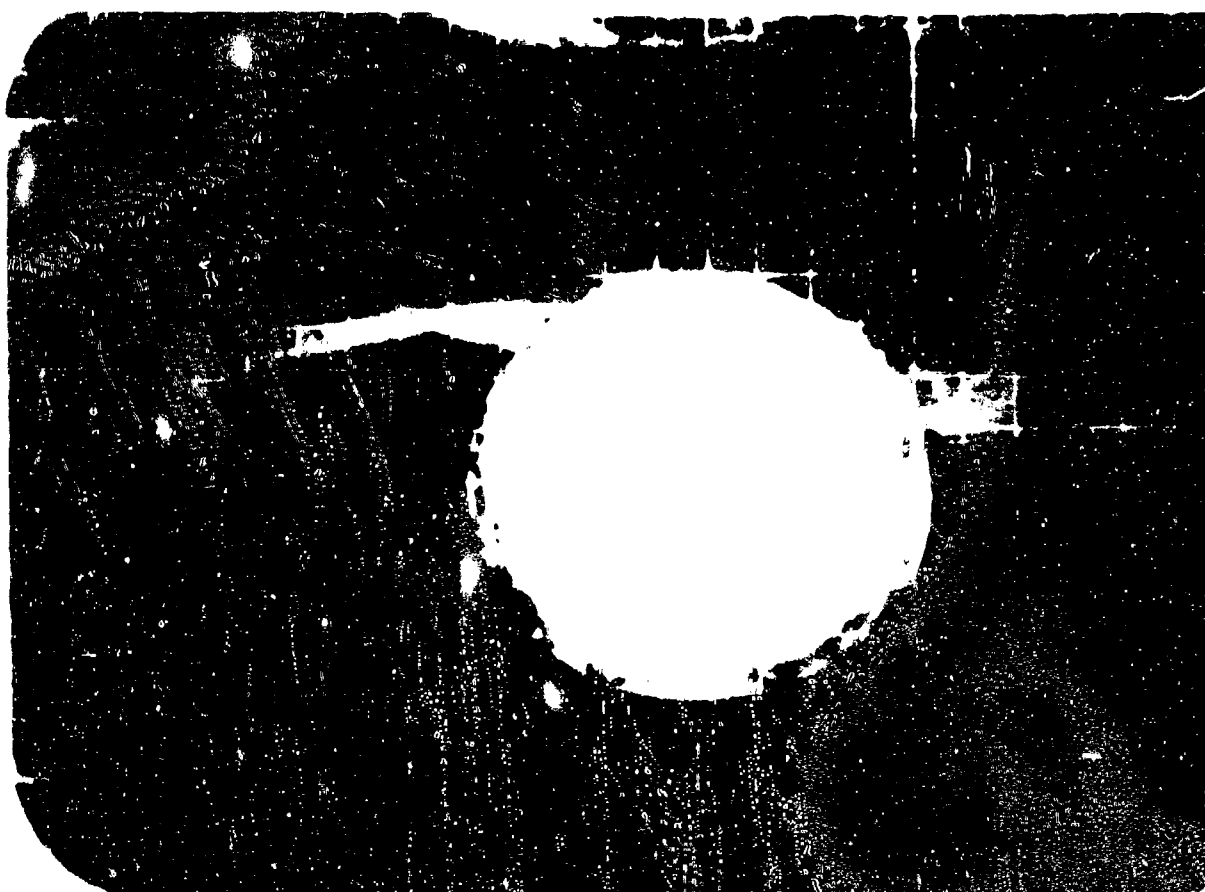


Figure A.8 Shot Erie, Series 34565, Frame 11. Red, 25 mm, B-57.

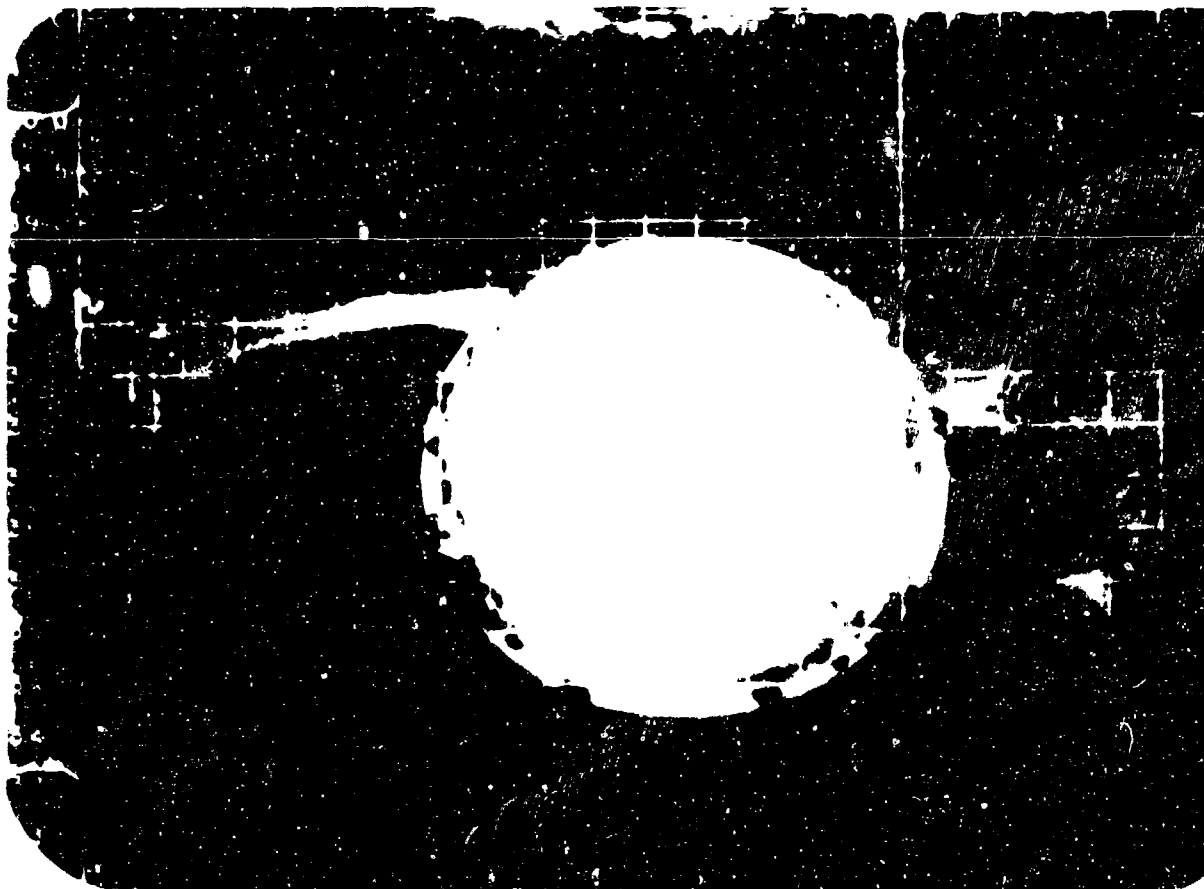


Figure A.9 Shot Erie, Series 34565, Frame 14, Red, 25 mm, B-57.

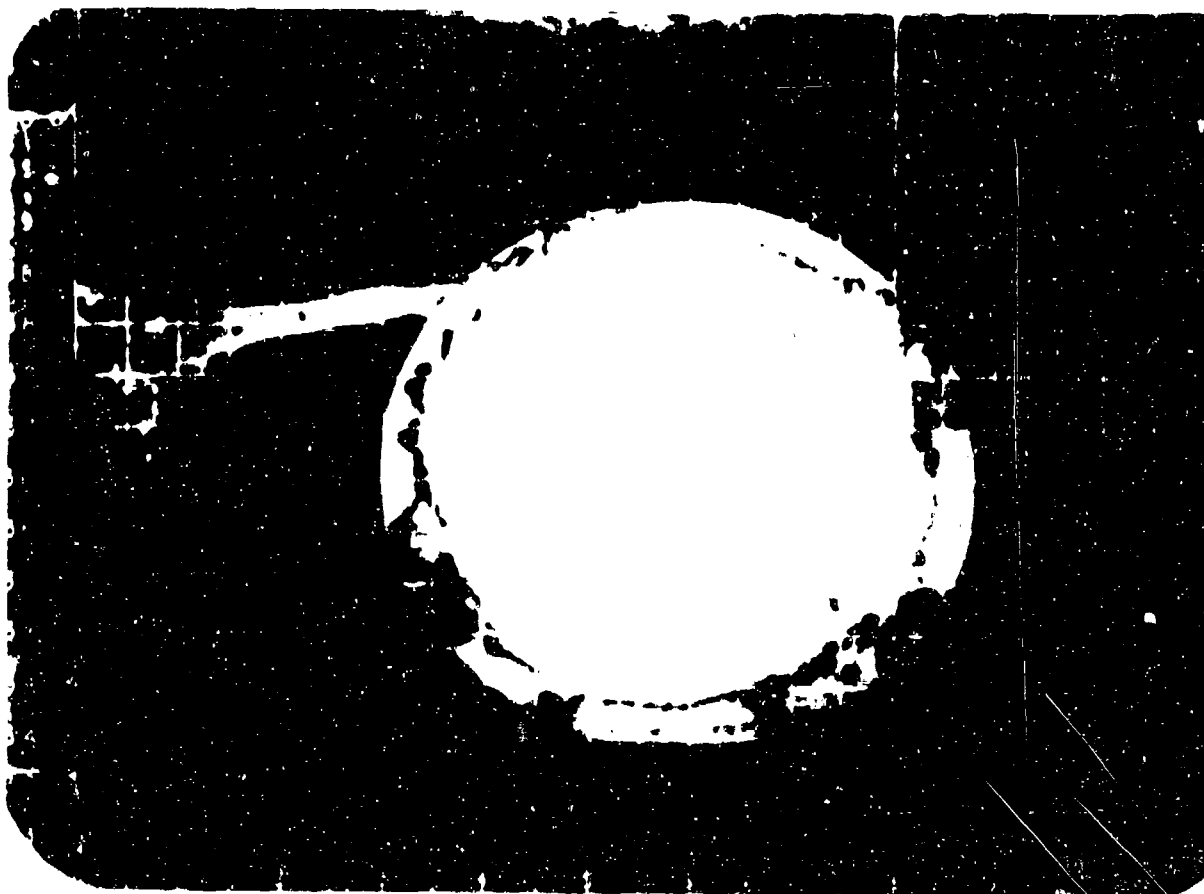


Figure A.10 Shot Erie, Series 34565, Frame 18, Red, 25 mm, B-57.

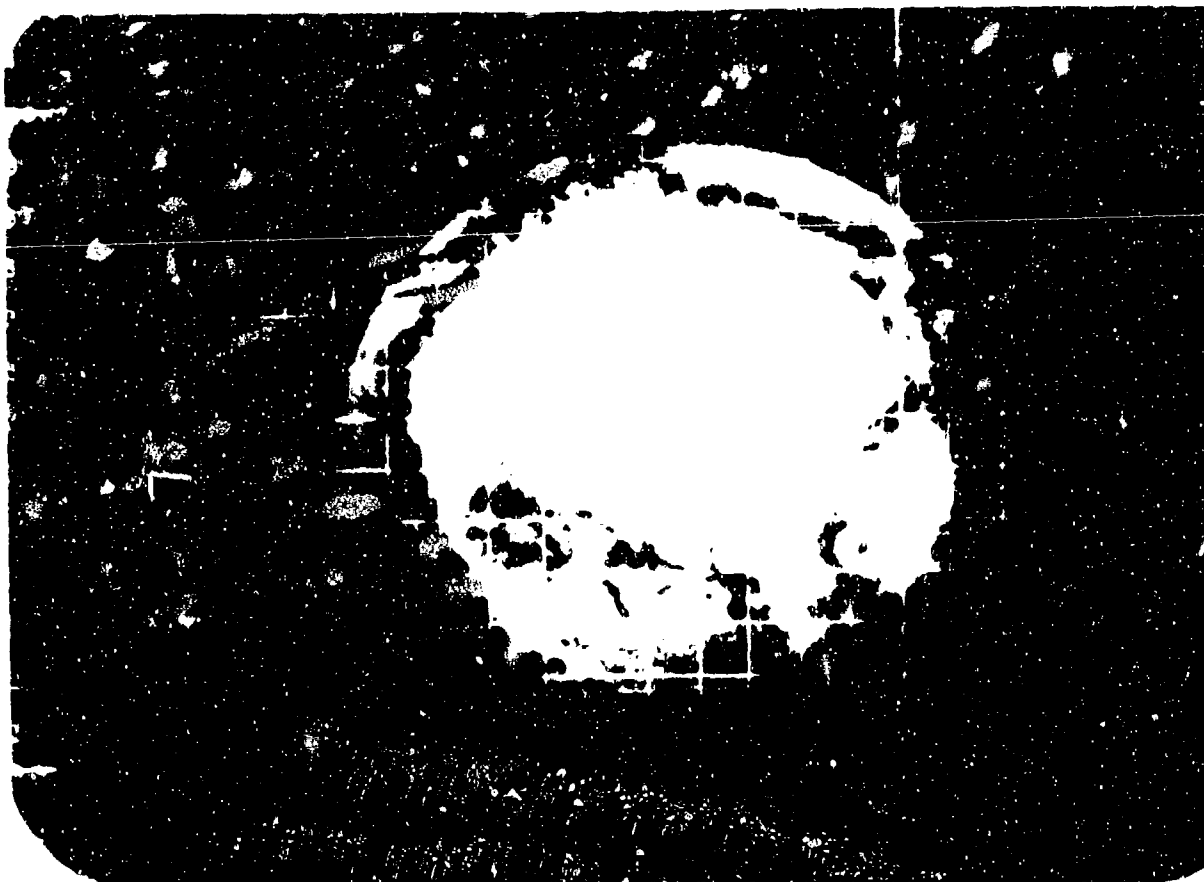


Figure A.11 Shot Erie, Series 34565, Frame 24, Red, 25 mm, B-57.

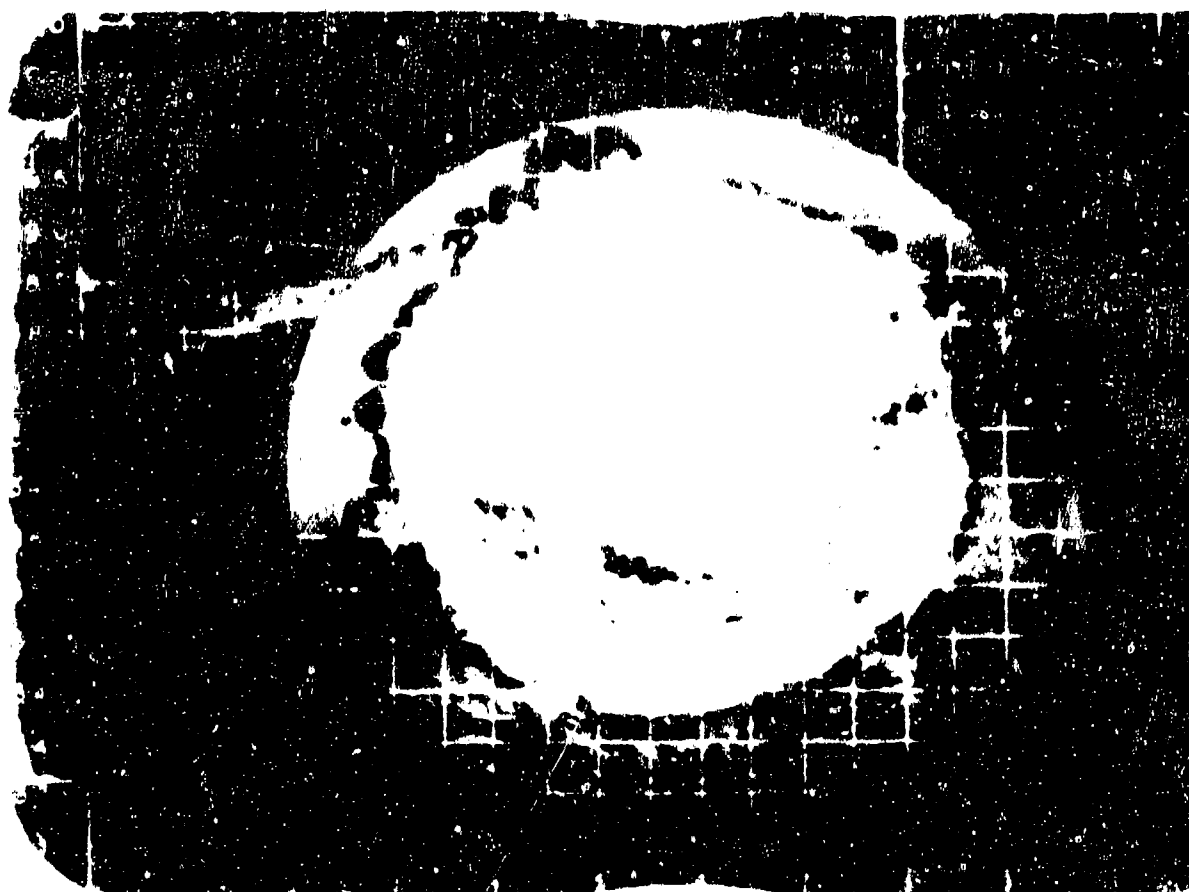


Figure A.12 Shot Erie, Series 34565, Frame 30, Red, 25 mm, B-57.



Figure A.13 Shot Erie, Series 34565, Frame 39, Red, 25 mm, B-57.

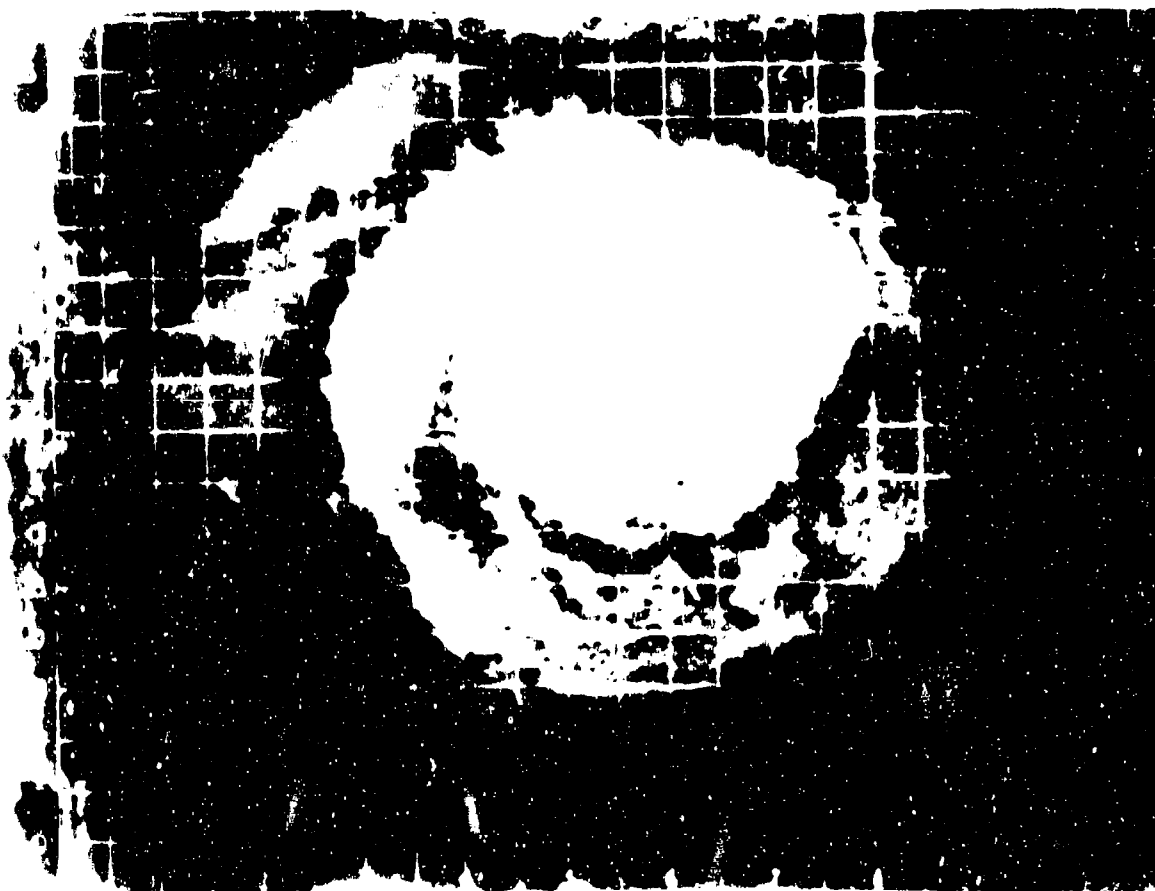


Figure A.14 Shot Erie, Series 34565, Frame 45, Red, 25 mm, B-57.

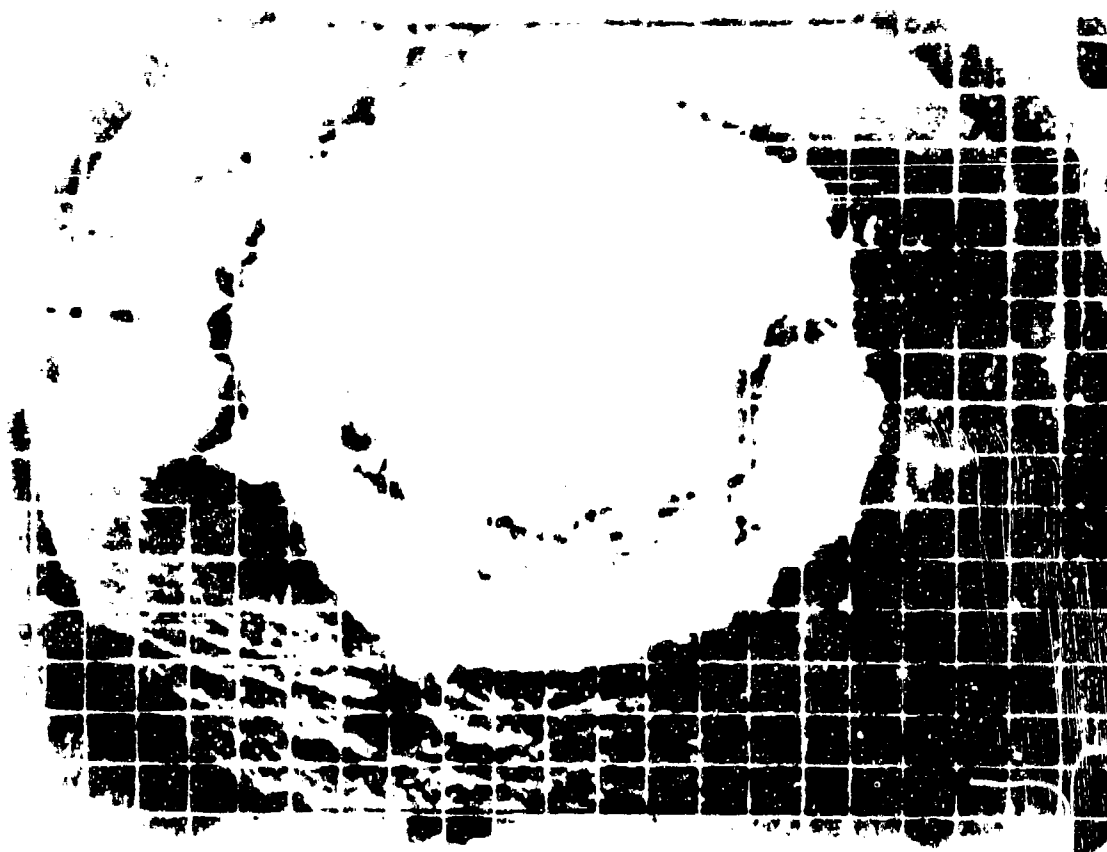


Figure A.15 Shot Erie, Series 34565, Frame 51, Red, 25 mm, B-57.

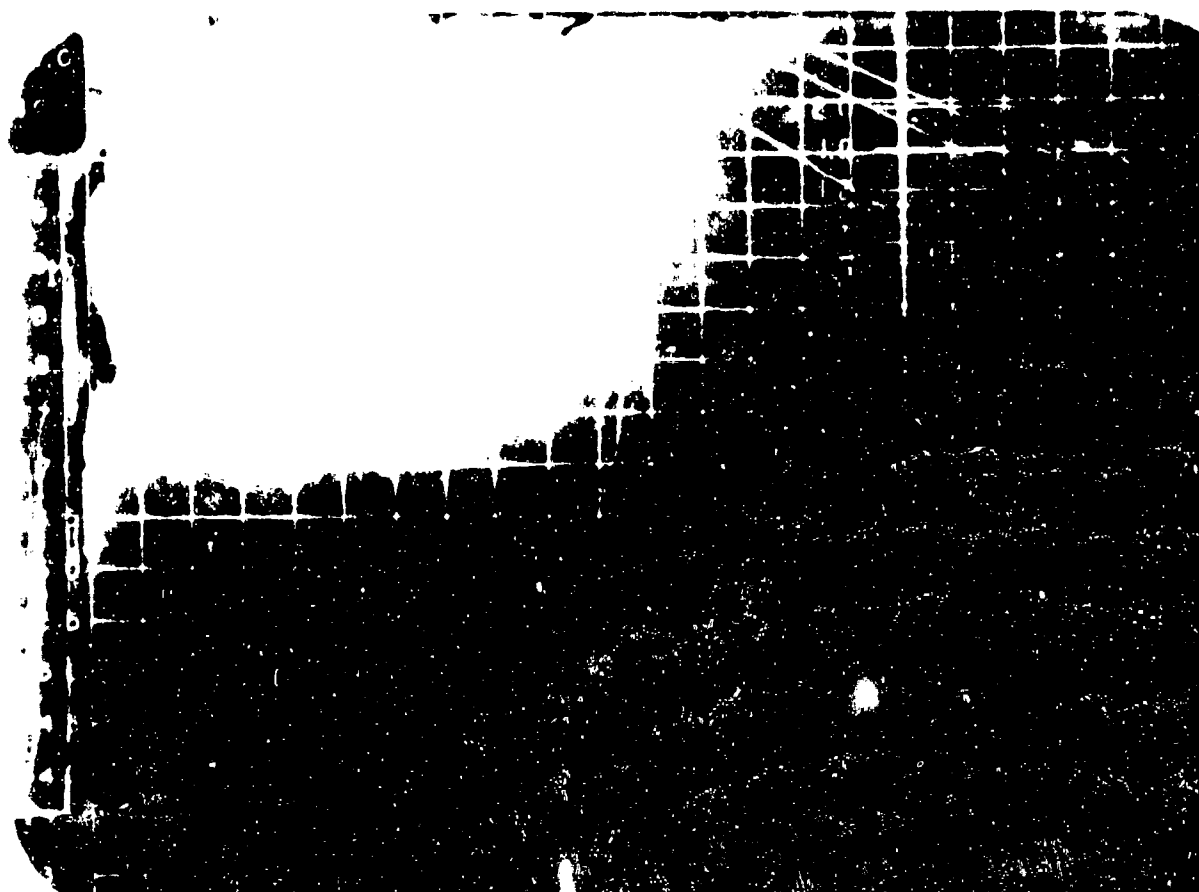


Figure A.16 Shot Lacrosse, Series 31587, Frame Zero, Blue, f.1., 25 mm, B-57.

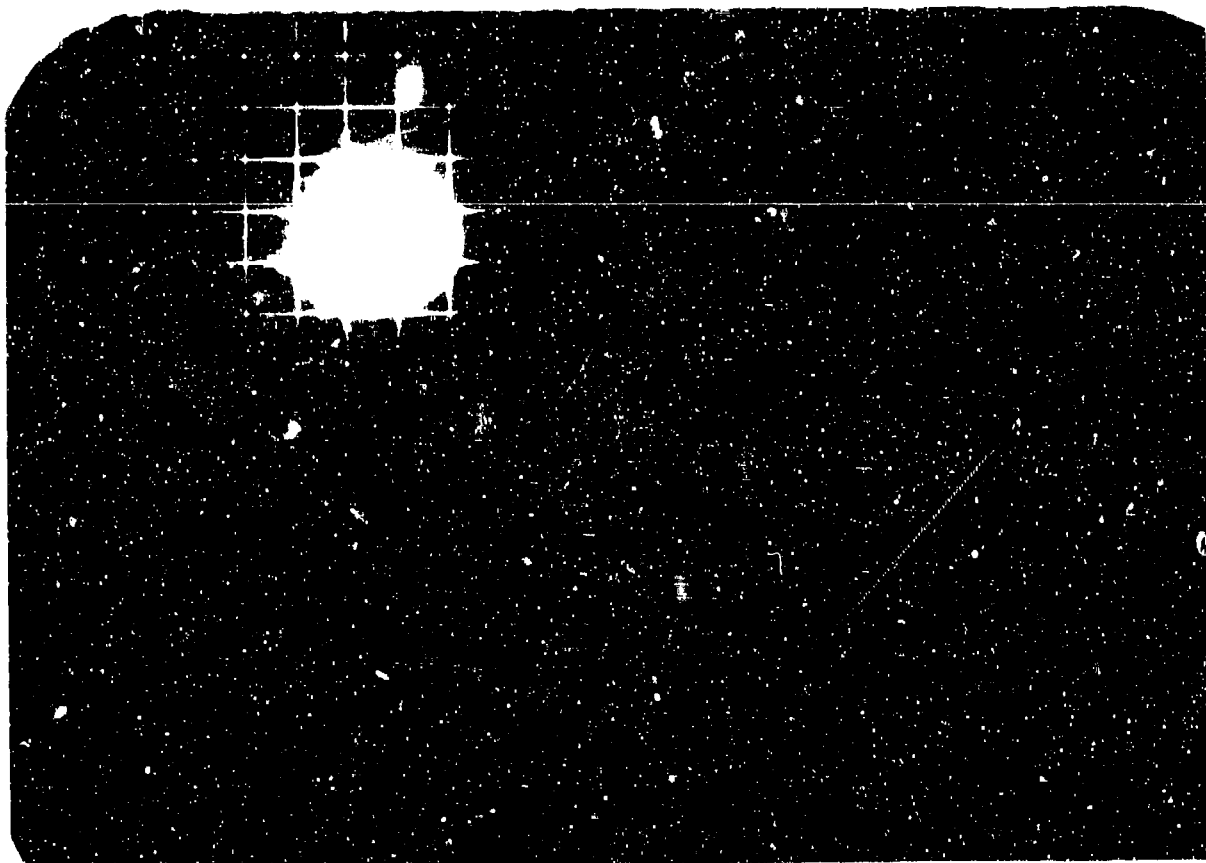


Figure A.17 Shot Lacrosse, Series 31587, Frame Zero, Blue, f.l., 25 mm, B-57.

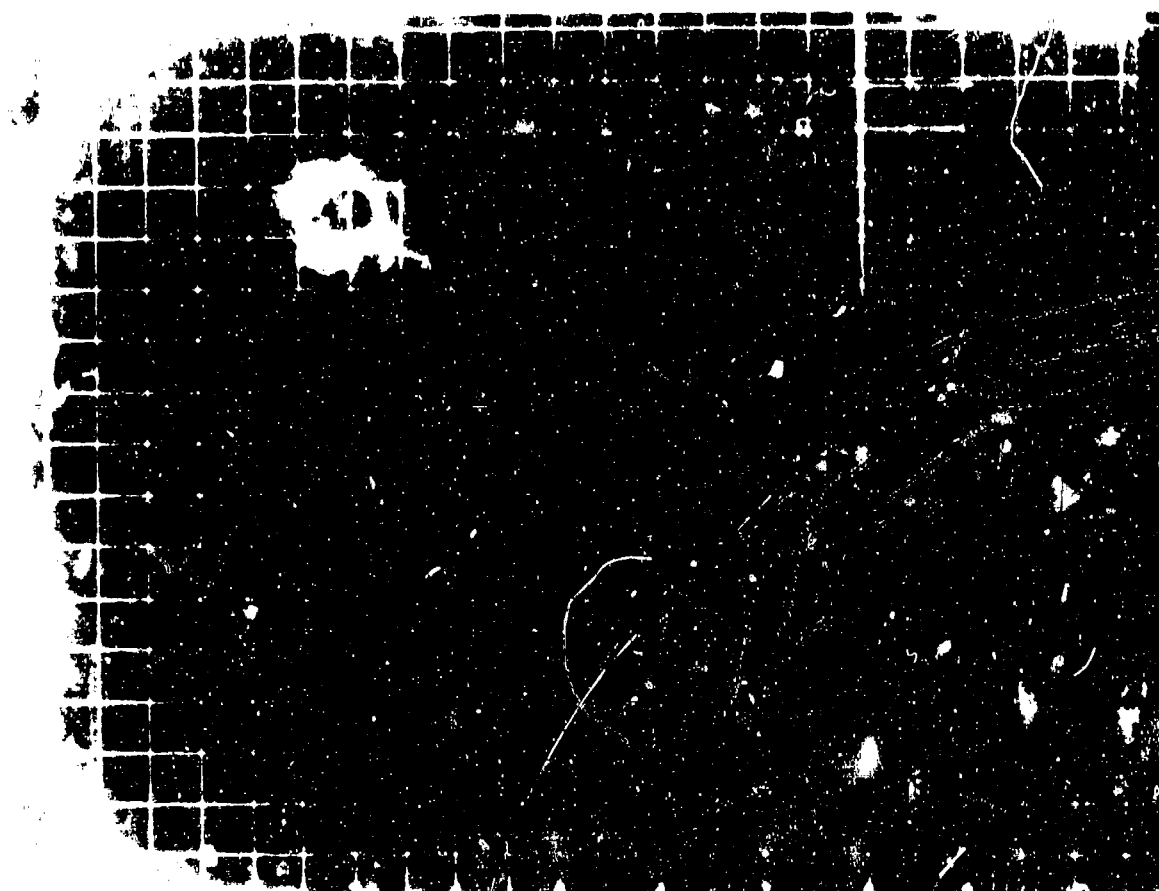


Figure A.18 Shot Lacrosse, Series 31587, Frame 1, Blue, f.l., 25 mm, B-57.

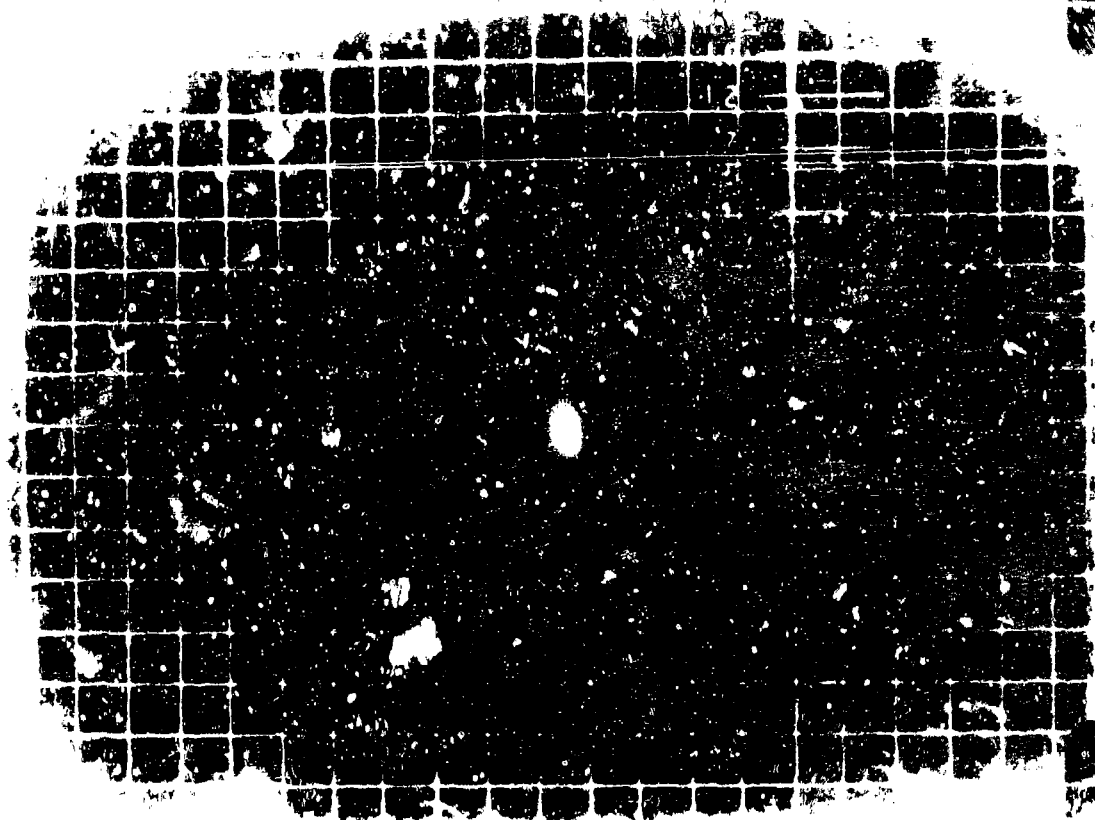


Figure A.19 Shot Lacrosse, Series 31587, Frame 2, Blue f.l., 25 mm, B-57.

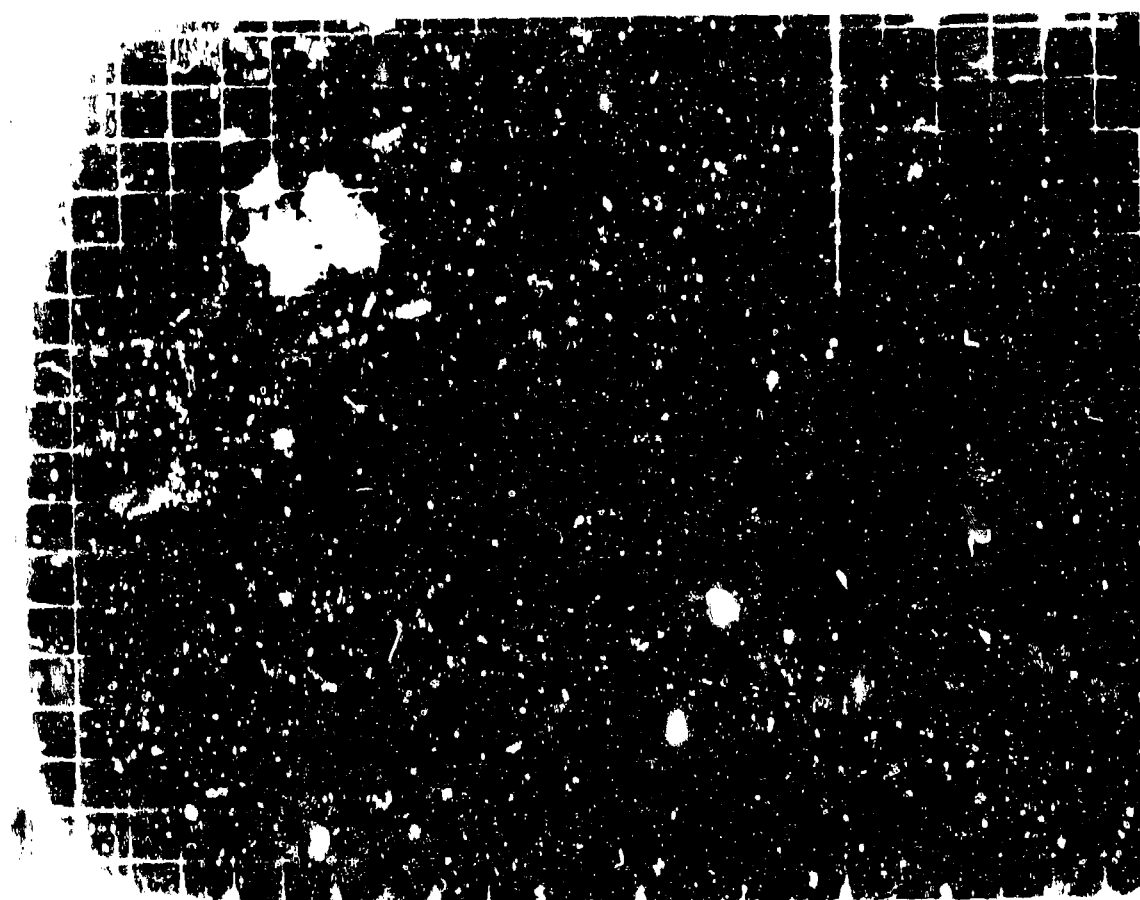


Figure A.20 Shot Lacrosse, Series 31587, Frame 3, Blue, f.l., 25 mm, B-57.

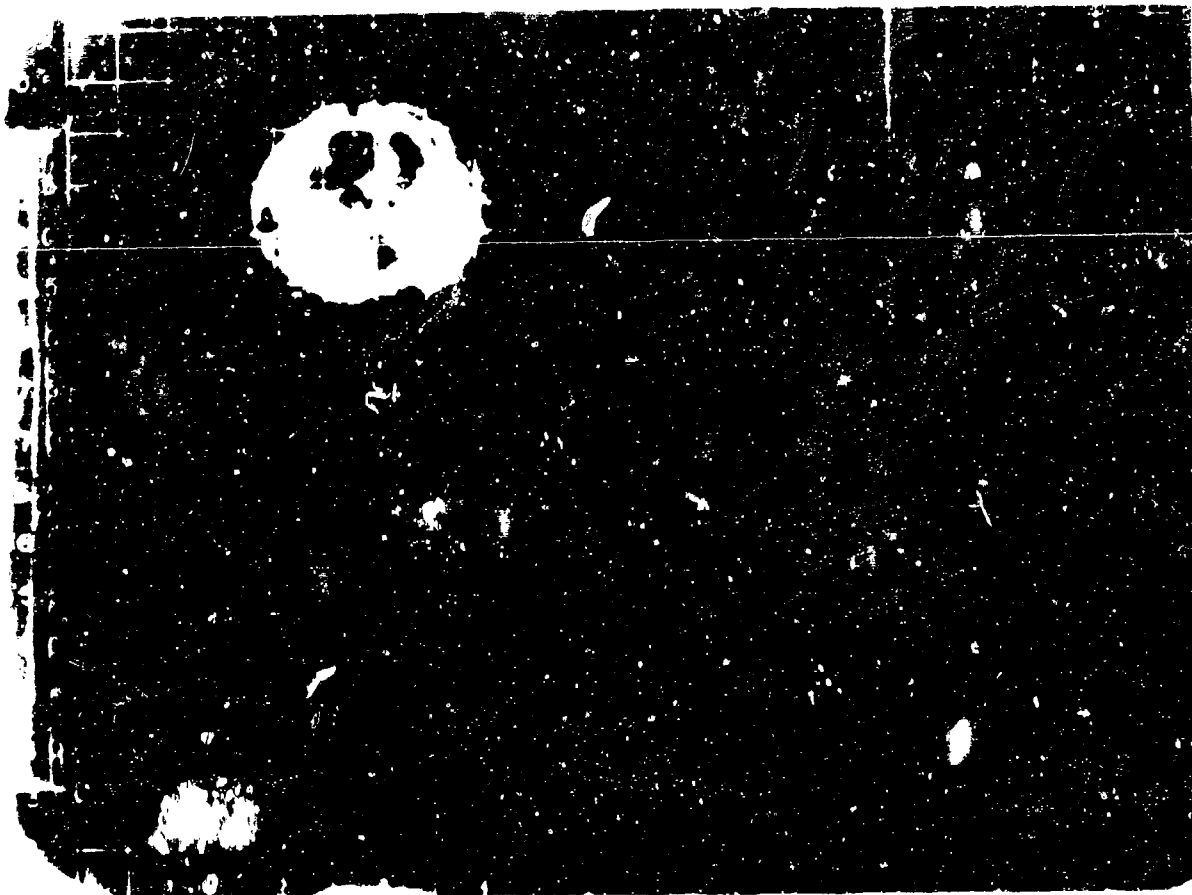


Figure A.21 Shot Lacrosse, Series 31587, Frame 6, Blue, f.l., 25 mm, B-57.

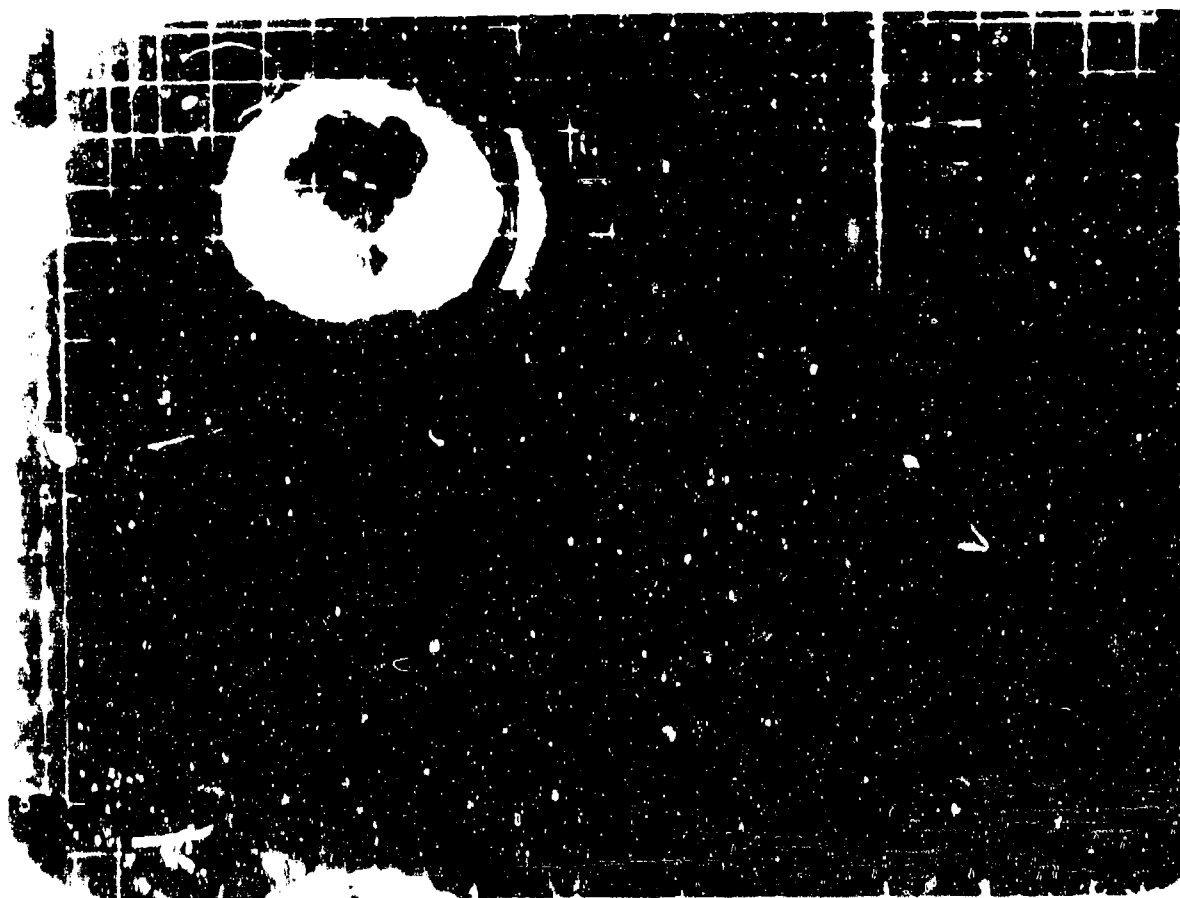


Figure A.22 Shot Lacrosse, Series 31587, Frame 9, Blue, f.l., 25 mm B-57.

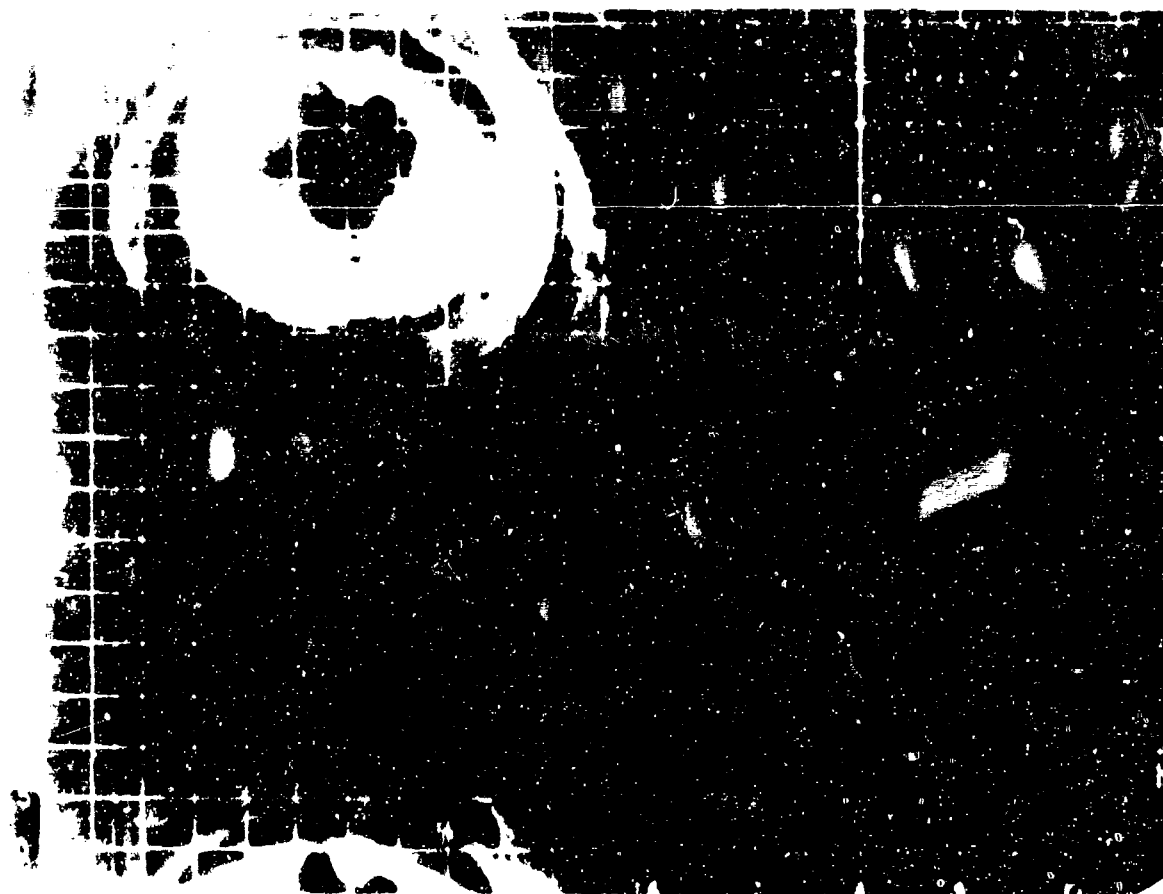


Figure A.23 Shot Lacrosse, Series 31587, Frame 13, Blue, f.l., 25 mm, B-57.

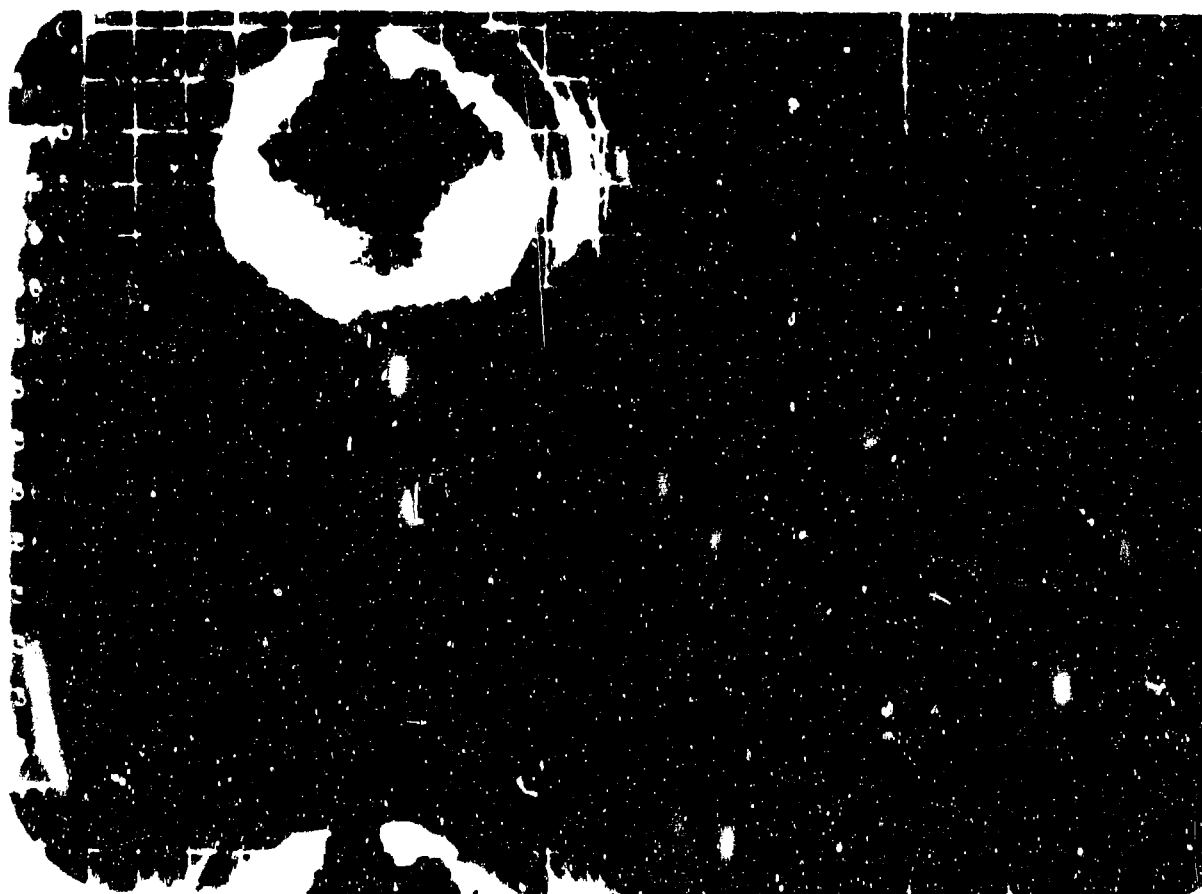


Figure A.24 Shot Lacrosse, Series 31587, Frame 18, Blue, f.l., 25 mm, B-57.

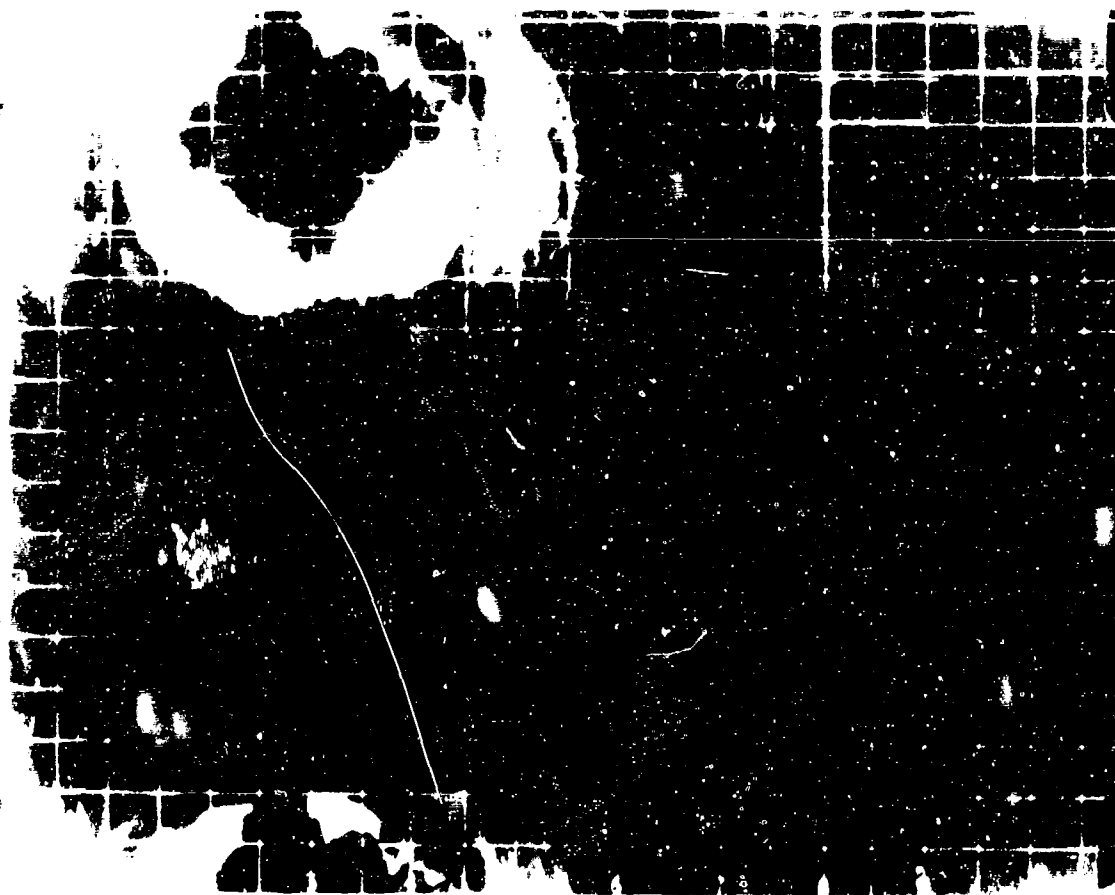


Figure A.25 Shot Lacrosse, Series 31587, Frame 23, Blue, f.l., 25 mm, B-57.

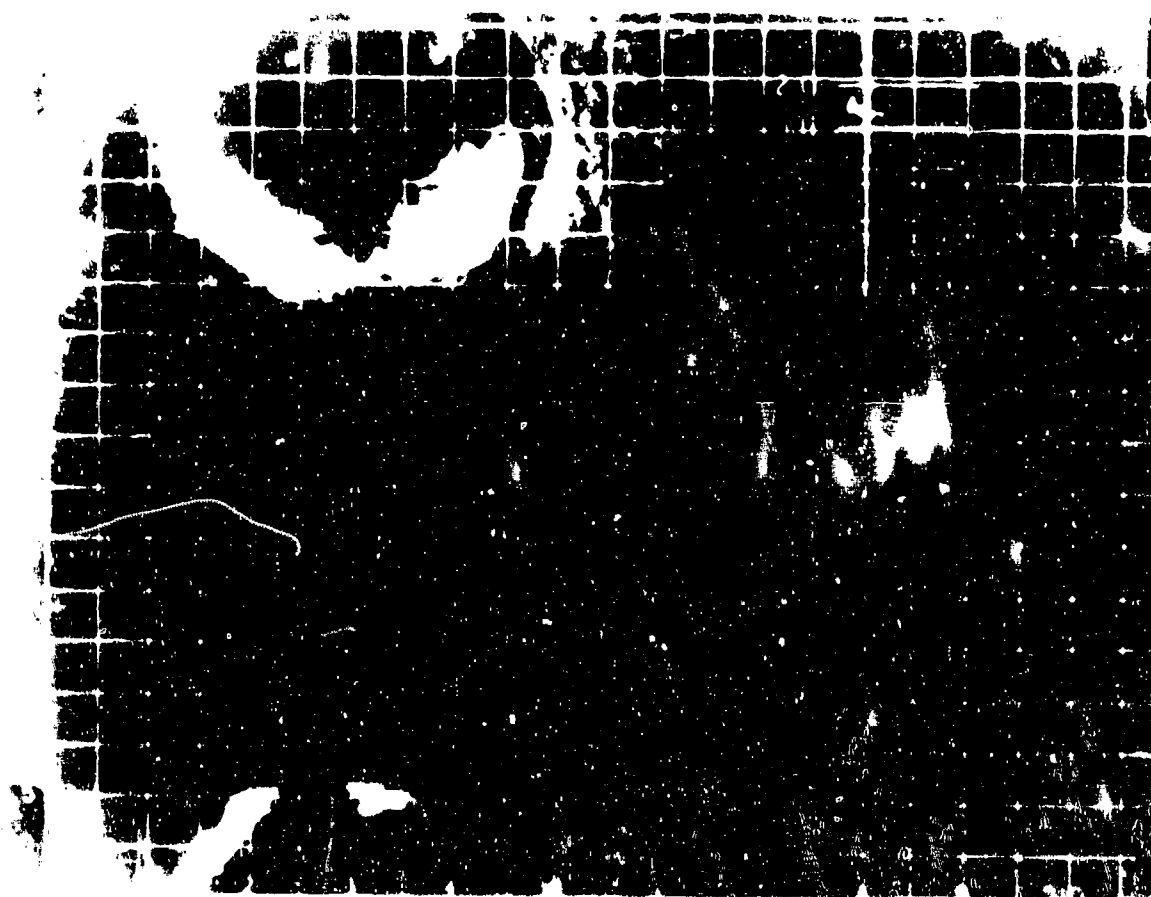


Figure A.26 Shot Lacrosse, Series 31587, Frame 30, Blue, f.l., 25 mm, B-57.

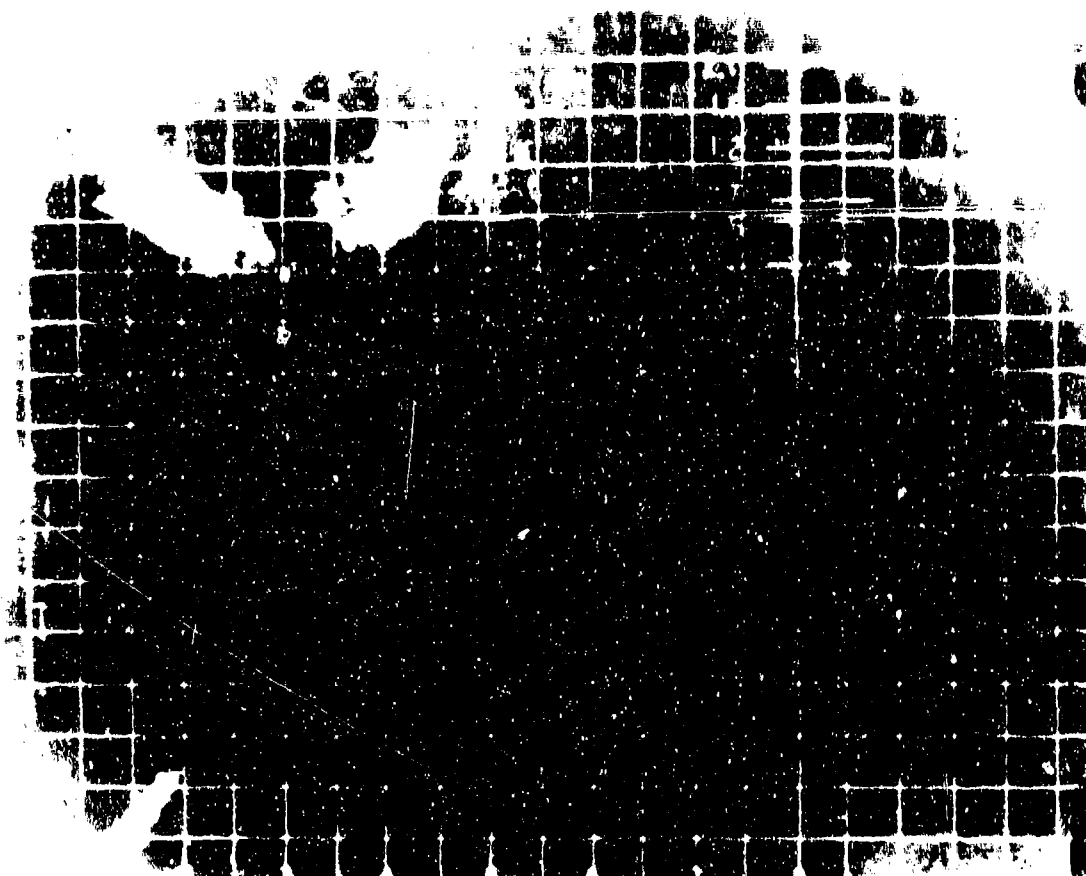


Figure A.27 Shot Lacrosse, Series 31587, Frame 39, Blue, f.l., 25 mm, B-57.



Figure A.28 Shot Lacrosse, Series 31587, Frame 49, Blue, f.l., 25 mm, B-57.

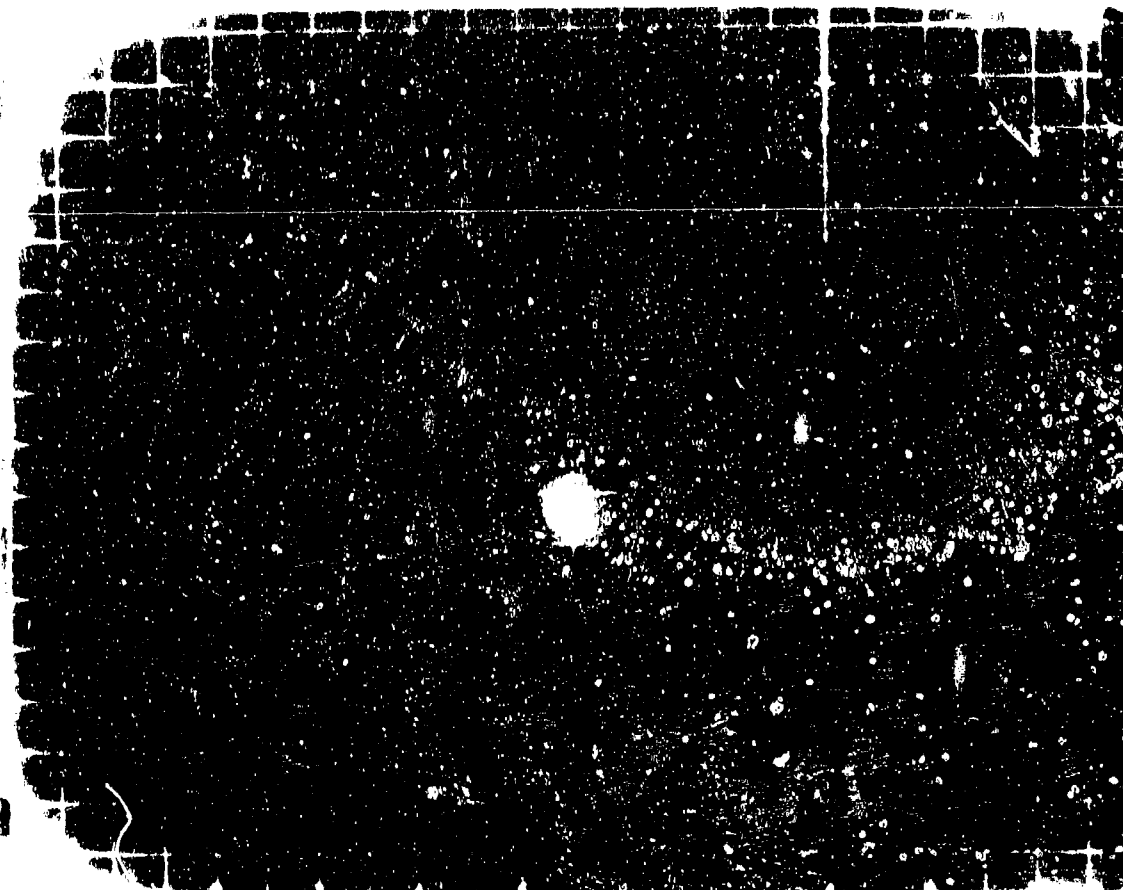


Figure A.29 Shot Huron, Series 37505, Frame Zero, Blue, B-57.

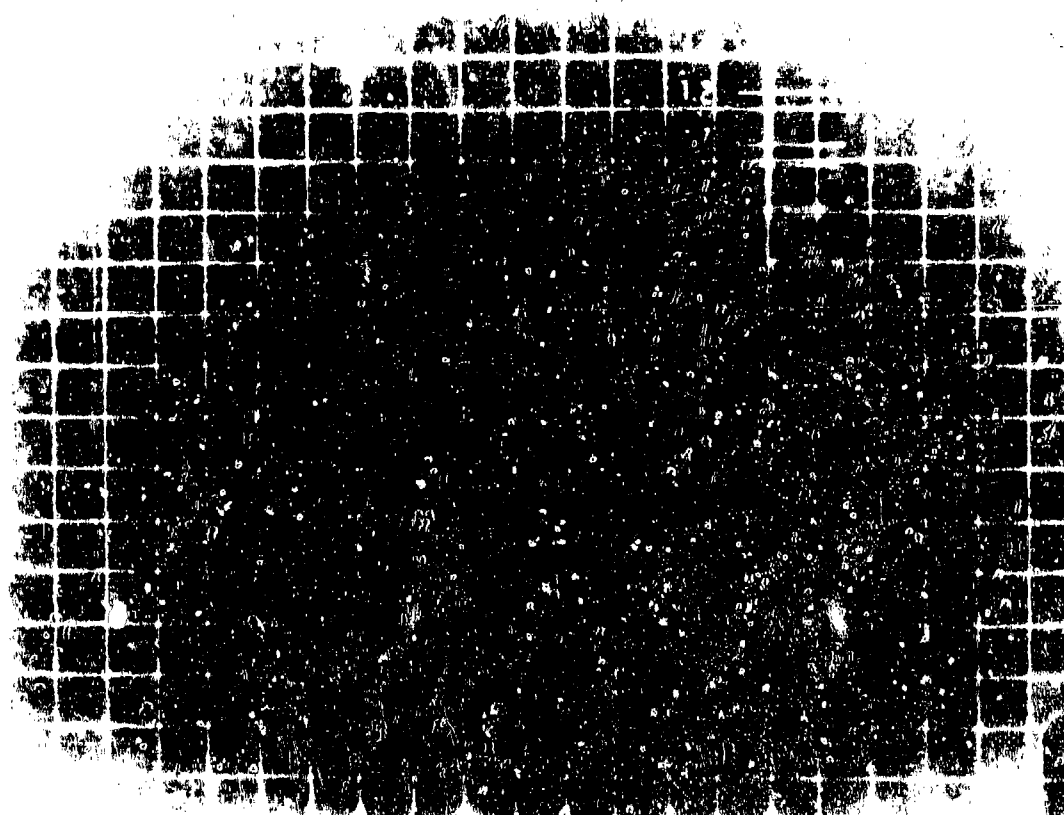


Figure A.30 Shot Huron, Series 37505, Frame 7, Blue, B-57.

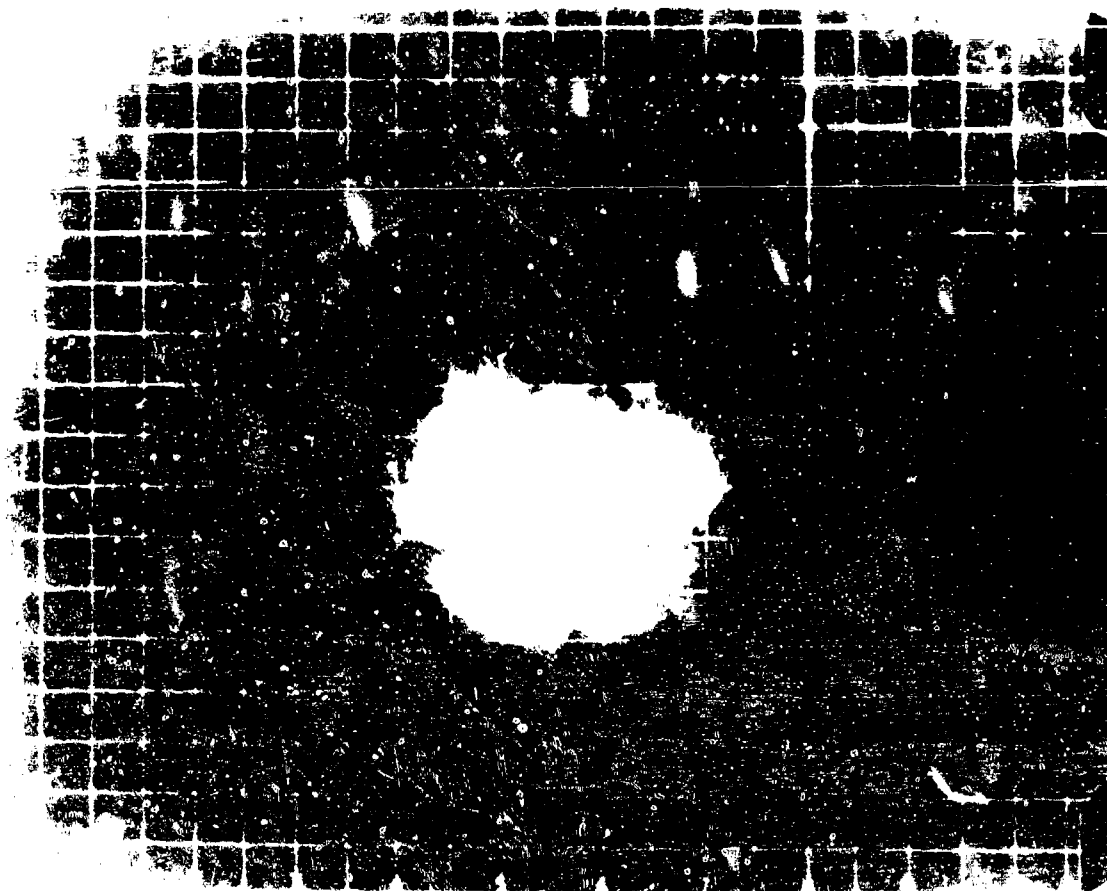


Figure A.31 Shot Huron, Series 37505, Frame 15, Blue, B-57.

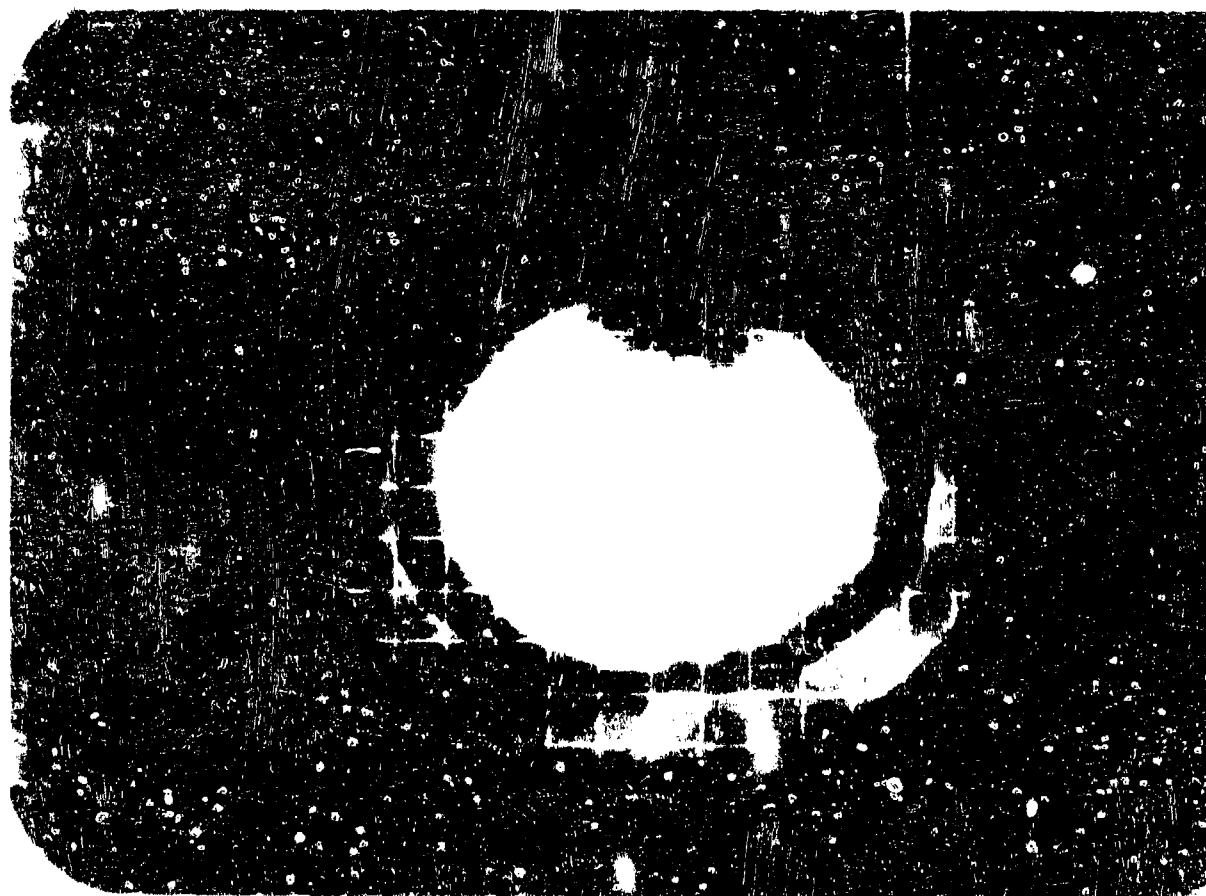


Figure A.32 Shot Huron, Series 37505, Frame 23, Blue, B-57.

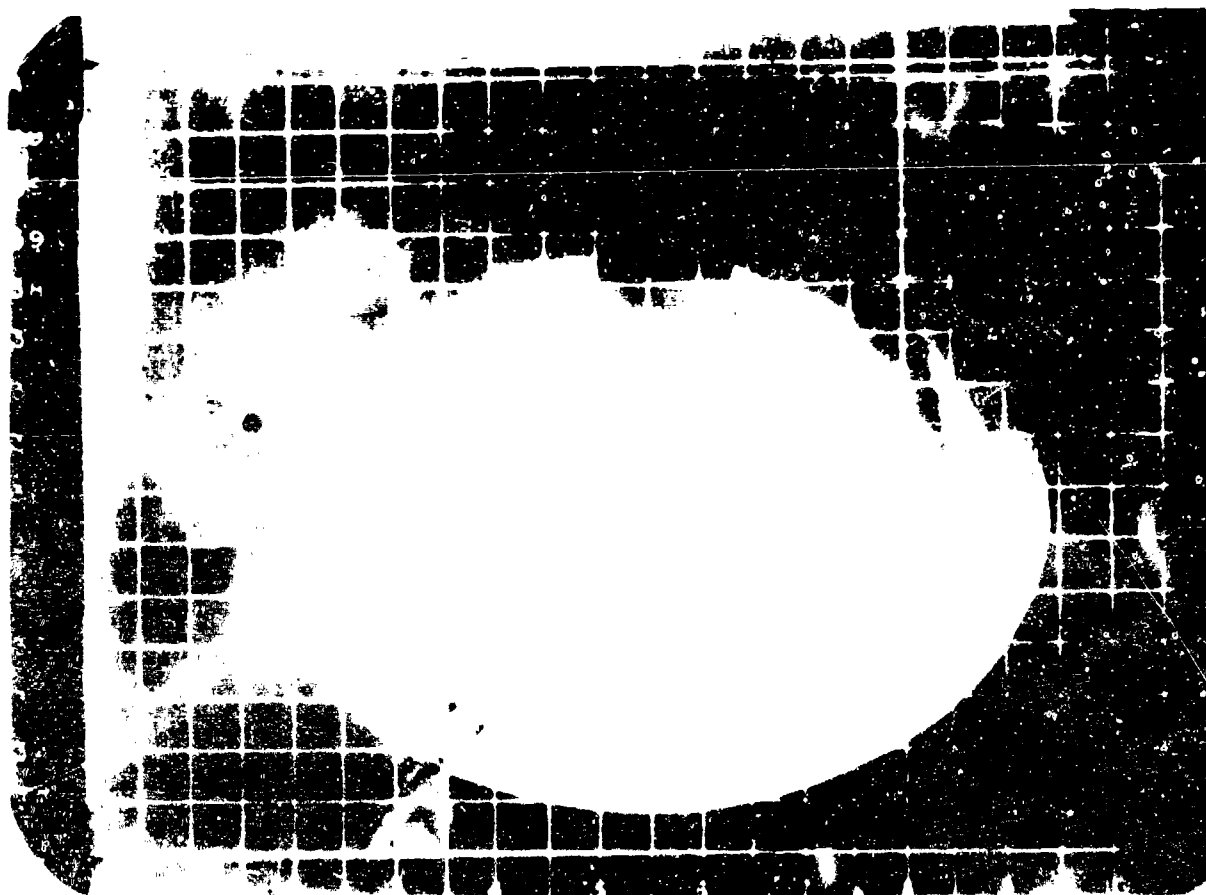


Figure A.33 Shot Huron, Series 37505, Frame 34, Blue, B-57.

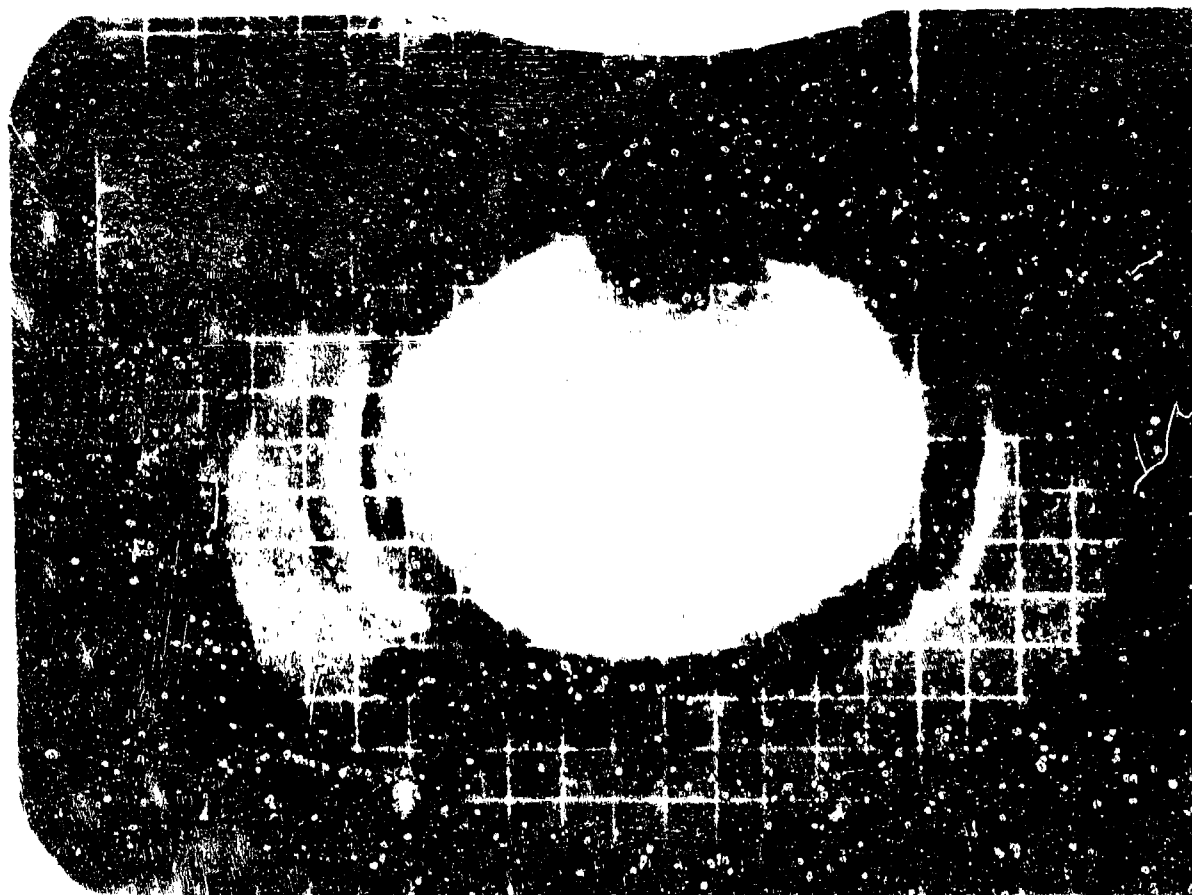


Figure A.34 Shot Huron, Series 37505, Frame 46, Blue, B-57.

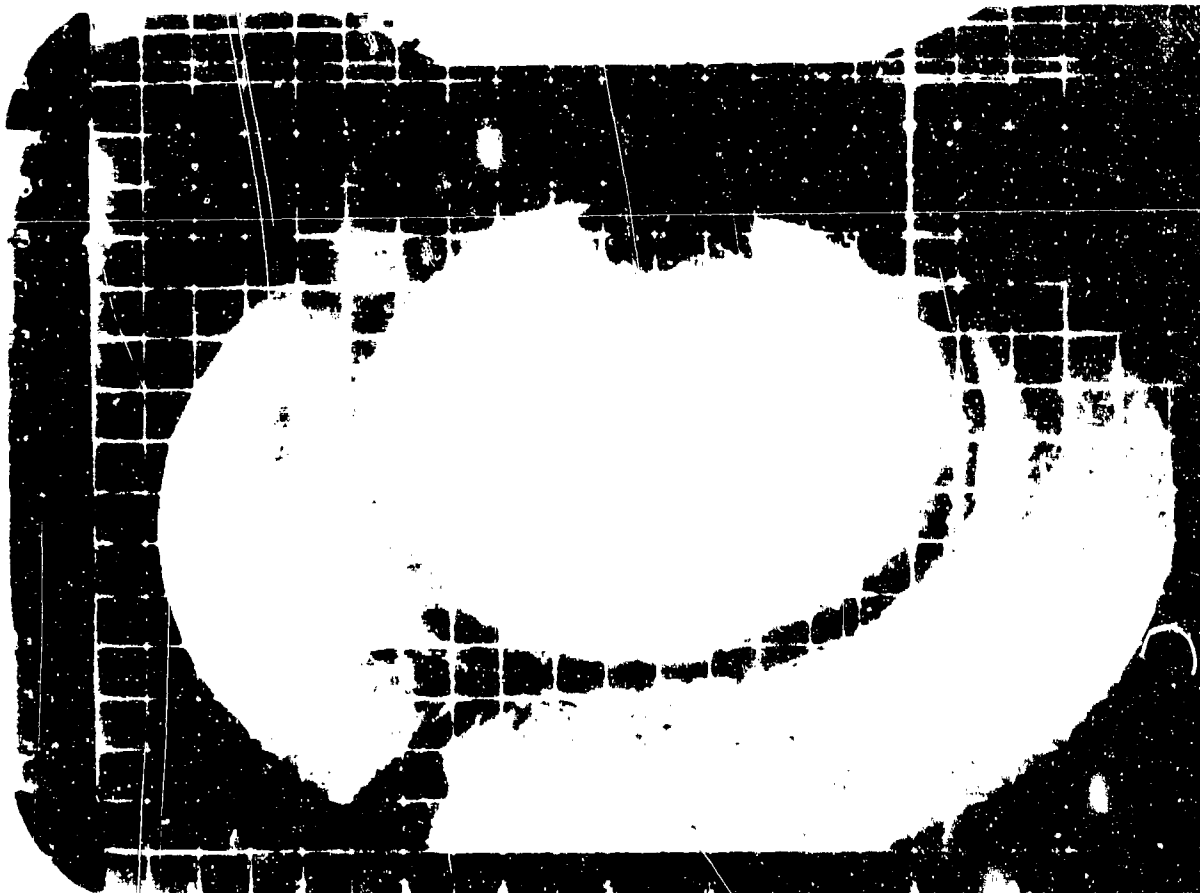


Figure A.35 Shot Huron, Series 37505, Frame 59, Blue, B-57.

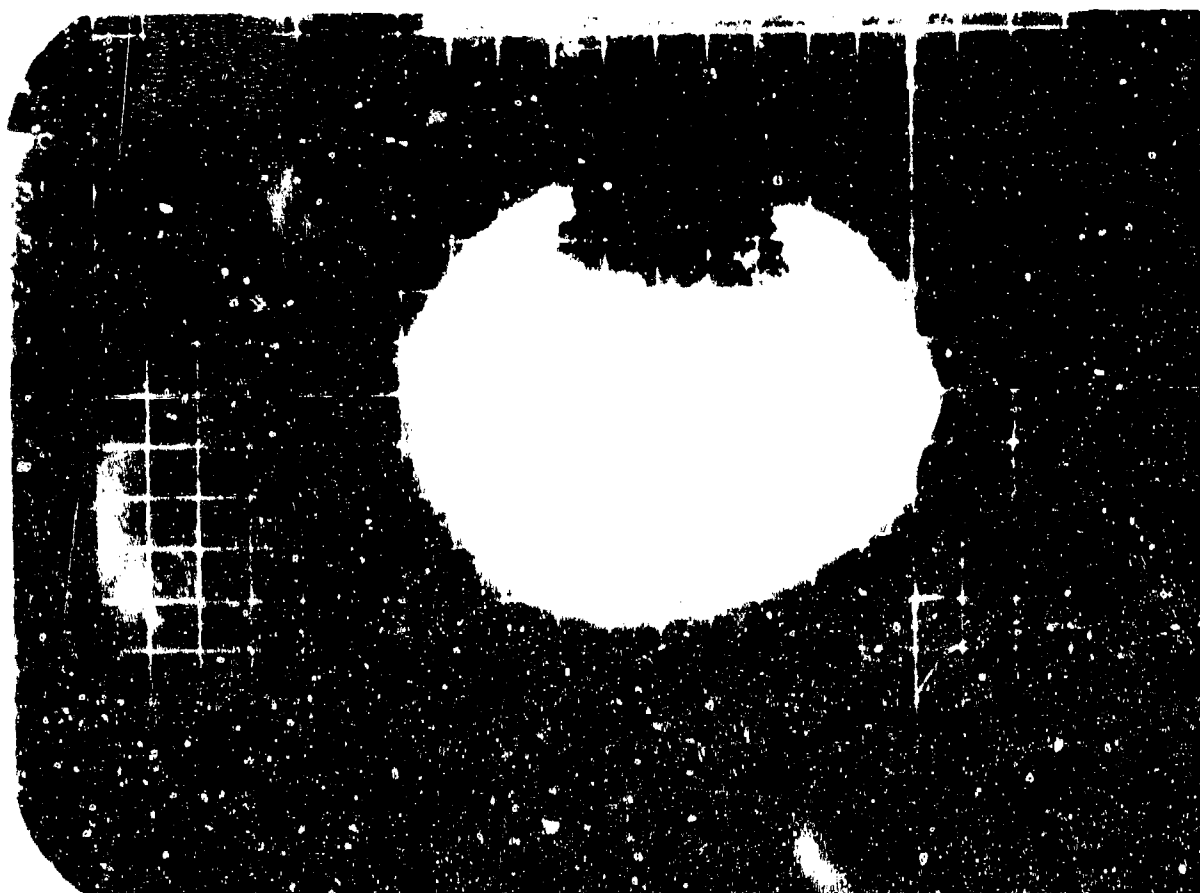


Figure A.36 Shot Huron, Series 37505, Frame 77, Blue, B-57.

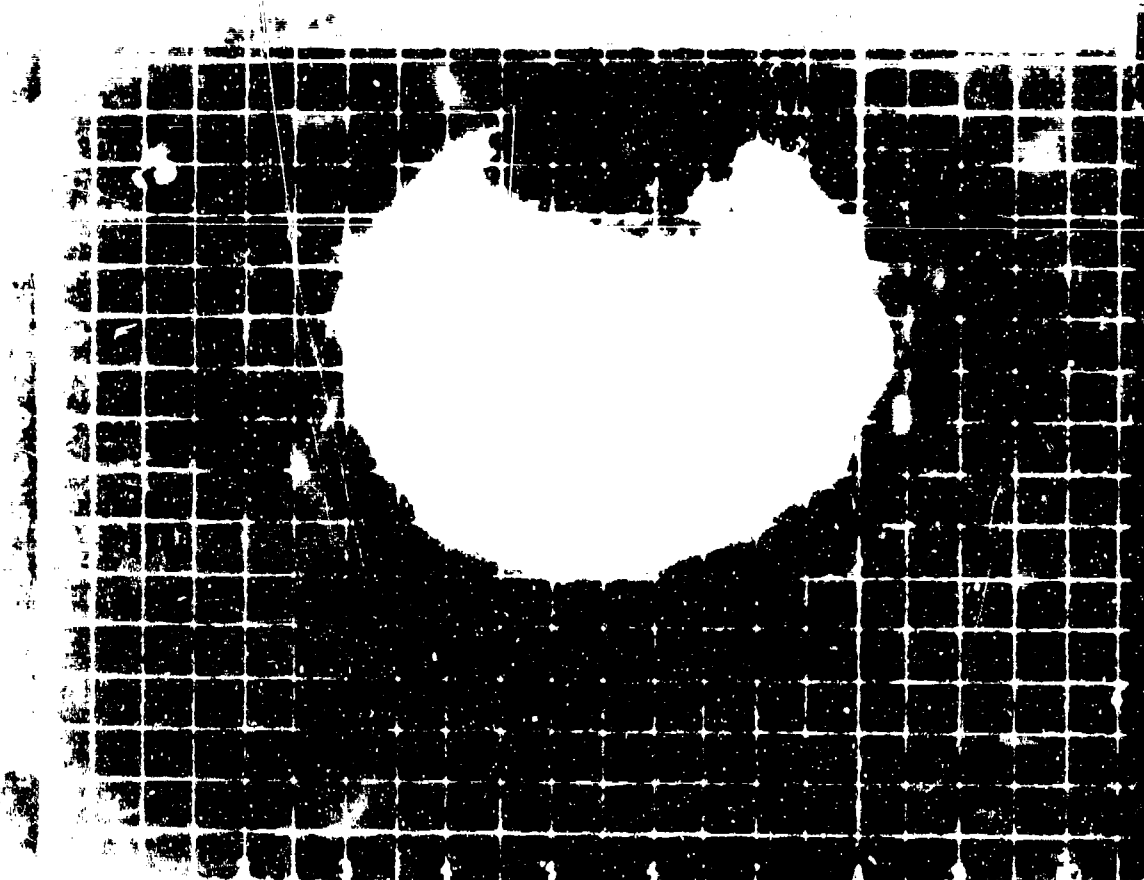


Figure A.37 Shot Huron, Series 37505, Frame 103, Blue, B-57.

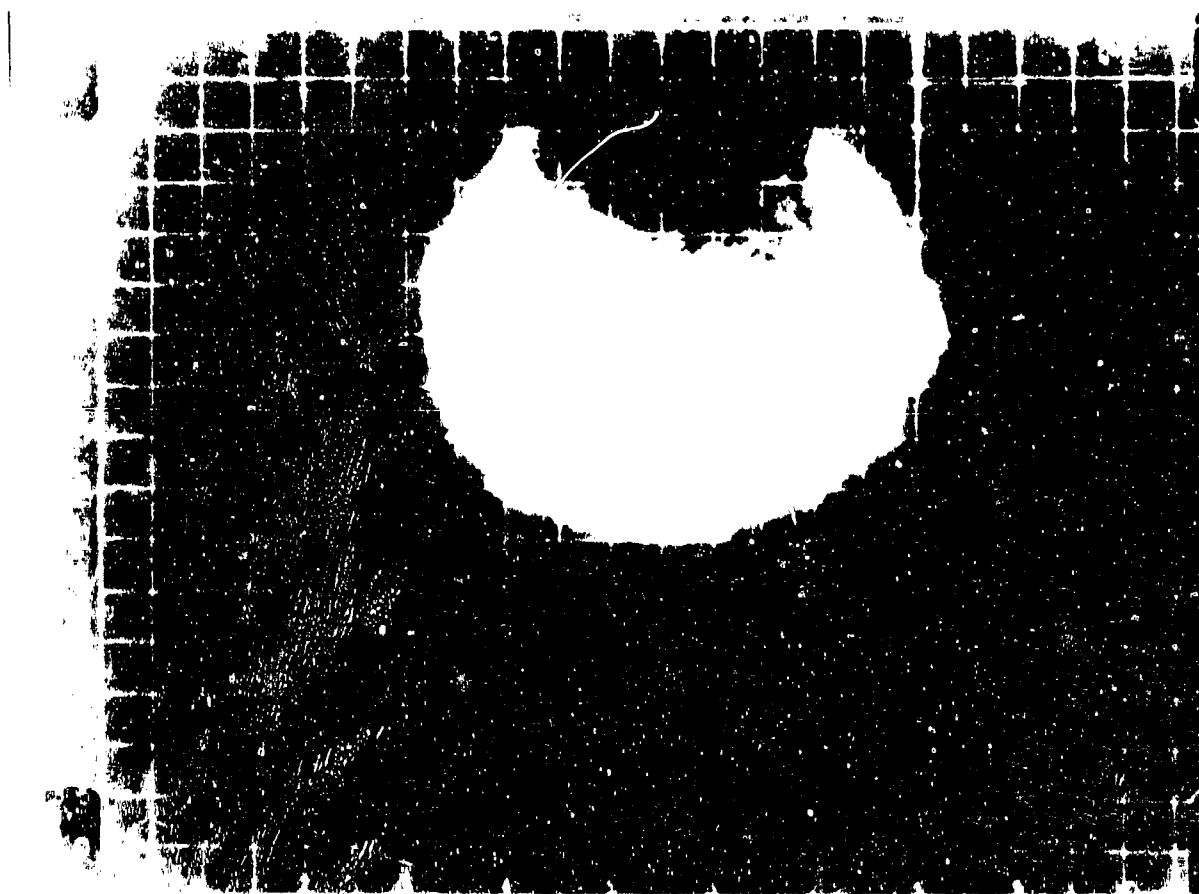


Figure A.38 Shot Huron, Series 37505, Frame 129, Blue, B-57.

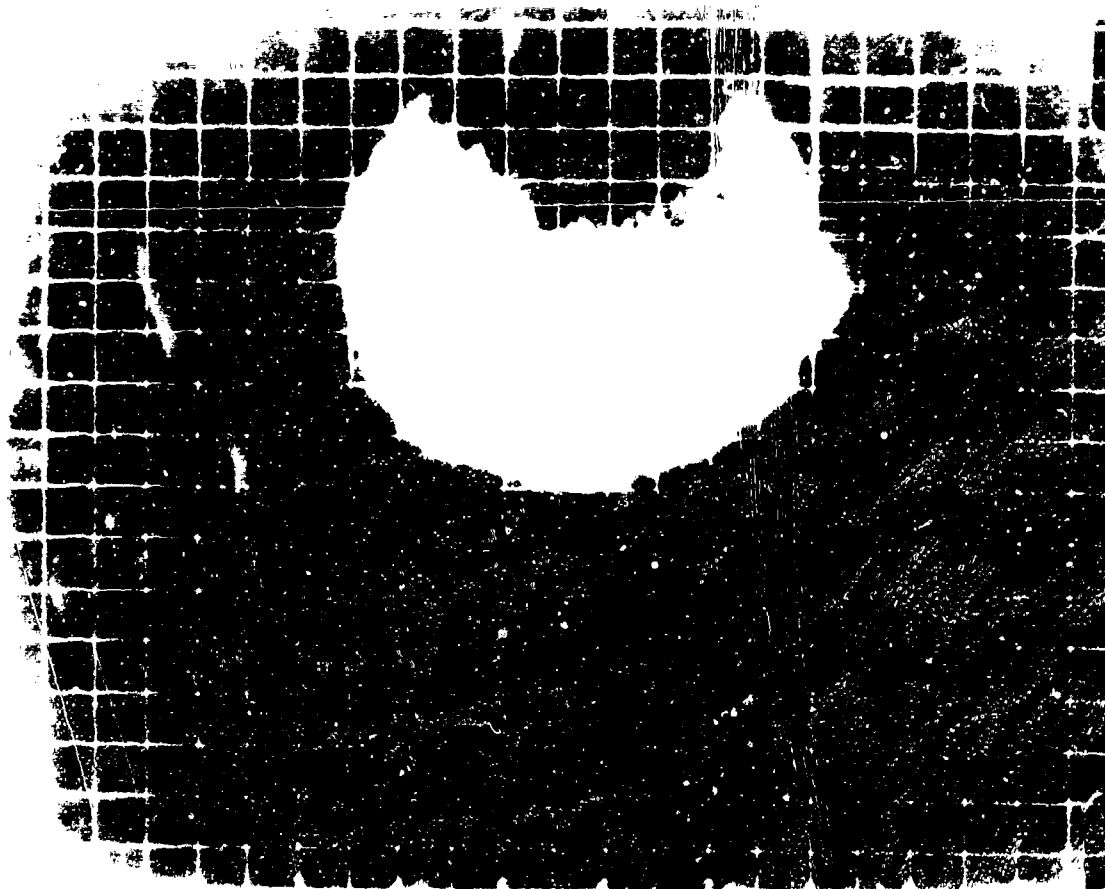


Figure A.39 Shot Huron, Series 37505, Frame 167, Blue, B-57.



Figure A.40 Shot Huron, Series 37505, Frame 193, Blue, B-57.



Figure A.41 Shot Huron, Series 37505, Frame 219, Blue, B-57.

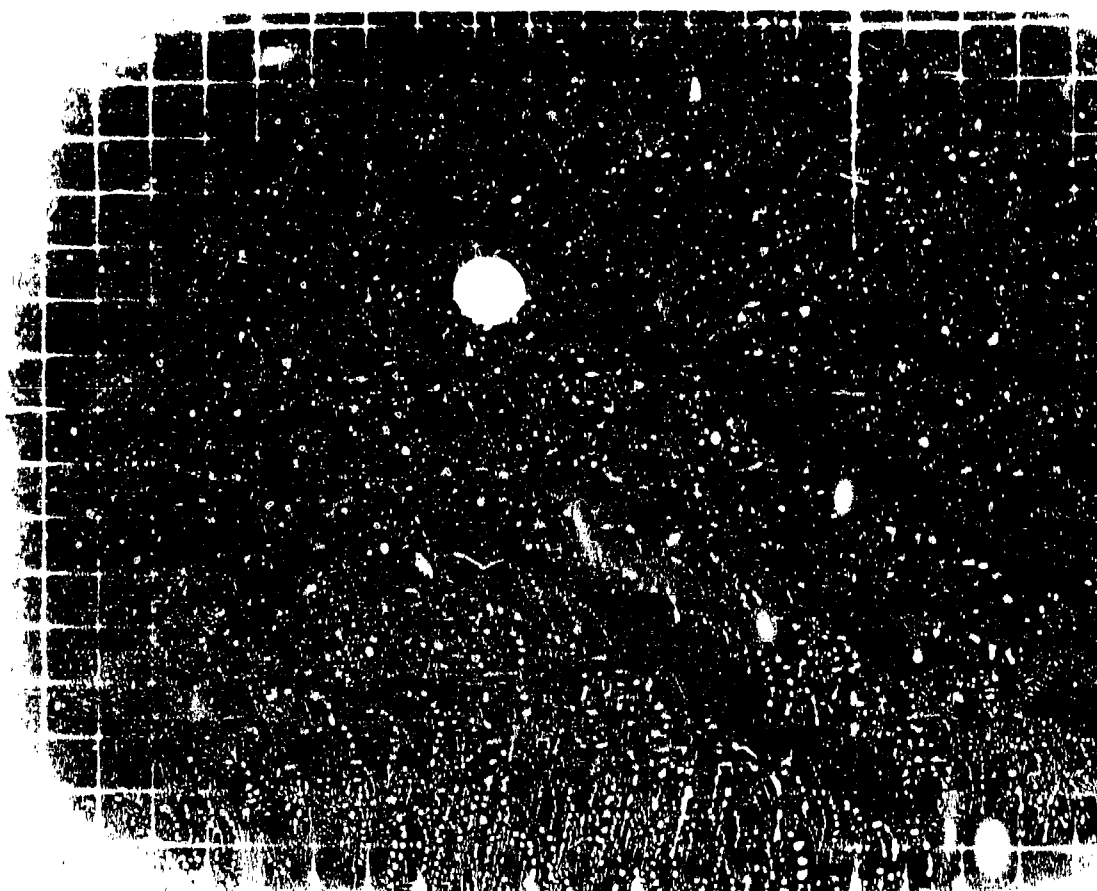


Figure A.42 Shot Flathead, Series 35153, Frame Zero, Blue, G.I., 25 mm, B-47.

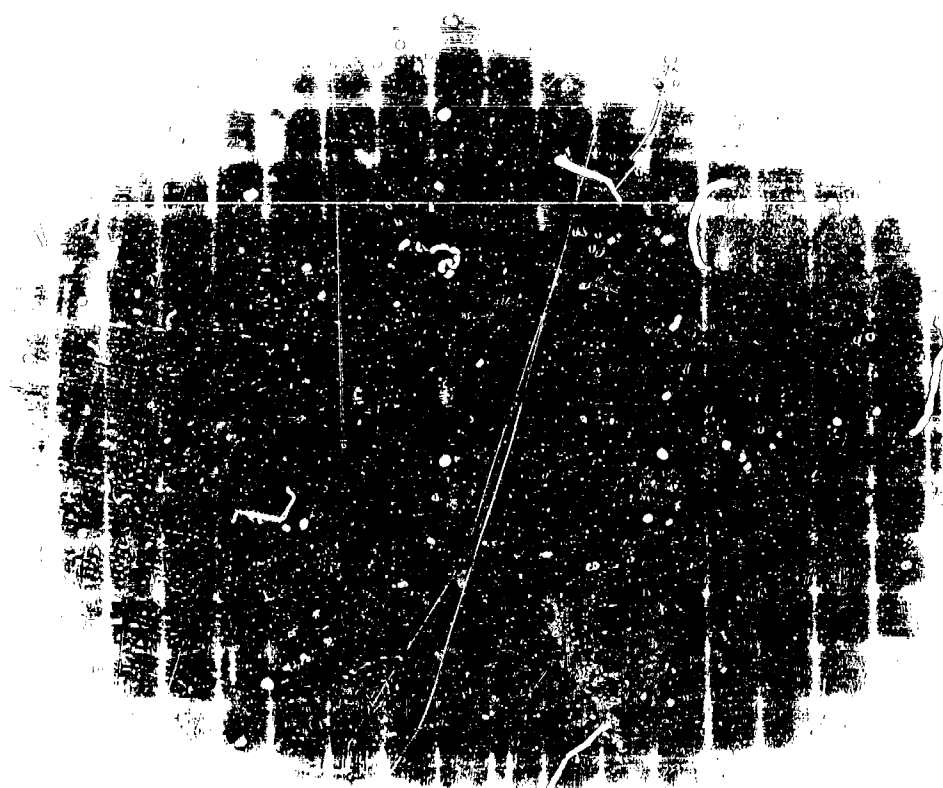


Figure 1. A dark, circular, textured object, possibly a fossil or a piece of wood, with a prominent diagonal line and some faint markings.

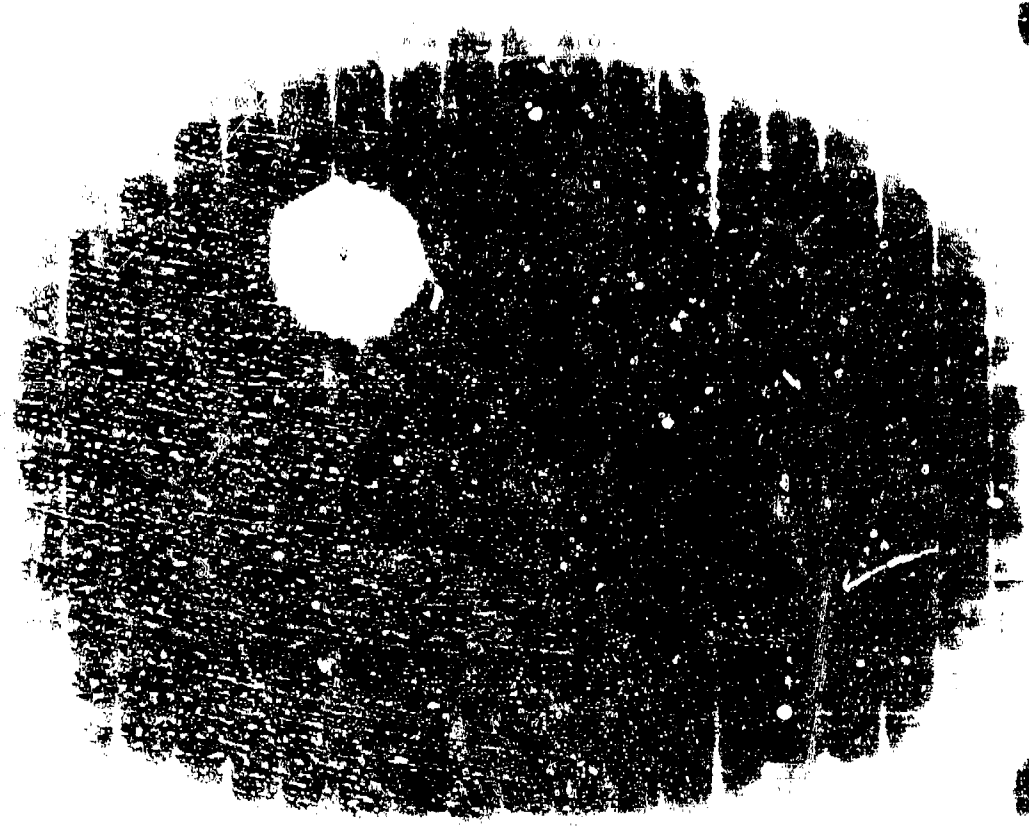


Figure 2. A dark, circular, textured object, similar to the one above, but with a distinct white circular spot in the upper left quadrant.

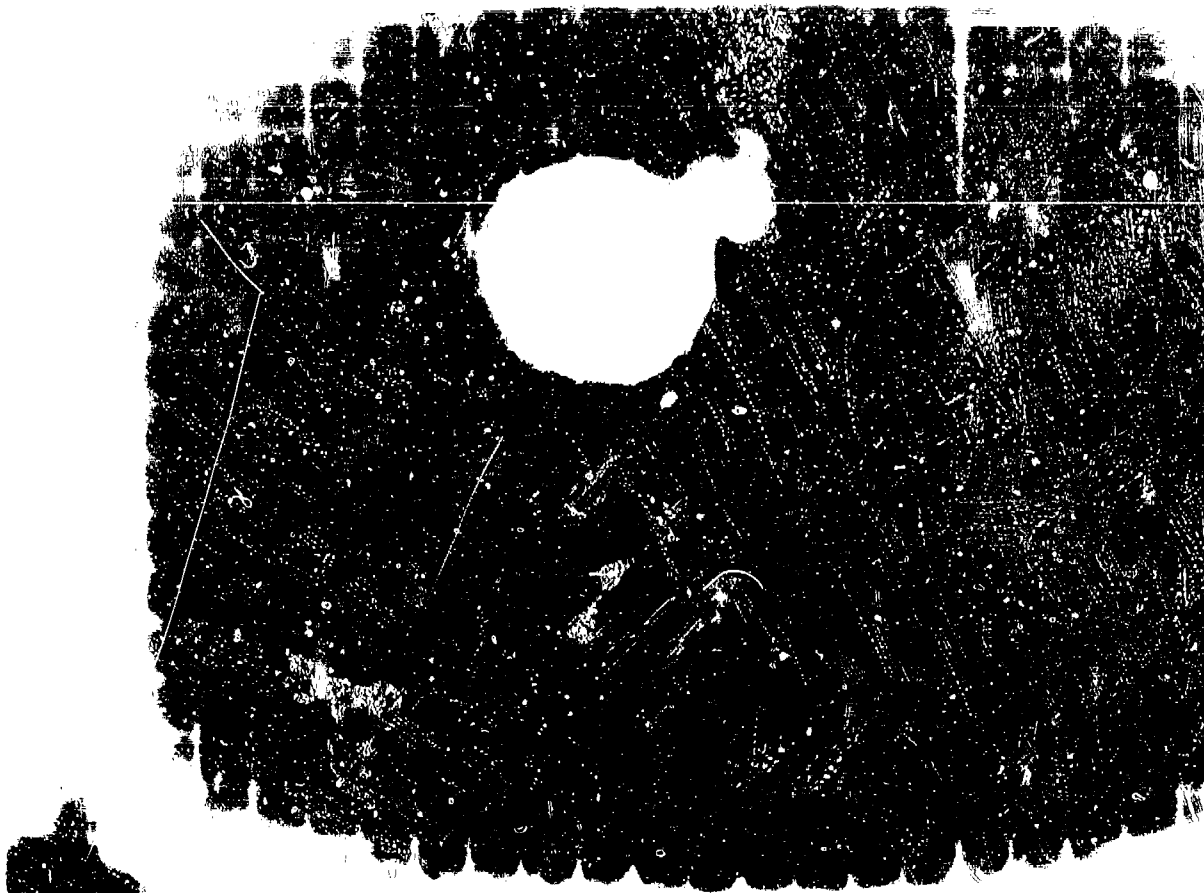


Figure 1. A photograph of a dark, textured surface with a large, bright, irregularly shaped hole in the upper center. The hole has a jagged, irregular edge. The surrounding surface is dark and grainy, with some lighter, speckled areas. The overall appearance is that of a heavily worn or damaged material.



Figure 2. A photograph of a dark, textured surface with a large, bright, irregularly shaped hole in the upper center. The hole has a jagged, irregular edge. The surrounding surface is dark and grainy, with some lighter, speckled areas. The overall appearance is that of a heavily worn or damaged material.

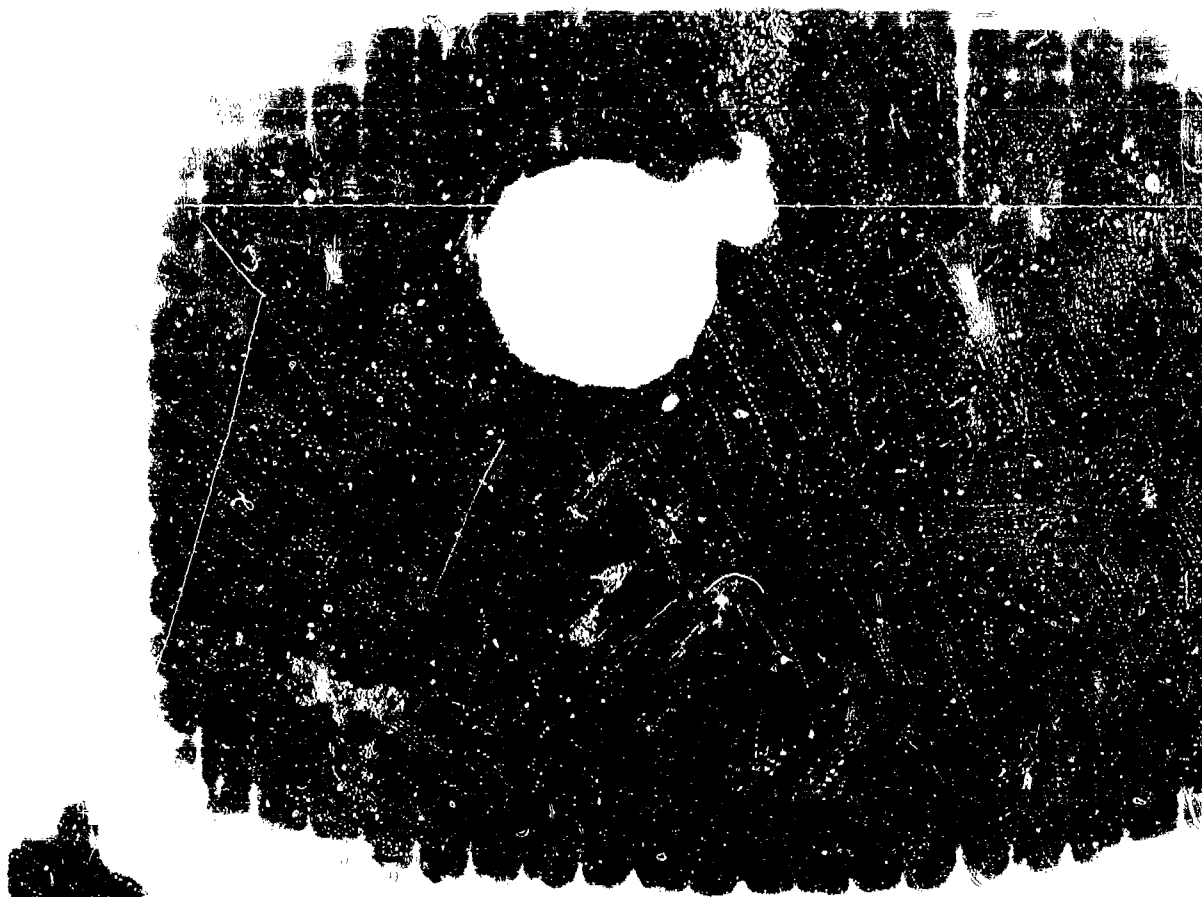


Figure 1. A dark, textured rectangular object with a large, irregular white hole in the center. The object has a rough, possibly metallic or plastic, surface with visible grain and some lighter spots. The hole is roughly circular but has jagged edges. The object is set against a plain white background.



Figure 2. A dark, textured rectangular object with a large, irregular white hole in the center. The object has a rough, possibly metallic or plastic, surface with visible grain and some lighter spots. The hole is roughly circular but has jagged edges. The object is set against a plain white background.



1. The first of the three photographs shows a view of the river from the bridge. The river is wide and shallow, with a sandy bottom. The water is clear and reflects the sky. The banks are covered with trees and bushes. The bridge is visible in the distance.



2. The second of the three photographs shows a view of the river from the bridge. The river is wide and shallow, with a sandy bottom. The water is clear and reflects the sky. The banks are covered with trees and bushes. The bridge is visible in the distance.



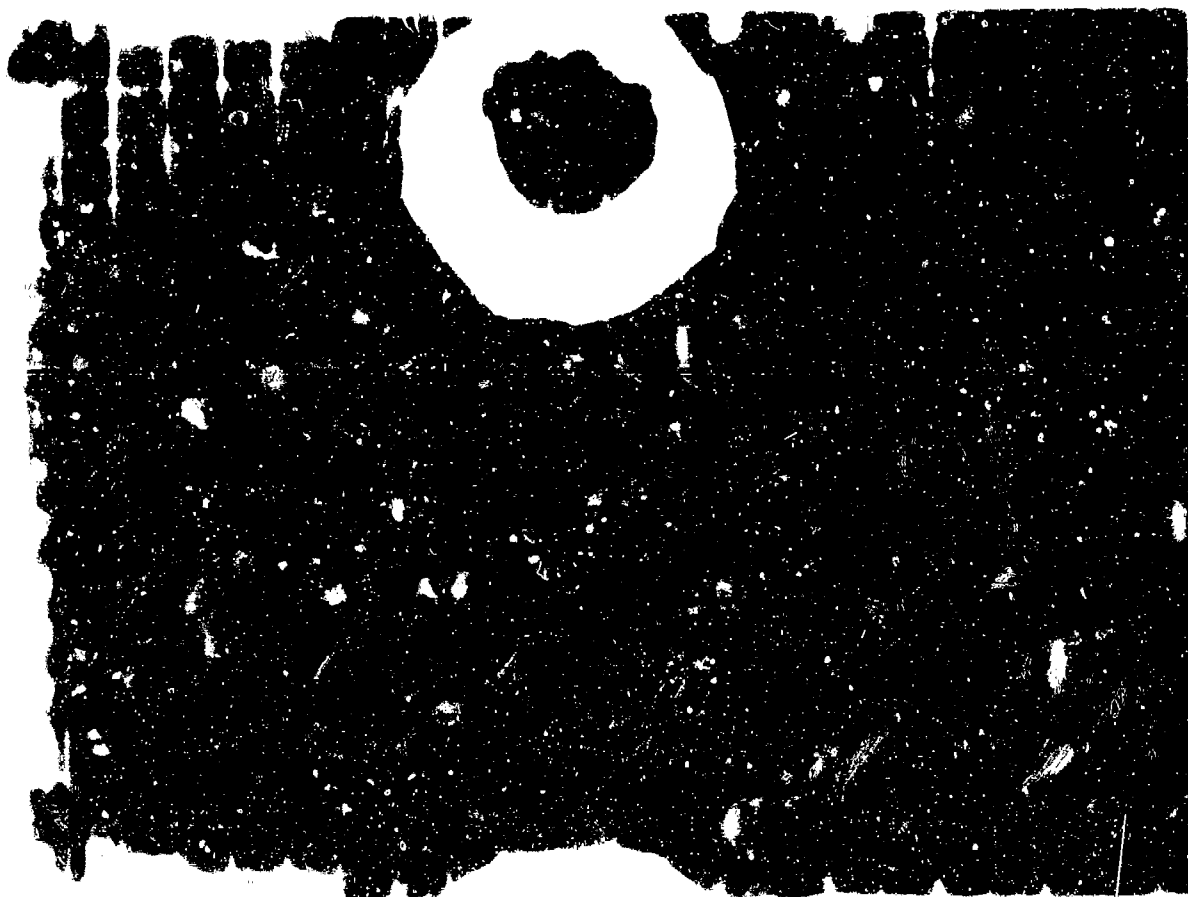
8 27 10 11 12 13 14 15 16 17 18 19 20 21 22 23 24 25 26 27 28 29 30 31 32 33 34 35 36 37 38 39 40 41 42 43 44 45 46 47 48 49 50 51 52 53 54 55 56 57 58 59 60 61 62 63 64 65 66 67 68 69 70 71 72 73 74 75 76 77 78 79 80 81 82 83 84 85 86 87 88 89 90 91 92 93 94 95 96 97 98 99 100



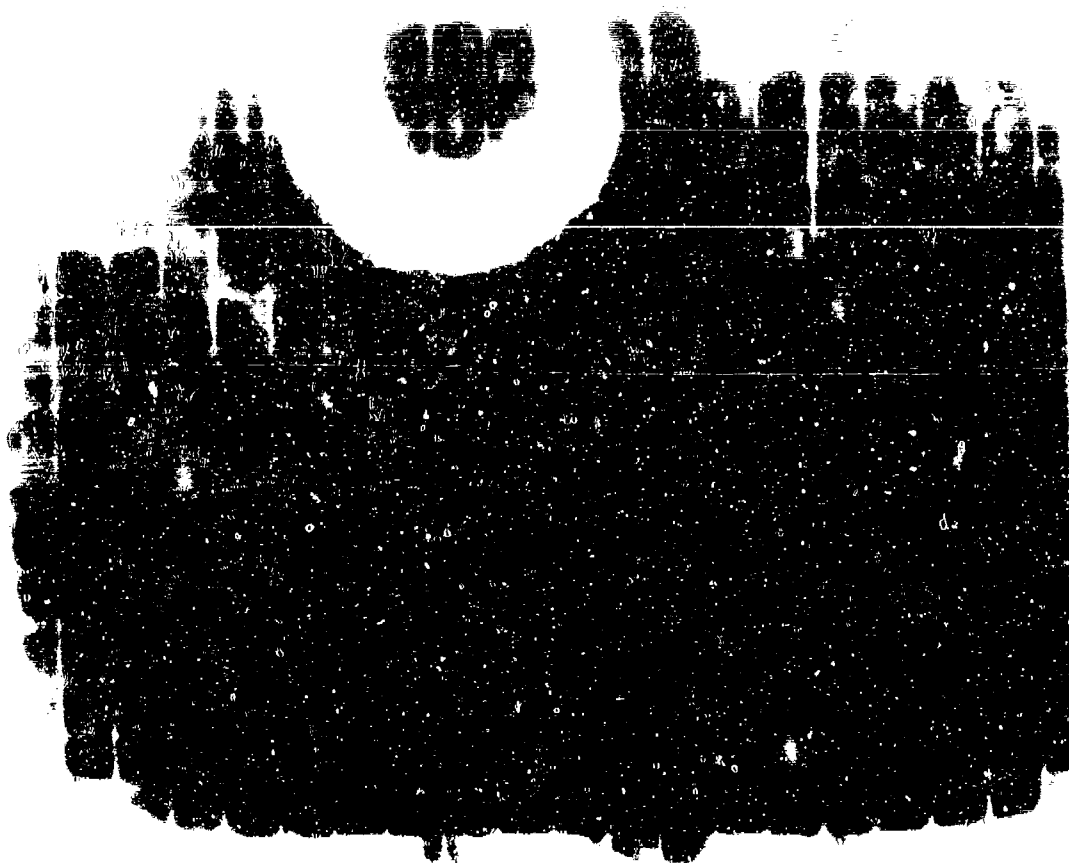
8 27 10 11 12 13 14 15 16 17 18 19 20 21 22 23 24 25 26 27 28 29 30 31 32 33 34 35 36 37 38 39 40 41 42 43 44 45 46 47 48 49 50 51 52 53 54 55 56 57 58 59 60 61 62 63 64 65 66 67 68 69 70 71 72 73 74 75 76 77 78 79 80 81 82 83 84 85 86 87 88 89 90 91 92 93 94 95 96 97 98 99 100

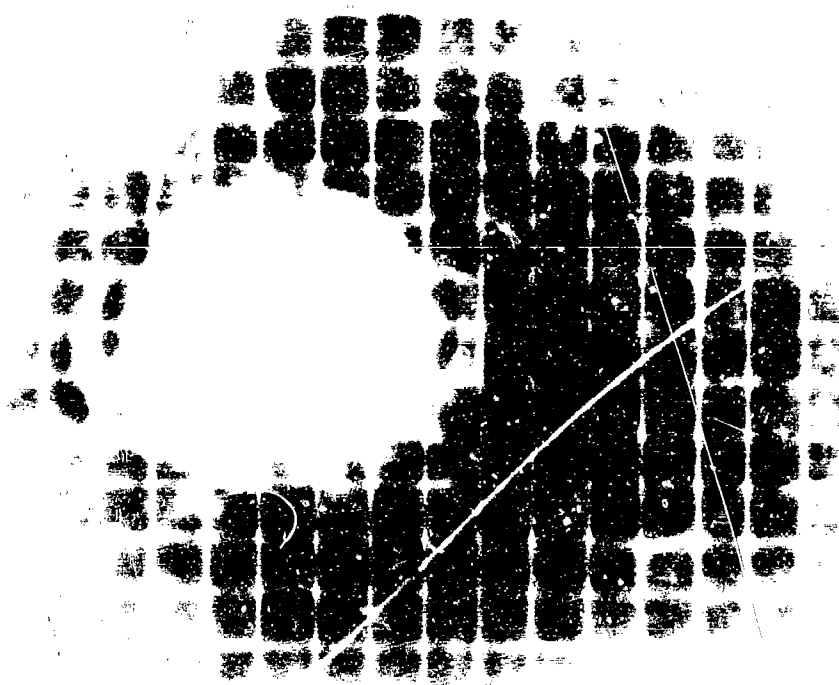


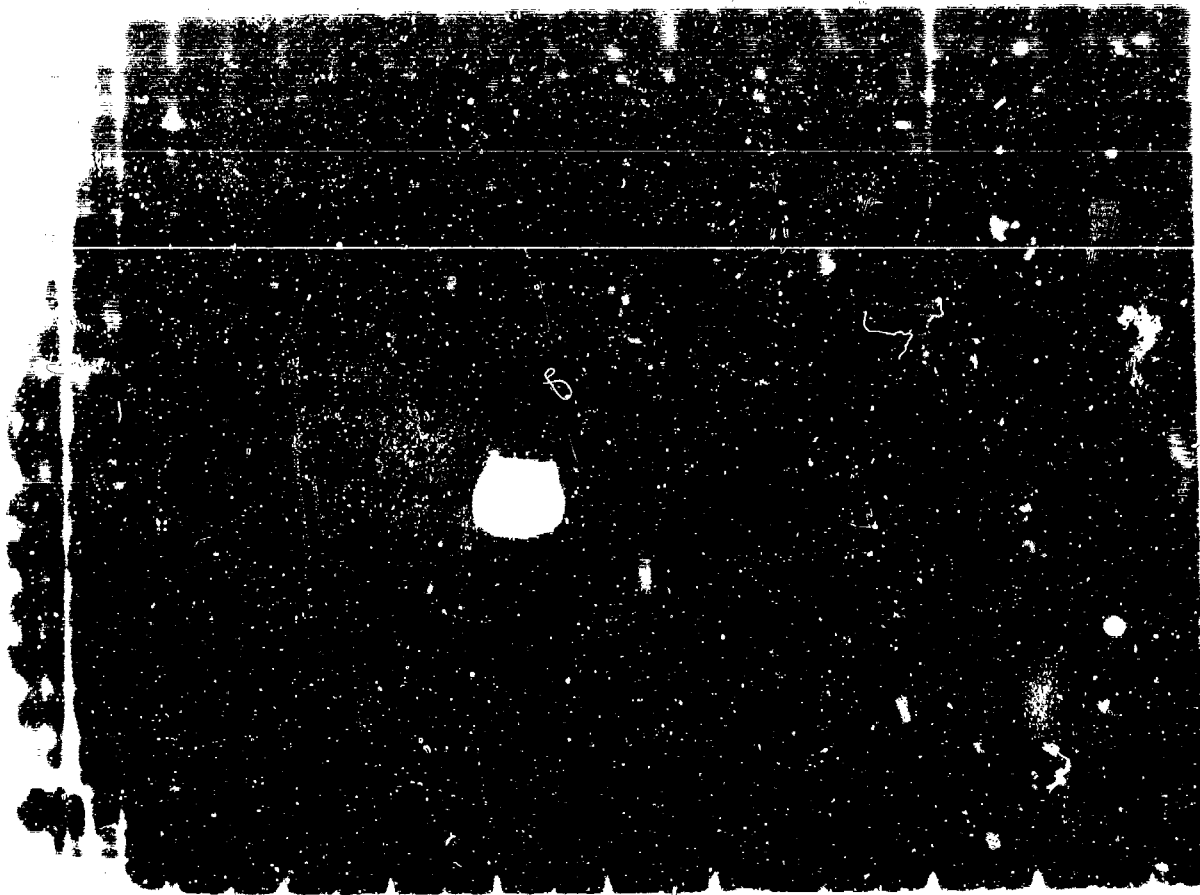
1. 2. 3. 4. 5. 6. 7. 8. 9. 10. 11. 12. 13. 14. 15. 16. 17. 18. 19. 20. 21. 22. 23. 24. 25. 26. 27. 28. 29. 30. 31. 32. 33. 34. 35. 36. 37. 38. 39. 40. 41. 42. 43. 44. 45. 46. 47. 48. 49. 50. 51. 52. 53. 54. 55. 56. 57. 58. 59. 60. 61. 62. 63. 64. 65. 66. 67. 68. 69. 70. 71. 72. 73. 74. 75. 76. 77. 78. 79. 80. 81. 82. 83. 84. 85. 86. 87. 88. 89. 90. 91. 92. 93. 94. 95. 96. 97. 98. 99. 100.

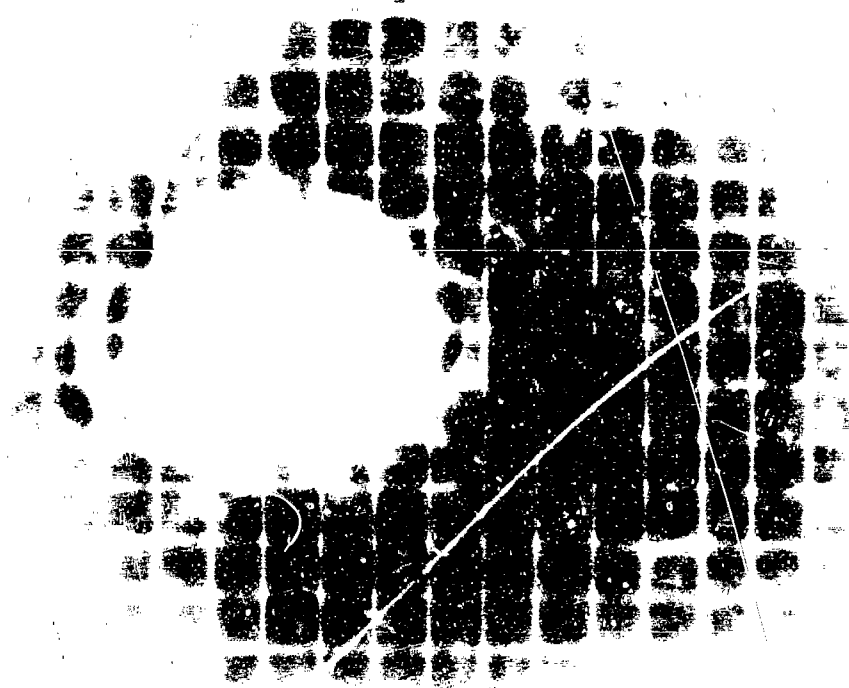


1. 2. 3. 4. 5. 6. 7. 8. 9. 10. 11. 12. 13. 14. 15. 16. 17. 18. 19. 20. 21. 22. 23. 24. 25. 26. 27. 28. 29. 30. 31. 32. 33. 34. 35. 36. 37. 38. 39. 40. 41. 42. 43. 44. 45. 46. 47. 48. 49. 50. 51. 52. 53. 54. 55. 56. 57. 58. 59. 60. 61. 62. 63. 64. 65. 66. 67. 68. 69. 70. 71. 72. 73. 74. 75. 76. 77. 78. 79. 80. 81. 82. 83. 84. 85. 86. 87. 88. 89. 90. 91. 92. 93. 94. 95. 96. 97. 98. 99. 100.









$\frac{1}{\sqrt{2}} \begin{pmatrix} 1 & i \\ -1 & i \end{pmatrix}$

[illegible]

1. The first part of the report is a summary of the work done during the year.

2. The second part of the report is a detailed account of the work done during the year.

1980年12月25日

1990年12月10日

SECRET

Figure 1. A 2D plot showing the relationship between the variables X and Y. The plot displays a series of data points forming a grid-like pattern, with a central cluster of points and several outliers. The axes are labeled X and Y, and the plot includes a title and axis labels.

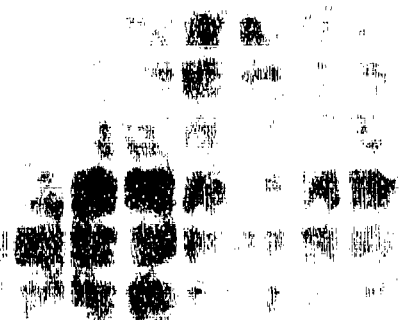


Figure 2. A 2D plot showing the relationship between the variables X and Y. The plot displays a series of data points forming a grid-like pattern, with a central cluster of points and several outliers. The axes are labeled X and Y, and the plot includes a title and axis labels.

Figure 8.80: Effect of the magnetic field on the plasma density profile for $B = 0.5$ T.

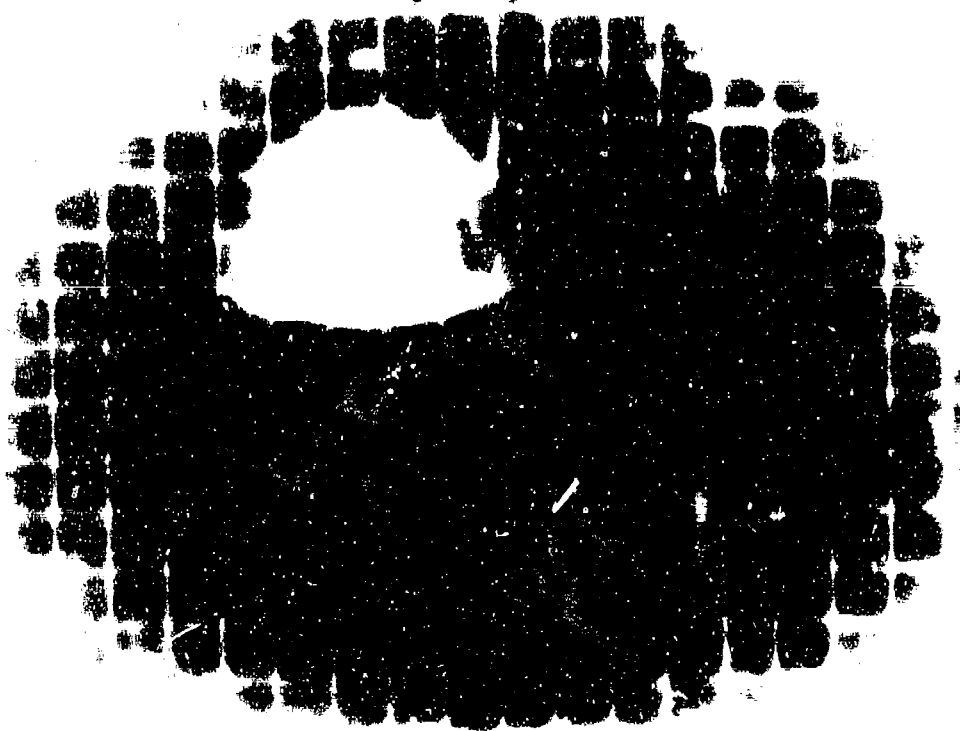
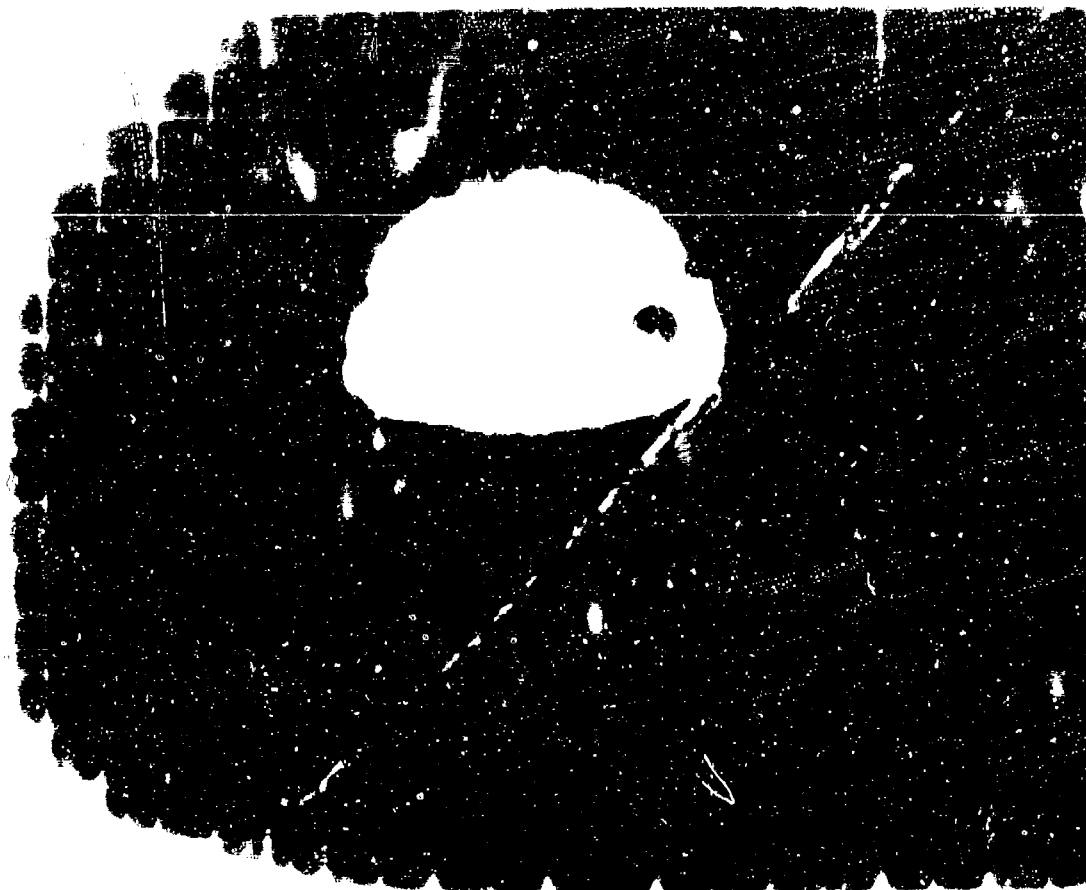


Figure 8.81: Effect of the magnetic field on the plasma density profile for $B = 1.0$ T.



1. 2010年12月31日，公司总资产为1,000,000,000.00元，净资产为500,000,000.00元。



姓名: _____ 性别: _____ 年龄: _____ 职业: _____
 联系电话: _____ 电子邮箱: _____



Figure 1. The image shows a circular object, possibly a face or mask, with a dark, textured background. The object is centrally located and appears to have some internal features, though they are obscured by the high contrast. The background is dark and grainy, with some lighter, irregular shapes.

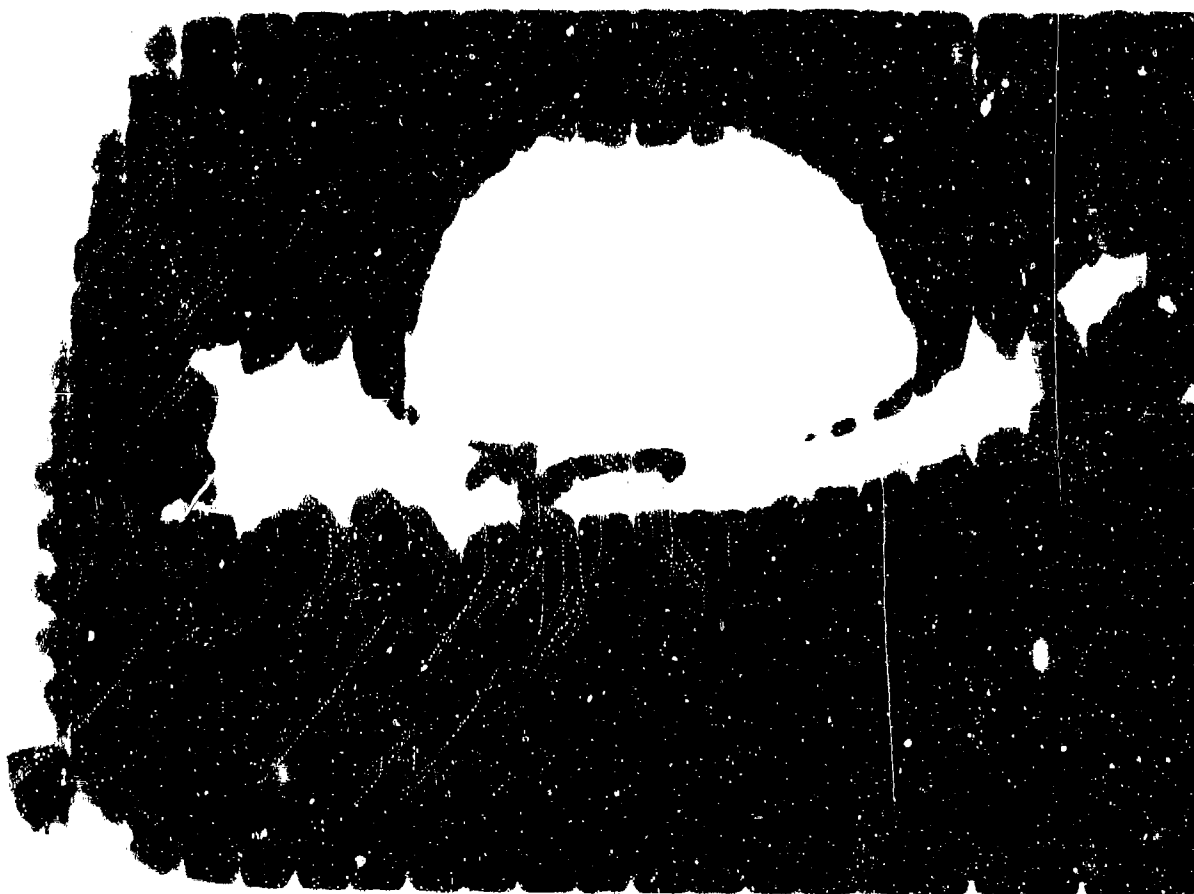


Figure 2. The image shows a circular object, possibly a face or mask, with a dark, textured background. The object is centrally located and appears to have some internal features, though they are obscured by the high contrast. The background is dark and grainy, with some lighter, irregular shapes.

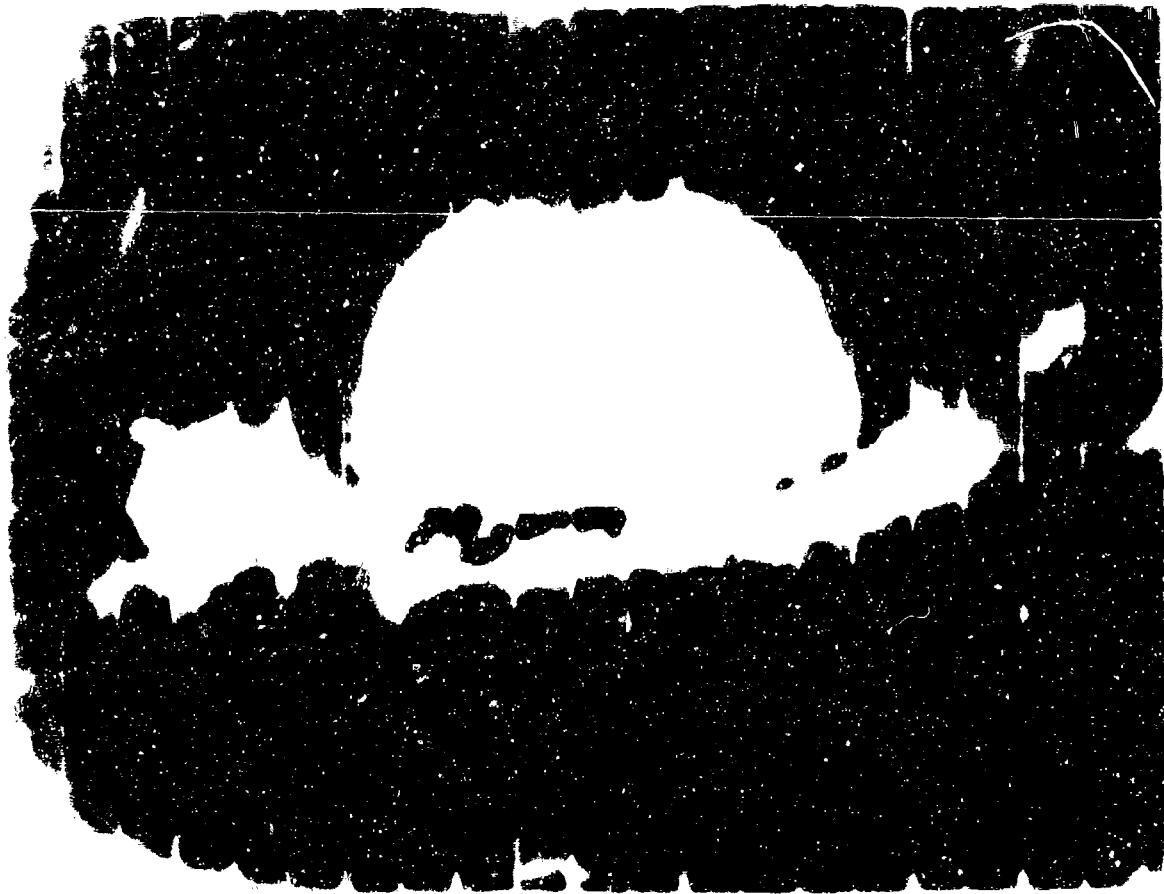


Figure 1. Skull of a human (Homo sapiens) showing the eye sockets and nasal cavity. The image is heavily degraded with significant noise and artifacts.

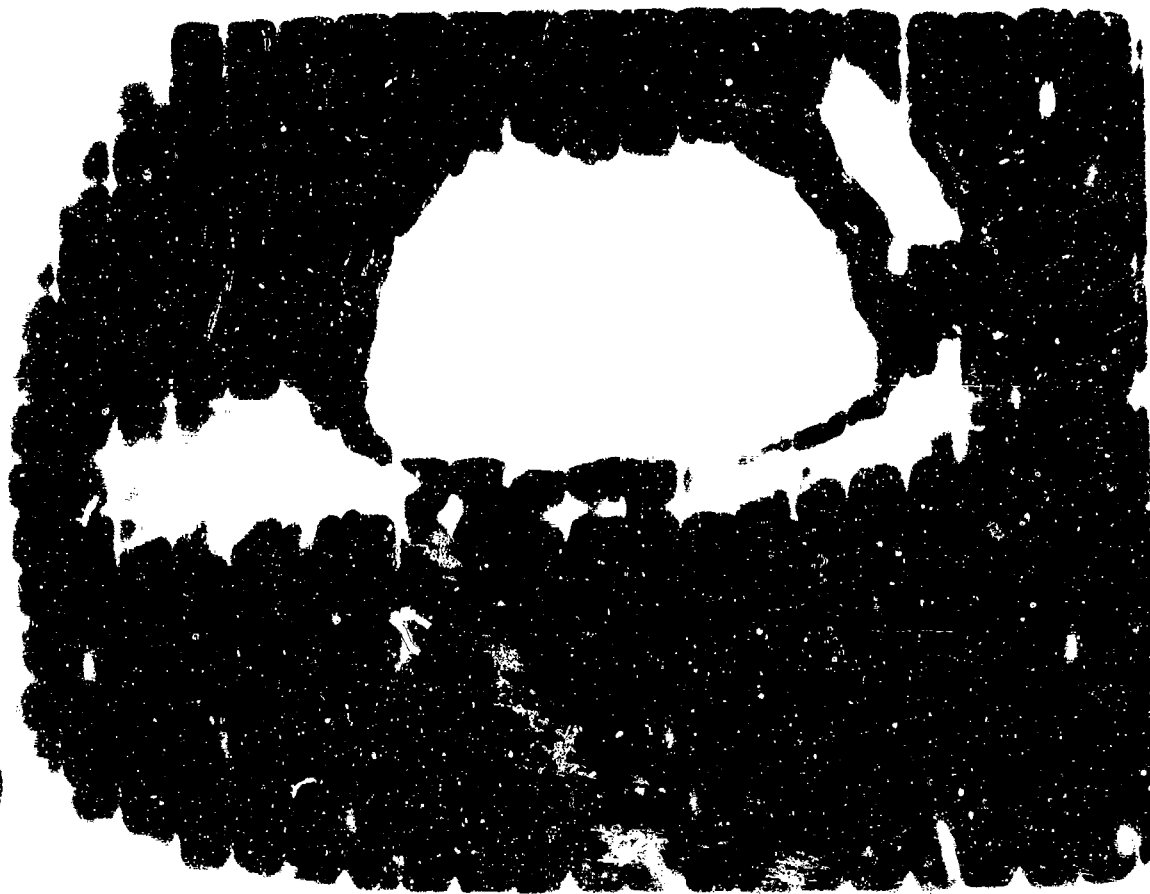


Figure 2. Skull of a human (Homo sapiens) showing the eye sockets and nasal cavity. The image is heavily degraded with significant noise and artifacts.

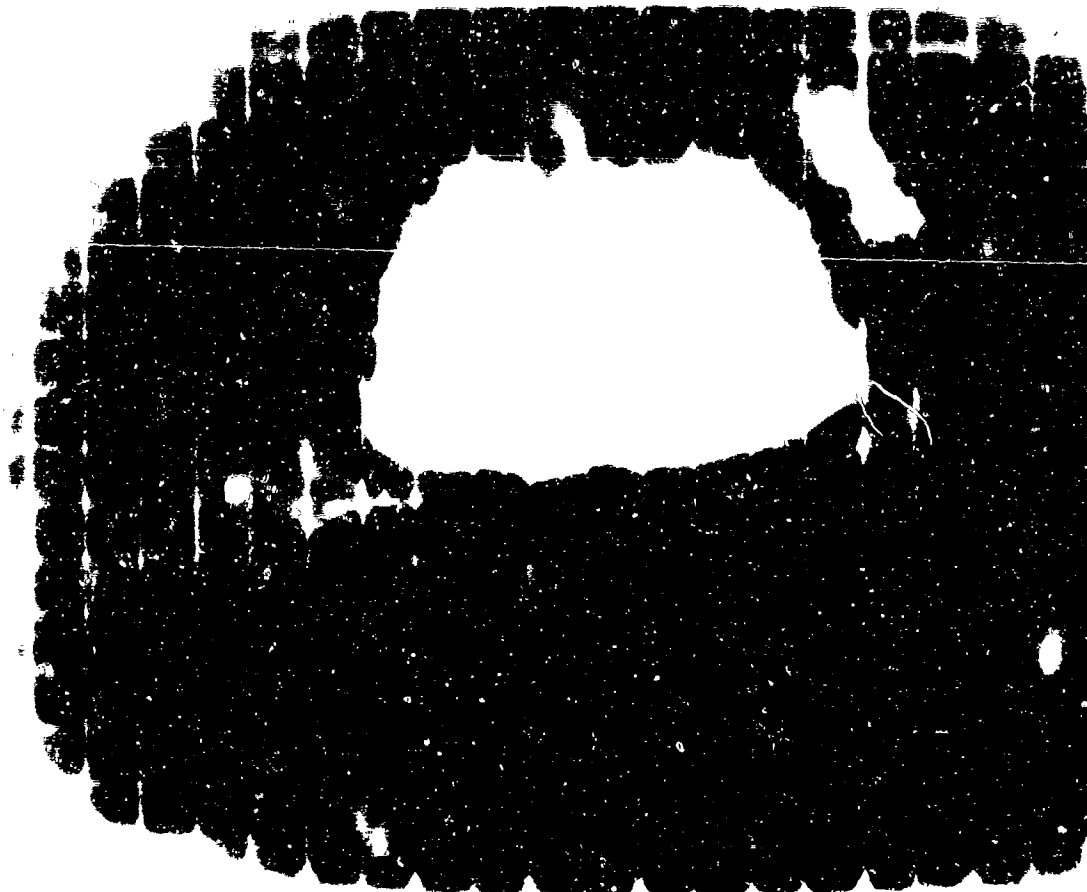


Figure 1. A dark, irregularly shaped object with a large, bright white circular hole in the center. The object has a rough, textured appearance, possibly made of wood or stone, and is set against a black background.



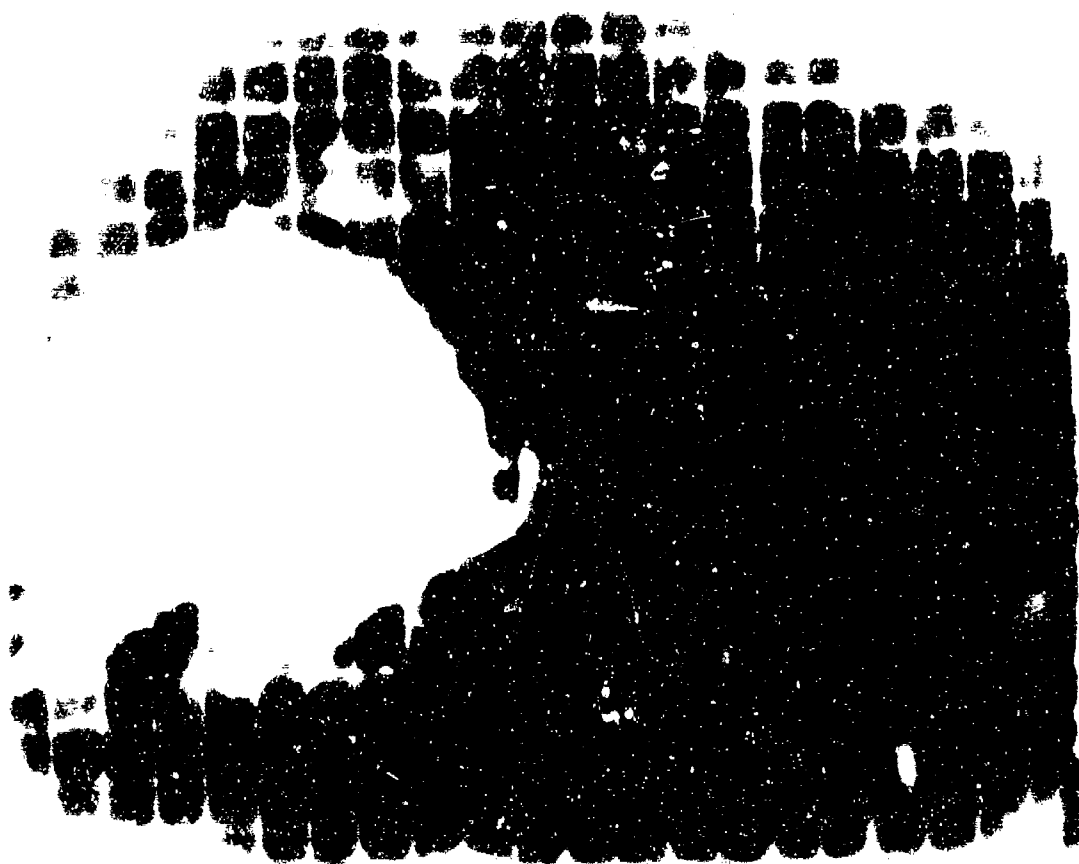
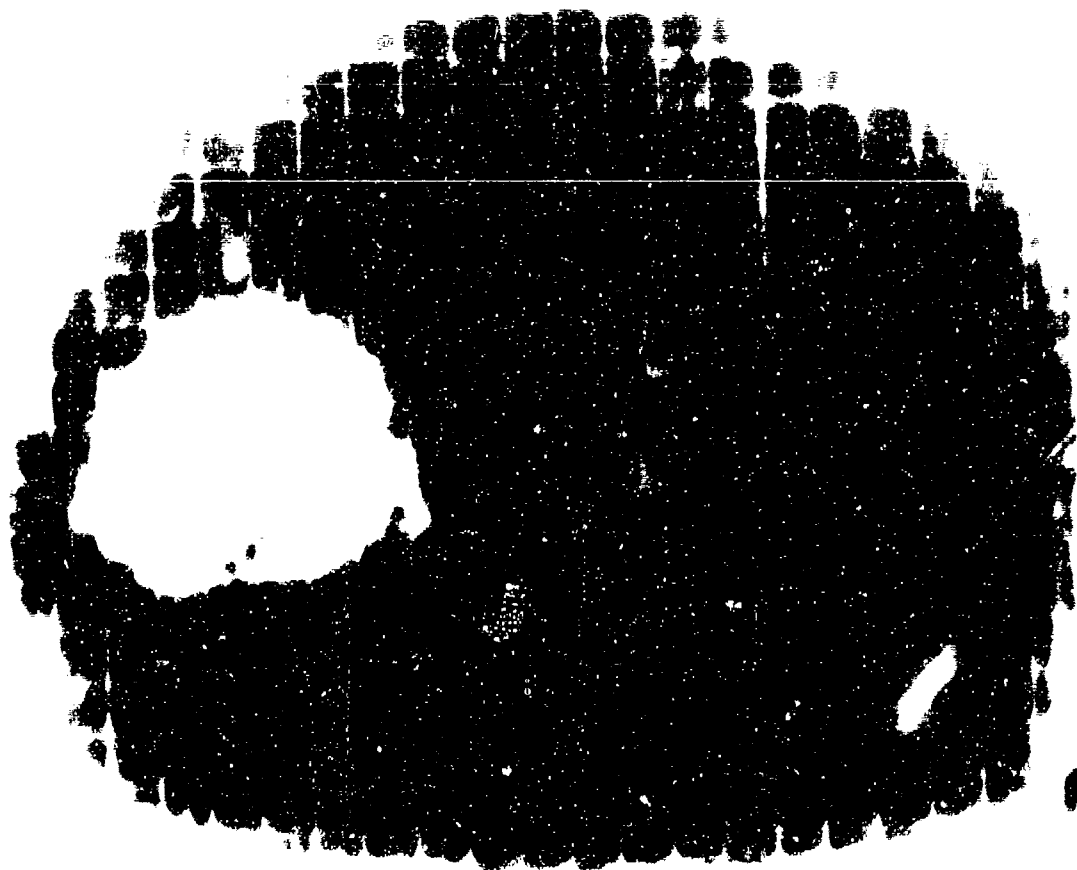
Figure 2. A dark, irregularly shaped object with a large, bright white circular hole in the center. The object has a rough, textured appearance, possibly made of wood or stone, and is set against a black background.



Figure 1. A dark, textured rectangular object with a large, irregular white hole in the center.



Figure 2. A dark, textured rectangular object with a large, irregular white hole in the center, showing more detail than the first image.



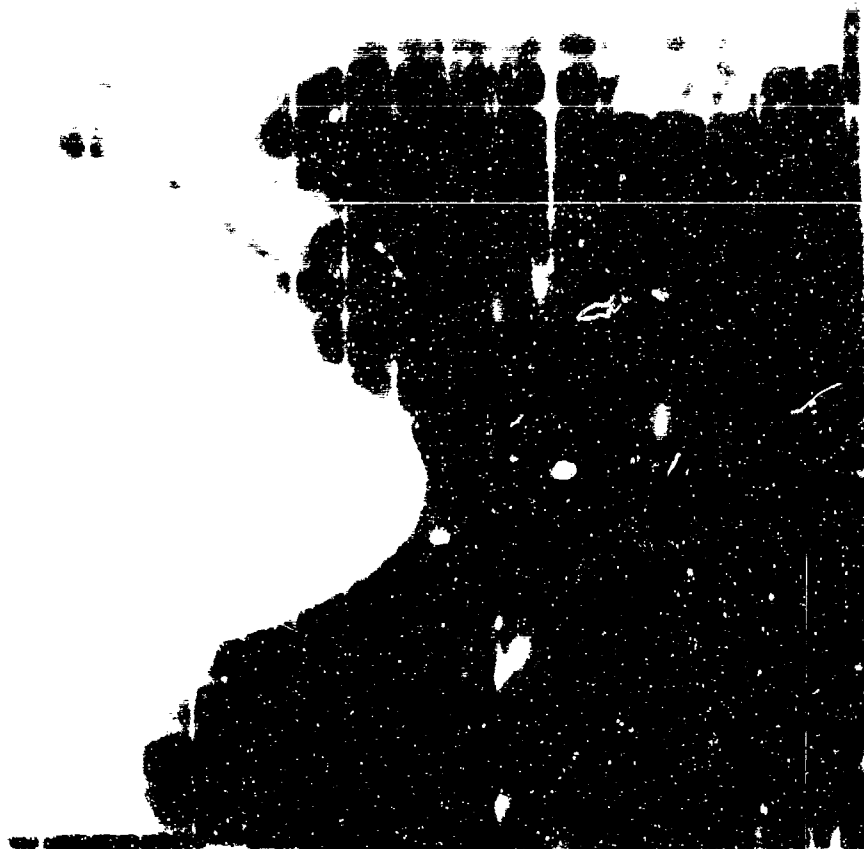




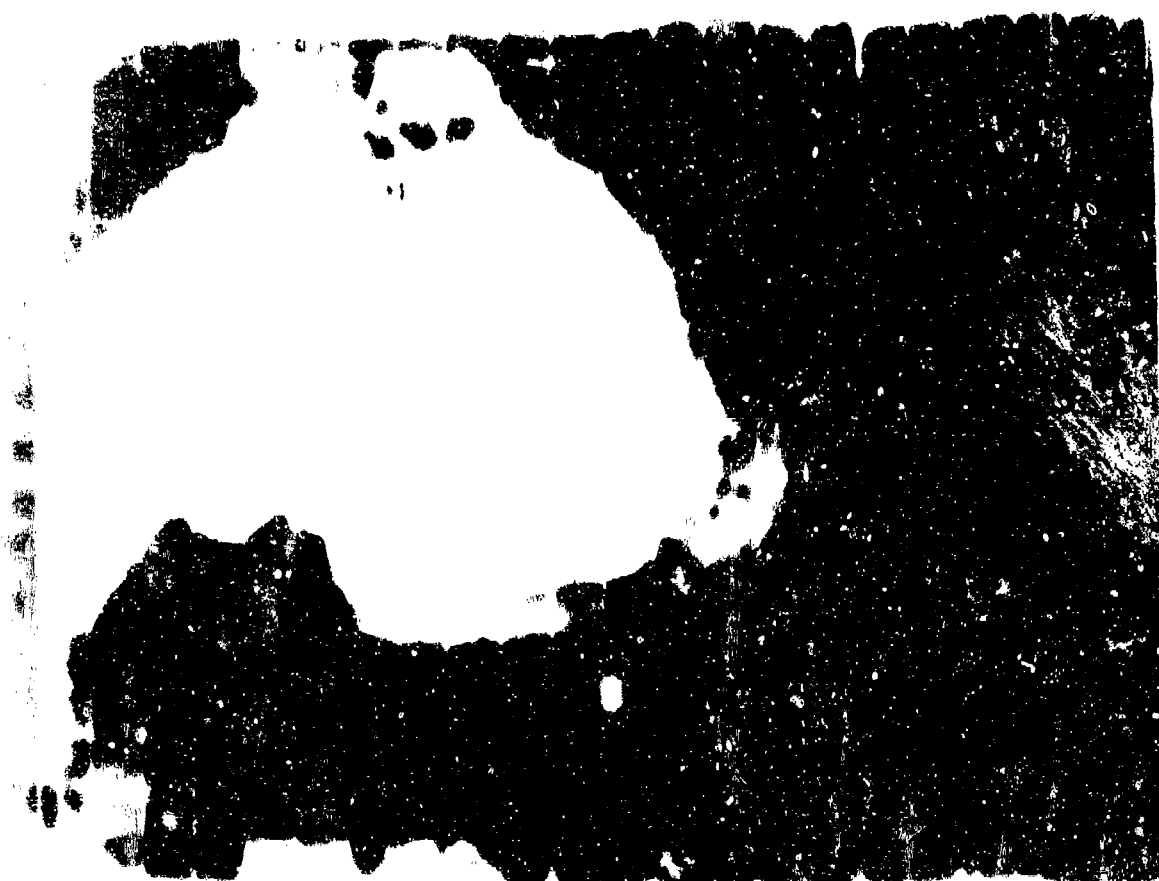
Figure 1. A photograph of a large, bright, irregularly shaped object, possibly a cloud or smoke plume, against a dark, textured background. The object has a jagged, irregular edge and a bright, almost white center. The background is dark and filled with numerous small, light-colored specks and larger, faint, irregular shapes, suggesting a complex, possibly organic or geological, structure. The overall image has a grainy, high-contrast quality typical of older film photography.



Figure 2. A photograph of a large, bright, irregularly shaped object, possibly a cloud or smoke plume, against a dark, textured background. The object has a jagged, irregular edge and a bright, almost white center. The background is dark and filled with numerous small, light-colored specks and larger, faint, irregular shapes, suggesting a complex, possibly organic or geological, structure. The overall image has a grainy, high-contrast quality typical of older film photography.



9. 10. 11. 12. 13. 14. 15. 16. 17. 18. 19. 20. 21. 22. 23. 24. 25. 26. 27. 28. 29. 30. 31. 32. 33. 34. 35. 36. 37. 38. 39. 40. 41. 42. 43. 44. 45. 46. 47. 48. 49. 50. 51. 52. 53. 54. 55. 56. 57. 58. 59. 60. 61. 62. 63. 64. 65. 66. 67. 68. 69. 70. 71. 72. 73. 74. 75. 76. 77. 78. 79. 80. 81. 82. 83. 84. 85. 86. 87. 88. 89. 90. 91. 92. 93. 94. 95. 96. 97. 98. 99. 100.



101. 102. 103. 104. 105. 106. 107. 108. 109. 110. 111. 112. 113. 114. 115. 116. 117. 118. 119. 120. 121. 122. 123. 124. 125. 126. 127. 128. 129. 130. 131. 132. 133. 134. 135. 136. 137. 138. 139. 140. 141. 142. 143. 144. 145. 146. 147. 148. 149. 150. 151. 152. 153. 154. 155. 156. 157. 158. 159. 160. 161. 162. 163. 164. 165. 166. 167. 168. 169. 170. 171. 172. 173. 174. 175. 176. 177. 178. 179. 180. 181. 182. 183. 184. 185. 186. 187. 188. 189. 190. 191. 192. 193. 194. 195. 196. 197. 198. 199. 200.



Figure 1. A photograph of a large, dark, irregularly shaped object, possibly a piece of debris or a heavily damaged component, with a lighter, circular area in the upper left corner.



Figure 2. A photograph of a large, dark, irregularly shaped object, possibly a piece of debris or a heavily damaged component, with a lighter, circular area in the upper left corner.

Figure 1. A 1000 Å image of the central region of the M87 galaxy. The image shows the central region of the galaxy, including the nucleus and the surrounding structure. The image is a grayscale representation of the light intensity in the 1000 Å band.

Figure 2. A 1000 Å image of the central region of the M87 galaxy. The image shows the central region of the galaxy, including the nucleus and the surrounding structure. The image is a grayscale representation of the light intensity in the 1000 Å band.

1000

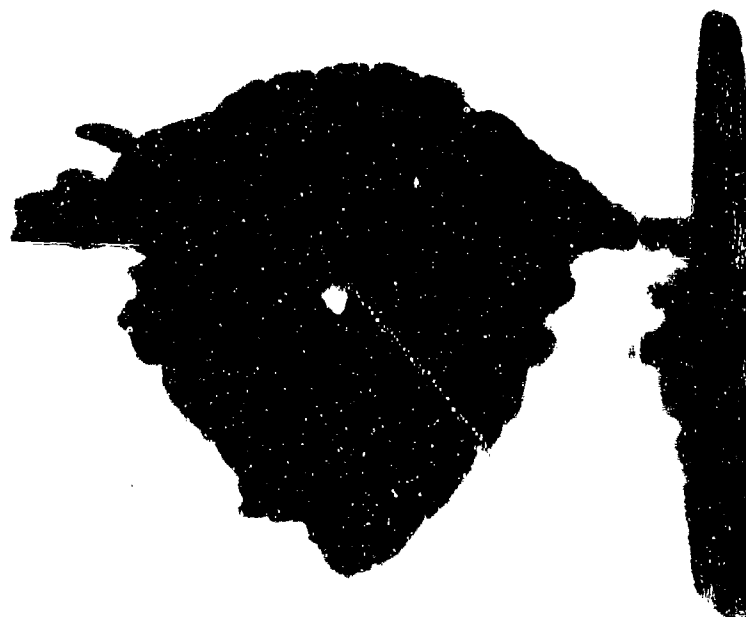
1000 1000

Figure 1. 1980-1981 Seasonal Distribution of the American Bittern in the Sacramento-San Joaquin River Delta

Figure 2. 1980-1981 Seasonal Distribution of the American Bittern in the Sacramento-San Joaquin River Delta



10-10-68



1. The first group of people who are not in the labor force are those who are not in the labor force because they are not in the labor force.



Figure 1. A. The most common form of the specimen. B. The specimen in a different form.



Figure 2. A. The most common form of the specimen. B. The specimen in a different form.



Figure 4. The effect of the concentration of the solution on the rate of the reaction.



Figure 5. The effect of the concentration of the solution on the rate of the reaction.

Figure 1. A. B. C. D. E. F. G. H. I. J. K. L. M. N. O. P. Q. R. S. T. U. V. W. X. Y. Z. AA. AB. AC. AD. AE. AF. AG. AH. AI. AJ. AK. AL. AM. AN. AO. AP. AQ. AR. AS. AT. AU. AV. AW. AX. AY. AZ. BA. BB. BC. BD. BE. BF. BG. BH. BI. BJ. BK. BL. BM. BN. BO. BP. BQ. BR. BS. BT. BU. BV. BW. BX. BY. BZ. CA. CB. CC. CD. CE. CF. CG. CH. CI. CJ. CK. CL. CM. CN. CO. CP. CQ. CR. CS. CT. CU. CV. CW. CX. CY. CZ. DA. DB. DC. DD. DE. DF. DG. DH. DI. DJ. DK. DL. DM. DN. DO. DP. DQ. DR. DS. DT. DU. DV. DW. DX. DY. DZ. EA. EB. EC. ED. EE. EF. EG. EH. EI. EJ. EK. EL. EM. EN. EO. EP. EQ. ER. ES. ET. EU. EV. EW. EX. EY. EZ. FA. FB. FC. FD. FE. FF. FG. FH. FI. FJ. FK. FL. FM. FN. FO. FP. FQ. FR. FS. FT. FU. FV. FW. FX. FY. FZ. GA. GB. GC. GD. GE. GF. GG. GH. GI. GJ. GK. GL. GM. GN. GO. GP. GQ. GR. GS. GT. GU. GV. GW. GX. GY. GZ. HA. HB. HC. HD. HE. HF. HG. HH. HI. HJ. HK. HL. HM. HN. HO. HP. HQ. HR. HS. HT. HU. HV. HW. HX. HY. HZ. IA. IB. IC. ID. IE. IF. IG. IH. II. IJ. IK. IL. IM. IN. IO. IP. IQ. IR. IS. IT. IU. IV. IW. IX. IY. IZ. JA. JB. JC. JD. JE. JF. JG. JH. JI. JJ. JK. JL. JM. JN. JO. JP. JQ. JR. JS. JT. JU. JV. JW. JX. JY. JZ. KA. KB. KC. KD. KE. KF. KG. KH. KI. KJ. KK. KL. KM. KN. KO. KP. KQ. KR. KS. KT. KU. KV. KW. KX. KY. KZ. LA. LB. LC. LD. LE. LF. LG. LH. LI. LJ. LK. LL. LM. LN. LO. LP. LQ. LR. LS. LT. LU. LV. LW. LX. LY. LZ. MA. MB. MC. MD. ME. MF. MG. MH. MI. MJ. MK. ML. MM. MN. MO. MP. MQ. MR. MS. MT. MU. MV. MW. MX. MY. MZ. NA. NB. NC. ND. NE. NF. NG. NH. NI. NJ. NK. NL. NM. NN. NO. NP. NQ. NR. NS. NT. NU. NV. NW. NX. NY. NZ. OA. OB. OC. OD. OE. OF. OG. OH. OI. OJ. OK. OL. OM. ON. OO. OP. OQ. OR. OS. OT. OU. OV. OW. OX. OY. OZ. PA. PB. PC. PD. PE. PF. PG. PH. PI. PJ. PK. PL. PM. PN. PO. PP. PQ. PR. PS. PT. PU. PV. PW. PX. PY. PZ. QA. QB. QC. QD. QE. QF. QG. QH. QI. QJ. QK. QL. QM. QN. QO. QP. QQ. QR. QS. QT. QU. QV. QW. QX. QY. QZ. RA. RB. RC. RD. RE. RF. RG. RH. RI. RJ. RK. RL. RM. RN. RO. RP. RQ. RR. RS. RT. RU. RV. RW. RX. RY. RZ. SA. SB. SC. SD. SE. SF. SG. SH. SI. SJ. SK. SL. SM. SN. SO. SP. SQ. SR. SS. ST. SU. SV. SW. SX. SY. SZ. TA. TB. TC. TD. TE. TF. TG. TH. TI. TJ. TK. TL. TM. TN. TO. TP. TQ. TR. TS. TT. TU. TV. TW. TX. TY. TZ. UA. UB. UC. UD. UE. UF. UG. UH. UI. UJ. UK. UL. UM. UN. UO. UP. UQ. UR. US. UT. UU. UV. UW. UX. UY. UZ. VA. VB. VC. VD. VE. VF. VG. VH. VI. VJ. VK. VL. VM. VN. VO. VP. VQ. VR. VS. VT. VU. VV. VW. VX. VY. VZ. WA. WB. WC. WD. WE. WF. WG. WH. WI. WJ. WK. WL. WM. WN. WO. WP. WQ. WR. WS. WT. WU. WV. WW. WX. WY. WZ. XA. XB. XC. XD. XE. XF. XG. XH. XI. XJ. XK. XL. XM. XN. XO. XP. XQ. XR. XS. XT. XU. XV. XW. XX. XY. XZ. YA. YB. YC. YD. YE. YF. YG. YH. YI. YJ. YK. YL. YM. YN. YO. YP. YQ. YR. YS. YT. YU. YV. YW. YX. YY. YZ. ZA. ZB. ZC. ZD. ZE. ZF. ZG. ZH. ZI. ZJ. ZK. ZL. ZM. ZN. ZO. ZP. ZQ. ZR. ZS. ZT. ZU. ZV. ZW. ZX. ZY. ZZ.

1. The first group of people who are interested in the results of the study are the researchers themselves. They want to know if the study was successful in achieving its objectives and if the results are consistent with their expectations.

1. 1990年12月，在《中国环境报》上刊登了“中国环境报”的“中国环境报”广告。

1 2 3 4 5 6



Figure 1. The structure of the ...



Figure 2. The structure of the ...



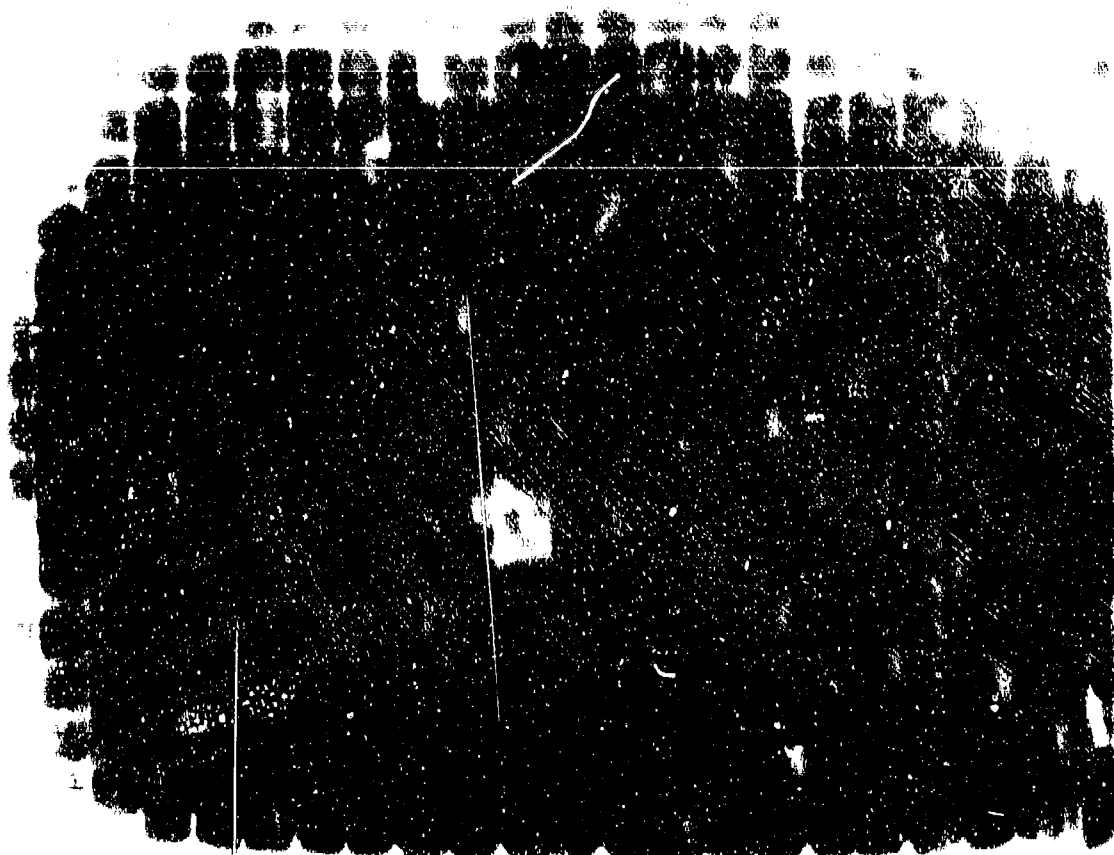
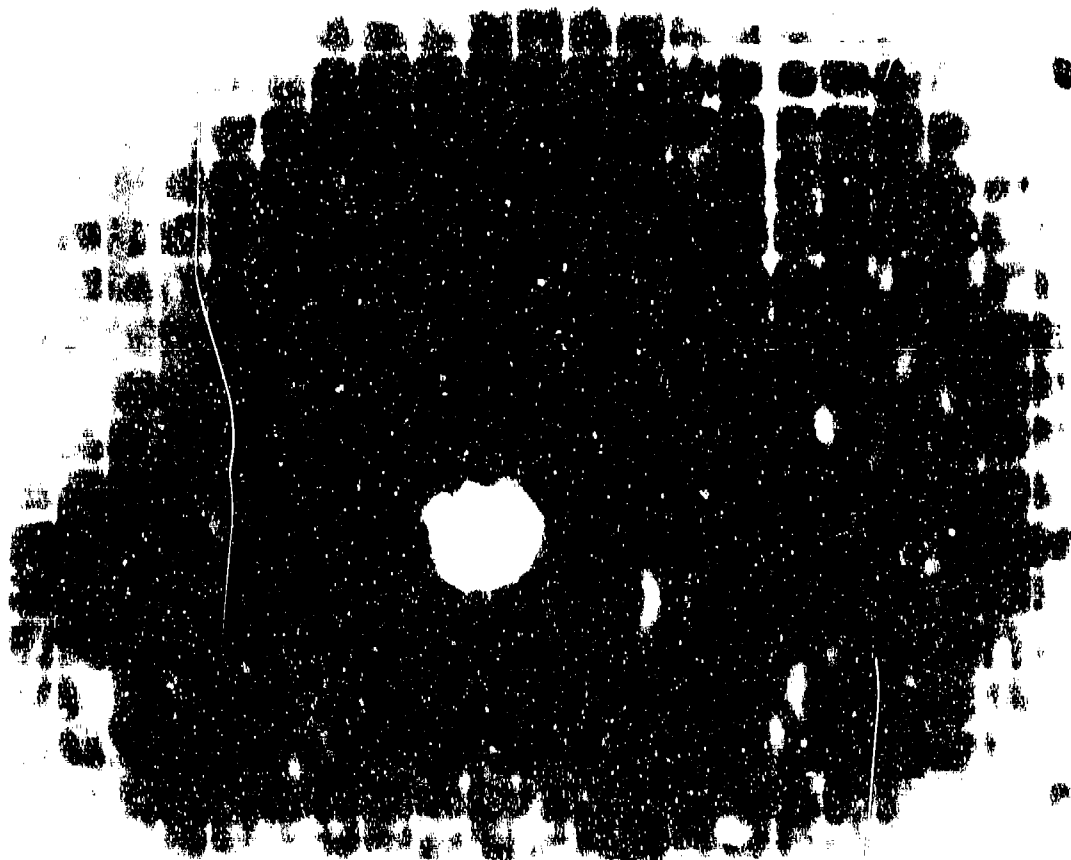


FIGURE 1.1. (a) (b) (c) (d) (e) (f) (g) (h) (i) (j) (k) (l) (m) (n) (o) (p) (q) (r) (s) (t) (u) (v) (w) (x) (y) (z) (aa) (ab) (ac) (ad) (ae) (af) (ag) (ah) (ai) (aj) (ak) (al) (am) (an) (ao) (ap) (aq) (ar) (as) (at) (au) (av) (aw) (ax) (ay) (az) (ba) (bb) (bc) (bd) (be) (bf) (bg) (bh) (bi) (bj) (bk) (bl) (bm) (bn) (bo) (bp) (bq) (br) (bs) (bt) (bu) (bv) (bw) (bx) (by) (bz) (ca) (cb) (cc) (cd) (ce) (cf) (cg) (ch) (ci) (cj) (ck) (cl) (cm) (cn) (co) (cp) (cq) (cr) (cs) (ct) (cu) (cv) (cw) (cx) (cy) (cz) (da) (db) (dc) (dd) (de) (df) (dg) (dh) (di) (dj) (dk) (dl) (dm) (dn) (do) (dp) (dq) (dr) (ds) (dt) (du) (dv) (dw) (dx) (dy) (dz) (ea) (eb) (ec) (ed) (ee) (ef) (eg) (eh) (ei) (ej) (ek) (el) (em) (en) (eo) (ep) (eq) (er) (es) (et) (eu) (ev) (ew) (ex) (ey) (ez) (fa) (fb) (fc) (fd) (fe) (ff) (fg) (fh) (fi) (fj) (fk) (fl) (fm) (fn) (fo) (fp) (fq) (fr) (fs) (ft) (fu) (fv) (fw) (fx) (fy) (fz) (ga) (gb) (gc) (gd) (ge) (gf) (gg) (gh) (gi) (gj) (gk) (gl) (gm) (gn) (go) (gp) (gq) (gr) (gs) (gt) (gu) (gv) (gw) (gx) (gy) (gz) (ha) (hb) (hc) (hd) (he) (hf) (hg) (hh) (hi) (hj) (hk) (hl) (hm) (hn) (ho) (hp) (hq) (hr) (hs) (ht) (hu) (hv) (hw) (hx) (hy) (hz) (ia) (ib) (ic) (id) (ie) (if) (ig) (ih) (ii) (ij) (ik) (il) (im) (in) (io) (ip) (iq) (ir) (is) (it) (iu) (iv) (iw) (ix) (iy) (iz) (ja) (jb) (jc) (jd) (je) (jf) (jg) (jh) (ji) (jj) (jk) (jl) (jm) (jn) (jo) (jp) (jq) (jr) (js) (jt) (ju) (jv) (jw) (jx) (jy) (jz) (ka) (kb) (kc) (kd) (ke) (kf) (kg) (kh) (ki) (kj) (kk) (kl) (km) (kn) (ko) (kp) (kq) (kr) (ks) (kt) (ku) (kv) (kw) (kx) (ky) (kz) (la) (lb) (lc) (ld) (le) (lf) (lg) (lh) (li) (lj) (lk) (ll) (lm) (ln) (lo) (lp) (lq) (lr) (ls) (lt) (lu) (lv) (lw) (lx) (ly) (lz) (ma) (mb) (mc) (md) (me) (mf) (mg) (mh) (mi) (mj) (mk) (ml) (mm) (mn) (mo) (mp) (mq) (mr) (ms) (mt) (mu) (mv) (mw) (mx) (my) (mz) (na) (nb) (nc) (nd) (ne) (nf) (ng) (nh) (ni) (nj) (nk) (nl) (nm) (nn) (no) (np) (nq) (nr) (ns) (nt) (nu) (nv) (nw) (nx) (ny) (nz) (oa) (ob) (oc) (od) (oe) (of) (og) (oh) (oi) (oj) (ok) (ol) (om) (on) (oo) (op) (oq) (or) (os) (ot) (ou) (ov) (ow) (ox) (oy) (oz) (pa) (pb) (pc) (pd) (pe) (pf) (pg) (ph) (pi) (pj) (pk) (pl) (pm) (pn) (po) (pp) (pq) (pr) (ps) (pt) (pu) (pv) (pw) (px) (py) (pz) (qa) (qb) (qc) (qd) (qe) (qf) (qg) (qh) (qi) (qj) (qk) (ql) (qm) (qn) (qo) (qp) (qq) (qr) (qs) (qt) (qu) (qv) (qw) (qx) (qy) (qz) (ra) (rb) (rc) (rd) (re) (rf) (rg) (rh) (ri) (rj) (rk) (rl) (rm) (rn) (ro) (rp) (rq) (rr) (rs) (rt) (ru) (rv) (rw) (rx) (ry) (rz) (sa) (sb) (sc) (sd) (se) (sf) (sg) (sh) (si) (sj) (sk) (sl) (sm) (sn) (so) (sp) (sq) (sr) (ss) (st) (su) (sv) (sw) (sx) (sy) (sz) (ta) (tb) (tc) (td) (te) (tf) (tg) (th) (ti) (tj) (tk) (tl) (tm) (tn) (to) (tp) (tq) (tr) (ts) (tt) (tu) (tv) (tw) (tx) (ty) (tz) (ua) (ub) (uc) (ud) (ue) (uf) (ug) (uh) (ui) (uj) (uk) (ul) (um) (un) (uo) (up) (uq) (ur) (us) (ut) (uu) (uv) (uw) (ux) (uy) (uz) (va) (vb) (vc) (vd) (ve) (vf) (vg) (vh) (vi) (vj) (vk) (vl) (vm) (vn) (vo) (vp) (vq) (vr) (vs) (vt) (vu) (vv) (vw) (vx) (vy) (vz) (wa) (wb) (wc) (wd) (we) (wf) (wg) (wh) (wi) (wj) (wk) (wl) (wm) (wn) (wo) (wp) (wq) (wr) (ws) (wt) (wu) (wv) (ww) (wx) (wy) (wz) (xa) (xb) (xc) (xd) (xe) (xf) (xg) (xh) (xi) (xj) (xk) (xl) (xm) (xn) (xo) (xp) (xq) (xr) (xs) (xt) (xu) (xv) (xw) (xx) (xy) (xz) (ya) (yb) (yc) (yd) (ye) (yf) (yg) (yh) (yi) (yj) (yk) (yl) (ym) (yn) (yo) (yp) (yq) (yr) (ys) (yt) (yu) (yv) (yw) (yx) (yy) (yz) (za) (zb) (zc) (zd) (ze) (zf) (zg) (zh) (zi) (zj) (zk) (zl) (zm) (zn) (zo) (zp) (zq) (zr) (zs) (zt) (zu) (zv) (zw) (zx) (zy) (zz)



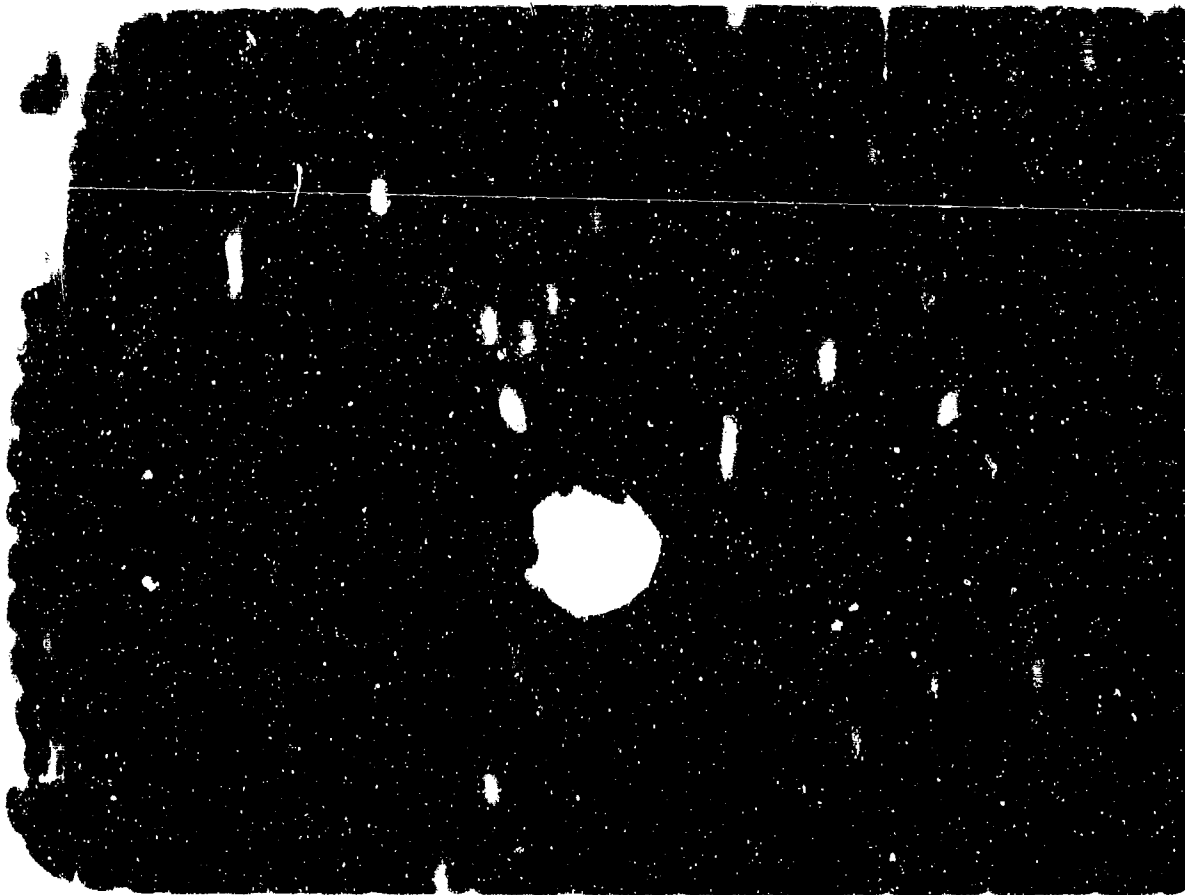


Figure 1. A 1.5 mm diameter hole in a 1.5 mm diameter plate. The hole is 1.5 mm in diameter. The plate is 1.5 mm in diameter. The hole is 1.5 mm in diameter. The plate is 1.5 mm in diameter.

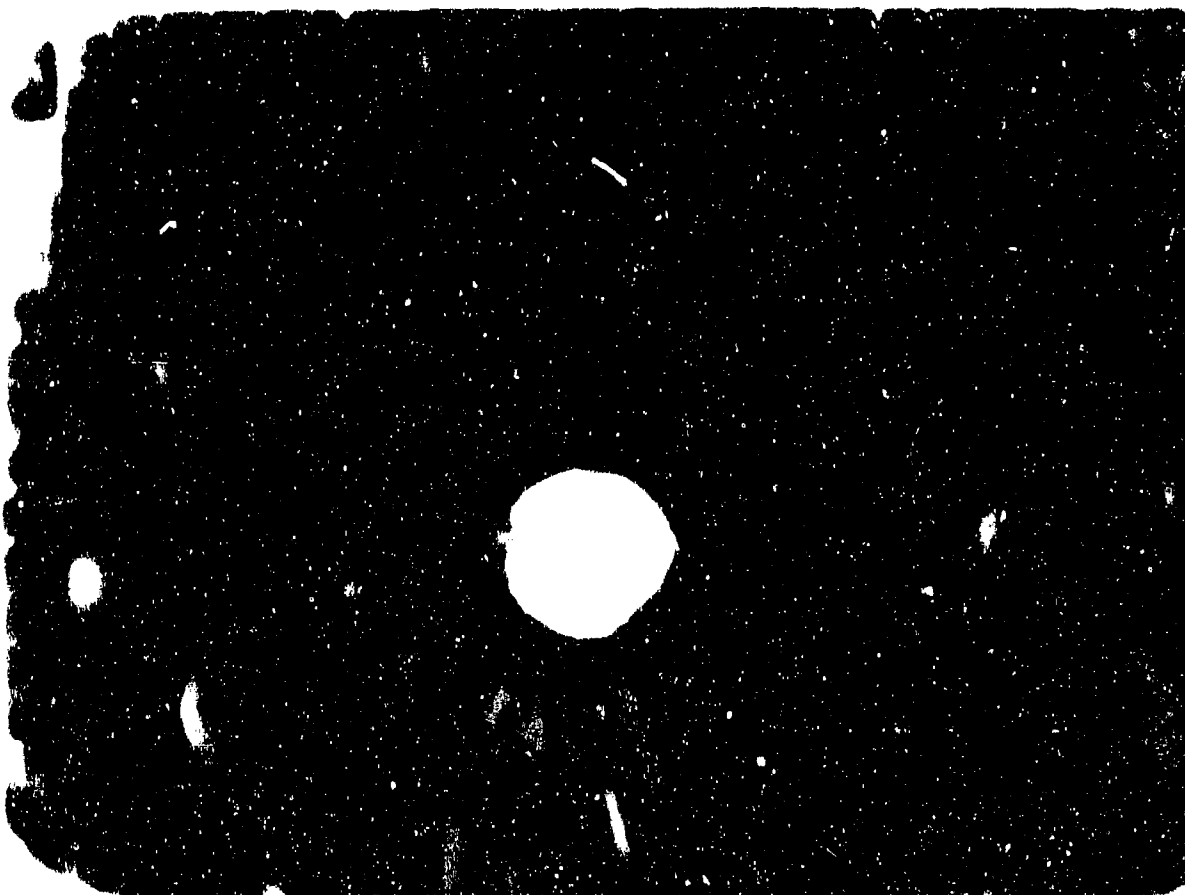


Figure 2. A 1.5 mm diameter hole in a 1.5 mm diameter plate. The hole is 1.5 mm in diameter. The plate is 1.5 mm in diameter. The hole is 1.5 mm in diameter. The plate is 1.5 mm in diameter.

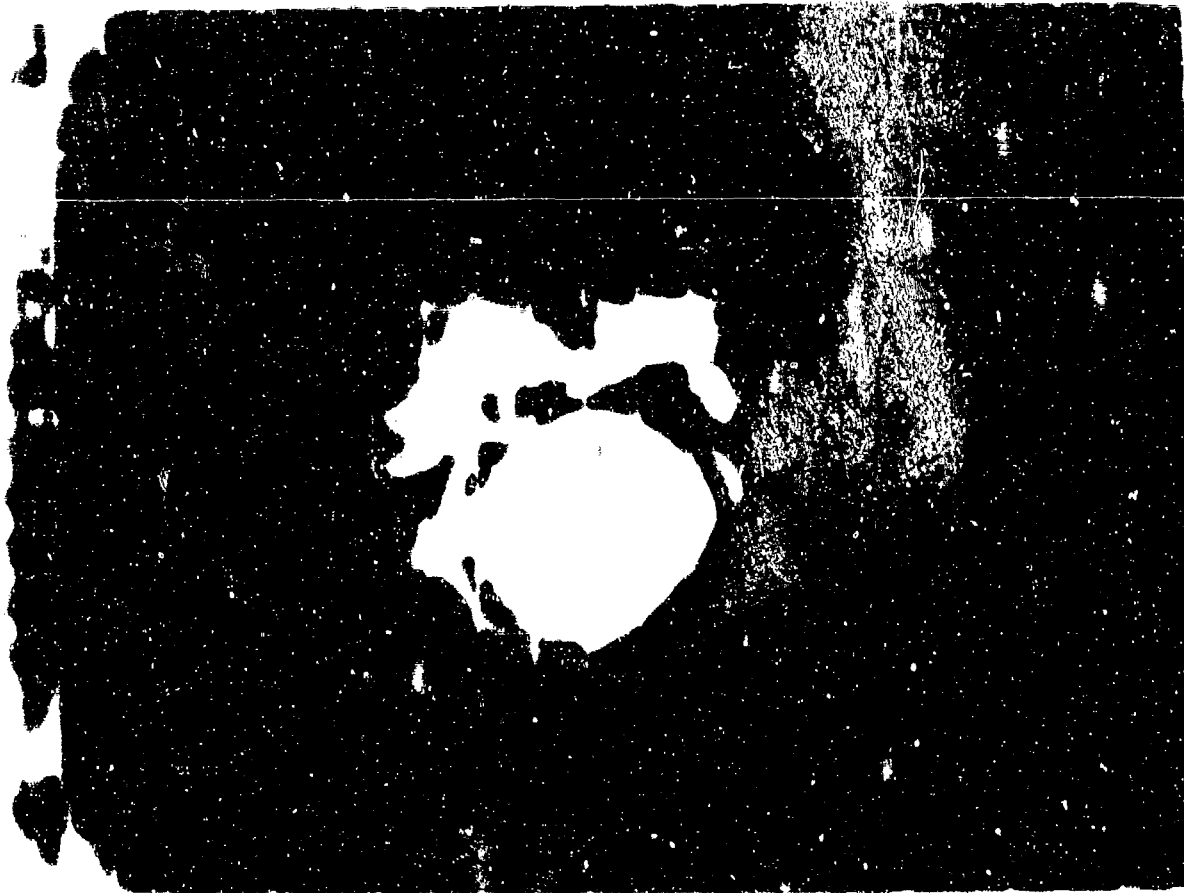


Figure 1. A 128 x 128 pixel image of a person's face, heavily obscured by shadows and noise, appearing as a bright, irregular shape against a dark background.



Figure 2. A 128 x 128 pixel image of a person's face, heavily obscured by shadows and noise, appearing as a bright, irregular shape against a dark background.

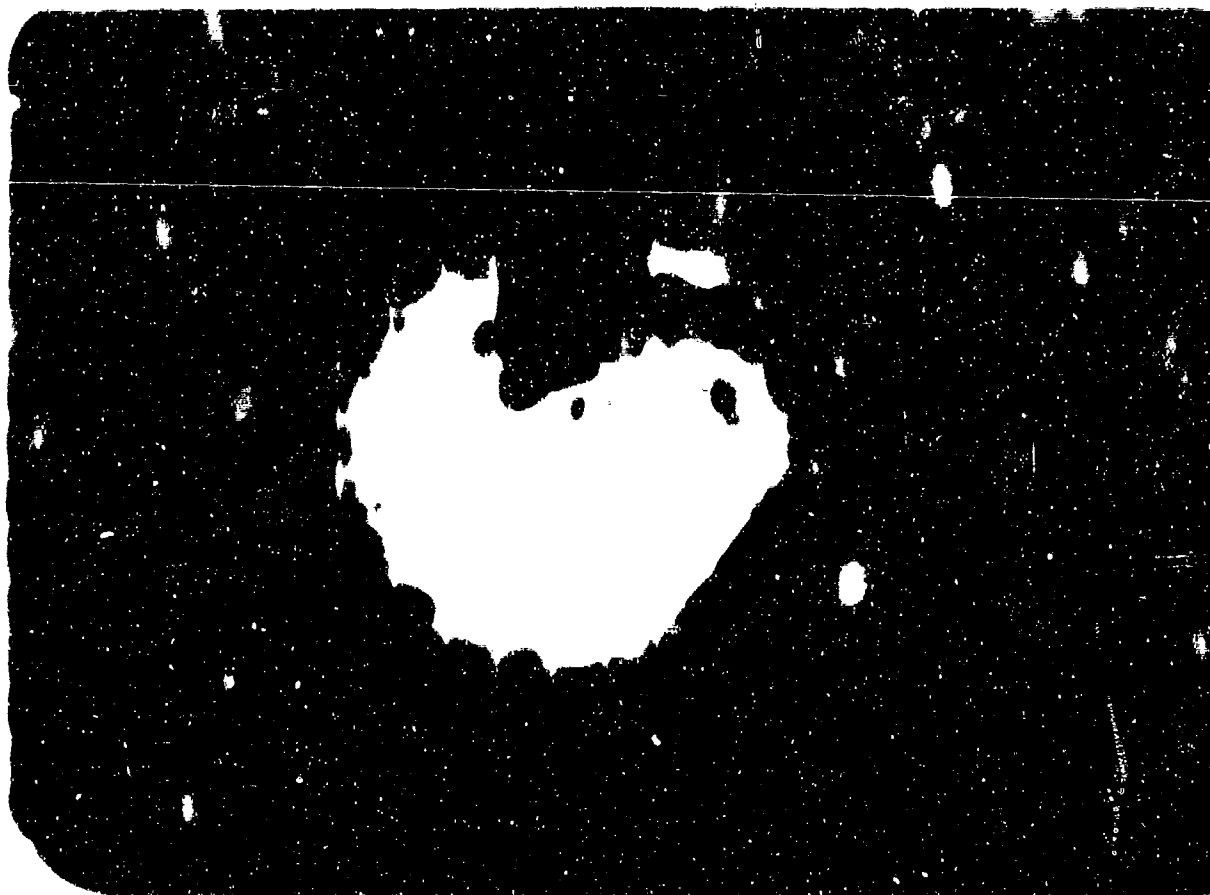


Figure 1.1. Subject 1940-1941. (a) 1940-1941.

1940-1941

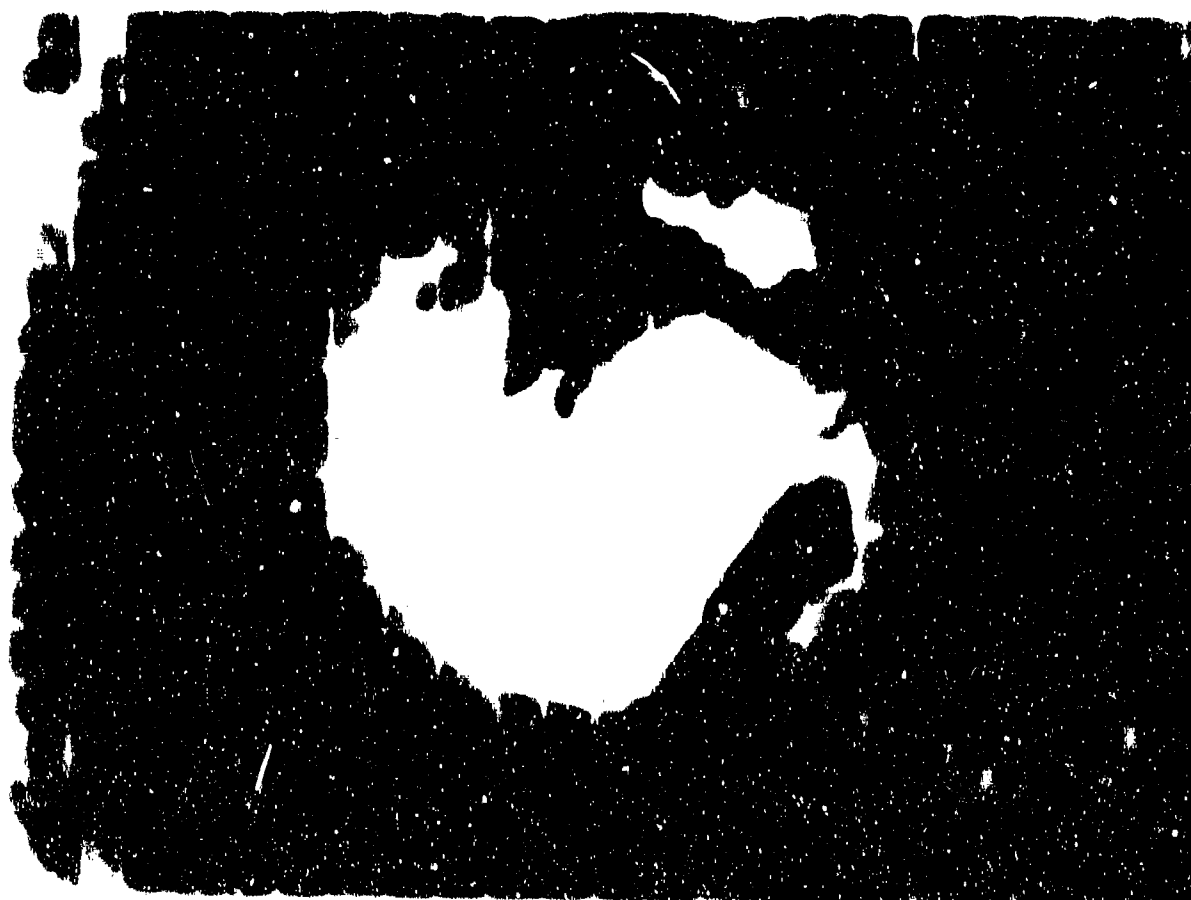


Figure 1.2. Subject 1940-1941. (b) 1940-1941.

1940-1941

1940-1941

1940-1941



1. The first group of variables includes the demographic characteristics of the respondents, such as age, gender, and education level. These variables are used to control for potential confounding factors that may influence the relationship between the independent and dependent variables.

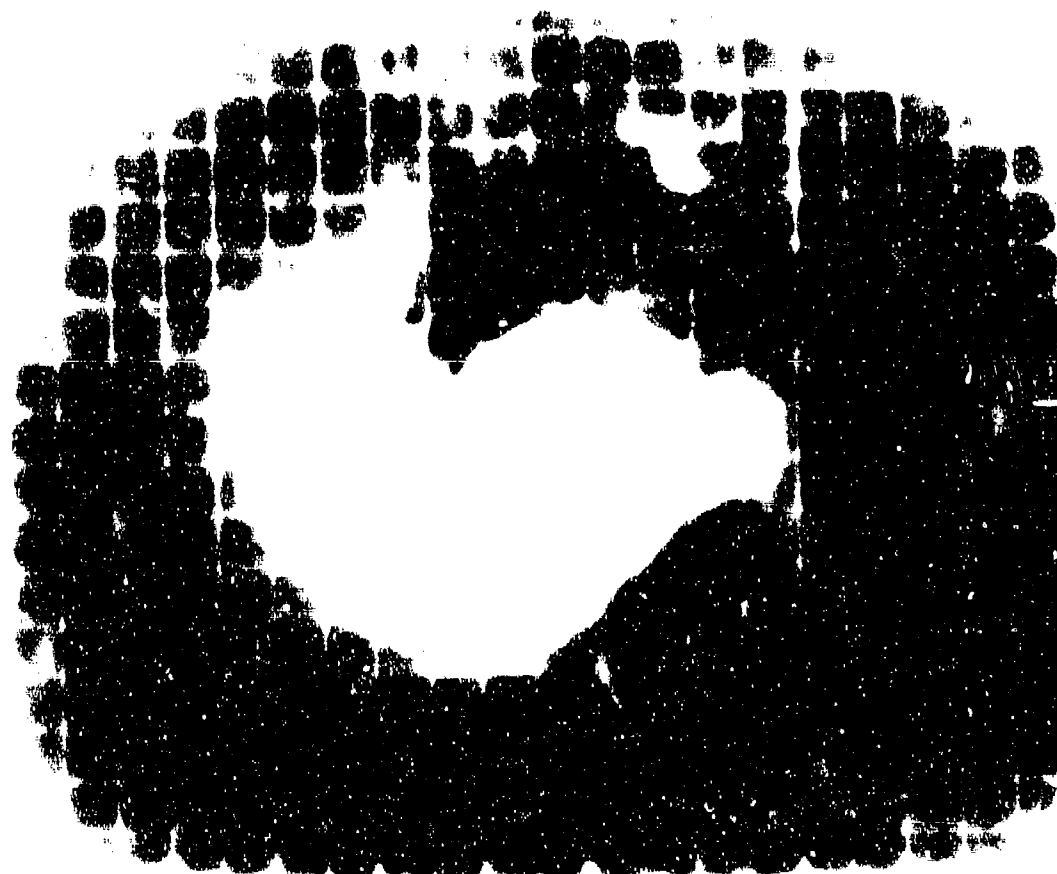
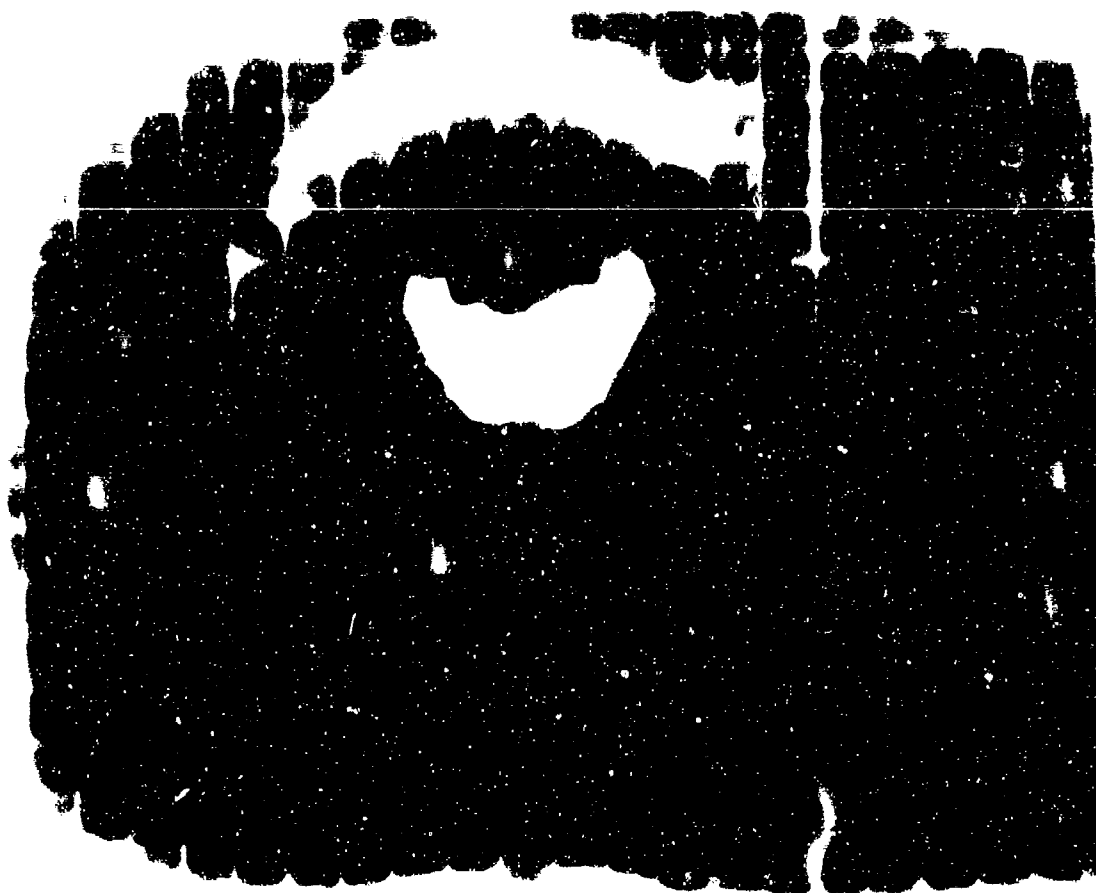
[illegible]



Figure 1. A high-contrast, black and white image showing a large, dark, irregular shape, possibly a silhouette or a heavily shadowed object, centered against a light background. The shape has a jagged, almost crystalline appearance with many small protrusions and indentations. Above the main shape, there is a smaller, more distinct, dark, rounded object.



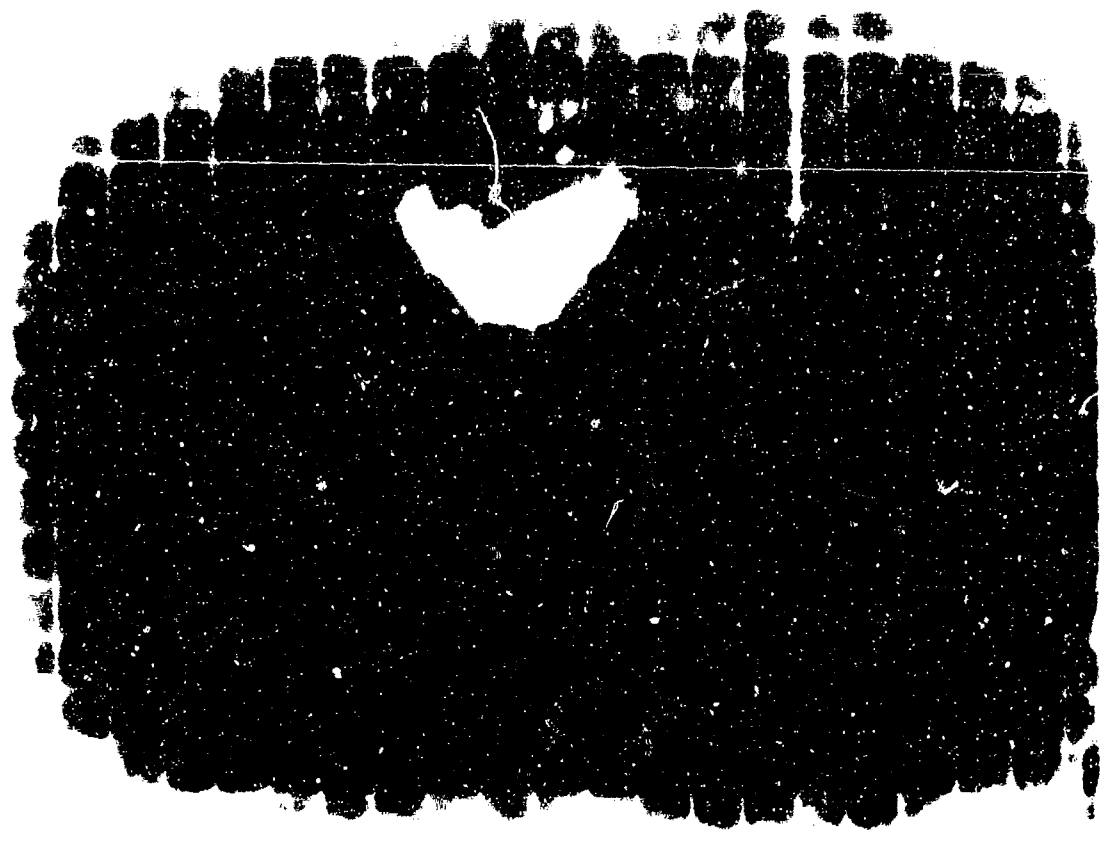
Figure 2. A high-contrast, black and white image showing a large, dark, irregular shape, possibly a silhouette or a heavily shadowed object, centered against a light background. The shape has a jagged, almost crystalline appearance with many small protrusions and indentations. Above the main shape, there is a smaller, more distinct, dark, rounded object.



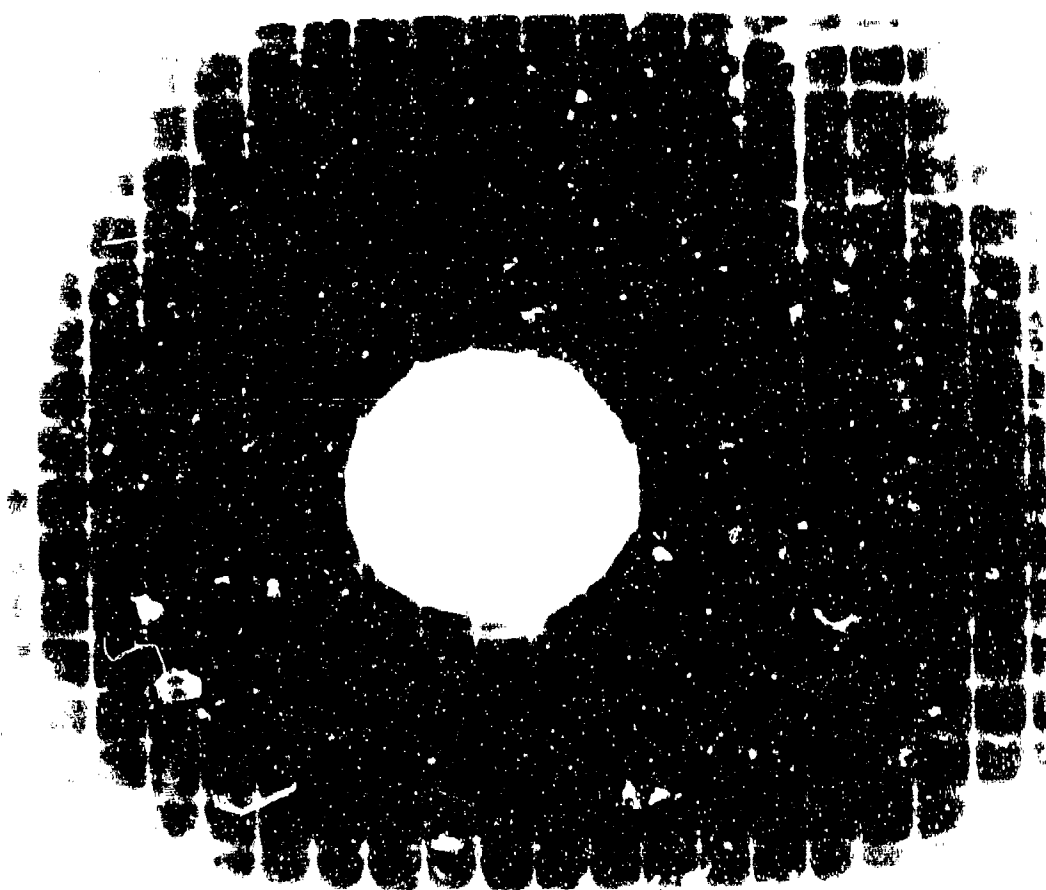
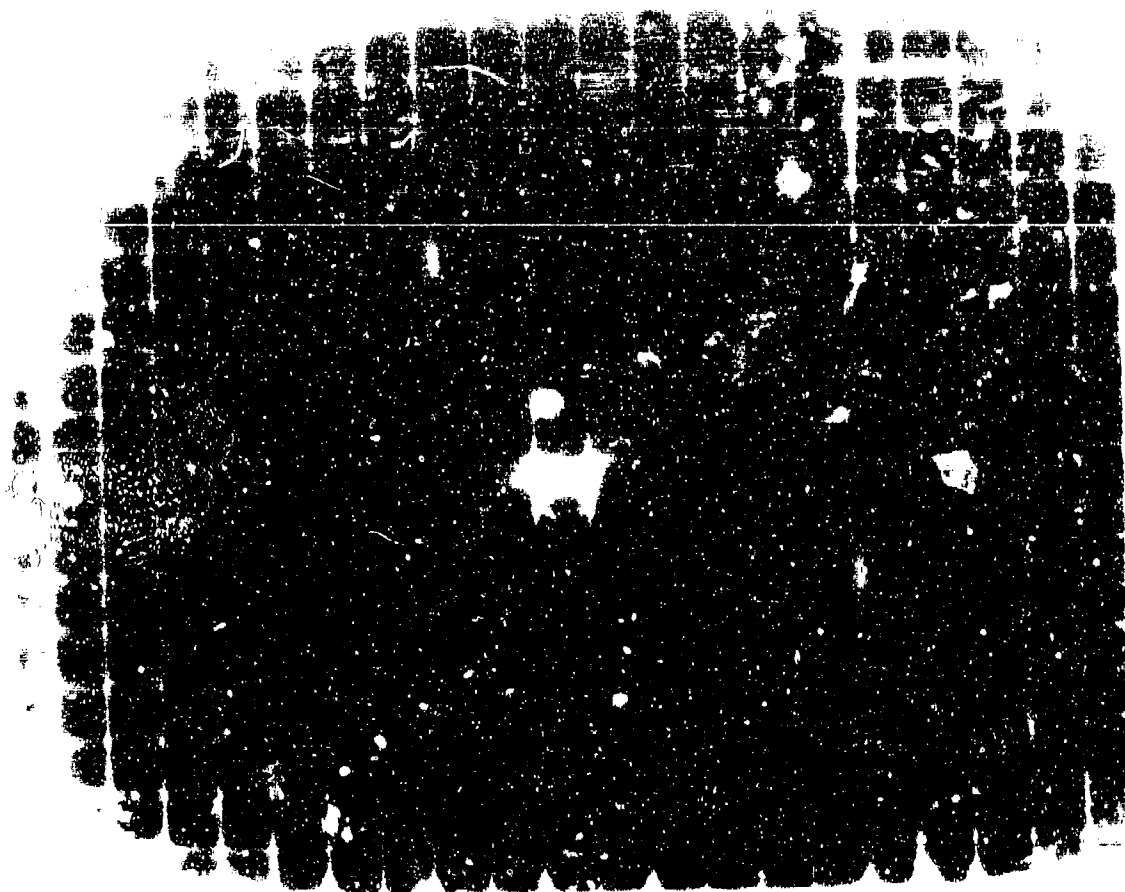
7. 1991年 2 月 25 日 星期四 晴 10 月 25 日 星期四 晴 11 月 25 日 星期四 晴 12 月 25 日 星期四 晴

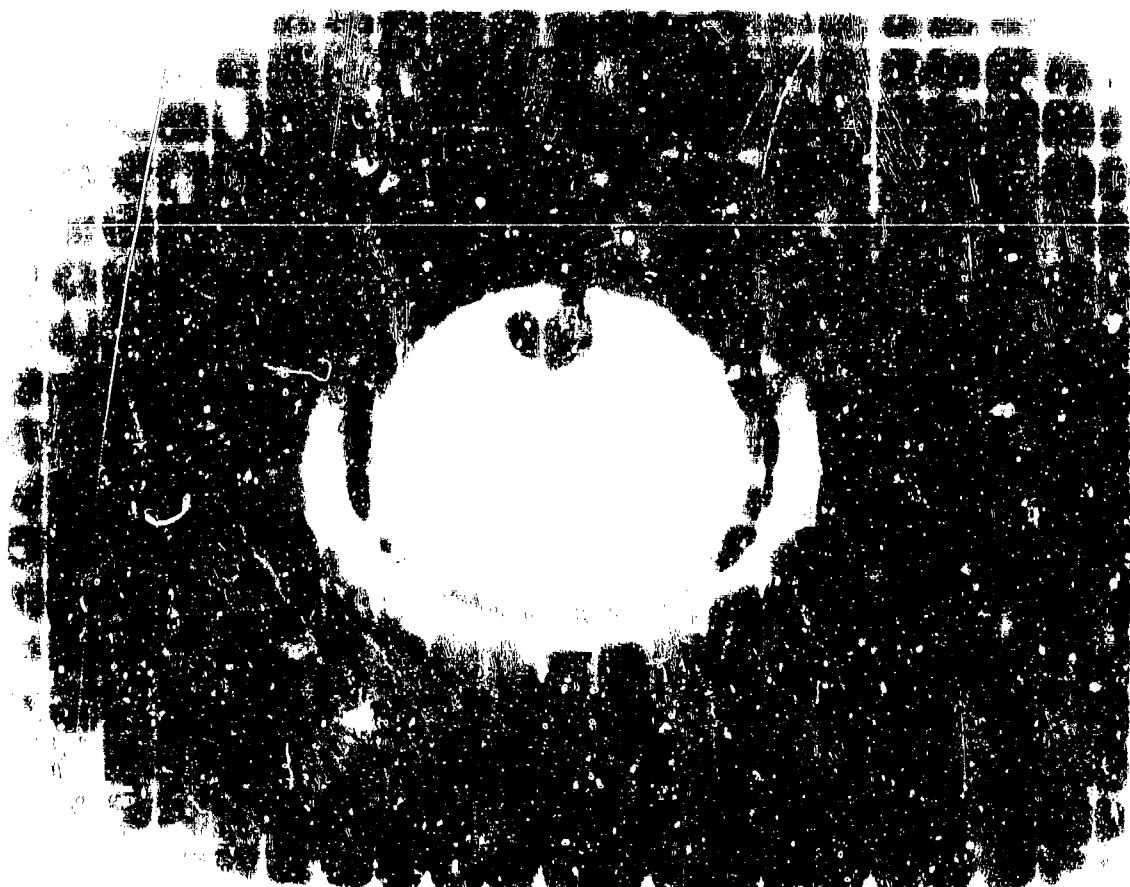


Figure 10. The effect of the initial concentration of the monomer on the polymerization rate.



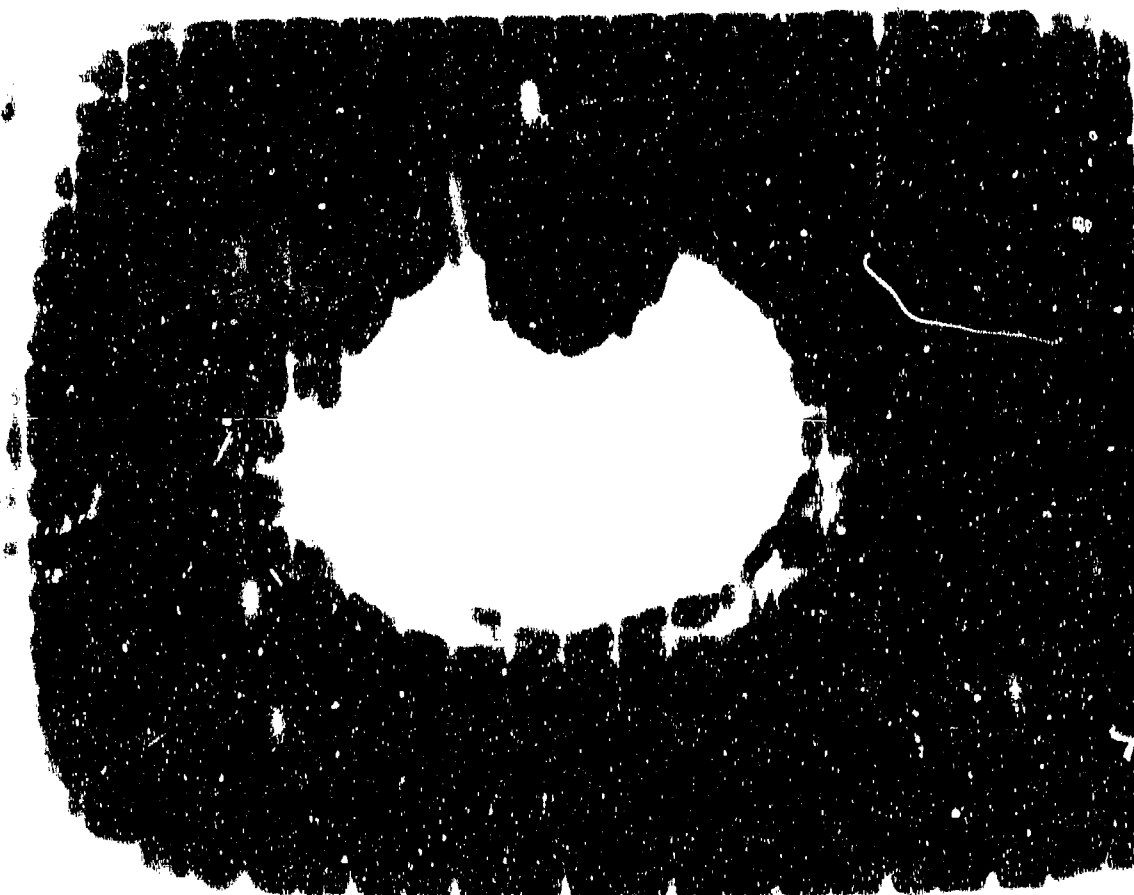
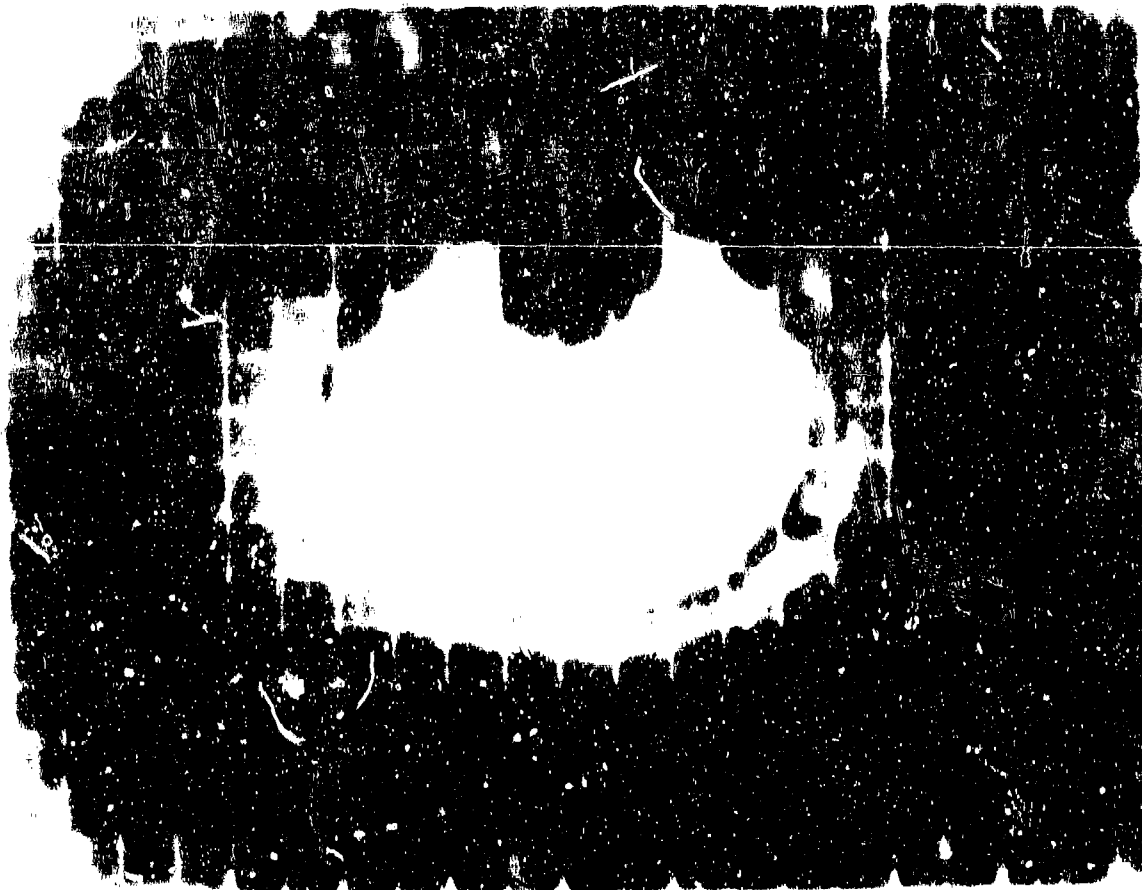
50000



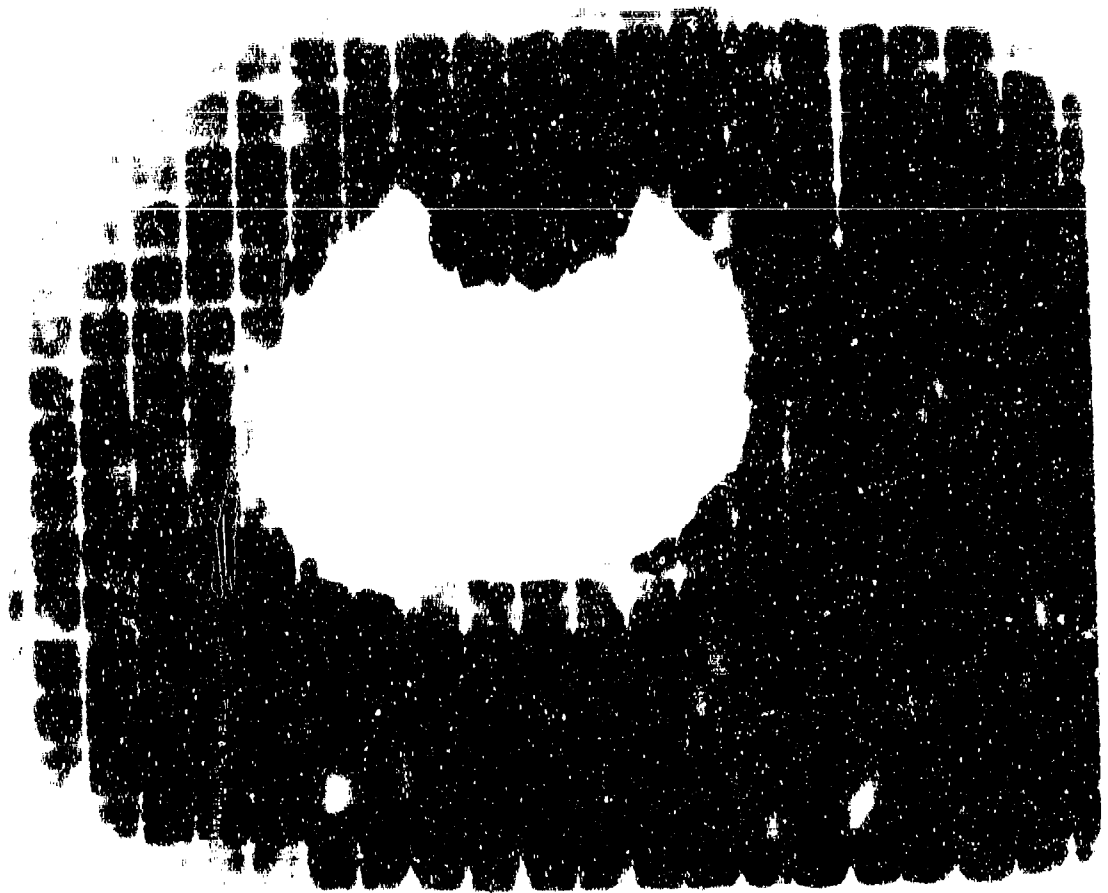


1. The first group of respondents (Group 1) consisted of 100 individuals who were randomly selected from the population of 1,000 individuals. This group was used to estimate the population mean and standard deviation.

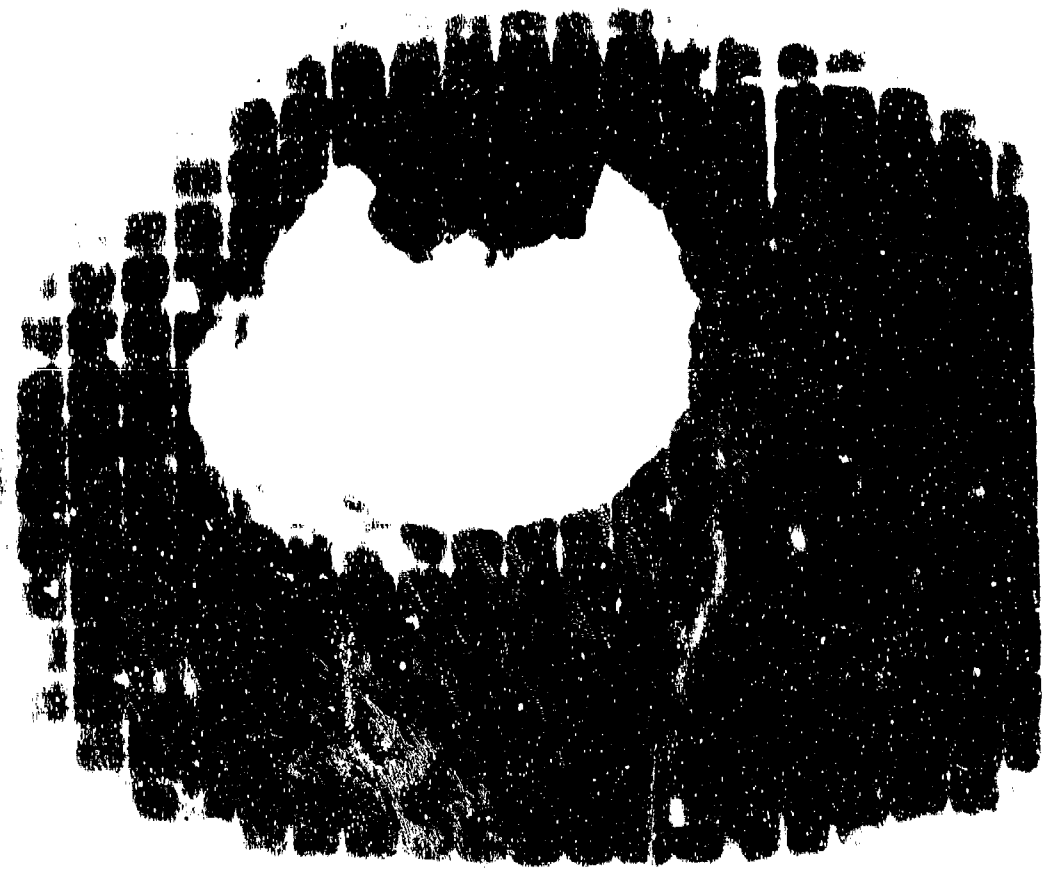




11
11111111



0 1 2 3 4 5 6 7 8 9 10 11 12 13 14 15 16 17 18 19 20 21 22 23 24 25 26 27 28 29 30 31 32 33 34 35 36 37 38 39 40 41 42 43 44 45 46 47 48 49 50 51 52 53 54 55 56 57 58 59 60 61 62 63 64 65 66 67 68 69 70 71 72 73 74 75 76 77 78 79 80 81 82 83 84 85 86 87 88 89 90 91 92 93 94 95 96 97 98 99



0 1 2 3 4 5 6 7 8 9 10 11 12 13 14 15 16 17 18 19 20 21 22 23 24 25 26 27 28 29 30 31 32 33 34 35 36 37 38 39 40 41 42 43 44 45 46 47 48 49 50 51 52 53 54 55 56 57 58 59 60 61 62 63 64 65 66 67 68 69 70 71 72 73 74 75 76 77 78 79 80 81 82 83 84 85 86 87 88 89 90 91 92 93 94 95 96 97 98 99

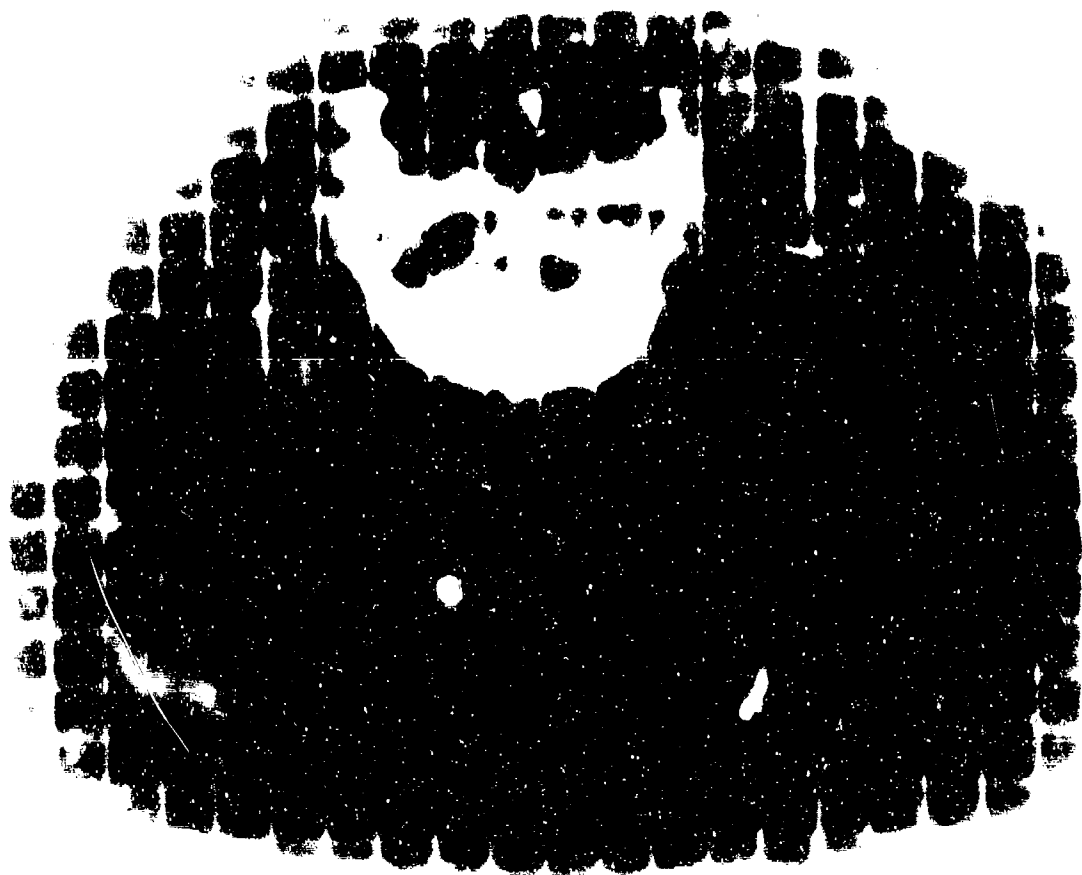
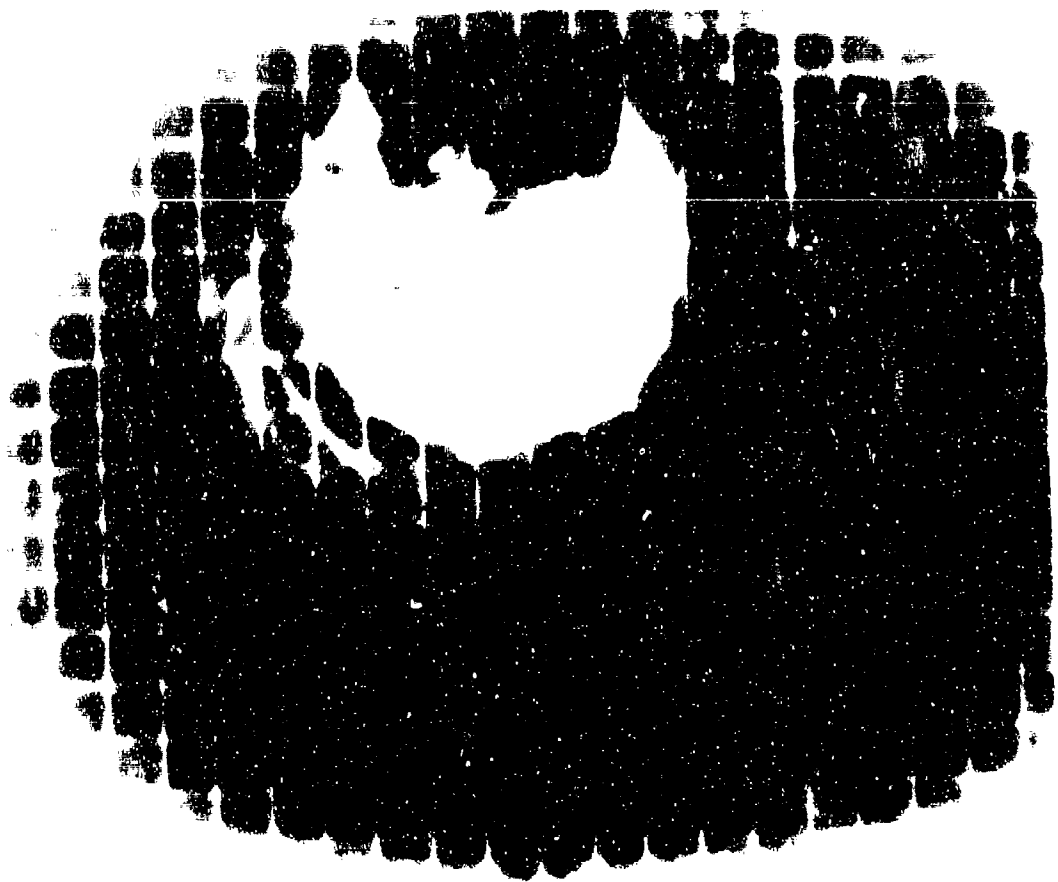




Figure 1. (a) and (b) show the same specimen from different angles. (c) shows the specimen from a different angle.

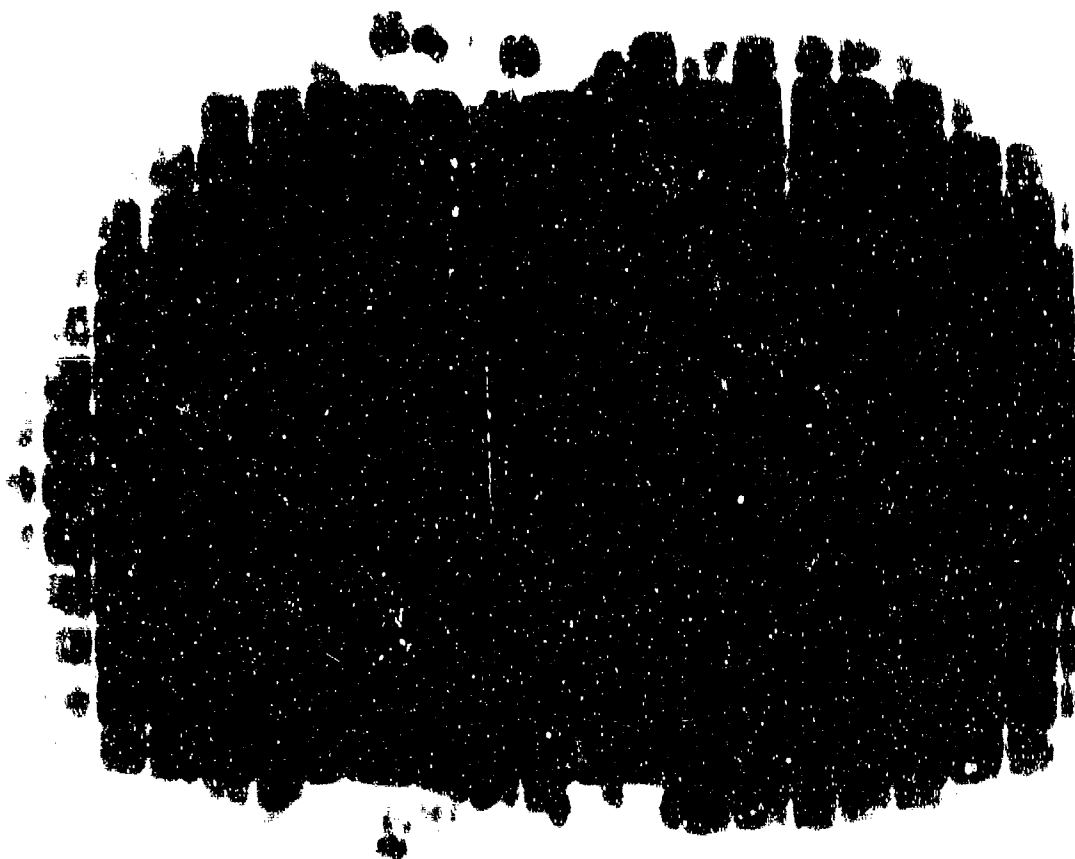
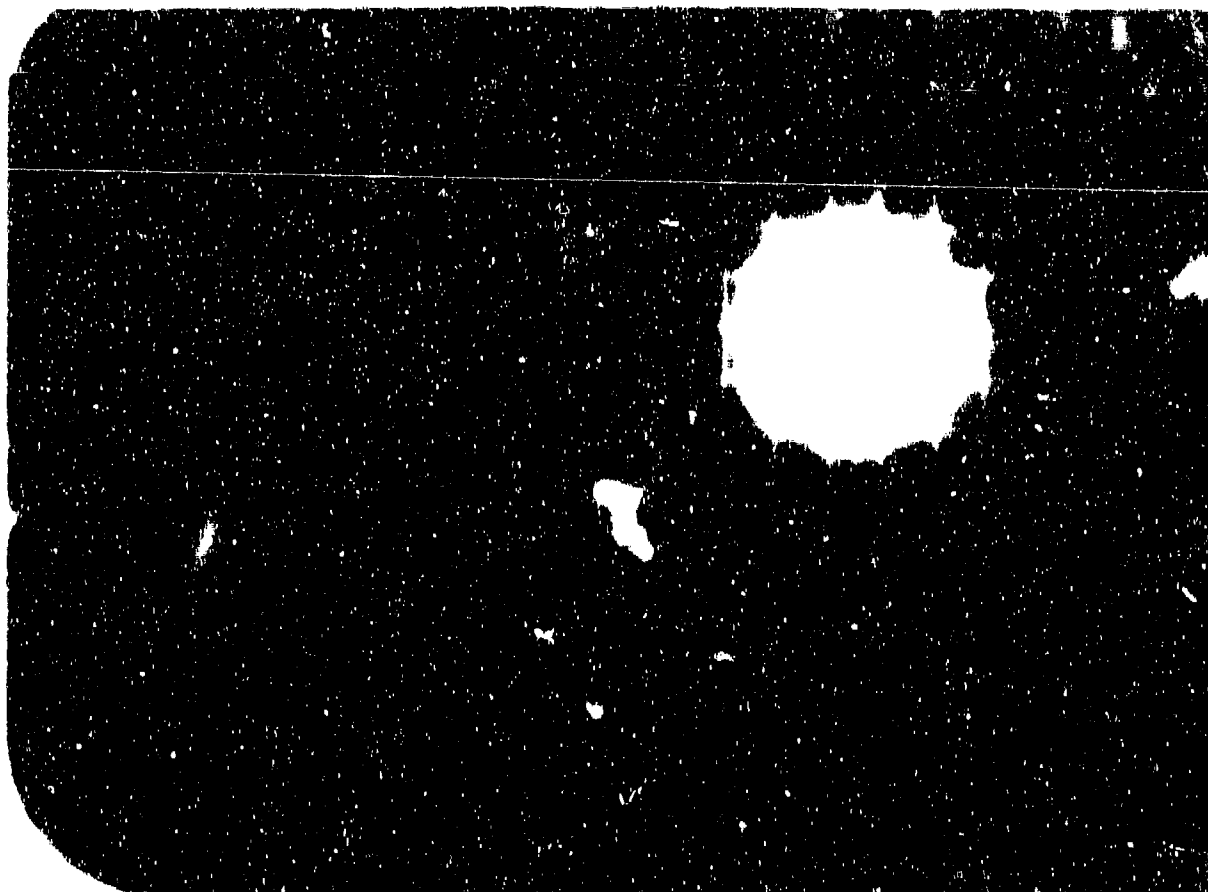
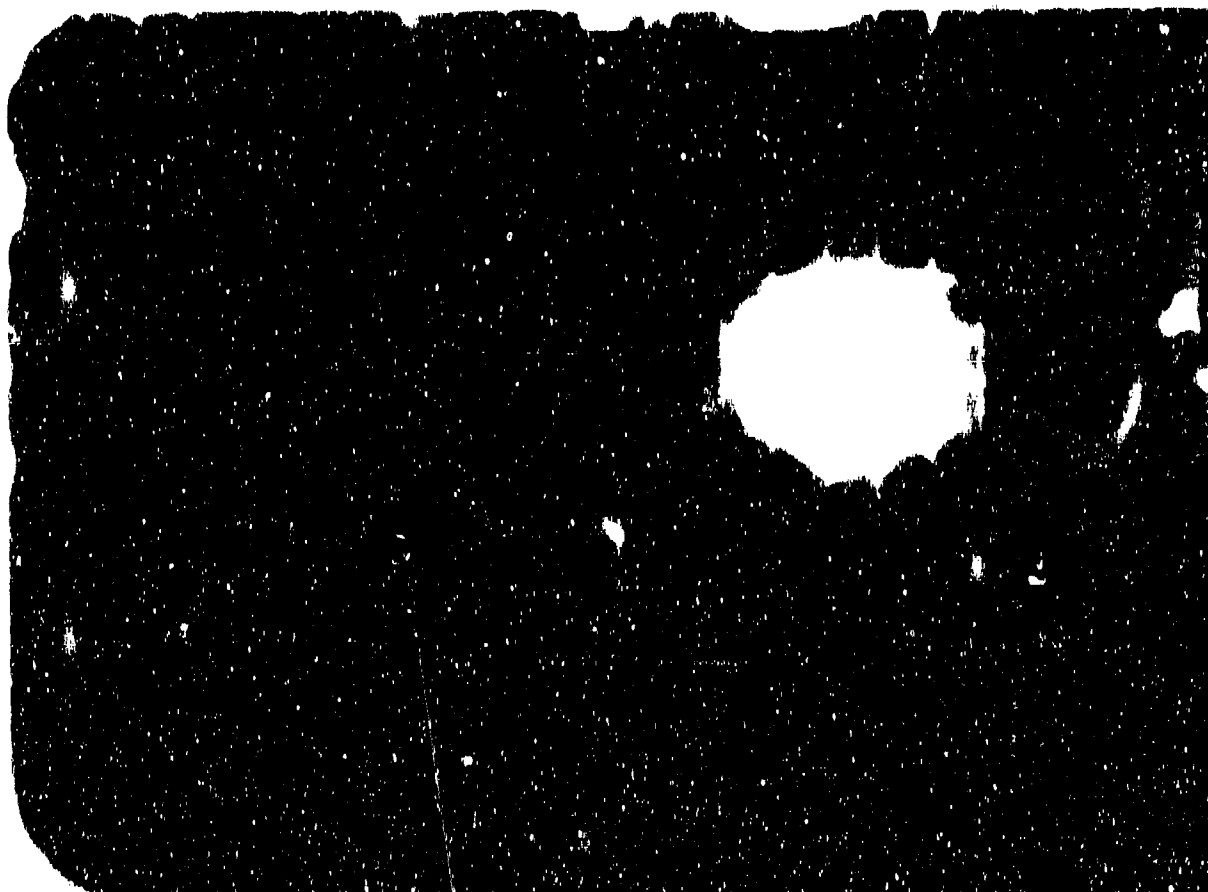


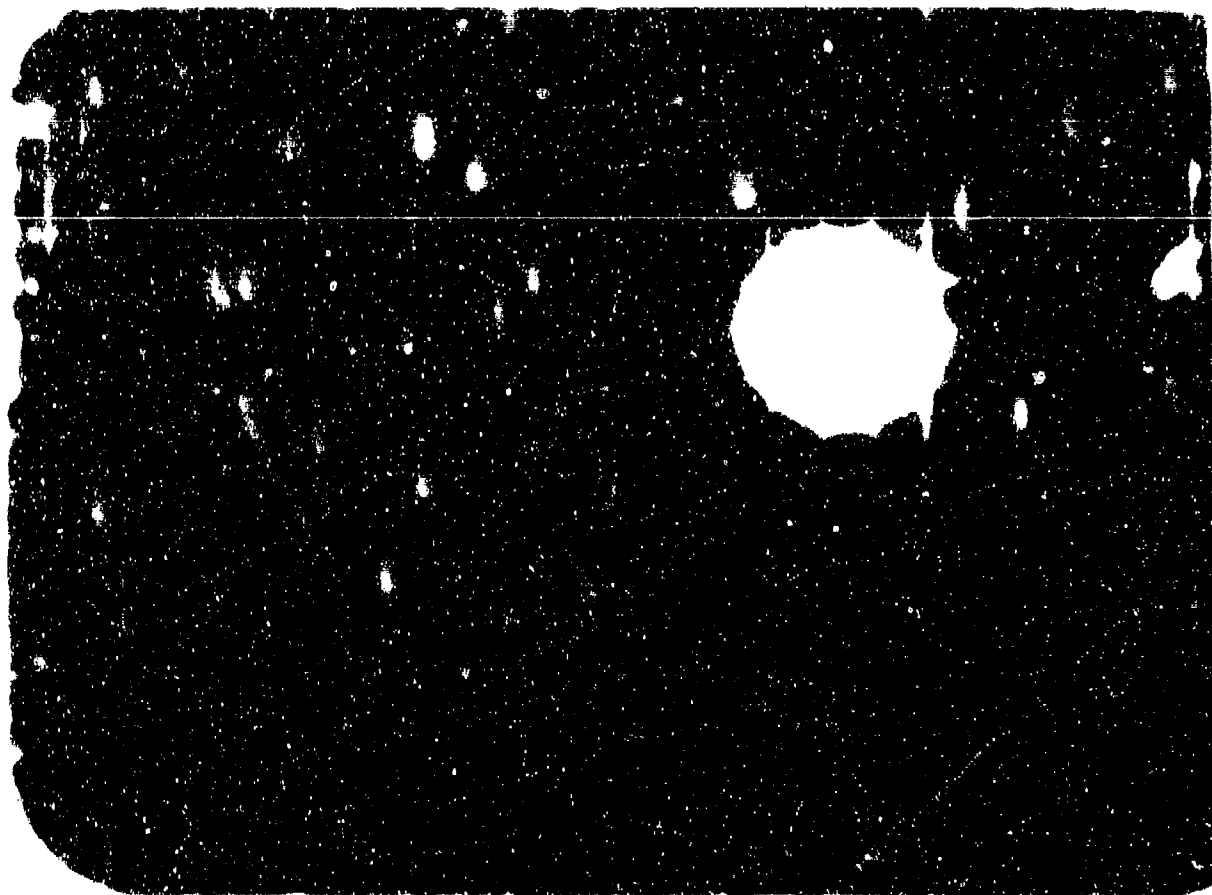
Figure 2. (a) and (b) show the same specimen from different angles. (c) shows the specimen from a different angle.



1944-1945



1944-1945



1. The first of the two objects is a dark, rectangular object with a large, irregular white circular hole in the upper right quadrant. The surface is heavily textured with numerous small white specks and larger irregular white patches, suggesting a worn or damaged material. The edges are slightly irregular and frayed.



2. The second of the two objects is a dark, rectangular object with a large, irregular white circular hole in the upper right quadrant. The surface is heavily textured with numerous small white specks and larger irregular white patches, suggesting a worn or damaged material. The edges are slightly irregular and frayed.

2000

1. The first of the two objects is a dark, rectangular object with a large, irregular white circular hole in the upper right quadrant. The surface is heavily textured with numerous small white specks and larger irregular white patches, suggesting a worn or damaged material. The edges are slightly irregular and frayed.

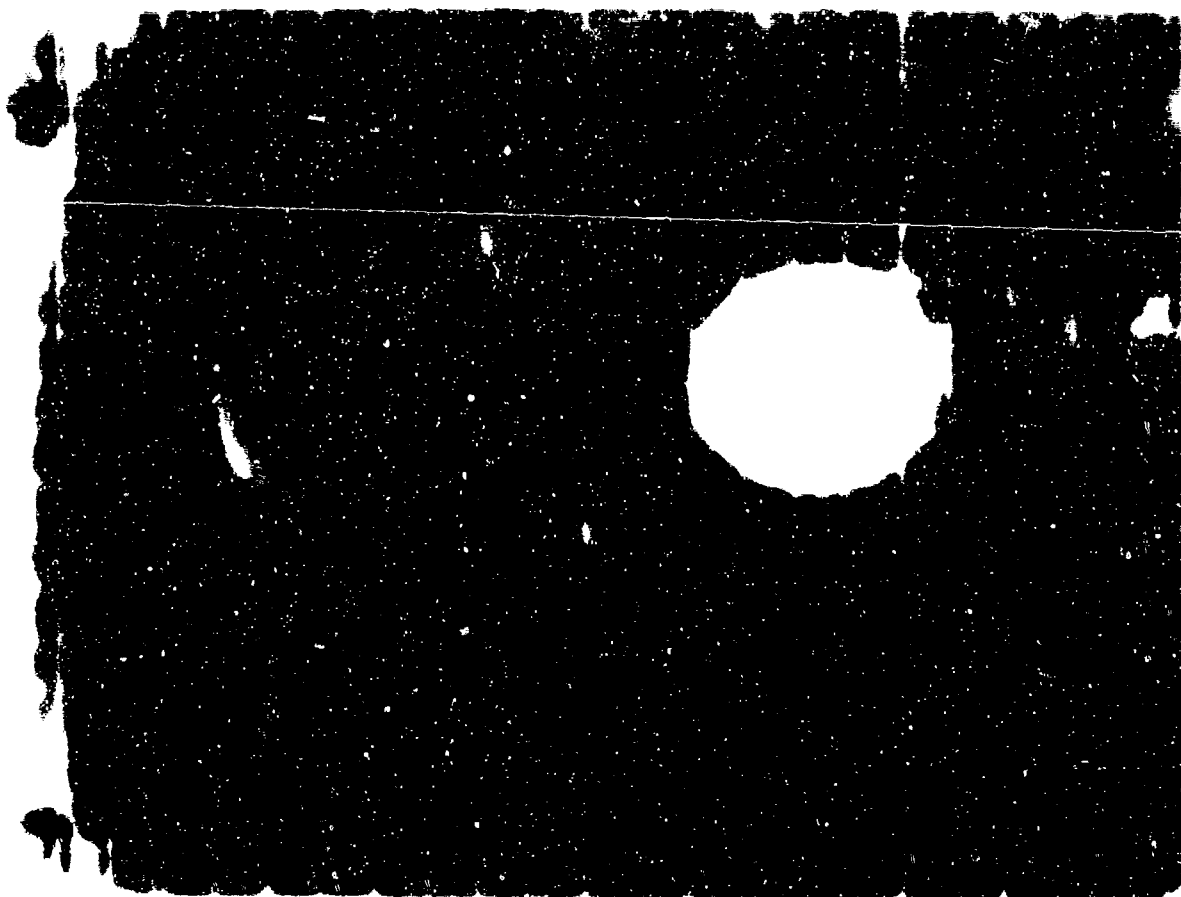


Figure 1. A. When the hole is closed. Figure 1. B. When the hole is open.

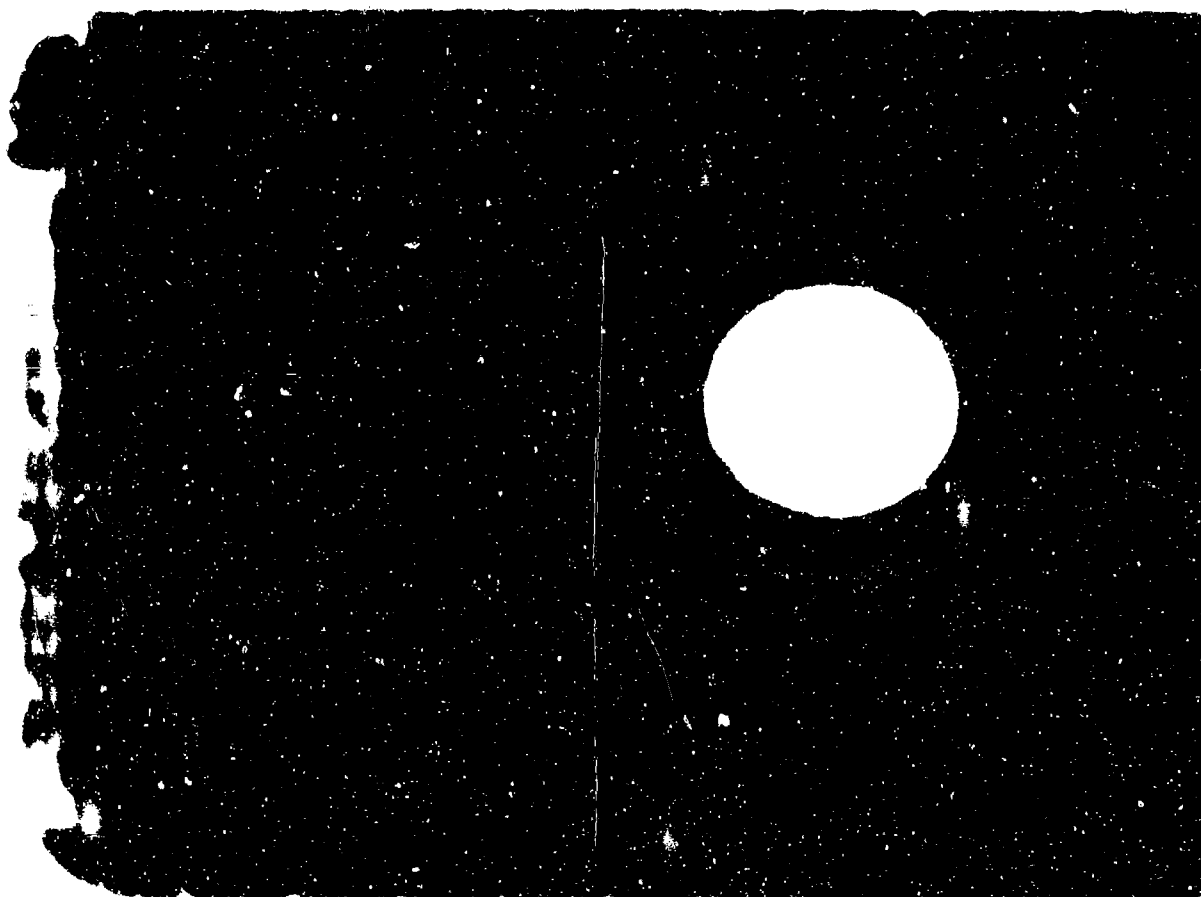


Figure 2. A. When the hole is closed. Figure 2. B. When the hole is open.

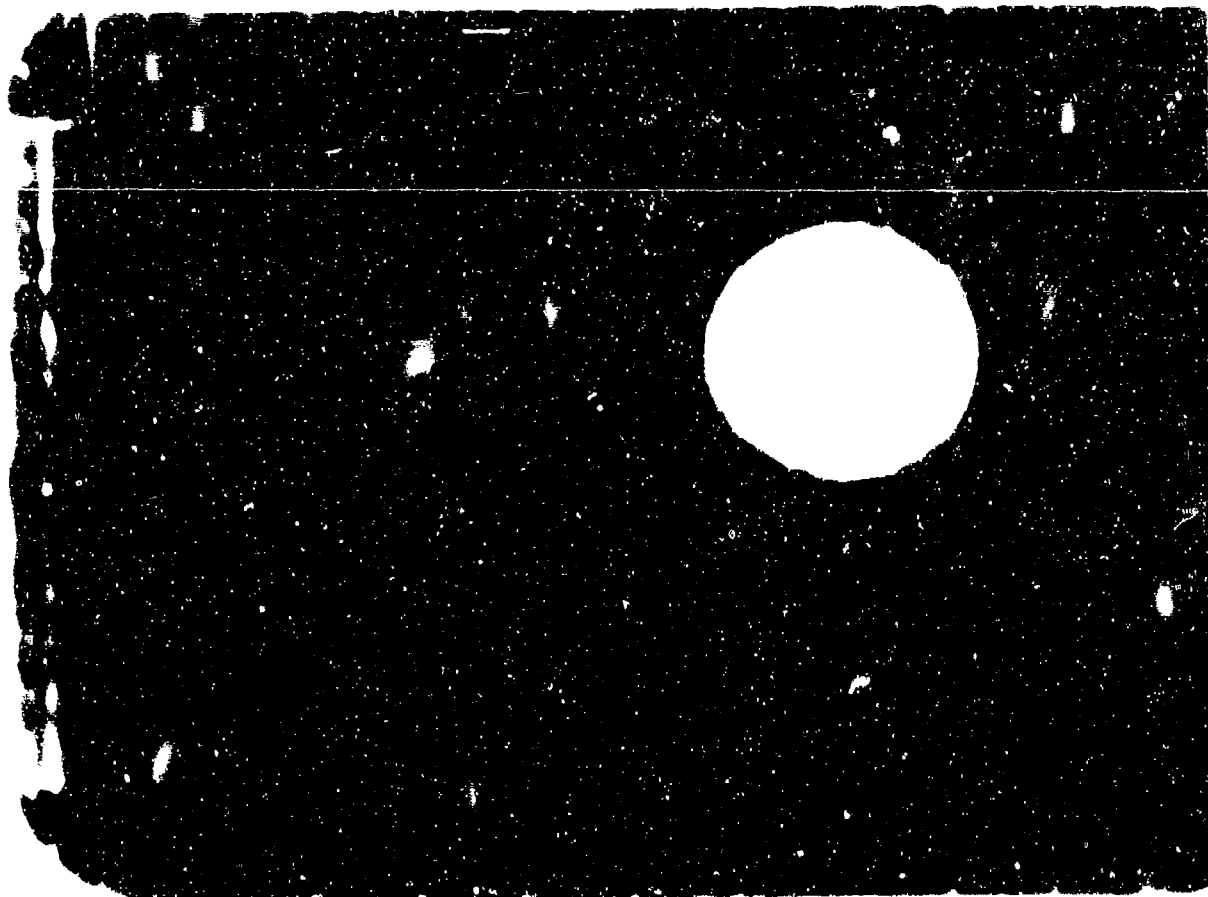


Figure 1. A dark, rectangular object with a large, bright, circular hole in the upper right quadrant.



Figure 2. A dark, rectangular object with a large, bright, circular hole in the upper right quadrant.

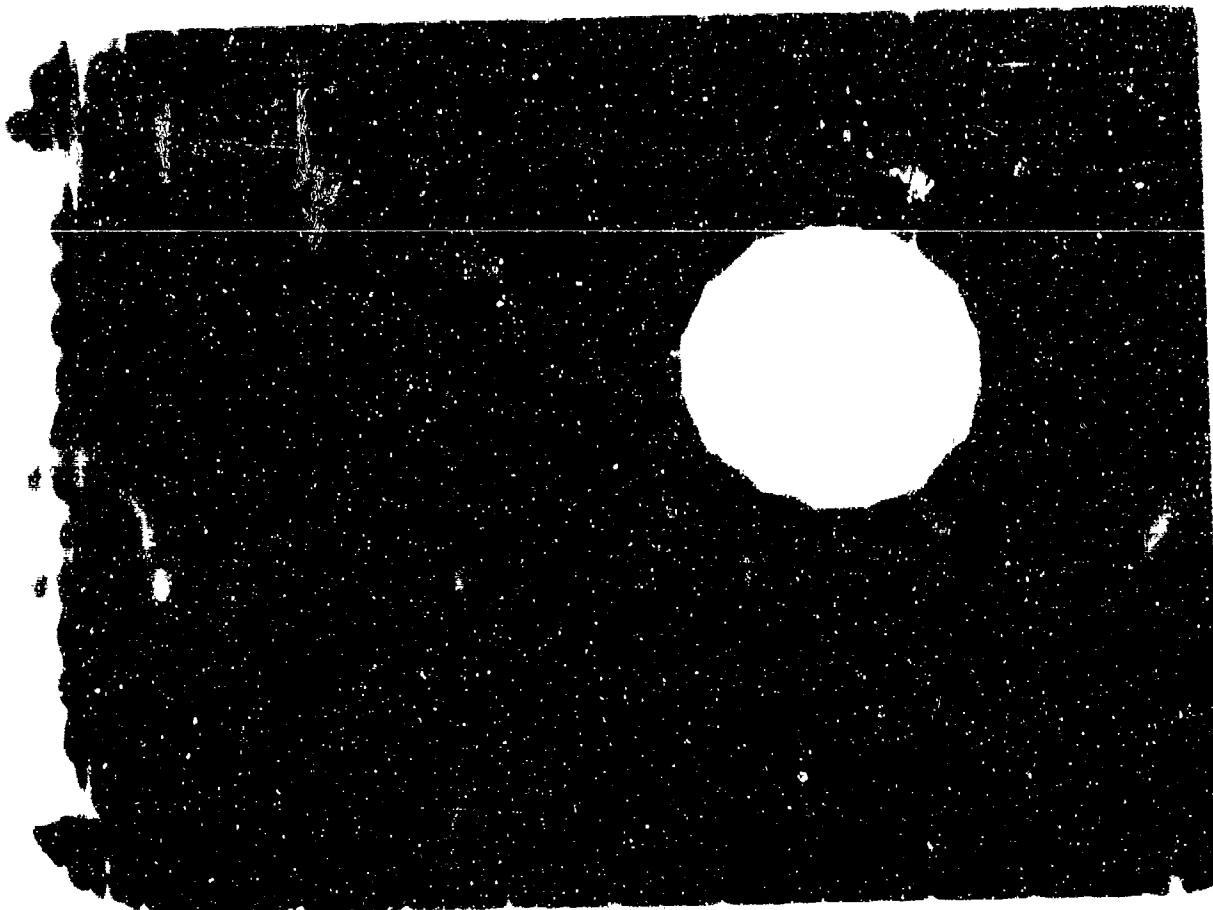


Figure 1. A 100-micron scale bar is shown in the upper right corner of the image.



Figure 2. A 100-micron scale bar is shown in the upper right corner of the image.

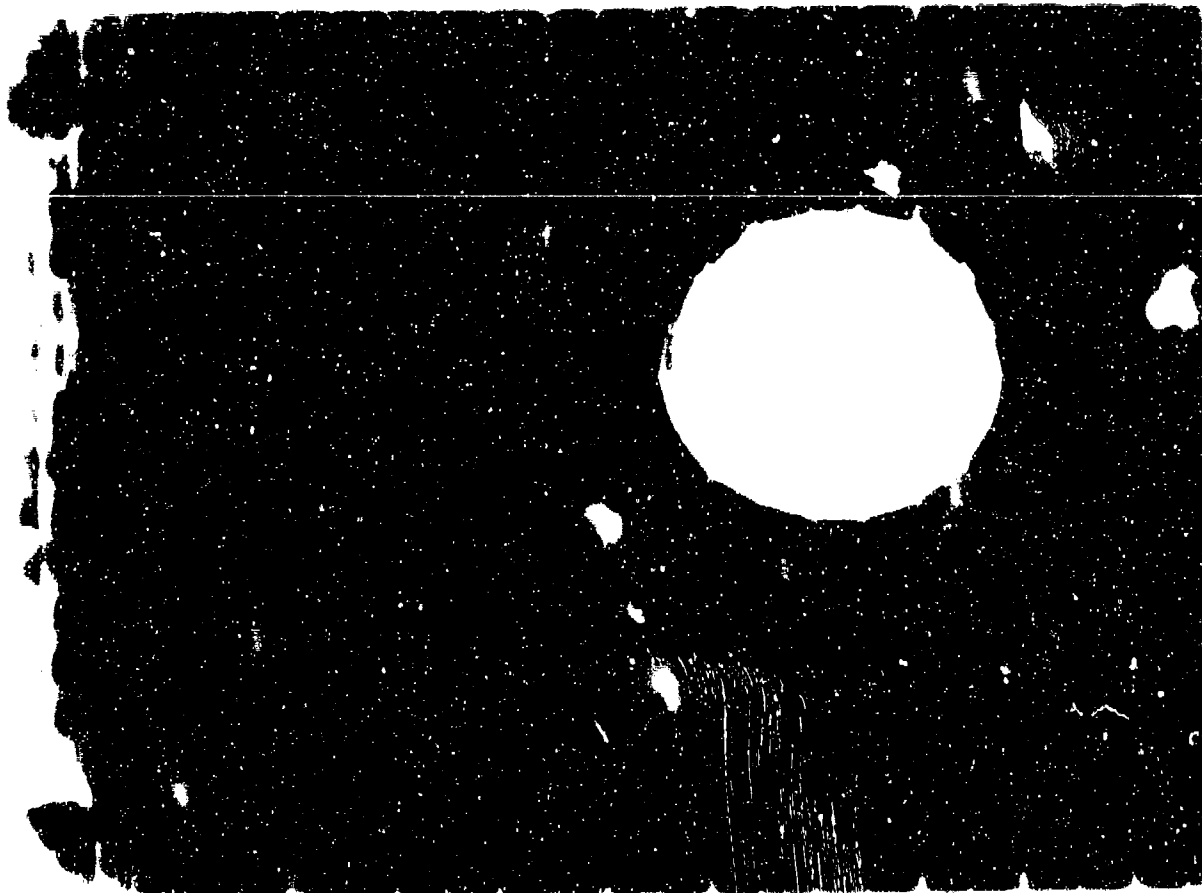


Figure 4. (a) (b) (c) (d) (e) (f) (g) (h) (i) (j) (k) (l) (m) (n) (o) (p) (q) (r) (s) (t) (u) (v) (w) (x) (y) (z)

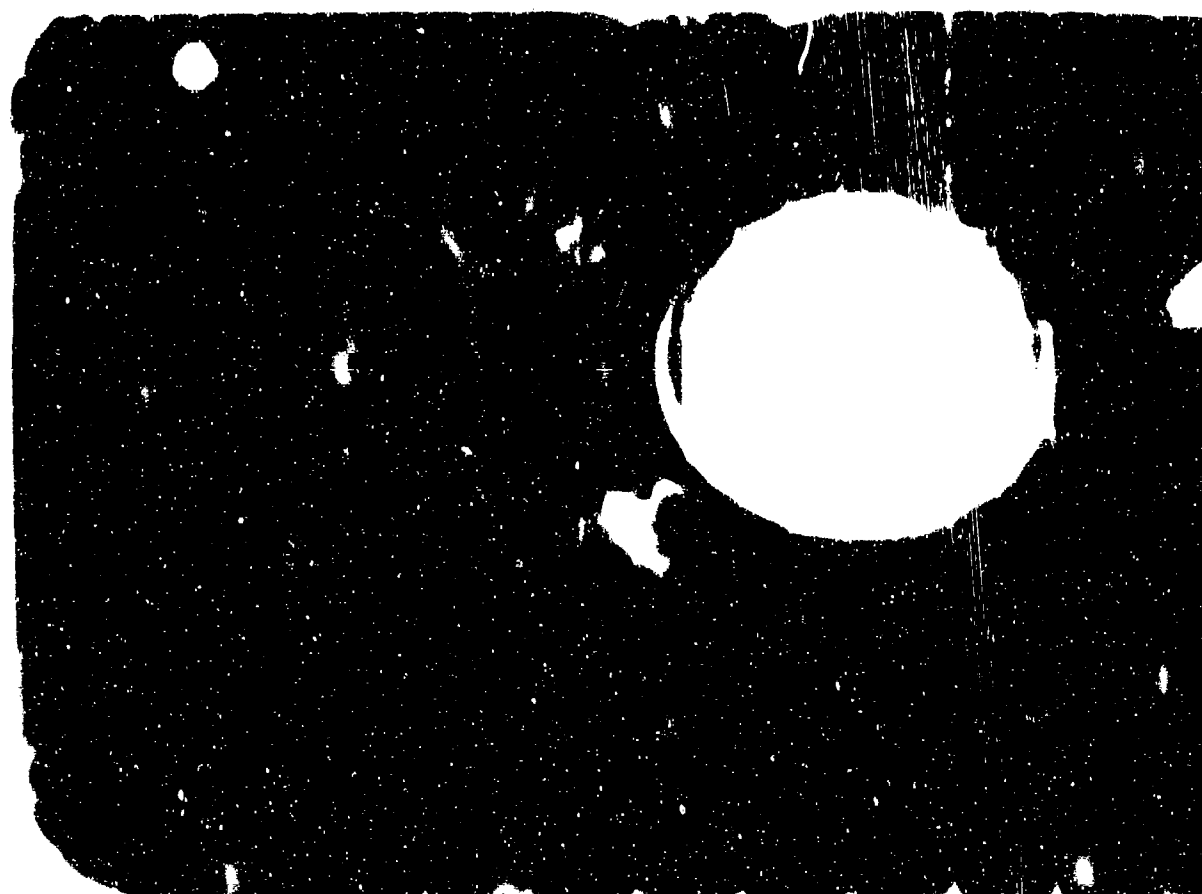


Figure 5. (a) (b) (c) (d) (e) (f) (g) (h) (i) (j) (k) (l) (m) (n) (o) (p) (q) (r) (s) (t) (u) (v) (w) (x) (y) (z)

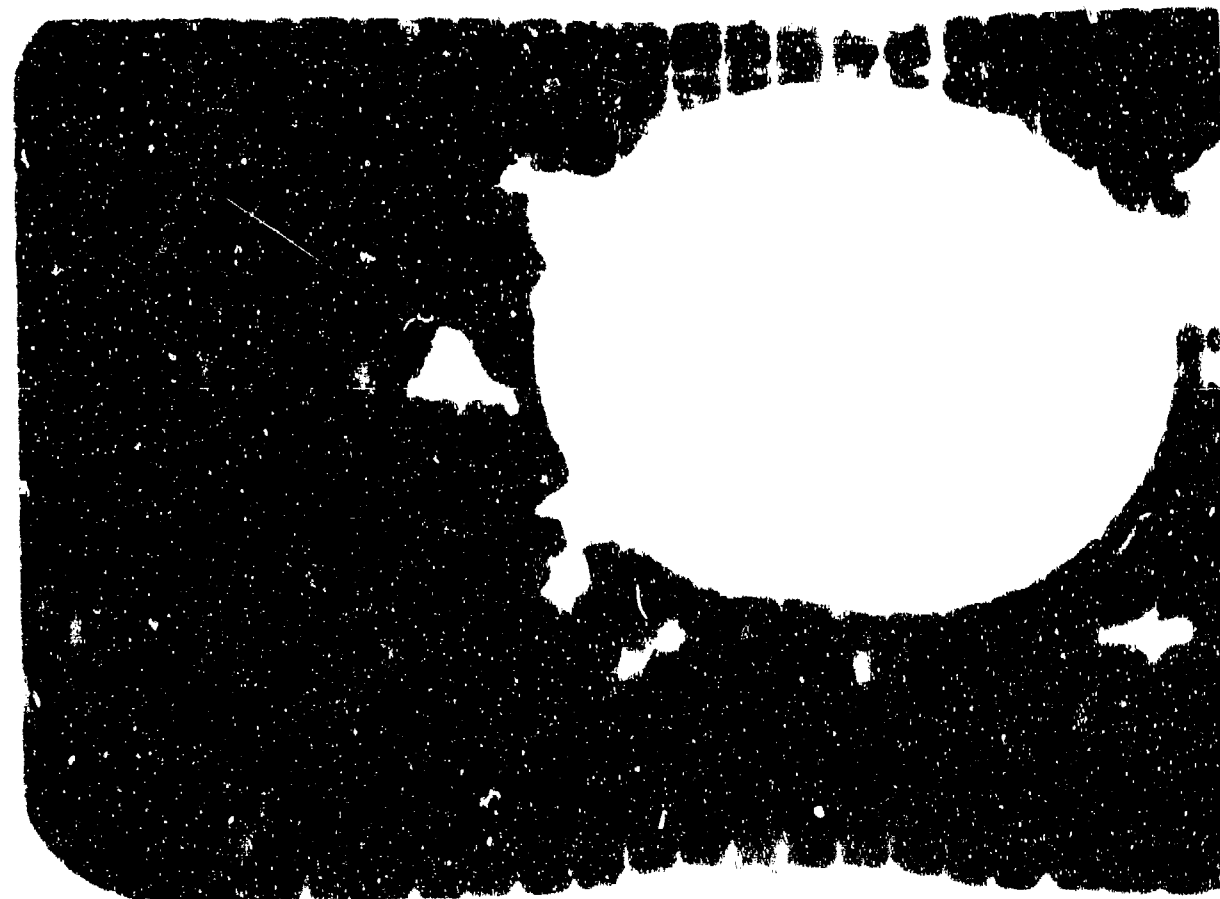
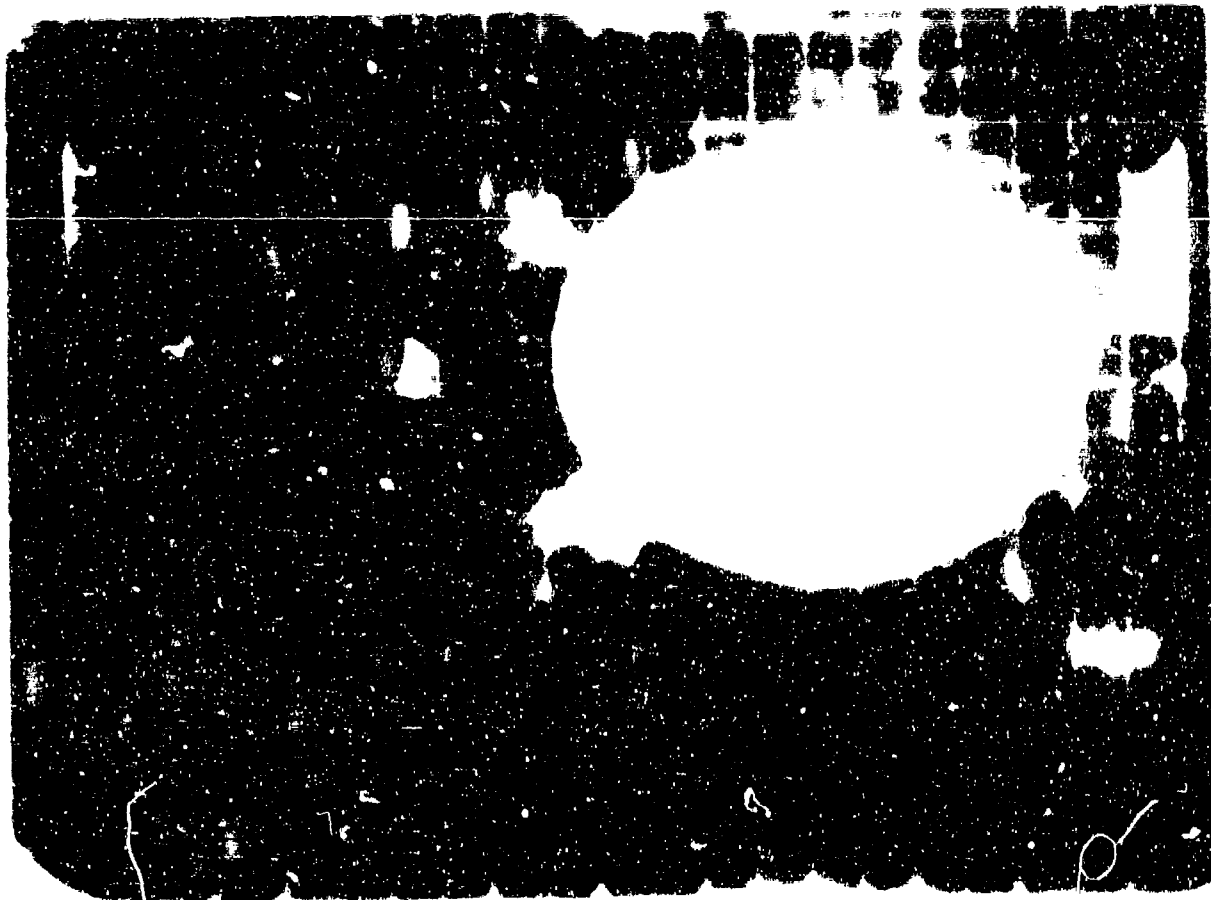
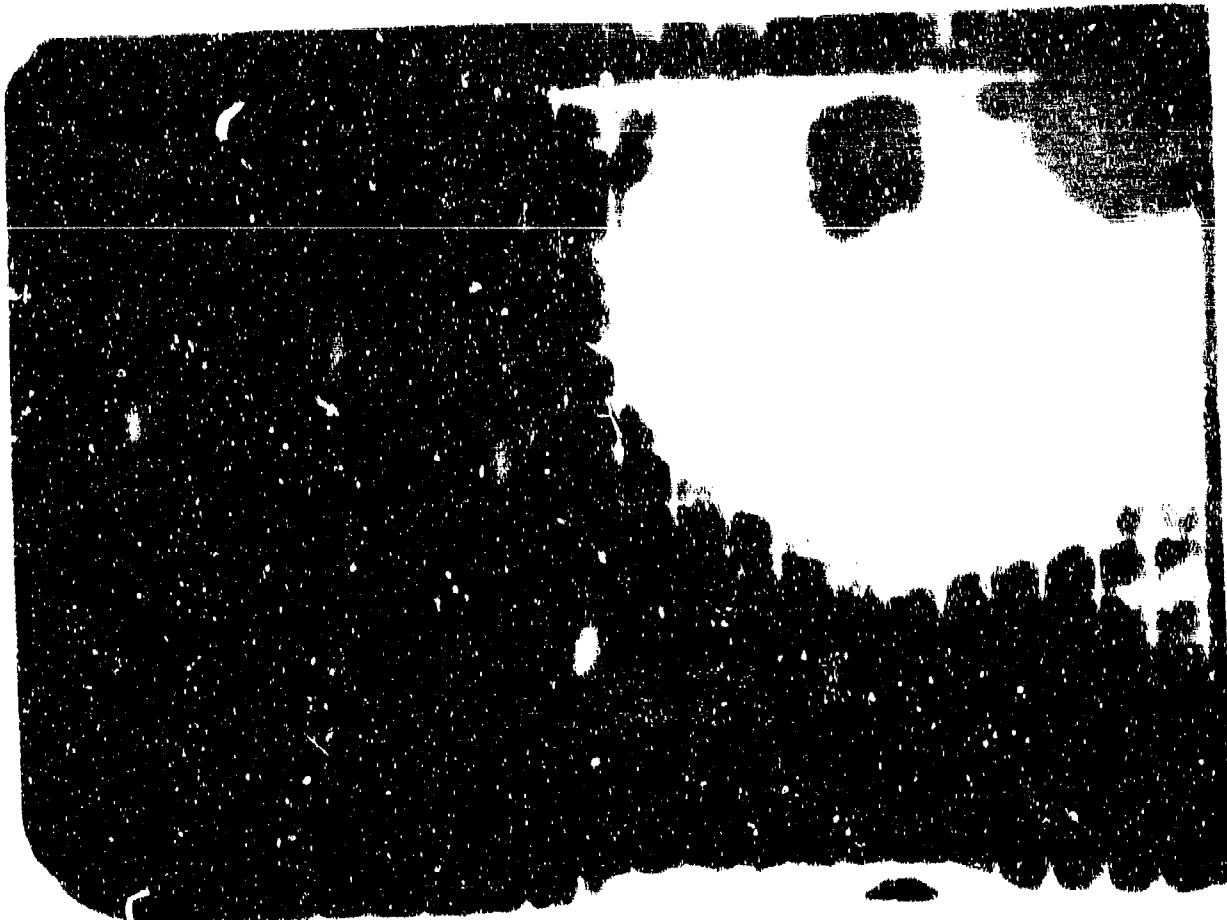


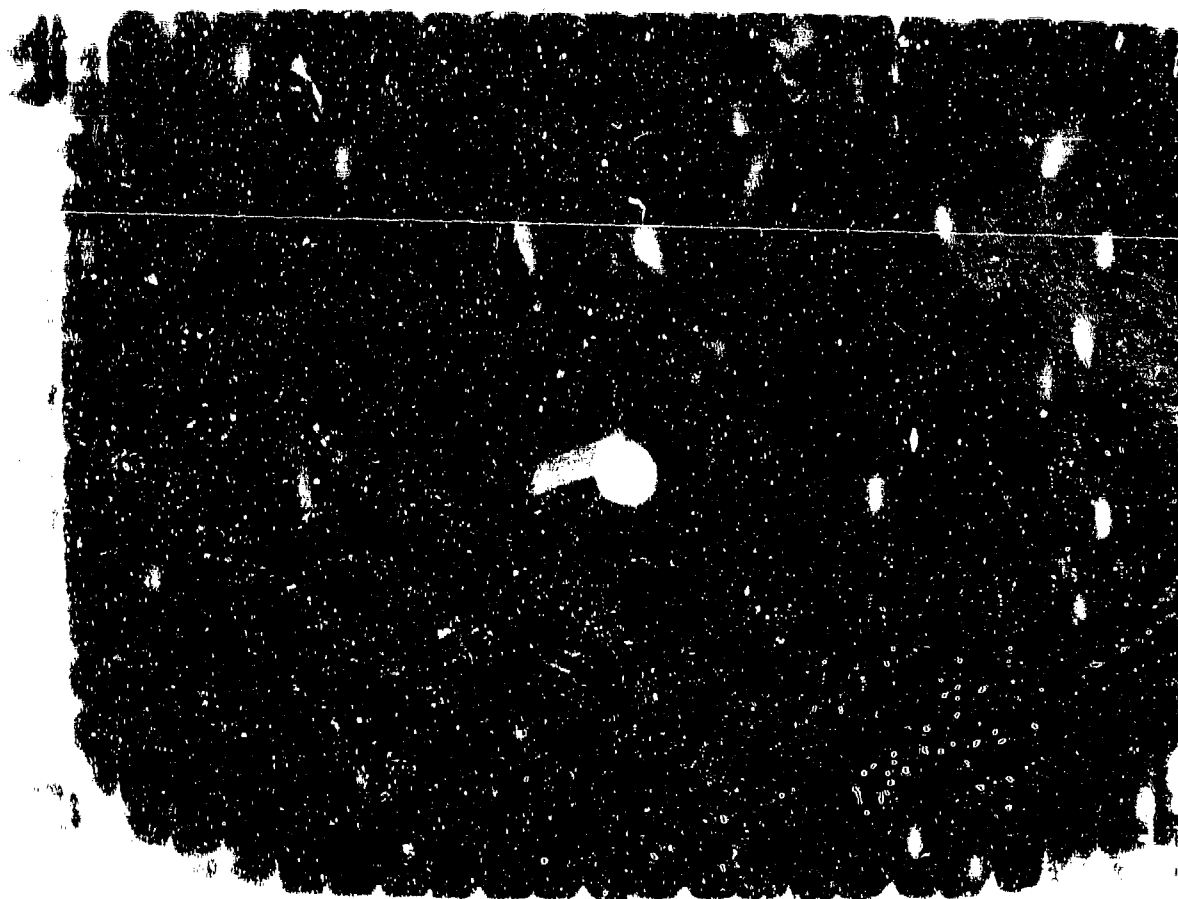


Figure 1. A high-contrast, black and white image showing a dark, irregular shape on the left side, possibly a silhouette or a heavily shadowed object, against a bright background. The shape has a jagged, textured appearance with some internal detail visible despite the high contrast.

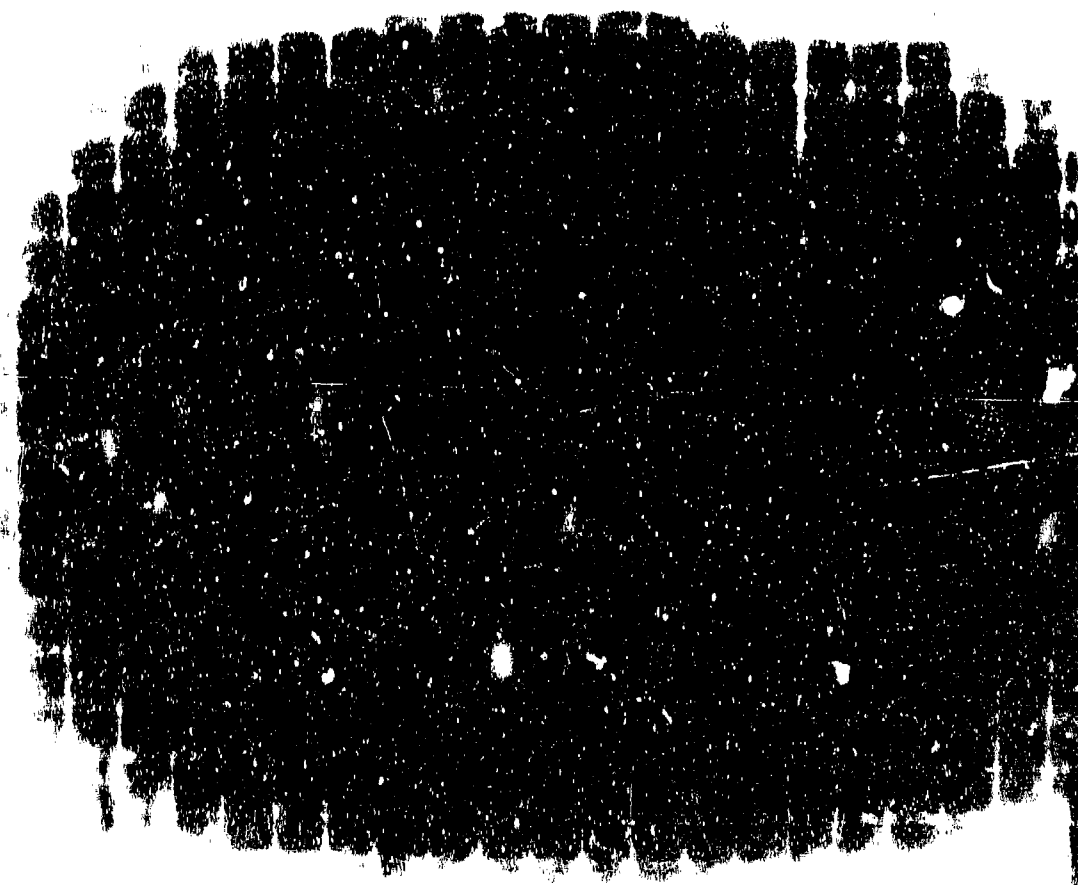


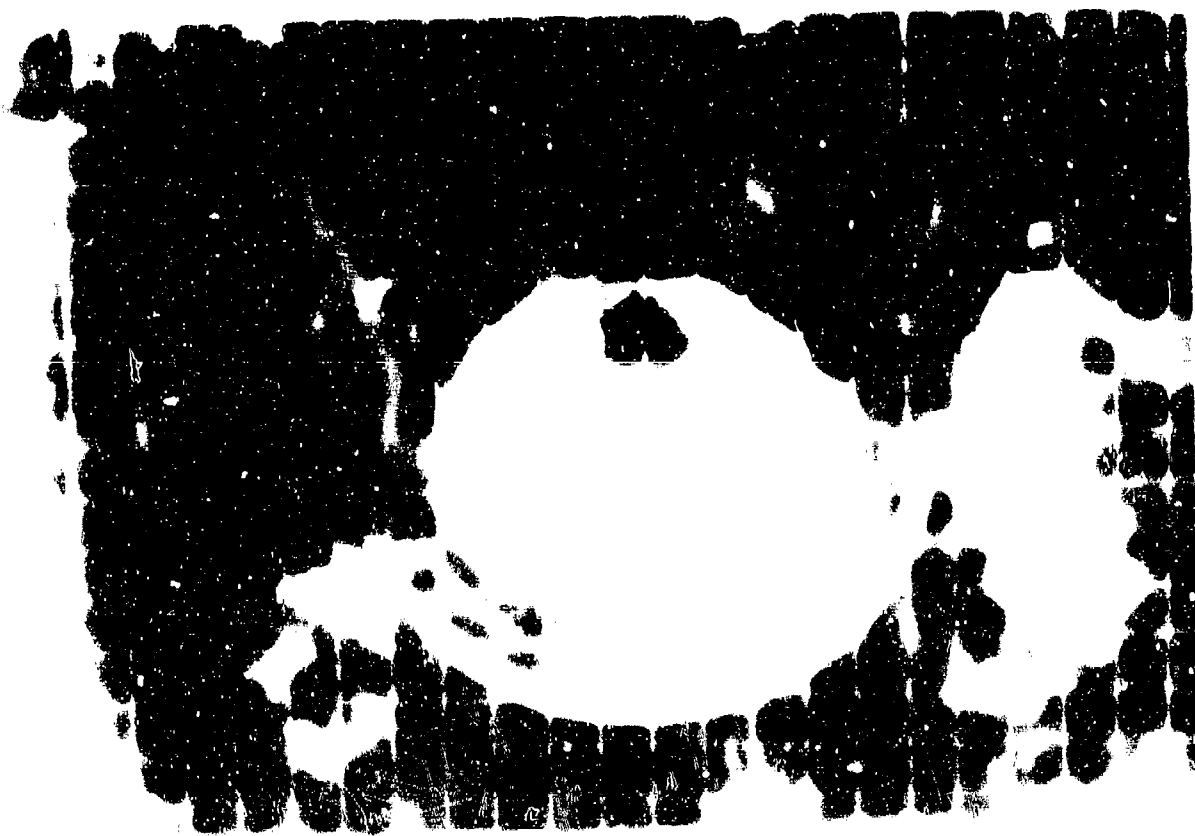
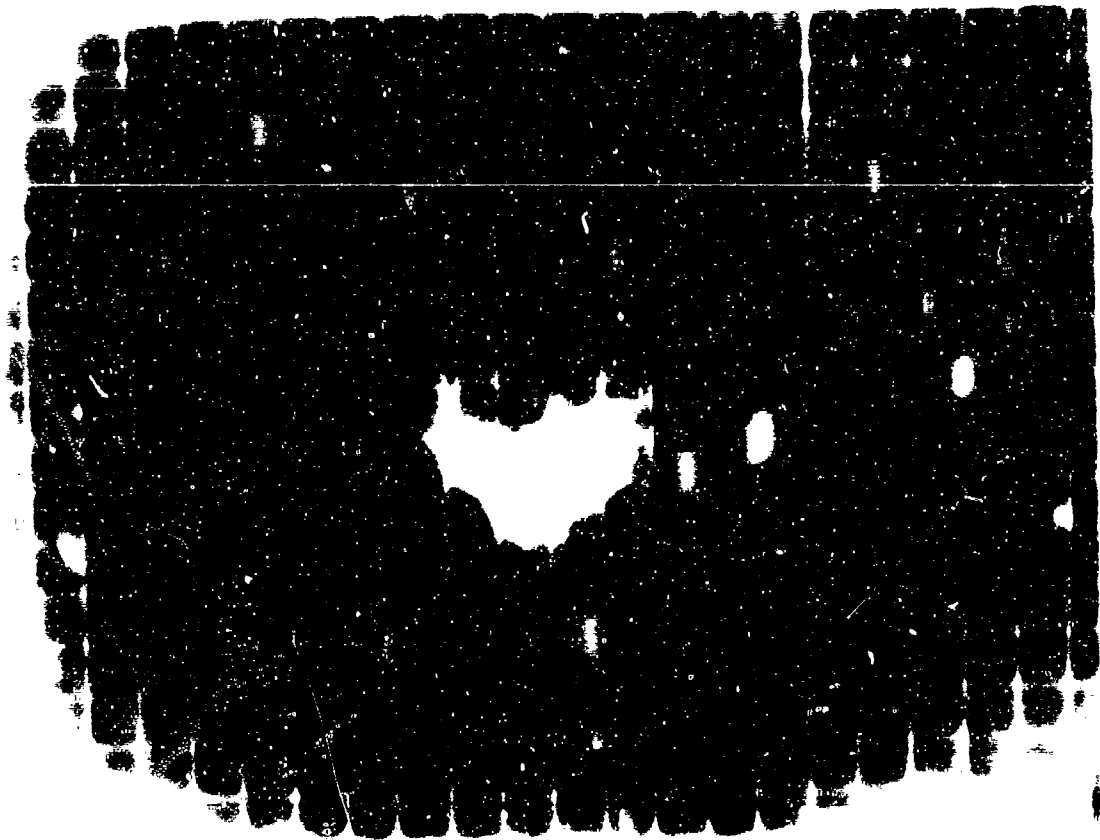
Figure 2. A high-contrast, black and white image showing a dark, irregular shape on the left side, similar to the one in the first image, but with a more defined, rounded top edge. The shape is set against a bright background, and its texture is highly visible.

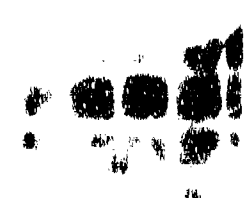
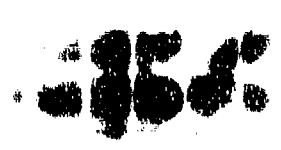
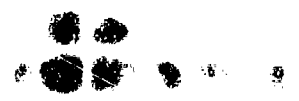




1. The first part of the document is a list of names and addresses, which is followed by a list of names and addresses. The list of names and addresses is as follows:







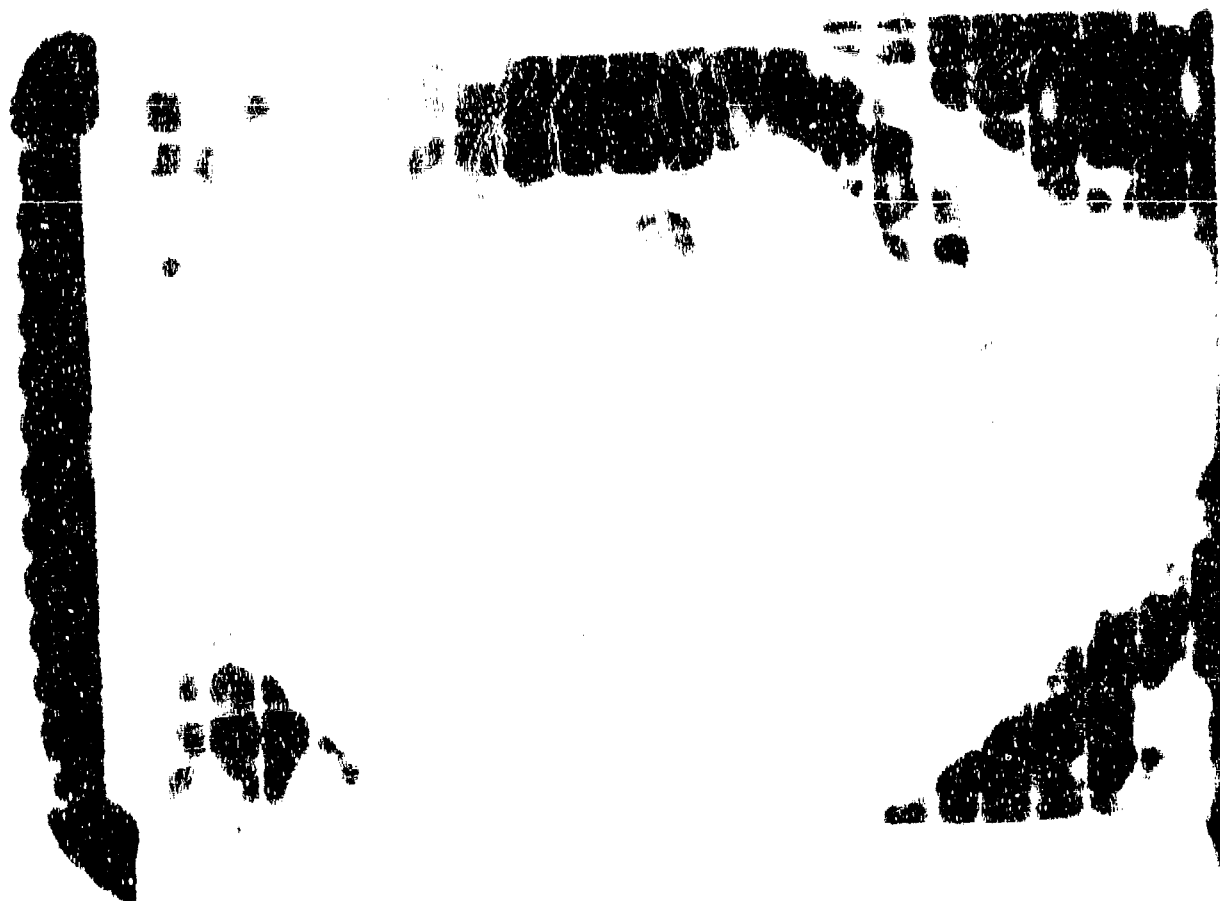


Figure 1. A high-contrast, black and white image showing a dark, irregular shape on the left side, possibly a shadow or a mark, against a lighter background.

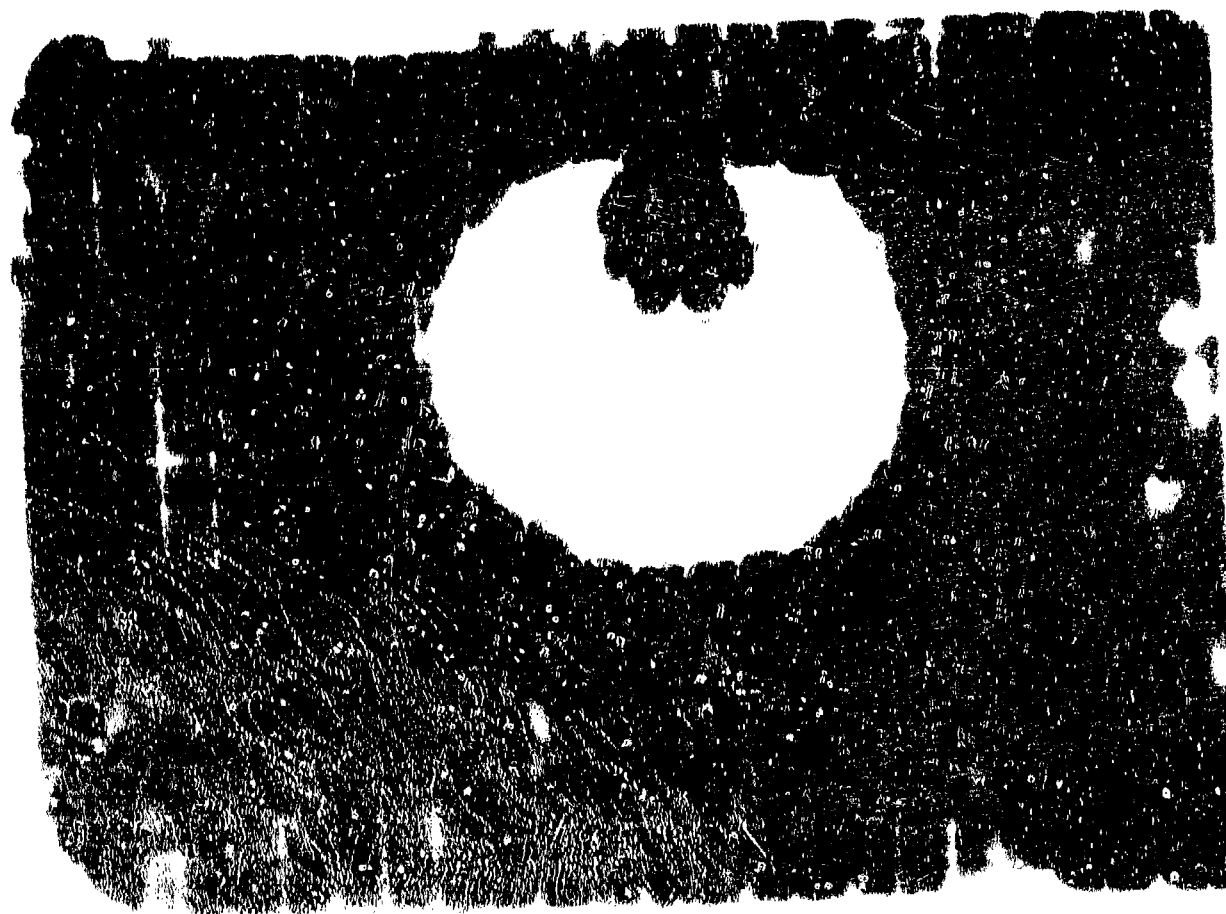
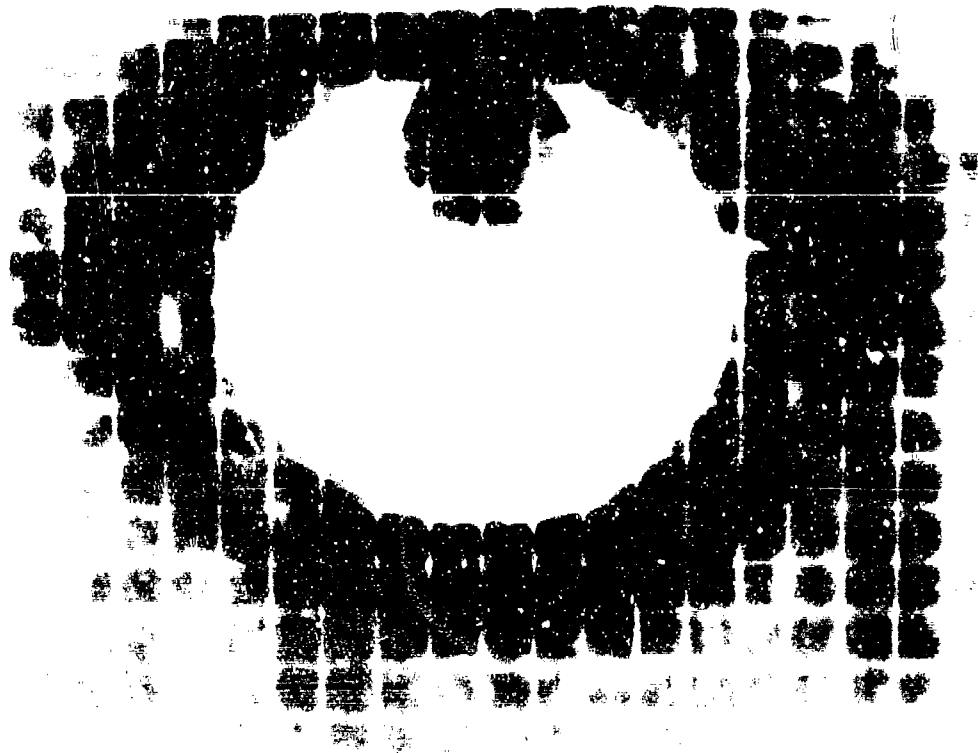


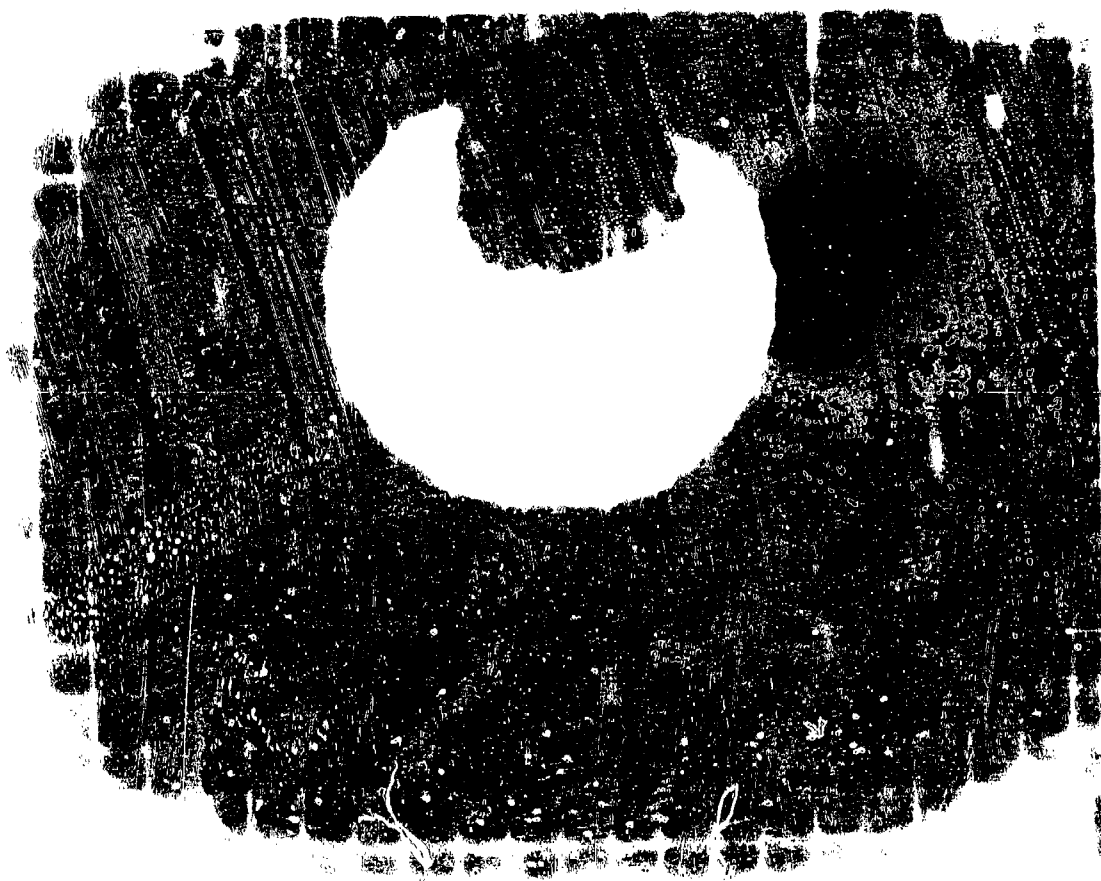
Figure 2. A high-contrast, black and white image showing a dark, irregular shape on the left side, possibly a shadow or a mark, against a lighter background.

Figure 3

Figure 4



1. The first image is a high-contrast, black and white photograph of a circular object, possibly a coin or a seal, with a prominent white circular center and a dark, textured outer ring. The texture of the ring appears granular or speckled. The entire object is set against a plain white background.



2. The second image is a high-contrast, black and white photograph of a circular object, similar to the first one, but with a different texture for the dark outer ring. The ring in this image appears more fibrous or striated, with visible vertical lines or ridges. The overall appearance is still high-contrast and grainy.

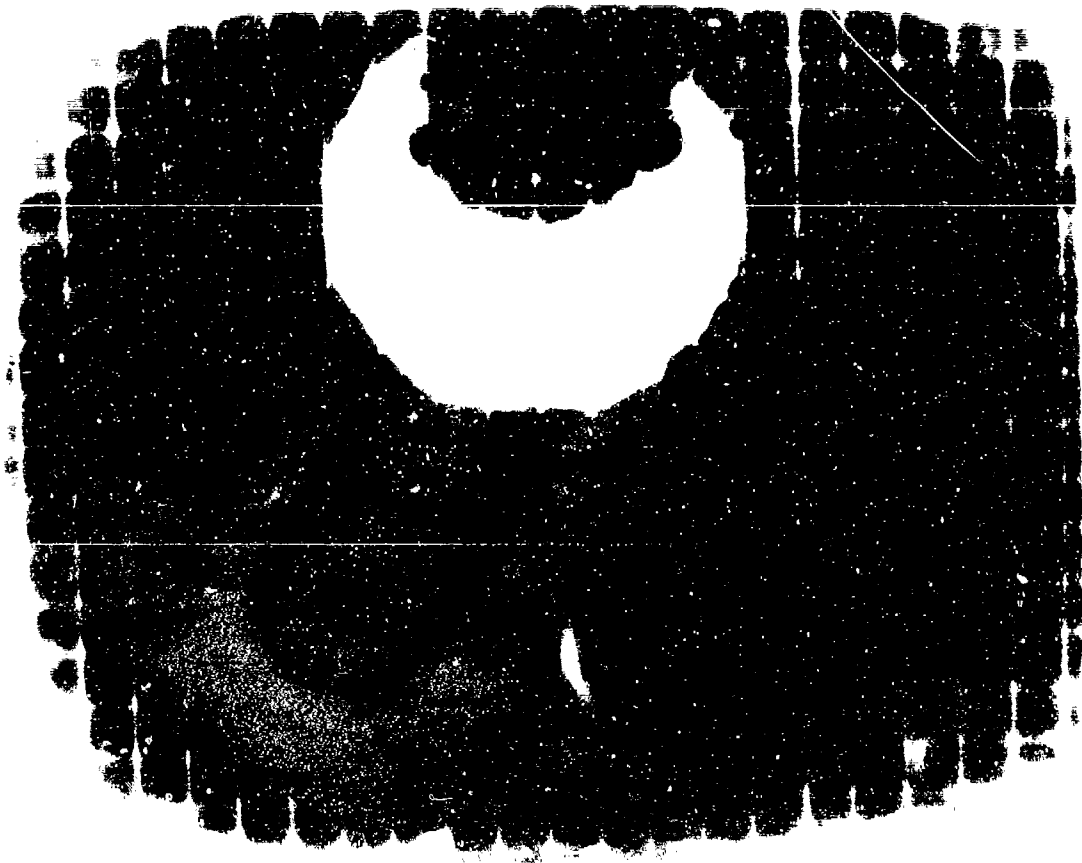


Figure 1: A dark, textured, roughly circular object with a large, irregular white hole in the center. The object has a frayed, irregular edge and a grainy, mottled texture.

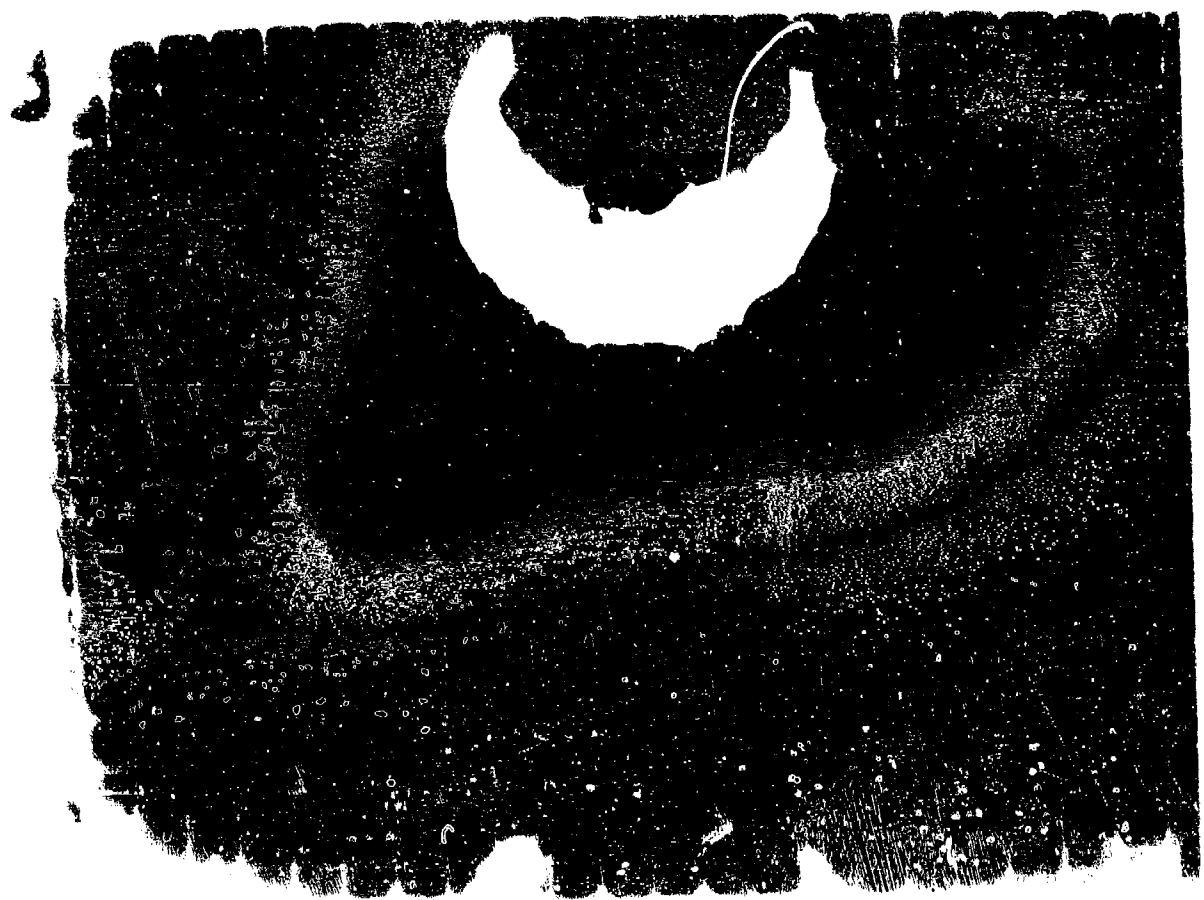


Figure 2: A dark, textured, roughly circular object with a large, irregular white hole in the center. The object has a frayed, irregular edge and a grainy, mottled texture, similar to the one above but with slightly different internal patterns.

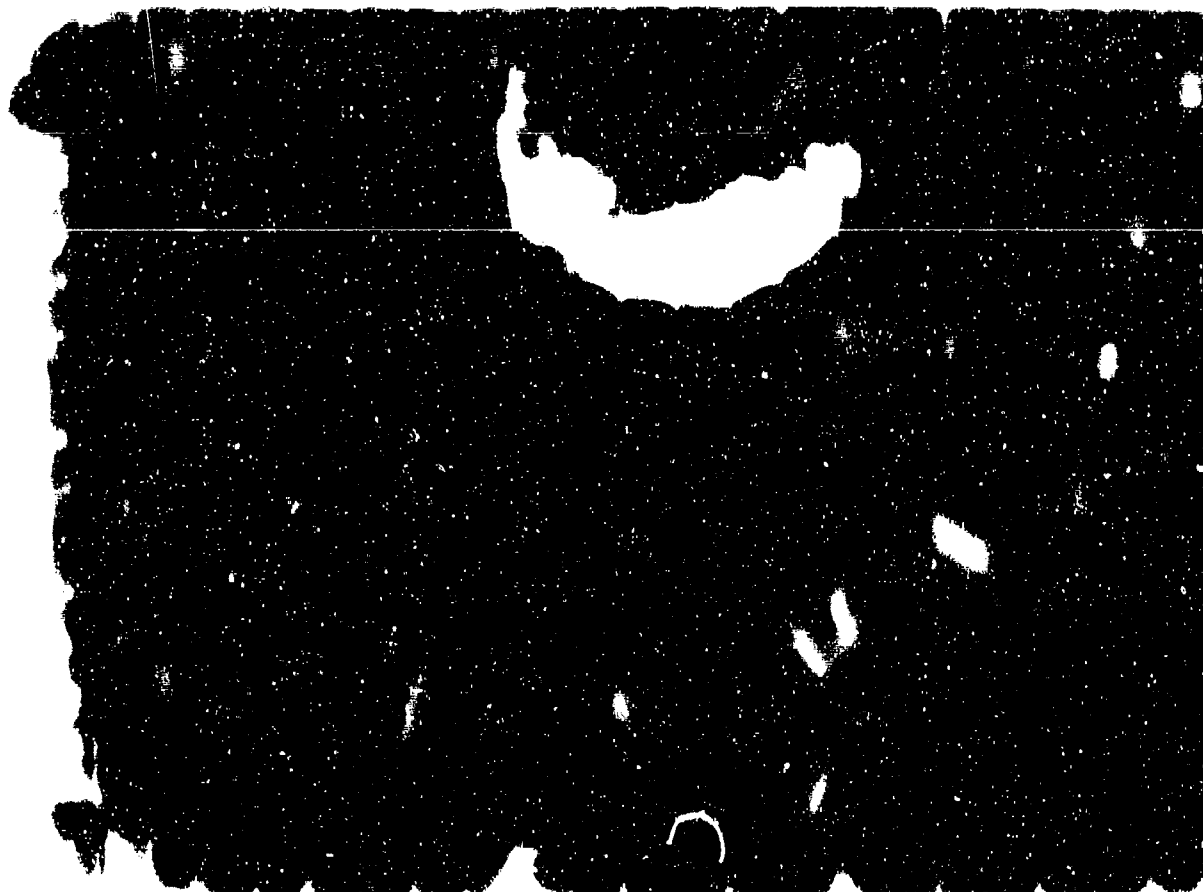


Figure 1. A dark, rectangular image with a large, irregular white shape in the upper center, resembling a torn piece of paper or a large hole. The background is black with visible vertical banding and numerous small white specks, suggesting a high-contrast scan of a dark surface.

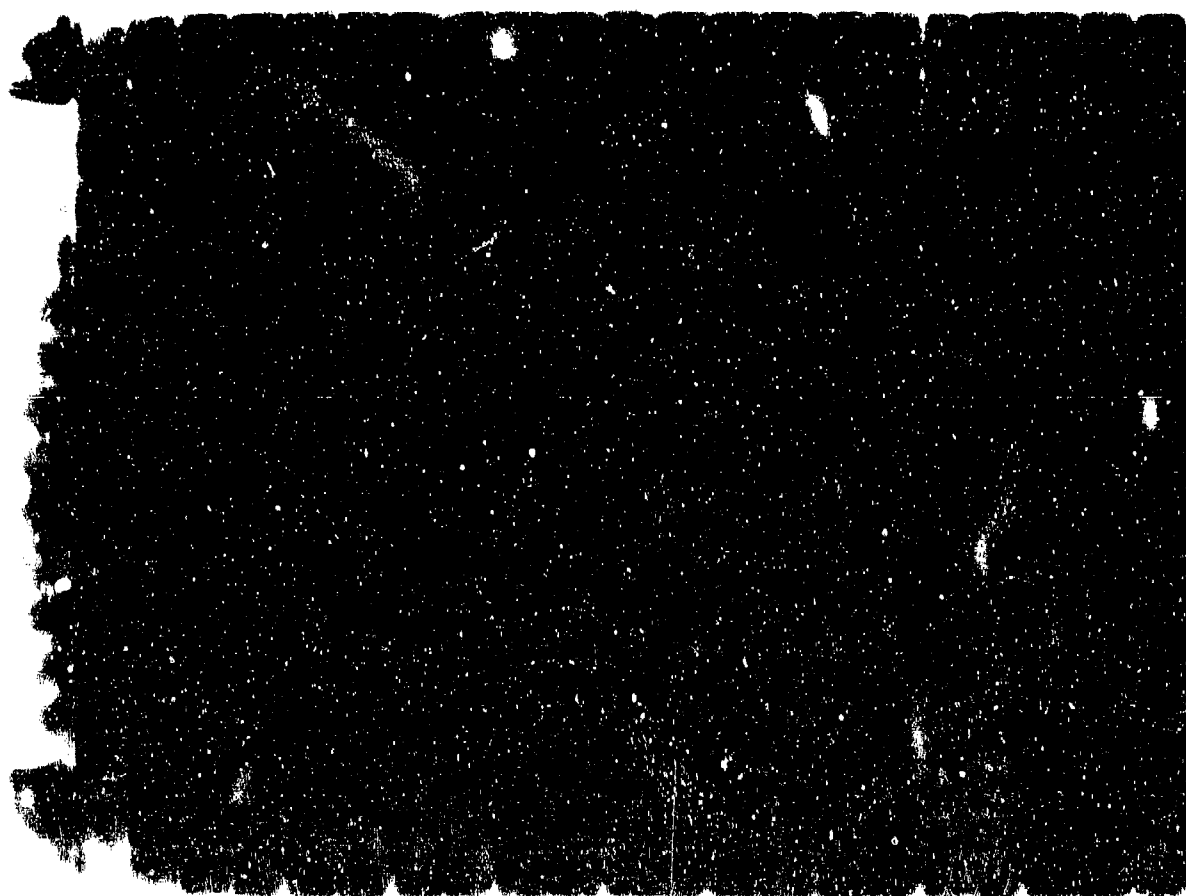


Figure 2. A dark, rectangular image, mostly black with visible vertical banding and numerous small white specks. There are a few small, bright white spots scattered across the surface, but no large distinct shapes are visible.

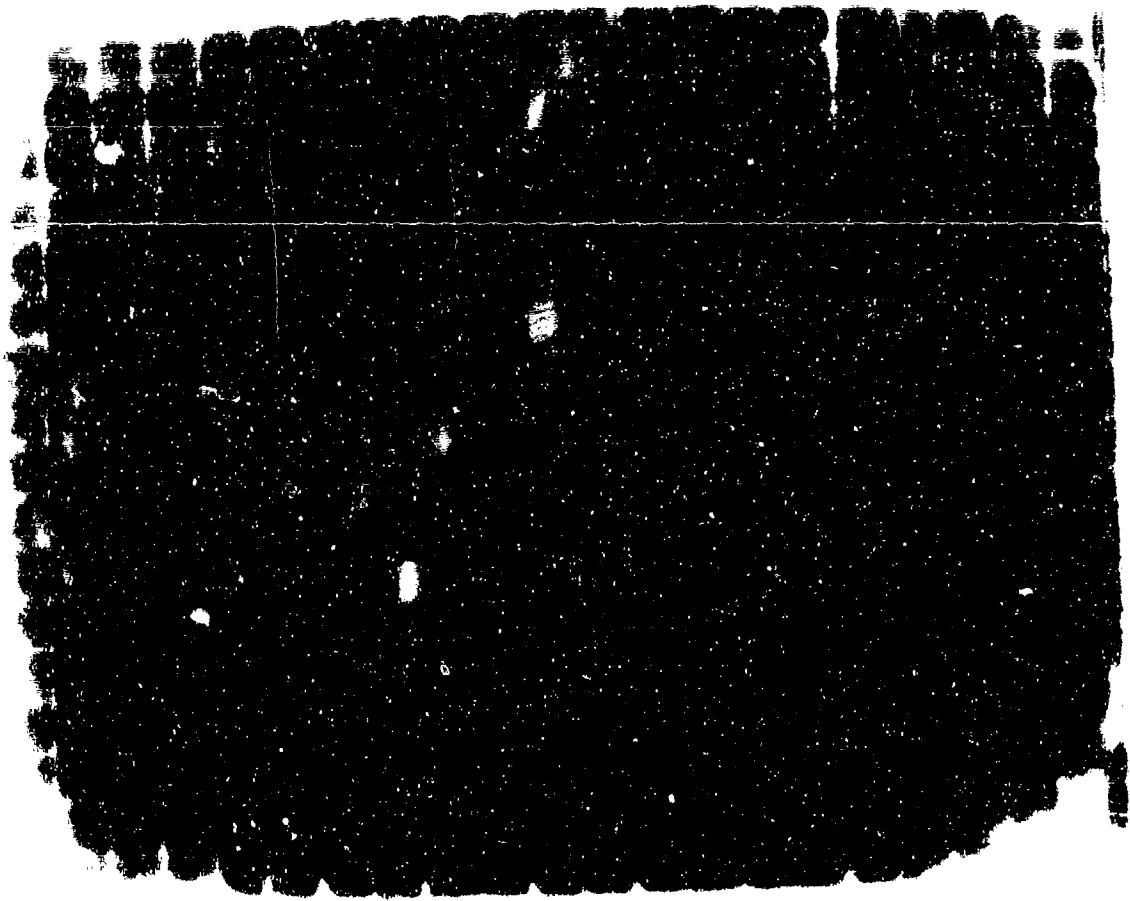
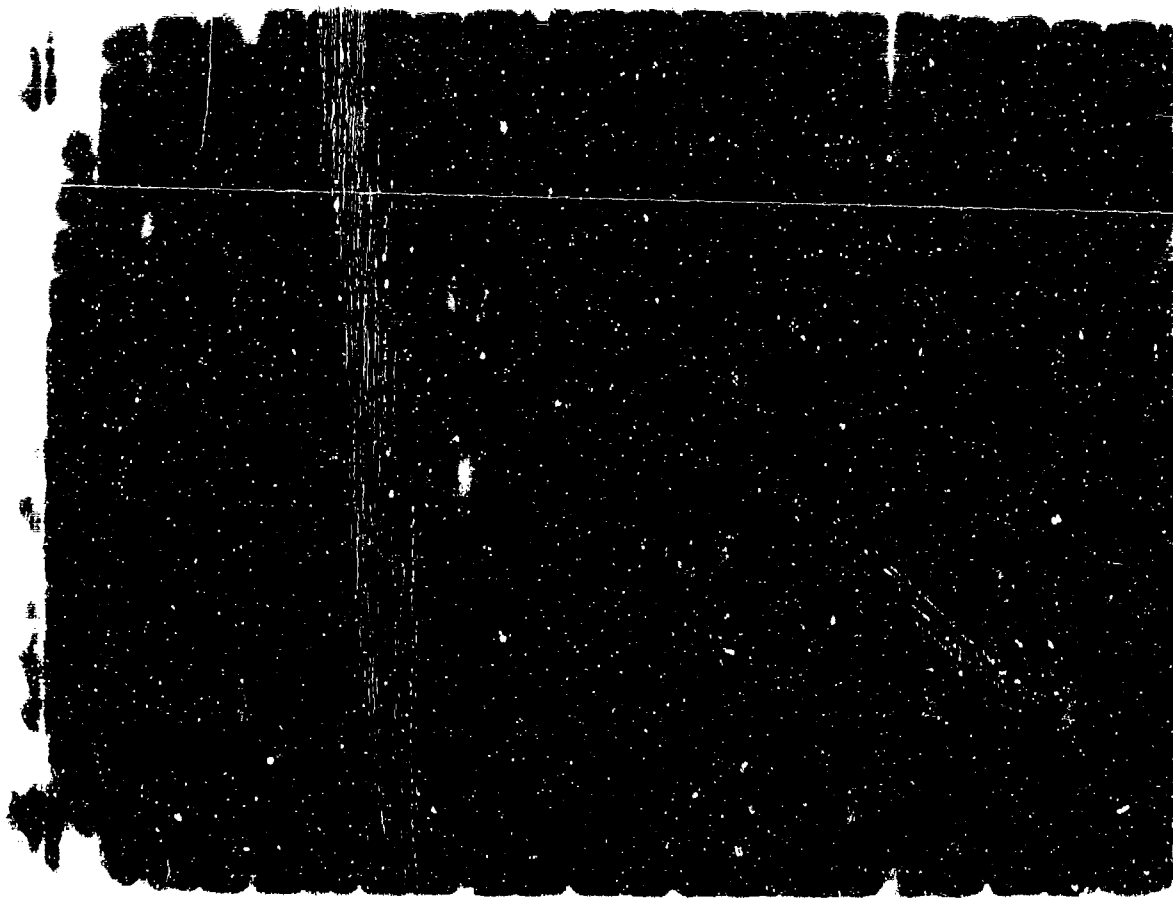


Figure 1. The first image in the sequence of images showing the initial state of the system.



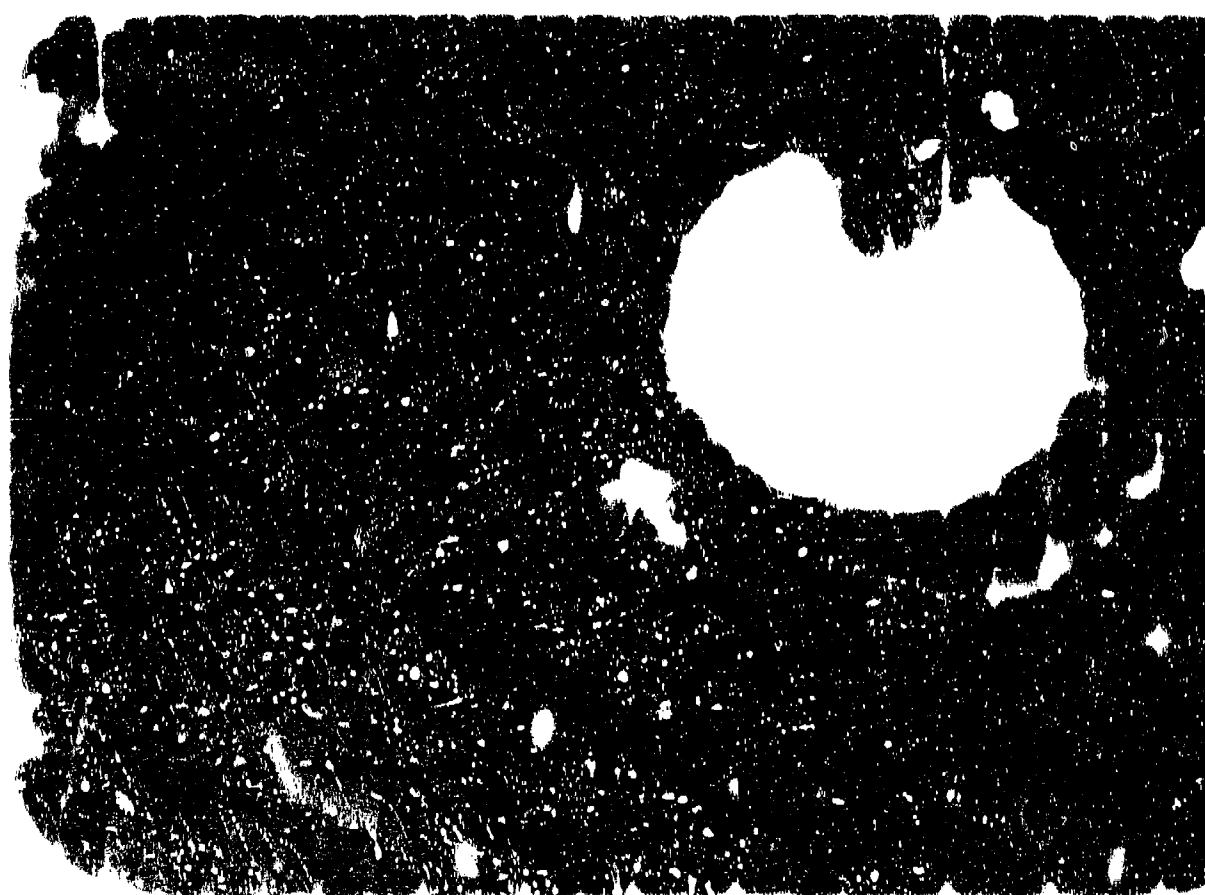
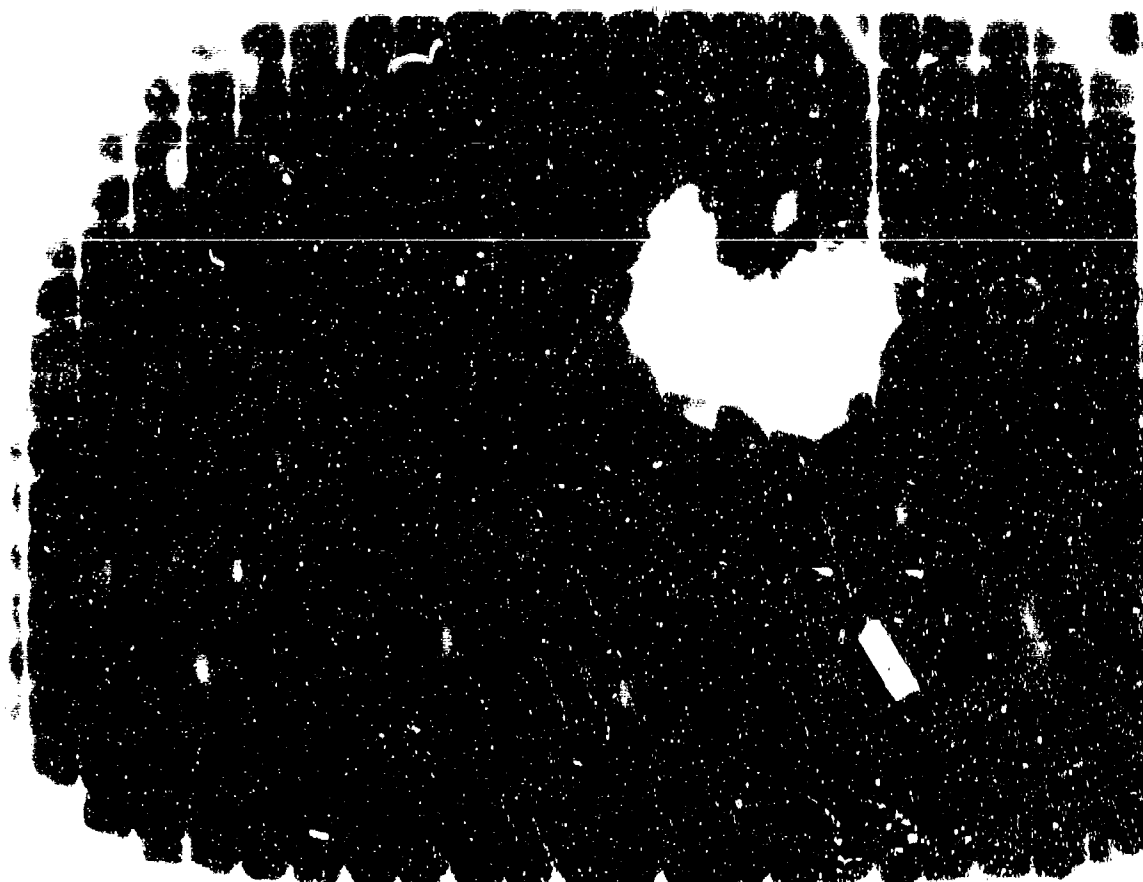
Figure 2. The second image in the sequence of images showing the initial state of the system.



0 100 200 300 400 500 600 700 800 900 1000



0 100 200 300 400 500 600 700 800 900 1000



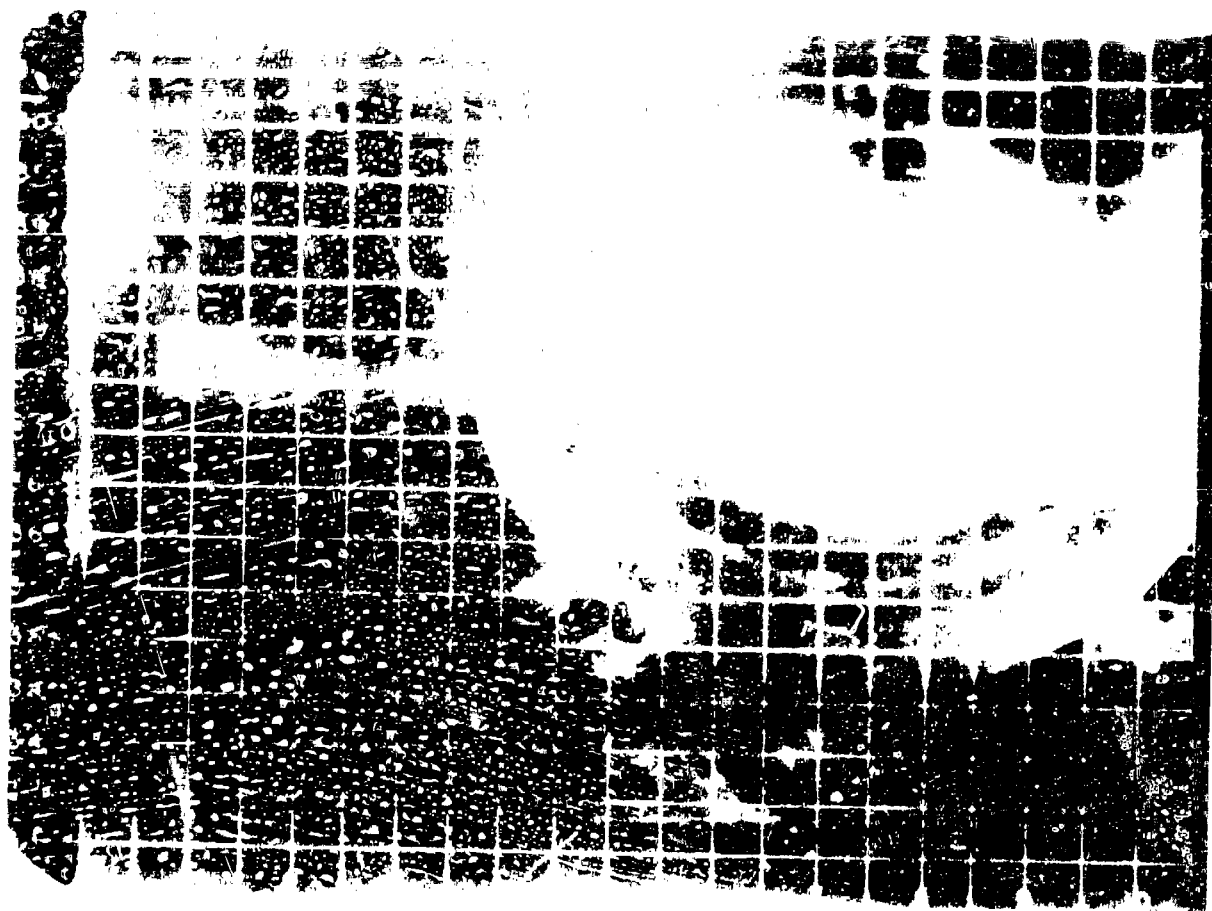


Figure A.179 Shot Dakota, Series 36231, Frame 66, Blue, f.1., 17 mm, B-52.

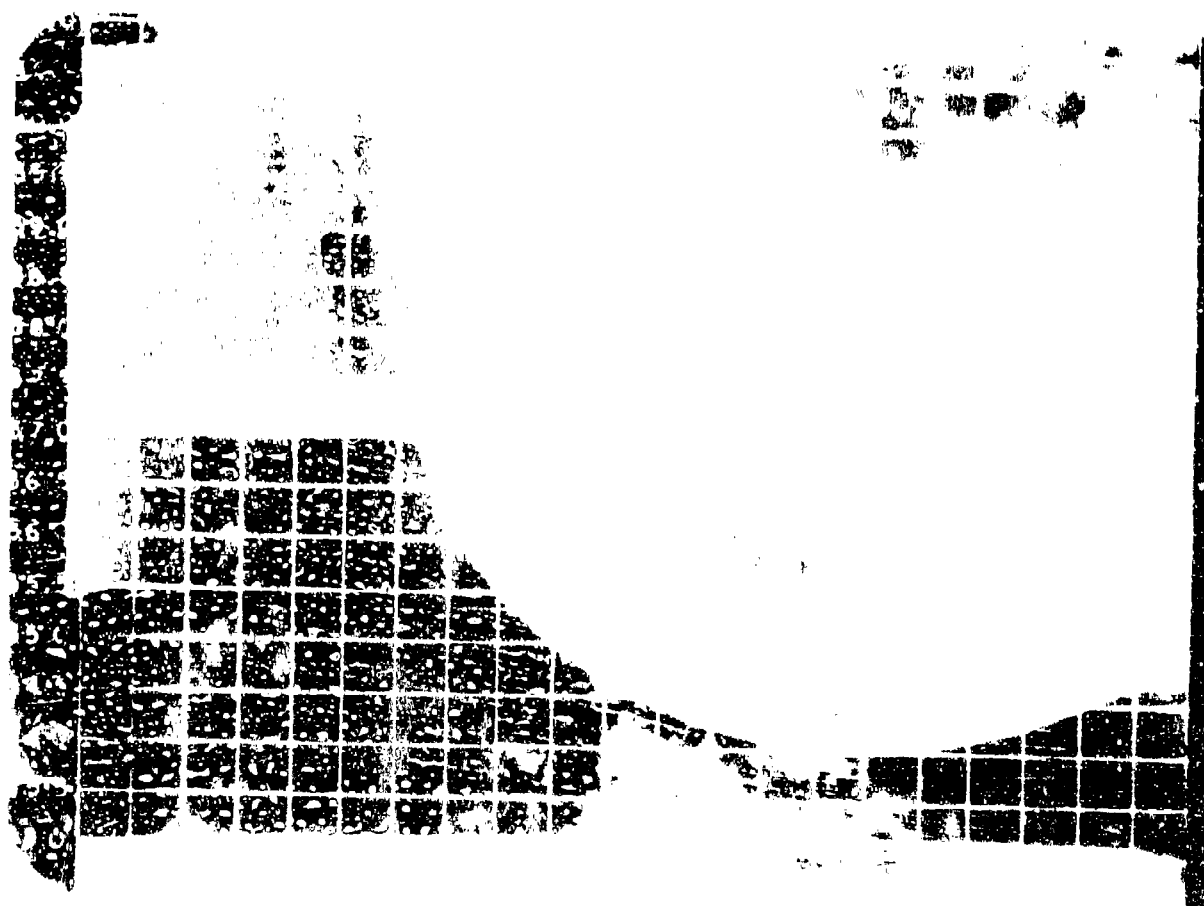


Figure A.180 Shot Dakota, Series 36231, Frame 60, Blue, f.1., 17 mm, B-52.

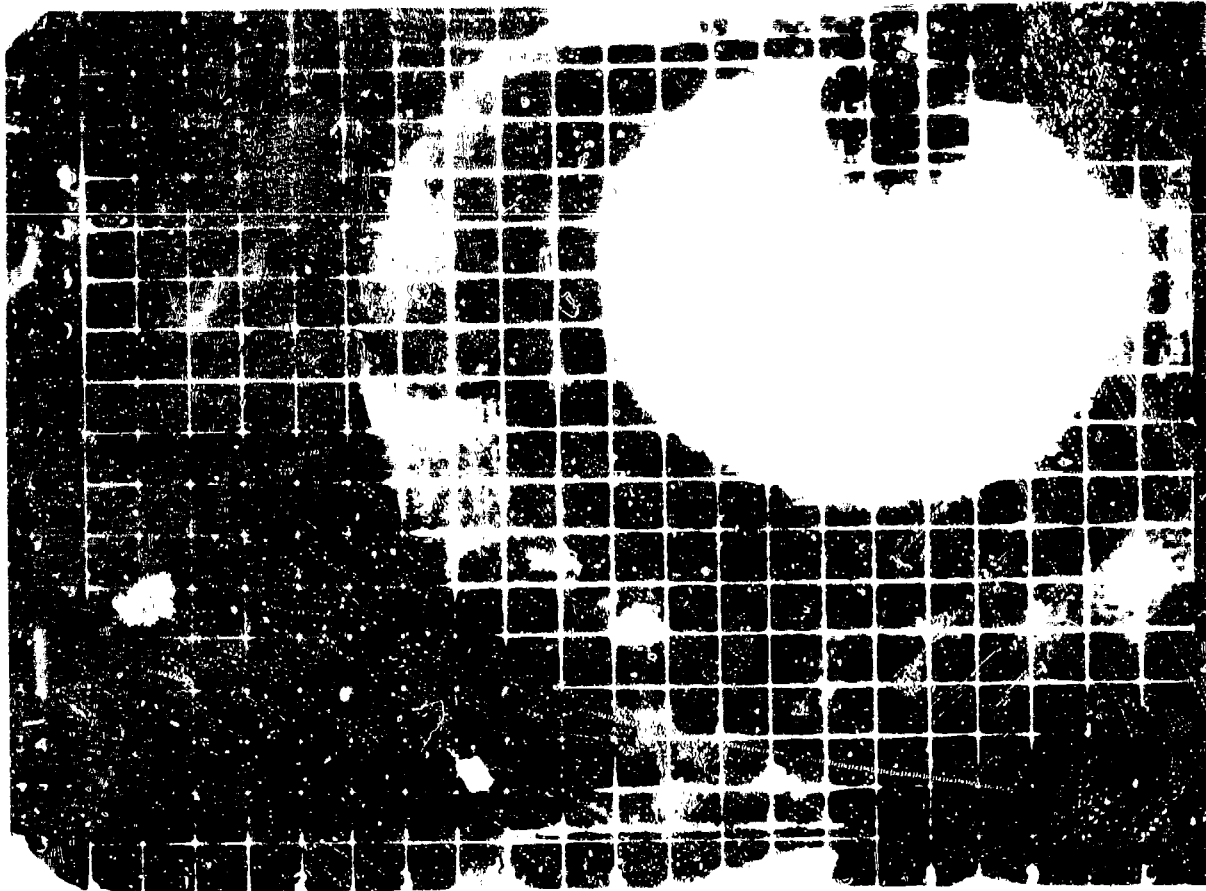


Figure A.181 Shot Dakota, Series 36231, Frame 115, Blue, f.1., 17 mm, B-52.

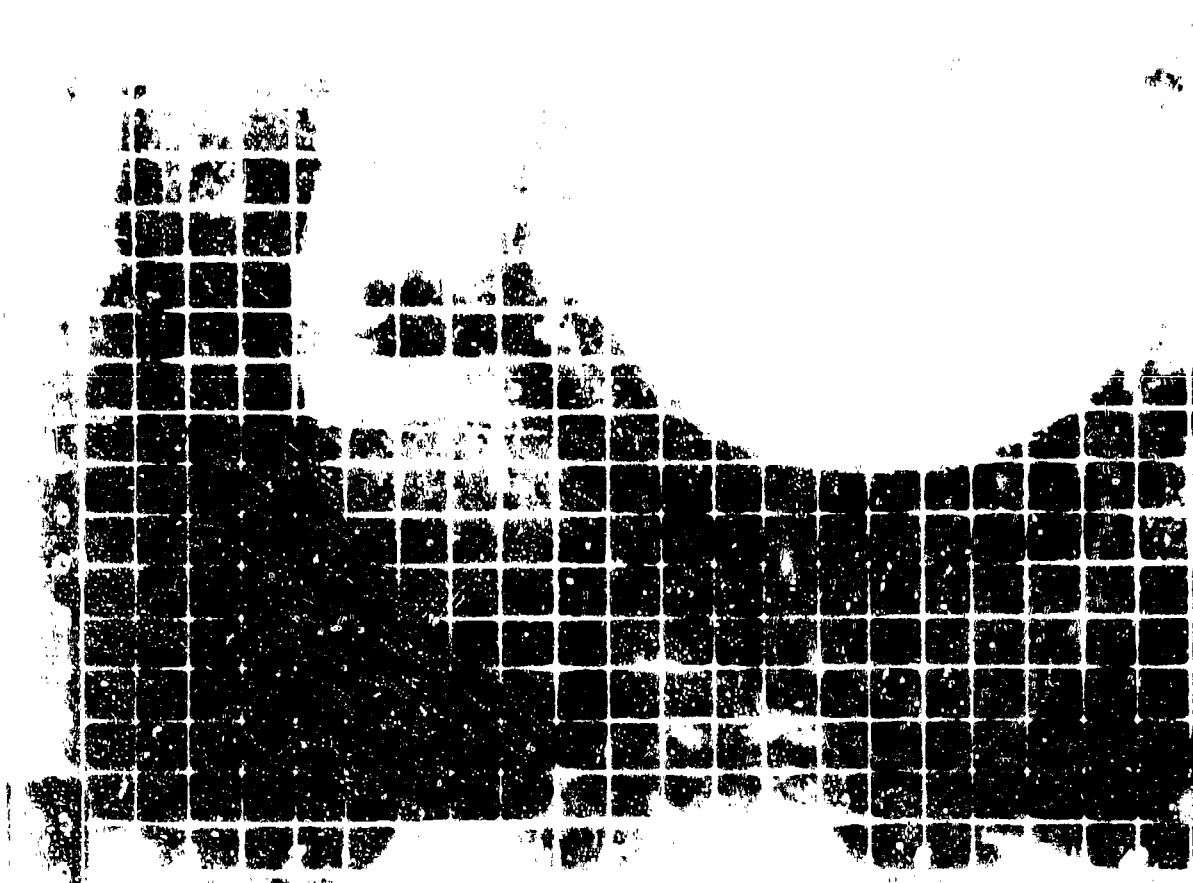


Figure A.182 Shot Dakota, Series 36231, Frame 150, Blue, f.1., 17 mm, B-52.

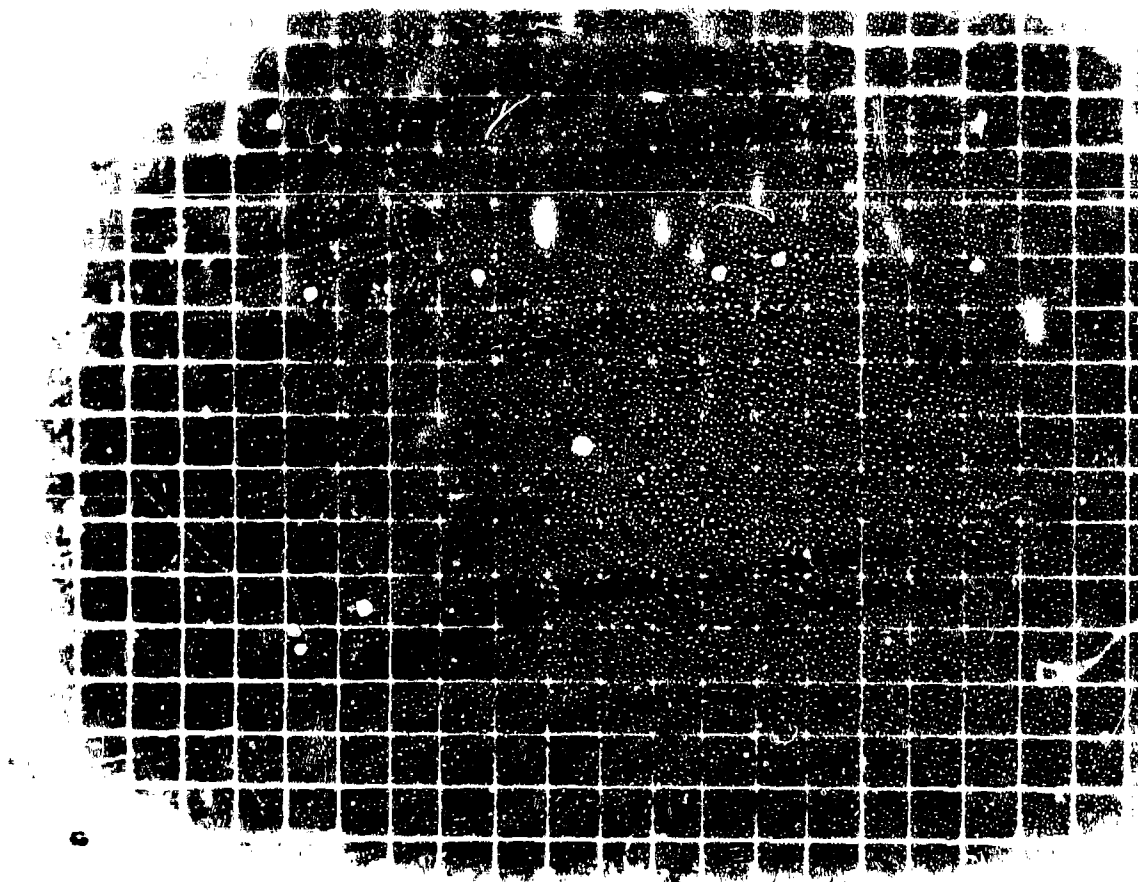


Figure A.183 Shot Dakota, Series 36233, Frame Zero, Blue, f.1., 10 mm, B-47.

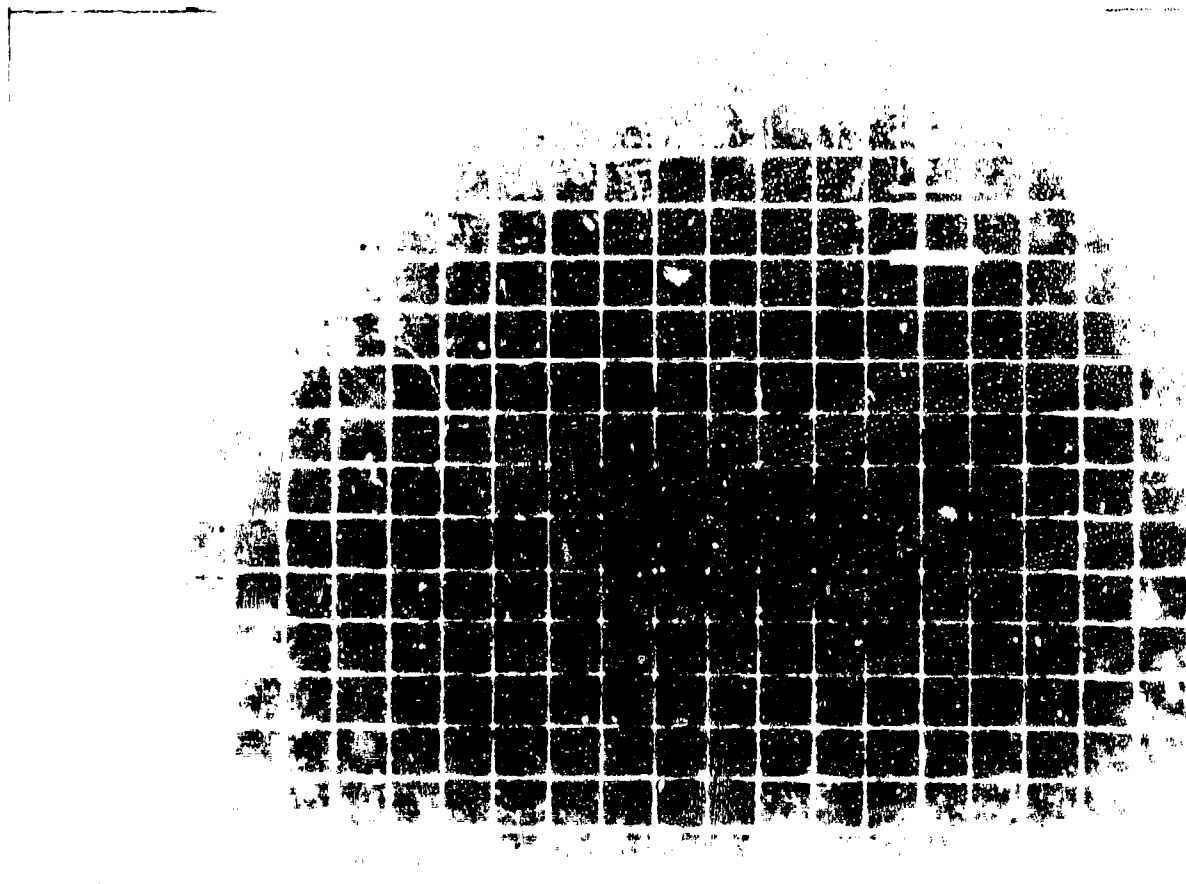


Figure A.184 Shot Dakota, Series 36233, Frame 30, Blue, f.1., 10 mm, B-47.

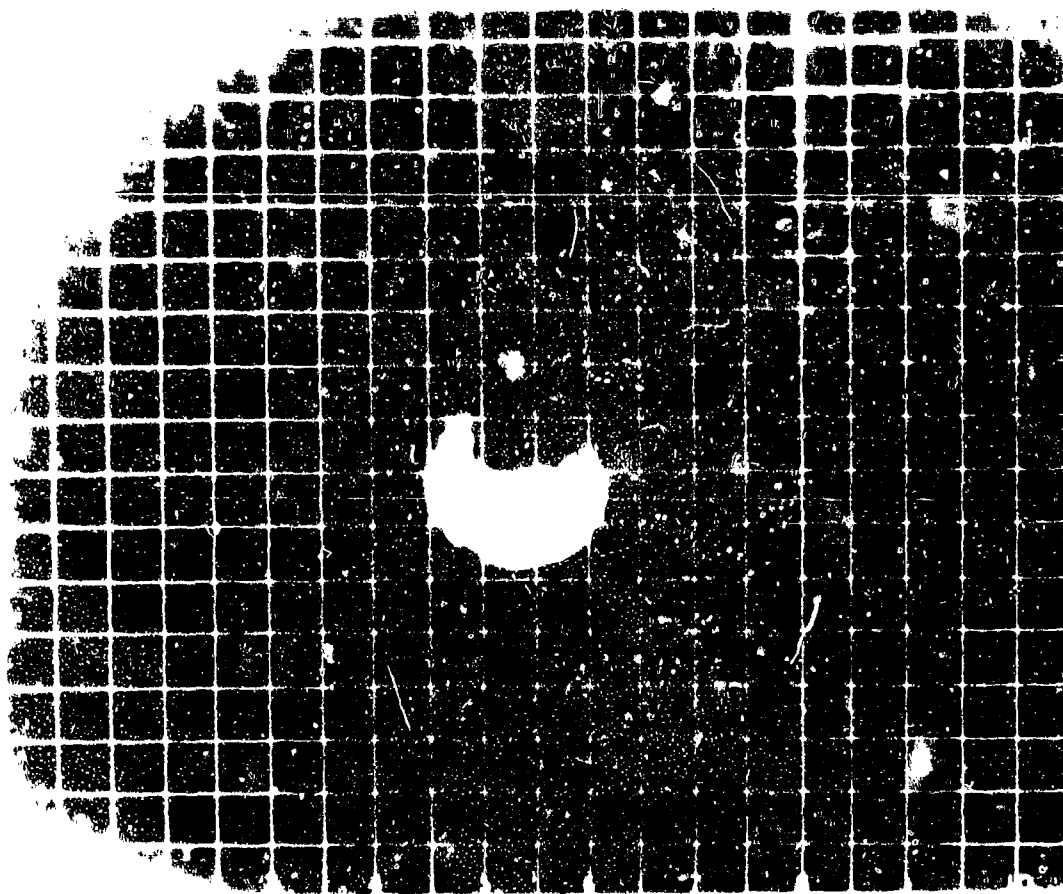


Figure A.185 Shot Dakota, Series 36233, Frame 45, Blue, f.1., 10 mm, B-47.



Figure A.186 Shot Dakota, Series 36233, Frame 50, Blue, f.1., 10 mm, B-47.

Figure A.187 Shot Dakota, Series 36233, Frame 65, Blue, f.l., 10 mm, B-47.

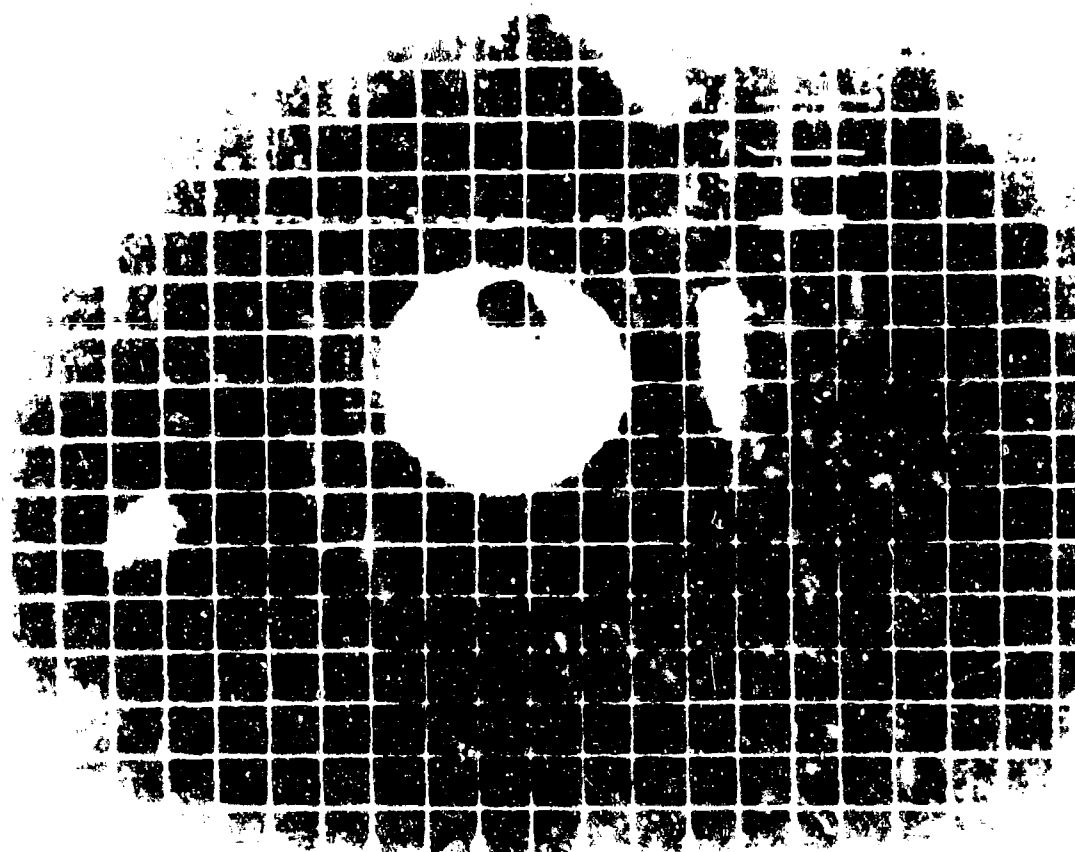


Figure A.188 Shot Dakota, Series 36233, Frame 99, Blue, f.l., 10 mm, B-47.

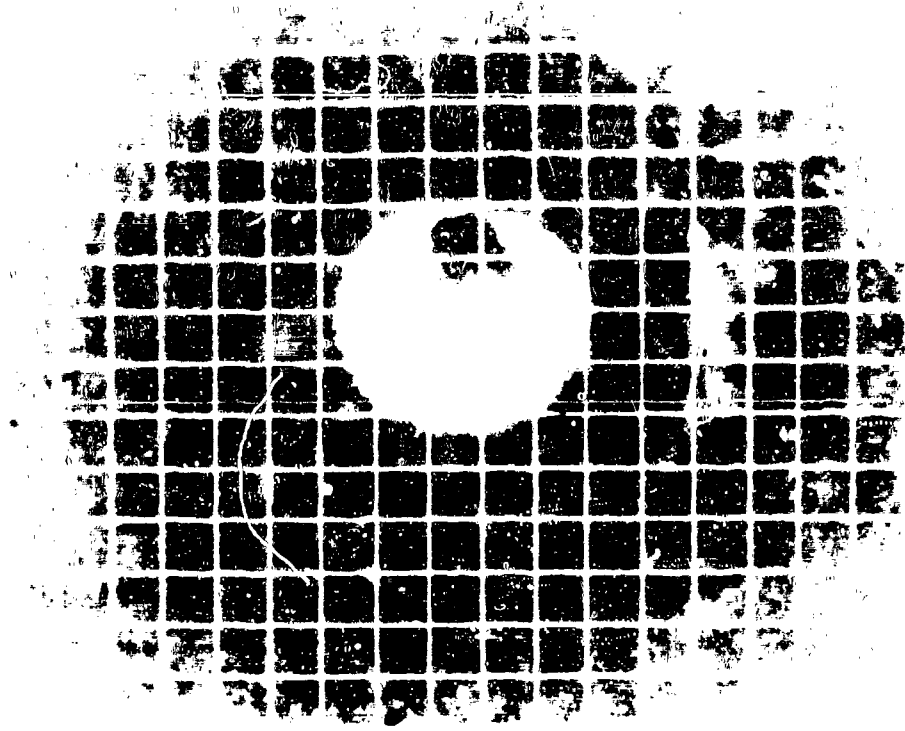


Figure A.189 Shot Dakota, Series 36233, Frame 115, Blue, f.l., 10 mm, B-47.

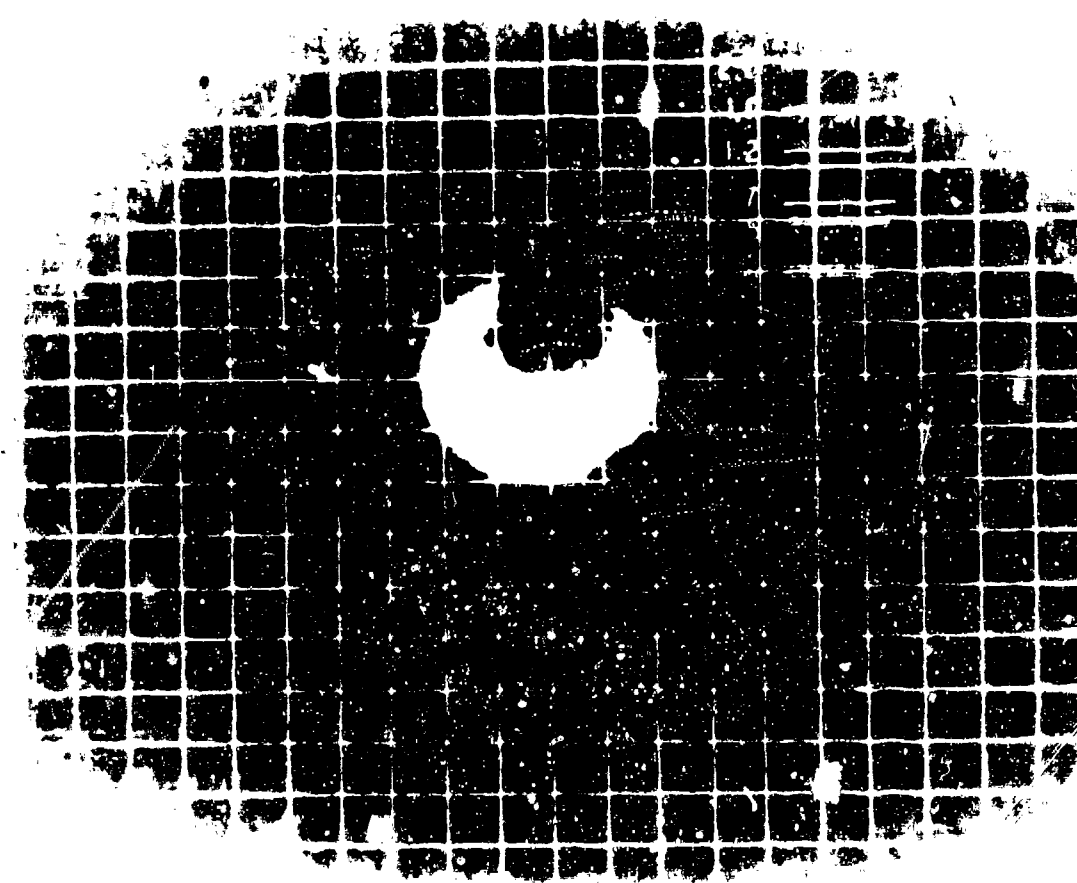


Figure A.190 Shot Dakota, Series 36233, Frame 150, Blue, f.l., 10 mm, B-47.

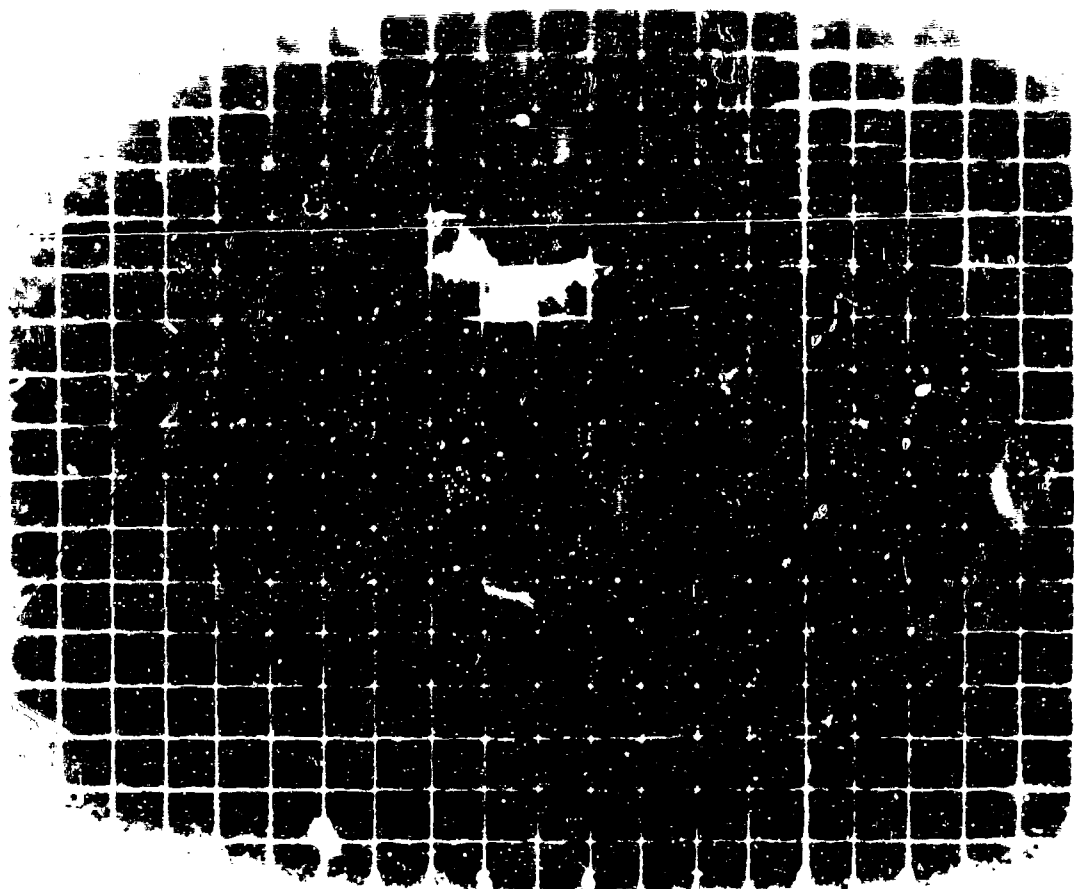


Figure A.191 Shot Dakota, Series 36233, Frame 250, Blue, f.1., 10 mm, B-47.

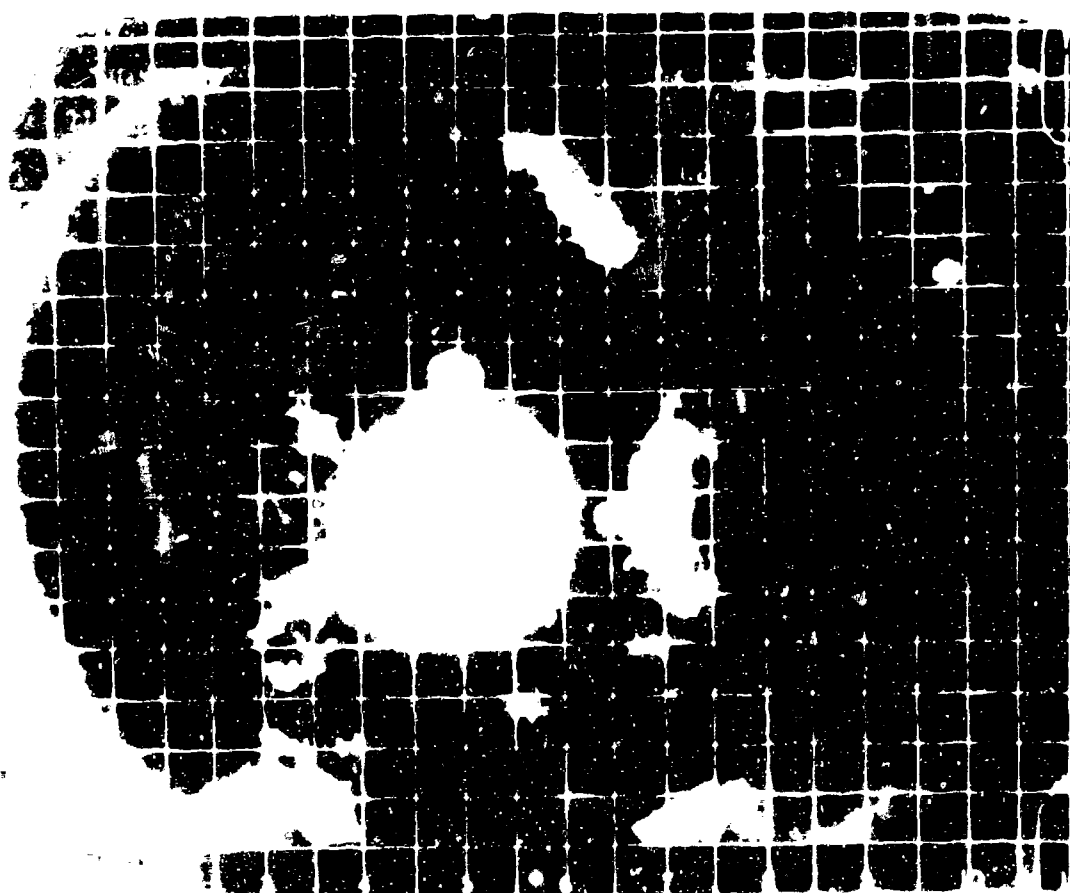


Figure A.192 Shot Dakota, Series 36236, Frame Zero, Red, f.1., 10 mm, B-47.

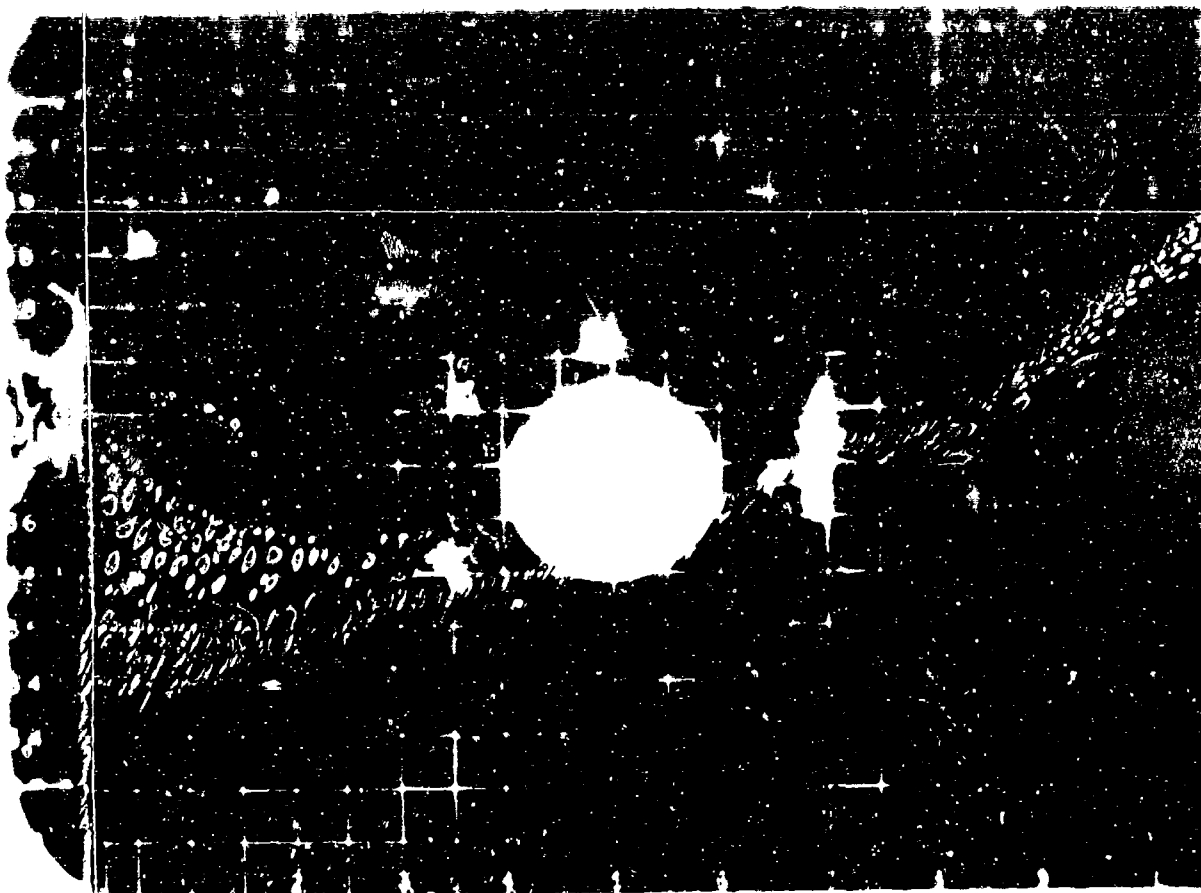


Figure A-13 Shot Dakota, Series 76236, Frame 15, Red, P1, 1000, B-47.

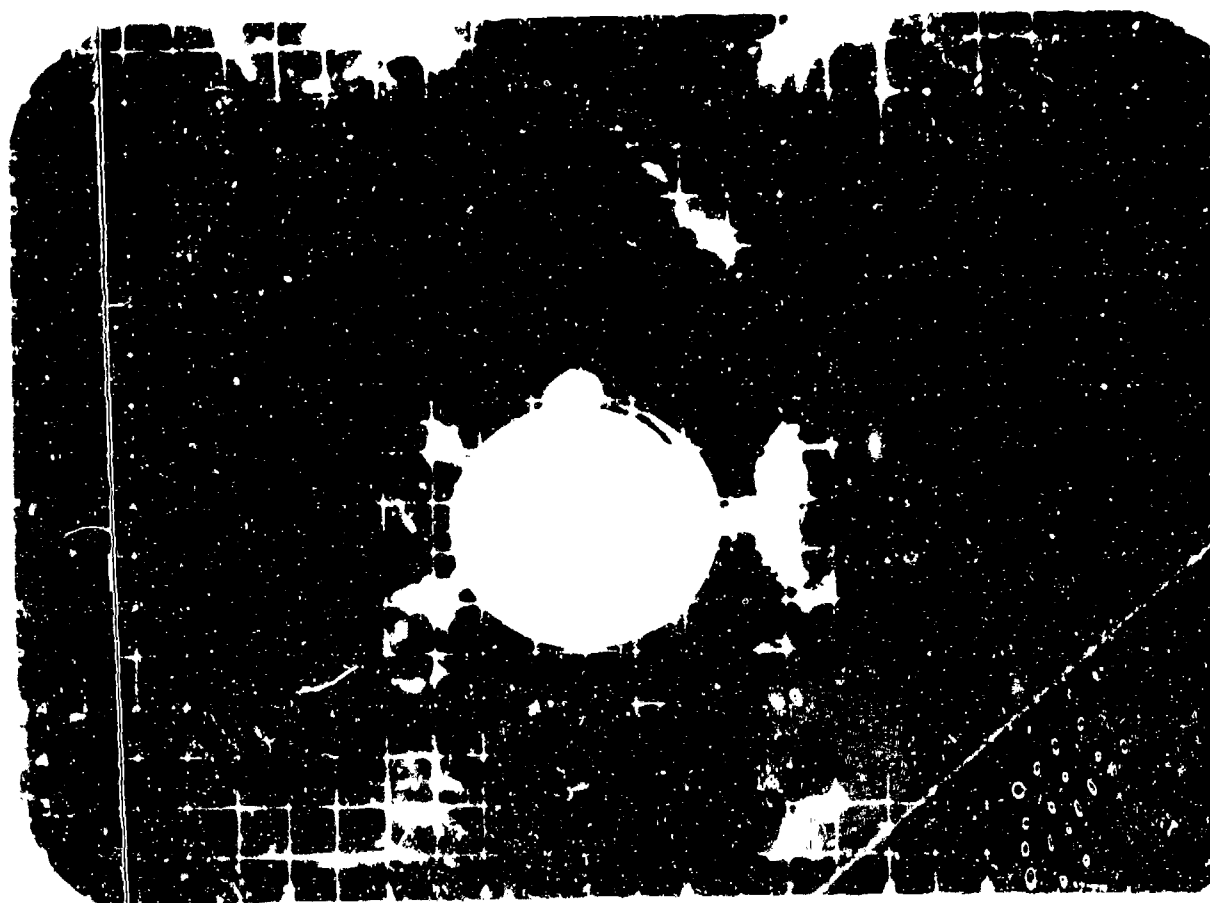


Figure A-14 Shot Dakota, Series 76236, Frame 16, Red, P1, 1000, B-47.

SECRET

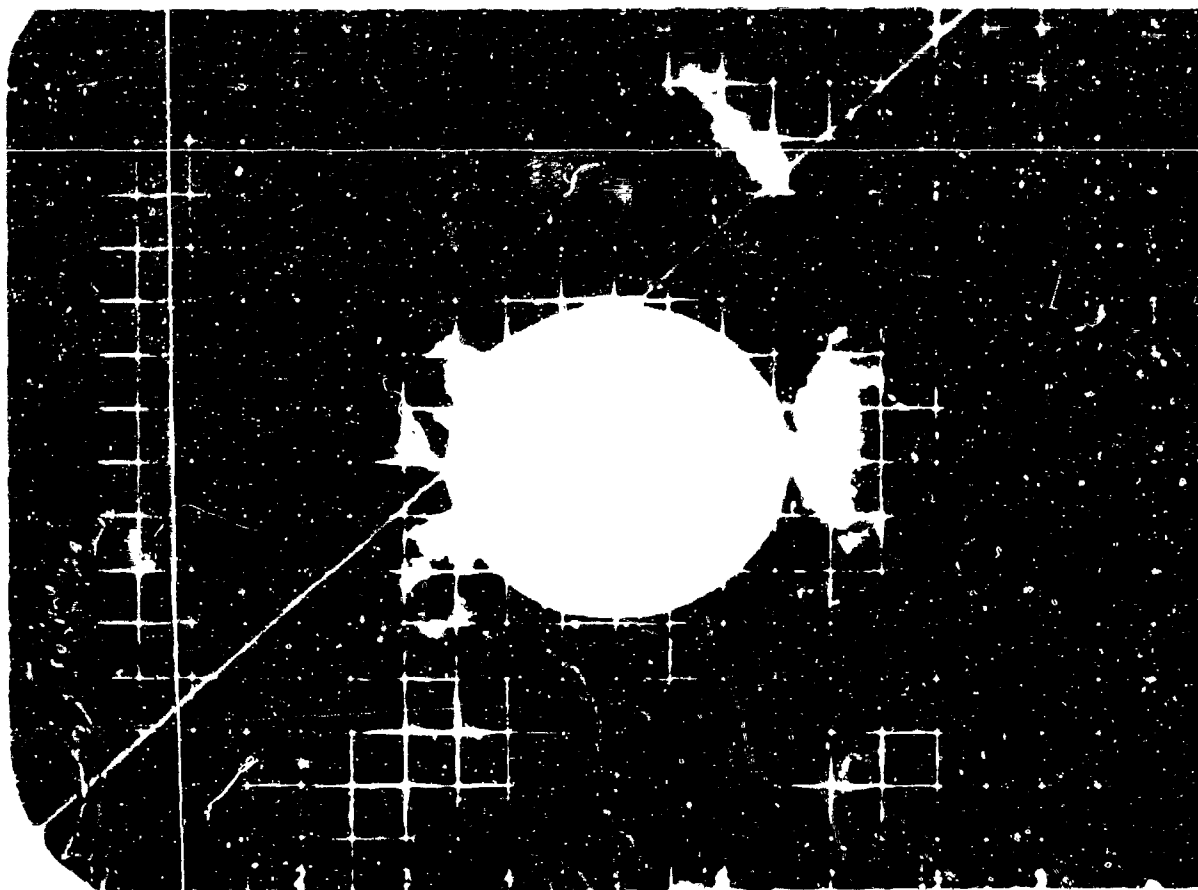


Figure 1. Object 1, Series 36236, Frame 15, Fed, I.L., 10 mm, B 47.

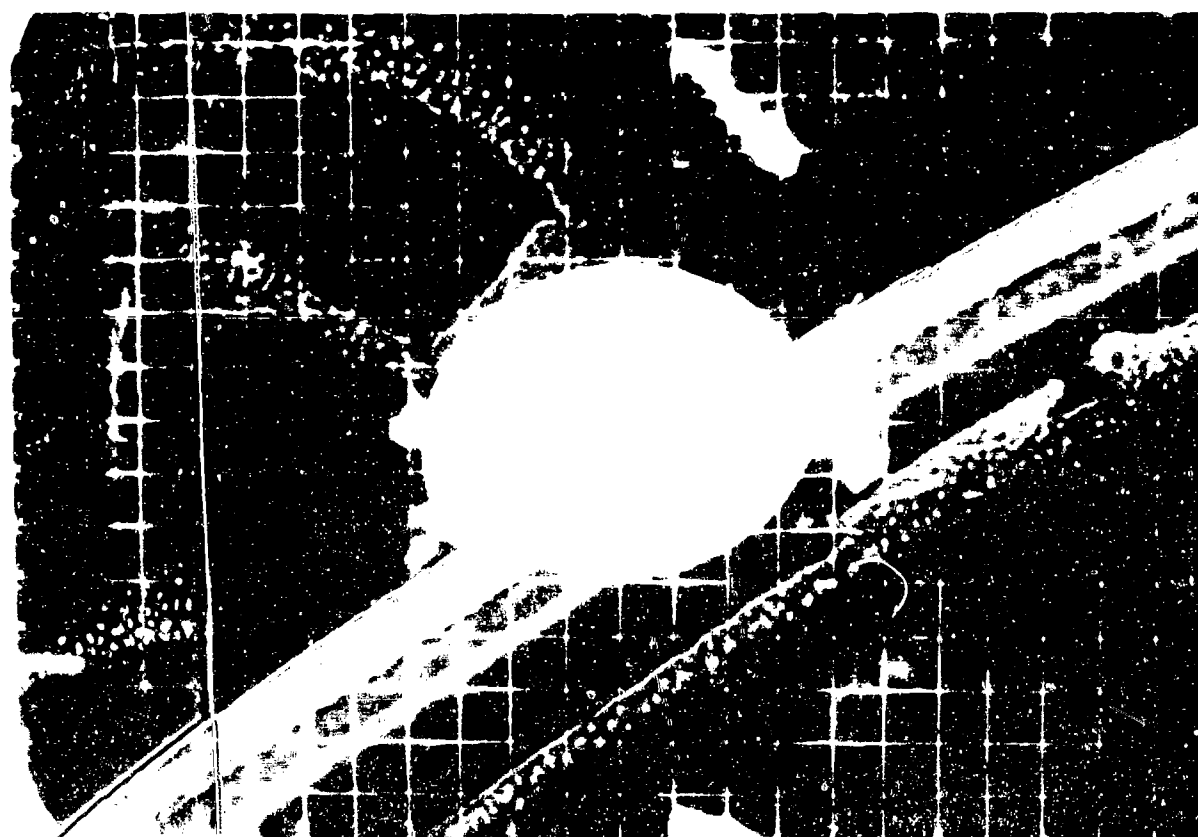


Figure 2. Object 1, Series 36236, Frame 35, Fed, I.L., 10 mm, B 47.

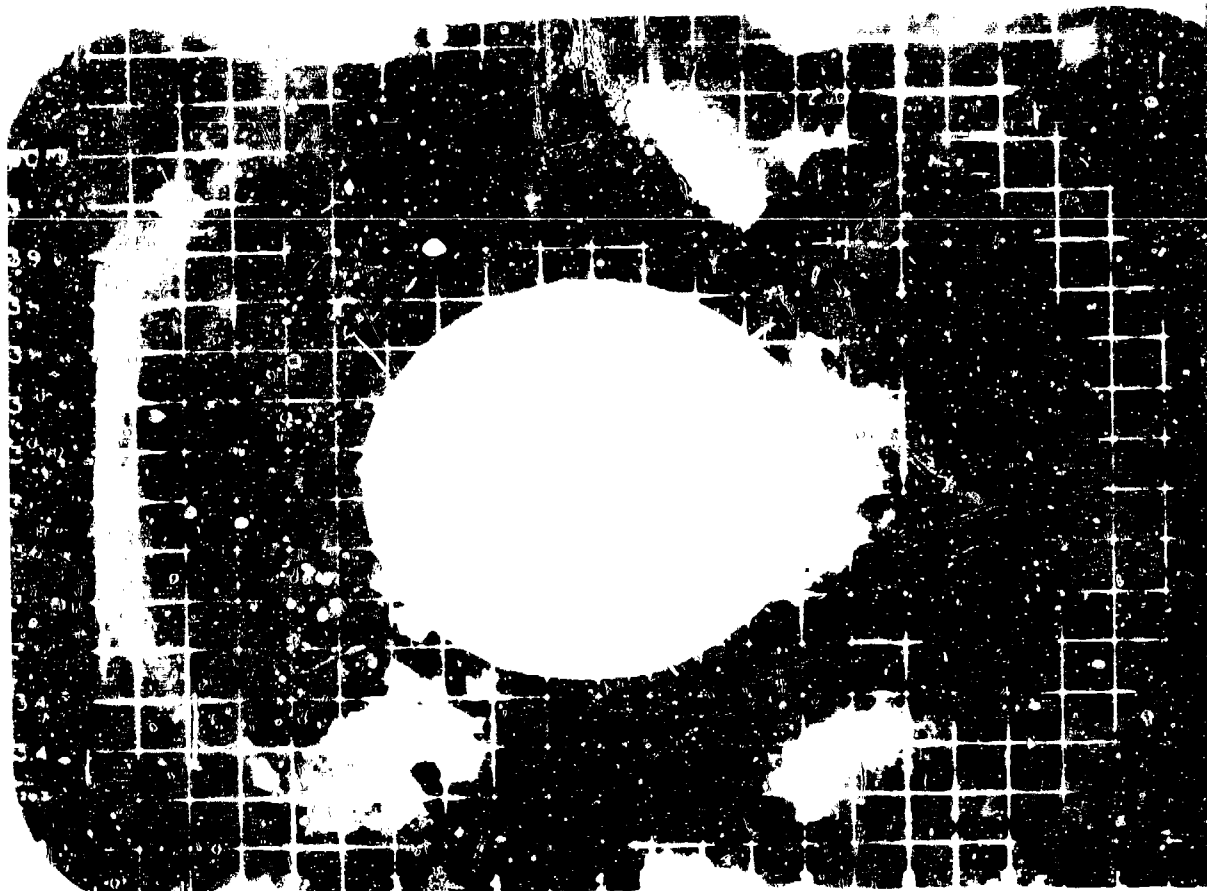


Figure A.197 Shot Dakota, Series 36238, Frame 90, Red, f.l., 10 mm, B-47.

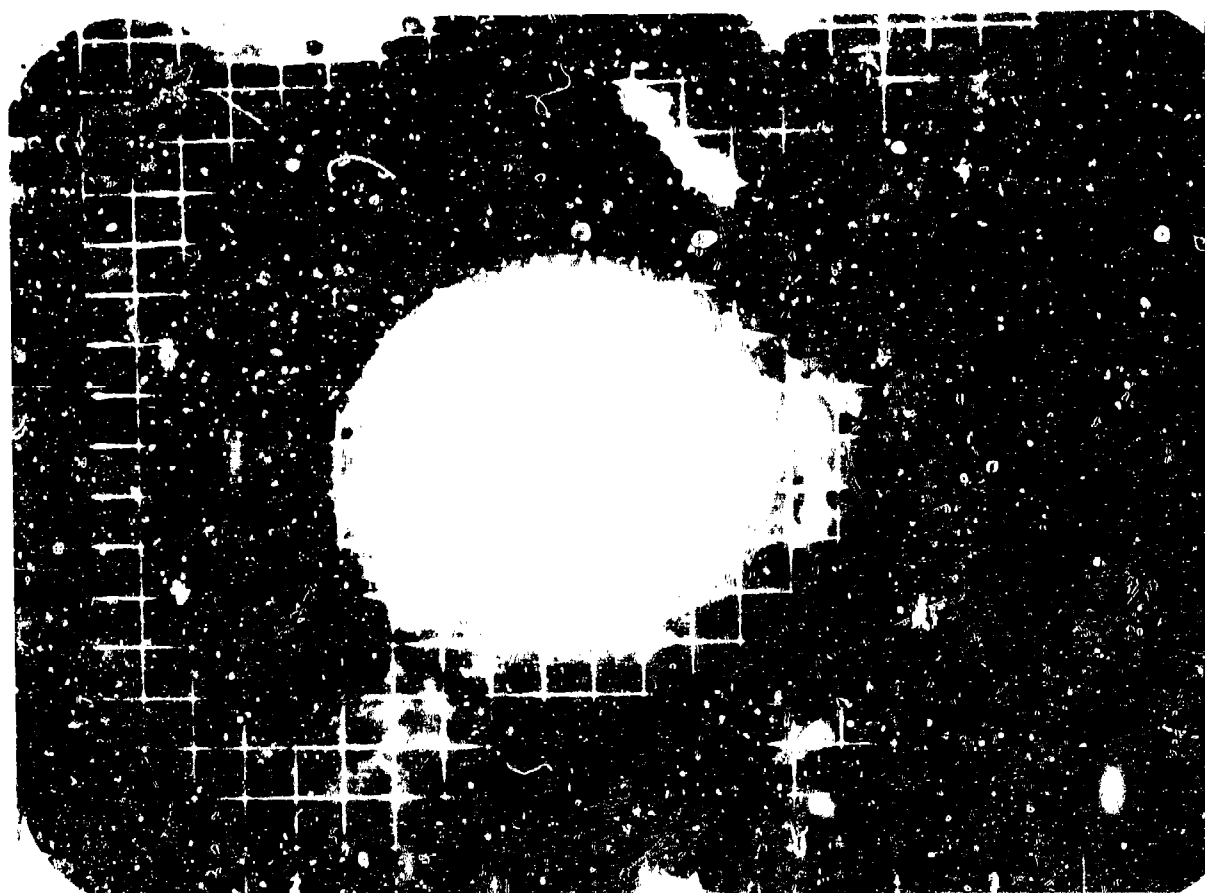


Figure A.198 Shot Dakota, Series 36236, Frame 115, Red, f.l., 10 mm, B-47.

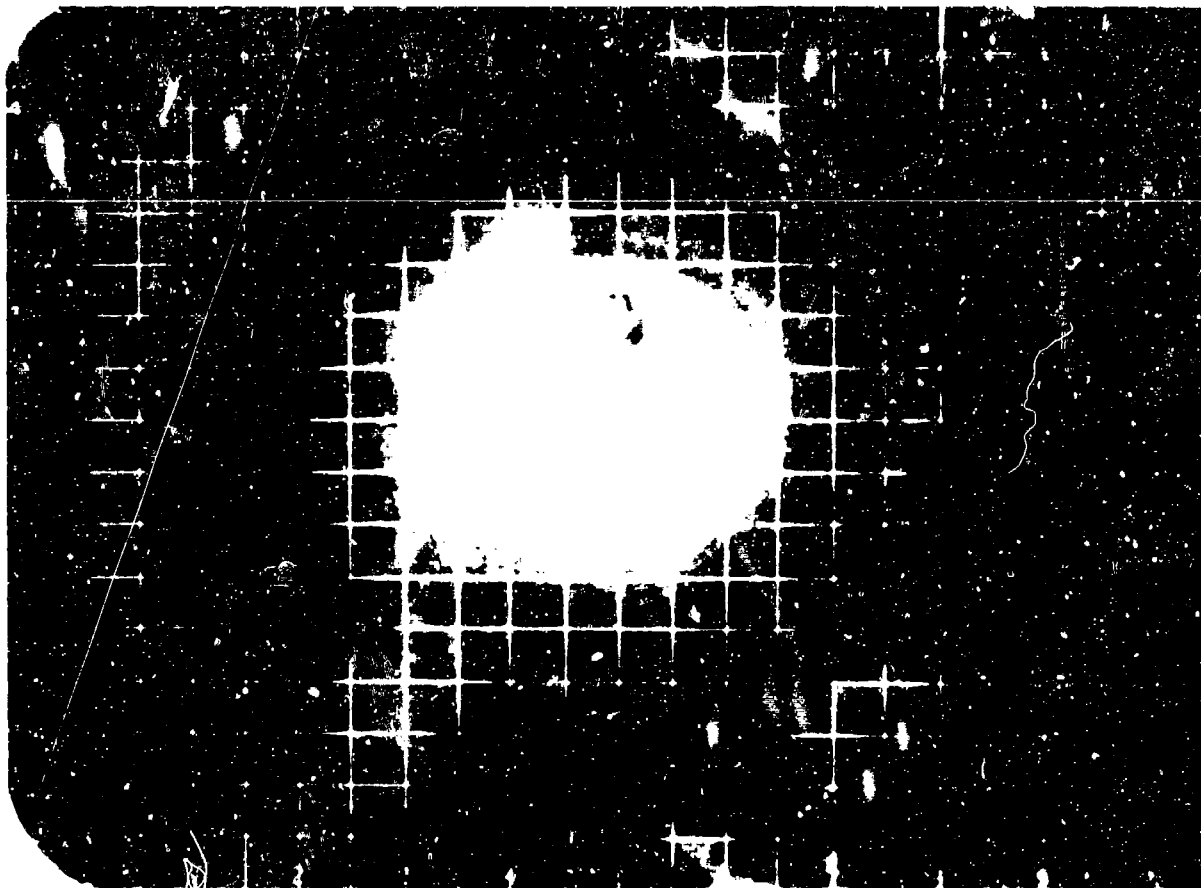


Figure A.199 Shot Dakota, Series 36236, Frame 150, Red, f.l., 10 mm, B-47.

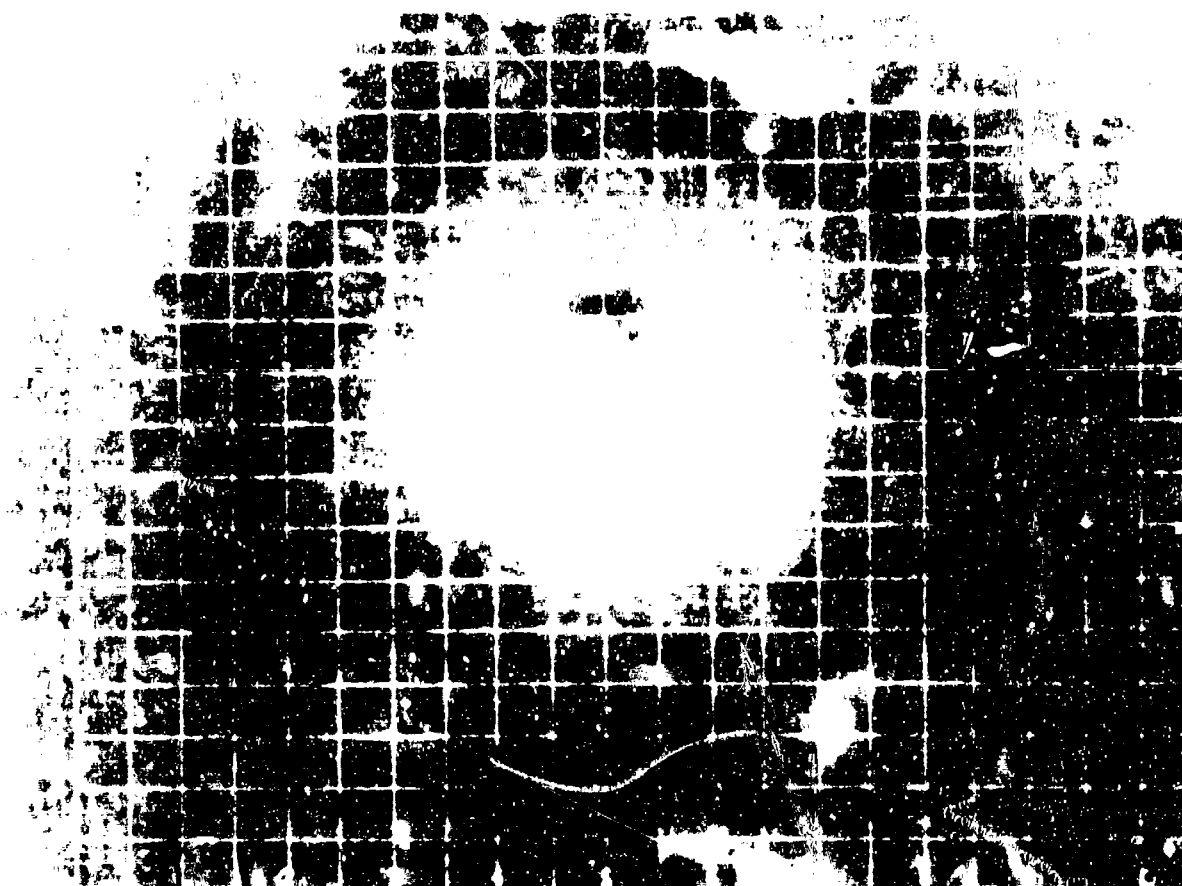


Figure A.200 Shot Dakota, Series 36236, Frame 200, Red, f.l., 10 mm, B-47.

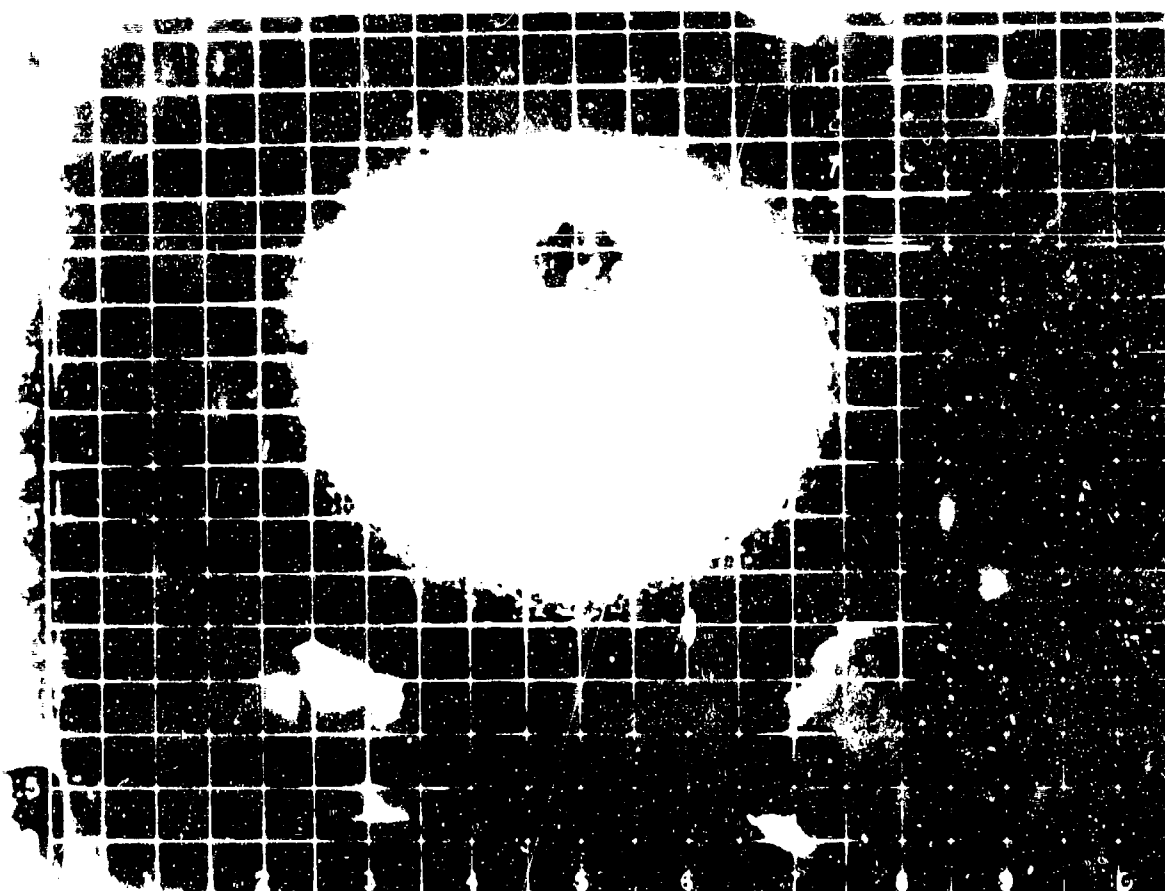


Figure A.201 Shot Dakota, Series 36236, Frame 250, Red, f.1., 10 mm, B-47



Figure A.202 Shot Dakota, Series 36236, Frame 325, Red, f.1., 10 mm, B-47.

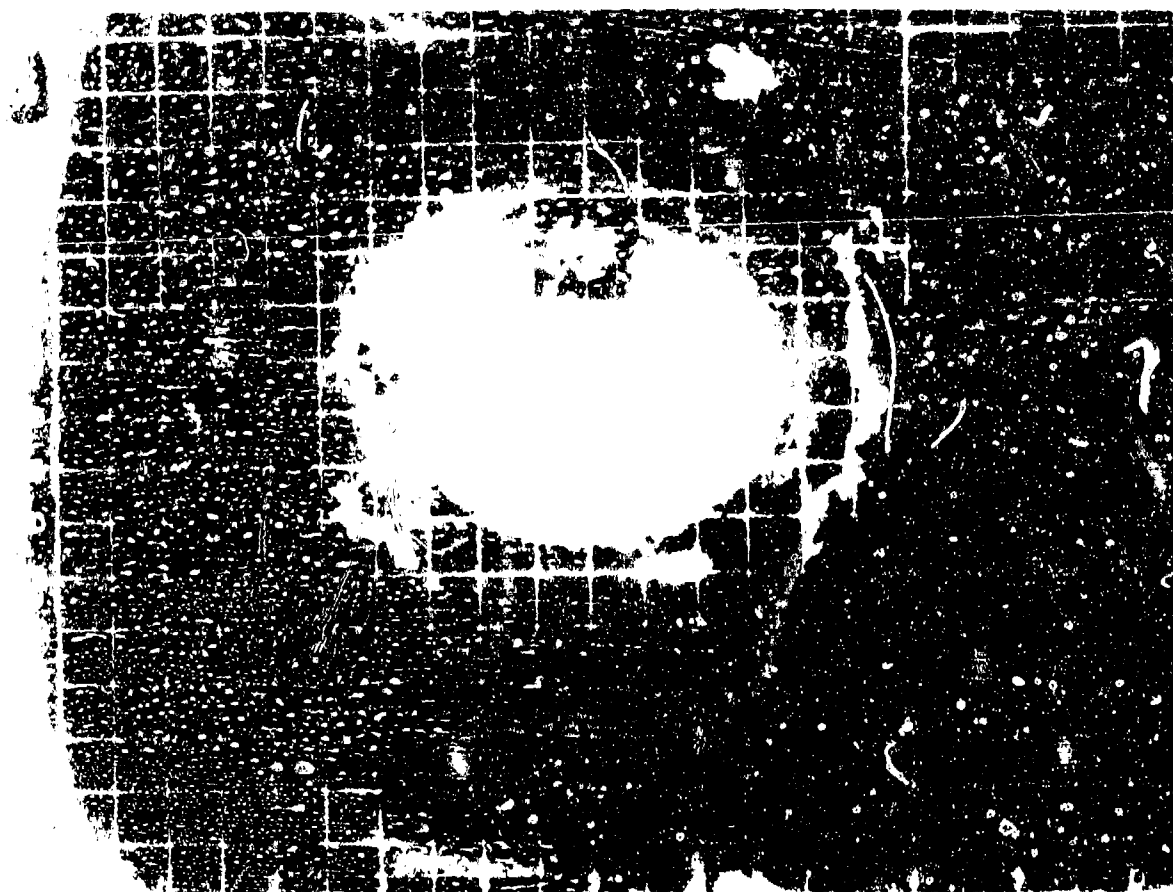


Figure A.203 Shot Dakota, Series 36236, Frame 375, Red, f.l., 10 mm, B-47.

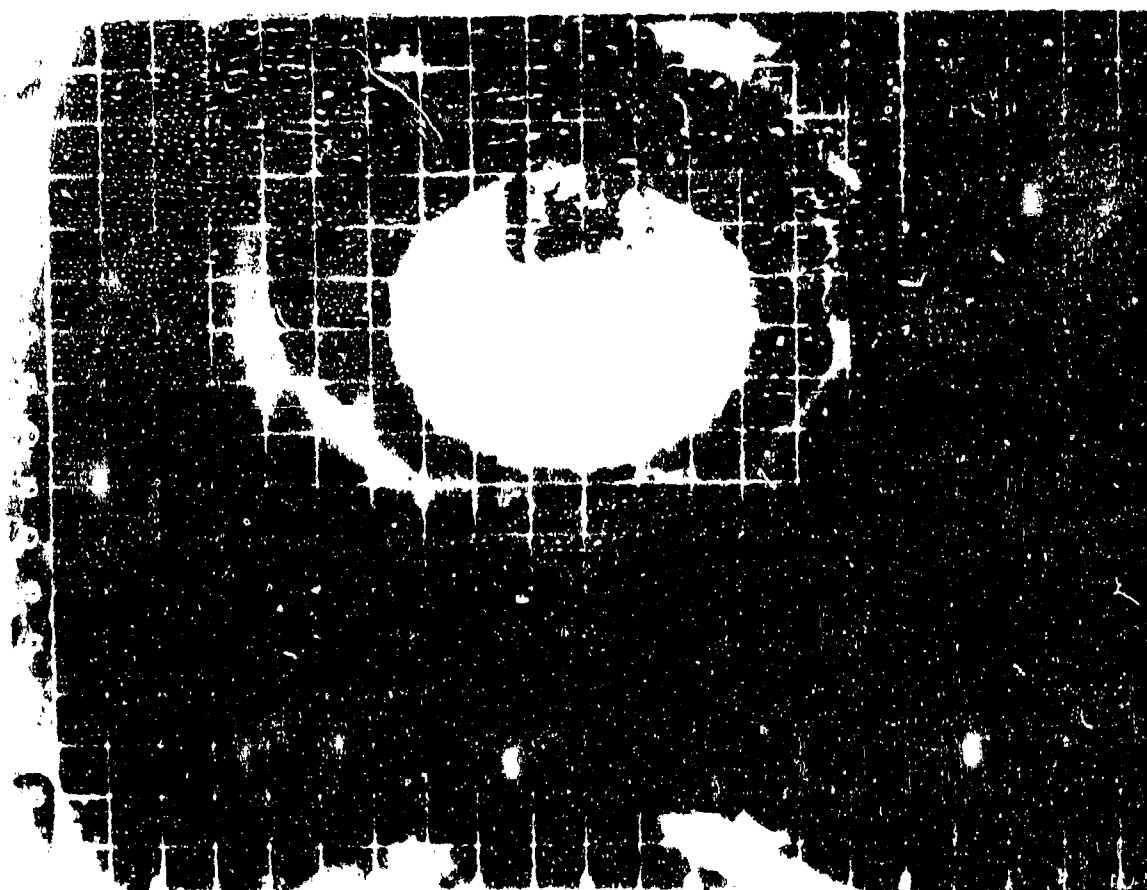


Figure A.204 Shot Dakota, Series 36236, Frame 425, Red, f.l., 10 mm, B-47.

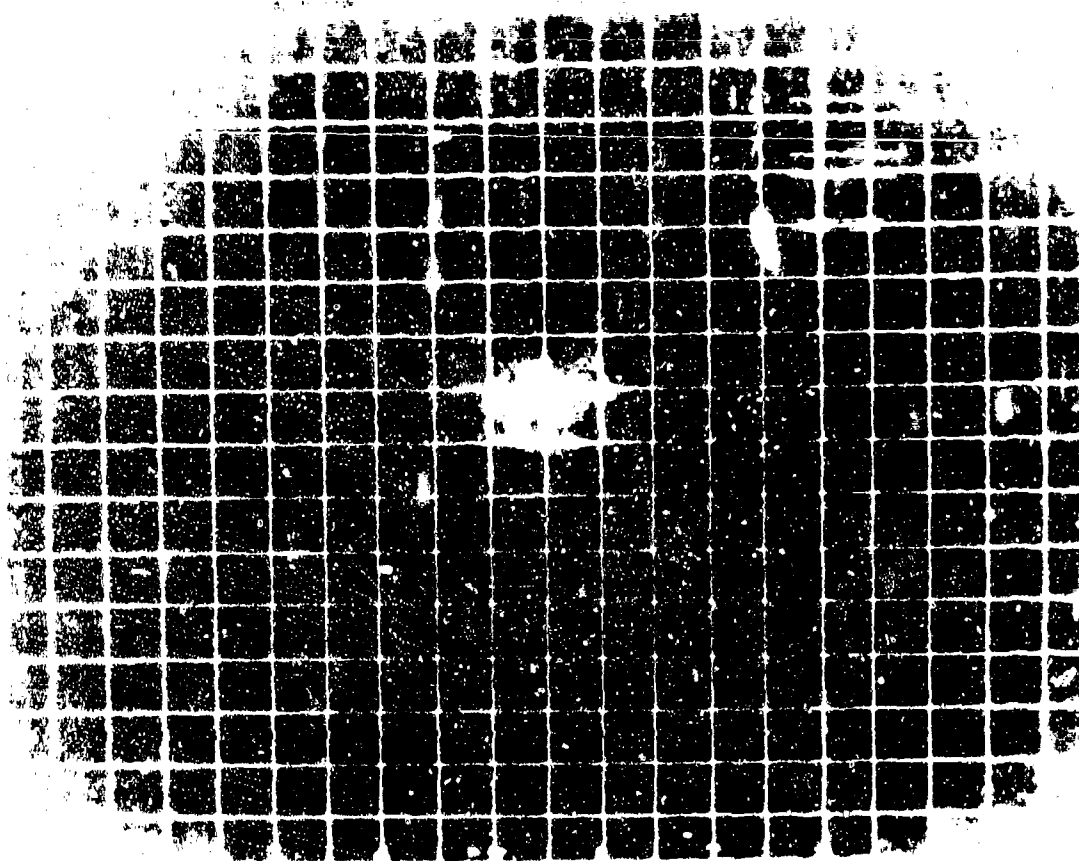


Figure A.205 Shot Dakota, Series 36241, Frame 35, Blue, f.l., 17 mm, B-66.

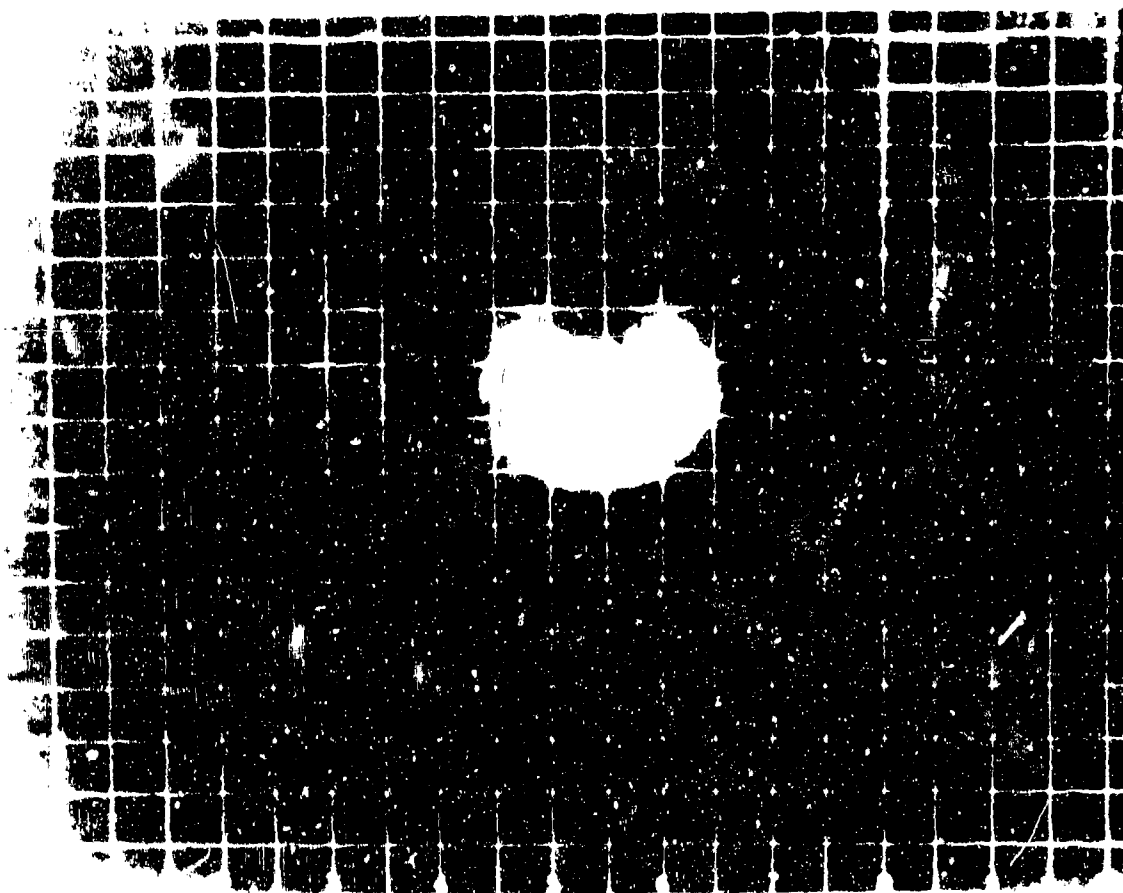


Figure A.206 Shot Dakota, Series 36241, Frame 45, Blue, f.l., 17 mm, B-66.

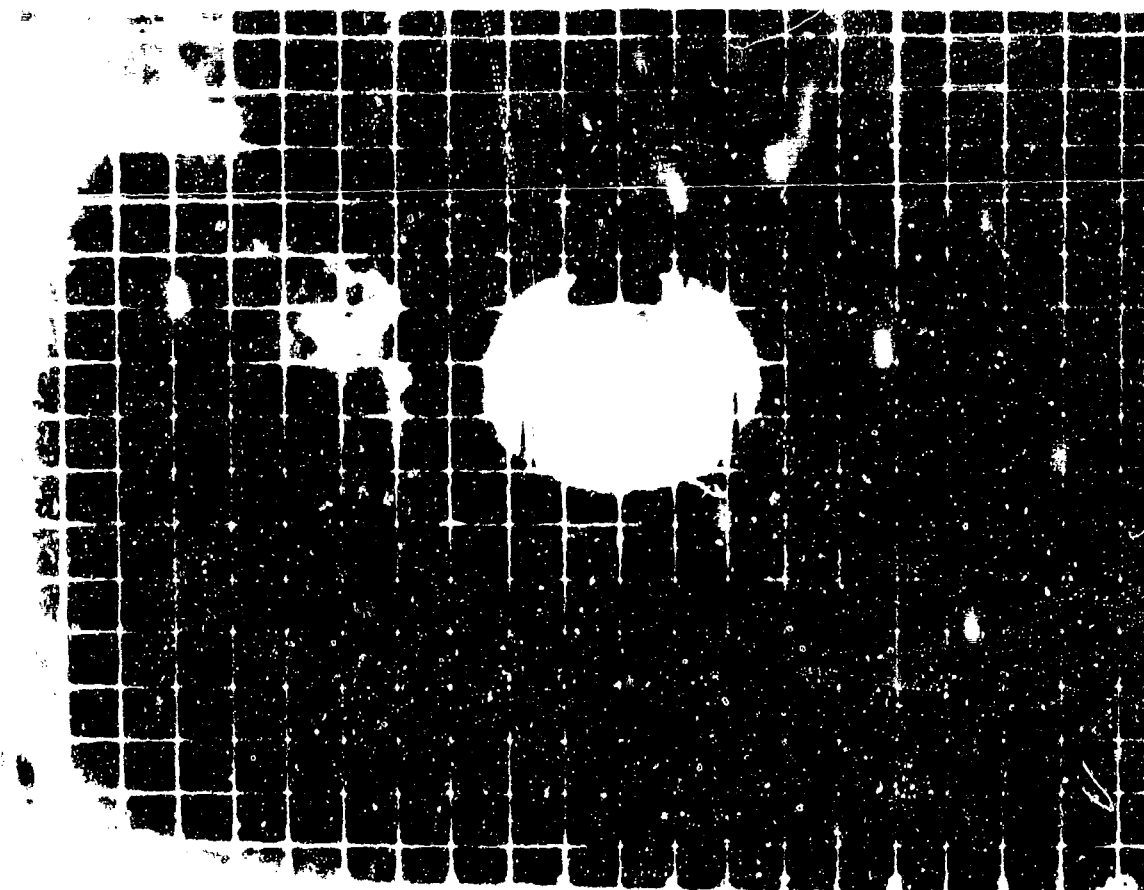


Figure A.207 Shot Dakota, Series 36241, Frame 65, Blue, f.l., 17 mm, B-66.

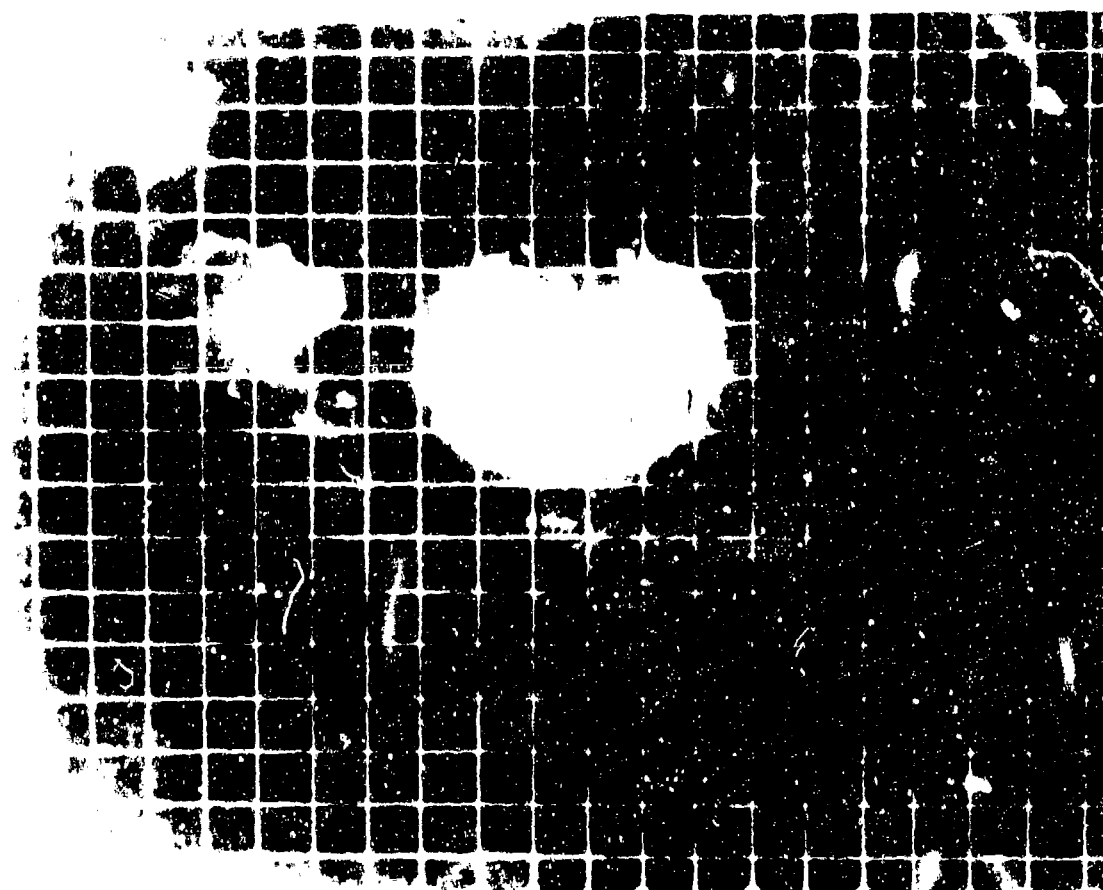


Figure A.208 Shot Dakota, Series 36241, Frame 100, Blue, f.l., 17 mm, B 66.

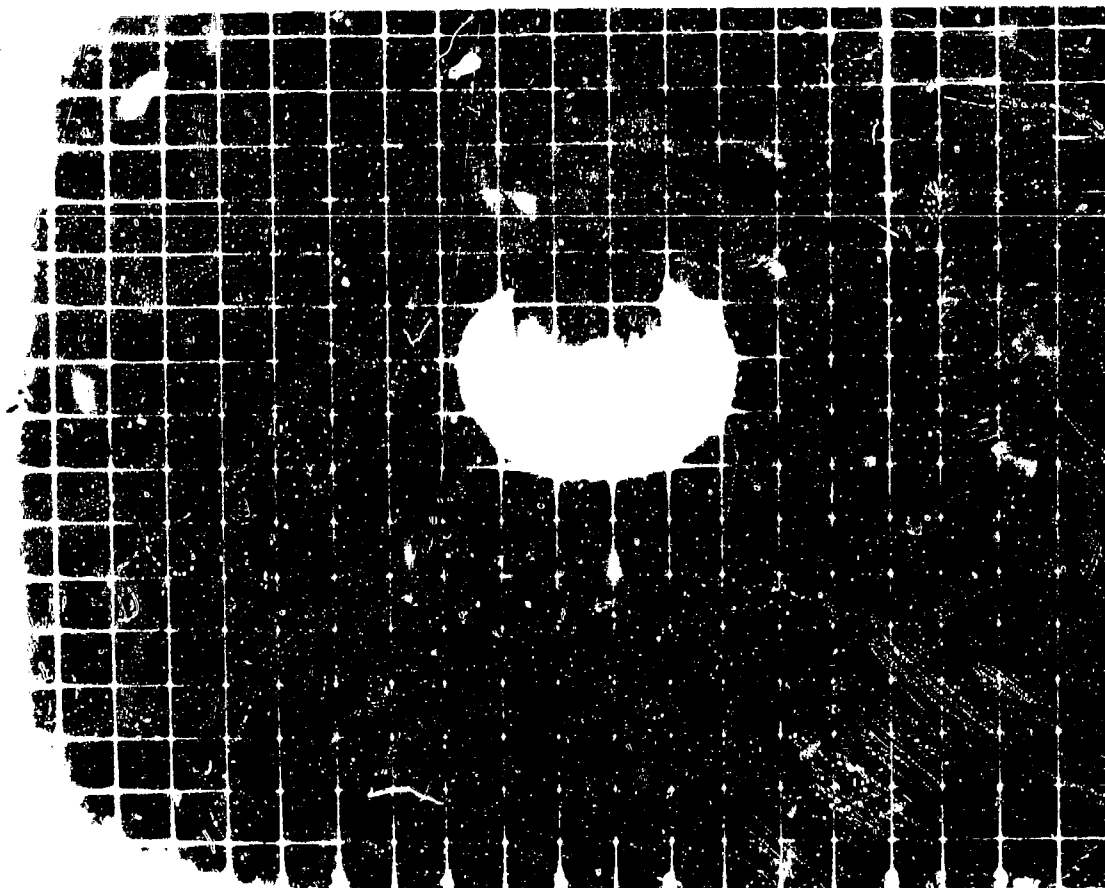


Figure A.209 Shot Dakota, Series 36241, Frame 150, Blue, f.l., 17 mm, B-66.

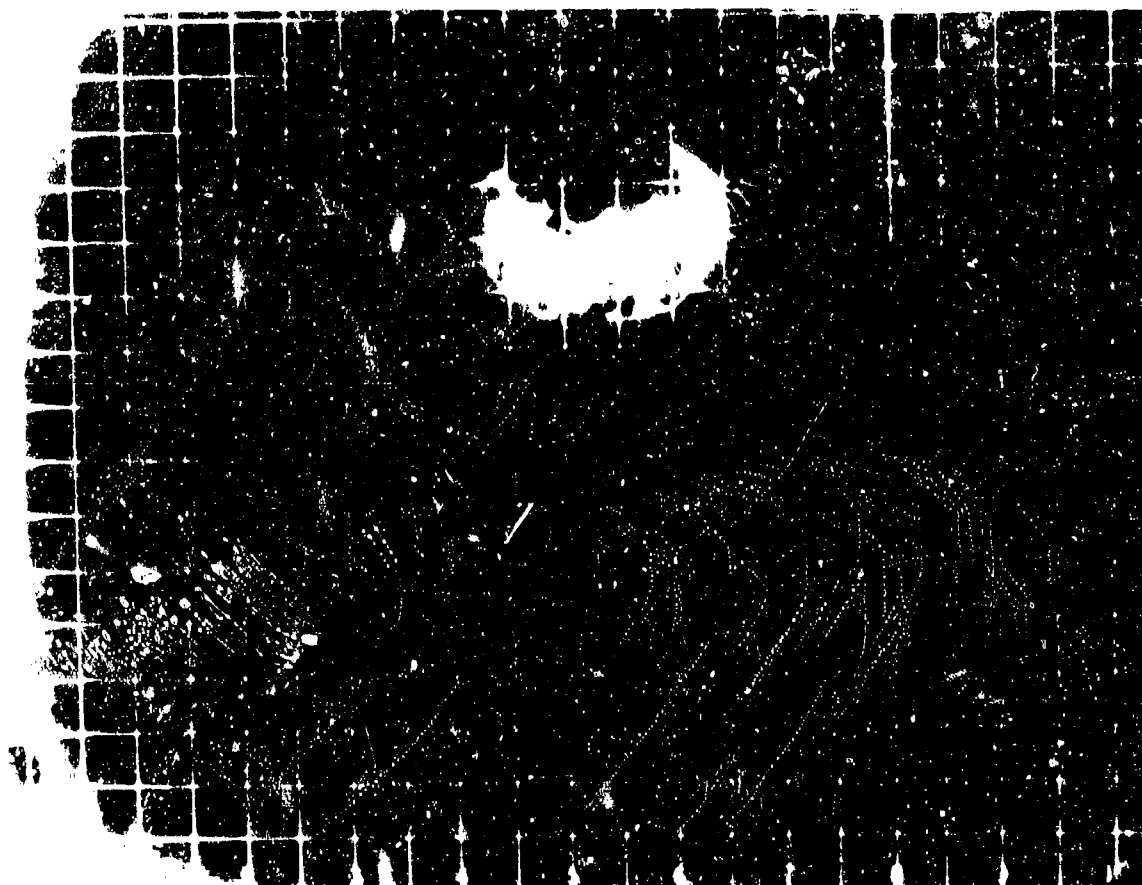


Figure A.210 Shot Dakota, Series 36241, Frame 250, Blue, f.l., 17 mm, B-66.

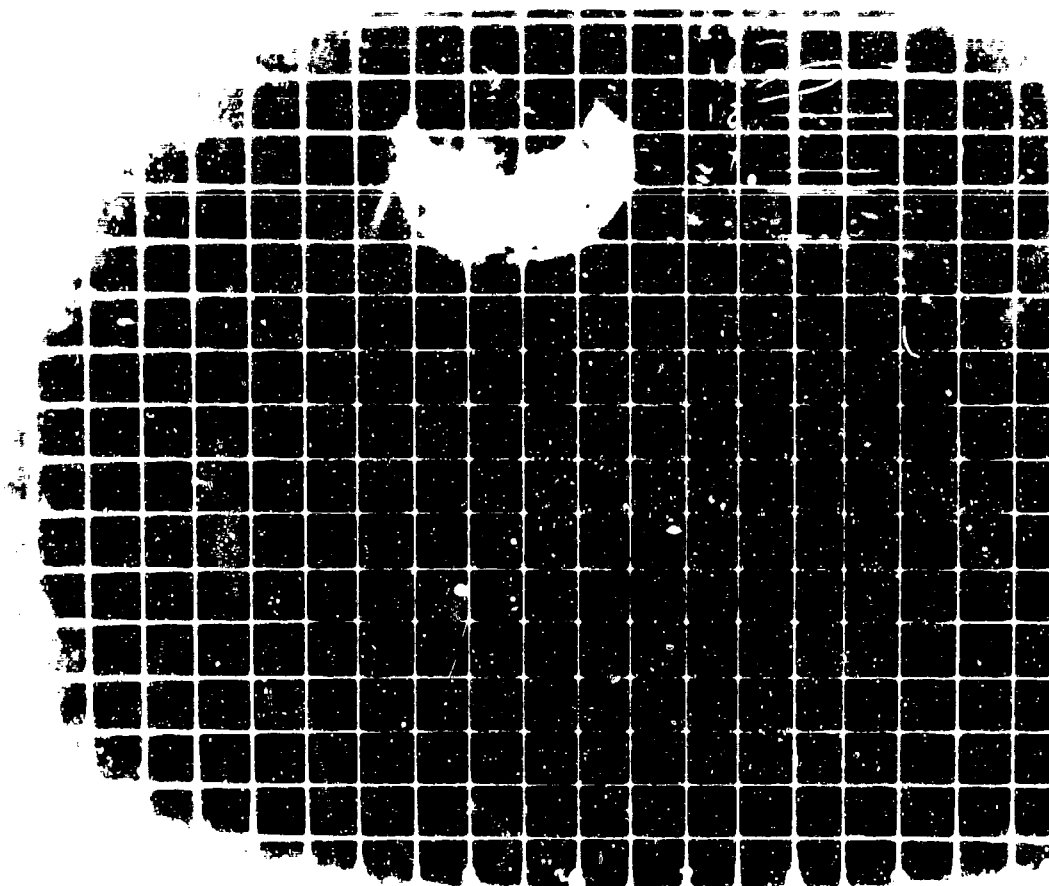


Figure A.211 Shot Dakota, Series 36241, Frame 350, Blue, f.l., 7 mm, B-66.

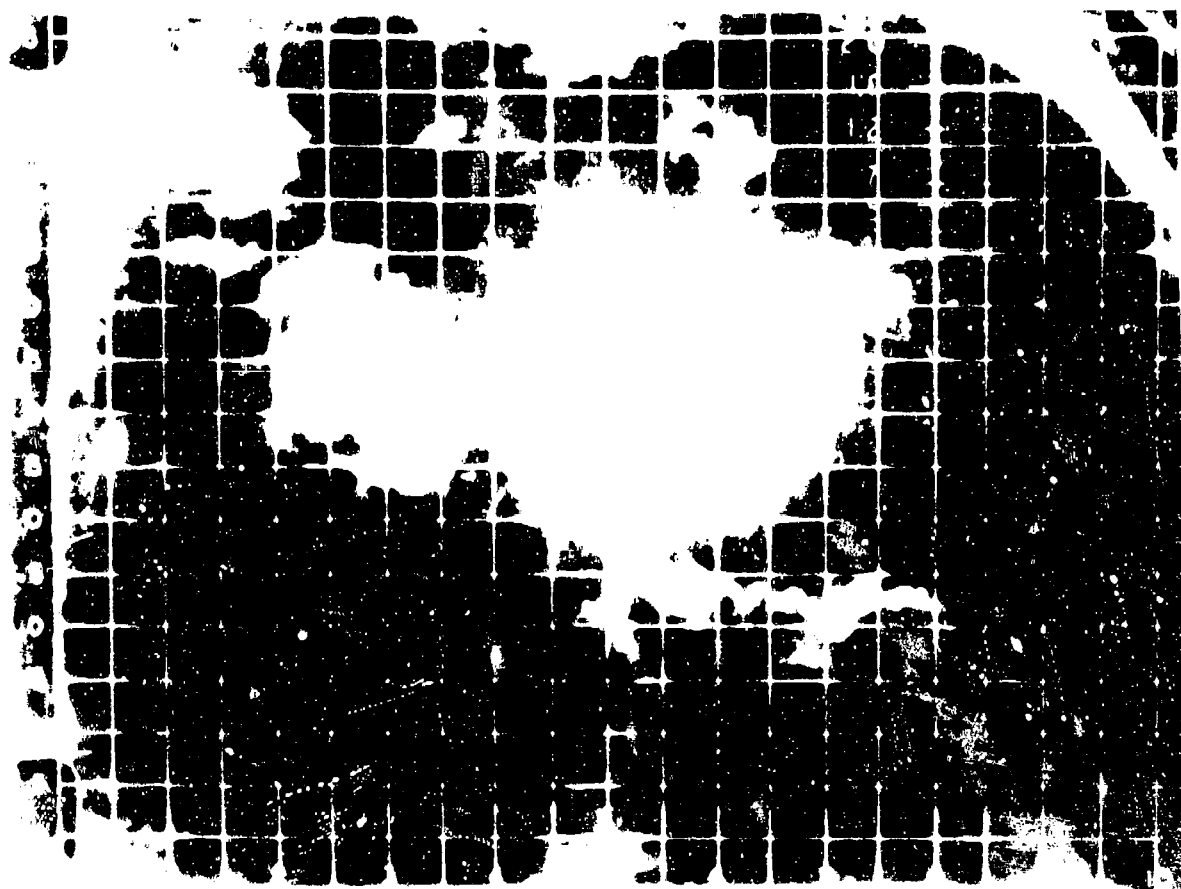


Figure A.212 Shot Dakota, Series 36242, Frame Zero, Red, f.l., 17 mm, B-66.

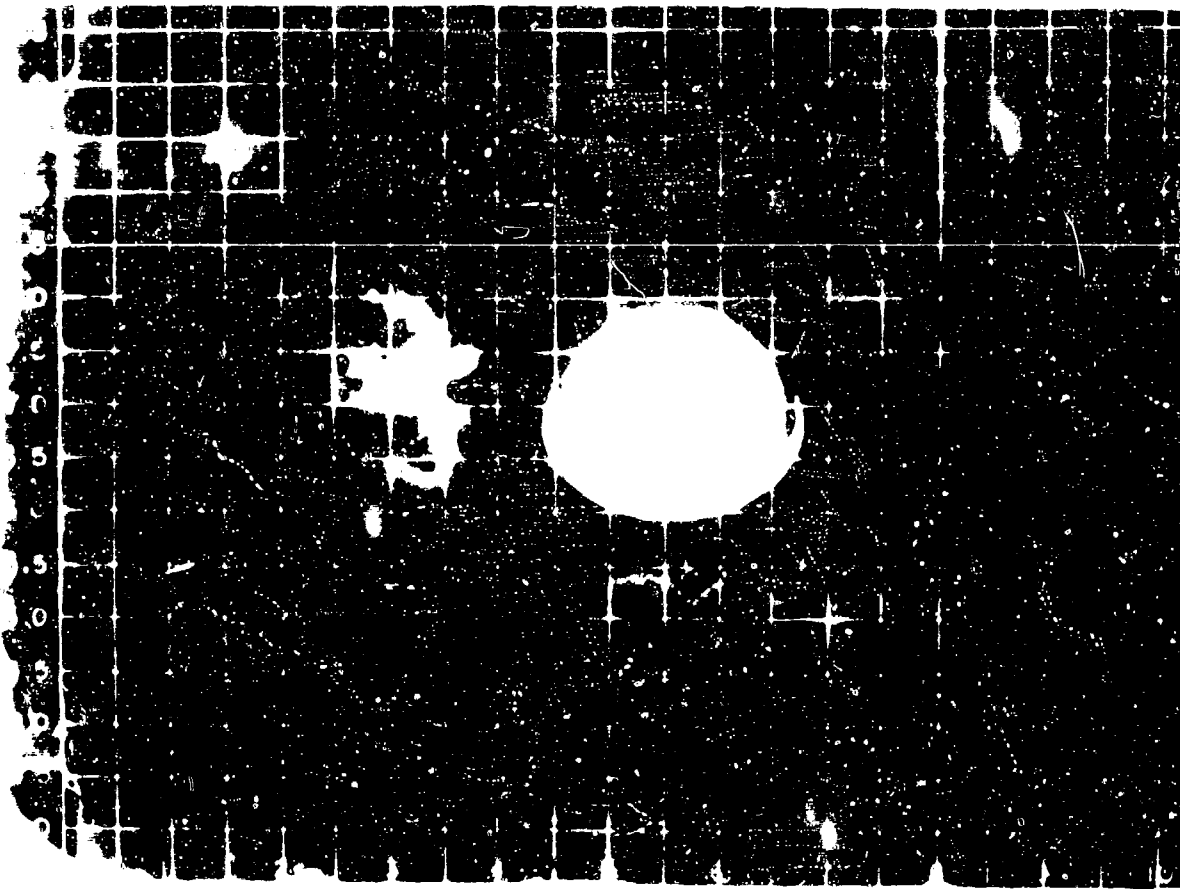


Figure A.213 Shot Dakota, Series 36242, Frame 15, Red, f.l., 17 mm, B-66.

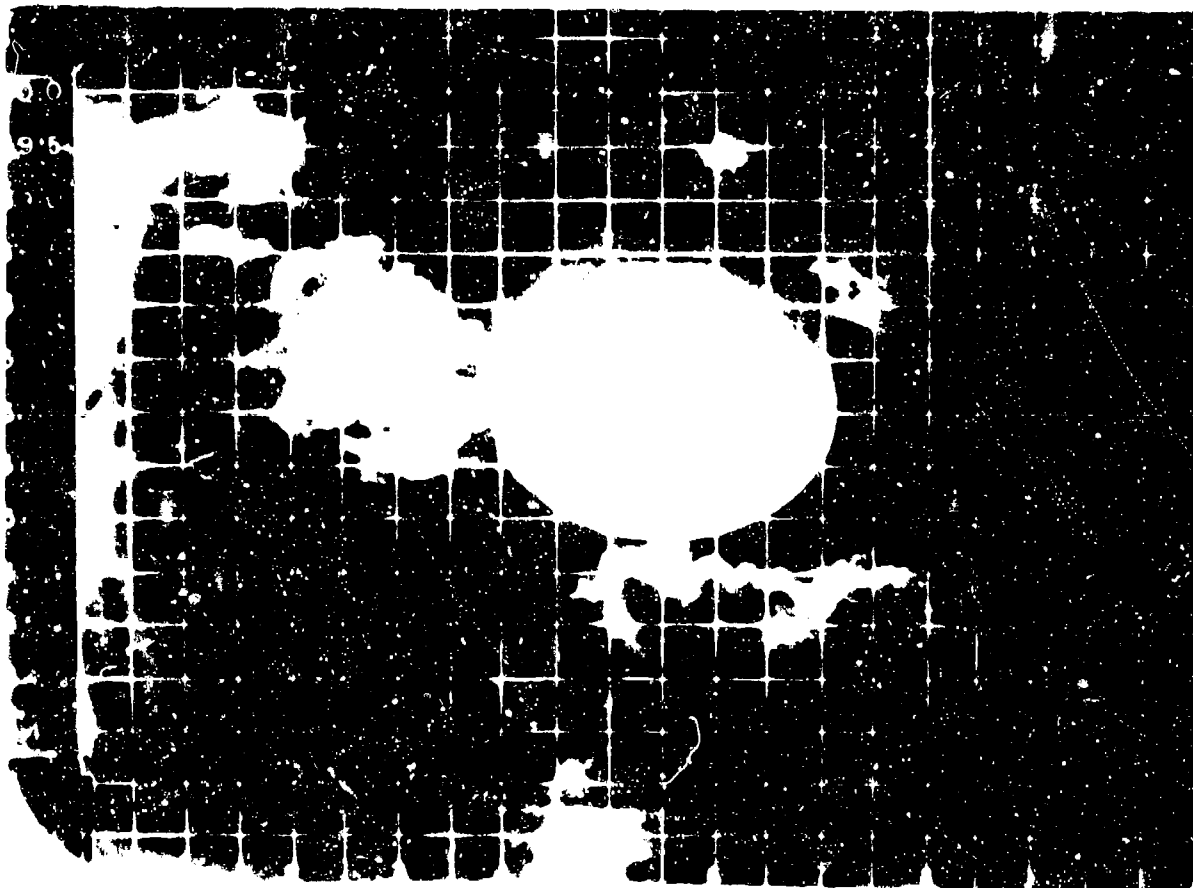


Figure A.214 Shot Dakota, Series 36242, Frame 30, Red, f.l., 17 mm, B-66.

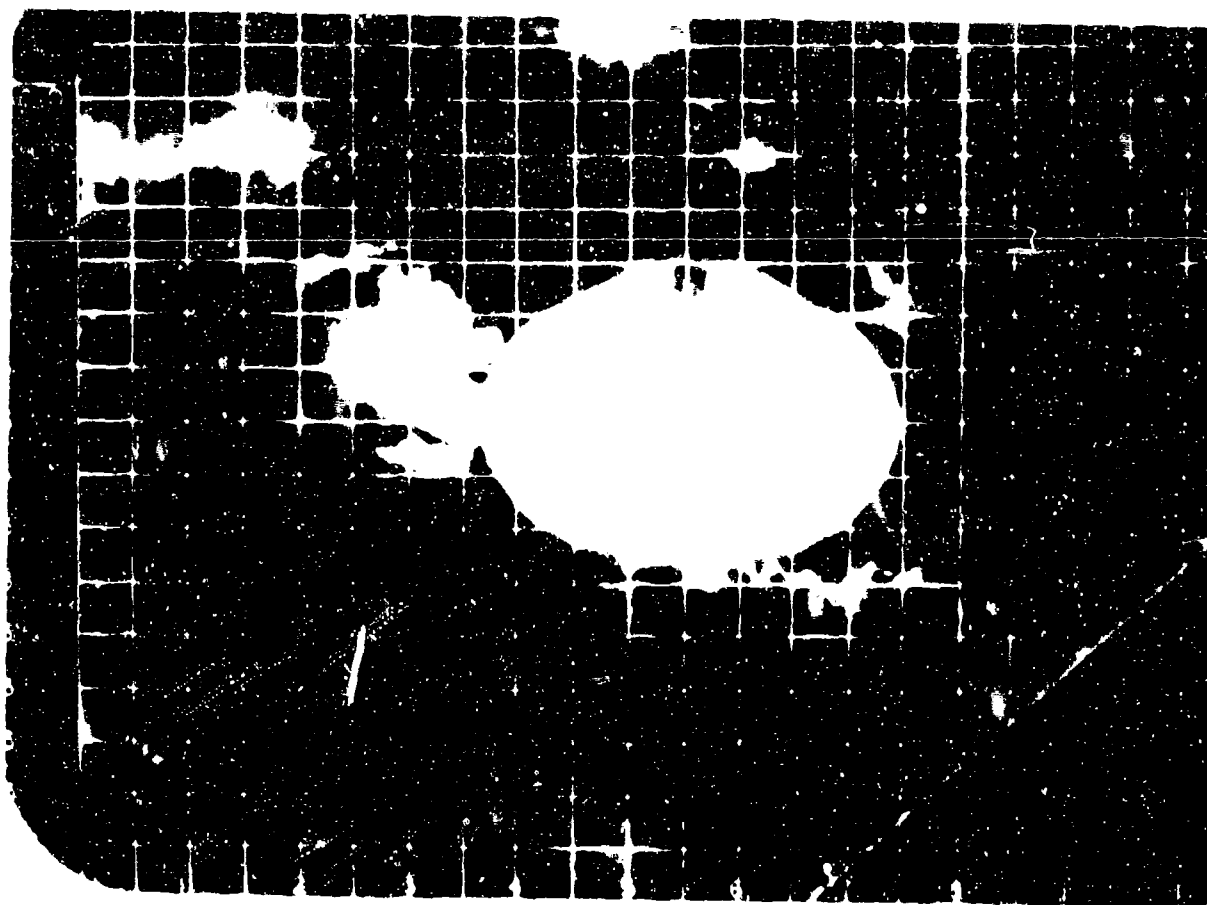


Figure A.215 Shot Dakota, Series 36242, Frame 45, Red, f.l., 17 mm, B-66.



Figure A.216 Shot Dakota, Series 36249, Frame 45, Red, f.l., 17 mm, B-66.

SECRET

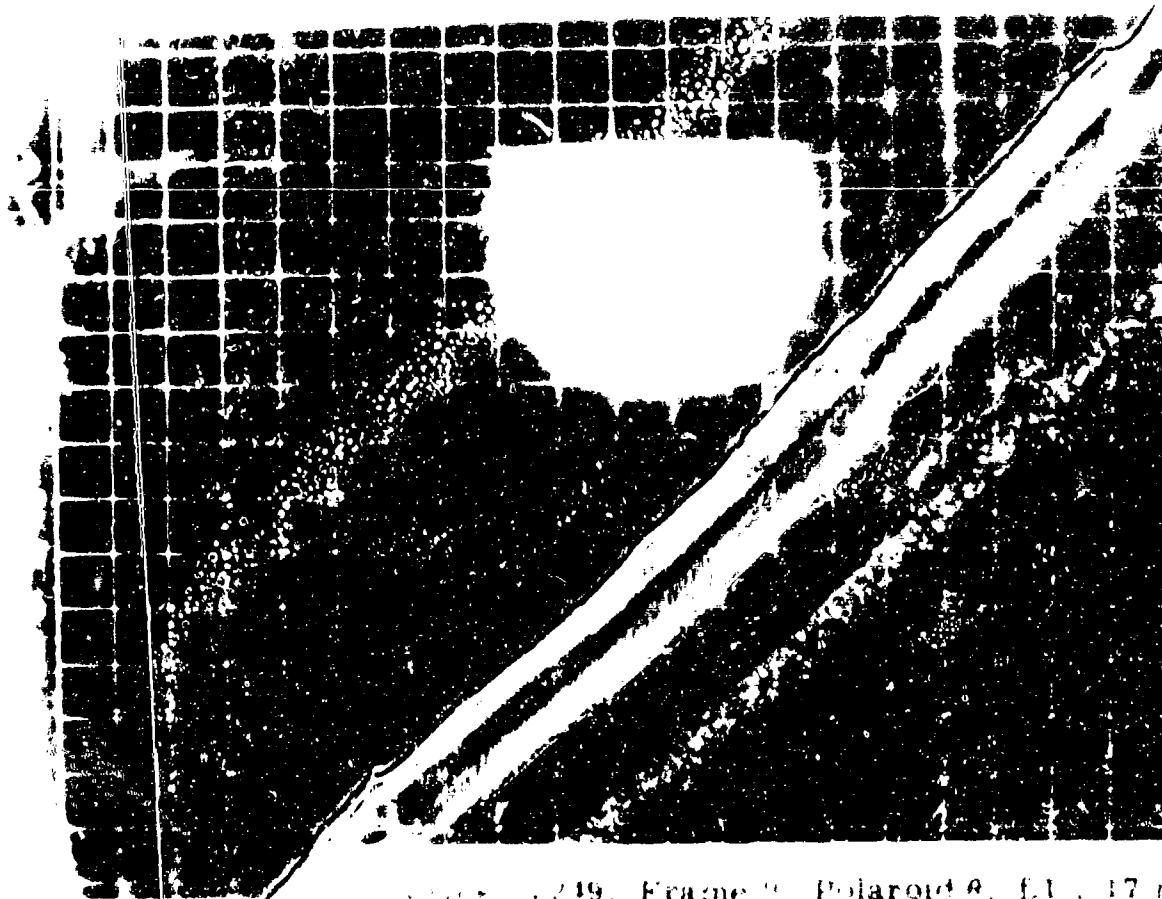


Figure A.219, Frame 9, Polaroid 8, f.1, 17 mm.

Figure
B-66



Figure A.218 Shpt Dakota, Series 36240, Frame 14, Polaroid 8, f.1, 17 mm.
B-66.

288

SECRET

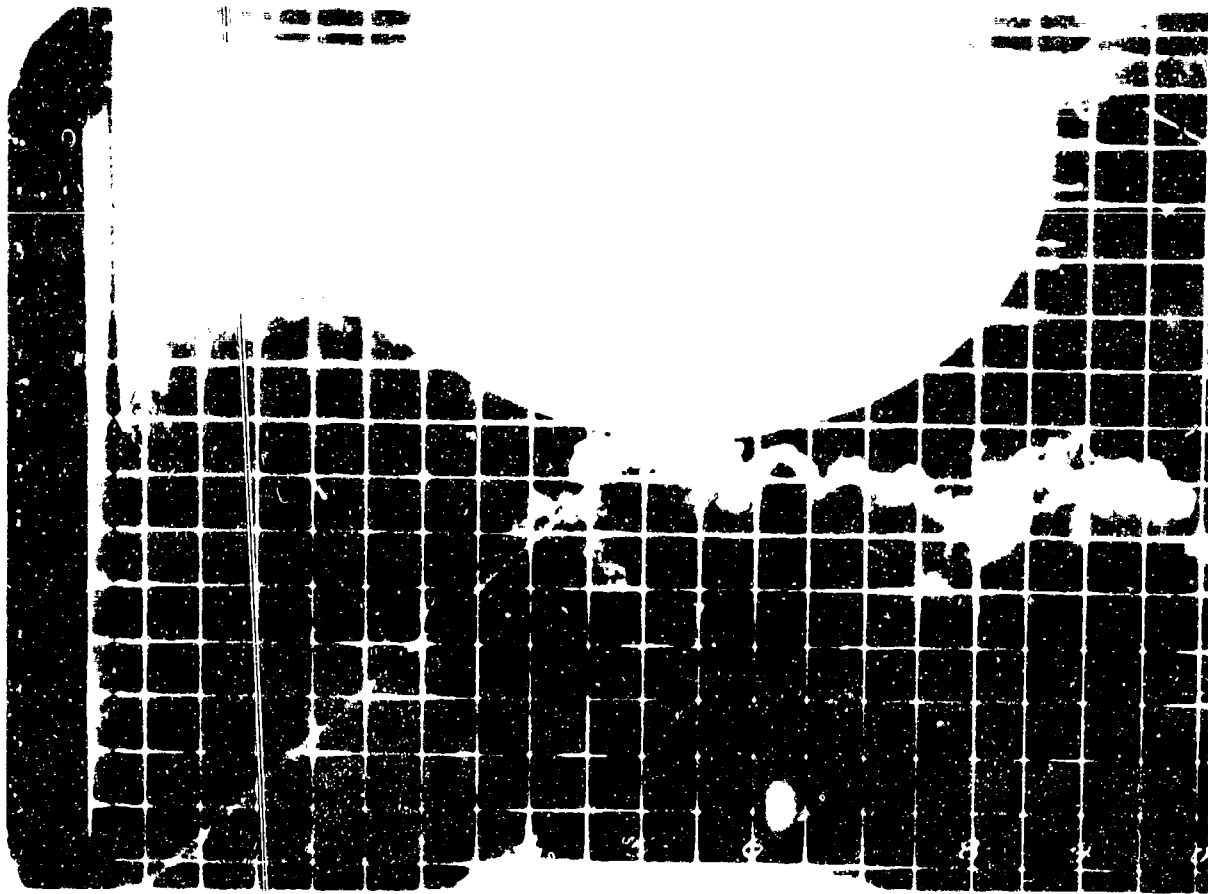


Figure A.219 Shot Dakota, Series 36249, Frame 34, Polaroid 0, f.l., 17 mm, B-66.



Figure A.220 Shot Dakota, Series 36249, Frame 44, Polaroid 0, f.l., 17 mm, B-66.

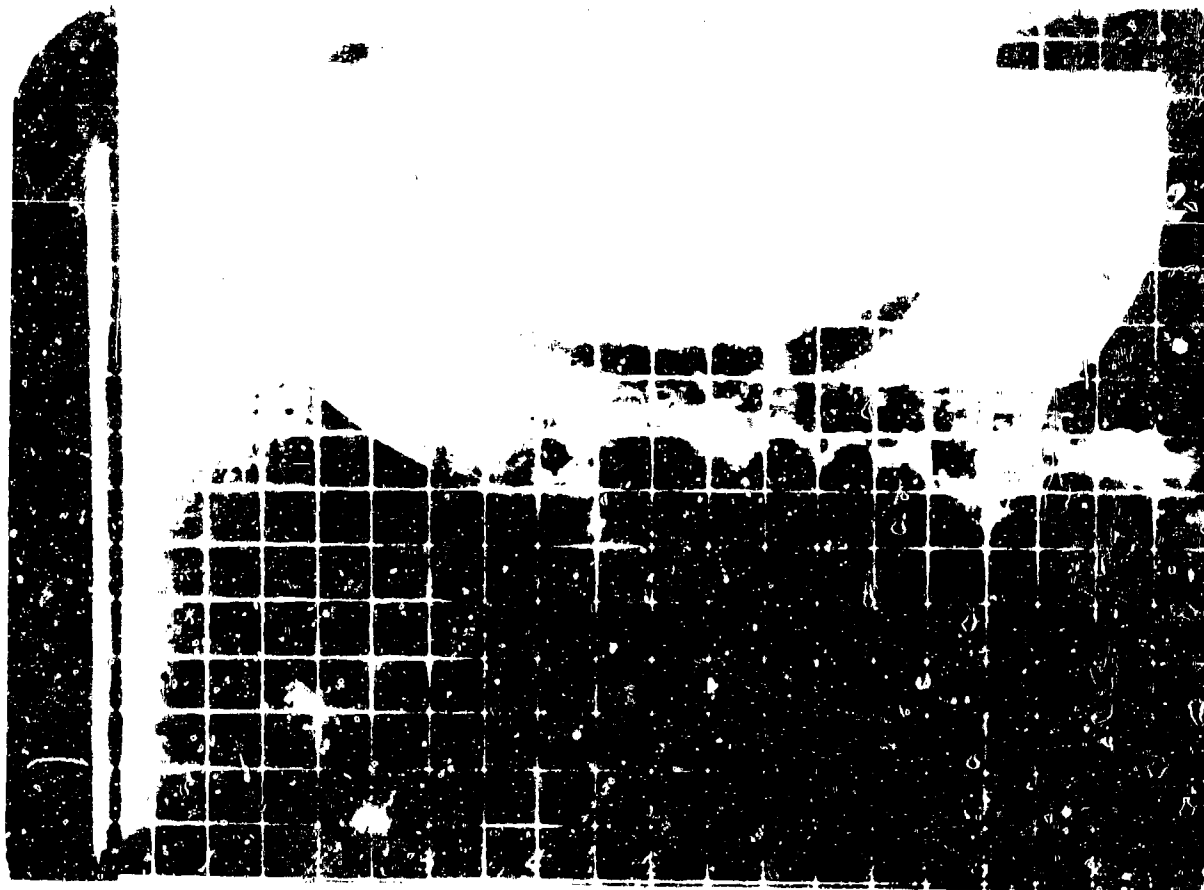


Figure A.221 Shot Dakota, Series 36249, Frame 64, Polaroid 8, f.l., 17 mm, B-66.

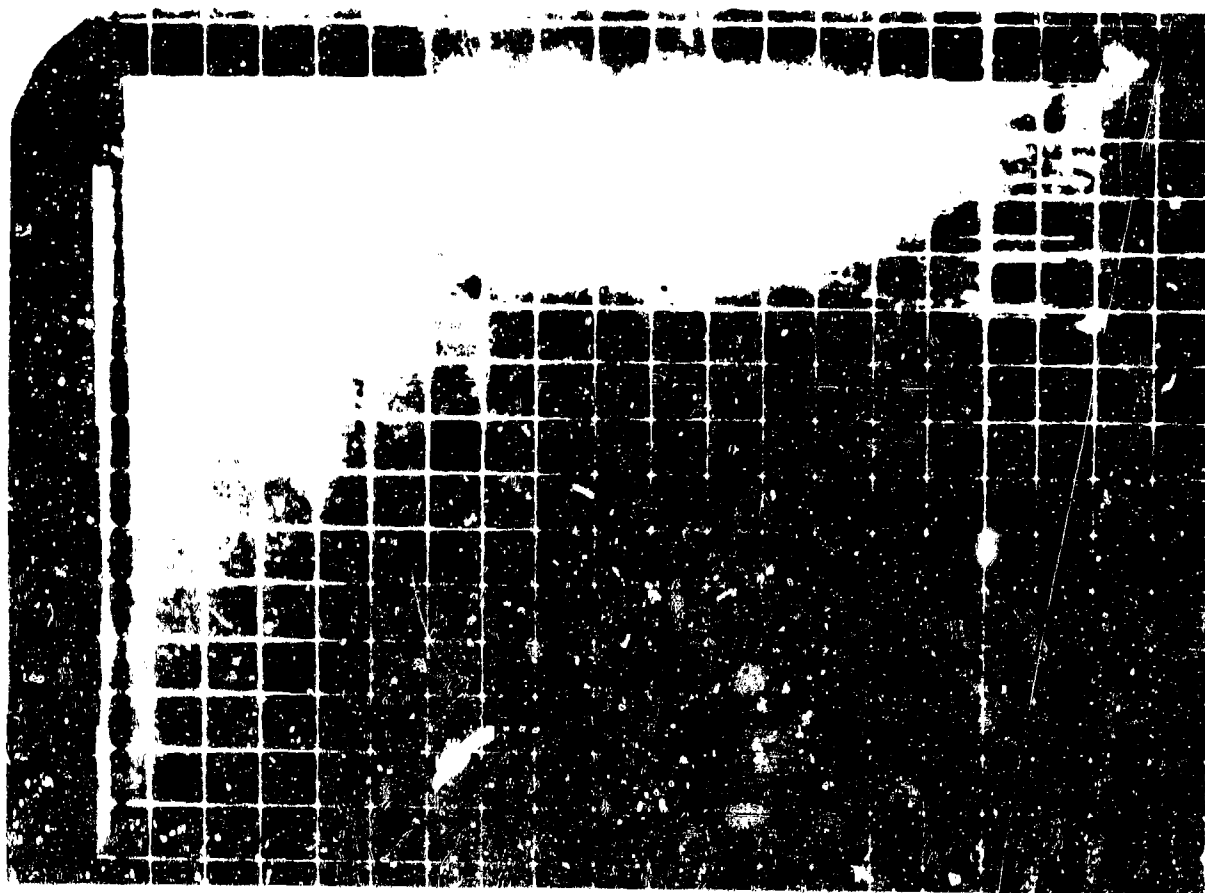


Figure A.222 Shot Dakota, Series 36249, Frame 80, Polaroid 9, f.l., 17 mm, B-66.

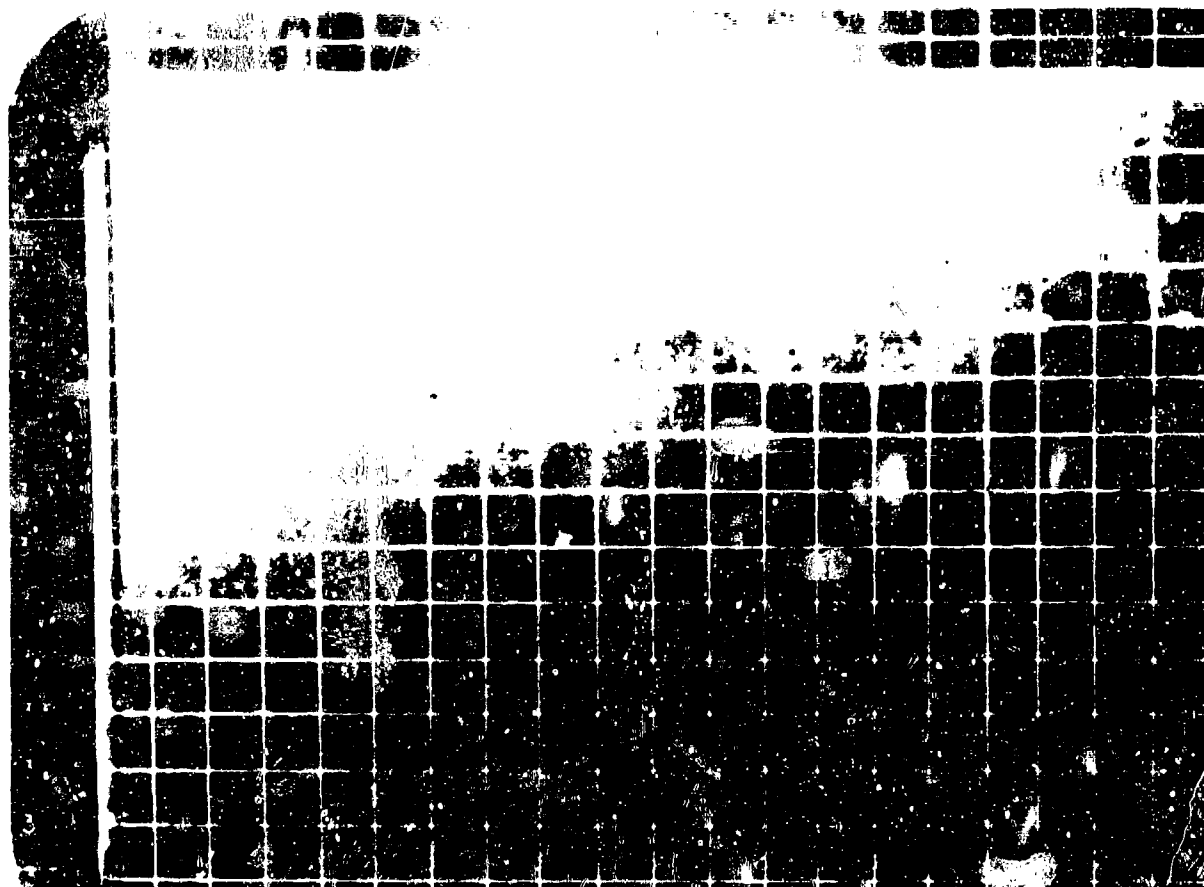


Figure A.223 Shot Dakota, Series 36249, Frame 199, Polaroid θ , f.l., 17 mm, B-66.

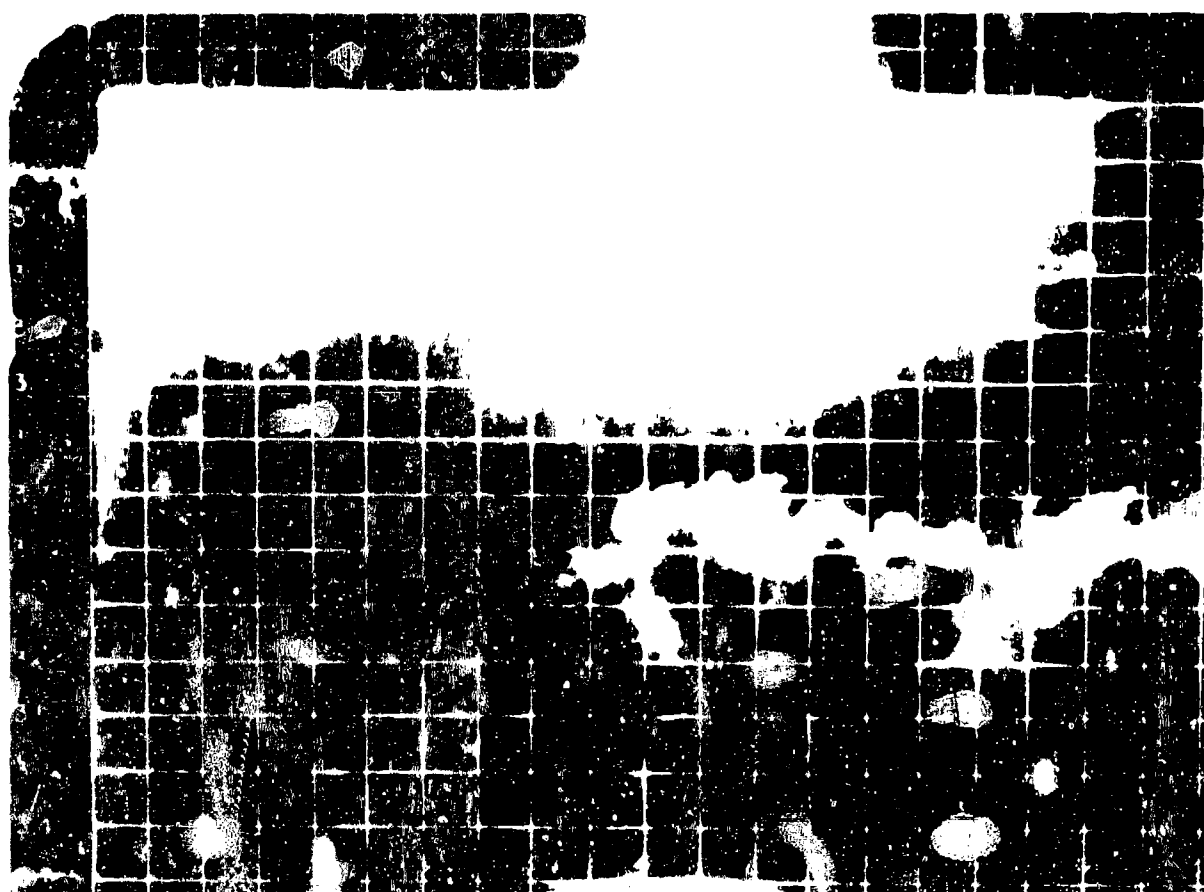


Figure A.224 Shot Dakota, Series 36250, Frame Zero, Polaroid ϕ , f.l., 17 mm, B-66.

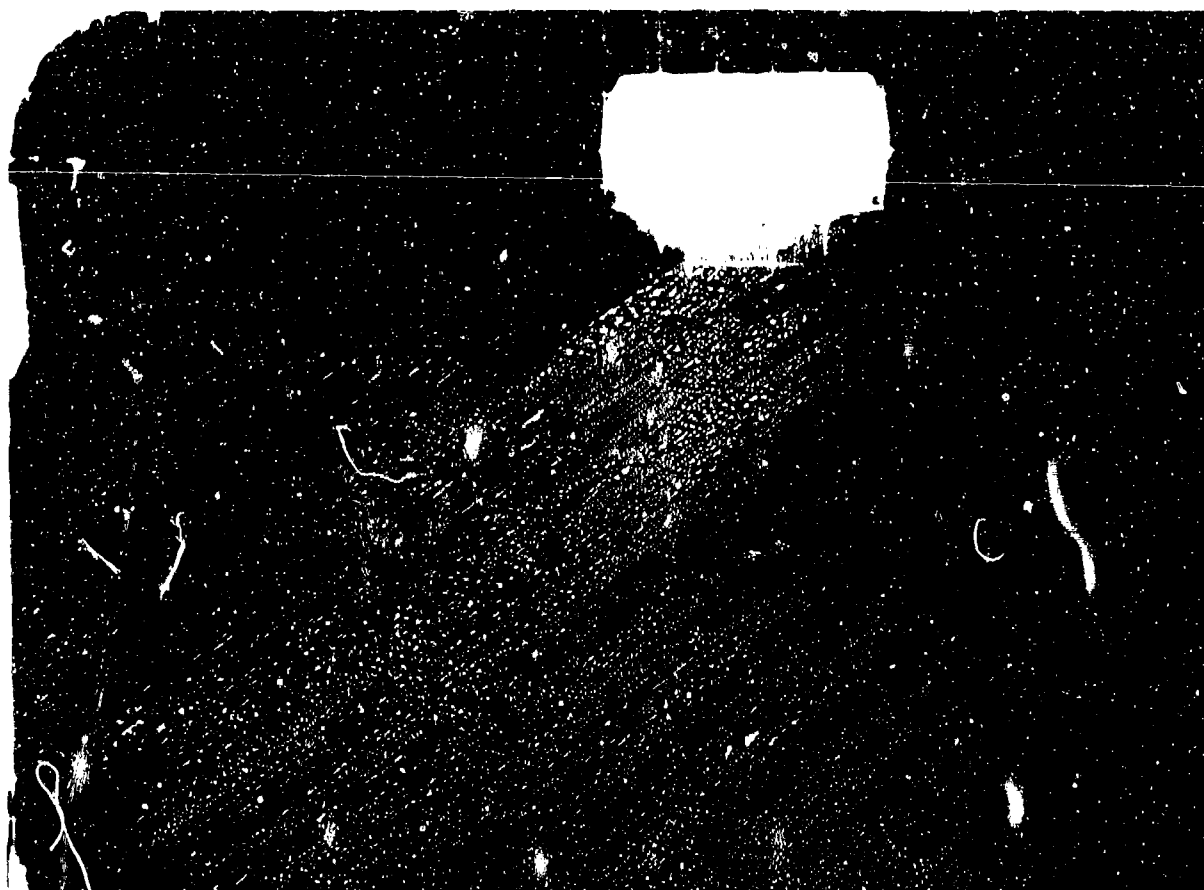


Figure A.225 Shot Dakota, Series 36250, Frame 4, Polaroid ϕ , f.l., 17 mm, B-66.

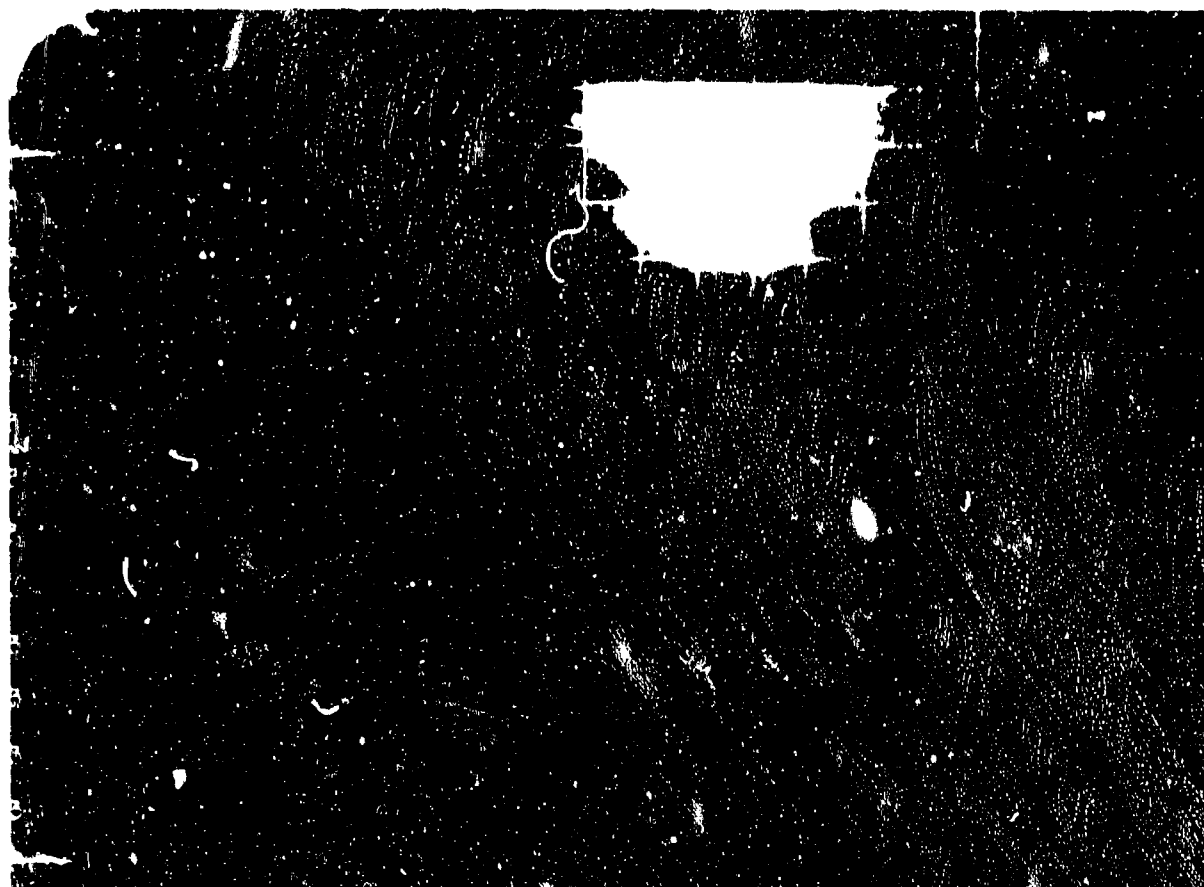


Figure A.226 Shot Dakota, Series 36250, Frame 9, Polaroid ϕ , f.l., 17 mm, B-66.

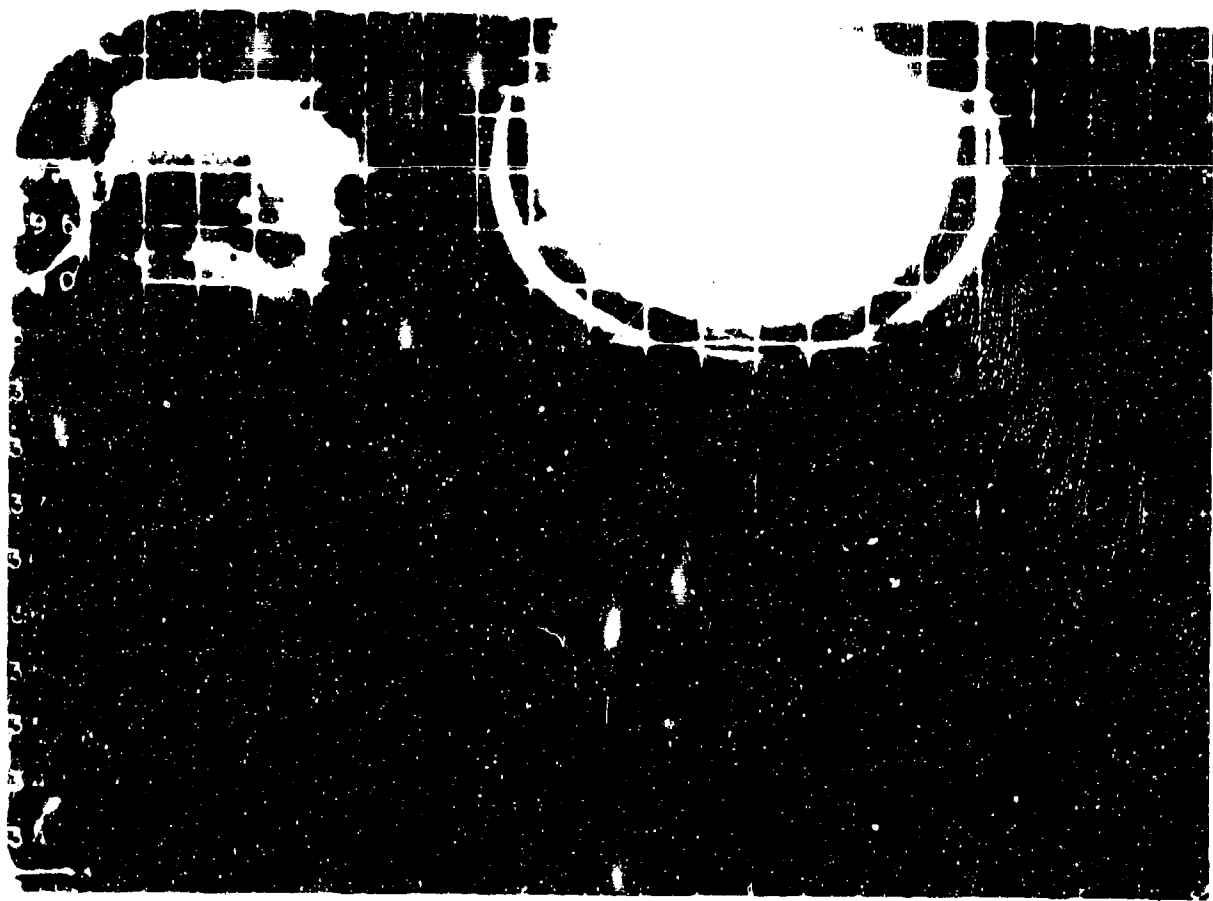


Figure A.227 Shot Dakota, Series 36250, Frame 16, Polaroid ϕ , f.l., 17 mm, B-66.

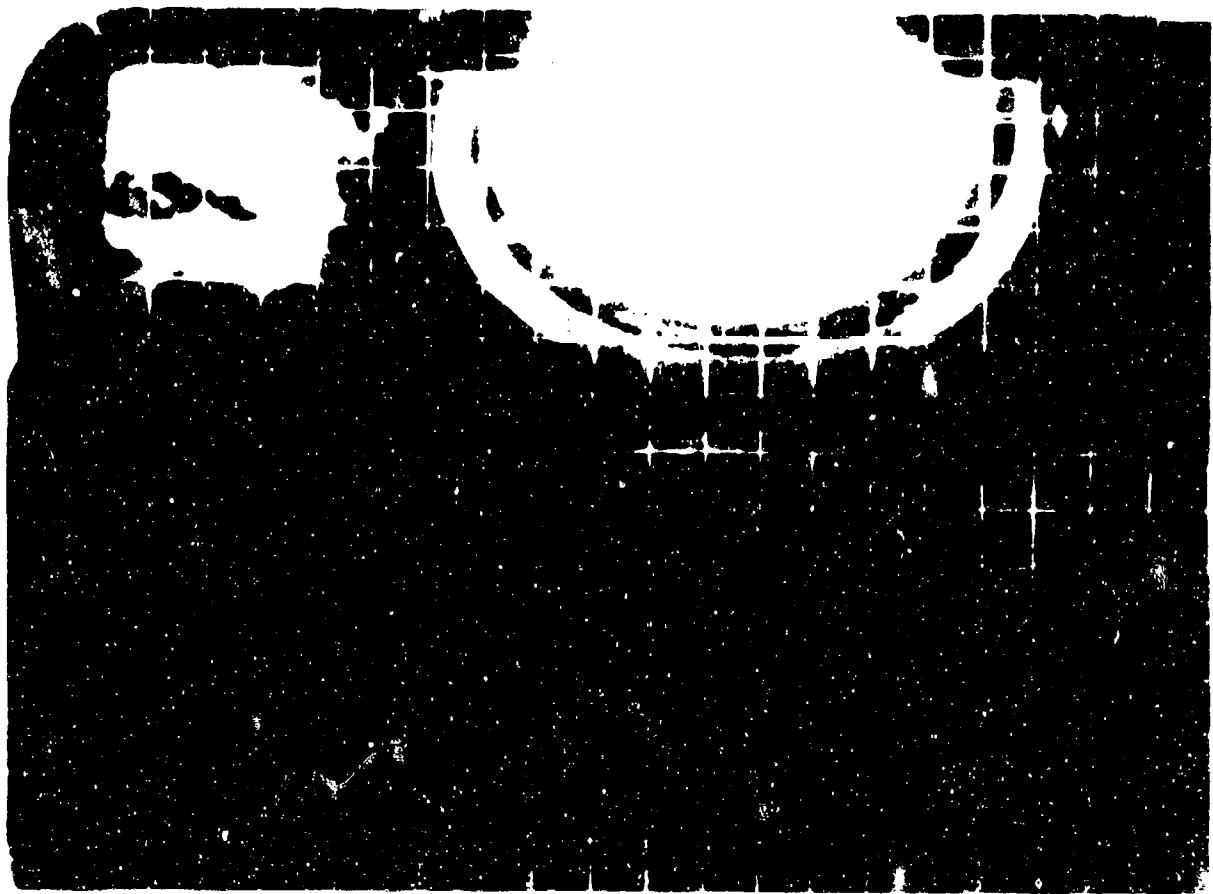


Figure A.228 Shot Dakota, Series 36250, Frame 24, Polaroid ϕ , f.l., 17 mm, B-66.

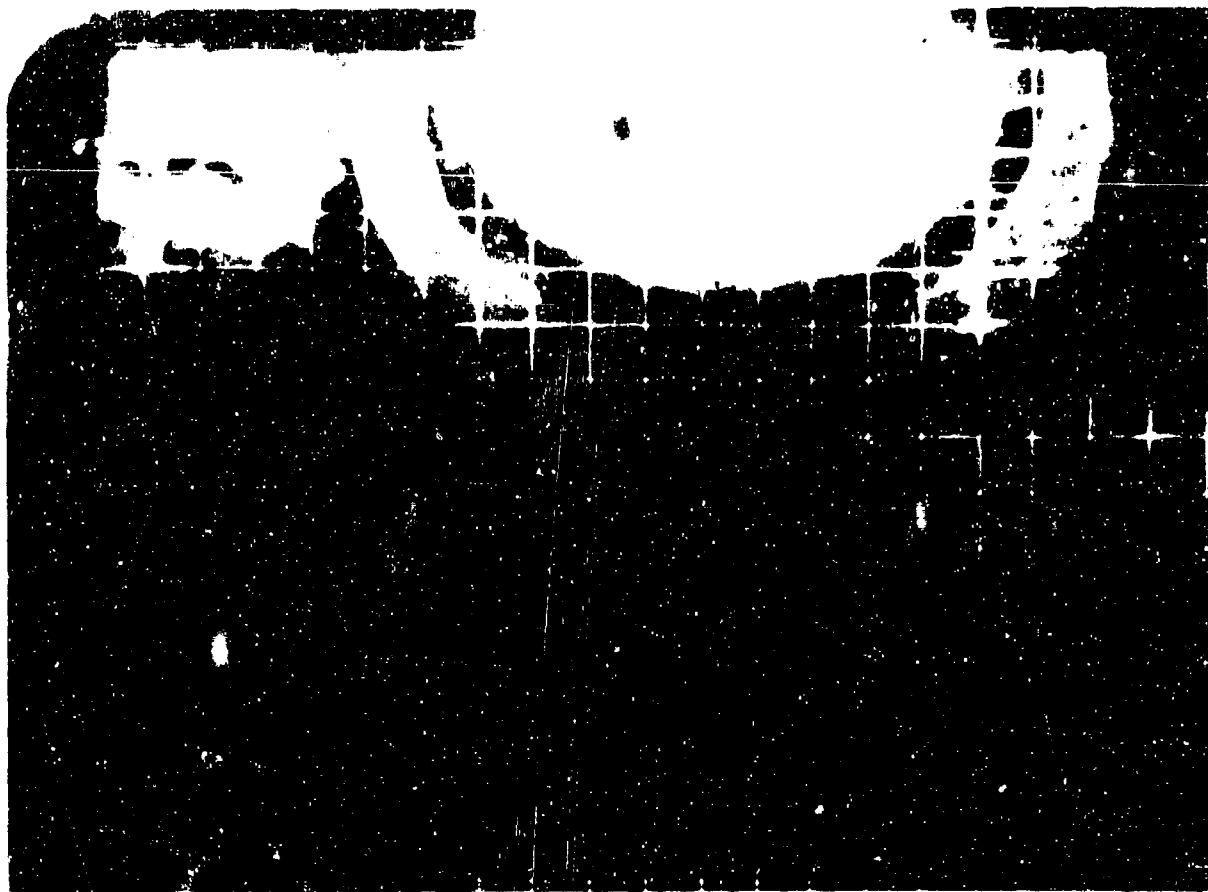


Figure A.229 Shot Dakota, Series 36250, Frame 39, Polaroid ϕ , f.l., 17 mm, B-66.



Figure A.230 Shot Dakota, Series 36250, Frame 64, Polaroid ϕ , f.l., 17 mm, B-66.

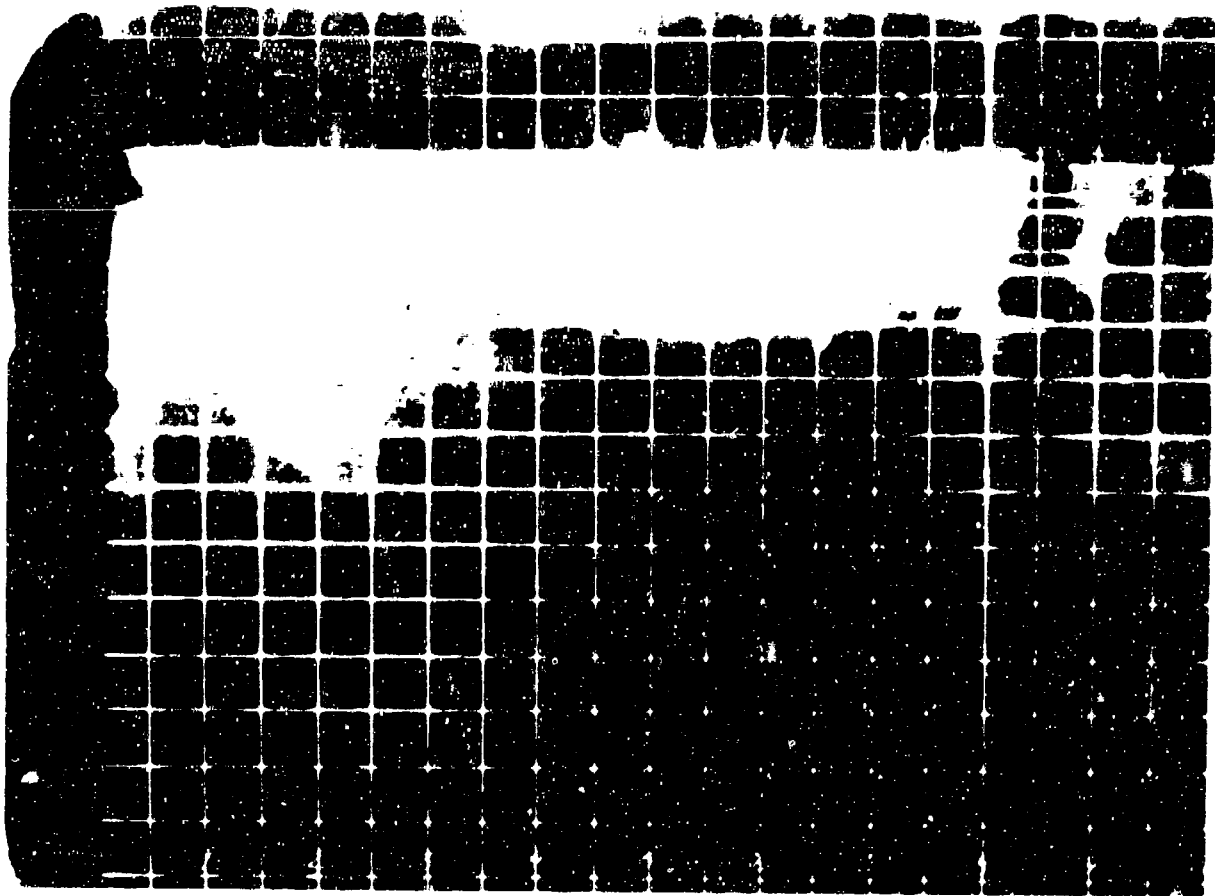


Figure A.231 Shot Dakota, Series 36250, Frame 89, Polaroid ϕ , f.l., 17 mm, B-66.

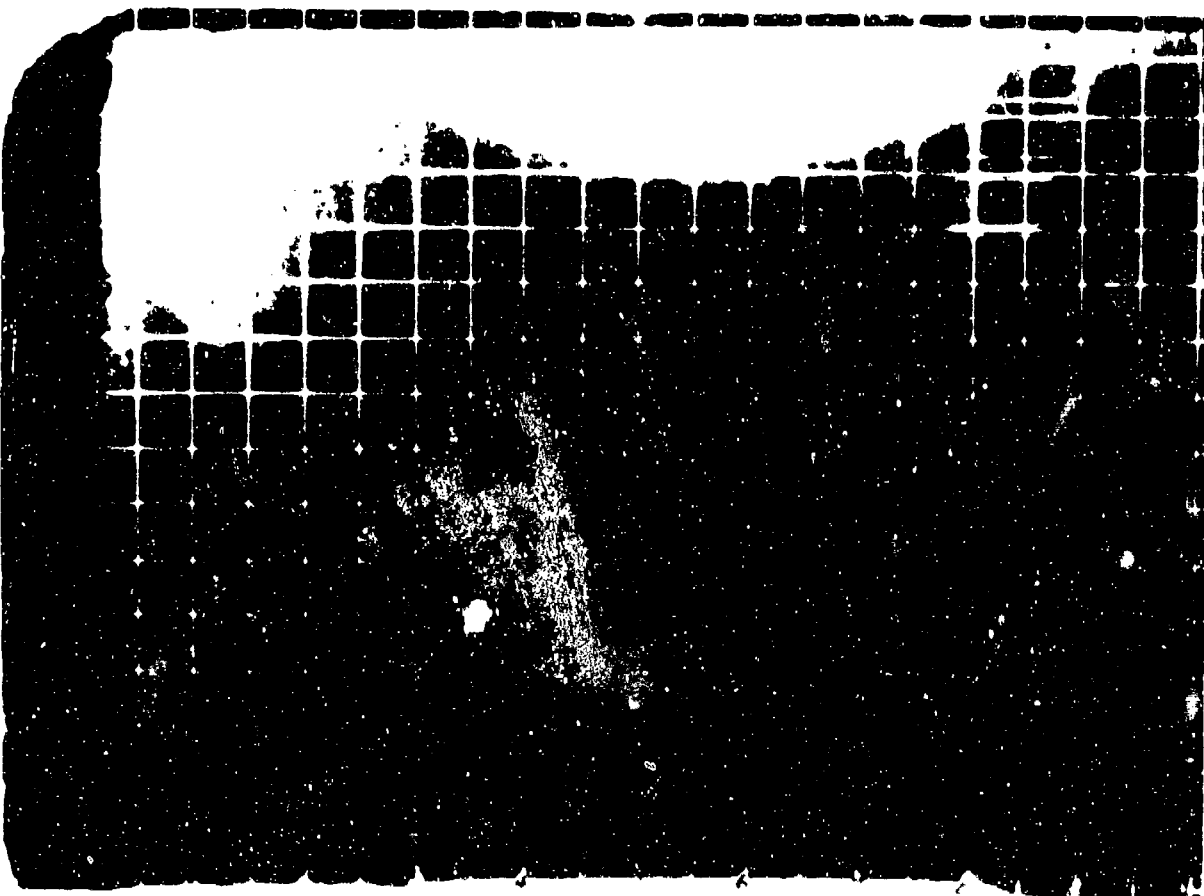


Figure A.232 Shot Dakota, Series 36250, Frame 114, Polaroid ϕ , f.l., 17 mm, B-66.

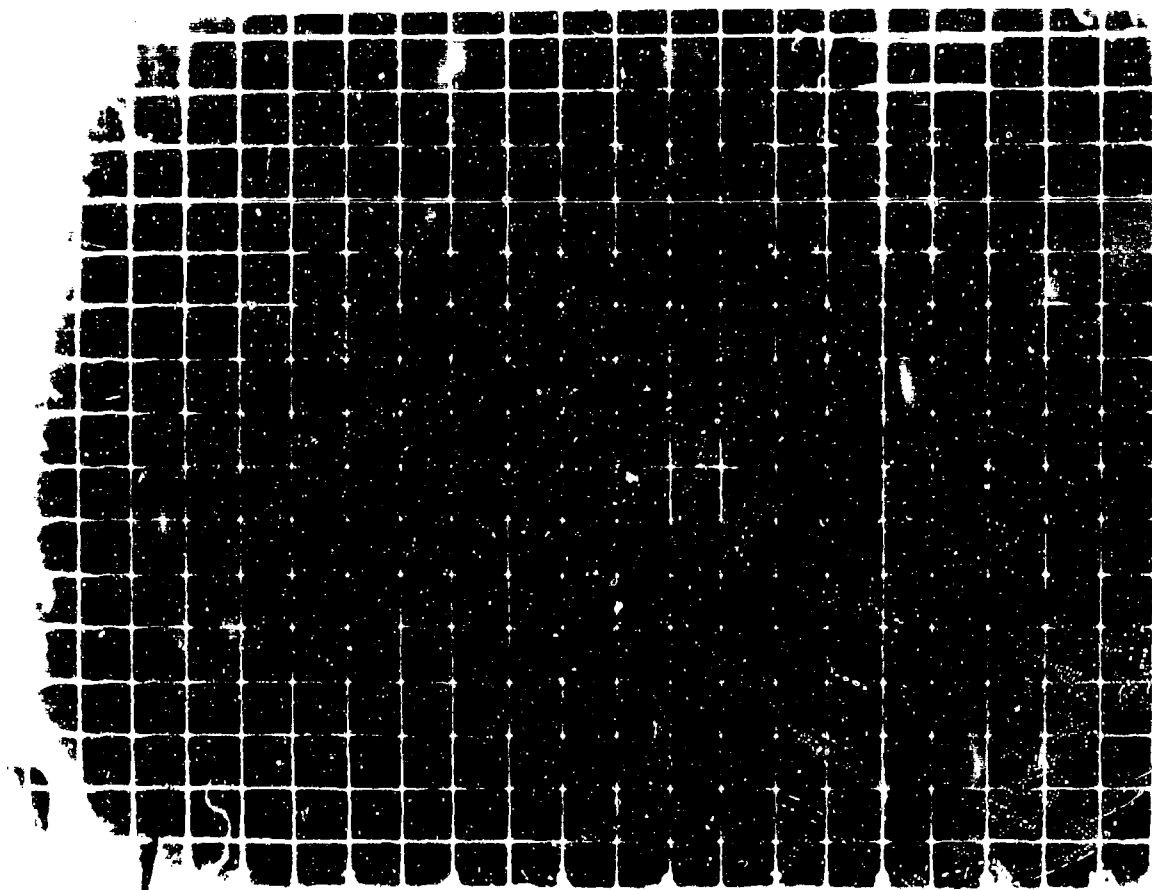


Figure A.233 Shot Dakota, Series 36299, Frame Zero, Blue, f.l., 17 mm, B-57.

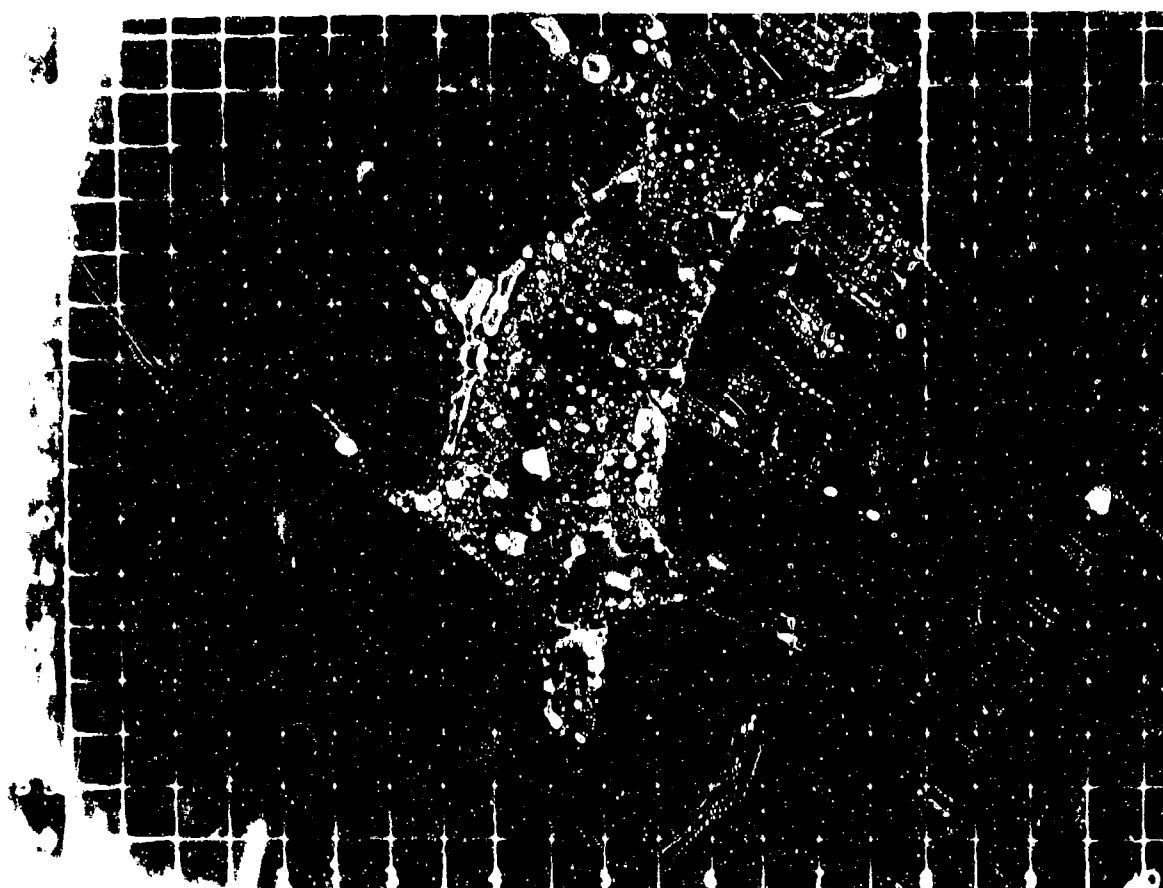


Figure A.234 Shot Dakota, Series 36299, Frame 1, Blue, f.l., 17 mm, B-57.

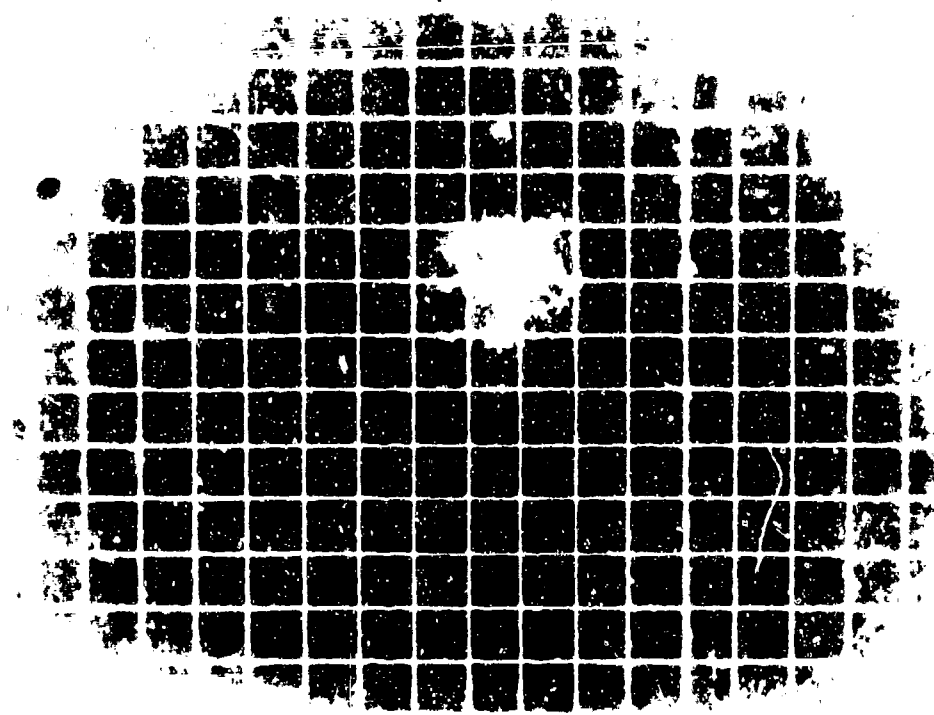


Figure A.235 Shot Dakota, Series 36299, Frame 20, Blue, f.1., 17 mm, B 57.

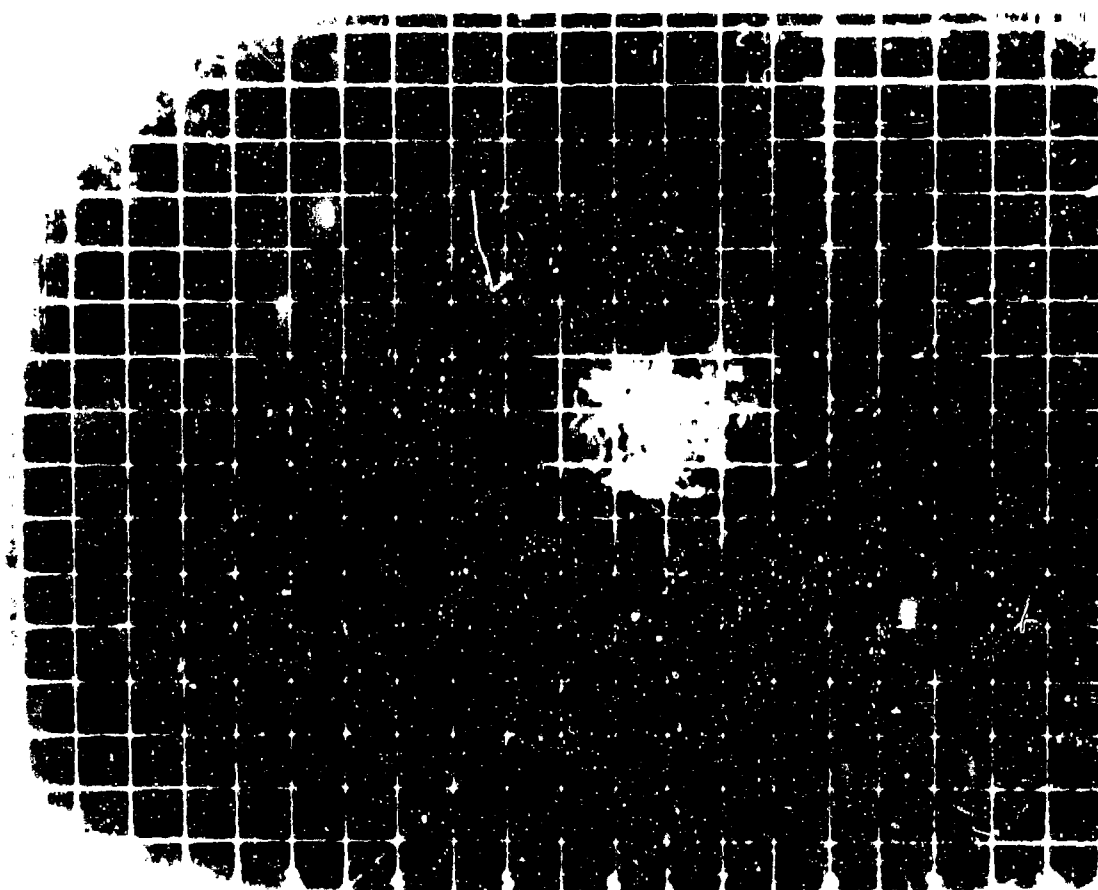


Figure A.236 Shot Dakota, Series 36299, Frame 30, Blue, f.1., 17 mm, B-57.

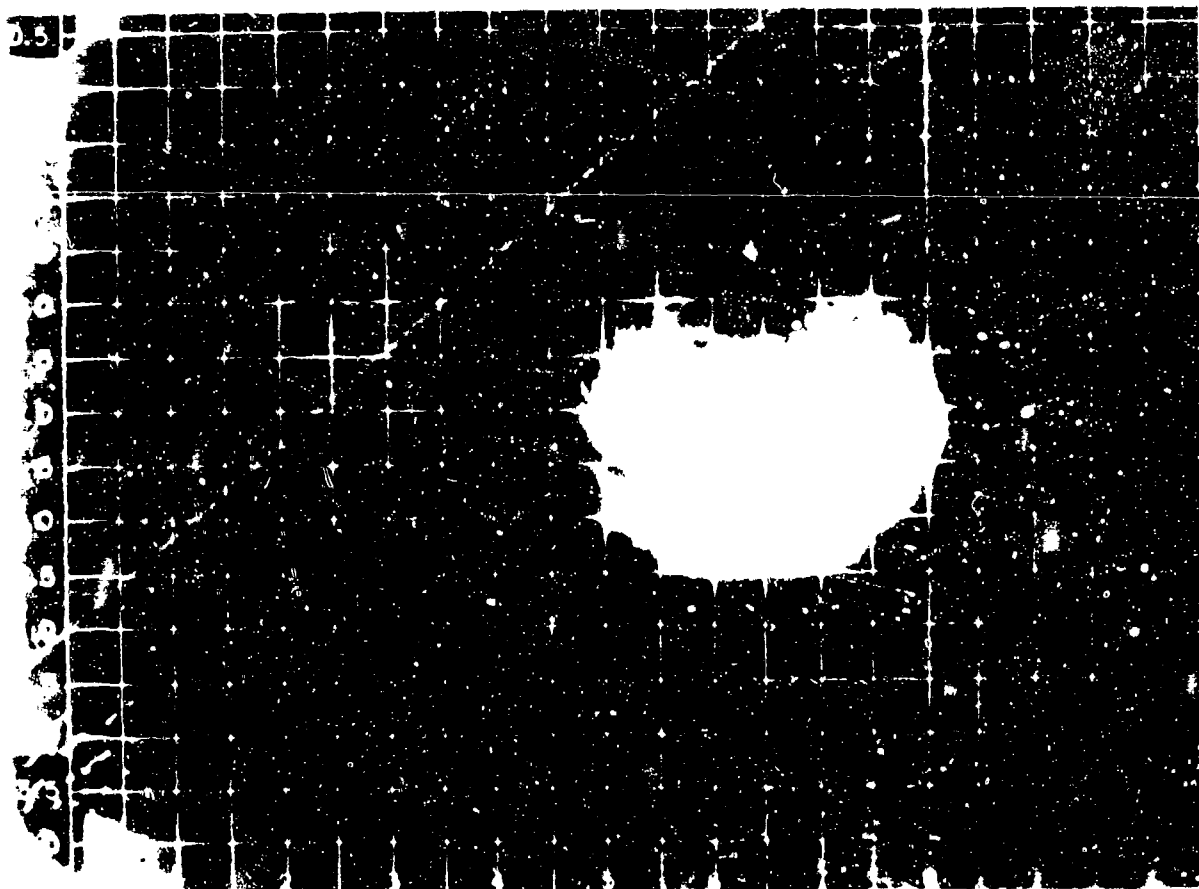
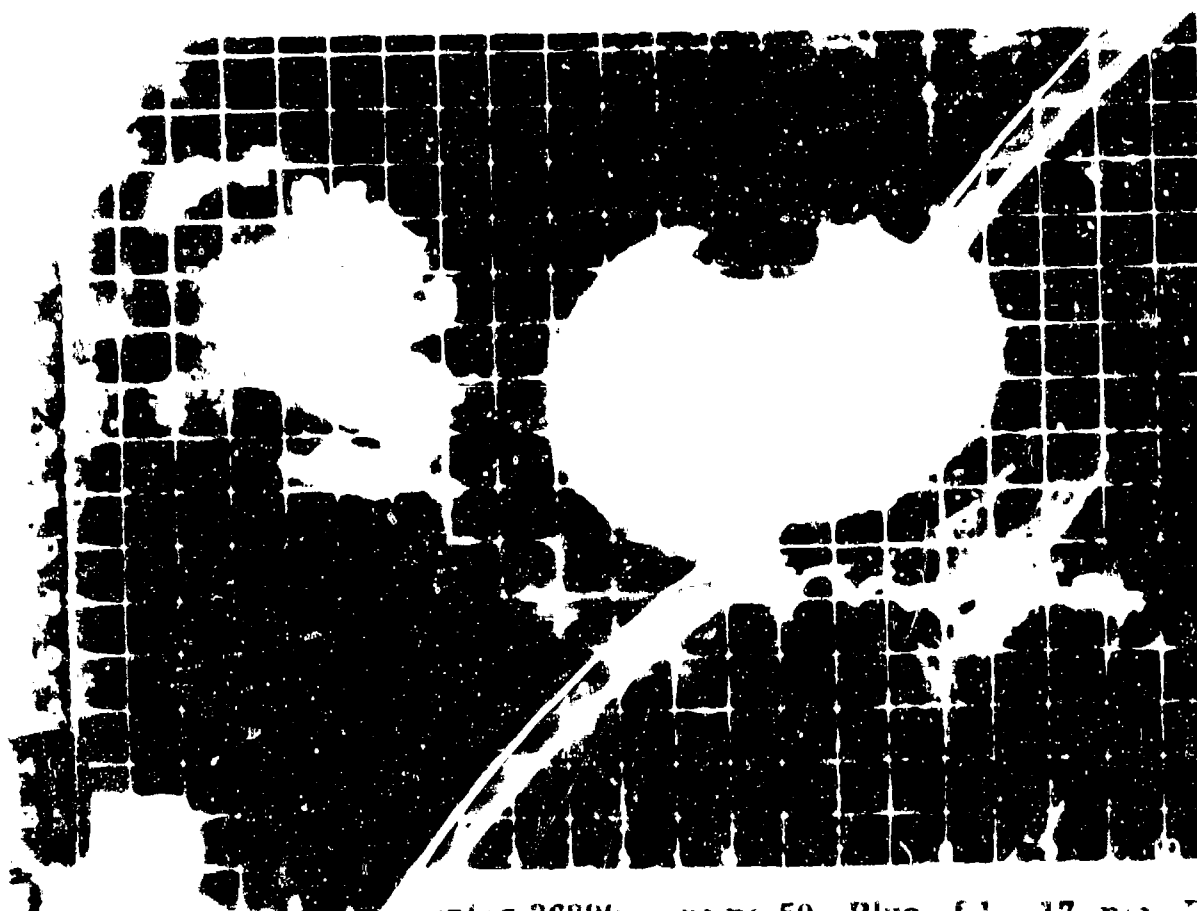


Figure A.237 Shot Dakota, Series 36299, Frame 40 Blue 1



Series 36299, Frame 50, Blue, f.l., 17 mm, B-67.

Figure A.238 Shot Dakota



Figure A.239 Shot Dakota, Series 36299, Frame 60, Blue, f.1., 17 mm, B-57.

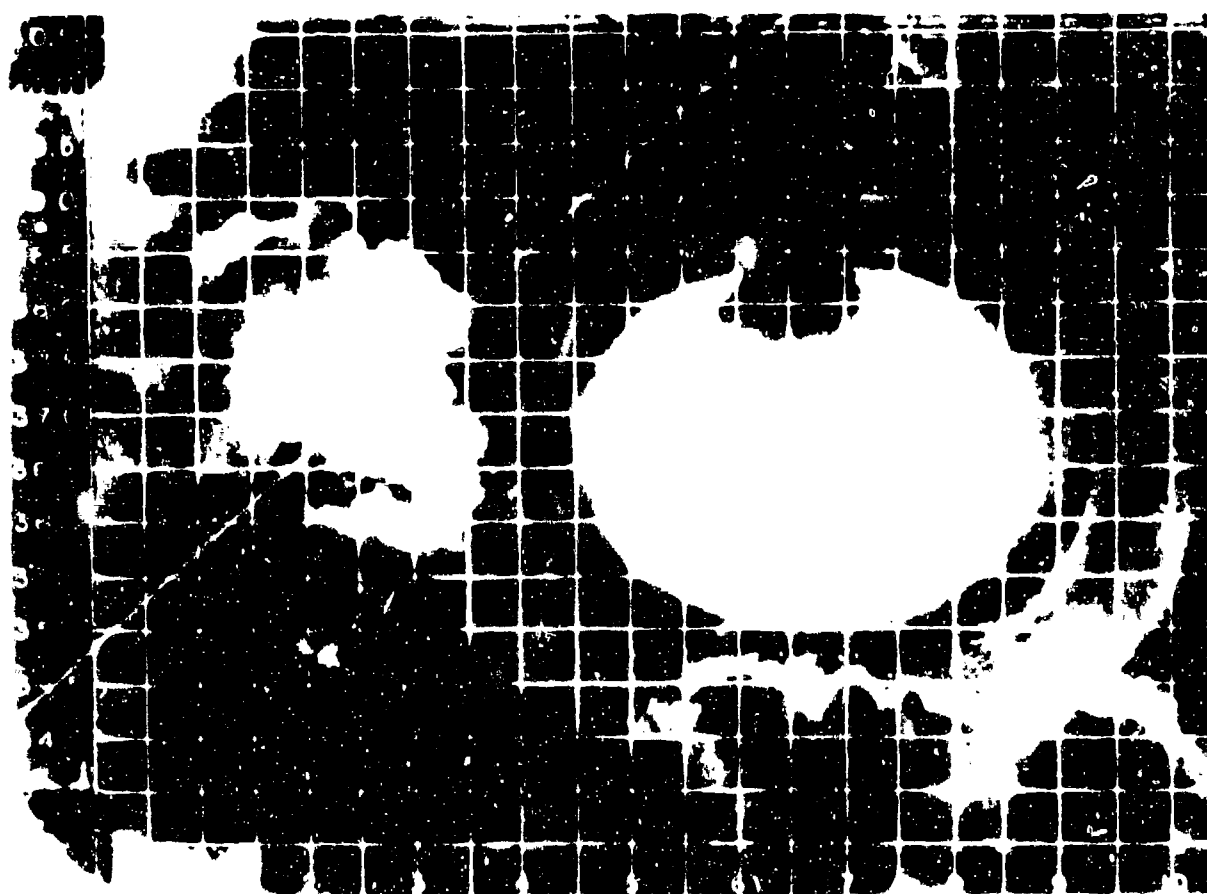


Figure A.240 Shot Dakota, Series 36299, Frame 63, Blue, f.1., 17 mm, B-57.

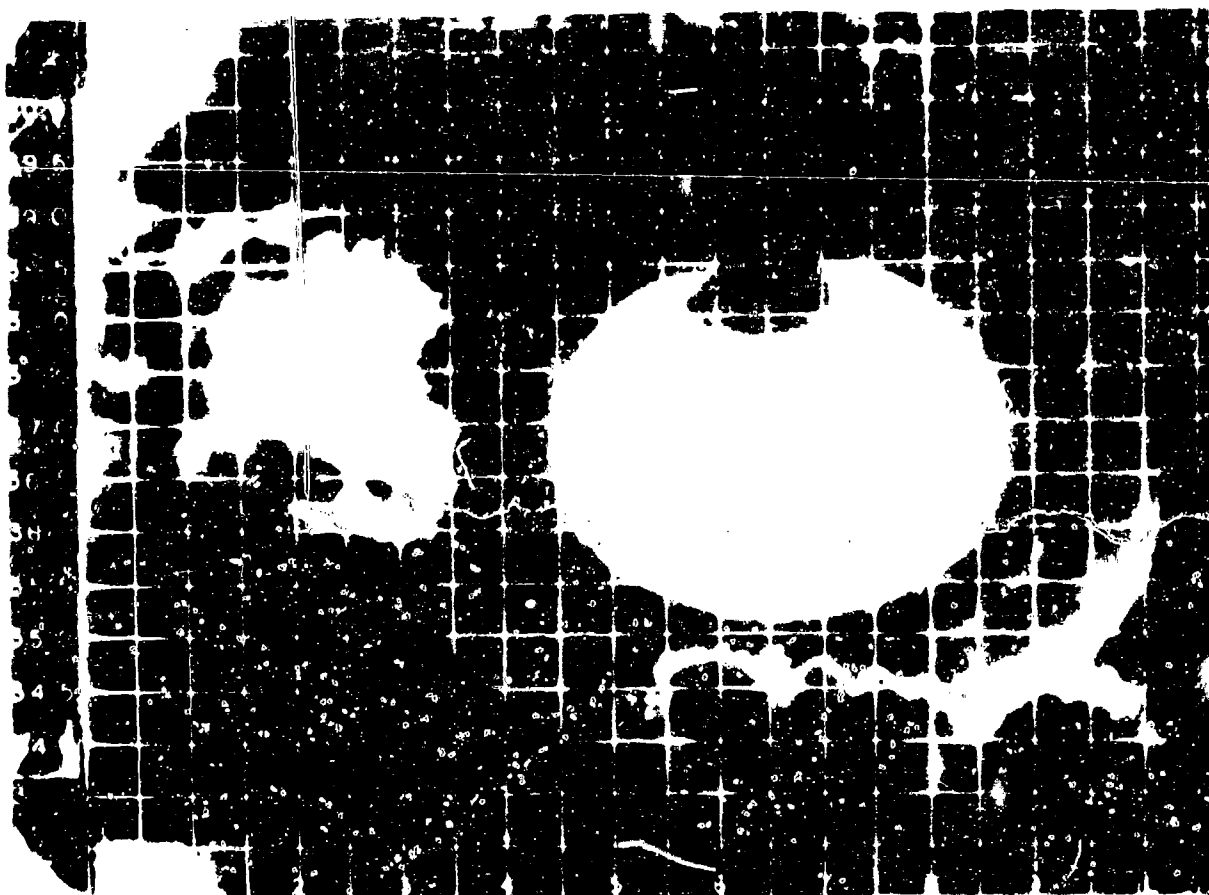


Figure A.241 Shot Dakota, Series 36299, Frame 65, Blue, f.l., 17 mm, B 57.

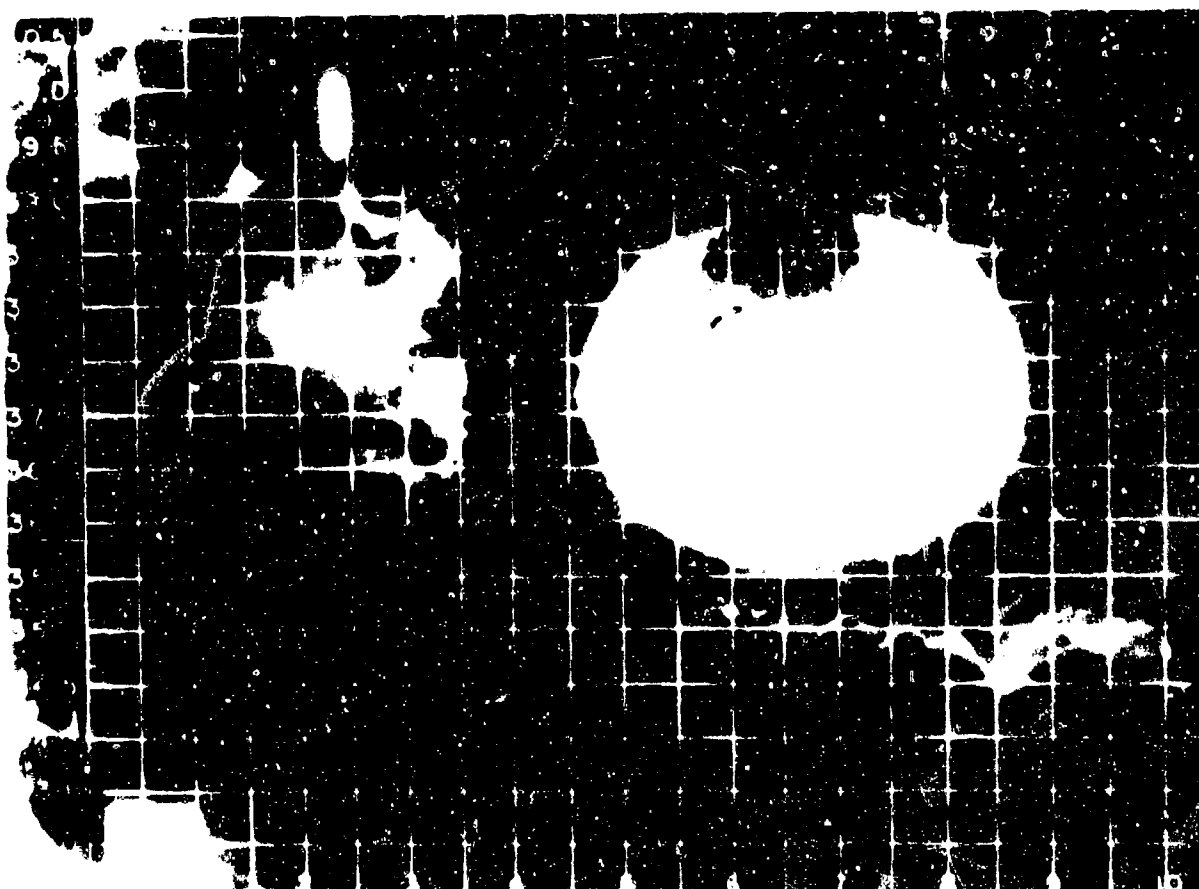


Figure A.242 Shot Dakota, Series 36299, Frame 70, Blue, f.l., 17 mm, B 57.

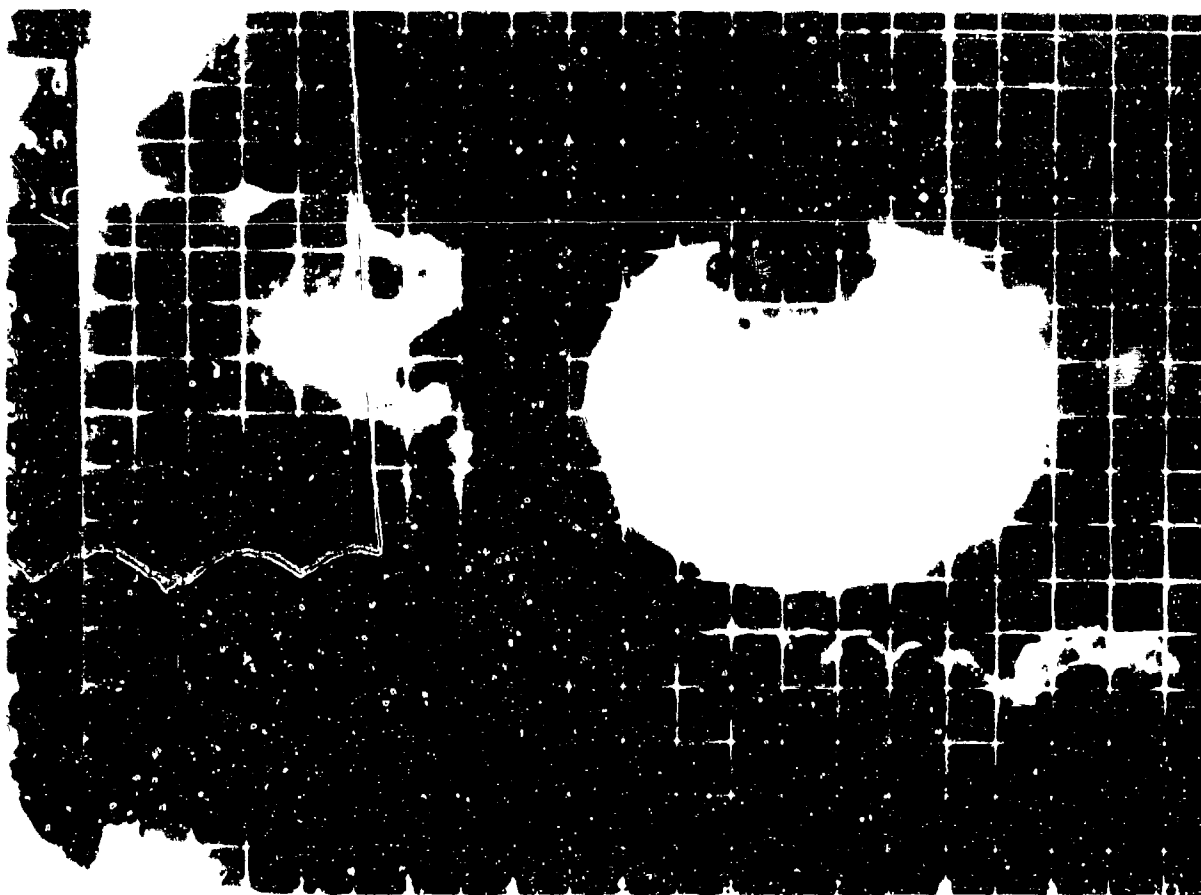


Figure A.243 Shot Dakota, Series 36299, Frame 80, Blue, f.l., 17 mm, B-57.

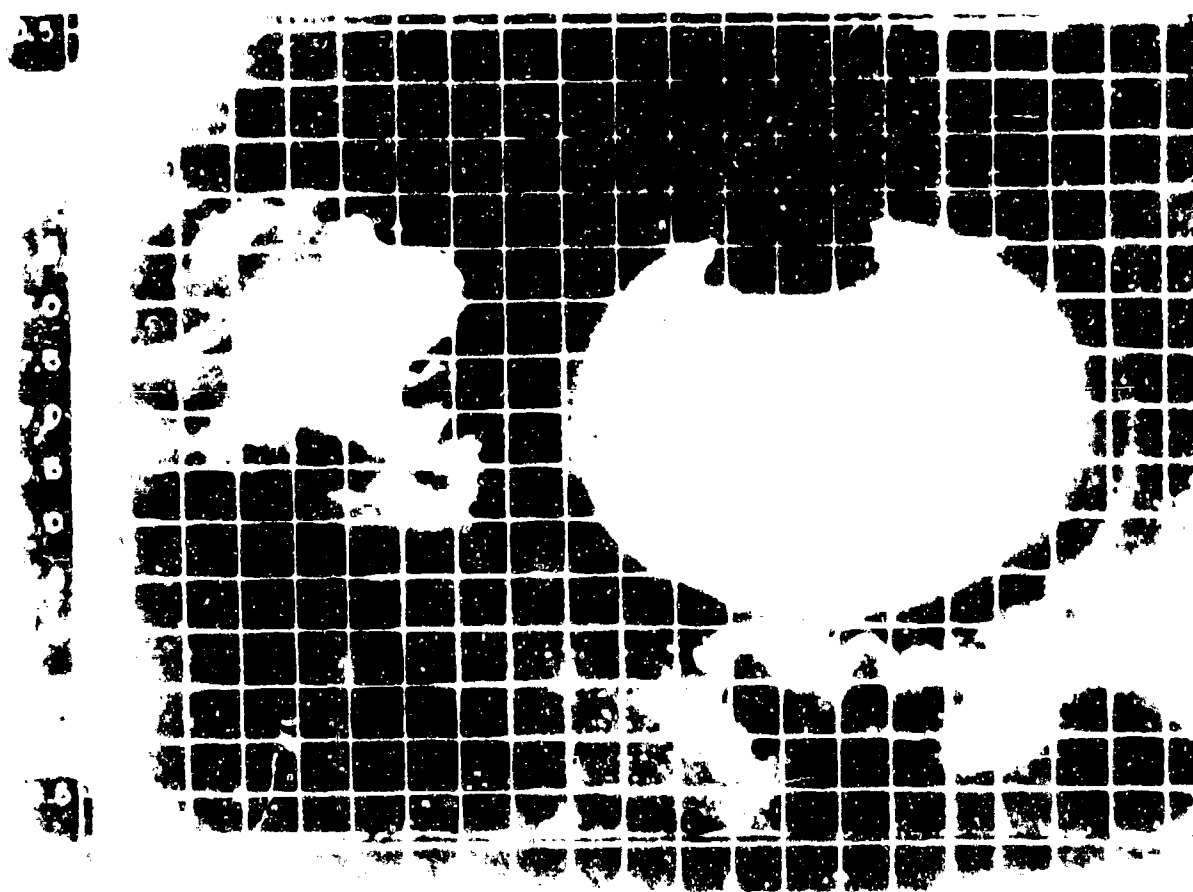


Figure A.244 Shot Dakota, Series 36299, Frame 90, Blue, f.l., 17 mm, B-57.

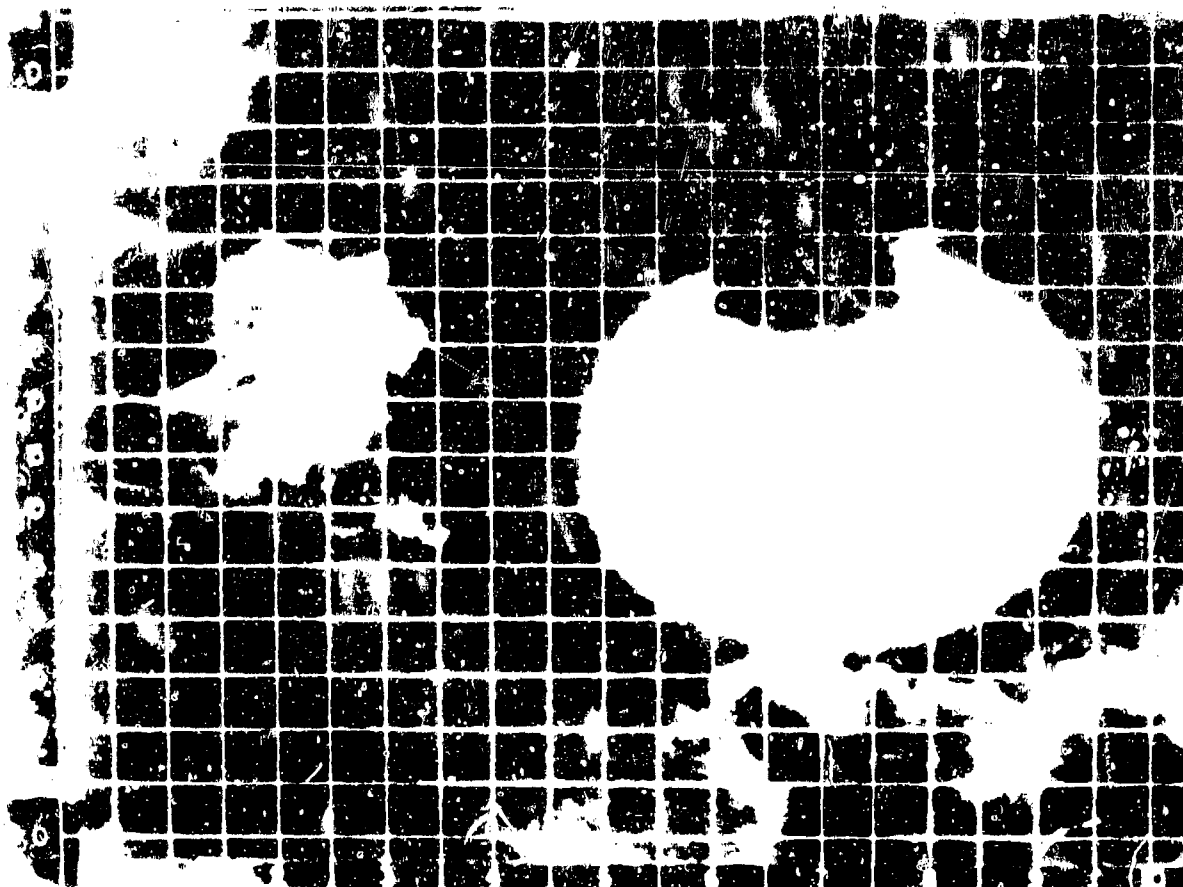


Figure A.245 Shot Dakota, Series 36299, Frame 115, Blue, f.l., 17 mm, B-57.

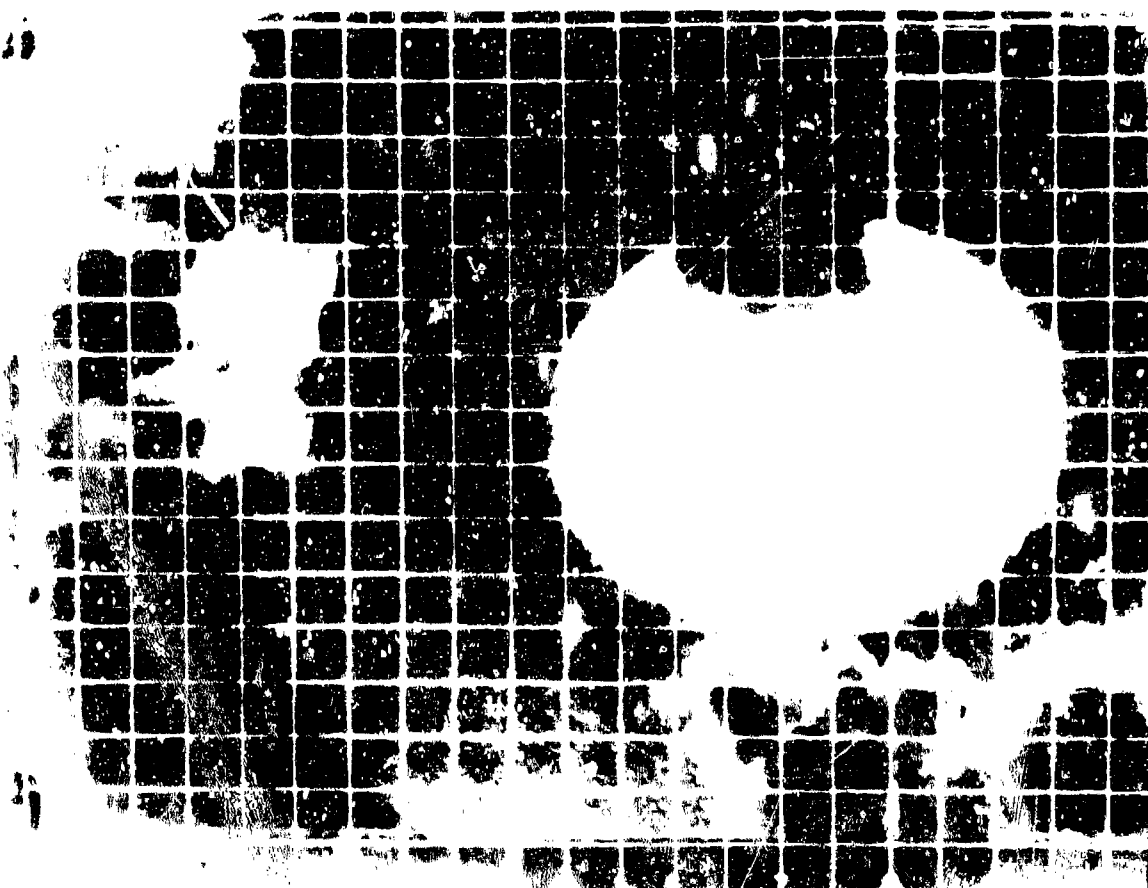


Figure A.246 Shot Dakota, Series 36299, Frame 130, Blue, f.l., 17 mm, B-57.



Figure A.247 Shot Dakota, Series 36299, Frame 150, Blue, f.1., 17 mm, B-57.

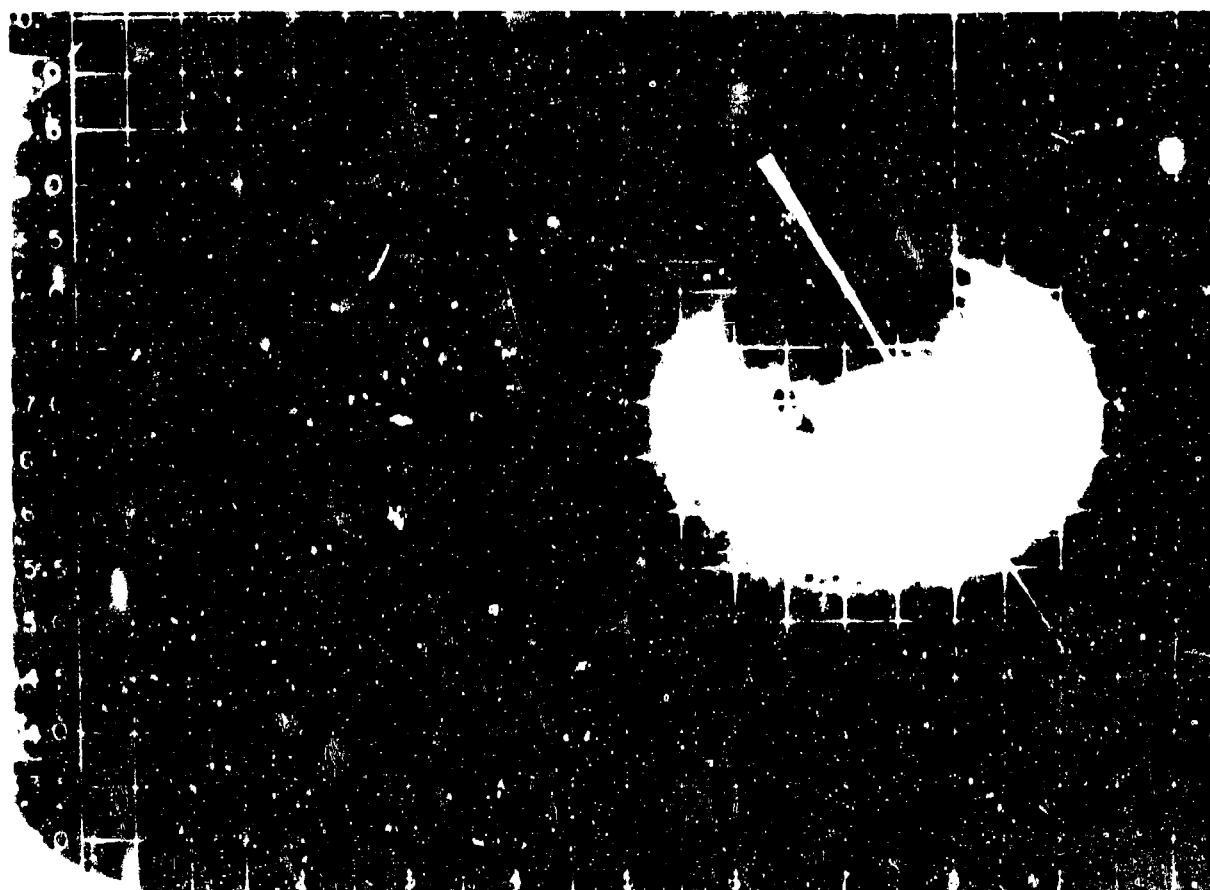


Figure A.248 Shot Dakota, Series 36299, Frame 170, Blue, f.1., 17 mm, B-57.

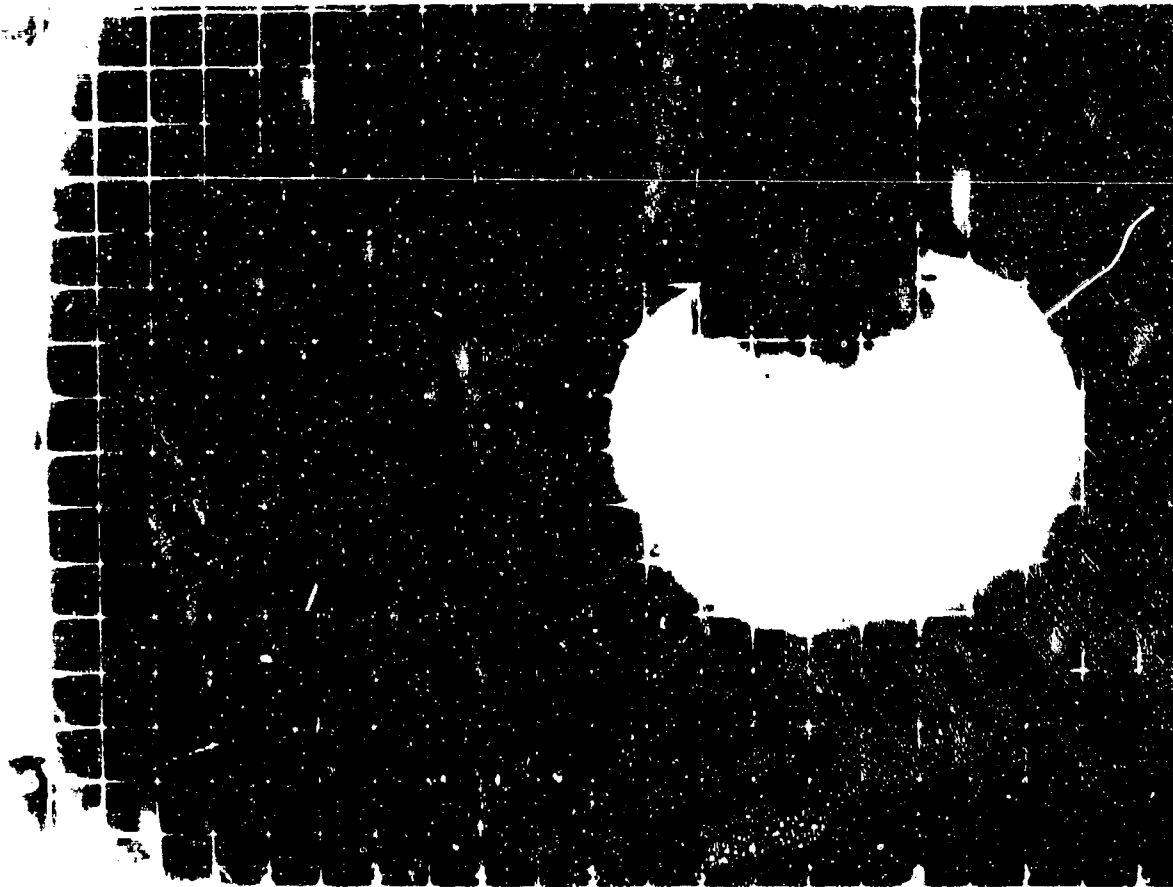


Figure A.249 Shot Dakota, Series 36299, Frame 190, Blue, f.l., 17 mm, B-57.

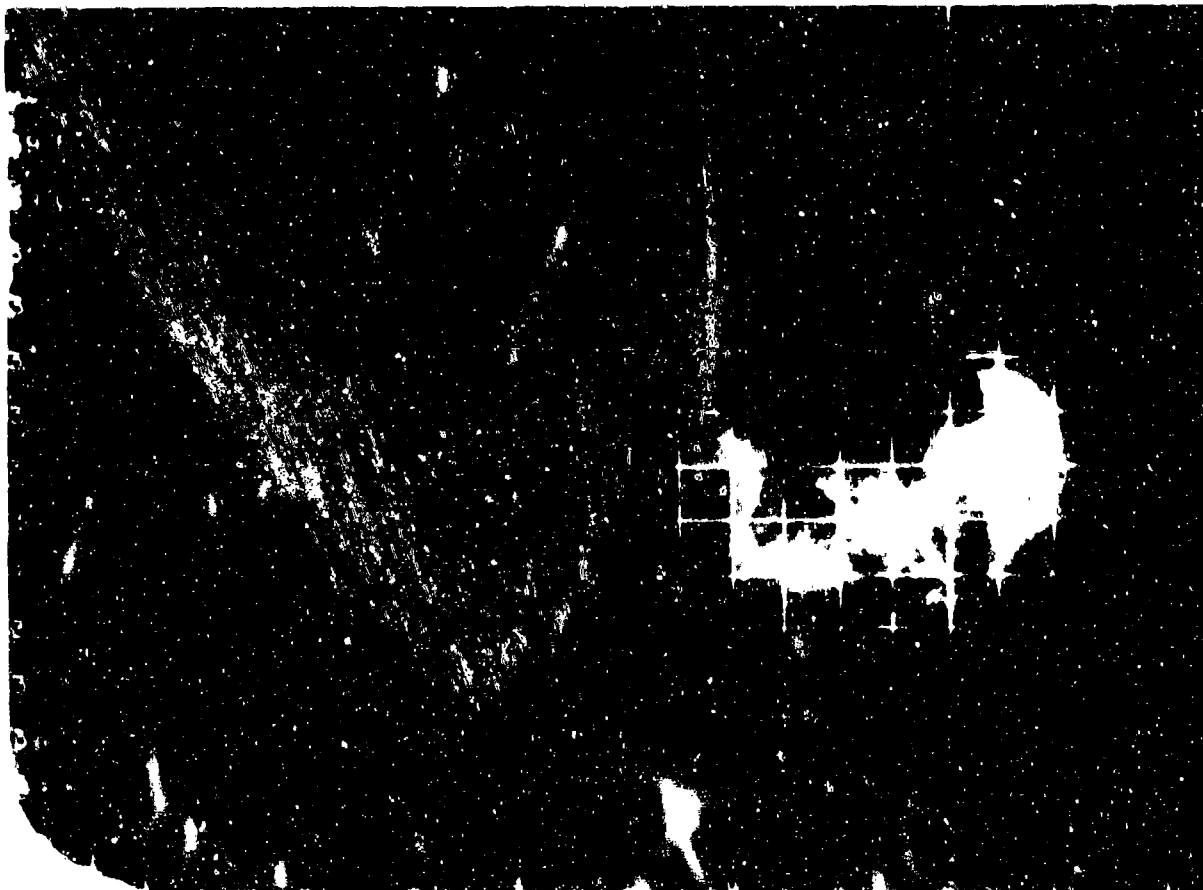


Figure A.250 Shot Dakota, Series 36299, Frame 225, Blue, f.l., 17 mm, B-57.

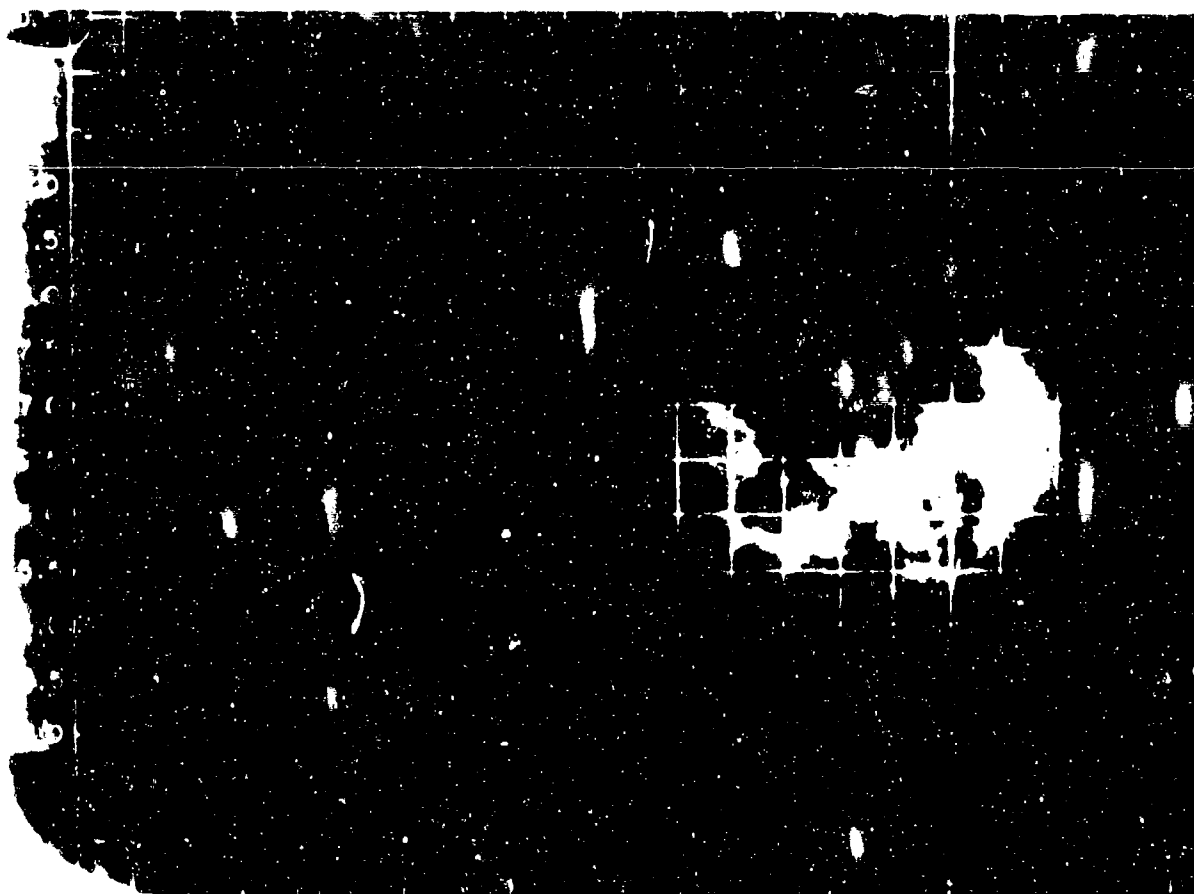


Figure A-251 Shot Dakota, Series 36299, Frame 275, Blue, f.l., 17 mm, B-57.

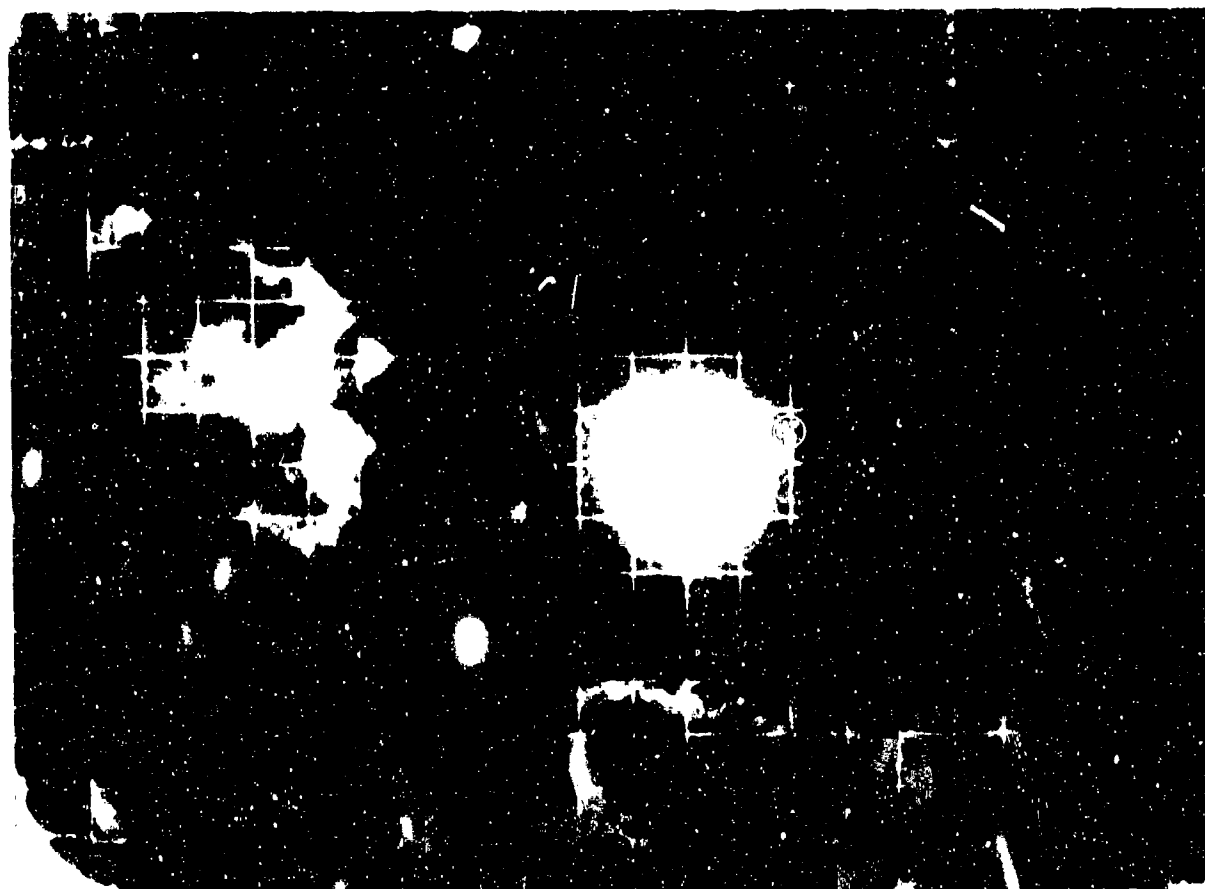


Figure A-252 Shot Dakota, Series 36300, Frame Zero, Red, f.l., 17 mm, B-57.

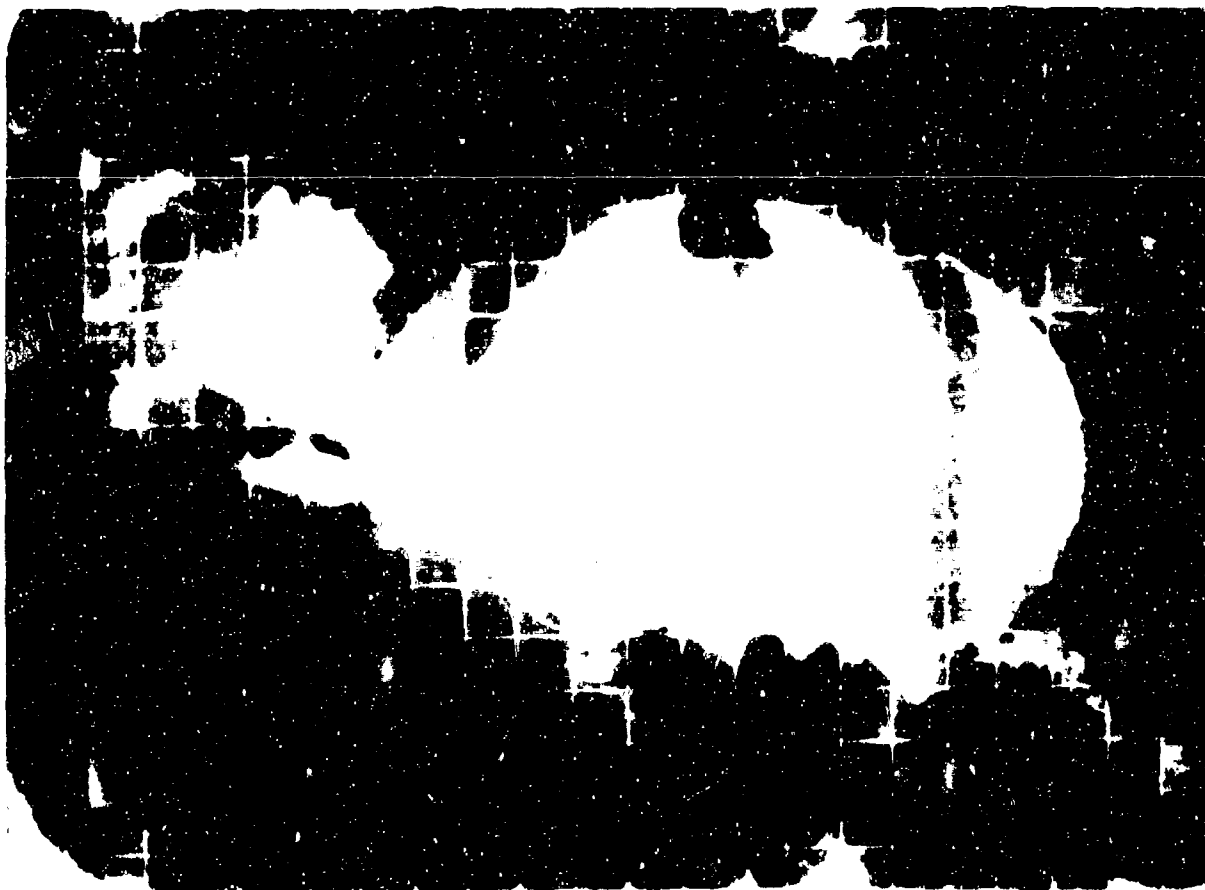


Figure A.253 Shot Dakota, Series 36300, Frame 57, Red, f.l., 17 mm, B-57.



Figure A.254 Shot Dakota, Series 36300, Frame 67, Red, f.l., 17 mm, B-57.

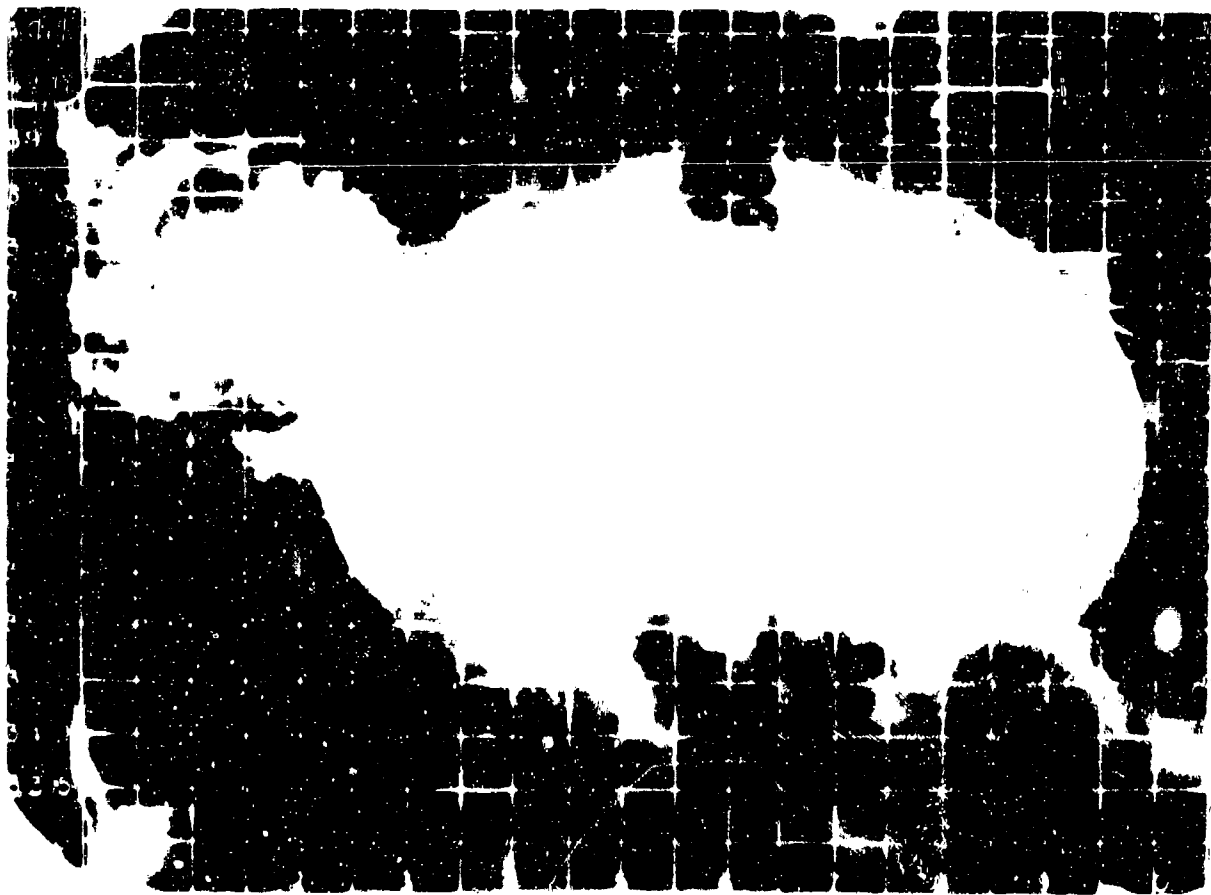


Figure A.255 Shot Dakota, Series 36300, Frame 77, Red, f.l., 17 mm, B-57.



Figure A.256 Shot Dakota, Series 36300, Frame 87, Red, f.l., 17 mm, B-57.

305 - 306

SECRET



Defense Threat Reduction Agency

45045 Aviation Drive
Dulles, VA 20166-7517

Rec'd 11/8/2000

CPWPT

October 11, 2000

MEMORANDUM TO THE DEFENSE TECHNICAL INFORMATION CENTER
ATTN: OCQ

SUBJECT: DOCUMENT UPDATES

The Defense Threat Reduction Agency Security Office has performed a classification review of the following two documents. The documents classification has been changed and the distribution statements added to read as stated below:

WT-1333, AD-361768, UNCLASSIFIED, STATEMENT A, Operational Redwing, Project 5.7, Thermal Flux and Albedo Measurements from Aircraft.

WT-1334, AD-339910, UNCLASSIFIED, STATEMENT A, Operation Redwing, Project 5.8, Evaluation of the A3D1 Aircraft for Special Weapons Delivery Capability.

If you have any questions, please call me at 703-325-1034.

Arldith Jarrett

ARDITH JARRETT
Chief, Technical Resource Center



DEFENSE THREAT REDUCTION AGENCY
Defense Threat Reduction Information Analysis Center (DTRIAC)
1680 TEXAS STREET SE
KIRTLAND AFB, NM 87117-5669

14 April 2004

BDQ (505) 846-0847

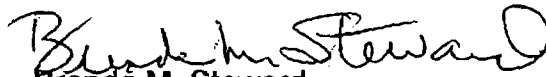
To: Larry Downing, DTIC

Subject: Re-Review of DNA reports

Here is the sixth increment of the results of the re-review project:

See Attached List

We will send more as they are reviewed.


Brenda M. Steward
COTR,
Defense Threat Reduction Information
Analysis Center (DTRIAC)

| REPORT NO. | AD NO. | CLASS | DISTRIBUTION |
|----------------------|---------|-------------|---------------------------|
| DASA 1254 | 333113 | Unc. | C, Software Documentation |
| DASA 1420 Chapter 7 | C020626 | Unc. | C, Admin - Operational |
| DASA 1420 Chapter 11 | C020628 | Unc. | C, Admin - Operational |
| DASA 1958 | 383870 | Unc. | C, Test and Evaluation |
| DNA 2808 | 519841 | Unc. | C, Test and Evaluation |
| DNA 3014F | 524387 | Unc. | C, Test and Evaluation |
| DNA 3070F | 526432 | Unc. | C, Test and Evaluation |
| DNA 3273F | 529507 | Unc. | C, Test and Evaluation |
| DNA 3315F | 530559 | Unc. | C, Test and Evaluation |
| POR 6723 | 531141 | SFRD | |
| WT 1333 | 361768 | Unc. | A |
| WT 1334 | 339910 | Unc. | A |